Agronomy Research

Established in 2003 by the Faculty of Agronomy, Estonian Agricultural University

Aims and Scope:

Agronomy Research is a peer-reviewed international Journal intended for publication of broad-spectrum original articles, reviews and short communications on actual problems of modern biosystems engineering incl. crop and animal science, genetics, economics, farm- and production engineering, environmental aspects, agro-ecology, renewable energy and bioenergy etc. in the temperate regions of the world.

Copyright:

Agronomy Research online:

Agronomy Research is available online at: http://agronomy.emu.ee/

Acknowledgement to Referees:

The Editors of *Agronomy Research* would like to thank the many scientists who gave so generously of their time and expertise to referee papers submitted to the Journal.

Abstracted and indexed:

SCOPUS, EBSCO, CABI Full Paper and Thompson Scientific database: (Zoological Records, Biological Abstracts and Biosis Previews, AGRIS, ISPI, CAB Abstracts, AGRICOLA (NAL; USA), VINITI, INIST-PASCAL.)

Subscription information:

Institute of Technology, EULS
St. Kreutzwaldi 56, 51014 Tartu, ESTONIA
E-mail: timo.kikas@emu.ee

Journal Policies:

Estonian University of Life Sciences, Estonian Research Institute of Agriculture, Latvia University of Agriculture, Aleksandras Stulginskis University, Lithuanian Institute of Agriculture and Lithuanian Institute of Horticulture and Editors of *Agronomy Research* assume no responsibility for views, statements and opinions expressed by contributors. Any reference to a pesticide, fertiliser, cultivar or other commercial or proprietary product does not constitute a recommendation or an endorsement of its use by the author(s), their institution or any person connected with preparation, publication or distribution of this Journal.

ISSN 1406-894X

CONTENTS

Agronomy Research **15**(S1), 941–951, 2017

Mechanical behaviour of selected bulk oilseeds under compression loading

O.L. Akangbe and D. Herak*

Czech University of Life Sciences, Faculty of Engineering, Department of Mechanical Engineering, Kamycka 129, Praha 6 – Suchdol, CZ16521 Prague, Czech Republic
*Correspondence: herak@tf.czu.cz

Abstract. Cold pressing or compressive mechanical expression of oil from bulk oilseeds without thermal treatments or appreciable thermal effects facilitates the preservation of quality in expressed oils and enhances their stability in storage. Mechanical response of bulk oilseeds during cold expression which are vital to equipment design vary with crops and are not completely understood. Mechanical behaviours of bulk seeds of camelina, pumpkin and sesame relevant to cold pressing were investigated at moisture contents of 7.04, 8.60 and 6.06% (d.b.), 80 mm pressing depth and a compressive force of 100 kN, applied uniformly at 10 mm min^{-1}. Deformation varied with incremental force and among crops at peak compression. Deformations in Camelina, Sesame and Pumpkin seeds were 40.2, 41.6 and 50.9 mm at peak compression. Oil point pressures of Sesame, Camelina and Pumpkin seeds were 3.83, 7.49 and 8.83 MPa, respectively. Oil recovery at the applied load was similar in Camelina and Sesame but significantly lower in pumpkin seeds. Volume energy requirement for the expression of oil from camelina, pumpkin and sesame seeds were 2.56, 1.72 and 1.46 MJ m^{-3}, respectively. An assessment of the pressed cake after oil expression revealed that the materials were capable of further deformation under compression.

Key words: oilseed, cold pressing, compressive stress, strain, energy.

INTRODUCTION

The main object of cold pressing of oilseeds is extracting oil at temperatures that guarantee the quality of the extracted oil (Kachel-Jakubowska et al., 2015; Ratusz et al., 2016). In large scale screw presses, process temperatures often reach 170 °C at 1,600 bars (Matthäus, 2012). Cold pressed oils are obtained at temperatures below 40 °C (Makała, 2015). Although considerable solvent–free expression is achieved with screw presses (Maurice, 2005), substantial quantities of residual oil are removed using supplemental techniques including solvent, super–critical fluids and temperature assisted processes and optimisation involves establishing combinations of geometrical, process and flow factors at which oil yields are high and quality as indicated by known process parameters is maintained (Voges et al., 2008; Willems et al., 2008; Honarvar et al., 2013). Hydraulic pressing refers to the mechanical expression of oil from bulk sections of oilseeds using compressive force (Mrema & McNulty, 1985; Owolarafe et al., 2008) and seldom involves significant changes in temperature of the pressed material, guaranteeing high oil quality (FAO/WHO, 2015a; 2015b). Different attempts

have been made to describe the mechanism of expression of oil from oilseeds using compressive force (Bargale, 1997; Bargale et al., 2000; Savoire et al., 2013). This process has been shown to be a function of several influence factors, including initial produce depths (Herák et al., 2013; Kabutey et al., 2013), moisture and temperature (Santoso & Inggrid, 2014; Kachel-Jakubowska et al., 2015), compressive force (Kabutey et al., 2014) and the rate of its application (Bargale et al., 2000; Santoso & Inggrid, 2014) and size or diameter of the constraining vessel (Kabutey et al., 2013; Owolarafe et al., 2007). Oil pressing indices of interest have also been shown to vary significantly across crop types and varietal lines (Herák et al., 2012; Rusinek et al., 2012). The main indicators of interest during compressive expression of oil from oilseeds have been oil points, oil yield, deformation and deformation energy (Faborode & Favier, 1996; Bargale et al., 2000; Kabutey et al., 2014). Deformation of bulk oilseed sections under compressive force has been described to occur in three phases (Mrema & McNulty, 1985; Faborode & Favier, 1996; Owolarafe et al., 2008). The reciprocal slope transform has been shown to be useful in describing only the initial phase during which reorganisation of seeds and settling–in occurs (Herák et al., 2014). Deformation behaviours in some crops have been described using the tangent–curve descriptor (Herák & Kabutey, 2014). The tangent curve relation provided fitting description of the reported process parameters up to some limit points (Divišová et al., 2014; Sigalingging et al., 2015) beyond which erratic behaviours or serration effects along the force–deformation profiles of different crops were established (Divišová et al., 2014; Kabutey et al., 2014). The limit point in question appears to be the bioyield point and this was not attained in some crops (Herák et al., 2012) with high strain resistance, at the applied force and pressing conditions. The behaviours reported in literature also varied significantly across oilseed crops.

Camelina, sesame and pumpkin seeds are emerging oilseed crops whose oils have received attention with regard to their qualities and potentials as food, biofuel and health oils (Tunde-Akintunde & Akintunde, 2004; Fruhwirth & Hermetter, 2007; Berti et al., 2016). In this study, the behaviours of these important oilseeds under compressive force were investigated and parameters essential to the expression of oil from them were determined.

MATERIALS AND METHODS

Samples

Whole and cleaned seeds of camelina (*Camelina sativa* (L.) Crantz), pumpkin (*Cucurbita pepo* L.) and sesame (*Sesamum indicum* L.) purchased in Czech Republic were used for this study.

Experimental setup and tests

A schematic view of the oil expression apparatus is shown in Fig. 1. It consisted of an 80 mm internal bore cylindrical steel pressing vessel with a 20 mm thick circular base plate stepped inwards diametrically at 10mm depth, 8mm from its circumference and 10 lateral orifices (ϕ3 mm) equispaced along the circumference of the pressing vessel, 15 mm from its base. The vessel had a close fitting solid piston, stepped 1mm, 30 mm from its base. The vessel is mounted on the bed of a Tempos ZDM 50 model test universal test rig and loaded compressively using a spherical base, flat topped disc. Bulk

columns of camelina, sesame and pumpkin seeds at 7.04, 8.60 and 6.06% moisture contents (d.b.), respectively, each 80mm deep and constrained within the pressing vessel were gradually compressed at 10 mm min-1 to a maximum force of 100 kN under laboratory condition of 20 °C. Each test was repeated three times. The experiment was considered as a completely randomised design. Test data were electronically logged using the Mark Mitchell Engauge Digitizer software (Version 4.1, 2002). Moisture measurements were conducted using the oven drying method as described in the ASAE standards S352.2 for moisture determination in unground grains and seeds. Each 15 g sample was oven dried in a Gallenkamp Memmert type hot air oven at 103 ± 2 °C. The masses of the samples used in the course of this study were weighed using the Kern 440–35N (Kern & Sohn GmbH, Stuttgart, Germany) weighing balance. The capacity of the standard calibrated cylinder used for initial bulk density measurement was 230 mm^3.

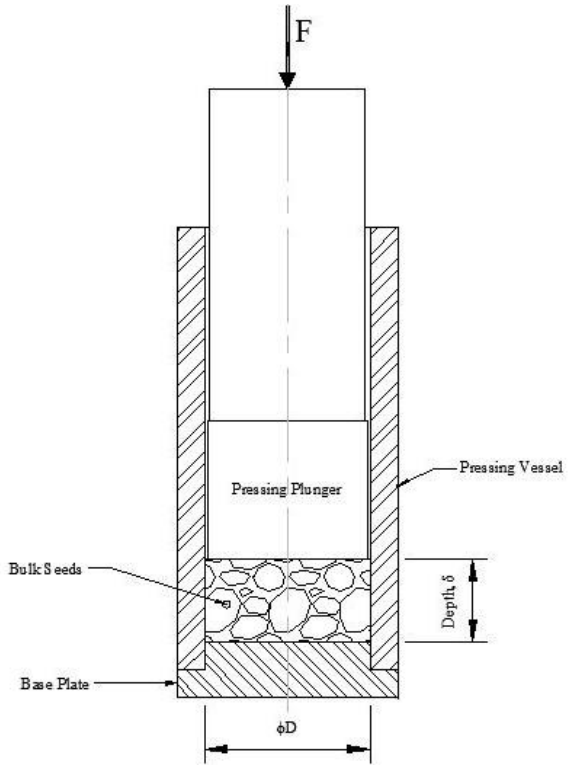

Figure 1. Schematic view of the oil expression apparatus.

Evaluation of properties of oilseeds and compression parameters

The porosity, P_f (%) of each batch of crop was calculated using the relationship given below (Eq. 1) (Mohensin, 1970; Sirisomboon et al., 2007):

$$P_f = \left(1 - \frac{\rho_b}{\rho_t}\right) \times 100 \quad (1)$$

where ρ_b (kg m^{-3}) and ρ_t (kg m^{-3}) are the bulk and true densities of each crop, respectively. Bulk densities of oilseeds prior to expression were determined as the ratio of the mass of a sample to the known free–fill volume it occupies without compaction,

as outlined in literature (Mohensin, 1970; Sirisomboon et al., 2007; Arozarena et al., 2012). True densities were determined using a solvent displacement technique – the method of the pycnometer and toluene, as described by Mohsenin (1970). True densities were computed (Eq. 2) as:

$$\gamma_s = \left(\gamma_T \times \frac{m_s}{m_{TD}}\right) \tag{2}$$

γ_S and γ_T are specific gravities of the crop and of the batch of toluene used while m_S and m_{TD} are masses of the sample and of the displaced quantity of toluene, respectively.

The highest value of deformation which was achieved for each crop at any given load was defined as δ_c (mm). Where δ_o (mm) is the initial height of pressed bulk seeds, the strain in the compressed material ϵ_l (–) is given by Eq. 3

$$\in_l = \frac{\delta_c}{\delta_o} \tag{3}$$

The initial volume of compressed material, V (mm^3) is given by Eq. 4

$$V = \frac{\pi \times D^2}{4} \times \delta_o \tag{4}$$

where, D (mm) is the inside diameter of the constraining cylindrical steel vessel.

Bulk density of the compressed oilseed material, ρ_{bc} (kg m^{-3}) after oil expression was determined as a function of the mass (m_c) and volume (V_c) of the final product volume following compression (Eq. 5)

$$\rho_{bc} = \frac{m_c}{V_c} \tag{5}$$

The final volume of the compressed material, V_c (mm^3) is given by Eq. 6

$$V_c = \frac{\pi \times D^2}{4} \times \delta_f \tag{6}$$

where, δ_f (mm) is the final height of the compressed oilseeds in the constraining. Oil yield, OY (%) was determined as a function of the ratio of expressed oil to the total seed mass (Eq. 7)

$$OY = \frac{m_o}{m_{ss}} \times 100 \tag{7}$$

where, m_O (g) is the mass of expressed oil and m_{ss} (g) is the mass of seeds pressed

Deformation energy E (J) is the energy required to achieve a given deformation of the compressed product mass, at the specified force and conditions (Eq. 8). This is the area beneath the force–deformation curve and is numerically computable as

$$E = \sum_{n=0}^{n=i-1} \left[\left(\frac{F_{n+1} + F_n}{2}\right) \times (\delta_{n+1} - \delta_n)\right] \tag{8}$$

i represents the number of subdivisions of the deformation axis, which in this case was done in step measurements of 0.01 mm, as logged by the test equipment and as set forth by Herák *et al.* (2012), F_n (N) being the compressive force for a known deformation, δ_n (mm) and E (J) the deformation energy. Volume deformation energy, e (N mm^{-3}) is a function of the induced volumetric strain and is determinable by Eq. 9

$$e = \frac{E}{V} \tag{9}$$

The Modulus of Elasticity of the compressed bulk material, M_n (MPa) was obtained as the slope of or stress and strain or deformation curve at the specified force, numerically computed using Eq. 10.

$$M_n = \left[\frac{4 \times \delta_o}{\pi \times D^2} \times \left(\frac{F_{n+1} - F_n}{\delta_{n+1} - \delta_n}\right)\right]_{n=0}^{n=i-1} \quad (10)$$

Data analysis

All test data were subjected to the analysis of variance using the generalised linear model in Minitab®, release 17. Numerical computations and graphical plots were carried on the MS Excel platform. Main treatment effects were compared using the Duncan's multiple range test.

RESULTS AND DISCUSSION

Some physical properties of the bulk camelina, pumpkin and sesame seeds relevant to oilseed pressing are presented in Table 1. Marked differences ($p < 0.0001$) were observed among mean values of these parameters for the three crops. Porosity, bulk and true densities ranged between 6.67–7.73%, 1,058.7–1,070.9 kg m^{-3} and 1,144.4–1,149.8 kg m^{-3}, 28.6–30.1%, 590.8–603.2 kg m^{-3} and 839.6–850.6 kg m^{-3} and 3.96–10.2%, 991.3–1,060.0 kg m^{-3} and 1,101.5–1,105.0 kg m^{-3} in bulk seeds of camelina, pumpkin and sesame, respectively. Packing factor was greatest in pumpkin seeds compared to the other oilseeds (Table 1). These observed physical properties were found to be comparable with those reported in literature (Tunde-Akintunde & Akintunde, 2004¸Darvishi, 2012; Khodabakhshian, 2012). There are however observable variations that are due mainly to the varieties of the crops reported and moisture contents at which the tests were conducted (Milani et al., 2007; Tunde-Akintunde & Akintunde, 2007). Physical and mechanical properties of biological materials have been shown to vary with crops, their varieties and moisture levels.

Table 1. Physical properties of bulk seeds (*Mean* ± *SD**)

Crop	Moisture content (%, d.b.)	Mass (g)	Porosity (%)	†Bulk density (kg m^{-3})	True density (kg m^{-3})
Camelina	7.04 ± 0.06	240.9 ± 3.6	8.73 ± 1.38	1,047.3 ± 15.9	1,147.4 ± 2.8
Pumpkin	8.60 ± 0.15	141.4 ± 3.5	27.25 ± 1.79	614.8 ± 15.2	845.1 ± 7.8
Sesame	6.06 ± 0.36	230.9 ± 5.3	9.05 ± 2.09	1,003.7 ± 23.0	1,103.6 ± 1.9

*SD = standard deviation. †n = 20.

Force–deformation diagrams of bulk sections of camelina, pumpkin and sesame seeds loaded gradually to 100 kN are presented in Fig. 2. Curvilineal trends were observed in the buildup of deformation forces with incremental deformation, in all the oilseeds. The observed trends were positive. Deformation varied significantly ($p < 0.0001$) among the three oilseeds with each incremental addition of force, as did the peak deformations when compressed to 100 kN. The least deformation at peak load occurred in camelina seeds, followed by sesame. The greatest deformation occurred in pumpkin seeds (Table 2). Pumpkin has a comparatively higher packing factor than the other seeds and this accounts for the relative amount of rearrangement that may be

necessary in its bulk section prior to pronounced induction of stresses to cause actual failure of the oil bearing material.

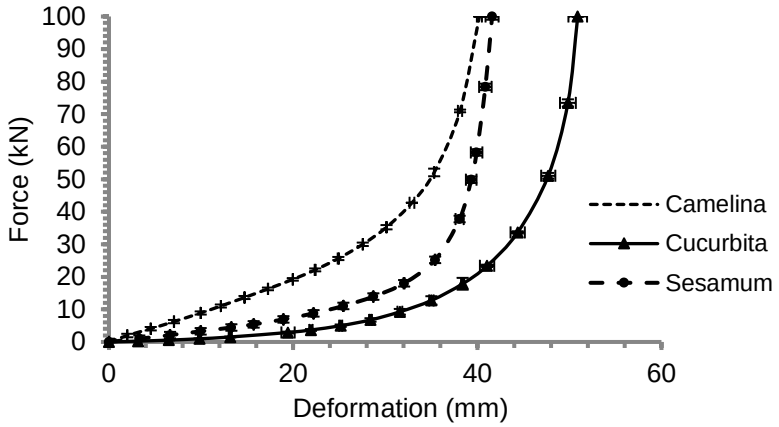

Figure 2. Measured mechanical characteristics of the selected oilseeds at pressing depths of 80 mm.

Table 2. Measured and calculated mechanical parameters of the selected bulk oilseeds uni-axially loaded to 100 kN at 10 mm min^{-1} and 9% moisture content (*Mean* ± *SD**)

Crop	Deformation (mm)	Volume deformation (10^4 mm^3)	Strain (-)	Deformation energy (J)	Volume deformation energy (MJ m^{-3})
Camelina	40.2 ± 0.3	20.2 ± 0.1	0.503 ± 0.003	1,027.3 ± 10.0	2.56 ± 0.02
Pumpkin	50.9 ± 1.0	25.6 ± 0.5	0.636 ± 0.013	693.3 ± 20.5	1.72 ± 0.05
Sesame	41.6 ± 0.7	20.9 ± 0.4	0.520 ± 0.009	585.2 ± 28.7	1.46 ± 0.07

* *SD* = standard deviation.

Oil point pressure (OPP), oil yield and bulk density of the pressed seeds after oil expression are presented in Table 3. At peak application of compressive force, slightly more oil was expressed from sesame than camelina; the least amount of oil was expressed from pumpkin seeds (Table 3). Pumpkin also attained the least bulk density after compression, indicating capacity for further densification (Table 3). Some studies reported slightly higher oil yields under at similar pressures through thermal conditioning of the oilseeds between 40–103 °C (Ajibola et al., 1993; Willems et al., 2008). Compressive oil expression has been correlated with applied pressure and strong interactions between this factor, moisture and temperature have also been reported (Min & Jeong, 1995). The show of oil was attained in pumpkin seeds at higher pressure than the other oilseeds. This indicates higher resistance of its oil bearing material to strain; sesame had very low OPP, the first show of oil being at 3.83 MPa. The oil point pressure for camelina observed in this study is lower than that reported in an earlier study which documented oil point pressures (Rusinek et al., 2012).

When deformation at peak load was compared with the relative yield of oil from each crop (Table 3), no particular trend could be inferred. Whereas the largest amount of deformation was observed in pumpkin seeds, the percent yield of oil with respect to total seed mass was low, compared to the other oilseeds (Table 3). It does appear however that a better correlation exists between relative yield of oil and oil point pressure in each oilseed (Table 3). The show of oil and therefore the onset of actual expression of oil from the oilseeds appeared to be slower in pumpkin compared to the other oilseeds. It may be inferred therefore that much of the deformation observed in pumpkin seeds at the applied force of 100 kN is attributable to rearrangement or packing in the oilseed material prior to actual occurrence of failure in the oilseed material, delaying the onset of oil.

Table 3. Oil expression and compression parameters (*Mean ± SD**)

Crop	Oil Point Pressure *(MPa)*	Oil Yield *(%)*	Bulk density of compressed seeds *(kg m^{-3})*
Camelina	7.49 ± 0.04	13.08 ± 0.26	1,220.9 ± 8.8
Pumpkin	8.83 ± 0.40	4.01 ± 0.22	1,125.5 ± 26.1
Sesame	3.83 ± 0.10	14.56 ± 0.58	1,180.5 ± 10.3

* *SD* = standard deviation.

Induced strains at maximum deformation ranged between 0.500–0.508, 0.619–0.646 and 0.512–0.533 in camelina, pumpkin and sesame seeds, respectively (Table 2). Similar amounts of strain and volumetric deformations were observed in camelina and sesame. Strain resistance is a property of the oilseed material. Some single seed quasi–static studies revealed higher rupture force requirement for pumkin than sesame seeds being in the ranges of 20.1–102.4 N and 9.10–10.6 N, respectively (Darvishi, 2012; Khodabakhshian, 2012).

The amounts of energy expended during the compression of the three oilseeds varied significantly ($p < 0.0001$) ranging from 1,016.0–1,040.3, 671.1–720.6 and 522.3–622.3 J in camelina, pumpkin and sesame seeds, respectively. The least amount of energy was expended during the compression of sesame seeds, being 585.2 J; energy expended during the compression of pumpkin was 693.3 J. The most amount of energy was expended during the compression of camelina seeds, being 1,027.3 J (Table 2).
When the volumes of oilseeds compressed were considered (Fig. 3), significant differences ($p < 0.0001$) were observed in the amount of energy expended per unit volume of compressed material. Volume energy demand ranged between 2,526–2,587, 1,669–1,792 and 1,373–1.548 MJ m^{-3} for the compression of camelina, pumpkin and sesame seeds, respectively. The mean volume energy requirement was 1.72 and 1.46 MJ m^{-3}, for pumpkin and sesame, respectively. The most amount of energy was required for the compression of Camelina being 2.55 MJ m^{-3}. This is lower than the value (8.3 MJ m^{-3}) reported by Rusinek et al. (2012) for spring camelina.Variations in the volume energy demands of the three oilseeds as deformation progressed can be seen in Fig. 3. For every measure of deformation, more energy was required to deform a unit volume of camelina seeds, compared to the other crops. This was followed by energy demand for the deformation of unit volumes of sesame seeds, which was higher than that required for pumpkin seeds.

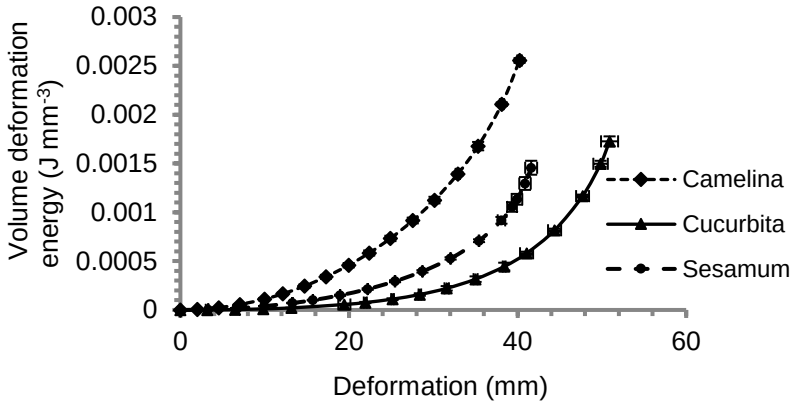

Figure 3. Changes in volume energy demands with incremental deformation of bulk camelina, pumpkin and sesame seeds loaded gradually to 100 kN.

Mean moduli of elasticity attained by the compressed oilseed materials at peak deformation, given the applied force are presented in Table 2. Fig. 3 shows the relative buildup of strain in each oilseed material, given the induced state of stress. At peak deformation and with respect to the applied force, pumpkin seeds offered the highest resistance to strain. This translated to a very low oil yield (Table 3).

Given its low oil yield at 100 kN, bulk pumpkin seeds appear to be capable of considerable amounts of increased deformation at higher stresses which would result in better oil yield.

Mean moduli of elasticity attained by the compressed oilseed materials at peak deformation, given the applied force are presented in Table 2. Fig. 4 shows the relative buildup of strain in each oilseed material, given the induced state of stress. At peak deformation and with respect to the applied force, pumpkin seeds offered the highest resistance to strain. This translated to a very low oil yield (Table 3). Given its low oil yield at 100 kN, bulk pumpkin seeds appear to be capable of considerable amounts of increased deformation at higher stresses which would result in better oil yield.

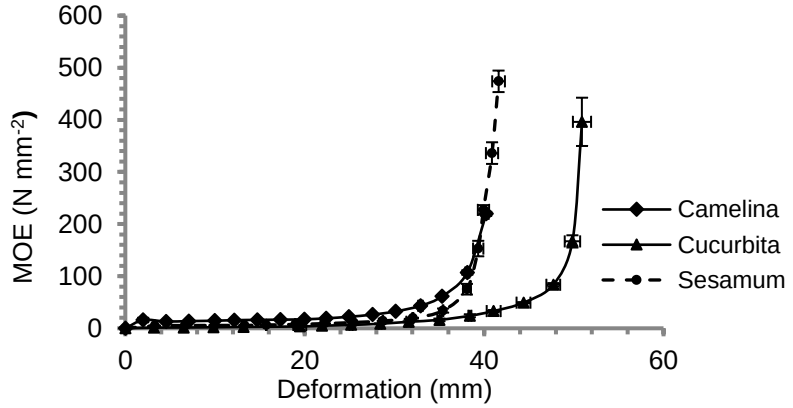

Figure 4. Moduli of elasticity of bulk camelina, pumpkin and sesame seeds gradually compressed to 100 kN.

CONCLUSIONS

Mechanical response of three important and emerging oilseed crops relevant to cold expression were determined at 80 mm pressing depth using a compressive force of 100 kN applied uniformly at 10 mm min^{-1} in an 80 mm diameter pressing vessel. Deformation, resistance to strain and deformation energy varied significantly among the three crops. Porosity, deformation and resistance to strain were greatest and mean oil recovery least in pumpkin seeds. Camelina, pumpkin and sesame had oil point pressures of 7.49, 8.83 and 3.83 MPa and volume deformation energy requirements of 2.56, 1.72 and 1.46 MJ m^{-3}, respectively, given the imposed pressing conditions. An assessment of the bulk densities of the seeds after compression indicated that the seeds are capable of further deformation under compression.

ACKNOWLEDGEMENTS. This study has been supported by Integral Grant Agency of Faculty of Engineering, Czech University of Life Sciences Prague, grant number: 2016: 31130/ 1312/ 3106.

REFERENCES

Ajibola, O.O., Owolarafe, O.K., Fasina, O.O. & Adeeko, K.A. 1993. Expression of oil from sesame seeds. *Canadian Agricultural Engineering* **35**(1), 83–88.

Arozarena, I., Iguaz, A., Noriega, M.J., Bobo, G. &Virseela, P. 2012. Physical properties of cereal products: measurement techniques and applications. In Arana, I. (ed.): *Physical properties of foods: novel measurement techniques and applications.* CRC Press, New York. pp303.

Bargale, P.C. 1997. *Mechanical oil expression from selected oilseeds under uniaxial compression*. University of Saskatchewan.

Bargale, P.C., Wulfsohn, D., Irudayaraj, J., Ford, R.J. & Sosulski, F.W. 2000. Prediction of oil expression by uniaxial compression using time-varying oilseed properties. *Journal of Agricultural Engineering Research* **77**(2), 171–181.

Berti, M., Gesch, R., Eynck, C., Anderson, J. & Cermak, S. 2016. Camelina uses, genetics, genomics, production, and management. *Industrial Crops & Products* **94**, 690–710.

Darvishi, H. 2012. Moisture-dependent physical and mechanical properties of white sesame seed. *American-Eurasian Journal of Agricultural & Environmental Sciences* **12**(2), 198–203.

Divišová, M., Herák, D., Kabutey, A., Šleger, V., Sigalingging, R. & Svatoňová, T. 2014. Deformation curve characteristics of rapeseeds and sunflower seeds under compression loading. *Scientia Agriculturae Bohemica* **45**(3), 180–186.

Faborode, M. O. & Favier, J.F. 1996. Identification and significance of the oil-point in seed-oil expression. *Journal of Agricultural Engineering Research* **65**(4), 335–345.

FAO/WHO. 2015a. *Standard for Edible Fats and Oils Not Covered by Individual Standards CODEX STAN 19-1981* (CODEX ALIMENTARIUS). FAO/WHO, Rome. Retrieved from www.fao.org/input/download/standards/74/CXS_019e_2015.pdf

FAO/WHO. 2015b. *Standard for named vegetable oils CODEX STAN 210-1999* (CODEX ALIMENTARIUS). FAO/WHO, Rome. Retrieved from www.fao.org/input/download/standards/336/CXS_210e_2015.pdf

Fruhwirth, G.O. & Hermetter, A. 2007. Seeds and oil of the Styrian oil pumpkin : components and biological activities. *European Journal of Lipid Science and Technology* **109**, 1128–1140.

Herák, D., Blahovec, J. & Kabutey, A. 2014. Analysis of the axial pressing of bulk Jatropha curcas L . seeds using reciprocal slope transformation. *Biosystems Engineering* **121**, 67–76.

Herák, D. & Kabutey, A. 2014. Tangent curve model for describing mechanical behavior of oil

bearing crops under compression loading. In L. Ševčík, P. Lepšík, M. Petrů, I. Mašín, & R. Martonka (Eds.), *Modern Design Construction Methods of Construction Design. Proceedings of ICMD 2013* (pp. 227–233. New York: Springer.

Herák, D., Kabutey, A. & Divišová, M. 2013. Analysis of tangential curve equation describing mechanical behaviour of rapeseeds (Brassica napus L .) mixture under compression loading **59**(1), 9–15.

Herák, D., Kabutey, A., Divišová, M. & Svatonova, T. 2012. Comparison of the Mechanical Behaviour of Selected Oilseeds under Compression Loading. *Notulae Botanicae Horti Agrobotanici Cluj-Napoca* **40**(2), 227–232.

Herák, D., Kabutey, A., Sedláček, A. & Gurdil, G. 2012. Mechanical behaviour of several layers of selected plant seeds under compression loading. *Research in Agricultural Engineering* **58**(1), 24–29.

Honarvar, B., Sajadian, S.A., Khorram, M. & Samimi, A. 2013. Mathematical modeling of supercritical fluid extraction of oil from canola and sesame seeds. *Brazilian Journal of Chemical Engineering* **30**(1), 159–166.

Kabutey, A., Herák, D., Dajbych, O., Divišová, M., Boatri, W.E. & Sigalingging, R. 2014. Deformation energy of Jatropha curcas L . seeds under compression loading. *Research in Agricultural Engeneering* **60**(2), 68–74.

Kabutey, A., Herák, D., Chotěborský, R., Dajbych, O., Divišová, M. & Boatri, W. 2013. Linear pressing analysis of Jatropha curcas L . seeds using different pressing vessel diameters and seed pressing heights. *Biosystems Engineering* **115**(1), 43–49.

Kachel-Jakubowska, M., Kraszkiewicz, A., Lorencowicz, E., Koszel, M. & Przywara, A. 2015. Effects of thermal treatment of seeds on quality and oxidative stability of oils. *Agriculture and Agricultural Science Procedia* **7**, 255–259.

Khodabakhshian, R. 2012. Mechanical strength and physical behavior of pumpkin seed and its kernel. *Thai Journal of Agricultural Science* **45**(1), 37–43.

Makała, H. 2015. Cold-pressed oils as functional food. In G. Budryn & D. Żyżelewicz (Eds.), *Plant Lipids Science, Technology, Nutritional Value and Benefits to Human Health* (pp. 185–200. Kerala, India. Retrieved from http://www.trnres.com/ebook/uploads/budryncontent/T_1427785049Budryn 4.pdf

Matthäus, B. 2012. Oil Technology. In S. K. Gupta (Ed.), *Technological Innovations in Major World Oil Crops, Volume 2: Perspectives* (Vol. 2, pp. 23–92). New York: Springer. https://doi.org/10.1007/978-1-4614-0827-7

Maurice A. Williams. 2005. Recovery of Oils and Fats from Oilseeds and Fatty Materials. In F. Shahidi (Ed.), *Bailey's Industrial Oil and Fat Products. Volume 5: Edible Oil and Fat Products: Processing Technologies.* (6th ed., Vol. 5, pp. 99–189). New York: John Wiley and Sons, Inc.

Milani, E., Razavi, M.S.A., Koocheki, A., Nikzadeh, V., Vahedi, N., Moeinfard, M. & Gholamhossein Pour, A. 2007. Moisture dependent physical properties of cucurbit seeds. *International Agrophysics* **21**, 157–168.

Min, Y.-K. & Jeong, H.-S. 1995. Optimisation of batch expression of sesame oil. *Journal of the Korean Society of Food Science and Nutrition* **24**(5), 785–789.

Mohensin, N.N. 1970. *Physical Properties of Plant and Animal Materials. Vol. I: Structure, Physical Characteristics and Mechanical Properties.* New York: Gordon and Breach Science Publishers. https://doi.org/10.1002/food.19870310724

Mrema, G.C. & McNulty, P.B. 1985. Mathematical model of mechanical oil expression from oilseeds. *Journal of Agricultural Engineering Research* **31**(4), 361–370.

Owolarafe, O.K., Osunleke, A.S., Odejobi, O.A., Ajadi, S.O. & Faborode, M.O. 2008. Mathematical modelling and simulation of the hydraulic expression of oil from oil palm fruit. *Biosystems Engineering* **101**(3), 331–340.

Ratusz, K., Popis, E., Ciemniewska-Zytkiewicz, H. & Wroniak, M. 2016. Oxidative stability of camelina (Camelina sativa L.) oil using pressure differential scanning calorimetry and Rancimat method. *Journal of Thermal Analysis and Calorimetry* **126**, 343–351.

Rusinek, R., Rybczyński, R., Tys, J., Gawrysiak-Witulska, M., Nogala-Kalucka, M. & Siger, A. 2012. The process parameters for non-typical seeds during simulated cold deep oil expression. *Czech Journal of Food Sciences* **30**(2), 126–134.

Santoso, H. & Inggrid, M. 2014. Effects of temperature, pressure, preheating time and pressing time on rubber seed oil extraction using hydraulic press. *Procedia Chemistry* **9**, 248–256.

Savoire, R., Lanoiselle, J.-L. & Vorobiev, E. 2013. Mechanical continuous oil expression from oilseeds : a review. *Food and Bioprocess Technology* **6**(1), 1–16.

Sigalingging, R., Herák, D., Kabutey, A., Dajbych, O., Hrabě, P. & Mizera, Č. 2015. Application of a tangent curve mathematical model for analysis of the mechanical behaviour of sunflower bulk seeds. *International Agrophysics* **29**, 517–524.

Sirisomboon, P., Kitchaiya, P., Pholpho, T. & Mahuttanyavanitch, W. 2007. Physical and mechanical properties of Jatropha curcas L. fruits, nuts and kernels. *Biosystems Engineering* **97**(2), 201–207. https://doi.org/10.1016/j.biosystemseng.2007.02.011

Tunde-Akintunde, T.Y. & Akintunde, B.O. 2004. Some Physical Properties of Sesame Seed. *Biosystems Engineering* **88**(1), 127–129.

Tunde-Akintunde, T.Y. & Akintunde, B.O. 2007. Effect of Moisture Content and Variety on Selected Physical Properties of Beniseed. *Agricultural Engineering International: The CIGR Ejournal IX*, 1–14.

Voges, S., Eggers, R. & Pietsch, A. 2008. Gas assisted oilseed pressing. *Separation and Purification Technology* **63**(1), 1–14.

Willems, P., Kuipers, N.J.M. & De Haan, A.B. 2008. Hydraulic pressing of oilseeds : Experimental determination and modeling of yield and pressing rates. *Journal of Food Engineering* **89**, 8–16.

Agronomy Research **15**(S1), 952–963, 2017

Effects of change in the weight of electric vehicles on their performance characteristics

D. Berjoza[1*] and I. Jurgena[2,*]

[1]Latvia University of Agriculture, Technical Faculty, Institute of Motor Vehicles, 5 J. Cakstes boulevard, LV-3001 Jelgava, Latvia
[2]Latvia University of Agriculture, Faculty of Economics and Social Development, Institute of Business and Management Science, 18 Svetes str., LV-3001 Jelgava, Latvia
[*]Correspondence: dainis.berjoza@llu.lv; inara.jurgena@llu.lv

Abstract. One of the parameters of electric vehicles that can affect their dynamic and range characteristics is their weight. Converting a vehicle with an internal combustion engine into an electric one, it is possible to vary its batteries and their placement. It is also possible to choose batteries of various capacities for serial electric vehicles, for example, Tesla Model S. Not only the costs of electric vehicles but also such performance characteristics as dynamics and travel range per charge depend on the number of batteries and the total weight of the electric vehicles. The research developed and approbated an algorithm for calculating comparative parameters for electric automobiles. The algorithm was approbated on 30 electric automobiles of various makes. Energy consumption per km distance travelled shows the exploitation cost of an electric automobile. According to this indicator, the most economical electric automobiles were as follows: Renault Twizy (67.8 Wh km^{-1}), Tazzari Zero (87.9 Wh km^{-1}) un Renault Zoe ZE22 (93.6 Wh km^{-1}).

Key words: batteries, range, batteries capacity, energy consumption, weight coefficient, gross weight.

INTRODUCTION

One of the technical parameters of vehicles is their weight. The weight of vehicles and its distribution on axles can affect such performance parameters as fuel consumption and acceleration dynamics. An analysis of the historical trends in vehicle weight change shows that auto manufacturers used the designs of massive automobiles in the 1950–70s, not seeking lower vehicle weight. Later, from the 1970s to the middle of the 1980s, the use of lightweight materials became popular, and steel was replaced with lightweight composite materials (plastics) in vehicle design. Consequently, the average weight of the same class automobiles decreased, on average, by 15–20%.

However, a too large decrease in the weight of vehicles resulted in lower passenger safety and design durability. To enhance the safety of passengers, in the 1980–90s vehicles started to be equipped with various safety systems, e.g. safety airbags, the automatic braking system (ABS) and stability control systems. A number of passive safety systems were designed as well. The introduction of new safety systems and their

installation on automobiles again resulted in higher vehicle weight, which was observed at the end of the 20th century.

Changes in the weight of internal combustion engine vehicles of the same model are usually insignificant. Small weight changes are usually observed if vehicles are equipped with the engines of different capacities and modifications and various devices. Changes in the weight of commercial cars are possible due to their freight compartments of different sizes.

A change in the weight of an automobile can affect the automobile's average fuel consumption. Such a trend is usually observed if driving in the urban driving regime when the automobile is often accelerated and stopped. An analysis of annual changes in automobile fuel consumption shows that in the middle of the 1980s the average fuel consumption for cars considerably decreased, while later this trend was not so explicit (Heavenrich, 2008). A similar trend in the historical evolution of automobiles was observed in relation to weight reduction; the smallest decrease in weight was specific to the automobiles manufactured in the period 1981–1987. The average weight of automobiles produced later tended to increase again. The weight increase trend does not considerably affect the acceleration dynamics of automobiles of new designs, which may be explained by the introduction of modern engine designs (Heavenrich, 2008).

Energy capacity per unit battery weight for electric vehicles (EV) is very high – from 60 to 96 Wh kg^{-1}. If an automobile is equipped with 20 kWh lithium batteries, their weight might reach 200 kg. The cost of batteries is high, up to 1,000 EUR kWh^{-1}. (Huh et al., 2011). To reduce the cost of vehicles, it is advised to choose a custom-made pack of EV batteries, as it is economically inefficient to carry the excessive weight of the batteries.

If an electric car is equipped with modern lithium-ion batteries, the current technologies allow achieving a travel range of 40–480 km per battery charge. Such batteries are not only heavy but also occupy a large space – 450–600 litres – inside the car. By using the fuel cell technology, the occupied space may be reduced by half (Thomas, 2009).

Electric vehicles may be equipped with batteries of various types. Electric vehicles are usually equipped with lead (PbA), nickel (NiMH) and lithium (Li-Ion) batteries. Today, electric vehicles have lithium-ion batteries, yet slow-moving electric vehicles are equipped with lead batteries as well. Lead batteries increase the weight of an electric vehicle the most, compared with the other kinds of batteries.

If an electric automobile is equipped with lead batteries for a range of 60 km per charge, the weight of the automobile can reach 1,700 kg. If the electric automobile is equipped with a greater number of batteries and its weight increases to 3,500 kg, the travel range increases to 170 km. If equipping electric automobiles with NiMH batteries, a medium class electric automobile with a weight of 1,500 kg can achieve a travel range of 100 km per charge. If using batteries of this kind, an automobile can reach a range of 300 km, yet its weight increases to 2,650 kg. To achieve a range of 100 km per charge by using modern lithium-ion batteries, the weight of an automobile reaches 1,350 kg and the weight of its batteries is approximately 150 kg. In order for an electric automobile to achieve a travel range that is similar to the travel range of internal combustion engine automobiles and exceeds 400 km, the weight of the electric automobile has to be increased to 2,000 kg (Thomas, 2009).

According to research investigations by other authors too, the travel range of electric vehicles is directly affected by the capacity of batteries, which depends on the weight of the batteries that can be installed on the electric vehicle. If using a 1.1 kWh lithium battery weighing 10 kg, a medium class automobile can travel a distance of 8 ± 1 km. A 7.4 kWh lithium battery weighing 80 ± 20 kg allows covering a distance of 50 ± 7 km. However, if using 31.8 kWh batteries weighing 290 ± 160 kg, the automobile can travel a distance of 250 ± 37 km (O. van Vliet et al., 2011).

Exploiting an internal combustion engine automobile after it has been fuelled up, regardless of the kind of fuel used, the weight of the fuel and therefore the weight of the automobile decreases; for a medium class automobile the weight decrease is in the range of 50–5 kg. In electric automobiles, the energy storage device – the battery – is many times heavier that the fuel tank; besides, its weight does not change depending of the battery's charge level – whether it is fully charged or fully discharged (Hauffe et al., 2008).

If equipping an electric automobile with higher capacity and heavier batteries, its total weight increases, and a higher power electric motor with a higher weight is necessary for dynamic driving. In this case, if purchasing an electric automobile, the cost increases owing to costlier accessory parts for the electric automobile as well as higher 'fuel' or electricity cost per 100 km kilometrage. By means of simulation methods, optimum parameters may be chosen for electric automobiles with various battery packs, motors and travel ranges (Hauffe et al., 2008). However, the key or at least a very important factor in choosing parameters for an electric automobile is the vehicle's driver's driving habits, daily kilometrage and maximum and average driving speeds. At present, the available assortment of electric automobiles in Latvia may not be characterised as being very broad and as meeting all the wishes of consumers, compared with that of internal combustion engine vehicles.

A comparison of the same class automobiles shows that the automobiles with a longer travel range are also heavier. The lowest average weight is specific to diesel and petrol engine automobiles, followed by HEVs (hybrid electric vehicles) and BEVs (battery electric vehicles). Besides, the average weight of BEVs can exceed that of other kinds of automobiles by up to 200 kg (Faria et al., 2012). A higher weight of an automobile can worsen not only the automobile's performance characteristics but also decrease the lifetime of assemblies of its suspension.

MATERIALS AND METHODS

The weight of vehicles and a change in it is an essential characteristic. For some vehicles when carrying the freight of various weights, the real exploitation weight can change even more than two times. Such changes are associated with the specifics of exploitation of vehicles and the structural qualities of the vehicles. Some transport enterprises calculate tonne-kilometres (t km) for their lorries, which indicate the work done by the lorries. The enterprises also set fuel consumption limits both for empty lorry runs and for full runs, i.e. t km done. Weight is also an essential factor for electric automobiles, especially in cases where large-size batteries are used, which are intended for traveling long distances.

To compare the efficiency in respect to electric vehicle weight, a specific weight coefficient for batteries has been introduced, which is calculated according to the formula:

$$k_m = \frac{m_{Acum}}{m_{EV}} \quad (1)$$

where: m_{Acum} – electric automobile's battery weight, kg; m_{EV} – electric automobile's weight, kg.

To identify the efficiency of a battery pack used in an electric automobile, the weight of the electric automobile is taken into consideration. The higher the km indicator, the higher weight batteries are used in the electric automobile and the more it is loaded. Serial electric automobiles are usually equipped with lithium-ion batteries that allow traveling a range of 120–150 km. The latest generation electric automobiles tend to increase their travel ranges. The specific weight coefficient for batteries does not completely indicate the efficiency of a battery pack, as the Eq. (1) does not include the battery pack's capacity.

The capacity of a battery pack for electric automobiles is measured in kWh. The higher the indicator is, the more electrical energy can be stored during charging the electric automobile. The simplest way how to identify this indicator for a particular electric automobile is to measure the electrical energy consumed during charging.

Batteries are different in terms of their chemical composition and therefore their weight per energy unit. Modern electric automobiles are equipped with lithium-ion batteries that have one of the highest energy densities. The energy capacity of a battery pack installed on an electric automobile is lower than that of all the individual battery elements combined, as a battery system involves a battery management system (BMS), an air conditioning and cooling system etc. The energy capacity of a battery is calculated by the following formula:

$$\rho_A = \frac{E_{Acum}}{m_{Acum}}, \text{Wh kg}^{-1} \quad (2)$$

where: E_{Acum} – energy capacity of a battery pack for an electric automobile, Wh.

Technical characteristics usually specify an electric automobile's travel range per charge based on comparable experimental cycles done on a roller test bench, e.g. in an NEDC (New European Driving Cycle) test. Since experiments are done under ideal conditions, the data acquired not always are consistent with an automobile's travel range identified under real conditions. Under real road conditions, an automobile's travel range is affected by the wind, the road's resistance (climbing resistance, rolling resistance), the speed as well as the driving style (Renault, 2017). Therefore, the results acquired performing an NEDC test could be even 25–30% higher than those identified under real conditions. Since the technical characteristics for any electric automobile specify its travel range identified performing an NEDC test, the further analysis is done based on the data acquired for electric automobiles through doing an experiment.

The performance of a battery pack installed on the particular experimental automobile may be characterised by energy consumption per km distance travelled:

$$l_{E-1} = \frac{E_{Acum}}{L_{EV}}, \quad (3)$$

where: L_{EV} – distance travelled by the electric automobile per charge (range), km.

To measure the performance of a battery pack per 100 km distance travelled, the Eq. (3) is supplemented:

$$l_{E-100} = \frac{100E_{Acum}}{L_{EV}} \quad (4)$$

Energy consumption per km distance travelled can indicate the effect of the total weight of an electric automobile as well as the total cost of electricity for the distance travelled.

The suitability of a battery pack for an electric automobile in terms of an energy storage criterion may be measured by a ratio of energy to gross weight:

$$k_E = \frac{E_{Acum}}{m_{EV-Gros}}, \text{Wh kg}^{-1} \quad (5)$$

where: $m_{EV-Gros}$ – gross weight of an electric automobile, kg.

The performance of an electric automobile per charge may be measured by the on-board energy-range factor:

$$F_{E-L} = \frac{E_{Acum}L_{EV}}{m_{EV-Gros}}, \quad (6)$$

where: E_{Acum} – energy capacity of a battery pack of the electric automobile, kWh.

A higher energy-range factor means the performance of an electric automobile is better in terms of battery capacity, distance travelled and gross weight.

The factor may be increased or decreased by either reducing the weight of an electric automobile, which is not always possible due the design of the automobile, or increasing the battery pack's capacity that can increase the travel range.

To perform an analysis of the parameters of electric automobiles, the research summarised data on 30 electric automobiles in a table. A fragment of the data needed for the analysis is presented in Table 1.

Table 1. Technical parameters of Renault electric automobiles

Automobile model	Power, kW	Curb weight, kg	Gross weight, kg	Battery weight, kg	On-board power, kWh	NEDC range, km
Renault Zoe Expression Nav R90 ZE22 New	68	1,470	1,965	290	22	235
Renault Zoe Dinamique Nav R90 ZE40	68	1,480	1,966	305	41	400
Renault Twizy	13	474	690	100	6.1	90
Renault Kangoo	44	1,410	2,126	260	22	170

RESULTS AND DISCUSSION

The Eq. (1) allows calculating the specific weight coefficient, and the data are summarised in Fig. 1. The higher the weight of a battery pack, the higher the gross weight of an electric automobile.

An analysis of specific weight coefficient values shows that high coefficient values were specific to both large class electric automobiles, e.g. Tesla Model S, reaching 0.25, and small class ones, e.g. Aixam Electric (0.27), Tazzari Zero (0.26) and Think City (0.28).

Average coefficient values were specific to the electric automobiles equipped with lightweight battery packs that consisted of either the latest technology batteries with a low weight or low-capacity battery packs, and, therefore, the per-charge distance travelled by the electric automobile was short. The specific weight coefficient values for selected electric automobiles were as follows: Nissan Leaf (24) – k_m = 0.15; Nissan e-NV200 and Kia Soul – k_m = 0.14; Mercedes B Class electric – k_m = 0.12. These electric automobiles are medium class ones with a relatively high curb weight.

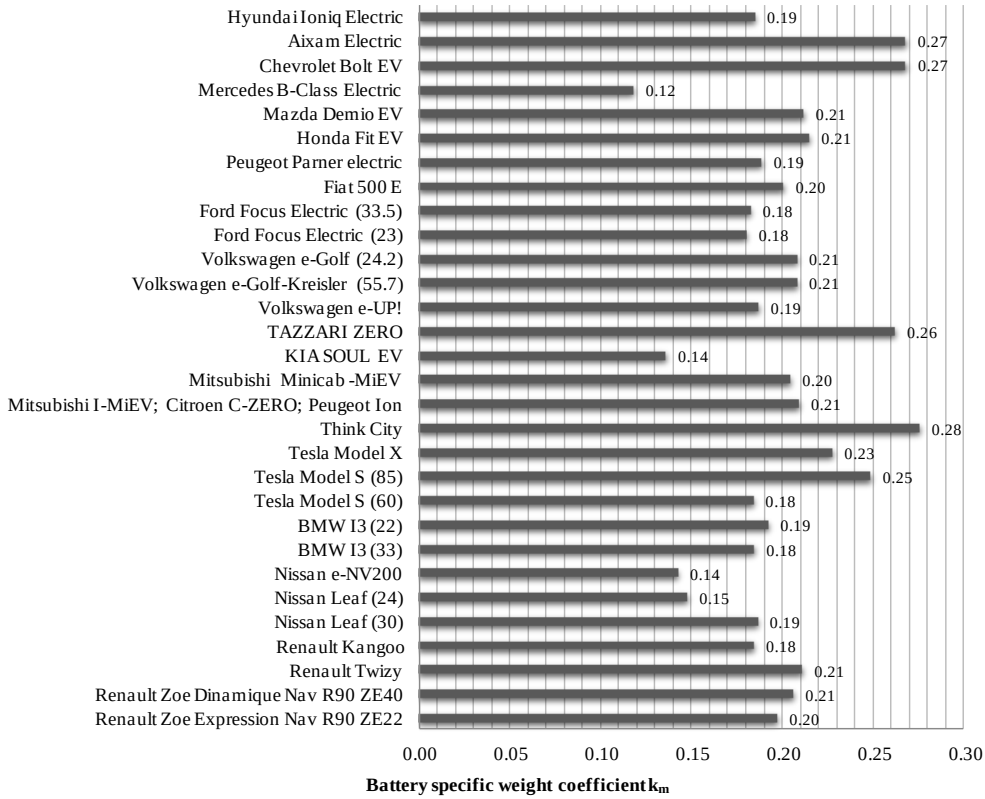

Figure 1. Battery specific weight coefficient for selected electric automobiles.
*Information in brackets represents the battery capacity.

The battery energy capacity coefficient values calculated according to the formula (2) are presented in Fig. 2. To analyse the problem of battery weight, the scientific literature often refers to energy capacity. The battery system of electric vehicles involves a number of elements for battery security, e.g. a hermetic cover that protects the battery from impacts and the surrounding environment.

Among the selected electric automobiles, Tesla Model X had the highest energy capacity value, ρ_A = 184 W kg^{-1}. The following models had the energy capacity in the range of 140–180 W kg^{-1}: BMW i3 (33), Tesla Model S (60), Tesla Model S (85), Kia Soul EV and experimental electric automobiles Volkswagen e-Golf-Kreisler (55.7). Tesla electric automobiles were still the best performers. The lowest energy capacity was

specific to small class electric automobiles Renault Twizy ρ_A = 61 W kg^{-1}, Honda Fit EV ρ_A = 63 W kg^{-1} and Aixam Electric ρ_A = 67 W kg^{-1}. These values were 2.5–3 times lower than those for the electric automobiles having the highest energy capacity values. Such a trend may be explained by the use of older technology batteries in such electric automobiles or heavy battery protection and management systems that result in a high weight percentage of the batteries installed on a small electric automobile.

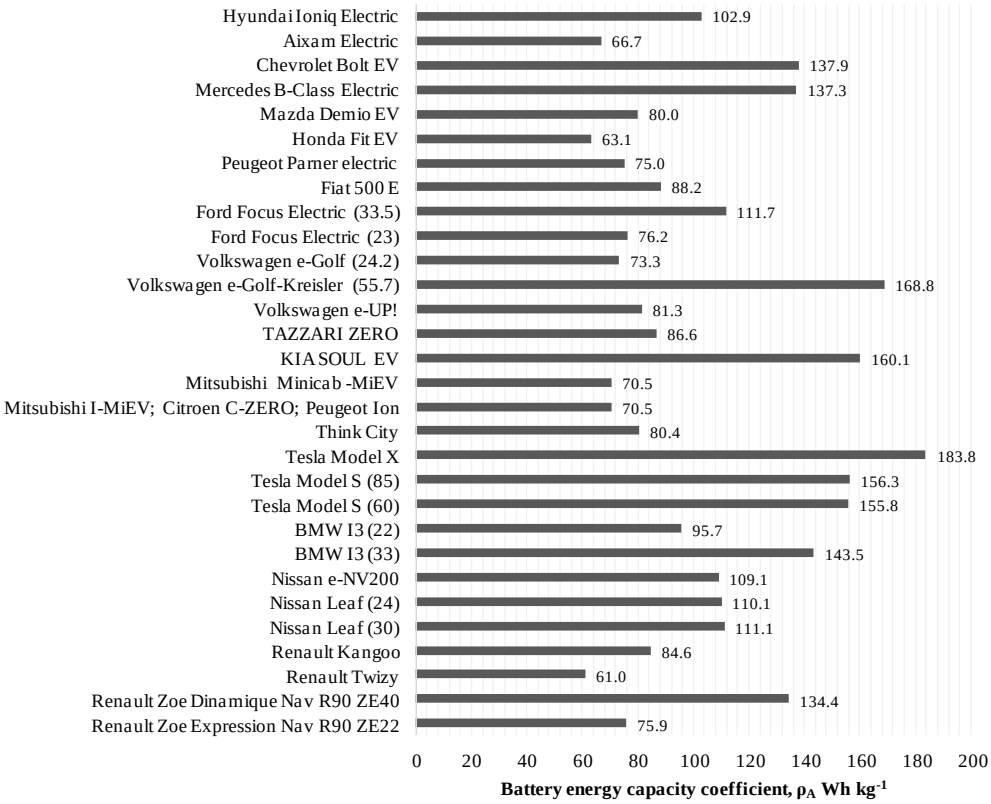

Figure 2. Battery energy capacity coefficient for selected electric automobiles.

The energy consumed per 1 km distance travelled is calculated according to the Eq. (3) and the results are summarised and showed in Fig. 3. The calculations took into account the travel ranges identified in an NEDC cycle test, and, under real road conditions, this indicator might be different from the calculated one. The best performers are the electric automobiles consuming the smallest amount of energy per 1 km distance travelled. The best performers are the following small class electric automobiles: Renault Twizy – 67.8 Wh km^{-1}, Tazzari Zero 87.9 Wh km^{-1} and Renault Zoe Expression with a 22 kWh battery (93.6 Wh km^{-1}). An analysis of electric automobiles of the same modification and design equipped with different capacity batteries revealed that in all cases the electric automobiles equipped with higher capacity batteries had a higher value of this indicator, showing lower performance, e.g. Tesla Model S (85) by 23.7%, Volkswagen e-Golf-Kreisler by 9.3% and Renault Zoe Dinamique (41) by 9.5%, compared with models equipped with lower capacity batteries. This indicates that with

the battery energy capacity increasing in electric automobiles, they become less economically efficient. The only electric automobile that was not subject to this trend was Nissan Leaf (30) whose energy consumption improved, compared with the base model, by 0.5%. The highest energy consumption was specific to the following electric automobile models: Tesla Model S (85) – 199.5 Wh km^{-1}, Tesla Model X – 200.0 Wh km^{-1} and Kia Soul EV –216.7 Wh km^{-1}. These electric automobiles were the most economically inefficient in terms of energy consumption.

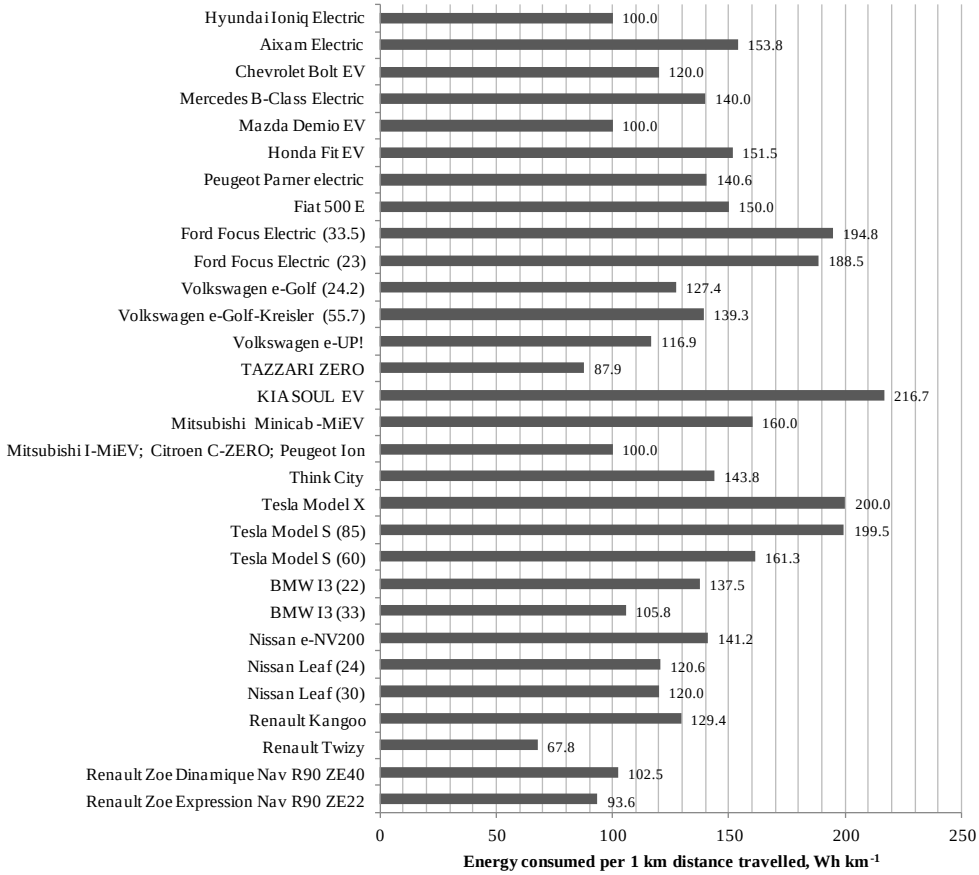

Figure 3. Energy consumed per 1 km distance travelled for selected electric automobiles.

The amounts of electrical energy stored per kg gross weight were calculated by the Eq. (5) and are showed in Fig. 4. The higher the indicator, the performance of an electric automobile is higher, and its batteries can store more energy. The highest indicator value is usually specific to the electric automobiles equipped with high capacity batteries.

The highest energy-gross weight values were specific to the following electric automobile models: Tesla Model S (85) – k_E = 30.36 Wh kg^{-1}, Tesla Model X – k_E = 32.57 Wh kg^{-1}, Volkswagen e-Golf Kreisler (55.7) – k_E = 28.42 Wh kg^{-1} and Chevrolet Bolt EV – k_E = 29.27 Wh kg^{-1}. The poorest performer was Renault Twizy with 8.84 Wh kg^{-1}. The energy-gross weight values for Peugeot Partner electric, Honda

Fit EV, Mitsubishi Minicab Miev, Nissan e-NV 200 and Renault Kango were in the range of 10.11–10.81 Wh kg^{-1}. The electric automobiles had low battery capacities relative to their gross weights. Based on this parameter, one can provisionally assume that this group of electric automobiles, compared with the other ones, has a short travel range.

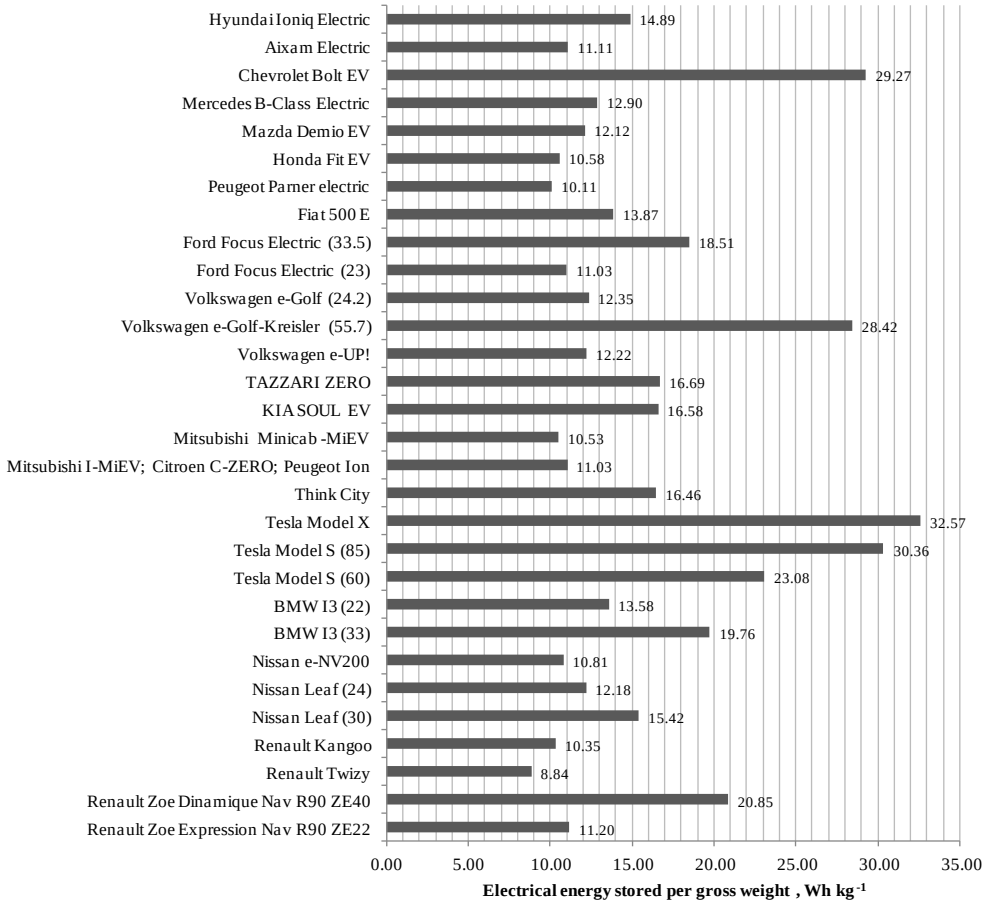

Figure 4. Electrical energy stored per kg gross weight for selected electric automobiles.

The energy-kilometrage factor was calculated by the Eq. (6) and the calculation results are summarised in Fig. 5. Electric automobiles with a factor of more than 6.0 are considered to be higher performance ones than those having a lower factor.

The best performers were the following automobile models: Tesla Model X – $F_{E\text{-}L}$ = 16.29, Chevrolet Bolt EV – $F_{E\text{-}L}$ = 14.63, Tesla Model S (85) – $F_{E\text{-}L}$ = 12.93 and Volkswagen e-Golf Kreisler – $F_{E\text{-}L}$ = 11.37. The electric automobiles with a relatively high gross weight and a low battery capacity had a factor value that was lower by about 2 kWh km kg^{-1}.

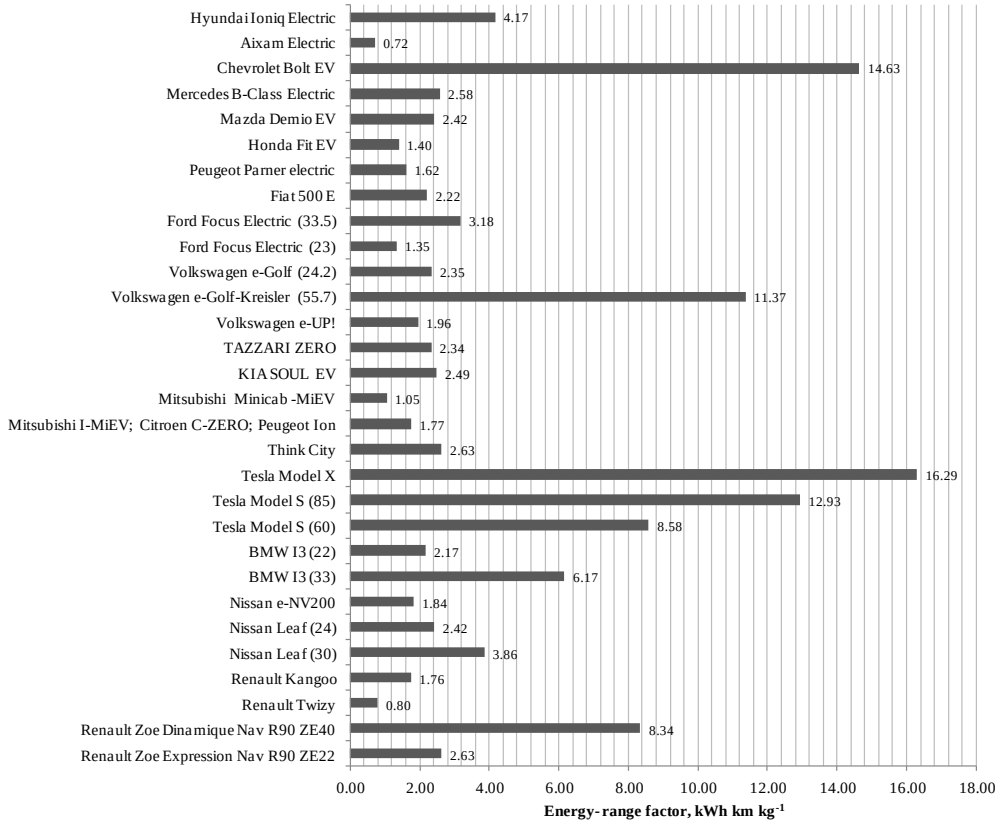

Figure 5. Energy-range factor for selected electric automobiles.

An analysis of the parameters regarding battery capacity and range showed that higher performance electric automobiles or models were as follows: Tesla brand electric automobiles, Volkswagen e-Golf Kreisler, Chevrolet Bolt EV and Renault Zoe ZE 40, yet in terms of energy consumption per 1 km distance travelled the electric automobiles with lower capacity batteries and lower weight were more economically efficient.

To perform an in-depth examination of the effects of increasing the weight of batteries for electric automobiles on such performance parameters as fuel consumption per 1 km distance travelled, range per battery charge, acceleration intensity, maximum acceleration etc., it is necessary to design a mathematical model for simulation of interrelationships among the parameters and to compare the calculated data with road experimental data. It is intended to design the model at the future stages of the research.

CONCLUSIONS

1. An analysis of the historical evolution of vehicles reveals that the average weight of automobiles decreased in the 1980s with the use of the latest generation materials, yet an increase in the weight was observed later, which was associated with higher safety standards.

2. The research developed a calculation algorithm (Eq. 1–6) for the most essential characteristics of electric automobiles based on their technical parameters, which was approbated on 30 electric automobiles of various models.

3. Specific weight coefficient values for a pack of batteries of electric automobiles do not explicitly tend to increase depending on the automobile class. High values are specific to both small, two-seater electric automobiles, e.g. Think City, k_m = 0.28, Axam Electric, k_m = 0.28 and Tazzary Zero, k_m = 0.26, and five-seater ones such as Tesla Model S (85), k_m = 0.25, and Chevrolet Bolt EV, k_m = 0.27.

4. Low values were identified for medium class electric automobiles with an average curb weight, e.g. Nissan e-NV200 and Kia Soul, k_m = 0.14; Mercedes B Class Electric, k_m = 0.12. The battery packs installed on such electric automobiles are relatively light and weigh less than 220 kg.

5. The highest battery energy densities were specific to the electric automobiles with high capacity batteries: Tesla Model X, ρ_A = 184 W kg^{-1}, Volkswagen e-Golf-Kreisler (55.7), ρ_A = 168.8 W kg^{-1} and Kia Soul EV, ρ_A = 160.1 W kg^{-1}.

6. The lowest battery energy densities were specific to the small electric automobiles: Renault Twizy, ρ_A = 61 W kg^{-1}, Honda Fit EV, ρ_A = 63 W kg^{-1} and Aixam Electric, ρ_A = 67 W kg^{-1}. These values were 2.5-3 times lower than those for the electric automobiles having the highest energy capacity values.

7. Energy consumption per km distance travelled is an essential indicator that directly affects the exploitation cost of an electric automobile. This indicator for electric automobiles with high capacity and weight batteries (Kia Soul EV, Tesla) was 80–95% higher than for the electric automobiles with a low gross weight.

8. Energy stored per kg EV gross weight for Tesla and Volkswagen e-Golf Kreisler (55.7) was the highest and ranged from 23.08–32.57 Wh km^{-1}. For most of the electric automobiles analysed, this indicator was in the range of 10.11–12.35 Wh kg^{-1}.

9. The highest energy-kilometrage factor values were identified for the electric automobile models Tesla Model X, $F_{E\text{-}L}$ = 16.29 and Chevrolet Bolt EV, $F_{E\text{-}L}$ = 14.63. This indicator for the electric automobiles with a relatively low gross weight and battery capacity was lower by 2.5 kWhkm kg^{-1}. Of the electric automobiles analysed, 56.6% belonged to this value group.

10. When purchasing an electric automobile, it is advised to carefully examine the need for a large capacity battery pack ($E_{Acum} \geq 50$ kWh) and choose an electric automobile that is best suited for the conditions of its exploitation and the average daily range, thus reducing the energy cost per 1 km distance covered.

REFERENCES

Faria, R., Moura, P., Delgado, J. & de Almeida, A.T. 2012. A sustainability assessment of electric vehicles as a personal mobility system. *Energy Conversion and Management* **61**, 19–30.

Hauffe, R., Samaras, C. & Michalek, J.J. 2008. Plug-in hybrid vehicle simulation: how battery weight and charging patterns impact cost, fuel consumption, and CO_2 emissions. In *Proceedings of the 2008 Design Engineering Technical Conferences & Computer and Information in Engineering Conferences*, New York City, NY, USA, IDETC2008-50027, 1–7.

Heavenrich, R.M. 2008. Light-Duty Automotive Technology and Fuel Economy Trends: 1975 through 2005 (EPA420-R-05-001) Office of Transportation and Air Quality's (OTAQ). U.S. Environmental Protection Agency, 79 pp.

Huh, J., Lee, W., Cho, G.-H., Lee, B. & Rim, C.-T. 2011. Characterization of novel inductive power transfer systems for on-line electric vehicles. Daejeon, Korea, 978-1-4244-8085-2/11.2011 IEEE – 1975–1979.

Renault ZOE. 2017. Genuine Brochure. Renault Passion for life. Z.E. 36 pp.

Thomas, C.E. 2009. Fuel cell and battery electric vehicles compared. *International Journal of Hidrogen Energy* **34**(15), 6005–6020.

van Vliet, O., Brouwer, A.S., Kuramochi, T., van den Broek, M. & Faaij, A. 2011. Energy use, cost and CO_2 emissions of electric cars. *Journal of Power Sources. International Journal of the Science Technology of Battery, Fuel Cell and other Electrochemical Systems*. Elsevier, **169**(4) ISSN 0378-7753, 2298–2310, doi:10.1016/j.jpowsour.2010.09.119

Agronomy Research **15**(S1), 964–970, 2017

Effect of commercial diesel fuel and hydrotreated vegetable oil blend on automobile performance

G. Birzietis[1,*], V. Pirs[1], I. Dukulis[1] and M. Gailis[1,2]

[1]Latvia University of Agriculture, Faculty of Engineering, Motor Vehicle institute, 5 J. Cakstes boulv., LV-3001 Jelgava, Latvia
[2]Riga Technical University, Faculty of Mechanical Engineering, Transport and Aeronautics, Department of Automotive Engineering, Viskalu 36, LV-1006 Riga, Latvia
[*]Correspondence: gints.birzietis@llu.lv

Abstract. The new fuel 'Pro Diesel' that contains hydrotreated vegetable oil (HVO) was recently introduced in Baltic market. It raised some interest on performance of the new fuel among fleet and individual consumers. The authors evaluated and compared performance of modern M1 class automobile, using regular fossil diesel fuel and Pro Diesel fuel.
Torque, power and fuel consumption of the vehicle have been evaluated on chassis dynamometer, in steady state and driving cycle mode.
Depending on test conditions, engine power and torque was increased up to 2%, and fuel consumption reduced up to 3.9%, when diesel fuel/ HVO blend was used.

Key words: Pro Diesel fuel, HVO, NexBTL, compression ignition engine, fuel consumption, power, torque.

INTRODUCTION

Since April 2016, the largest Neste Oil fuel retail stations in Latvia started to offer new brand of fuel – 'Neste Pro Diesel', which contain hydrotreated vegetable oil (HVO) approximately 15% by volume.

HVO can be produced from many kinds of fats. Their production need not be based only on processing of raw vegetable oils, but other kinds of waste triglycerides-rich materials (used cooking oil, animal fats) can be used as well (Huber et al., 2007).

Renewable feedstocks such as vegetable oils may be processed by variations of conventional petroleum refining, including hydrotreatment. These refining methods produce saturated paraffinic hydrocarbon molecules with extremely low aromatic levels and a very narrow distillation range, and properly processed, they can provide the required cold flow properties (Worldwide Fuel Charter, 2013).

The different physical and chemical properties of the fuel affects the combustion processes in the engine. As a result, the power and torque performance of the vehicle as well as fuel consumption and exhaust emission composition is changing.

The aim of this study was evaluate and compare performance and fuel consumption of modern M1 class automobile, using regular fossil diesel fuel and Pro Diesel fuel.

There are number of studies done on performance and fuel consumption characteristics of HVO and its blends with fossil diesel fuel in diesel engines during the last years.

Extensive studies have been done in Finland (Nylund et al., 2011) within the frame of OPTIBIO project, where the HVO fuel was tested in 300 urban buses. The test fuels were a 30% HVO blend and 100% HVO. In this study the fuel consumption measurements was carried out with 11 different buses. It was concluded that maximum increase in volumetric fuel consumption was 1.4% for the 30% HVO blend and 5.2% for 100%.

Within the same project the effects of injection timing on exhaust emissions and fuel consumption was studied at Aalto University with an engine equipped with an adjustable common-rail fuel injection system and running on 100% HVO. There was concluded that choosing a calibration that delivers NOx at the same level as with regular diesel fuel results in a 4% reduction in energy consumption and a reduction of some 40% in filter smoke number. If a slight increase (4%) in NOx can be allowed, energy consumption can be reduced as much as 6% (Nylund et al., 2011).

The difference in power and fuel consumption of tractor Claas Ares running with pure HVO fuel and fossil diesel have been studied in Latvian University of Agriculture. In these studies it was found that the engine effective power and torque using HVO fuel decreases relatively to fossil diesel fuel. The average PTO (power take-off) power and torque reduction was about 5.0%. It can be explained by the 5.5% difference in the volume-based lowest heating values of both fuels. The average hourly fuel consumption in PTO revolutions range from 300 to 625 min^{-1} using HVO was by about 1% lower comparing to diesel fuel, but due to the lower developed engine power the increase of the specific fuel consumption was in average by 4.1% higher (Sondors et al., 2014).

Aatola et al. (2008) have studied NO_x – particulate emission trade-off and NO_x – fuel consumption trade-off using different fuel injection timings in a turbocharged charge air cooled common rail heavy duty diesel engine with sulfur free diesel fuel, neat HVO, and a 30% HVO + 70% diesel fuel blend. Results showed that the use of 100% HVO decreases the specific fuel consumption (SFC)of the engine at all engine speeds and loads at each measured injection timing when comparing with EN 590 and EN 590-30 diesel fuels. With EN 590-30 diesel fuel, the decrease of SFC compared to EN 590 diesel fuel is, of course, not that clear.

Kim et al. (2014) carried out the study of engine performance to compare iso-HVO (isomerized-hydrotreated vegetable oil) with BD (Biodiesel). The test samples were prepared 16 kinds of fuels, which are fossil diesel and 2%, 10%, 20%, 30%, 50% of BD, HVO, and iso-HVO blended diesel, respectively. The engine performances and emission were tested on engine dynamometer and chassis dynamometer with 1.5 l diesel engine and passenger car, for evaluating maximum power, fuel consumption, and emission, especially PM (Particulate Matter) and NO_x. Iso-HVO has much better engine performance than BD and slightly better than HVO, but slightly worse than fossil diesel. In this study HVO blended diesel show decreases in the power, meaning that the more HVO or iso-HVO blended, the more power decreased. Decrease of maximum power depends on the driving conditions, and normally, fuel injection control of the engine in the maximum power mode is conducted by fuel volume. Kim et al. (2014) also reports,

that HVO and iso-HVO show slightly decrease of fuel consumption while blending ratios of them increase.

Pellegrini et al. (2015) have studied the potential of HVO as blending component of diesel fuel to be used in advanced combustion systems at different compression ratios and at high EGR rates. The experiments were carried out in a single cylinder research engine at three steady state operating conditions and at three compression ratios (CR) by changing the piston. The two of test fuels comprised 15 and 30% of HVO. They found that as the engine compression is reduced, the use of HVO fuel blends allows for more efficient combustion timing and so reduces the fuel consumption.

Also Pexa et al. (2015) carried out the study of 100% rapeseed methyl ester and 100% hydrogenated oil impact on the operational characteristics of a turbocharged internal combustion engine of the tractor Zetor Foretrra 8641 using a dynamometer to the PTO. It was observed that during the operation with HVO fuel, the engine maximum torque reduces by approx. 0.9% and the maximum performance reduces by approx. 6%. The specific fuel consumption of the HVO fuel reduces in comparison to the RME fuel almost in the whole speed range.

Most of the researchers, who tested blends of paraffinic fuel (HVO, gas to liquid (GTL)) with diesel fuel, using compression ignition (CI) engines with CR above 17:1, reported decrease of engine maximal torque and power, comparing to diesel fuel (Uchida et al., 2008; Wang et al., 2009; Kim et al., 2014). It was explained by lower volumetric heating value of paraffinic fuel. Kitano et al. (2005) tested GTL fuel, using engine with CR 16:1 and reported no change in engine power and torque, comparing GTL to diesel fuel.

MATERIALS AND METHODS

Two fuels were used in this study – Neste Pro Diesel (ProD), which contained hydrogenated vegetable oil, and regular fossil fuel Neste Futura. General properties of test fuels according the certificates of conformity are presented in Table 1.

Table 1. Basic parameters of tested fuels

Parameter	Fossil Diesel Fuel	HVO Blended Diesel Fuel
Fuel designation	Neste Futura	Neste Pro Diesel
Density at 15 °C, kg m^{-3}	824.4	822.2
Cetane number	51.1	55
Viscosity at 40 °C, mm^2 s^{-1}	1.937	2.537
Flash point, °C	62	67.5
Content of HVO, % vol	0	9.15

The four-wheel drive car Mazda CX-5 of 2015 equipped with a 2.2-liter Euro 6 engine with compression ratio 14.0:1 was used in this study. The effective power of the vehicle was 129 kW and it was equipped with Common-rail fuel system. The torque was transmitted to the wheels through a 6-speed automatic transmission. The rear axle drive of the test car was mechanically unlocked for the tests on chassis dynamometer.

The study was performed in Scientific Laboratory of Alternative Fuels of Latvia University of Agriculture on chassis dynamometer Mustang MD-1750. For measurement of power and torque on driving axle and fuel consumption the following

tests were performed: power test, idle running test, constant speed tests (50 km h^{-1}, 90 km h^{-1} and 110 km h^{-1}), driving cycle IM-240 and especially worked driving cycle 'Jelgava'. The driving cycle IM-240 represents the combined driving cycle. The cycle simulates both the urban driving conditions where the maximum speed doesn't exceed 50 km h^{-1} and driving in non-urban area. The total duration of cycle is 240 seconds and the covered distance is 3.10 km. The driving cycle 'Jelgava' is localy eleborated city driving cycle that simulates as close as possible the real driving in one of the cities of Latvia – Jelgava. The total duration of this cycle is 360 seconds and covered distance is 2.36 km. Technical characteristic of driving cycle 'Jelgava' and peculiarities of elaboration are described in publication (Dukulis & Pirs, 2009).

Constant speed tests were performed for 60 seconds with the reading step of 1 second. Three repetitions were made in each testing mode. The gear shifter was set in automatic mode.

Load conditions were simulated in the laboratory on the eddy current roll type chassis dynamometer Mustang MD1750.

Fuel consumption was measured using the high precision and accuracy fuel consumption measurement system AVL KMA Mobile. System measuring range is 0.35–150 L h^{-1} and measuring error – 0.1%.

The layout of test equipment are shown in Fig. 1.

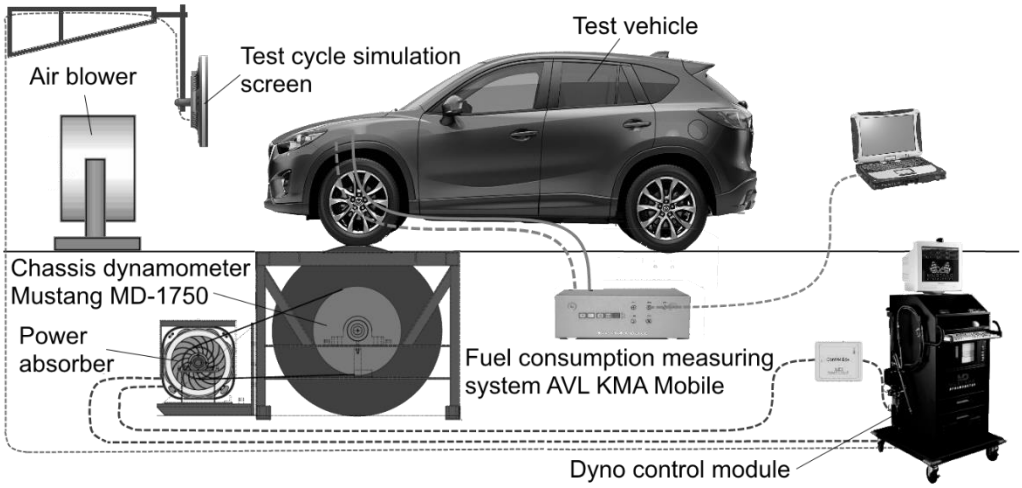

Figure 1. Test object and measuring equipment.

RESULTS AND DISCUSSION

The results of vehicle power and torque tests with both test fuels are presented in Fig. 2. At medium and high engine speeds the vehicle power and torque values are very similar. Significant power and torque increase was observed at low engine speeds (up to ~ 2,200 min^{-1}), during vehicle operation with Neste Prodiesel fuel.

The maximum power value of 106.8 ± 0.6 kW was reached during vehicle operation with ProDiesel fuel which is by 1.2% higher than in case of fossil diesel use. The maximum torque value also was higher for Pro Diesel fuel by 2%.

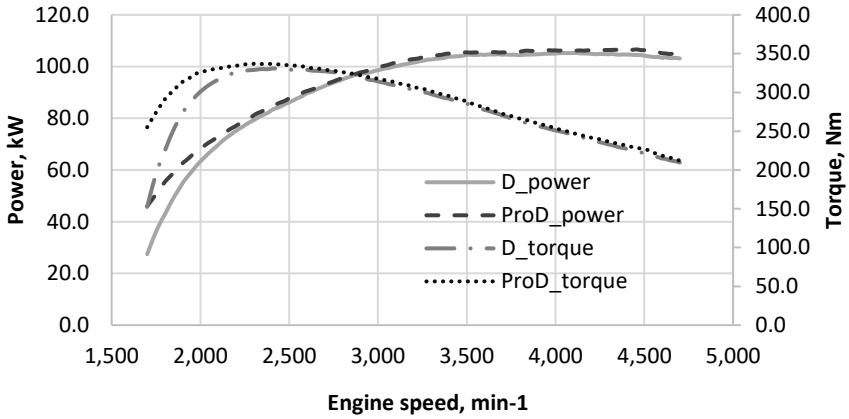

Figure 2. Vehicle power and torque curves.

The difference in power and torque values between test fuels within the whole speed range is shown in Fig. 3. The power and torque increase in vehicle operation with ProDiesel fuel at crankshaft speed 1,700 min^{-1} reach 67% compare to fossil fuel Futura.

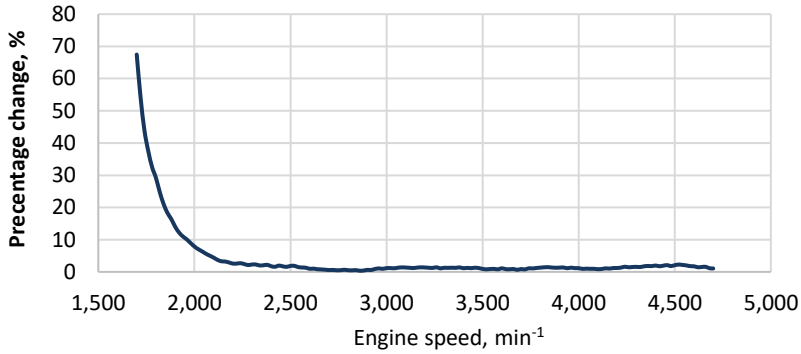

Figure 3. Vehicle power and torque percentage changes.

The difference in power and torque values can be attributed to to fuel properties, as well as a suitability of specific engine design (low compression ratio) and engine management system setup for fossil or ProDiesel fuel. Comparing to work of other researchers, commercial fuel blend was used and engine compression ratio was lower. In order to find explanation of above mentioned difference in power and torque the further studies on impact of HVO containing fuel properties on combustion process are necessary.

The difference in fuel consumption at vehicle idle operation between tested fuels were not observed. Both in case of Neste Pro Diesel and Neste Futura fuel the idling fuel consumption was 0.50 ± 0.02 L h^{-1}. The vehicle operation with HVO containing fuel in steady speed mode shows the overall trend of fuel consumption decrease (see Fig. 4.). The fuel consumption decrease with ProDiesel fuel at steady speed modes of 50, 90 and 110 km h^{-1} was 1.5%, 0.7% and 3.7% respectively.

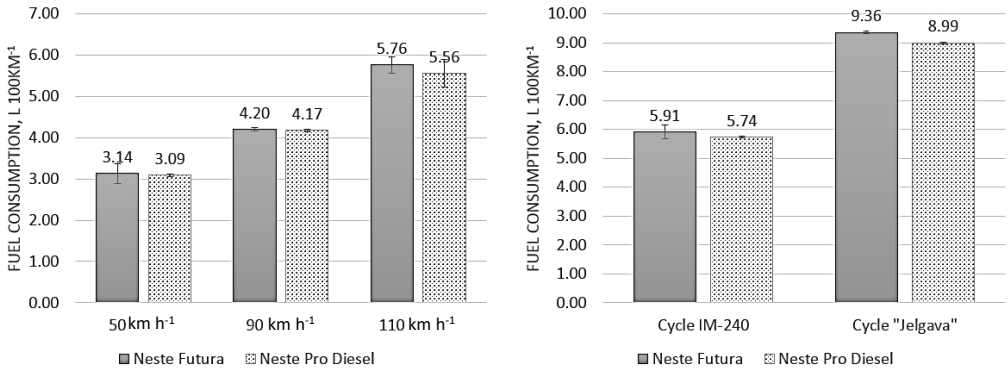

Figure 4. Fuel consumption in steady speed and driving cycle modes.

More evident fuel consumption changes was observed at variable load drive conditions or driving cycles. The vehicle operation with fuel containing HVO at driving cycle IM-240 showed the reduction in fuel consumption by 0.17 L 100 km^{-1} or 2.9% comparing to operation with fossil diesel. Whereas, the fuel consumption decrease at driving cycle 'Jelgava', which represents the movement of the vehicle in an intensive city traffic was 0.37 L 100 km^{-1} or 3.9%.

The observed decrease in fuel consumption partially could be explained by reduced engine compression ratio according to the studies performed by Pellegrini et al. (2015).

CONCLUSIONS

The results of the study show that test vehicle operating on fuel with admixture of hydrogenated vegetable oil at 9.15% by volume develops about 1.2% higher maximum power and 2% higher peak torque. However, the most significant difference between test fuels appear especially at low engine speed. The methodology and measuring equipment used in this study do not allow reveal the reason for that parameter changes. The partial impact on the result would leave both the different fuel physically - chemical properties as well as specific characteristic of vehicle engine and engine management system program set up.

The data of fuel consumption analysis showed that operation on fuel with admixture of hydrogenated vegetable oil at 9.15% by volume reduces the vehicle fuel consumption both in steady and transient driving modes. In steady driving modes at 50, 90 and 110 km h^{-1} the fuel consumption decreases by 1.5%, 0.7% and 3.7%. The vehicle operation with ProDiesel fuel in driving cycles IM-240 and 'Jelgava' shows 2.9% and 3.9% reduction of fuel consumption respectively compare to fossil diesel.

For reasonable explanation of obtained results the relation of particularities of engine design, fuel system and engine control system with the fuel physically-chemical characteristics of ProDiesel fuel must be analyzed in a further studies.

ACKNOWLEDGEMENTS. The authors acknowledge the Neste Latvia Ltd. for the supply of the test vehicle and test fuels.

REFERENCES

Aatola, H, Larmi, M., Sarjovaara, T. & Mikkonen, S. 2008. Hydrotreated Vegetable Oil (HVO) as a Renewable Diesel Fuel: Trade-off between NOx, Particulate Emission, and Fuel Consumption of a Heavy Duty Engine. SAE Technical Paper 2008-01-2500. 12 p.

Dukulis, I. & Pirs, V. 2009. Development of Driving Cycles for Dynamometer Control Software Corresponding to Peculiarities of Latvia. In: Proceedings of the 15th International Scientific Conference '*Research for Rural Development*'. Latvia University of Agriculture, Jelgava, pp. 95–102.

Huber, G. W., O'Connor, P. & Corma, A. 2007. Processing biomass in conventional oil refineries: Production of high quality diesel by hydrotreating vegetable oils in heavy vacuum oil mixtures. *Applied Catalysis A*: General. Volume **329**, 120–129.

Kim, D., Kim, S., Oh, S. & No, S.-Y. 2014. Engine performance and emission characteristics of hydrotreated vegetable oil in light duty diesel engines. *Fuel* **125**, 36–43

Kitano, K., Sakata, I. & Clark, R. 2005. Engine performance and emission characteristics of hydrotreated vegetable oil in light duty diesel engines. SAE 2005 *Transactions Journal of Fuels and Lubricants* **114**, 4–13.

Nylund, N.-O., Erkkilä, K., Ahtiainen, M., Murtonen, T., Saikkonen, P., Amberla, A. & Aatola, H. 2011. Optimized usage of NExBTL renewable diesel fuel. OPTIBIO. VTT Tiedotteita – Research Notes 2604, Espoo. 167 p.

Pellegrini, L., Beatrice, C. & Di Blasio, G. 2015. Investigation of the Effect of Compression Ratio on the Combustion Behavior and Emission Performance of HVO Blended Diesel Fuels in a Single-Cylinder Light-Duty Diesel Engine. SAE Technical Paper 2015-01-0898. 15 p.

Pexa, M., Čedík, J., Mařík, J., Hönig, V., Horníčková, Š. & Kubín, K. 2015. Comparison of the operating characteristics of the internal combustion engine using rapeseed oil methyl ester and hydrogenated oil. *Agronomy Research* **13**(2), 613–620.

Sondors, K., Birkavs, A., Dukulis, I., Pirs, V. & Jesko, Z. 2014. Investigation in tractor Claas Ares 557ATX operating parameters using hydrotreated vegetable oil fuel. In: Proceedings of the 13th International Scientific Conference '*Research for Rural Development*'. Latvia University of Agriculture, Jelgava, pp. 63–68.

Uchida, N., Hirabayashi, H., Sakata, I., Kitano, K., Yoshida, H. & Okabe, N. 2008. Diesel Engine Emissions and Performance Optimization for Neat GTL Fuel. *SAE International Journal of Fuels and Lubricants* **1**(1), 748–762

Wang, H., Hao, H., Li, X., Zhang, K. & Ouyang, M. 2009. Performance of Euro III common rail heavy duty diesel engine fueled with Gas to Liquid. *Applied Energy* **86**(10), 2257–2261.

Worldwide Fuel Charter. 2013. Fifth edition.

Agronomy Research **15**(S1), 971–980, 2017

Wear and stress analysis of chisel

R. Chotěborský[1,*], M. Linda[2] and M. Hromasová[2]

[1]Czech University of Life Sciences, Faculty of Engineering, Department of Material Science and Manufacturing, Kamycka 129, CZ165 21 Prague, Czech Republic
[2]Czech University of Life Sciences, Faculty of Engineering, Department of Electrical Engineering and Automation, Kamycka 129, CZ165 21 Prague, Czech Republic
[*]Correspondence: choteborsky@tf.czu.cz

Abstract. The object of research is stress analysis of worn chisel. The interaction between soil particles and chisel leads to change of shape and dimension of a worn chisel or other agriculture tools. The wear rate depends on the velocity of the chisel in the soil, position in the soil and shape of a chisel. These factors change the dimension and shape of chisel during its service life. The modern chisel includes sintered carbides on a tip. Sintered carbides plates are effective protection for wear resistance. But the body of the chisel is not protected and its wear resistance is lower than the tip. The service life of the tip is much higher than the body of the chisel. Stresses of the body of the chisel are stationary during the service life. The aim of this study is determining of optimising process of the strength of steel for chisels.

Key words: agriculture tools, FEM, soil, wear.

INTRODUCTION

Agriculture tools like chisel are most used for a non-tillage agriculture operation. Soil as particular media content a different ratio of particle size, usually sand particles and other, and its mineral composition depend on the place of land. A lot of researchers have been described a mineralogical composition (Singh et al., 2015), particular composition (De Pellegrin & Stachowiak, 2001), moisture content and other chemical and physical properties of soil (Rajaram & Erbach, 1998; Mouazen, 2002; Vogel et al., 2005; Asaf et al., 2007; Tagar et al., 2014). Some researchers have been focused on rheological properties of the soil and they have been described mechanical properties of soil for a prediction its behaviour under loading, wetting and drying (Rajaram & Erbach, 1998; Coetzee & Els, 2009; Tang et al., 2011; Chen et al., 2013; Sima, Jiang, & Zhou, 2014). Mathematical models of soil we can develop by finite element methods, discrete element methods or boundary element methods. Mechanical properties of soil are mostly described by finite element method, ex. under press loading. But drying of soil has been described by discrete element methods or more complicated by finite element methods. The interaction between soil and agriculture tools can be developed by a complex method where the first solver solve flow of soil around the tools, ex. Discrete element method and second solver transform force and velocity to the stress-strain analysis of tools, ex. Finite or discrete element method (Araya & Gao, 1995; Mouazen & Neményi, 1999; Mouazen & Ramon, 2002; Karmakar et al., 2007; Maksarov & Olt, 2008; Rojek

et al., 2011; Guo et al., 2012; Mak et al., 2012; Bentaher et al., 2013; Jørgensen, 2014; van Wyk et al., 2014; Farid Eltom et al., 2015; Borys & Küüt, 2016; Zhu et al., 2016). Although stress analysis in finite element method can be solved by steady state, the flow of soil is transient solver in discrete element method. Also present model of interaction between soil and agriculture tools used a modern mathematical methods (Abu-Hamdeh, 2003; Abo-Elnor et al., 2004; Aluko & Chandler, 2004), but the solution has unexpected change of shape during soil processing, thanks to wearing process in soil (Stachowiak, 2000; Stachowiak & Stachowiak, 2001; Waoldman et al., 2012; Woldman et al., 2015). A complex model of interaction can be generalized with heat treatment of steel and input to the mathematical model, it can be wide for optimizing the process for manufactory production, where we can solve interaction of soil with tools and their heat treatment for the best service life and fuel consumption.

Some study showed that the microstructure, mechanical properties and wear can be predicted by mathematical models (Natsis et al., 2008).

The aim of this study is to present an idea of optimising process for a chisel, its heat treatment and stress analysis for best service life.

MATERIALS AND METHODS

The process of heat transfer during quenching of a steel chisel (Fig. 1) is nonstationary due to the variation of temperature with time. In this work, the problem of heat transfer, austenite phase transformation, flow, stress analysis in a three-dimensional phase was examined.

Figure 1. Real chisel computerization.

The structure composition of steel cooling depends on the actual hardness defined as:

$$HV = V_P \times HV_P + V_B \times HV_B + V_M \times HV_M \quad (1)$$

Where V_P is the volume of pearlite, V_B is the volume of bainite and V_M is the volume of martensite.

The amount of phases proportion is an equal unity defined by (Li et al., 2001; Liu et al., 2003; Pietrzyk & Kuziak, 2011; Xie et al., 2013) as:

$$HV_M = 127 + 949 \times C + 27 \times Si + 8 \times Ni + 16 \times Cr + 21 \times lnV_r \quad (2)$$

$$HV_B = -323 + 185 \times C + 330 \times Si + 153 \times Mn + 65 \times Ni + 144 \times Cr + 191 \times Mo + (89 + 53 \times C - 55 \times Si - 22 \times Mn - 10 \times Ni - 20 \times Cr - 33 \times Mo) \times lnV_r \quad (3)$$

$$HV_{F,P} = 42 + 233 \times C + 53 \times Si + 30 \times Mn + 12.6 \times Ni + 7 \times Cr + 19 \times Mo + (10 - 19 \times Si + 4 \times Ni + 8 \times Cr + 130 \times V) \times lnV_r \quad (4)$$

Where *C*, *Si*, *Mn* and others represent different kinds of chemical elements respectively (wt. %), V_r represents cooling speed at 700 °C (°C h^{-1}). The material was steel 25CrMo4 and heat treatment quenching in water.

From Eq. 1, it is not difficult to predict the fraction of phases if the hardness of cooling microstructure and the hardness of microstructure constituents' are separately known (Eqs 2 to 4). Results of austenite decomposition depend on the chemical composition and steel history. The characteristic cooling time relevant for structure transformation for most steel is the time $t_{8\text{-}5}$, this time is determined from temperature 800 °C to 500 °C. The characteristic cooling time was determined through series of algorithm where an average value of heat gradient between 500 °C and 800 °C.

The calculation of hardness was done by retrieving the temperature of nodes file. The analysis was performed for N nodes corresponding to the mesh of model. The temperature parameters of the nodes of the model were introduced (inlet) into the calculation of the volumetric representation of ferrite, pearlite, bainite and martensite.

The abrasive wear rate was determined according to ASTM G65 (ASTM G65-04, 2010). Samples were loaded by force 17 N, 35 N, 57 N, 78 N a 100 N in testing schema 3–1–3–1–3 (three times at 17 N, ones at 35 N, three times at 57 N). Repeated testing were used for elimination of testing errors according to DoE methods. The signification of slope the results of cumulative wear at same loading were tested on statistical dependency. The total track was 1890 m for one sample, the part track was 210 m. The mass loss was determined after part track on digital balance with accuracy 0.1 mg. The volume loss or wear was recalculated from mass loss divided by the density of steel 7,800 kg m^{-3}. The hardness of abrasive was Ha = 1,100 HV30.

Discrete element method was used for determination of flow soil particles around the chisel. Soil DEM model was determined from an experimental data of soil (sandy-loam) from land (GPS 50°23'36.2"N 16°01'47.2"E), where we done a practical tests. Experimental evaluation included pressing, relaxation, creep in pressing vessel and also included a shear test of soil at different loading. The output data included poison ratio, the coefficient of friction soil particle between itself, the dependency between young modulus and strain. These data were input for a DEM model of soil. Step size was 1 km. Results of DEM model (force and velocity) were applied on boundary nodes of surface chisel mesh model. The algorithm is schematically presented in Fig. 2.

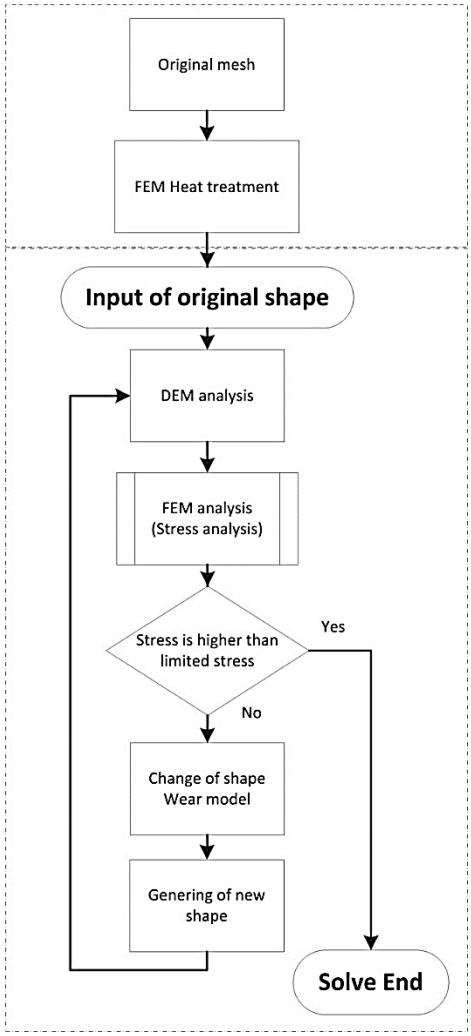

Figure 2. Schema of the algorithm.

Intel Xeon CPU E5-2640 v3 @ 2.60 GHz, 128 GB DDR3 RAM was used for an algorithm which was written in SciLab 5.5.2 (Scilab Enterprises, 2016).

RESULTS AND DISCUSSION

According to the schema of the algorithm (Fig. 2), the first step was determining of chisel microstructure and calculation of hardness. The result of quenched steel in cross section is presented in Fig. 3. FEM model showed that the microstructure and hardness were not homogenous although steel content hard martensitic structure and bainite after quenching. So, each of node in mesh model content a different ration two phases and according to Eq. 1 we determined hardness in this position of the node. This procedure we applied for all nodes in the model (Chotěborský & Linda, 2015). After then we

applied a model of wear rate. The original shape of the chisel was solved in DEM solver (Fig. 4) and results of particle flow (force and velocity) were applied in FEM model.

Figure 3. Hardness in cross section (near the hole in Fig. 4) of chisel after heat treatment.

Figure 4. Vectors of force (a) and velocity (b) from DEM.

The mathematical model of wear W ($\mathrm{mm^3\ m^{-1}}$) was determined by using of general linear method with step by step solver in Statistica software. Mathematical models with and without interaction of variables were compared between themselves. Comparison criteria were quality of fitting (R), residua normality and half normality, F and p value for a models with and without intercept. The best model no include interception but with interaction of variables in factorial schema.

General mathematical model (5–8):

$$W = A \times \frac{F}{S} + B \times \frac{Ha}{Hm} + C \times \frac{F \times Ha}{S \times Hm} \tag{5}$$

where:

$$A = 9 \times 10^{-5} \pm 2 \times 10^{-5} \tag{6}$$

$$B = 1.03 \times 10^{-3} \pm 0.057 \times 10^{-3} \tag{7}$$

$$C = 7 \times 10^{-5} \pm 1 \times 10^{-5} \tag{8}$$

Total quality of model:

$R = 0.96; F = 6043; p \ll 0.001$

The limited factors:

$Ha \in \{600; 1100\}; Hm \in \{200; 800\}$ Vickers hardness at load 30 kg HV30, Ha–abrasive hardness, Hm–material–steel hardness calculated from Eq. 1 and *S* is area.

$F \in \{10; 100\}\ N; S = 2.64\ cm^2$

Full mathematical model for a simulation:

$$W = 9 \times 10^{-5} \times \frac{F}{S} + 1.03 \times 10^{-3} \times \frac{Ha}{Hm} + 7 \times 10^{-5} \times \frac{F \times Ha}{S \times Hm} \qquad (9)$$

Where the ratio of force F and area A can be changed by stress in kPa for a simulation. Although these model no include other variables like sharpness according to (Stachowiak, 1998; Stachowiak, 2000; Stachowiak & Stachowiak, 2001), we can use it as a simple for a next modelling. The results of DEM simulation of soil flow (force and velocity) are transformed to an algorithm for an each node on the surface boundary. Boundary nodes moving depend on results according to Eq. 9 and after then the mesh generator design a new mesh (Fig. 5). This algorithm continuously calculates stress analysis in FEM for a new mesh dimension.

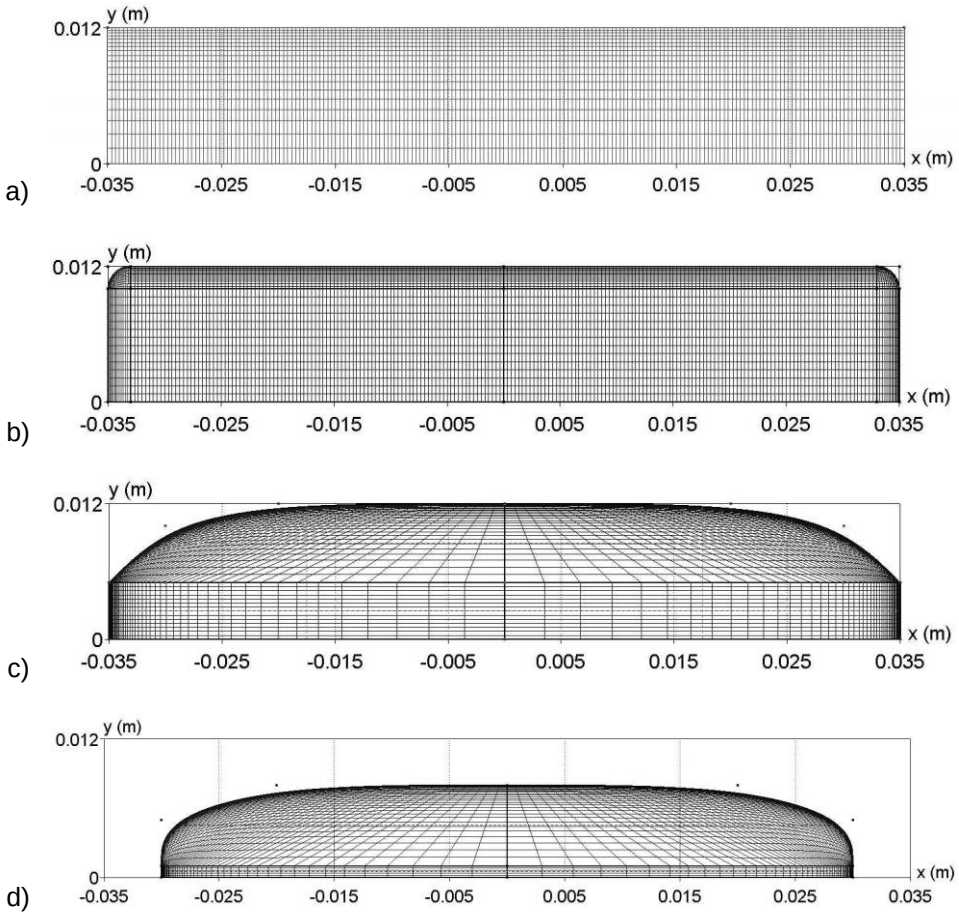

Figure 5. Cross section area of chisel mesh model; a) new chisel; b) 1 km distance; c) 5 km distance; d) 15 km distance.

Full new chisel model and worn chisel are presented in Fig. 7.

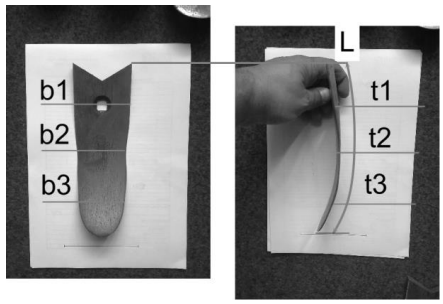

Figure 6. Real worn chisel after 15 km distance.

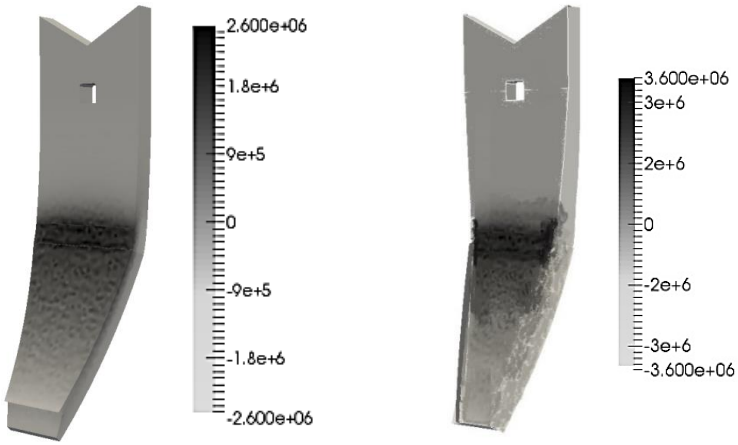

Figure 7. 3D Model of stress fields a new and worn chisel after 5 km.

Modelled and experimental measured data of thickness and width of chisel are presented in Fig. 8. The data showed good a correlation between modelled and measured the shape of chisel but residua are higher than 10%. Residues can be caused by larger abrasive particles of soil in the testing field, which were carried out practical field tests. Although the model showed similar soil moisture content. It can be caused by the mineral composition of soil, and that the soil contained a larger volume alumina silicates (Chotěborský & Linda, 2016), which are harder than sand and there are also sharper (Singh et al., 2006). Nevertheless, it is possible above procedure successfully applied for an overview of changes in shape during no-tillage. It is also possible to predict the traction resistance with the change of shape. However, our goal was to developed algorithms involving complex calculation chisel from the design of heat treatment to wear with an estimated stress in chisel, which leads to rupture or plastic deformation of the chisel during no-tillage agriculture operations. Especially, when the tip of chisel is protected by WC–Co sintered carbide with high wear resistance properties. This procedure is time-consuming for processor time, however, in our opinion is more accurate than the mathematical model based on experimental description change of

shape of chisel or ploughshare, for example as shown example GLM model (Arvidsson et al., 2004) or description of neural networks.

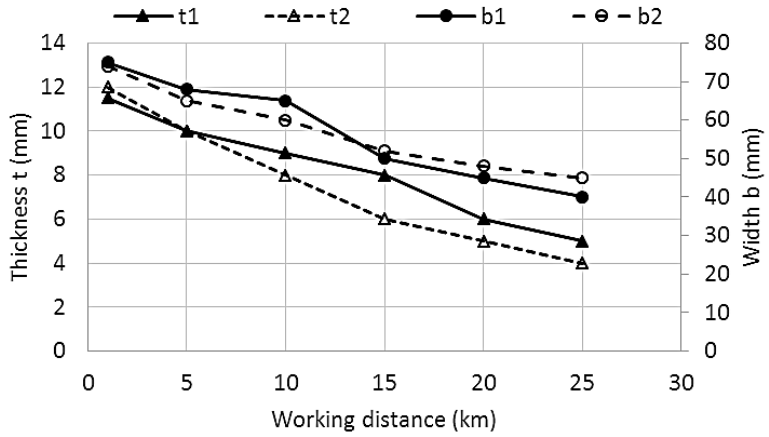

Figure 8. Thickness and width of the chisel, where t1 – measured thickness, t1 – modelled thickness, b1 – measured width (means) and b2 – modelled width.

CONCLUSIONS

The results presented in this article can be summarized in the following conclusions:

The algorithm is applicable for analysing stress of worn chisel. The results showed a good correlation between the measured data of shape changes in soil and modelled shape during wear.

The algorithm is time-consuming in case of one treated processing.

ACKNOWLEDGEMENTS. Supported by 31140/1414/314107 Technological agency of Czech Republic, 'R & D of working tools for agricultural machines'.

REFERENCES

Abo-Elnor, M., Hamilton, R. & Boyle, J. 2004. Simulation of soil–blade interaction for sandy soil using advanced 3D finite element analysis. *Soil and Tillage Research* **75**(1), 61–73.

Abu-Hamdeh, N. 2003. A nonlinear 3D finite element analysis of the soil forces acting on a disk plow. *Soil and Tillage Research* **74**(2), 115–124.

Aluko, O. B. & Chandler, H. W. 2004. Characterisation and Modelling of Brittle Fracture in Two-dimensional Soil Cutting. *Biosystems Engineering* **88**(3), 369–381.

Araya, K. & Gao, R. 1995. A Non-linear Three-Dimensional Finite Element Analysis of Subsoiler Cutting with Pressurized Air Injection. *Journal of Agricultural Engineering Research* **61**(2), 115–128.

Arvidsson, J., Keller, T. & Gustafsson, K. 2004. Specific draught for mouldboard plough, chisel plough and disc harrow at different water contents. *Soil and Tillage Research* **79**(2), 221–231.

Asaf, Z., Rubinstein, D. & Shmulevich, I. 2007. Determination of discrete element model parameters required for soil tillage. *Soil and Tillage Research* **92**(1–2), 227–242.

ASTM G65-04. Standard Test Method for Measuring Abrasion Using the Dry Sand/Rubber Wheel Apparatus (2010).

Bentaher, H., Ibrahmi, A., Hamza, E., Hbaieb, M., Kantchev, G., Maalej, A. & Arnold, W. 2013. *Finite element simulation of moldboard–soil interaction*. *Soil and Tillage Research* **134**.

Borys, N. & Küüt, A. 2016. The influence of basic soil tillage methods and weather conditions on the yield of spring barley in forest-steppe conditions. *Agronomy Research* **14**(2), 317–326.

Coetzee, C.J. & Els, D.N.J. 2009. Calibration of granular material parameters for DEM modelling and numerical verification by blade–granular material interaction. *Journal of Terramechanics* **46**(1), 15–26.

De Pellegrin, D. & Stachowiak, G.W. 2001. New technique for measuring particle angularity using cone fit analysis. *Wear* **247**(1), 109–119.

Farid Eltom, A.E., Ding, W., Ding, Q., Ali, A. baker B. & Eisa Adam, B. 2015. Effect of trash board on moldboard plough performance at low speed and under two straw conditions. *Journal of Terramechanics* **59**, 27–34.

Guo, L., Jirigalantu, & Zhang, F.C. 2012. The Load Analysis of Chisel-Edge Ruling Tool for Diffraction Gratings. *Applied Mechanics and Materials* **182–183**, 1596–1599.

Chen, Y., Munkholm, L.J. & Nyord, T. 2013. A discrete element model for soil–sweep interaction in three different soils. *Soil and Tillage Research* 126, 34–41.

Chotěborský, R. & Linda, M. 2015. FEM based numerical simulation for heat treatment of the agricultural tools. *Agronomy Research* **13**(3).

Chotěborský, R. & Linda, M. 2016. Determination of chemical content of soil particle for abrasive wear test. *Agronomy Research* **14**.

Jørgensen, M.H. 2014. Adaptive tillage systems. *Agronomy Research* 12(1), 95–100.

Karmakar, S., Kushwaha, R.L. & Laguë, C. 2007. Numerical modelling of soil stress and pressure distribution on a flat tillage tool using computational fluid dynamics. *Biosystems Engineering* **97**(3), 407–414.

Li, X., Miodownik, A.P. & Saunders, N. 2001. Simultaneous calculation of mechanical properties and phase equilibria. *Journal of Phase Equilibria* **22**(3), 247–253.

Liu, C.C., Xu, X.J. & Liu, Z. 2003. A FEM modeling of quenching and tempering and its application in industrial engineering. *Finite Elements in Analysis and Design* **39**(11), 1053–1070.

Mak, J., Chen, Y. & Sadek, M.A. 2012. Determining parameters of a discrete element model for soil–tool interaction. *Soil and Tillage Research* **118**, 117–122.

Maksarov, V. & Olt, J. 2008. Analysis of the rheological model of the process of chip formation with metal machining. *Agronomy Research* **6**, 249–253.

Mouazen, A. M. 2002. Mechanical behaviour of the upper layers of a sandy loam soil under shear loading. *Journal of Terramechanics* **39**(3), 115–126.

Mouazen, A.M. & Neményi, M. 1999. Finite element analysis of subsoiler cutting in non-homogeneous sandy loam soil. *Soil and Tillage Research* **51**(1), 1–15.

Mouazen, A.M. & Ramon, H. 2002. A numerical–statistical hybrid modelling scheme for evaluation of draught requirements of a subsoiler cutting a sandy loam soil, as affected by moisture content, bulk density and depth. *Soil and Tillage Research* **63**(3), 155–165.

Natsis, A., Petropoulos, G. & Pandazaras, C. 2008. Influence of local soil conditions on mouldboard ploughshare abrasive wear. *Tribology International* **41**(3), 151–157.

Pietrzyk, M. & Kuziak, R. 2011. Computer aided interpretation of results of the Jominy test. *Archives of Civil and Mechanical Engineering* **11**(3), 707–722.

Rajaram, G. & Erbach, D. 1998. Drying stress effect on mechanical behaviour of a clay-loam soil. *Soil and Tillage Research* **49**(1–2), 147–158.

Rojek, J., Oñate, E., Labra, C. & Kargl, H. 2011. Discrete element simulation of rock cutting. *International Journal of Rock Mechanics and Mining Sciences* **48**(6), 996–1010.

Scilab Enterprises. 2016. Scilab. France. *http://www.scilab.org/.* Accessed 21.11.2016

Sima, J., Jiang, M. & Zhou, C. 2014. Numerical simulation of desiccation cracking in a thin clay layer using 3D discrete element modeling. *Computers and Geotechnics* **56**, 168–180.

Singh, C.K., Kumar, P., Kumar, A. & Mukherjee, S. 2015. Depositional environment in great Indian desert using grain size parameters and its chemical characterization. *Journal of the Geological Society of India* **86**(4), 412–420.

Singh, M., Mondal, D.P. & Das, S. 2006. Abrasive wear response of aluminium alloy-sillimanite particle reinforced composite under low stress condition. *Materials Science and Engineering A* **419**(1–2), 59–68.

Stachowiak, G. & Stachowiak, G. 2001. The effects of particle characteristics on three-body abrasive wear. *Wear* **249**(3–4), 201–207.

Stachowiak, G.W. 1998. Numerical characterization of wear particles morphology and angularity of particles and surfaces. *Tribology International* **31**(1–3), 139–157.

Stachowiak, G.W. 2000. Particle angularity and its relationship to abrasive and erosive wear. In *Wear* **241**, 214–219.

Tagar, A.A., Ji, C., Ding, Q., Adamowski, J., Chandio, F.A. & Mari, I.A. 2014. Soil failure patterns and draft as influenced by consistency limits: An evaluation of the remolded soil cutting test. *Soil and Tillage Research* **137**, 58–66.

Tang, C.-S., Shi, B., Liu, C., Suo, W.-B. & Gao, L. 2011. Experimental characterization of shrinkage and desiccation cracking in thin clay layer. *Applied Clay Science* **52**(1–2), 69–77.

van Wyk, G., Els, D.N.J., Akdogan, G., Bradshaw, S.M. & Sacks, N. 2014. Discrete element simulation of tribological interactions in rock cutting. *International Journal of Rock Mechanics and Mining Sciences* **65**, 8–19.

Vogel, H.-J., Hoffmann, H. & Roth, K. 2005. Studies of crack dynamics in clay soil. *Geoderma* **125**(3–4), 203–211.

Woldman, M., Tinga, T., Van Der Heide, E. & Masen, M.A. 2015. Abrasive wear based predictive maintenance for systems operating in sandy conditions. *Wear* **338–339**, 316–324.

Woldman, M., van der Heide, E., Schipper, D.J., Tinga, T. & Masen, M.A. 2012. Investigating the influence of sand particle properties on abrasive wear behaviour. *Wear* **294–295**, 419–426.

Xie, J. Bin, Wu, C.C., Fan, J., Fu, M. & Hu, D.F. 2013. Numerical Simulation on the Temperature Field of Steel 1045 Quenched by Different Hardening Media. *Applied Mechanics and Materials* **444–445**, 1222–1228.

Zhu, L., Cheng, X., Peng, S.-S., Qi, Y.-Y., Zhang, W.-F., Jiang, R. & Yin, C.-L. 2016. Three dimensional computational fluid dynamic interaction between soil and plowbreast of horizontally reversal plow. *Computers and Electronics in Agriculture* **123**, 1–9.

Agronomy Research **15**(S1), 981–998, 2017

Experimental analysis of combustion process in SI Engine using ethanol and ethanol-gasoline blend

M. Gailis[1,2*] and V. Pirs[2]

[1]Riga Technical University, Faculty of Mechanical Engineering, Transport and Aeronautics, Department of Automotive Engineering, Viskalu 36A, LV 1006 Riga, Latvia
[2]Latvia University of Agriculture, Faculty of Engineering, Motor Vehicle Institute, Liela street 2, LV 3001 Jelgava, Latvia
[*]Correspondence: maris.gailis@rtu.lv

Abstract. Effect of fuel composition and ignition timing on combustion parameters of spark ignition (SI) port fuel injection (PFI) engine had been studied experimentally. The engine was fuelled with an ethanol and ethanol-gasoline blend E85. The engine was operated at steady speed at 1,500 min^{-1} and four load points have been used. Minimal ignition timing advance for maximal brake torque (MBT) at stoichiometric air/ fuel ratio for the tested fuels were found. The fuels were tested at their respective MBT timing and gasoline MBT timing. MBT timing was retarded by 8–11% for ethanol and 5–10% for E85 fuel, comparing to gasoline MBT timing. Indicated mean effective pressure (IMEP) was not affected by ignition timing in tested conditions. Maximal cylinder pressure was increased and flame development phase was extended, when gasoline MBT was used with fuels with high ethanol content at tested conditions.

Key words: Spark ignition, MBT, E85, bio fuel, renewable fuel, heat release, burn duration, combustion, IMEP.

INTRODUCTION

Spark ignition (SI) engine can be fuelled with different fuel types. In Baltic States, most common fuels are of fossil origin, such as gasoline and liquefied petrol gas (LPG). There are commercial fuels that are made from or partially contain renewable resources. For SI engine, these so called 'drop-in fuels', where bioethanol is blended with gasoline. In Latvia, gasoline with research octane number RON95 contain 5% vol. of anhydrous bioethanol. Gasoline-ethanol blend E85 contain approximately 75…85% vol. of anhydrous bioethanol, depending on season. In contrary to RON95, E85 is suitable as fuel only for specially designed or converted automobiles, commonly known as 'Flex-fuel vehicles' (FFV). Primary reason for it is different air-fuel ratio, comparing ethanol and typical gasoline. Fuel supply system material compatibility with ethanol is another issue.

Fuel type conversion of SI engine equipped automobiles is a common practise, particularly in Lithuania and Latvia. For economic reasons, most vehicle fuel type conversions Latvia and Lithuania nowadays are gasoline-LPG conversions. According to report of European Commission (2015), at time of the report there were 1,000 LPG

vehicles in Estonia, 48,368 in Latvia and 210,000 in Lithuania. The conversion to LPG cost up to 600–3,000 EUR for passenger vehicle and is followed by additional regular maintenance costs (European Commission, 2015).

First generation biofuels, such as fatty acid methyl-ester (FAME) and bioethanol, compete with land use for food production. Second generation biofuels are produced from biomass, that cannot be used as food or feed. Production of bioethanol as second generation biofuel, from agricultural waste, has been started at commercial scale in Italy, Spain and other EU countries. Tax incentives for fuel containing high ratio of bioethanol currently are applied several EU countries, including Lithuania and Latvia (European Commission, 2015). Variations in oil price may rise interest for gasoline-E85 conversion of passenger vehicles, equipped with SI engines.

Kotek et al. (2015) investigated injection timing using fuel with high ethanol ratio in SI port injection engine. They found that injection timing adaptation range of original engine control unit (ECU) was limited and additional control unit (ACU) can be successfully used to extend injection pulse and allow operation of the engine, designed for gasoline use, on E85.

Küüt et al. (2011) performed comparative performance tests on test engine, equipped with commercial Flex-fuel adapter. They used regular gasoline, pure ethanol and farmstead bioethanol. Comparing ethnol fuels, higher engine power was observed using ethanol, and higher efficency was observed in case of farmstead bioethnol.

Čedík et al. (2014) investigated effect of E85 in SI engine on harmful exhaust emissions. Test, using unmodified ECU yielded increased NOx emissions, comparing to gasoline use, which can be attributed to lean air-fuel mixture. Use of adapter for injection pulse extension resulted in lower NOx emissions but increase of HC and CO emissions, comparing to use of E85 and gasoline with unmodified ECU. The obtained results can be attributed to poor adaptation of air-fuel mixture in transient conditions and non-optimal ignition advance for E85 fuel.

Costagliola et al. (2013) investigated combustion efficiency and engine-out emissions using instrumented conventional SI engine, using gasoline-ethanol splash blends from E10 up to E85. Air-fuel ratio was kept close to stoichiometric and ignition advance optimized for each type of test fuel. Ignition advance reduced up to 3% with increase in ethanol content in fuel. They reported slightly shorter flame development and main combustion phase for E85 fuel, comparing to other test fuels. Differences in combustion phasing between fuels were reported as insignificant. Thermal load of engine head was not affected by fuel composition. Use of E85 increased global efficiency and significant reduction of regulated exhaust emissions – NOx, HC and CO. Using E85, aldehyde emissions were increased twice, and benzene emissions reduced by 50%, comparing to gasoline.

Melo et al. (2012) tested combustion and emission characteristics using hydrous ethanol and gasoline blends at different volumetric ratios, up to 100% hydrous ethanol (H100). Ignition advance was knock and exhaust gas temperature limited and increased with increase of ethanol content. Variations in ignition advance between fuels strongly influenced combustion phasing and made difficult to compare and evaluate results. CO and HC emissions were reduced, aldehyde emissions increased with increase of ethanol content. H100 showed highest thermal efficiency among tested blends. Results of NOx emissions were inconsistent.

Yoon & Lee (2012) studied effects of anhydrous bioethanol on exhaust emissions and engine performance. They performed engine speed sweep at wide open throttle conditions. Ethanol and regular gasoline, both at respective MBT ignition timing was used. Combustion pressure, brake mean effective pressure was increased and brake specific emissions of CO, HC and NOx were reduced using ethanol, comparing to gasoline. Increased cylinder pressure was explained with increased volumetric efficiency due to high heat of vaporization and heat capacity of ethanol.

Dirrenberger et al. (2014) measured laminar burning velocity of gasoline and gasoline-ethanol blend. They found that ethanol content up to 15% vol. in gasoline blend does not significantly change laminar burning velocity. Ethanol had higher laminar burning velocity, comparing to gasoline. Difference in burning velocity was larger at mixture equivalence ratio from 0.8 to 1.4. Higher laminar burning velocity of ethanol may indicate, that at non-knocking combustion conditions ignition timing should be retarded for ethanol fuel, comparing to regular gasoline.

Literature studies show that use of ethanol or gasoline blends with high ethanol content have potential for rising SI engine thermal efficiency and decreasing of regulated exhaust emissions. Best results were reported, when both air-fuel ratio and ignition timing was controlled and adjusted to match fuel requirements.

It is generally understood, that for normal engine operation air/ fuel ratio (AFR) must be corrected, if gasoline SI engine is being converted to use high ethanol content fuel (Pirs & Gailis, 2013). Various methods for AFR correction are developed and commercialized, employing ethanol concertation sensor (Wang et al., 2008, McKay et al., 2012), exhaust gas oxygen sensor (Ahn et al., 2008) and in-cylinder pressure (Oliverio et al., 2009). Effect of ignition timing less addressed in research, connected with fuel type conversion. Difference between laminar flame speed between ethanol and gasoline diminishes with increase of pressure (Aleiferis et al. 2013), and most the research is performed in wide open throttle (WOT) mode.

The aim of this study is to evaluate effect of non-optimal (gasoline MBT) ignition timing on combustion phasing using ethanol and E85 fuel at stoichiometric AFR and part load steady state conditions. The results provide insight of combustion behaviour of high ethanol content fuels in case when ignition timing is adjusted gasoline use.

MATERIALS AND METHODS

Test Fuels

Two samples of fuel were used in this study – bioethanol-gasoline blend (E85) and neat hydrous bioethanol (E96). E85 was purchased at commercial gasoline station 'Lukoil'. E96 was obtained from ethanol producer 'Jaunpagasts Plus'. Properties of test fuels are included in Table 1. Ethanol content was taken from quality certificates. Density was measured using aerometer. Other parameters were found in the literature. Commercial gasoline RON98 in this study was used as reference fuel for finding gasoline MBT timing.

Table 1. Properties of test fuels

Fuel	E85	E96
Ethanol content, % vol.	84.5	96.2
Density at 15 °C, kg m^{-3}	784	792
Research octane number	101.5[b]	106.0[a]
Motor octane number	90.1[b]	87.0[a]
Lower heating value, MJ kg^{-1}	29.2[b]	26.9[a]
Laminar flame velocity, m s^{-1}	-	0.39[c]

[a] Heywood (1988); [b] Szybist et al. (2010); [c] Turner et al. (2011).

Research equippment

The experimental setup consisted of spark ignition engine equipped automobile, which was placed on chassis dynamometer, and instrumented for in-cylinder pressure measurement. Fuel consumption was measurement using *AVL KMA Mobile*. Surrounding air temperature during the tests was 20…23 °C and air pressure 101.4…101.6 kPa.

The test automobile was Renault Twingo, model C068 and production year 2003, equipped with manual gearbox. The engine was equipped with port fuel injection and static two coil ignition system. Characteristics the test engine are listed in Table 2. Original engine control unit (ECU) was replaced by user configurable ECU of type VEMS 3.6. Original oxygen sensor was replaced by wideband sensor Bosch LSU 4.2. Oxygen sensor signal was used for closed loop operation at defined air-fuel ratio. Original fuel injectors Siemens DEKA 873774 (fuel flow rate 100 cc min^{-1} at 3 bar) were replaced by Siemens DEKA 863409 with increased fuel flow rate 182 cc min^{-1} at 3 bar. Increased fuel supply rate of replaced injectors ensured sufficient fuel amount in case of E85 and E96 fuel. Spray angles for both injector types were similar. The experimental engine setup for cylinder pressure measurement is shown in Fig. 1.

Table 2. Characteristics of test engine (Renault S. A., 1996)

Parameter	Value
Producer and type	Renault D7F 702
Air supply	naturally aspirated
Cylinder setup	4 cylinder, in-line arrangement
Displacement volume, cm^3	1,149
Torque at 2,500 min^{-1}, Nm	93
Power at 5,250 min^{-1}, kW	43
Piston stroke and bore, mm	76.8 x 69.0
Compression ratio	9.65
Valves per cylinder	2
Opening of inlet valve, CAD ATDC	350
Closing of inlet valve, CAD BTDC	141
Opening of exhaust valve, CAD ATDC	148
Closing of exhaust valve, CAD BTDC	354

To enable fully sequential injection, camshaft position sensor was installed. External fuel tank and pump was used to make fuel change quick and complete. Altered fuel supply and engine control allowed operation and monitoring of the test engine with

any of test fuels at freely selected ignition advance and within necessary fuel–air ratio, which was controlled in closed loop mode.

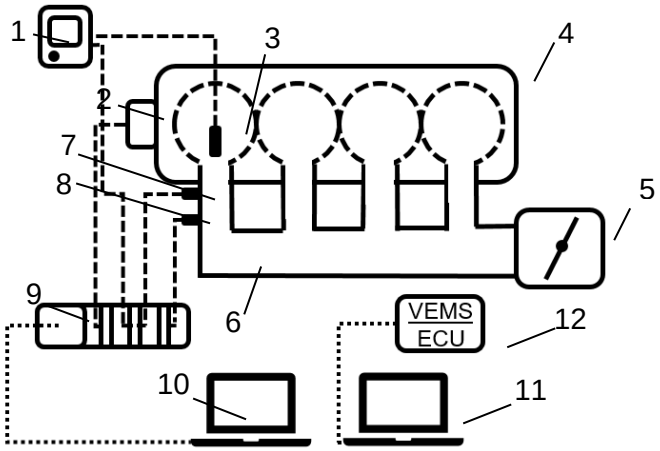

Figure 1. Cylinder pressure measurement setup: 1 – charge amplifier; 2 – crankshaft encoder; 3 – measuring spark plug; 4 – test engine; 5 – adjustable throttle valve; 6 – inlet manifold; 7 – inlet manifold pressure sensor; 8 – temperature sensor; 9 – data acquisition module; 10 – data acquisition control PC; 11 – ECU control PC; 12 – user controllable ECU.

To control inlet manifold pressure and engine load, engine throttle valve was equipped with screw type adjustor.

Engine synchronous measurement of cylinder pressure is taken using modified spark plug with pressure transducer Kistler 6118BD16 and charge amplifier Kistler 5018A. Crankshaft position and speed was detected using optical encoder Kistler 2613B, with resolution 0.1 crank angle degree (CAD). Inlet manifold pressure measurement was taken using GM039 absolute pressure sensor. Inlet air and exhaust gas temperature were measured using K-type thermocouples. Data acquisition was performed using National Instruments equipment, consisting of signal-specific modules and FPGA based controller. Cylinder pressure signal and manifold pressure signal were registered with module NI 9222. Inlet and exhaust temperature was registered using module NI 9214. Crankshaft encoder and camshaft signals were registered using NI 9752 module. Signal-specific modules were installed in NI cRIO 9068 chassis. LabVIEW code was developed, allowing monitoring of cylinder pressure and saving of data. Amplified cylinder pressure signal and manifold pressure sensor signal, synchronized with crankshaft position, and time data were registered in lossless manner with resolution 0.1 CAD.

Chassis dynamometer Mustang MD1750 was used to limit engine speed and absorb power. Dynamometer is equipped with large rollers with diameter 1.27 m and total inertial mass 1148 kg. Power is absorbed using eddy current brake. Combining large inertial mass of the rollers and PID control of the edgy current brake ensured stable rotational speed of the test engine during steady state test conditions.

Test Methodology

Automobile was placed and secured on the chassis dynamometer, engine started and warmed up to nominal coolant temperature at 90 ± 5 °C. Inlet air temperature was held at 42 ± 3 °C and fuel temperature was held at 41 ± 3 °C. Fuel/ air ratio was held close to stoichiometric ratio at all test conditions. Testing was conducted at steady state conditions at selected test points. Selected test points for this report are listed in Table 3. Part load points and engine speed for this report were selected, basing on increased differences in MBT timing for gasoline and ethanol fuels, comparing to conditions of higher engine speed and higher load.

Table 3. Selected test points

Engine speed, min^{-1}	Inlet manifold pressure, kPa
1,500	40
	50
	60
	70

At first stage of the research MBT ignition timing for all three test fuels at all selected test conditions were determined within limits of 0.5 CAD. 50% of cumulative heat release at 10 CAD after piston top dead centre (TDC) was chosen as criteria for MBT timing, according to Heywood (1988). Engine stabilization time at selected conditions before the measurement was 300 s. In case of fuel change engine was run for 1,200 s before measurement was taken. At each test point data of 150 consecutive engine cycles were collected. To statistically evaluate the results, each test was non-consecutively repeated five times.

Data Processing

MATLAB code for data post processing and report generation was developed. Apparent heat release rate (AHRR) was calculated for each engine cycle using Eq. 1) according to Stone (1999).

$$\frac{dQ_n}{d\varphi} = \frac{\gamma}{\gamma - 1} p \frac{dV}{d\varphi} + \frac{\gamma}{\gamma - 1} V \frac{dp}{d\varphi} \quad (1)$$

where: dQ_n – apparent heat release rate, J deg^{-1}; φ – crank angle degree; γ – ratio of specific heats; V – cylinder volume, m^3; p – cylinder pressure, Pa.

To partially compensate heat losses, motoring AHRR was calculated and subtracted from firing AHRR. Mean value of 150 consecutive engine cycles was used as test result.

Ratio of specific heats γ was calculated by finding polynomial fit coefficient for cylinder pressure and volume relation in logarithmic scale. Ratio of specific heats was calculated separately for compression and expansion stroke of each engine cycle and mean value was used for AHRR calculation.

Cumulative heat release (CHR) was calculated using Eq. (2) according to Heywood (1988).

$$Q_n = \int_{\varphi start}^{\varphi_{end}} \frac{dQ_n}{d\varphi} d\varphi \quad (2)$$

where: Q_n – cumulative heat release rate, J.

Relative cumulative heat release (HR) was calculated from CHR and stated in percent. HR was used for combustion phasing analysis. Flame development angle (FDA) was assumed as duration in CAD from spark discharge till 10% of HR. Rapid burning

angle (RBA) was assumed as duration in CAD from 10% till 90% of HR. Overall burning angle was assumed as sum of flame development and rapid burning angle.

Indicated work is calculated using Eq. (3) according to Heywood (1988).

$$W_i = \int_{\varphi start}^{\varphi_{end}} p\, dV \tag{3}$$

where: W_i – indicated work, J.

Gross indicated work is calculated only in compression and expansion strokes, so gas exchange work is excluded from the result. Indicated mean effective pressure ($IMEP$) is calculated from gross indicated work, using Eq. (4) according to Heywood (1988).

$$IMEP = \frac{W_i}{V_d} \tag{4}$$

where: $IMEP$ – indicated mean effective pressure, bar; V_d – displaced cylinder volume, m^3.

RESULTS AND DISCUSSION

The results present burn rate and burn phasing characteristics, using E85 and E96 fuels at MBT timing and for comparison, at gasoline MBT.

Ignition timing

Example of relative cumulative heat release (RCHR) trace is shown in Fig. 2. Lines, labelled 'MBT', correspond to fuel's respective MBT ignition timing. Lines, labelled 'MBT G' represent RCHR trace for respective fuel, tested with ignition advance, which matches gasoline MBT. At fuel's respective MBT, 50% of HR is achieved at 10 CAD after TDC. In case, when E96 and E85 are used with RON98 MBT ignition timing, start of heat release is over advanced for optimal timing. Comparing RCHR trace for all three test fuels at their respective MBT, heat release in case of RON98 appears retarded in late combustion phase, from 40 to 95 CAD.

Table 4. MBT ignition timing at engine speed 1,500 min^{-1}

Inlet manifold pressure, kPa	Test fuel	MBT ignition advance, CAD BTDC
40	E96	27.0
	E85	27.5
	RON98	30.5
50	E96	22.0
	E85	22.0
	RON98	24.0
60	E96	19.5
	E85	19.5
	RON98	21.5
70	E96	18.0
	E85	18.5
	RON98	19.5

Results of experimentally obtained MBT values for test fuels are shown in Table 4. Relatively small difference in MBT timing between E96 and E85 is found at 40 kPa and 70 kPa test conditions. Ignition timing is not limited by detonation, as no detonation was observed.

Results of RCHR trace for other test conditions repeated trend, shown in Fig. 2, and are omitted from this paper for a sake of brevity. The results are discussed in combustion phasing analysis subchapter.

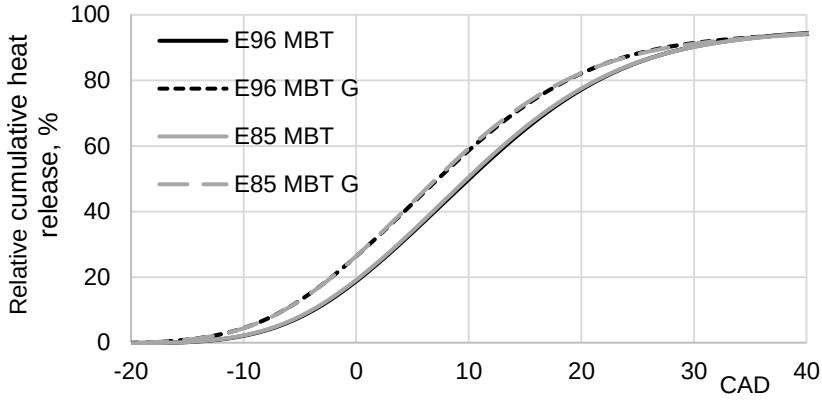

Figure 2. Relative cumulative heat release, engine speed 1,500 min^{-1}, inlet manifold pressure 40 kPa, stoichiometric air/ fuel ratio.

Relative difference of MBT ignition advance for E96 and E85 fuels, comparing to MBT ignition advance for RON98 is shown in Fig. 3.

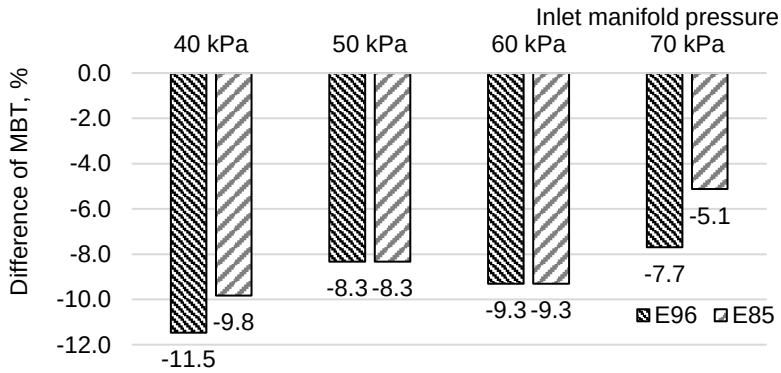

Figure 3. Relative difference of MBT advance, comparing to RON98 MBT, engine speed 1,500 min^{-1}, stoichiometric air/ fuel ratio.

Difference of MBT ignition advance between fuels with high bioethanol content and regular gasoline appears to be decreasing with increase of inlet manifold pressure and thus, increase in charge mass and cylinder pressure. The trend of differences agrees with findings of other researchers (Yücesu et al. 2006; Yoon et al., 2009; Costagliola et al., 2013). The relative difference which is reported in this paper is larger.

Indicated metrics and heat release analysis

Fuel consumption results are shown in Table 5. The data was used for calculation of theoretical energy input for heat release plots.

Fired and motored cylinder pressure trace and AHRR for E96 and E85 in case of inlet manifold pressure 40 kPa are shown in Fig. 4, a and c. MBT spark advance for E96 fuel is 27.0 CAD and 27.5 CAD for E85 fuel. MBT spark advance in case of RON98 is 30.5 CAD. In case where E96 and E85 are fired with ignition timing, which corresponds to gasoline MBT, both fuels show slightly higher AHRR and higher maximal cylinder pressure, comparing to test fuel's MBT timing. At MBT timing maximal cylinder pressure is phased at approximately 16 CAD ATDC. In case of over advanced timing, pressure is rising too early in engine cycle. Greater compression work and unnecessary mechanical stress on the engine parts is expected.

Ratio of specific heats was not significantly affected by ignition advance in tested range. The results are shown in Table 6. Mean value of compression and expansion was used in calculation of heat release.

Cumulative heat release trace and theoretical energy input are shown in Fig. 4, b & d.

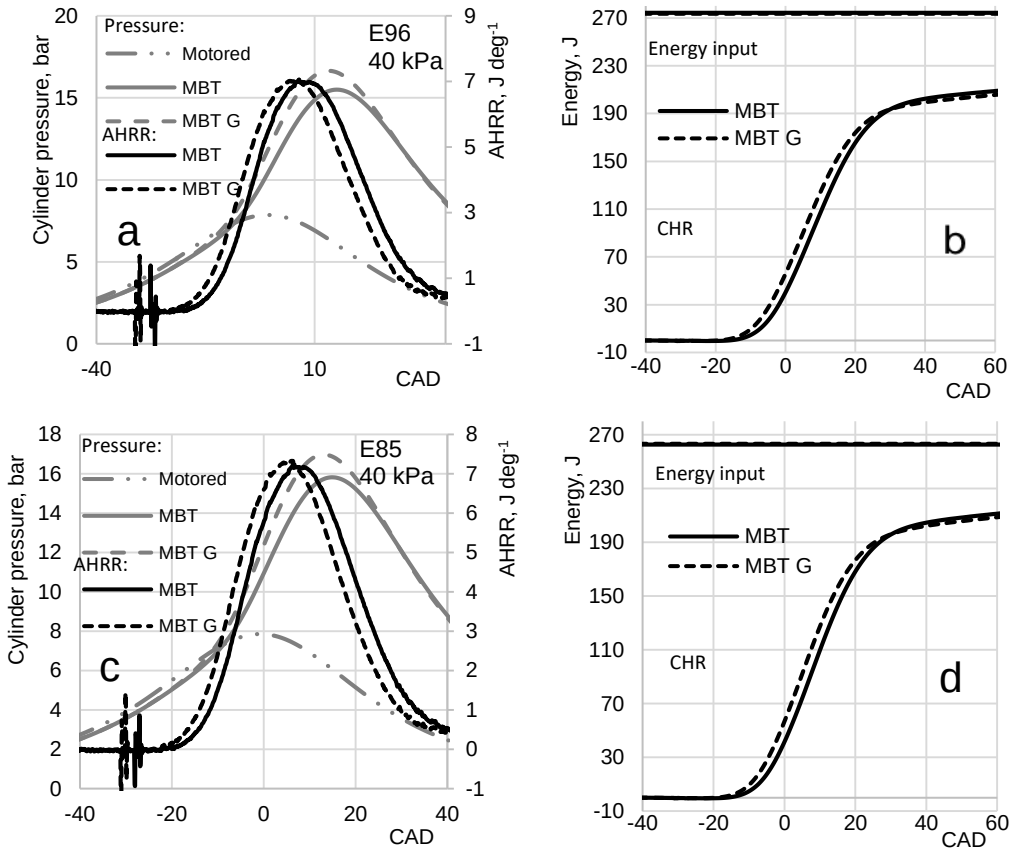

Figure 4. Cylinder pressure, apparent heat release rate and cumulative heat release, inlet manifold pressure 40 kPa. MBT – fuel's MBT timing, MBT G – gasoline MBT timing.

Table 5. Fuel consumption at engine speed 1,500 min^{-1}

Inlet Manifold pressure, kPa	Test fuel	Engine fuel consumption, kg h^{-1}
40	E96	0.46
	E85	0.41
50	E96	0.61
	E85	0.54
60	E96	0.76
	E85	0.68
70	E96	0.89
	E85	0.79

Table 6. Ratio of specific heats at engine speed 1,500 min^{-1}

Inlet manifold pressure, kPa	Test fuel	Compression	Expansion
40	E96	1.34	1.25
	E85	1.35	1.24
50	E96	1.34	1.25
	E85	1.35	1.24
60	E96	1.34	1.24
	E85	1.35	1.24
70	E96	1.34	1.24
	E85	1.35	1.24

Fired and motored cylinder pressure trace and AHRR for E96 and E85 in case of inlet manifold pressure 50 kPa are shown in Fig. 5, a & c. MBT spark advance for E96 and E85 fuel is 22.0 CAD. MBT spark advance in case of RON98 is 24.0 CAD. Start of heat release and pressure rise is advanced in engine cycle in case of gasoline MBT timing for E96 and E85 fuels, comparing to test fuel's MBT timing.

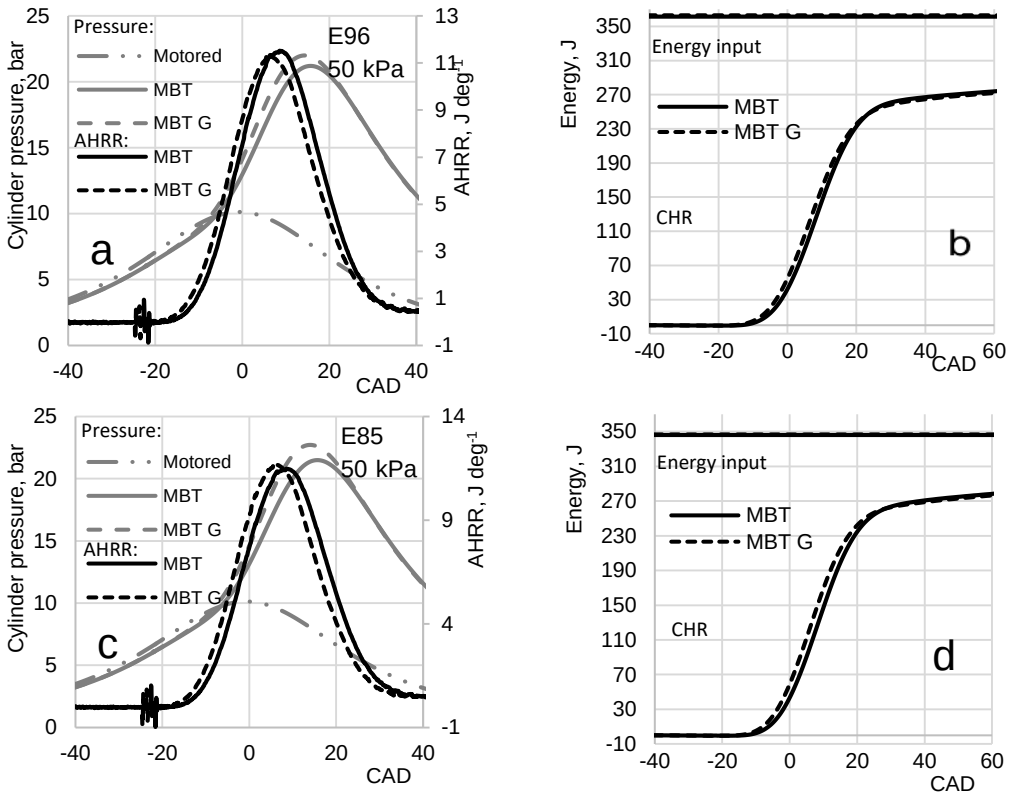

Figure 5. Cylinder pressure, apparent heat release rate and cumulative heat release, inlet manifold pressure 50 kPa. MBT – fuel's MBT timing, MBT G – gasoline MBT timing.

Fired and motored cylinder pressure trace and AHRR for E96 and E85 in case of inlet manifold pressure 60 kPa are shown in Fig. 6, a & c. MBT spark advance for E96 and E85 fuel is 19.5 CAD. MBT spark advance in case of RON98 is 21.5 CAD.

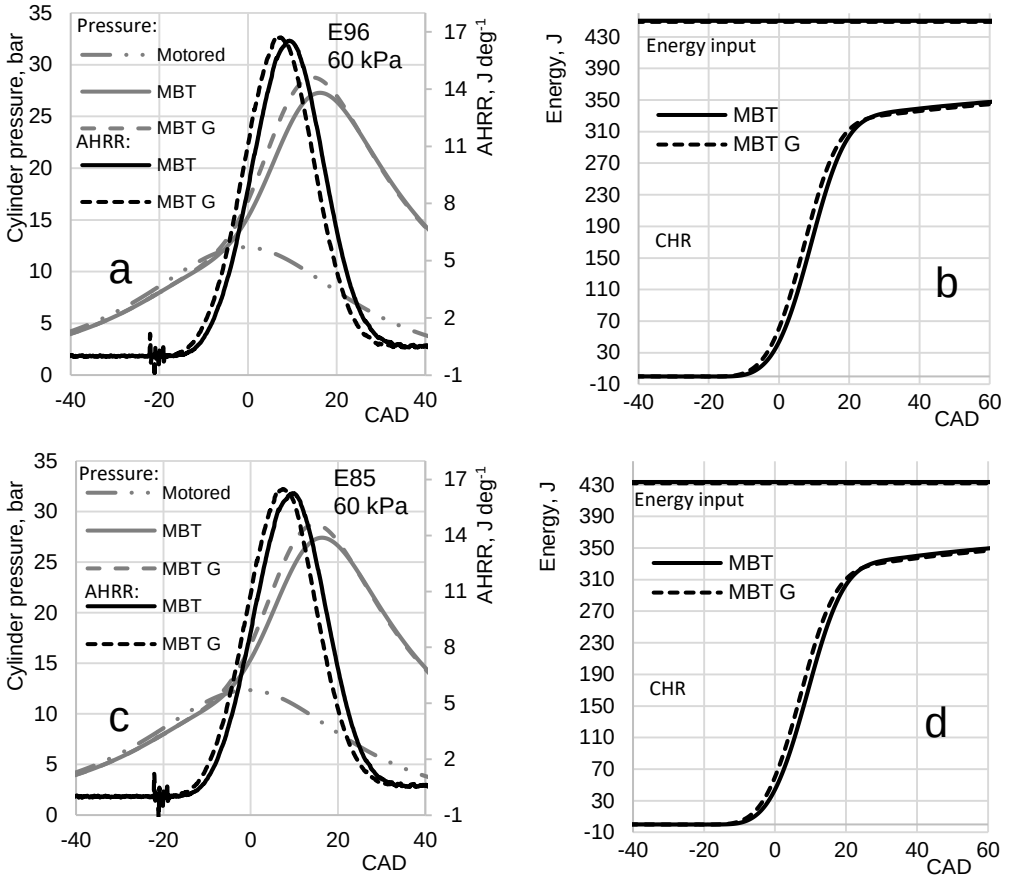

Figure 6. Cylinder pressure, apparent heat release rate and cumulative heat release, inlet manifold pressure 60 kPa. MBT – fuel's MBT timing, MBT G – gasoline MBT timing.

Fired and motored cylinder pressure trace and AHRR for E96 and E85 in case of inlet manifold pressure 70 kPa are shown in Fig. 7, a & c. MBT spark advance for E96 is 18.0 CAD and for E85 fuel is 18.5 CAD. MBT spark advance in case of RON98 is 19.5 CAD. Difference in MBT timing between fuels with high bioethanol content and pure gasoline is reducing with increase of inlet manifold pressure.

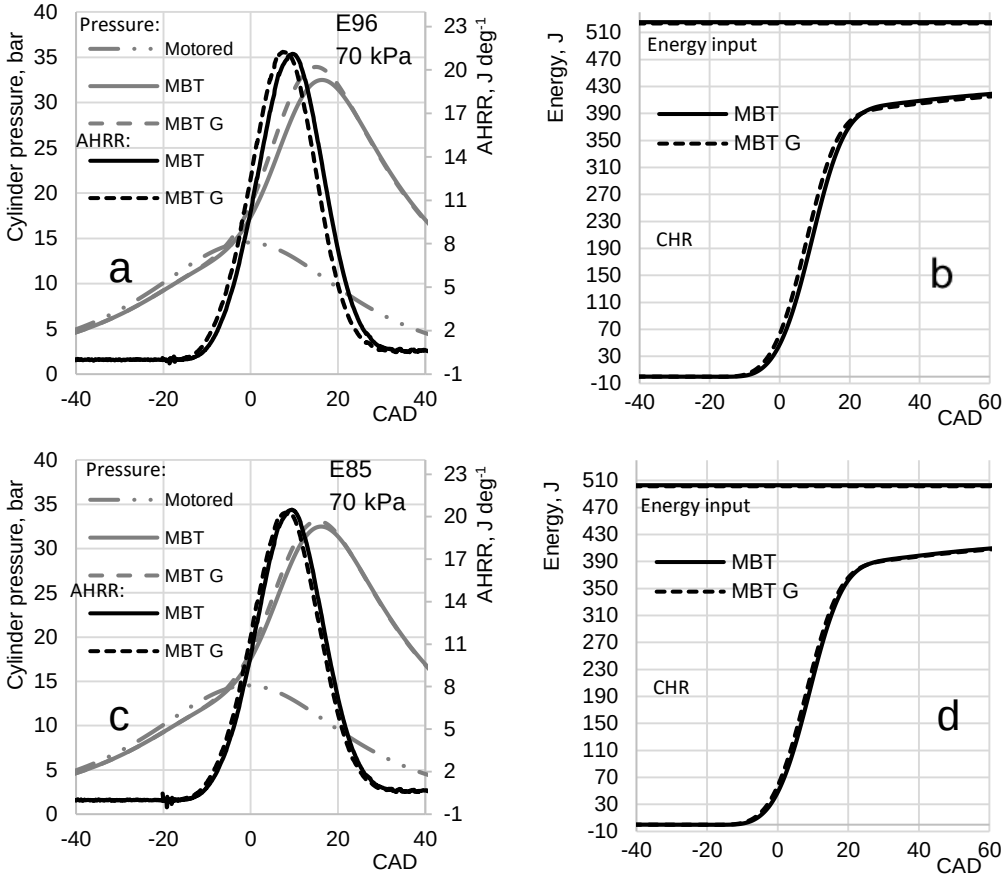

Figure 7. Cylinder pressure, apparent heat release rate and cumulative heat release, inlet manifold pressure70 kPa. MBT – fuel's MBT timing, MBT G – gasoline MBT timing.

Maximal cylinder pressure for all test conditions is shown in Fig. 8. Error bars in this and all following diagrams represent confidence interval, calculated with the significance $P = 0.05$. The difference of maximal cylinder pressure is statistically significant, comparing results at fuel's respective MBT and gasoline MBT. The difference can be attributed to ignition advance but engine temperature and environmental parameters might be influencing factors for maximal cylinder pressure. Increased maximal cylinder pressure may reduce engine life and affect exhaust emissions. Yoon et al. (2009) reported increased maximal cylinder pressure using ethanol, comparing to E85, both set at equal ignition timing. Increase of maximal cylinder pressure was attributed to increased volumetric efficiency caused by charge cooling effect of ethanol. As shown in Fig. 8, no significant differences in maximal cylinder pressure between test fuels were found in this research. Different load control method was used in this research, comparing to Yoon et al. (2009). The authors of this study controlled load by inlet manifold pressure, Yoon et al. (2009) controlled throttle valve position.

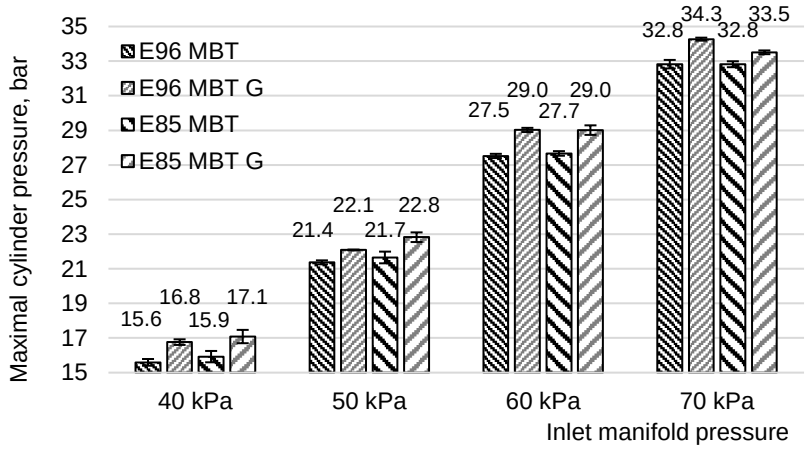

Figure 8. Maximal cylinder pressure at all test conditions.

Effect of variation of ignition advance close to MBT point on engine efficiency is expected to be insignificant. Gross IMEP, calculated for all test conditions, is shown in Fig. 9. Difference of IMEP at fuel's MBT and gasoline MBT is statistically insignificant. IMEP was larger for E85 fuel at test conditions when inlet manifold pressure is from 40 to 60 kPa, comparing to E96 fuel. At test conditions, when inlet manifold pressure is 70 kPa, IMEP is larger for E96 fuel, comparing to E85 fuel.

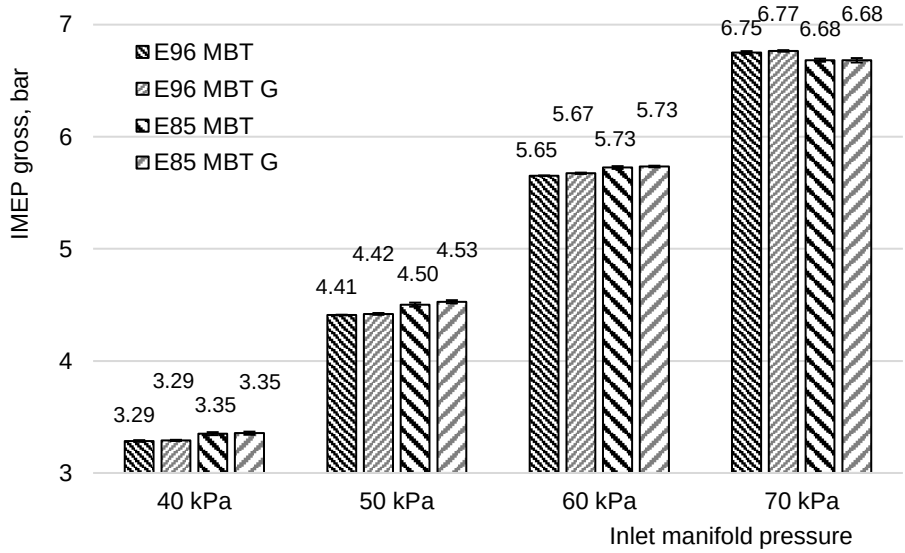

Figure 9. Gross indicated mean effective pressure at all test conditions.

Flame-development angle (FDA) is shown in Fig. 10. It is affected mainly by the mixture composition, pressure, temperature and motion in the close area of the spark plug discharge electrodes. As shown in Fig. 2, during FDA heat is being released at lower rate, comparing to following burning phase. In case of over-advanced ignition

timing (MBT G), flame-development phase is extended in all test conditions for E96 and E85 fuels, comparing to MBT timing. It can be attributed to lower pressure and temperature at the spark discharge in case of MBT G ignition timing. Difference between FDA of specific fuel (E85 or E96) appears to be decreasing with increase of inlet manifold pressure. In case of highest tested load, when inlet manifold pressure is 70 kPa, FDA of E85 appears to be extended, comparing to E96, with both MBT and MBT G ignition timing. The difference is small and statistically insignificant.

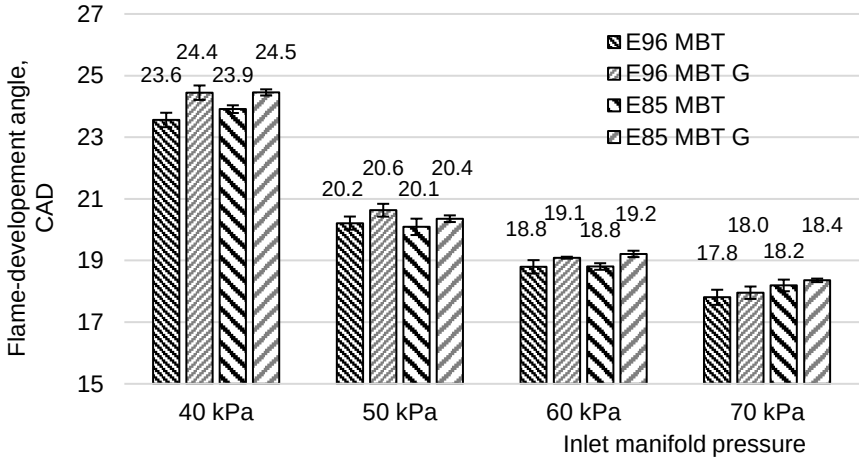

Figure 10. Flame-development angle at all test conditions.

End of flame-development phase is shown in Fig. 11. At MBT timing, flame development end phasing is close for both test fuels. At MBT timing, phasing of 50% of heat release is approximately 16 CAD after TDC. So, duration of heat release between 10% to 50% is approximately the same for both test fuels.

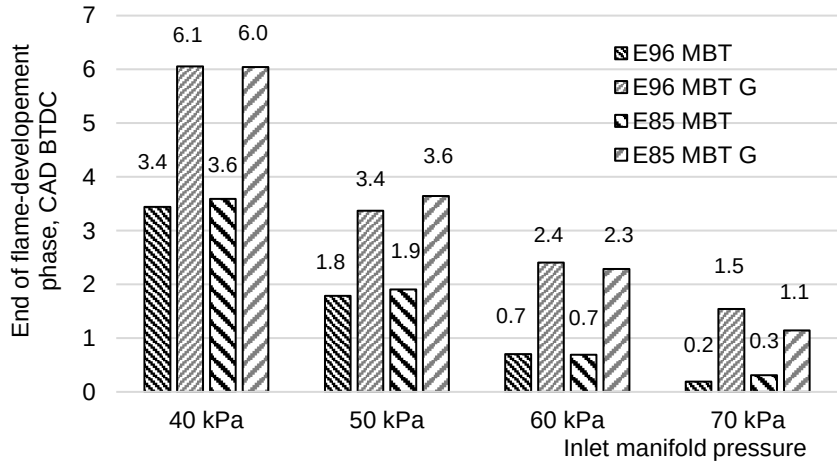

Figure 11. End of flame-development phase at all test conditions.

Combustion analysis, conducted in optically accessible engine using schlieren technique, reveals that at the beginning of combustion flame develops in near spherical form at spark plug electrodes. Surface of flame front is small at the early phase of combustion and it affects energy release rate. As flame front area increases, rate of energy release increases (Heywood, 1988).

In case of MBT G ignition timing, flame-development phase ends early in engine cycle. Comparing to MBT timing, more energy is released before TDC, while cylinder volume is still decreasing. Energy, which is released before TDC, does not contribute to useful work but unnecessary increase in-cylinder pressure. Rapid-burning angle (RBA) is shown in Fig. 12. At low load operating points (40 and 50 kPa), rapid-burning phase (RBP) appears to be extended in case of MBT G spark timing, comparing to MBT timing for both test fuels, but difference is statistically insignificant.

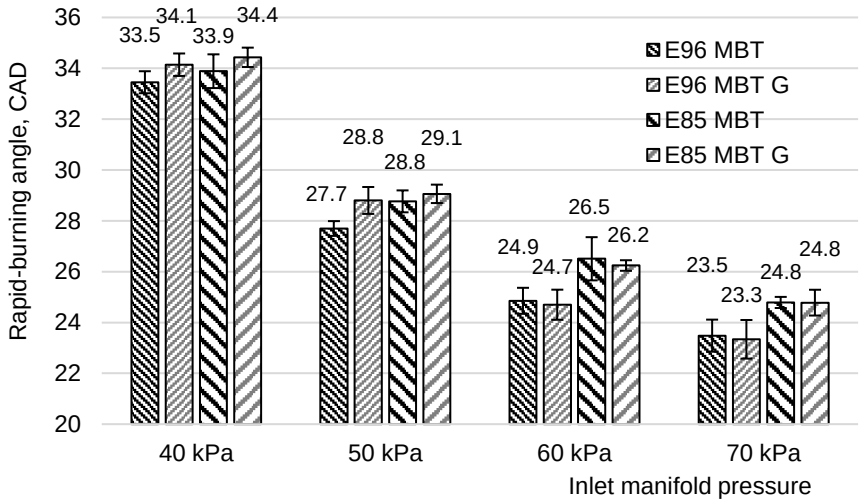

Figure 12. Rapid burn angle at all test conditions.

At higher load (60 and 70 kPa), effect of ignition advance on RBA is small, but difference between test fuels is large and statistically significant, which is in agreement with the findings of Yoon et al. (2009).

As shown in Fig. 11, at higher load (60 and 70 kPa), relatively larger part of RBP is located close to TDC in case of MBT G ignition timing for both test fuels. That may contribute to shorter RBA in those cases, comparing to MBT ignition timing.

Overall burning angle is the sum of FDA and RBA. As major part of combustion occurs during rapid-burning phase, the trend observed in RBA analysis is also present in overall burning angle, which is shown in Fig. 13. As inlet manifold pressure and engine load is increasing, influence of ignition timing is decreasing and influence of fuel chemical and physical properties of fuel is increasing. In case of MBT ignition timing, phasing of 10% and 50% of heat energy release for both test fuels, E96 and E85, are similar. Difference between test fuels increases at late part of combustion, when flame front is reaching combustion chamber wall.

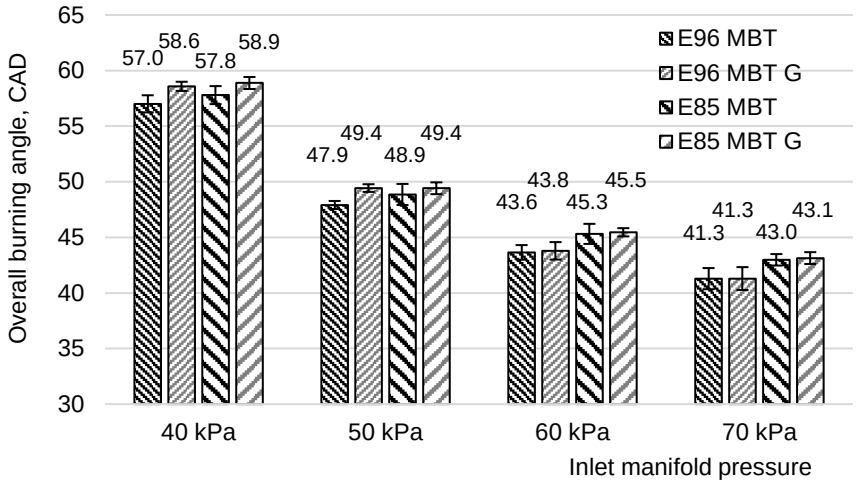

Figure 13. Overall burn angle at all test conditions.

CONCLUSIONS

Hydrous bioethanol and commercial grade ethanol-gasoline blend E85 were tested at steady state operating points using SI PFI engine. Following conclusions from this study can be made:

- MBT timing was retarded for high-ethanol content fuels, comparing to gasoline MBT timing. It can be attributed to faster laminar flame velocity of ethanol and fact, that detonation was not observed at tested conditions.
- Relative difference in MBT timing advance between pure gasoline and high-ethanol content fuels was decreasing with increase in engine load. The effect can be attributed to increasing relative importance of in-cylinder conditions over chemical properties of fuel.
- IMEP was not affected by over-advanced ignition timing in case of gasoline MBT. Increased cylinder pressure did not result in increase of useful engine output work but rather increased mechanical stress on engine parts and changed combustion phasing.
- At low load conditions IMEP was larger for E85 fuel and at highest tested load IMEP was larger for neat hydrous ethanol.
- Flame development angle was increased when gasoline MBT timing was used for high-ethanol content fuels. It can be attributed to lower pressure and temperature at combustion initialization.
- Rapid burning angle was increased at low load conditions when gasoline MBT timing was used for high-ethanol content fuels. Adverse effect was observed at high load conditions. It can be attributed to placement of combustion phases relative to TDC.
- E85 showed extended overall burning angle at high load conditions, comparing to hydrous ethanol. Overall burning angle my affect engine thermal efficiency, engine-out emissions and conditions in exhaust after treatment systems.

The results, presented in this paper are part of larger study on combustion efficiency and exhaust emissions, using and comparing gasoline and high-ethanol content blends. The results provide some insight in effect of fuel composition and ignition timing on combustion phasing in SI PFI engine. The results may useful in further analysis on requirements and potential benefits of converting gasoline SI engine for high-ethanol content fuel.

REFERENCES

Ahn, K., Stefanopoulou, A.G. & Jankovic, M. 2008. Estimation of Ethanol Content in Flex-Fuel Vehicles Using an Exhaust Gas Oxygen Sensor: Model, Tuning and Sensitivity. In: *ASME 2008 Dynamic Systems and Control Conference, Parts A and B.* Ann Arbor, p. 8 (In USA)

Aleiferis, P.G., Serras-Pereira, J. & Richardson, D. 2013. Characterisation of flame development with ethanol, butanol, iso-octane, gasoline and methane in a direct-injection spark-ignition engine. *Fuel* **109**, 256–278.

Costagliola, A. a., de Simio, L., Iannaccone, S. & Prati, M. V. 2013. Combustion Efficiency and Engine Out Emissions of a S.I. Engine Fueled with Alcohol/Gasoline Blends. *Applied Energy* **111**, 1162–1171.

Čedík, J., Pexa, M., Kotek, M. & Hromádko, J. 2014. Effect of E85 Fuel on Harmful Emissions – Škoda Fabia 1 . 2 HTP. *Agronomy Research* **12(**2), 315–322.

Dirrenberger, P., Glaude, P. A., Bounaceur, R., le Gall, H., Pires da Cruz, A., Konnov, A. A. & Battin-Leclerc, F. 2014. Laminar Burning Velocity of Gasolines with Addition of Ethanol. *Fuel* **115**, 162–169.

Heywood, J.B. 1988. *Internal Combustion Engine Fundamentals.* McGraw-Hill, New York, 930 p.

Kotek, T., Kotek, M., Jindra, P. & Pexa, M. 2015. Determination of the Optimal Injection Time for Adaptation SI Engine on E85 Fuel Using Self-designed Auxiliary Control Unit. *Agronomy Research* **13(**2), 577–584.

Küüt, A., Ritslaid, K. & Olt, J. 2011. Study of potential uses for farmstead ethanol as motor fuel. *Agronomy Research Biosystem Engineering Special Issue* **1**, 125–134.

McKay, B., VanVelzen, I., Guth, C., Achleitner, E. & Biber, P. 2012. An Onboard Ethanol Concentration Sensor for the Brazilian Market. In: *21st SAE Brasil International Congress and Exhibition.* São Paulo, p. 11 (In Brasil)

Oliverio, N.H., Jiang, L., Yilmaz, H. & Stefanopoulou, A.G. 2009. Modeling the effect of fuel ethanol concentration on cylinder pressure evolution in Direct-Injection Flex-Fuel engines. In: *2009 American Control Conference.* St. Louis, p. 8 (In USA)

Pirs, V. & Gailis, M. 2013. Research in use of fuel conversion adapters in automobiles running on bioethanol and gasoline mixtures. *Agronomy Research* **11**(1), 205–214.

Renault S. A., 1996. *Manual de reparation moteur D*. Renault, Bologne-Billancourt, 46 p.

Melo, T. C., Machado, G. B., Belchior, C. R. P., Colaço, M. J., Barros, J. E. M., de Oliveira, E. J. & de Oliveira, D. G. 2012. Hydrous ethanol–gasoline blends – Combustion and emission investigations on a Flex-Fuel engine. *Fuel* **97**, 796–804.

State of the Art on Alternative Fuels Transport Systems in the European Union 2015. http://ec.europa.eu/transport/sites/transport/files/themes/urban/studies/doc/2015-07-alter-fuels-transport-syst-in-eu.pdf. Accessed 20.1.2017.

Stone, R. 1999. *Introduction to Internal Combusiton Engines*. Third Edition. Palgrave Macmillian, New York . 641 p.

Szybist, J., Foster, M., Moore, W. R., Confer, K., Youngquist, A. & Wagner, R. 2010, Investigation of Knock Limited Compression Ratio of Ethanol Gasoline Blends. In : *Proceedings of SAE 2010 World Congress & Exhibition.* Detroit, p. 16 (In USA)

Turner, D., Xu, H., Cracknell, R. F., Natarajan, V. & Chen, X. 2011. Combustion performance of bio-ethanol at various blend ratios in a gasoline direct injection engine. *Fuel* **90**(5), 1999–2006.

Wang, S.S., Lin, Y., Resendiz, N.H., Granados, Luis E. & Rodriguez, H.H. 2008. Ethanol Concentration Sensor. In: *Proceedings SAE Powertrains, Fuels and Lubricants Meeting 2008.* Detroit, p. 8 (In USA)

Yoon, S.H., Ha, S.Y., Roh, H.G. & Lee, C.S. 2009. Effect of bioethanol as an alternative fuel on the emissions reduction characteristics and combustion stability in a spark ignition engine. Proceedings of the Institution of Mechanical Engineers, Part D: *Journal of Automobile Engineering* **7**(1), 941–951.

Yoon, S.H. & Lee, C.S. 2012. Effect of undiluted bioethanol on combustion and emissions reduction in a SI engine at various charge air conditions. *Fuel* **97**(1), 887–890.

Yücesu, H.S., Topgül, T., Çinar, C. & Okur, M. 2006. Effect of ethanol–gasoline blends on engine performance and exhaust emissions in different compression ratios. *Applied Thermal Engineering* **26**(17–18), 2272–2278.

Agronomy Research **15**(S1), 999–1005, 2017

Comparison of reliability of false rejection rate by monocriterial and multi-criteria of biometric identification systems

V. Hartová[1,*] and J. Hart[2]

[1]Czech University of Life Sciences Prague (CULS), Faculty of Engineering, Department of Vehicles and Ground Transport, Kamýcká 129, CZ165 21 Prague, Czech Republic
[2]Czech University of Life Sciences Prague (CULS), Faculty of Engineering, Department of Technological Equipment of Buildings, Kamýcká 129, CZ165 21 Prague, Czech Republic
[*]Correspondence: nverca@seznam.cz

Abstract. Biometric user identification is a highly topical theme these days. The most widespread areas are identification of a person on the basis of fingerprints and identification on the basis of facial features. Testing was performed on the 4 biometric systems. Systems using fingerprint were LA 2000M and iEvo ULTIMATE, and systems disposing even the scan faces were D-Station, IFace 800. Measurements showed that the higher reliability have biometric identification systems which identify the person on the basis of one parameter. From the results it is also seen that sabotage of biometric identification devices that identifies on the the basis of two or more parameters is much simpler than those that identify only using fingerprint or scan of face.

Key words: fingerprint, false rejection rates, false acceptance rates, identification.

INTRODUCTION

At present, identification based on biometric characteristics is being used ever more often. This method of identification of persons is user friendly, as it is not necessary to remember passwords or codes, and there is no need to carry around chips or RFID cards. The development of biometric systems was very extensive in the beginning of this scientific direction, and over time the development of new systems slowed and more attention was paid to the improvement of existing systems. Initially, systems identifying a user were created based on a single feature (fingerprints, face shape, bloodstream and others), while in recent years the trend of combined reading identification devices, e.g. a combination of fingerprint and facial scan, has spread (Rak, 2012; Stroica, 2012; Jazzar, 2013).

One of the most important parameters of biometric identification systems is reliability. These systems are used mainly in places where it is necessary to restrict access to people for whatever reason. We are increasingly seeing cases where these systems were compromised from a security standpoint and an unauthorized user broke into a guarded area. It is therefore important to continuously develop this branch of science by constantly inspecting and testing the correct functionality of existing biometric systems, all whilst designing improvements to existing systems from the obtained results (Jain & Feng, 2009; Yoon et al., 2012).

MATERIALS AND METHODS

Testing was focused on the reliability of dual biometric identification systems in comparison with the reliability of systems that identify only on the basis of one biometric method. Measurements were carried out in the security technology laboratory at the Technical Faculty of the Czech University of Life Sciences in Prague, and the measurements were carried out under laboratory conditions. These conditions are based on standards ČSN EN 50133, ČSN ISO/IEC 19794, ČSN ISO/IEC 19794, ČSN ISO/IEC 27006, ČSN ETSI EN 302 77, as well as on the recommendations of the relevant manufactures.

80 test subjects participated in the measurements. The testing was always done in twenty cycles. The test subjects were 16 women and 64 men aged 21–62. Two devices were selected for the measurements that only identified on the basis of fingerprints (scanner LA 2000M and scanner iEvo ULTIMATE), and two dual systems that identified on the basis of fingerprints and facial features (D-Station and IFace 800). Their basic parameters are shown in Table 1. All of these devices have optic sensors. These systems were selected on the recommendations of the manufacturer. Manufacturers recommend these device to use even in places with difficult conditions.

Table 1. The basic parameters of biometric devices (Information from the datasheet)

LA 2000M	iEvo ULTIMATE	D-Station	IFace 800
			
FRR	FRR	FRR	FRR
< 0.001%	< 0.001%	< 0.001%	< 0.001%
FAR	FAR	FAR	FAR
< 0.00001%	< 0.00001%	< 0.00001%	< 0.00001%
Fingerprint Capacity	Fingerprint Capacity	Fingerprint Capacity	Fingerprint Capacity
8 000	10 000	200 000	2 000
Operating Temperature	Operating Temperature	Operating Temperature	Operating Temperature
0 ~ 45 °C	-20 ~70 °C	-20 ~ 50 °C	0 ~ 45 °C
Matching Speed	Matching Speed	Matching Speed	Matching Speed
< 1sec	< 0.7 sec	< 1sec	≤ 1 sec
Sensor	Sensor	Sensor	Sensor
Optical	Optical	Optical	Optical

The use of the first optic sensors was recorded between the 1960s and 1970s. These sensors work on the basis of FTIR – Frustrated Total Internal Reflection technology. This is a laser beam or a thick bundle of optical fibres illuminating the surface of the

finger beds from below, which is placed to the transparent plate of the sensor. The reflected light flux is scanned by the CCD (Charge Couplet Device) element. Papillary lines and furrows determine the amount of reflected light, wherein the ridges reflect more light than the furrows. However, the CCD element does not use the reflection of light from the furrows as a means of evaluation (Rak, 2012; Stroica et al., 2012; Jazzar & Muhammad, 2013).

False rejection rates of a user. Such a situation means that an authorized user is not let into a building via the identification devices. If this happens rarely, the user repeats the entire identification process and is then admitted into the building. False rejection rates of a person can have many causes (incorrectly placed finger on the scanner, wet finger, cold finger, injured finger, dirty finger, etc.). The probability of the false rejection rates of a user can be calculated via the following formula:

$$FRR = \frac{NFR}{NEIA} 100[\%] \quad (1)$$

FRR – False Rejection Rates, NFR – Number of False Rejection, NEIA – Number of Enrolle Identification Attemps (Svozil, 2009).

The measurements were performed both under standard and difficult conditions, focusing on the different types of tests that can arise under realistic conditions. Tests were divided into the following:

- **standard identification –** this identification was carried out on washed, cleaned hands.
- **cold fingers** – it was first necessary to cool the fingers of the test subjects to the same temperature range from 20–25 °C. This was done using ice prepared into moulds. Each mould was treated with waterproof foil in order to prevent dampening the measured finger. This simulated the cold outdoor environment. Each measurement was preceded by a fifteen minute cooling of the finger and then the finger was placed on the surface of the sensor.
- **cooling of a damp finger** – for cooling a damp finger, the measurements were carried out in the same manner as for cooling a dry finger, except for the part with the waterproof foil. During the measurement the finger was cooled directly with the ice. As the ice melted it slightly dampened the skin of the finger. The finger was then not dried, which caused the required wet surface.
- **heated finger** – during this measurement, it was first necessary to determine a method for heating a finger to temperature range from 50–55 °C. Initially, the finger was heated with hot water in a container, but this method was rejected because the water cooled. In order to ensure the same conditions for all of the test subjects, and that the measurement was relevant, a USB (Universal Serial Bus) heater was chosen to heat the finger, to which a digital temperature sensor was attached. The heating temperature was constantly 55 °C, but it is necessary to expect temperature losses during the short movement of the finger from the heater to the sensor of the scanner. That is why the specified temperature range is from 50–55 °C.
- **soaked finger** – soaking of the finger was very important for the testing. Such a case may occur during normal work and domestic situations. The finger beds were soaked using water in a container. The liquid was heated to 40 °C using the USB

heater. Each subject dipped their finger for 20 minutes. After removing the finger from the water bath, it was dried with gauze and tested on the measuring panel.

- **blackened finger** – testing a blackened finger was chosen on the basis of practical experience. Hands are usually not washed before being scanned into the system. Smeared hands are common both at work and in private lives. A black washable marker with incomplete covering was used to simulate blackening and smeared hands. The test focused only on the hue rather than the micro particles of impurities, such as dirt, dust, etc.
- **finger with a layer of glue** – Testing with a layer of glue was selected as a substitute for similar materials such as silicone, adhesives and other lubricants which we encounter in practice in normal life. A thin layer of the glue was applied to the finger and the scan we done after five minutes, during which the glue only partially solidified. After each scan the surface of the scanner sensor was cleaned.
- **finger with a layer of instant glue** – instant glue was selected because it creates a solid hard coating. This coating is transparent and very thin. When the glue is applied and dries, the papillary lines are deteriorated and individual scanners make verifications according to these lines.
- **injured finger** – fingers are injured every day, and it was therefore necessary to also test such cases. The 80 test subjects were asked to evaluate the most common injuries, which included cuts, burnt finger beds and deterioration of the skin from grinding and pressure. These four types of injuries were divided amongst the test subjects.
- **dirty finger (soil)** – dust was used for these measurements acquired from a vacuum cleaner bag. The dust was mixed with peat and the required mixture was created. Each test subject rubbed this mixture between their palms before the measurement was carried out.

RESULTS AND DISCUSSION

The measurement results clearly show that the use of more modern, dual biometric readers is less secure. It is evident from Fig. 1 that identification is not one hundred percent accurate. Based on the results acquired from the standard identification, the measurements were then expanded to test under difficult conditions.

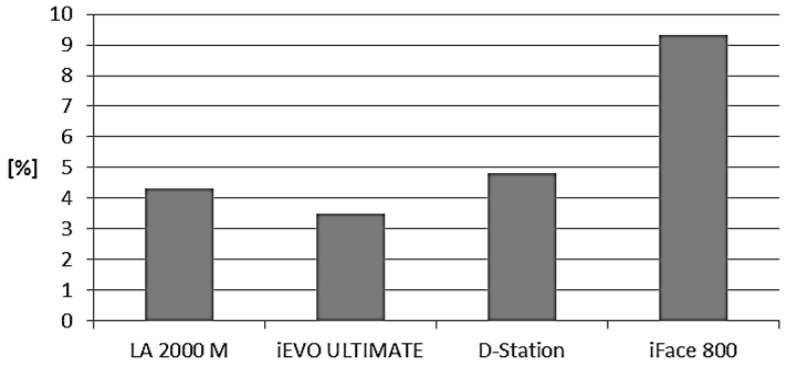

Figure 1. False rejection rates under standard conditions.

Measurement of systems reliability under difficult conditions unequivocally showed that the rate of FRR increased several fold. Fig. 2 shows the average value of errors (FRR) under adverse conditions.

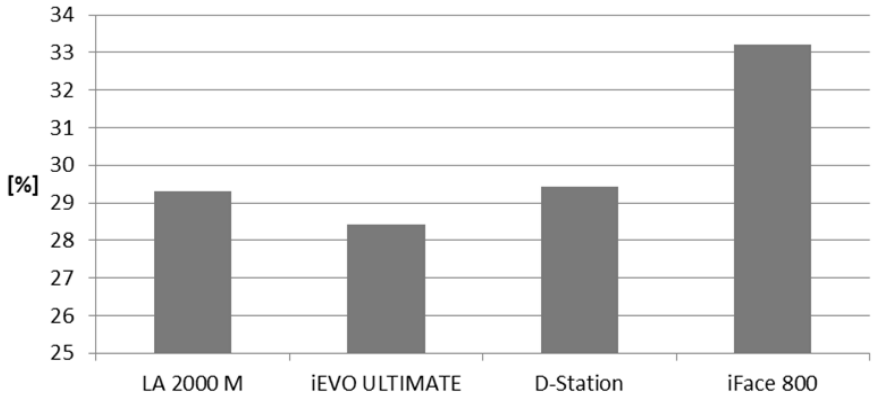

Figure 2. Average false rejection rates of adverse conditions.

Furthermore, using the of chi square test statistical method, a hypothesis was defined regarding whether the results of a standard FRR test on individual readers are consistent with FRR testing under adverse conditions. We will compare the calculated value of the test criterion with the corresponding quartile distribution $\chi 2$ (k - 1), i.e. with three degrees of freedom. For the 5% significance level, we will use $\chi 2$ (1 - α), i.e. quartile $\chi^2_{0,95} = 7.815$. The values of the tested criterion for the individual tests are given in Table 2.

Table 2. Chi square for testing under difficult conditions

	LA 2000M	iEVO ULTIMATE	D-Station	iFace 800	$\sum \chi 2$
cold fingers	0.032609	0.188616071	0.098214	0.006711409	0.3261505
cooling of a damp finger	2.264493	3.135044643	2.545455	0.167785235	8.1127772
heated finger	0.612319	0.251116071	0.207792	0.006711409	1.0779385
soaked finger	2.355978	4.152901786	4.444805	0.184983221	11.138668
finger with a layer of instant glue	2024.479	2534.652902	1858.092	881.9211409	7299.1449
dirty finger (soil)	532.8705	665.1607143	507.858	271.147651	1977.0368

The hypothesis is not rejected in the first and third cases, which means testing using cold fingers and a heated finger. For these statistical results we do not exceed the limits defining the critical field (7.815), and it is found in the field and on the 5% significance level. For tests using a soaked finger, cooling of a damp finger, a finger with a layer of instant glue and a dirty finger (soil), the calculated value of the test criterion exceeds the limit of defining the critical field (7.815), and we reject the hypothesis of the conformity of FRR results under adverse conditions and standard tests.

H0: The value of FRR of readers LA 2000 M and iEVO ULTIMATE (monocriterial readers) is the same as D-Station P (2) = 0.00127 and IFAC 800 (readers combined). Statistics was performed separately so that the results was relevant and so that each monocriterial reader was compared with each reader combined. They were used two-sample paired t-test with a fixed level of significance 0.05. Achieved statistical significance for two-sided test P (2) was for readers LA 2000 M and D-Station P(2) = 0.00127, for LA 200 M and iFace 800 P(2) = 0.000642, for iEVO ULTIMATE and D-Station P(2) = 0.000115 and for iEVO ULTIMATE and iFace 800 P(2) = 0.000528, which is in all cases less than the determination level of importance, and we therefore reject the hypothesis.

It is unnecessary to continue to develop new devices and new biometric methods unless the reliability of existing systems is improved. It is important for new systems to avoid the errors of the existing systems. These issues are also discussed by the author Yoon, who in his article 'Altered Fingerprints: Analysis and Detection', refers to the possibility of sabotaging systems through the creation of a synthetic fingerprint, etc. He also modifies the algorithm in order to be immune to this sabotage. In contrast, author Jain focused on the development of a new device for identification of a person. As a unique characteristic, he chose the entire surface of the palm. Compared to a small fingerprint, minutiae are more clearly visible on entire surface of the palms. The tests showed that the new device operates with 78% reliability, and it can thus be tested in practice (Jain & Feng, 2009; Yoon et al., 2012). Similar testing indicates Veronica Nídlová just right for readers destined into normal environments. (Nídlová, 2015)

Before purchasing an access biometric identification system, it is necessary to consult with professionals in the field and pay attention to the reliability of individual biometric systems. It is important to understand what areas or information we want to protect, and to adapt the choice of the biometric identification device with regard to this.

CONCLUSIONS

Today, the reliability of biometric identification systems is a very current issue. The measured values show that the first two scanners that identify a person solely on the basis of a fingerprint are much more reliable than dual scanners.

These results: for readers LA 2000 M and D-Station P(2) = 0.00127, for LA 200 M and iFace 800 P(2) = 0.000642, for iEVO ULTIMATE and D-Station P(2) = 0.000115 and for iEVO ULTIMATE and iFace 800 P(2) = 0.000528 show that the combined biometric identification systems are less reliable and can therefore not be recommended for practical use. It is necessary to continuously improve these systems in order to get closer to the values given by the manufacturers. The value of erroneous acceptance given by the manufacturers for all of the tested readers is $\leq 0.0001\%$, and the value of false rejection ratesof a user is $\leq 1\%$. When comparing these values with the values obtained from the standard measurements, it is evident that in dual systems the value of reliability decreased by almost 10%, which is very user-unfavourable.

ACKNOWLEDGEMENTS. It is a project supported by the CULS IGA TF 2016 'The University Internal Grant Agency' (2016:31150/1312/3110).

REFERENCES

Jain, A.K. & Feng, J.J. 2009. Latent Palmprint Matching. *IEEE Transactions on pattern analysis and machine intelligence*. 1032–1047 p.

Jazzar, M.M. & Muhammad, G. 2013. Feature Selection Based Verification/Identification System Using Fingerprints and Palm Print. *Arabian journal for science and engineering* 849–857.

Nídlová, V. & Hart, J. 2015. Reliability of Identification Based on Fingerprints in Dual Biometric Identification Systems. *Applied Mechanics and Materials* **752–753**, 1040–1044.

Rak, R., Matyáš, V. & Říha, Z. 2012. Biometrics and identity of man – in forensic and commercial applications, 664 p. (in Czech).

Stroica, P. & Vladescu, M .2012. Implementation of a multiple biometric identification system based on face, fingerprints and iris recognition. *Advanced topics in optoelectronics, microelectronics, and nanotechnologies VI*.

Svozil, L. 2009. Aspects of biometric identification of persons using facial recognition. *Bachelor thesis*, Univerzita Tomáše Bati ve Zlíně. (in Czech)

Yoon, S., Feng, J.J., & Jain, A.K. 2012. Altered Fingerprints: Analysis and Detection. *IEEE Transactions on pattern analysis and machine intelligence*. 451–464 p.

Agronomy Research **15**(S1), 1006–1013, 2017

Utilization of the elementary mathematical model for description of mechanical behaviour of composites reinforced by Ensete Ventricosium fibres

P. Hrabě[1,*], D. Herak[2] and Č. Mizera[2]

[1]Czech University of Life Sciences, Faculty of Engineering, Department of Material Science and Manufacturing Technology, Kamýcká 129, CZ165 21 Prague, Czech Republic
[2]Czech University of Life Sciences, Faculty of Engineering, Department of Mechanical Engineering, Kamýcká 129, CZ165 21 Prague, Czech Republic
[*]Correspondence: hrabe@tf.czu.cz

Abstract. This article is focused on the utilization of elementary mathematical model for description of mechanical behaviour of composites materials reinforced by fibres of Ensete Ventricosium under tension loading. Elementary mathematical model was derived for unidirectional fibres oriented in the direction of tension loading and it was experimentally verified. As a matrix it was used a two-component resin Gluepox Rapid and as a reinforcement they were used fibres of Ensete Ventricosum. Experimental samples with different volume fibres ratio contained 40, 60, 80, 100, 120 and 140 fibres were tested on tensile equipment MP Test – 5.050. In this study the elementary mathematical model was utilized for description of dependency between modulus of elasticity, rupture stress and volume fibres ratio. From this research follows that data determined from derived elementary mathematical model are significant (on the level of significance 0.05) with experimentally determined data. This derived elementary mathematical model can be used as background for further research related to the modelling of mechanical behaviour of composites reinforced by fibres.

Key words: modulus of elasticity, stress at rupture, natural material.

INTRODUCTION

Natural fibres such as flax, sisal, coconut fibres as well as banana fibres were used in a historical age. Products from these natural fibres were of wide range of use from clothes to a roof of a house. Nowadays these fibres have been evaluated as ecological materials because of their biological dissolubility and renewability (Müller, 2015). Except for this lignocellulose fibres are CO_2 emission neutral. Except for plants which are grown for the production of fibres the fibre of other plants is of secondary or no commercial use. This is a case of a banana plant Ensete Ventricosium which is grown like food of inhabitants. Fibres with very good mechanical properties can be gained from remaining leaves and a bark of the banana plant (Mizera et al., 2015; Müller, 2016).

A modern technology uses the composites various ways including bearing constructions which a resistance to static, dynamic and fatigue loadings. Numerical modelling can help to interpret results gained from common portable equipment's which

have been nowadays used for metals. Modifications of these methods can be used for composites (Atuanya et al., 2011).

A current research is focused on the numerical modelling of the problem through hybrid rack to an irregular quadrilateral rack (Magomedov & Kholodov, 1988; Chelnokov, 2006; Beklemysheva et al., 2015). This method is based on characteristic properties of elastically deformable bodies as a set of equations and models for spreading of a reflection and a quarry among areas including their mutual transformation on various boundaries and contact types. The method was verified at various problematic examples, in a comparison with experiments in various scientific branches including a seismology (Petrov et al., 2011; Petrov & Kvasov, 2012), materials science (Beklemysheva et al., 2014; Petrov et al., 2014) and a biomechanics (Agapov et al., 2006; Beklemysheva et al., 2015). One-way carbon fibres of the polymeric composite are modelled as orthotropic medium by means of one direction, namely according to the fibres (Petrov et al., 2014).

The numerical modelling was performed in publications (Daynes et al., 2008; Daynes et al., 2010¸ Petrov et al., 2014). Most of analyses according to theoretical and numerical methods were performed only in limited cases. A primary mistake at a derivation of original loading is stated in the published theoretical study which led to a wrong form of equations (Mostafa et al., 2016). However, most of previous studies used one-way composites in their analyses. Only the paper of Potluri & Thammandra (2007) was focused on the numerical modeling of 2-D fabrics of composites exposed to one-axis and two-axis loading of fibres in a molding material (Kejval & Müller 2013).

By now no publication was dealing with the mathematical description of composites reinforced by Ensete fibres. Ensete fibres have a good mechanical behaviour (Mizera et al., 2016). From already published studies is evident that Ensete ventricosum fiber has very similar rupture stress as other fibers produced from other materials such as vakka, coconut, abaca or sisal (Munawar et al., 2006; Rao & Rao 2007).

This paper is focused on the elementary mathematical model for the description of the mechanical behaviour of composite materials reinforced with Ensete Ventricosium fibres. In order to the elementary mathematical model, mechanical test of composites were performed.

MATERIALS AND METHODS

Materials

As reinforcement of composite material the fibres from the plant *Ensete ventricosum*, obtained from Hawassa region, Ethiopia were used. The moisture content $M_c = 9.12 \pm 1.81\%$ *(w. b.)* of the fibres was determined using standard oven method, ASAE method (ASAE S410.1 DEC97, ASAE, 1998). Samples of *100 g* mass from a batch of Ensete fibres were randomly selected for the moisture content determination. The mass of each sample m_s *(g)* was determined using an electronic balance (Kern 440–35, Kern & Sohn GmbH, Balingen, Germany). The average diameter of fibres $D_f = 205 \pm 17\ \mu m$ was determined by using optical microscope (Zeiss Jenavert, Carl Zeiss, Jena, Germany). The average tension rupture stress of Ensete fibres after 20 tests was 385.12 ± 26.69 MPa. The epoxy resin GlueEpox Rapid was used as a matrix. It is a two-component resin prepared from a bisphenol (A) and epichlorhydrin (B).

Composite preparation

The composite material was created by pre-mixture containing of matrix and added fibres. The matrix was prepared by mixing of the parts A and B in ratio 100:45 (w/w) at room temperature. The final fluid matrix was poured in forms, which were prepared from a material Lukapren N, according to the standards. Into the liquid matrix were inserted the fibres in one direction (Fig. 2). The mixture was then left to cure for 24 h. Finally, the samples were removed from the forms and stored for posterior tests. The dimensions of samples (obtained from forms) are shown in Fig. 1. Composite samples were prepared with a different number of fibres in a sample 40, 60, 80, 100, 120 and 140, which corresponds to the percentage volume of 3.8, 5.8, 7.8, 9.8, 11.8 and 13.8%, respectively. For comparison of measured values of composite materials the pure matrix without fibres were created.

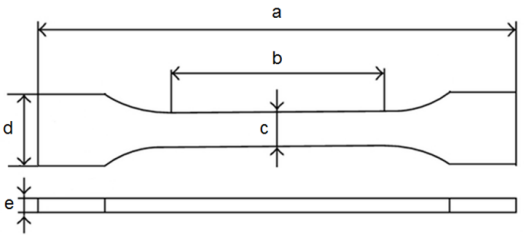

Figure 1. Test sample – Tensile strength (CSN EN ISO 3167, 2004).

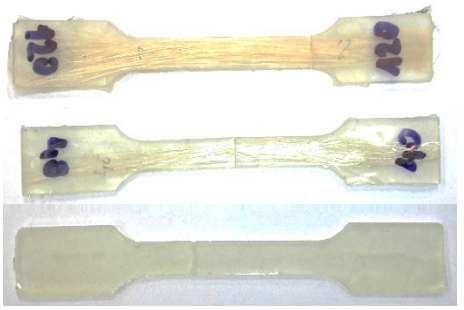

Figure 2. Samples of composite materials.

Laboratory tests

To determine the relationship between tension force and deformation, a device (Labortech, MPTest 5.050, Czech Republic) was used to record the course of deformation function. The tensile test was performed according to (ČSN EN ISO 527-2, 2012). A deformation speed at the tensile test was 10 mm min^{-1}. Determined amounts of tension force and deformation were transformed into stress and strain using Eqs. 2 & 3 respectively.

$$\sigma = \frac{F}{S} \tag{1}$$

where: σ – tensile stress in sample, MPa; F – tensile force, N; S – appropriate cross section area of sample after tensile test, mm^2,

$$\varepsilon = \frac{x}{L_0} \tag{2}$$

where: ε – strain, - ; ε – elongation of sample, mm; L_0 – gauge length, mm.

From measured values was determined the modulus of elasticity by Eq. 3.

$$E = \frac{\sigma}{\varepsilon} \tag{3}$$

where: E – modulus of elasticity, MPa; σ – tensile stress in sample, MPa; ε – strain, -.

Model determination

Simple model of composites assembled from two parts, matrix and fibres, (Fig. 3) was used for model derivation.

Basic assumption of this model is that strain of composite is equal to the strain of matrix as to the strain of fibres and that internal forces acting between the matrix and the fibres were neglected. Therefore it follows that force acting on composites can be described by Eq. 4.

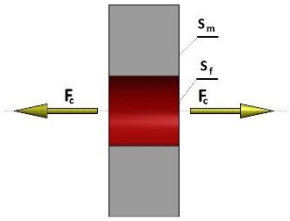

Figure 3. The basic model of composite material.

$$F_c = F_m + F_f \tag{4}$$

Where F_m (N) is force acting on matrix and F_f (N) is force acting on fibres. Previous formula (Eq. 4) can be expressed using Hooke's law as Eq. 5.

$$E_c \times (S_m + S_f) \times \varepsilon = E_m \times S_m \times \varepsilon + E_f \times S_f \times \varepsilon \tag{5}$$

Where E_c (MPa) is modulus of elasticity of composite, E_c (MPa) is modulus of elasticity of matrix, E_f (MPa) is modulus of elasticity of fibres, S_m (mm^2) is cross section area of matrix, S_f (mm^2) is cross section area of fibres and ε (-) is strain of composite. From Eq. 5 it can be expressed formula for modulus of elasticity of composites (Eq. 6) and this equation can be simplified with aid of Eq. 7 into general formula (Eq. 8).

$$E_c = E_m \times \frac{S_m}{(S_m + S_f)} + E_f \times \frac{S_f}{(S_m + S_f)} \tag{6}$$

$$\alpha = \frac{S_f}{S_m} \tag{7}$$

Where α (-) is fibre volume ratio.

$$E_c = E_m \times \frac{1}{1 + \alpha} + E_f \times \frac{\alpha}{1 + \alpha} \tag{8}$$

Strain of composites can be described by Eq. 9, where σ_m (MPa) is tension stress in matrix and σ_f (MPa) is tension stress in fibres.

$$\varepsilon = \frac{\sigma_m}{E_m} = \frac{\sigma_f}{E_f} = \frac{F_m}{S_m \times E_m} = \frac{F_f}{S_f \times E_f} \tag{9}$$

Eq. 10 can be derived using Eq. 9 into Eq. 4.

$$F_c = F_m + F_m \times \frac{S_f \times E_f}{S_m \times E_m} \tag{10}$$

Eq. 10 was divided by cross section area of composites (S$S_m + S_f$) (mm^2) and thus it was transformed in stress form (Eq. 11)

$$\sigma_c = \left(\sigma_m + \sigma_m \times \frac{S_f \times E_f}{S_m \times E_m}\right) \times \frac{S_m}{S_m + S_f} \tag{11}$$

With aid of Eq. 12, where β (-) is modulus of elasticity ratio, the general formula for description tension stress of composites can be derived (Eq. 13).

$$\beta = \frac{E_f}{E_m} \tag{12}$$

$$\sigma_c = \sigma_m \times \frac{1+\alpha\times\beta}{1+\alpha} \tag{13}$$

RESULTS AND DISCUSSION

Measured and determined values of composite materials are shown in Table 1.

Table 1. Measured and determined values of samples

Number of fibres (-)	Fibre volume ratio (-)	Composite cross section area (mm^2)	Rupture force (N)	Rupture strain (-)	Rupture stress (MPa)	Modulus of elasticity (MPa)
40	0.038 ± 0.004	33.23 ± 3.02	1,482 ± 107	0.031 ± 0.002	44.6 ± 6.2	1,439 ± 103
60	0.058 ± 0.006	23.89 ± 3.94	1,075 ± 85	0.028 ± 0.004	45.0 ± 7.3	1,607 ± 115
80	0.078 ± 0.008	36.75 ± 3.93	1,687 ± 56	0.029 ± 0.005	45.9 ± 7.0	1,583 ± 106
100	0.098 ± 0.010	24.36 ± 3.44	1,196 ± 90	0.026 ± 0.004	49.1 ± 6.9	1,888 ± 114
120	0.118 ± 0.012	33.99 ± 2.59	1,893 ± 80	0.030 ± 0.004	55.7 ± 6.1	1,857 ± 137
140	0.138 ± 0.014	38.27 ± 2.20	2,216 ± 95	0.029 ± 0.003	57.9 ± 6.6	1,997 ± 145

Measured values of modulus of elasticity and obtained values from model are shown in Fig. 4. High modulus of elasticity 1997 ± 145 MPa was achieved in the composite material at the maximum number of fibres 140 pcs. Individual samples of the composite material were compared with the pure epoxy resin without fibres. From the Fig. 4 is evident that the modulus of elasticity increased continuously with increase the number of fibres. For statistical comparison of measured and obtained values the statistical analysis ANOVA was used.

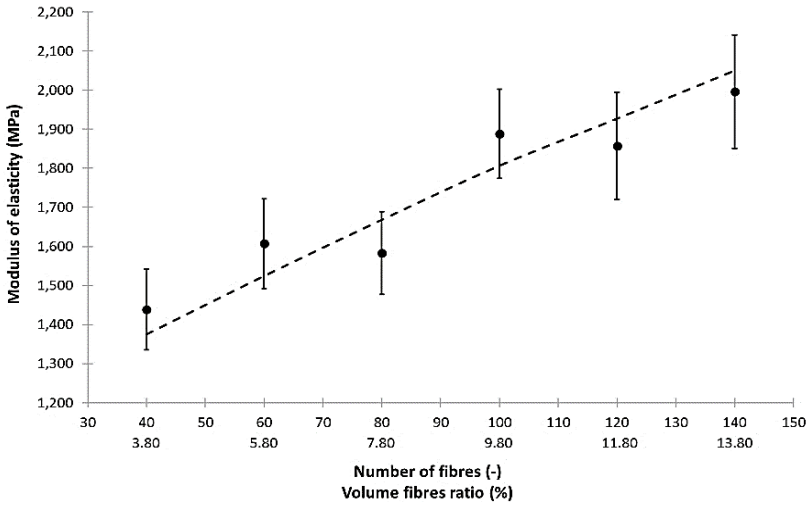

Figure 4. Effect of number of fibres in composite material on modulus of elasticity.

Statistical analysis ANOVA (Table 2) shows that the measured values of modulus of elasticity and the results from the general model (Eq. 8) were statistically significant at significance level 0.05, that is, the values of F_{crit} (critical value comparing a pair of models) were higher than the F_{rat} values (value of the F – test) for all the measured composites and values of P_{value} (significance level at which it can be rejected the hypothesis of equality of models) (Table 2) were higher than 0.05 which is also confirmed by very high coefficients of determination R^2.

Table 2. Statistical analysis of general models

	F_{rat} (-)	P_v (-)	F_{crit} (-)	R^2 (-)
Modulus of elasticity	0.005	0.945	5.32	0.91
Rupture stress	0.489	0.504	5.32	0.86

F_{rat} – value of the F test, *F_{crit}* – critical value that compares a pair of models, *P_{value}* – hypothesis of the study outcomes significant level, *R^2* – coefficient of determination.

Measured and determined values of tension stress at rupture are shown in Fig. 5. The obtained results from general model of tension stress of composite material (Eq. 13) are shown in Fig. 5. The highest stress was obtained at 57.9 ± 6.6 MPa. From the Fig. 5 it is clear that increased number of fibres increased the stress at rupture. Statistical analysis of results is shown in Table 2. From the statistical analysis (Table 2) is evident that the measured values of rupture and the results from the general model (Eq. 13) were statistically significant at significance level 0.05.

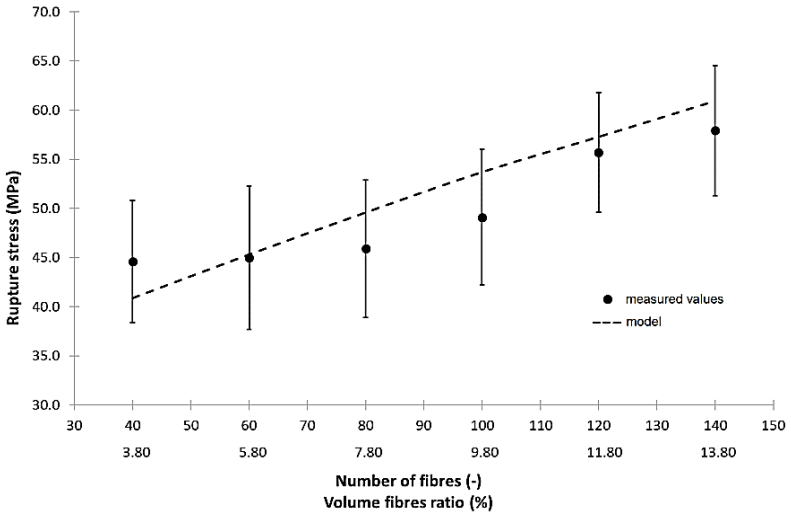

Figure 5. Effect of number of fibres in composite material on stress at rupture.

Modelling of behaviour of composite materials researched also authors Mostafa et al., 2016. They examined the tensile tests of composite materials reinforced by glass fibres. The effect of addition of Ensete fibres into two-component resin on mechanical behaviour of composite material described authors Mizera et al., 2015. Ensete fibres have good mechanical properties and that is why they can have great potential for use in

composite materials. By adding various natural fillers in composite materials, can modify their mechanical properties (Müller et al., 2015). Authors Mostafa et al., 2016 also published a mathematical model for synthetic fibres with preloading.

Modelling of mechanical behaviour of composites brings new knowledge which can be used in construction by using of natural materials.

This material can be used in the automotive industry.

ACKNOWLEDGEMENTS. This paper has been made with the assistance of the grant IGA TF CZU No. 2017:31130/1312/3111.

CONCLUSIONS

The aims of this study were to create basic mathematical models describing the dependency between number of Ensete fibres in composite material and modulus of elasticity and stress at rupture. It was found as follows:

- an increasing number of Ensete fibres in composite increases the modulus of elasticity and stress at rupture,
- the general models describing effect the number of Ensete fibres in composite material on modulus of elasticity and on stress at rupture were determined and also statistically confirmed,
- in this study determined models can help to design further models which will describe the mechanical behaviour of composite materials reinforced by natural fibres.

ACKNOWLEDGEMENTS. This paper has been supported by Internal Grant Agency of Faculty of Engineering – Czech University of Life Sciences Prague – IGA 2016: 31130/1312/3106.

REFERENCES

Agapov, P.I., Belotserkovskii, O.M. & Petrov, I.B. 2006. Numerical modeling of the effects of mechanical effects on the human brain in cases of head injury (Chislennoe modelirovanie posledstvii mekhanicheskogo vozdeistviia na mozg cheloveka při cherepno-mozgovoi travme=. *Zhurnal vychislitelnoi matematiki i matematicheskoi fiziki* **46**, 1711–1720.

Atuanya, C.U., Ibhadode, A.O.A. & Igboanugo, A.C. 2011. Potential of using recycled low-density polyethylene in wood composites board. *African Journal of Environmental Science and Technology* **5**, 389–396.

Beklemysheva, K.A., Petrov, I.B. & Favorskaya, A.V. 2014. Numerical simulation of processes in solid deformable media in the presence of dynamic contacts using the grid-characteristic method. *Mathematical Models and Computer Simulations* **4**, 294–304.

Beklemysheva, K.A., Danilov, A.A., Petrov, I.B., Vassilevsky, Y.V. & Vasyukov, A.V. 2015. Virtual blunt injury of human thorax: Age-dependent response of vascular system. *Russian Journal Of Numerical Analysis And Mathematical Modelling* **5**, 259–268.

Daynes, S., Potter, K.D. & Weaver, P.M. 2008. Bistable prestressed buckled laminates. *Composites Science and Technology* **68**, 3431–3437.

Daynes, S., Diaconu, C.G., Potter, K.D. & Weaver, P.M. 2010. Bistable prestressed symmetric laminates. *Journal of Composite Materials* **44**, 1119–1137.

Chelnokov, F.B. 2006. Iavnoe predstavlenie setochno-kharakteristicheskikh skhem dlia uravenii uprugosti v dvumernom i trekhmernom prostranstvakh. *Matematicheskoe modelirovanie* **18**, 96–108.

Kejval, J. & Müller, M. 2013. Mechanical properties of multi-component polymeric composite with particles of AL2O3/SIC. *Scientia Agriculturae Bohemica* **44**, 237–242.

Magomedov, K.M. & Kholodov, A.S. 1988. Setochno-kharakteristicheskie chislenye metody. *M.: Nauka*. 1988.

Mizera, Č., Herák, D., Müller, M. & Hrabě, P. 2015. Mechanical behaviour of polymeric composite with fibres of false banana (Ensete ventricosum). *Agronomy Research* **13**, 680–689.

Mizera, Č., Herak, P., Hrabe, P., Muller, P. & Kabutey, A. 2016. Mechanical Behavior of Ensete ventricosum Fiber Under Tension Loading. *Journal of Natural Fibers* **14**, 287–296.

Mostafa, H.N., Ismarrubie, N.Z., Sapuan, M.S. & Sultan, H.T.M. 2016. Fibre prestressed polymer-matrix composites: a review. *Journal of Composite Materials* **51**, 39–66.

Müller, M. 2015. Hybrid composite materials on basis of reactoplastic matrix reinforced with textile fibres from process of tyres recyclation. *Agronomy Research* **13**, 700–708.

Müller, M., Cidlina, J., Dědičová, K. & Krofová, A. 2015. Mechanical properties of polymeric composite based on aluminium microparticles. *Manufacturing Technology* **15**, 624–628.

Müller, M. 2016. Mechanical properties of composite material reinforced with textile waste from the process of tyres recycling. *Research in Agricultural Engineering* **62**, 99–105.

Munawar, S.S., Umenura, S. & Kawai, S. 2006. Characterization of the morphological, physical and mechanical properties of seven nonwood plant fiber bundles. *Journal of Wood Science* **53**, 108–113.

Petrov, I.B., Kvasov, I.E. & Pankratov, S.A. 2011. Numerical simulation of seismic responses in multilayer geologic media by the grid-characteristic method. *Mathematical Models and Computer Simulations* **3**, 196–204.

Petrov, I.B. & Kvasov, I.E. 2012. High-performance computer simulation of wave processes in geological media in seismic exploration. *Computational Mathematics and Mathematical Physics* **52**, 302–313.

Petrov, I.B., Vasyukov, A.V., Beklemysheva, K.A., Ermakov, A.S., Dzuba, A.S. & Golovan, V.I., 2014. Chislennoye modelirovalie dynamicheskih processov pri nizkoskorostnom udare po kompozitnoy stringernoi paneli. *Matematicheskoye modelirovanie* **4**, 96–110.

Petrov, I.B., Favorskaya, A.V., Vasyukov, A.V., Ermakov, A.S., Beklemysheva, K.A., Kazakov, A.O. & Novikov, A.V. 2014. Numerical simulation of wave propagation in anisotropic media. *Doklady Mathematics* **4**, 778–780.

Potluri, P. & Thammandra, V.S. 2007. Influence of uniaxial and biaxial tension on mesoscale geometry and strain fields in a woven composite. *Composite Structures* **7**, 405–418.

Rao, K.M.M. & Rao, K.M. 2007. Extraction and tensile properties of natural fibres: Vakka, date and bamboo. *Composite Structures* **77**, 288–295.

Agronomy Research **15**(S1), 1014–1023, 2017

Evaluation of quality and efficiency of ventilation equipment by scanning electron microscopy

M. Hromasová[1,*], P. Kic[2], M. Müller[3] and M. Linda[1]

[1]Czech University of Life Sciences in Prague, Faculty of Engineering, Department of Electrical Engineering and Automation, Kamýcká 129, CZ165 21 Prague, Czech Republic
[2]Czech University of Life Sciences in Prague, Faculty of Engineering, Department of Technological Equipment of Buildings, Kamýcká 129, CZ165 21 Prague, Czech Republic
[3]Czech University of Life Sciences in Prague, Faculty of Engineering, Department of Material Science and Manufacturing Technology, Kamýcká 129, CZ165 21 Prague, Czech Republic
[*]Correspondence: hromasova@tf.czu.cz

Abstract. The aim of this research is an evaluation of the quality and function of ventilation equipment in basement rooms. There was analysed the function of ventilation system in relation to the quality of outdoor and indoor environment. The concentration of air dust was measured by exact instrument DustTRAK II Model 8530 aerosol monitor inside and outside the building. Using the special impactors the PM_1, $PM_{2.5}$, PM_4, PM_{10} size fractions were also measured. Particles separated from the ventilation equipment were examined with SEM (scanning electron microscopy) using a microscope TESCAN MIRA 3 GMX. Obtained results of measurements were evaluated by statistical instruments and concentrations of different size of dust particles were analysed. The size of particles outlet the ventilation equipment was ca. of 55% lower than the size of the particles inlet the ventilation equipment. The difference in tested sizes of the dust particles in the ventilation equipment and outlet the ventilation equipment, i.e. in the place of cleaned air inlet into the basement room, was statistically proved. The diversity of impurities caught by the ventilation equipment and impurities moving in the air in the tested room is obvious from the results of SEM analysis.

Key words: dust, fraction, scanning electron microscopy, ventilation.

INTRODUCTION

Dust is one of the most common pollutants, which people face in everyday life and in their work activities. By dust we understand air pollution particles of matter that dispersed in the air create aerosols. Dust is characterized by a concentration, size and properties of dispersed particles. On all of those characteristics depends the influence on health. The harmful effect of dust on humans is very wide. Evaluation of dust depends on the origin, nature and size of the dust particles, on its concentration in the air, but also on the length and conditions of action, and on the human individual sensitivity to dust.

The attention to dust is paid in many research works, e.g. Skulberg et al. (2004), Bouillard et al. (2005), Mølhave (2008), Mølhave et al. (2009), Buchholz et al. (2011), Nõu & Viljasoo (2011), Brodka et al. (2012), Traumann et al. (2013), Traumann et al.

(2014), Kic (2015), Kic (2016). The methodology and the results of measurements correspond to the research topic, especially to factors that are specific to studied space. There are studied e.g. the impact of outdoor particulates transferred into the indoor space, the impact of processed and handled material, the influence of floor surface, the influence of sports equipment, particles released from special plastic materials used indoor etc.

The quality of indoor environment in some buildings and rooms depends on the efficient function of ventilation systems and equipment. The rooms, corridors and other spaces situated in basements of buildings are completely depending on the well-functioning forced ventilation with filtration of intake air. The quality and efficiency of the ventilation is partly depending on the elimination of undesirable dust particles and microorganisms transported together with fresh air by air streams in the air inlet from outside.

Basement spaces in many university buildings are because of the worse microclimate conditions most commonly used for warehouses in which workers or students cannot be. In many buildings there are also problems occurring with the underground moisture that penetrates from the surrounding terrain into the external walls which thus become wet (Krofova & Kic, 2016a).

Spaces which depend on the ventilation equipment are located in various offices, institutions etc. Filters are used for the elimination of dust particles from outdoor environment. The filter is an equipment which separates solid dust particles from the airstream going through the ventilation equipment during the filtration process. The function of the filter is to hold the impurities on its fibres by means of the filtration mechanisms. The elimination of the dust particles is essential not only owing to the health protection of persons in a given space but also at the production processes which are prone to the contamination from outside (Krofova & Müller, 2015; Krofova & Kic, 2016a; Krofova & Kic, 2016b).

The aim of this research is an evaluation of the quality and function of ventilation equipment in basement rooms. There was analysed the function of ventilation system in relation to the quality of outdoor and indoor environment.

MATERIALS AND METHODS

The indoor air quality depends also on the efficient function of filters installed in air inlet part of ventilation system for cleaning of intake air. To study the quality and function of filters this research was focused on the composition of particles separated by the filter. Tested filters are of G4 level. The filter G4 is used for catching and holding most gross dust particles.

The dust particles were removed from filters by shaking. A preparation of particles for the analysis by the scanning electron microscopy includes bonding of separated dust particles on a special carbon tape and gilding by a thin layer of gold in the apparatus Quorum Q150R ES.

Particles separated from the ventilation equipment were examined with SEM (scanning electron microscopy) using a microscope TESCAN MIRA 3 GMX at the accelerating voltage of the pack (HV) 15 kV or 5 kV, the working distance WD was 15.02 mm. The difference of the saturation of the various types of particles from the filter G4 was observed by SEM (scanning electron microscopy).

The spectral analysis (EDX) was performed at the filter by means of the auto-emission scanning electron microscope managed by the computer SEM (Tescan Mira 3 GXM). The EDX method detects X-ray and it is used for a quick analysis of a chemical composition of samples.

10 mm target with a carbon adhesive tape determined for testing of samples in SEM was placed in the tested basement room (without windows) in the inlet place of the cleaned air, i.e. from the ventilation equipment, for a comparison of the effectivity of the function of the ventilation equipment staffed with the filter G4 (Fig. 1). The particles moving in the basement room were sedimented on this plate during 7 days. A common working was during 7 days in the basement room (a laboratory of the Department of material science and manufacturing technology), i.e. it came to alternating on and off the ventilation equipment according to the needs. Sampling of dust particles in the indoor basement room is visible in Fig. 2. Collected samples were analysed by SEM according to the above mentioned procedures.

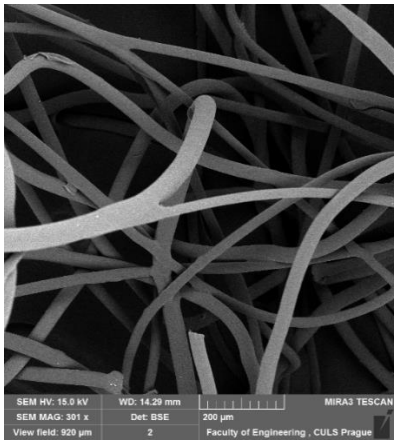

Figure 1. SEM images of filter G4 (MAG 301x).

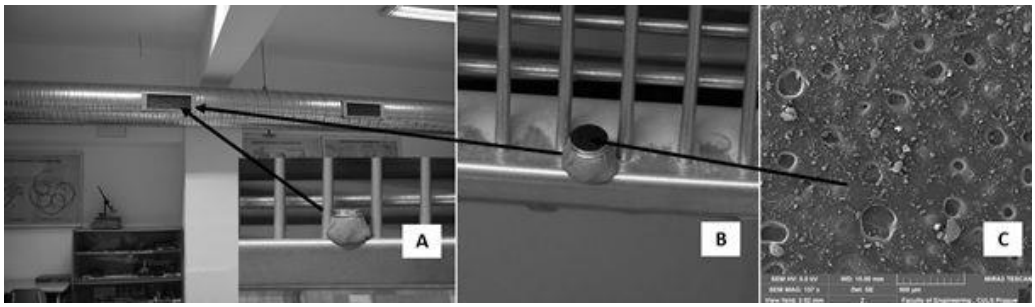

Figure 2. Sampling from indoor basement room: A: Inlet part of ventilation – exit from ventilation equipment and placing of sampling target, B: detailed view on dust particle sampling, C: SEM images of target area (MAG 137x).

An evaluation of the shape and the dimensions of impurities gained by SEM analysis was performed using the program Gwyddion. The program Gwyddion visualizes and analyzes data form microscopy. The results of measuring were statistically analysed by *Anova F-test*.

The total concentration of air dust was measured by special exact instrument Dust–Track II Model 8530 aerosol monitor. After the installation of different impactors the $PM_{10,}$ PM_4, $PM_{2.5}$, PM_1 size fractions of dust were also measured. The 90 data of dust concentration for total dust as well as of each fraction size outside and inside the empty room were collected, in representative places, which can be used for measurement without technological problems. The position of measuring instrument was usually at

75 cm above the floor. The dust measurements were carried out first without ventilation and the same dust measurements were carried out later with standard ventilation.

According to the Air Protection Act No. 201/2012 PM_{10} limit value in 24 hours is 50 μg m^{-3}, one year limit value is 40 μg m^{-3} and one year limit value $PM_{2.5}$ is 25 μg m^{-3}. The 90 data of dust concentration for total dust as well as of each fraction size in each room were collected. The obtained results of dust measurements were processed by Excel software and verified by statistical software Statistica 12 *(ANOVA* and *TUKEY HSD Test*). Different superscript letters (a, b, c) in common are significantly different from each other in the rows of the tables *(ANOVA; Tukey HSD Test; P ≤ 0.05)*, e.g. if there are the same superscript letters in all the rows it means the differences between the values are not statistically significant at the significance level of *0.05*.

The level of filtration and quality of filter function is usually expressed by the efficiency of filtration and penetration of dust through the filter (Szekyova et al. 2006). In this paper these parameters are used for evaluation of function of the ventilation system from the point of view of quality of dust removal. The efficiency of air filter O_c describes how well an air filter removes microscopic particles. It can be calculated according to the Eq. (1).

$$O_c = \frac{c_e - c_i}{c_e} 100 \quad (1)$$

where: O_c – total efficiency of air filter, %; c_e – concentration of pollutant in the inlet air before the filter, μg m^{-3}; c_i – concentration of pollutant in outlet air after filtration, μg m^{-3}.

The penetration of dust through the air filter P_c describes how many dust particles pass through the air filter. It can be calculated according to the Eq. (2).

$$P_c = \frac{c_i}{c_e} 100 \quad (2)$$

where: P_c – penetration of dust through an air filter, %.

RESULTS AND DISCUSSION

Principal results of dust measurement are summarized and presented in the Tables 1, 2 and Figs 3, 4. The measurements were during the day of rather high dust concentration outside the building. The measurements inside the empty, but not ventilated room (Table 1) show us that total dust concentrations and also concentrations of all dust fractions were lower that outside, but higher than 0.050 mg m^{-3}, which is dangerous for the human health. From the Table 1 it is apparent a statistically significant effect of ventilation on dust reduction, nevertheless the total dust concentration and also the concentrations of $PM_{10,}$ PM_4, $PM_{2.5}$ and PM_1 dust fractions were higher than 0.050 mg m^{-3}.

The evaluation of filtration quality is presented in the Table 1. The efficiency of filtration was higher than 55% and penetration of dust through the filter was therefore lower than 45%. These results are influenced not only by the quality of filters, but also by the sedimentation of dust inside the room and low level of dust suction by the ventilation equipment.

Table 1. Total dust concentration and concentration of dust fractions PM_{10}, PM_4, $PM_{2.5}$ and PM_1 outside and inside the empty room without and with ventilation. Different superscript letters (a, b) are the sign of high significant difference between the dust concentration in ventilated and not ventilated room (*ANOVA; Tukey HSD Test*; $P \leq 0.05$)

Room	Total $\mu g\ m^{-3} \pm SD$	PM_{10} $\mu g\ m^{-3} \pm SD$	PM_4 $\mu g\ m^{-3} \pm SD$	$PM_{2.5}$ $\mu g\ m^{-3} \pm SD$	PM_1 $\mu g\ m^{-3} \pm SD$
Outside	131.5 ± 3.4	127.8 ± 1.8	127.7 ± 1.6	126.4 ± 1.9	116.3 ± 1.3
Inside without ventilation	62.3 ± 2.6^a	61.6 ± 1.9^a	59.9 ± 1^a	58.1 ± 1.1^a	53.9 ± 0.9^a
Inside with ventilation	57.3 ± 1.9^b	57.1 ± 1.4^b	55.4 ± 1.2^b	54.6 ± 1^b	49.4 ± 0.8^b

SD – Standard deviation.

Table 2. The efficiency of air filtration O_c and penetration of dust through the ventilation system and the air filter P_c in the room, calculated from total dust concentration and concentration of dust fractions PM_{10}, PM_4, $PM_{2.5}$ and PM_1 outside and inside the empty room with ventilation

Parameter of dust filtration	Total %	PM_{10} %	PM_4 %	$PM_{2.5}$ %	PM_1 %
O_c	56.5	55.3	56.6	56.8	57.5
P_c	43.5	44.7	43.4	43.2	42.5

The Fig. 3 presents graph of the distribution of dust size of particles outside the building. The main parts (88%) of the dust in external air are the particles smaller than 1 μm (size fraction PM_1) and 8% are the particles bigger than 1 μm and smaller than 2.5 μm. The air contains the biggest dust particles in very low percentage (3% of the particles bigger than 10 μm, and 0.1% of the particles smaller than 10 μm and bigger than 4 μm).

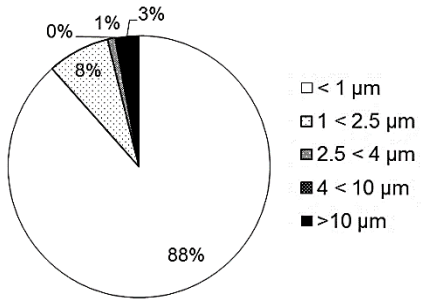

Figure 3. Percentage of dust fractions in the air outside the building.

The Fig. 4 presents the graph of the distribution of dust size of particles inside the room without and with the ventilation. The main parts (86%) of the dust in the room with and without ventilation are the particles smaller than 1 μm (size fraction PM_1), 7% are the particles bigger than 1 μm and smaller than 2.5 μm in non-ventilated, 9% in ventilated room. The air contains the biggest dust particles in very low percentage (1% of the particles bigger than 10 μm in non-ventilated and 0.1% in ventilated room). It is obvious that the small particles can move around freely in the air and the large particles settle down.

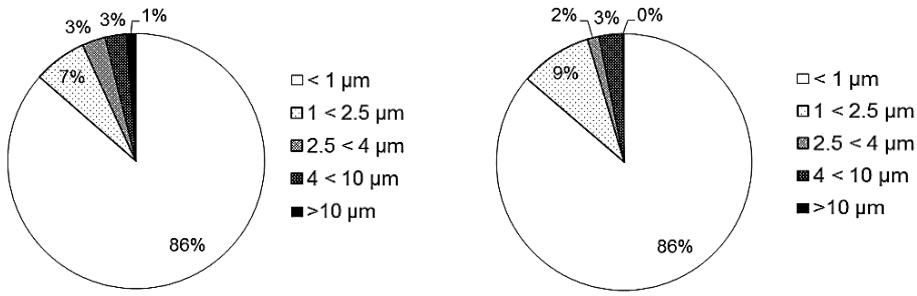

Figure 4. Percentage of dust fractions inside the empty room without ventilation (left) and with ventilation (right).

The fraction size caught by the filter G4 was measured as 37.8 ± 41.5 µm. Measured dust particles were distinguished for considerably different size. The size differed up of 109.8% (the variation coefficient). The fraction size caught in the exit of the filtration equipment, i.e. in the place of cleaned air inlet, was 20.8 ± 18.1 µm. The size differed up of 87.2% (the variation coefficient). The size of the dust particles in the exit was of ca. 55% lower than the size in the input. Results presented in the Fig. 5 provide more detailed view on the fraction size.

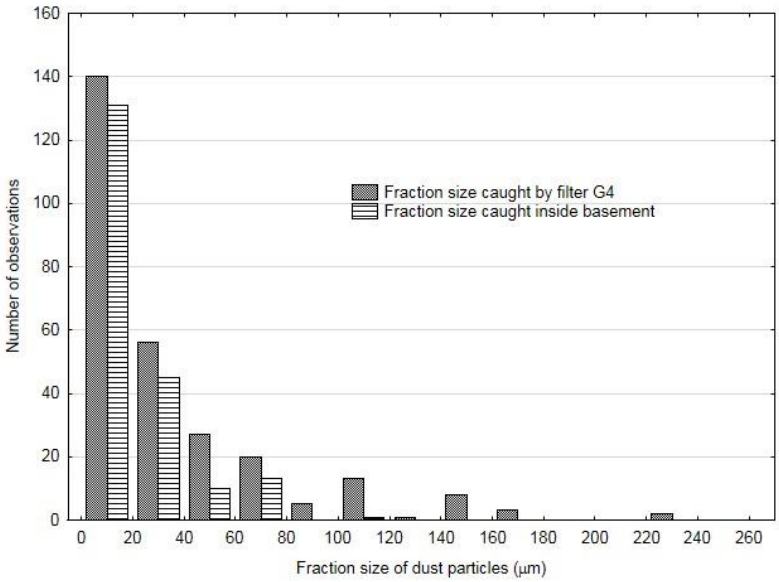

Figure 5. Histogram – dust particles.

Anova F-test was used for the statistical comparison of measured geometrical data of various sizes of dust particles gained from the input filter G4 and from the sediment of dust particles from indoor room (the exit from the ventilation equipment). The zero hypothesis H_0 shows the state when there is no statistically significant difference ($p > 0.05$) among single tested sets of data in terms of their mean values.

It is possible to say in terms of the statistical testing of the size of the dust particles gained from the input filter G4 and at the exit from the ventilation equipment, i.e. in the place of cleaned air inlet to the indoor room that the sizes are statistically non-homogeneous groups, i.e. there is a difference in the size of particles gained from outside filter and particles moving in the indoor room.

The hypothesis H_0 was not certified, i.e. there is a difference among single tested sets in the significance level, i.e. $p < 0.05$ ($p = 0.000$). The difference in tested sizes of dust particles in the ventilation equipment and in the exit from the ventilation equipment, i.e. in the place of the cleaned air inlet to the basement room was statistically proved.

It is obvious from the results that the filter catches all sizes of the particles. It entirely removes impurities higher than 100 μm from the ventilation equipment. It was ascertained by the analysis that ca. 11% of the impurities of the dimension higher than 100 μm was caught in the filter G4. On the contrary great amount of particles to 10 μm (ca. 30%) and 10 to 20 μm (ca. 36%) goes through the filter G4. However, the filter G4 should be efficient for the impurities ≥ 10 μm (according to EN 779). The percentage representation of impurities of higher dimension subsequently significantly decreases, i.e. it does not exceed 13%.

The specification of the particle dimension is essential, but it is also important to determine the chemical composition of impurities. This analysis was performed by means of the spectral analysis (EDX) - the auto-emission scanning electron microscope managed by the computer SEM (Tescan Mira 3 GXM) using the analyser Oxford X Max 7. The principle of measuring is visible from Fig. 6.

The result of EDX analysis is a detection of single chemical elements in the filters and their amount. EDX analysis set a presence 64.52% C, 28.65% O, 2.62% Si, 1.38% Ca, 0.88% Al, 0.68% Fe, 0.36% S, 0.27% K, 0.26% Na, 0.24% Cl and 0.15% Mg. The data are presented in mass percentage portion.

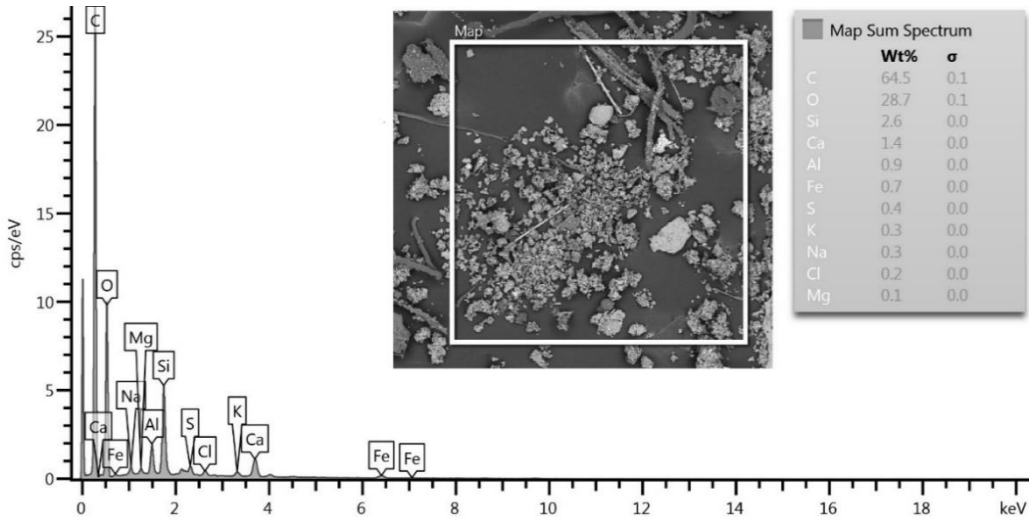

Figure 6. Results of EDX analysis of impurities in filter G4.

Fig. 7 and 8 show captured impurities. The impurities were heterogeneous according to the chemical composition as well as according to the geometrical shape.

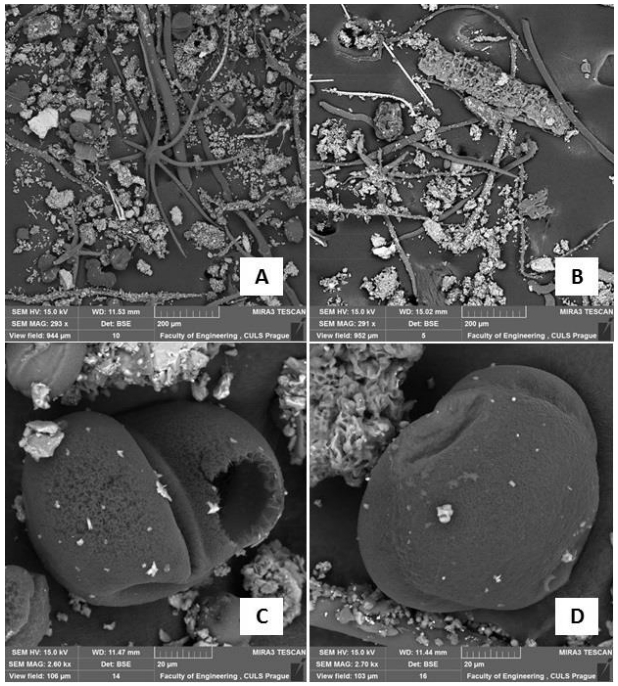

Figure 7. SEM images – impurities separated from filter G4: A: MAG 293x, B: MAG 291x, C: MAG 2.60kx, D: MAG 2.70kx.

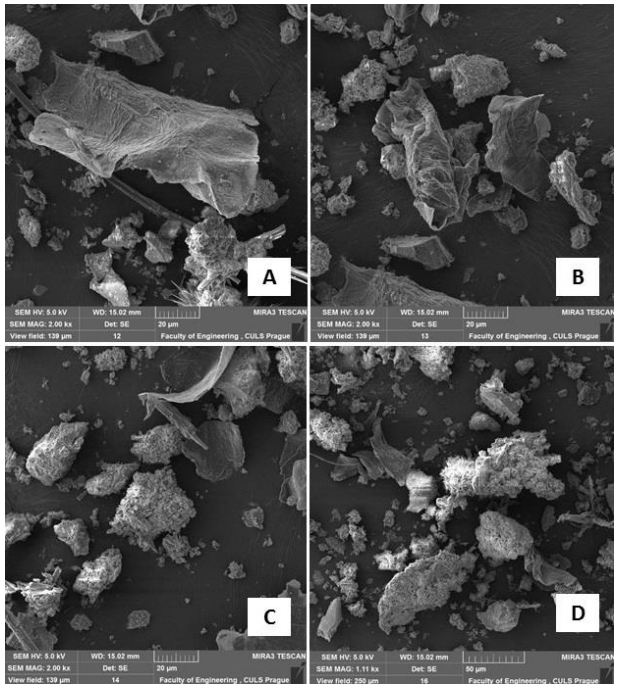

Figure 8. SEM images – impurities caught in exit from ventilation equipment: A: MAG 2.00kx, B: MAG 2.00kx, C: MAG 2.00kx, D: MAG 1.11kx.

CONCLUSIONS

The results of measurements of dust concentration showed that the ventilation system used in the tested basement room has sufficient system of air inlet and fresh air distribution, but the suction and outlet of polluted air from the room is situated (at the same level like inlet) near to the ceiling and therefore it is not able to remove sufficient quantity of dust particles, which are swirling inside the room.

The research with the aim to evaluate the quality and the function of the ventilation equipment by means of the analysis of impurities has following conclusions:

- The filter G4 is able to catch larger particles above all. The size of the particles in the exit was of ca. 55% smaller than the size in the input of the ventilation equipment. The filter G4 removes most of impurities over 100 μm. On the contrary, great amount of impurities smaller than 20 μm goes through the filter G4.
- The difference in tested sizes of the dust particles in the filter and in the exit from the ventilation equipment, i.e. in the place of cleaned air inlet to the basement room was statistically proved.

The heterogeneity (the shape, the chemical composition) of the impurities caught by the filter and the impurities moving in the air in the tested room is obvious from the results of SEM analysis.

REFERENCES

Act No. 201/2012 Coll. Air Protection Act. (in Czech).

Bouillard, L., Michel, O., Dramaix, M. & Devleeschouwer, M. 2005. Bacterial contamination of indoor air, surafaces, and settled dust, and related dust endotoxin concentrations in healthy office builgings. *Ann. Agric. Environ. Med*. **12**, 187–192.

Brodka, K., Sowiak, M., Kozajda, A., Cyprowski, M. & Szadkowska-Stanczyk, I. 2012. Biological contamination in office buildings related to ventilation/air conditioning system. *Medycyna Pracy* **63**(3), 303–315. (in Polish).

Buchholz, S., Krein, A., Junk, J., Gutleb, A.C., Pfister, L. & Hoffmann, L. 2011. Modelling, measuring, and characterizing airborne particles: Case studies from southwestern Luxembourg. Critical reviews in environmental science and technology 41(23), 2077–2096.

Kic, P. 2015. Dust pollution in university offices. *Agronomy Research* **13**(3), 759–764.

Kic, P. 2016. Dust pollution in the sport facilities. *Agronomy Research* **14**(1), 75–81.

Krofová, A. & Kic, P. 2016a. Heat recuperation in ventilation system of basement laboratory. In *15th International Scientific Conference on Engineering for Rural Development.* Jelgava; Latvia, Latvia University of Agriculture. pp. 56–61.

Krofová, A. & Müller, M. 2015. Influence of dusty micro-particles contamination on adhesive bond strength. *Agronomy Research* **13**(3), 654–661.

Krofová, A. & Kic, P. 2016b Ventilation and microclimatic conditions in the laboratory of adhesive bonding. *Agronomy Research* **14(**4), 1342–1350.

Mølhave, L. 2008. Inflammatory and allergic responses to airborne office dust in five human provocation experiments. *Indoor air* **18**(4), 261–270.

Mølhave, L., Pan, Z., Kjærgaard, S.K., Bønløkke, J.H., Juto, J., Andersson, K., Stridh, G., Löfstedt, H., Bodin, L. & Sigsgaard, T. 2009. Effects on human eyes caused by experimental exposures to office dust with and without addition of aldehydes or glucan. *Indoor air* **19**(1), 68–74.

Nõu, T. & Viljasoo, V. 2011. The effect of heating systems on dust, an indoor climate factor. *Agronomy Research* **9**(1), 165–174.

Skulberg, K., Skyberg, K., Kruse, K., Eduard, W., Djupesland, P., Levy, F. & Kjuus, H. 2004. The effect of cleaning on dust and the health of office workers: an intervention study. *Epidemiology* **15**(1), 71–78.

Standard ČSN EN 779. 2012. *Particulate air filters for general ventilation – Determination of the filtration performance.* (in Czech).

Szekyova, M., Ferstl, K. & Novy, R. 2006. *Ventilation and air-conditioning*. JAGA GROUP, Bratislava, 359 pp. (in Czech)

Traumann, A., Reinhold, K. & Tint, P. 2013. The model for assessment of health risks of dust connected with wood manufacturing in Estonia. *Agronomy Research* **11**(2), 471–478.

Traumann, A., Kritsevskaja, M., Tint, P. & Klauson, D. 2014. Air quality as an important indicator for ergonomic offices and school premises. *Agronomy Research* **12**(3), 925–934.

Agronomy Research **15**(S1), 1024–1032, 2017

Dry sorption stabilization of flue gases in biological waste incinerating facility with heating power under 5 MW

P. Jirsa* and J. Malaťák

Czech University of Life Sciences Prague, Faculty of Engineering, Department of Technological Equipment of Buildings, Kamýcká 129, CZ165 21 Praha-Suchdol, Czech Republic
*Correspondence: pjirsa@tf.czu.cz, jirsa.petr@gmail.com

Abstract. Biological and medical waste is always classified as hazardous material such as it must be treated according to its hazardous characteristics. One of the best methods for disposal seems to be a thermal degradation. This research examines the effect of finely crushed sorbent $Ca(OH)_2$ and $NaHCO_3$ to eliminate these hazardous substances in a small incinerating facility with heating power under 5 MW. The experiment took place in an existing incinerating plant with capacity 250 kg h^{-1}. Sorbents were injected into a flue gas flow at two different places. It was observed that the temperature of flue gas and the residence time significantly influence the sorbent refining effect that is caused by quantity of collision in flue gas stream. Sorbents were dosed into a system with a theoretical consumption excess to serve sufficient refining effect. At dosing rate of 7 kg h^{-1} $Ca(OH)_2$ the concentration of SO_2 decreased by 34.5% and HCl by 59.0% referring to the initial concentration. At dosing rate of 5 kg h^{-1} $NaHCO_3$ the concentration of SO_2 decreased by 32% and HCl by 44.8% referring to an initial concentration. Tested sorbents react with acidic compounds with different efficiency and preferably react with different acid compounds.

Key words: hospital waste, Calcium hydroxide, Sodium bicarbonate, HCl, SO_2.

INTRODUCTION

Hazardous particles and compounds form while waste incineration occurs. According to an enacted legislation, particular substances in a stream of flue gas have to be eliminated according to emission limit (Act No. 201/2012, Czech Republic). It includes sulphur oxides (SO_x), nitrogen oxides (NO_x), halogen hydrogens and persistent organic pollutants (POP) such as polychlorinated dibenzodioxins and dibenzofurans compounds (PCDD/F) that are resistant to environmental degradation (Wey et al., 2001).

Elimination of sulphur oxides and halogen hydrogens in flue gas can be done by several methods. They are classified as the wet process, semi-dry process and dry process. In the wet flue gas cleaning process the flue gas is stabilized by circulating water in a scrubber, the water is enhanced by lime milk. In semi-dry flue gas cleaning process an alkaline sorbent agent is injected to a flue gas flow in a liquid form as a suspension or a solution. The water part is vaporized and dry powdered sorbent captures heavy metals, sulphur oxides and halogen hydrogens then on its surface (Brna, 1990).

Dry refining technology is based on injection of sorbents in a form of a dry powder. The agent is sprayed directly into the flue gas flow (Allen et al., 2001) or mixed with waste going into the reactor (Cunill et al., 1991). Neutral compounds are formed by sorbent reaction with acid components. Solid particles are captured on mechanical separators. Sorbents can be calcium or sodium based, calcium hydroxide ($Ca(OH)_2$) or sodium bicarbonate ($NaHCO_3$). There are other synthesized sorbents at the market that can reach higher efficiency in flue gases stabilization under specific condition such as calcium-magnesium-aluminum (Ca-Mg-Al) mixed oxide sorbent or hydrogarnet (Cao et al., 2014).

Calcium oxide can stabilize hydrogen chloride with 54% efficiency at the temperature of 800 °C. However with 80% efficiency at 600 °C (Shemwell et al., 2001). The efficiency is highly dependent on sorbent faction and porosity (Daoudi & Walters, 1991) as well as on ambient temperature (Partanen et al., 2005). Conversion rate of hydrogen chloride grows with increasing size of calcium oxide. However, conversion rate of sulphur oxide increases with decreasing size of calcium oxide. Sulphation greatly accelerates in the presence of hydrogen chloride (Matsukata et al., 1996). Some researchers suggest that calcium carbonate under certain conditions is able to stabilize PCDD/F (Lu et al., 2007). Higher concentration of sulphur oxide in flue gases significantly reduces the formation of these compounds (Van Caneghem et al., 2012).

The research work focuses on the dry sorption refining technology in a small biological and medical waste incinerating plant. According to the Air protection Act, heating power of the small incinerating plant is lower than 5 MW (Act No. 201/2012, Czech Republic). The dry sorption refining technology seems to be very efficient for such application. However, it is not commonly used in a waste utilization plants with heating power higher than 5 MW, because there is a very high volume of flue gas transfer in the system. It is difficult to stabilize flue gases sufficiently under such conditions. Wet or semi-dry sorption technologies are usually used for plants with greater thermal output.

The aim of the study is to determine the refining effect of calcium hydroxide and sodium bicarbonate on HCl and SO_2 in relation with process conditions in the dry sorption refining system.

MATERIALS AND METHODS

The experiment took place in the incinerating facility for biological and hospital waste complex Johnson Controls Fabrics Strakonice a.s., Czech Republic. The incinerating plant consists of a pyrolysis-incinerating furnace Hoval – Schiestl GG 24, thermoreactor TR 24 and a steam boiler THD IV 0580 with heating power 1,508 kW. The capacity of the plant was 250 kg h^{-1} and the burned material was injected discontinuously 60–65 kg per every 15 minutes.

The input material was biological and hospital waste. Waste code according to waste catalogue (European Waste Catalogue): 180102, 180103, 180104, 200301, 150202, 150110. The elemental characteristic of incinerated waste in Table 1.

Table 1. Biological waste characteristics

	Share of component	H_2O	Ash	Cl	F	S	Heating value
	[%]	[%]	[%]	[%]	[%]	[%]	[MJ kg^{-1}]
Paper	24	5.8	5	0.5	-	4.2	15.4
Plastic	23	0.1	0.5	18	3	6.7	24.8
Textile	29	6.6	14.2	13.2	1.8	9.5	15.1
Biological component	14	32.1	18.6	5.3	2.1	12	11.4
Solvent, oil	10	0.6	0.8	16.1	1.3	21.3	39.6
Weighted average		7.9	8.1	10.4	1.6	9.1	19.3

Temperature in the furnace chamber was 900 to 950 °C. Two burners for natural gas automatically control the heat to the required temperature. The waste was carbonized and formed gas was mixed with the air and burned in thermoreactor at the temperature 1,100 to 1,150 °C. Formed flue gases flowed to the boiler where the temperature was reduced to 200 to 250 °C. First device for dosing a tested sorbent was placed after the boiler, position A. Flowingly the flue gas passed through the pipe labyrinth_1 which was 8 m long and a heat exchanger where the temperature was reduced to 130 to 135 °C. The second sorbent dosing device was placed after the cooler, position B. Flue gas went through the pipe labyrinth_2 which was 17 m long. All solid particles involving hazardous compounds and sorbents injected into the system previously were captured on a tied filter subsequently. The block diagram of the incinerating facility is given on the Fig. 1.

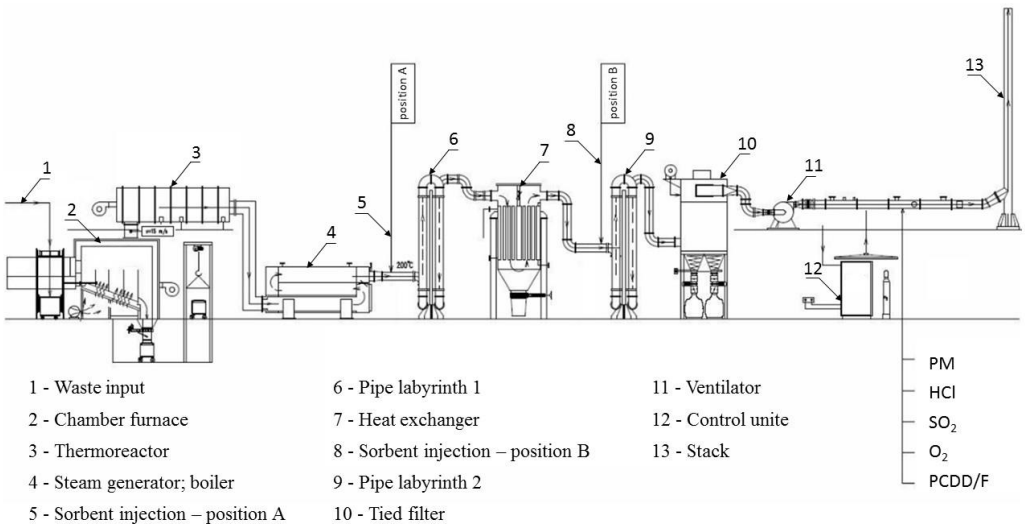

Figure 1. Incinerating facility block diagram.

The measurement of emissions in flue gas was taken according to appropriate legislative (Act No. 201/2012, Czech Republic). The measuring point was placed at the horizontal flue pipe with diameter 355 mm after a ventilator according to ISO 9096 and EN 13284-1.

Flue gas properties and the concentration of particulate matter (PM), hydrogen chloride (HCl), sulfur dioxide (SO_2), oxygen (O_2) were determined according to technical standards:

- Gravimetric determination of the mass concentration of particulate matter (ISO 9096 EN 13284-1);
- Determining flow velocity and volume flow (ISO 10780);
- Determination of moisture in the gas pipeline (EN 14790);
- Paramagnetic determination of oxygen (EN 14789);
- Photometric determination of the mass concentrations in inorganic chloride compounds (EN 1911);
- Determination of sulphur dioxide mass concentration, automated system - UVF fluorescence NDUV (ISO 7935, EN 14212);
- Determination of carbon oxide mass concentration, automated system – NDIR (ISO 10396, EN 15058).

All volumes, weights of combustion air and emission concentration are given for normal conditions, i.e., at t = 0 °C, p = 101.325 kPa and the reference oxygen content in the flue gases O_r = 11%.

Some results (Figs 3, 4) are given as a value of conversion. The conversion is expressed by following equation:

$$x_i = \frac{(c_{i,0} - c_i)}{c_{i,0}} \tag{1}$$

It is a volume of substance eliminated by tested sorbent given as a share of initial concentration.

For the experimental measurement, two different sorbents were tested on efficiency to eliminate hazardous particles in flue gases.

- Calcium hydroxide: $Ca(OH)_2$;
- Sodium Bicarbonate: $NaHCO_3$.

Sorbents react with acidic components of flue gas according to following chemical equations:

$$SO_2 + Ca(OH)_2 = CaSO_4 + H_2O \tag{2}$$

$$2HCl + Ca(OH)_2 = CaCl_2 + 2H_2O \tag{3}$$

$$SO_2 + 2NaHCO_3 + 1/2\ O_2 = Na_2SO_4 + 2CO_2 + H_2O \tag{4}$$

$$HCl + NaHCO_3 = NaCl + CO_2 + H_2O \tag{5}$$

The theoretical consumption of the sorbent was calculated for every experiment according to stoichiometric relation expressed in following equations:

$$G^T_{Ca(OH)_2} = M_{Ca(OH)_2} \times V \times \left(\frac{c_{SO_2}}{M_{SO_2}} + \frac{c_{HCl}}{\frac{1}{2}M_{HCl}}\right) \tag{6}$$

$$G^T_{NaHCO_3} = M_{NaHCO_3} \times V \times \left(\frac{c_{SO_2}}{\frac{1}{2}M_{SO_2}} + \frac{c_{HCl}}{M_{HCl}}\right) \tag{7}$$

where: $M(SO_2)$ = 64.066 g mol^{-1}; $M(HCl)$ = 36.461 g mol^{-1}; $M(Ca(OH)_2)$ = 74.093 g mol^{-1}; $M(NaHCO_3)$ = 84.007 g mol^{-1}; V = flue gas flow [$Nm^3\ h^{-1}$]; C_{SO2}, C_{HCl} = concentration [mg m^{-3}].

RESULTS AND DISCUSSION

Elimination of HCl and SO_2 by Calcium Hydroxide

Calcium hydroxide was injected into a flue gas pipe after the heat exchanger (position A). Concentration of hydrogen chloride and sulphur dioxide was measured in relation to various volume of calcium oxide that was added into a system.

The flue gas went through the pipe labyrinth_1 where the mean residence time was 0.6 s. Then it went through the cooler with the mean residence time of 1.1 s. The flue gas went through pipe labyrinth_2 with the mean residence time of 1.3 s. The sorbent was captured on a mechanical filter then. The total time of possible reaction between the injected sorbent and acid flue gas elements in the system was approximately 3 s.

The measuring point was after a heat exchanger where the temperature of flue gas was 225 °C. The mean volume of flue gas was 3,629 $Nm^3\ h^{-1}$ and mean volume of O_2 was 10.1 ± 0.98%. Theoretical consumption of $Ca(OH)_2$ was calculated according to Eq. (6). The theoretical sorbent consumption was determined at level 2.553 kg h^{-1} for stated conditions. During the test 2.5 to 7 kg h^{-1} of $Ca(OH)_2$ was dosed into the system and the concentration of HCl and SO_2 was measured based on injected sorbent volume.

The first value represents the reference point for evaluation when no sorbent was injected into the system. The dependence of HCl and SO_2 concentration in flue gas on volume of $Ca(OH)_2$ consumed by 1 m^3 of flue gas in the system is shown on the graph (Fig. 2).

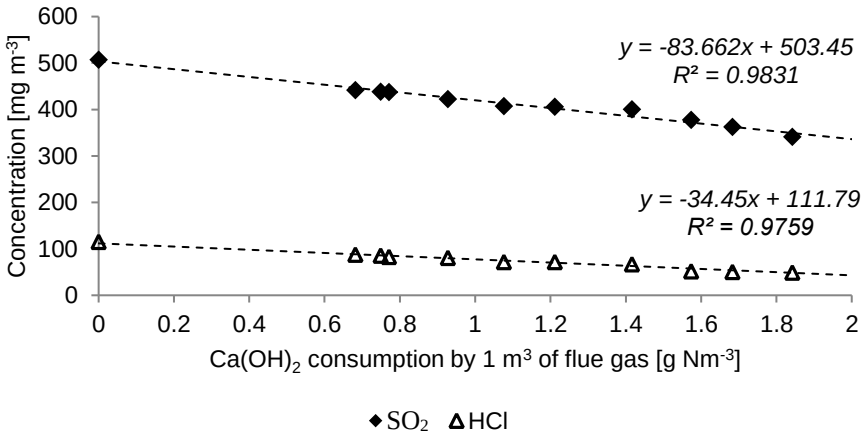

Figure 2. Reduction of HCl and SO_2 concentration in flue gas based on dosing $Ca(OH)_2$.

The results show that calcium hydroxide reacts with both hydrogen chloride and sulphur dioxide. The concentration of acid flue gas elements linearly decreases based on surplus of injected calcium hydroxide. At dosing rate of 7 kg h^{-1} $Ca(OH)_2$ the concentration of SO_2 decreased by 34.5% and HCl decreased by 59.0% referring to the initial concentration. The analysis of ash captured on a filter showed the conversion of

injected calcium oxide in the system was 30%. The volume of sulphur in the ash was 5.8% and volume of chlorides was 4.1%. It means that calcium hydroxide reacts preferably with sulphur oxides rather than chlorides.

Next experiment is focused on determining an influence of injected point on sorbent refining effectivity. The measurement was conducted under the same condition as the previous one. However, the place of sorbent injection was changed. It was placed after the cooler, before pipe labyrinth_2 (position B). The temperature at this point was 135 °C.

Graphs (Figs 3, 4) display the conversion of SO_2 and HCl that is caused by dosing $Ca(OH)_2$ into the system on different places. The conversion is calculated according to Eq. (1).

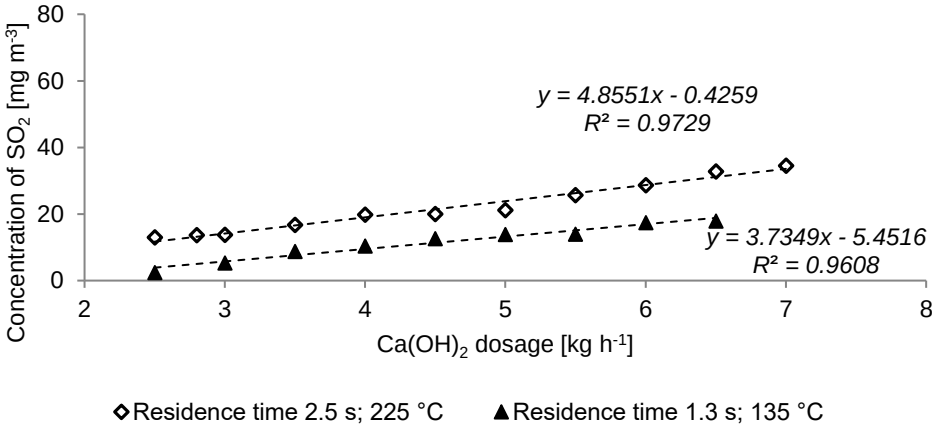

Figure 3. The effect of doosing place on $Ca(OH)_2$ efficiency to reduce SO_2 concetration.

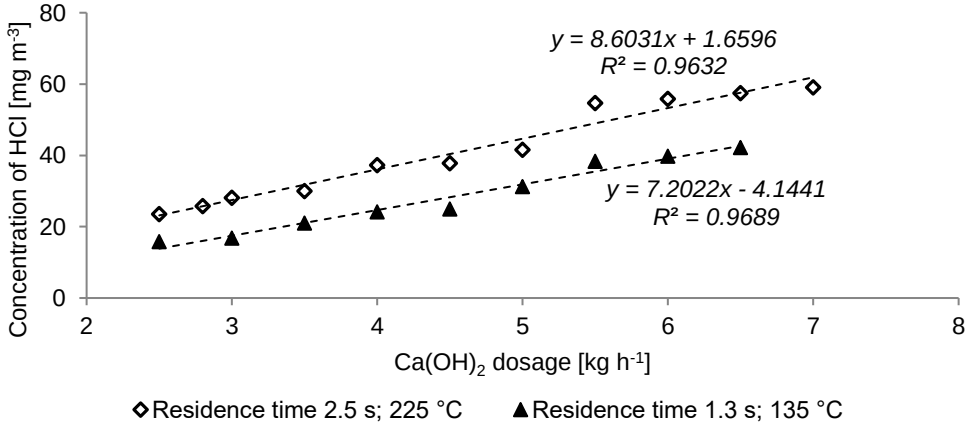

Figure 4. The effect of doosing place on $Ca(OH)_2$ efficiency to reduce HCl concetration.

The conversion rate of HCl is higher for dosing place at position A. The maximum conversion of HCl was 59.0% when 7 kg h^{-1} was dosed.

The dosing place highly influences the sorbent ability to react with acidic flue gas elements. There are mainly two parameters that influence number of collisions and reactions in flue gas flow, residence time in the system and the temperature (Bradna et al., 2016). In the first case, when the sorbent was injected in front of pipe labyrinth_1 (position A), the residence time was 3 s. However, in second case (position B) was the residence time 1. s. The experiment proves that sorbent effectiveness is dependent of kinetic conditions in the flue gas. With decreasing temperature and shorter residence time, the number of collusions reduce and subsequently decreases the sorbent effectiveness.

The conversion rate of SO_2 is higher for dosing place at position A. The maximum conversion of SO_2 was 34.5% when 7 kg h^{-1} was dosed.

Elimination of HCl and SO_2 by Sodium Bicarbonate

Powdered sodium bicarbonate ($NaHCO_3$) was injected into a flue gas pipe after the heat exchanger (position A). Concentration of hydrogen chloride and sulphur dioxide was measured based on various volume of sodium bicarbonate that was added into the system. The mean volume of glue gas flow was 3,380 Nm^3 h^{-1} and mean volume of O_2 was 10.5 ± 1.13%. Theoretical consumption of $NaHCO_3$ was calculated according to Eq. (7). The theoretical sorbent consumption was determined at level 2.341 kg h^{-1} for stated conditions. During the test 1.8 to 5 kg h^{-1} of $NaHCO_3$was dosed into the system and the concentration of HCl and SO_2 was measured based on injected sorbent volume.

The first value represents the reference point for evaluation. It was measured when no sorbent was injected into a system. The dependence of HCl and SO_2 concentration in flue gas on volume of $NaHCO_3$ injected to a system is shown on following graph (Fig. 5).

The dependence of HCl and SO_2 concentration in flue gas on volume of $NaHCO_3$ consumed by 1 m^3 of flue gas in the system is shown on the graph (Fig. 5).

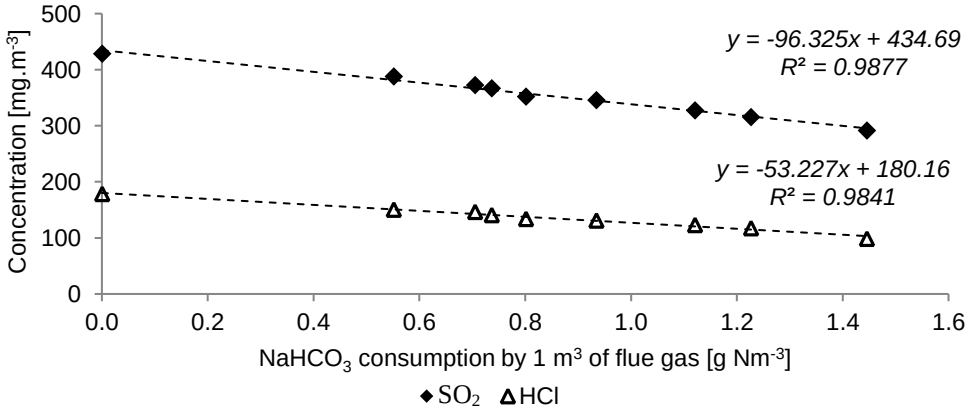

Figure 5. Reduction of HCl and SO_2 concentration in flue gas based on dosing $NaHCO_3$.

The results show that sodium bicarbonate reacts with both hydrogen chloride and sulphur dioxide. The concentration of acid flue gas elements linearly decreases based on surplus of injected $NaHCO_3$. At dosing rate of 5 kg h^{-1} $NaHCO_3$ the concentration of SO_2 decreased by 32% and HCl by 44.8% referring to an initial concentration. The analysis of ash captured on the filter showed the conversion of injected sodium bicarbonate in the system was 53%. The volume of sulphur in the ash was 3.2% and volume of chlorides was 5.1%. It means that sodium bicarbonate reacts preferably with chlorides rather than sulphur oxides. It also shows that $NaHCO_3$ can eliminate the content of HCl in flue gas better that calcium oxide. The development of these new technologies is the subject of further research, not only on this solved issue (Hart & Hartova, 2016).

CONCLUSIONS

The research focuses on the dry sorption refining technology in a small biological and hospital waste incinerating plant with heating power under 5 MW. Two different sorbents calcium hydroxide and sodium bicarbonate were tested on ability to eliminate concentration of HCl and SO_2 in flue gases. Theoretical consumption of tested sorbent was calculated for stated condition. It was obvious that theoretical amount of injected sorbent wasn´t enough to reduce the concentration of measured acidic compounds to sufficient level. It was caused by low quantity of collisions in flue gas flow between sorbent and eliminated compounds. During experiments, the excess of theoretical amount for each sorbent was injected into the system and the refining effect was observed. Both sorbents react with acidic compounds with different efficiency. Calcium hydroxide reacts preferably with sulphur oxides rather than chlorides. At dosing rate of 7 kg h^{-1} $Ca(OH)_2$ the concentration of SO_2 decreased by 34.5% and HCl by 59.0% referring to the initial concentration. Sodium bicarbonate reacts preferably with chlorides rather than sulphur oxides. It can eliminate the content of HCl in flue gas better that calcium oxide. At dosing rate of 5 kg h^{-1} $NaHCO_3$ the concentration of SO_2 decreased by 32% and HCl by 44.8% referring to an initial concentration. The most suitable arrangement would be probably a combination of both sorbents at different dosing places.

ACKNOWLEDGEMENTS. The article was financially supported by the Internal Grant Agency of the Czech University of Life Sciences Prague, Czech Republic, Grant No. 20173002.

REFERENCES

Act No. 201/2012 Coll. Air Protection. Czech Republic.

Allen, R.W., Archer, E. & MacInnes, J. 2001. Adsorption by particles injected into a gas stream. *Chemical Engineering Journal* **83**, 165–174.

Bradna, J., Malaťák, J. & Hájek, D. 2016. The properties of wheat straw combustion and use of fly ash as a soil amendment. *Agronomy Research* **14**, 1257–1265.

Brna, T.G. 1990. Cleaning of flue gases from waste combustors. *Combustion Science and Technology* **74**, 83–98.

Cao, J., Zhong, W., Jin, B., Wang, Z. & Wang, K. 2014. Treatment of hydrochloric acid in flue gas from municipal solid waste incineration with Ca-Mg-Al mixed oxides at medium-high temperatures. *Energy & Fuels* **28**, 4112–4117.

Cunill, F., Izquierdo, J.F., Martínez, J.C., Tejero, J. & Querol, J. 1991. Influence of different additives on the reaction between hydrated lime and sulfur dioxide. *Environmental Progress* **10**, 273–277.

Daoudi, M. & Walters, J.K. 1991. The reaction of HCl gas with calcined commercial limestone particles: The effect of particle size. *The Chemical Engineering Journal* **47**, 11–16.

Environmental Protection Agency. 2002. European Waste Catalogue and Hazardous Waste List.

Hart, J. & Hartova, V. 2016. Development of new testers to improve quality for data transmissions in intrusion and hold-up alarm systems, In: *15th International Scientific Conference on Engineering for Rural Development*, Jelgava, Latvia, volume: **15**, 523–528.

Lu, S.Y., Chen, T., Yan, J.H., Li, X.D., Ni, Y.L.M.J. & Cen, K.F. 2007. Effects of calcium-based sorbents on PCDD/F formation from pentachlorophenol combustion process. *Journal of Hazardous Materials* **147**, 663–671.

Matsukata, M., Takeda, K., Miyatani, T. & Ueyama, K. 1996. Simultaneous chlorination and sulphation of calcined limestone. *Chemical Engineering Science* **51**, 2529–2534.

Partanen, J., Backman, P., Backman, R. & Hupa, M. 2005. Absorption of HCl by limestone in hot flue gases. Part I: the effects of temperature, gas atmosphere and absorbent quality. *Fuel* **84**, 1664–1673.

Shemwell, B., Levendis, Y.A. & Simons, G.A. 2001. Laboratory study on the high-temperature capture of HCl gas by dry-injection of calcium-based sorbents. *Chemosphere* **42**, 785–796.

Van Caneghem, J., Brems, A., Lievens, P., Block, C., Billen, P., Vermeulen, I. & Vandecasteele, C. 2012. Fluidized bed waste incinerators: Design, operational and environmental issues. *Progress in Energy and Combustion Science* **38**, 551–582.

Wey, M.-Y., Ou, W.Y., Liu, Z.S., Tseng, H.H., Yang, W.Y. & Chiang, B.C. 2001. Pollutants in incineration flue gas. *Journal of Hazardous Materials* **82**, 247–262.

Agronomy Research **15**(S1), 1033–1040, 2017

Determining the specific heat capacity and thermal conductivity for adjusting boundary conditions of FEM model

A. Kešner[1,*], R. Chotěborský[1] and M. Linda[2]

[1]Department of Material Science and Manufacturing Technology Faculty of Engineering, Czech University of Life Sciences Prague, Kamýcká 129, CZ165 21 Prague – Suchdol, Czech Republic
[2]Department of Electrical Engineering and Automation, Faculty of Engineering, Czech University of Life Sciences Prague, Kamýcká 129, CZ165 21 Prague – Suchdol, Czech Republic
[*]Correspondence: kesner@tf.czu.cz

Abstract: One of modern way of the heat treatment process of agricultural tools such as chisels or tines is FEM modelling. FEM models needs the accurate boundary conditions for successful solution. Specific heat capacity and thermal conductivity are important parameters for the design of the physical properties of heat treatment. These parameters are used for the formation of the temperature field during the cooling process at the heat treatment. More accurate parameters allow you to better estimate the final microstructure in the entire cross-section of the material. Specific heat capacity and thermal conductivity are known from material sheets, but they are stated as constant values. This is the reason why this work is focused on the determination of specific heat capacity and thermal conductivity of steel during the quenching. For the experiment in this work was chosen material 25CrMo4. The values of specific heat capacity and thermal conductivity were determined by comparing the experimentally measured cooling curves and cooling curves generated by the mathematical model. The dependences of specific heat capacity and thermal conductivity were compared in temperature, so that the relationships of cooling curves were statistically significant under alfa level 0.05.

Key words: specific heat capacity, thermal conductivity, FEM model, quenching.

INTRODUCTION

Mechanical properties and production efficiency are important aspects in the production of agricultural tools. Combining these requirements need a correct preparation of production as the correct selection of materials including heat treatment. The simulation of heat treatment can be designed by FEM models nowadays allows. FEM models shown good prediction of microstructure, mechanical properties and deformation of the material (Rabin et al., 2013).

Bainitic structure or combination of bainitic and martensitic structures are suitable for agricultural tools. (Narayanaswamy et al., 2016a; Narayanaswamy et al., 2016b). The boundary conditions of FEM models is neccesary set to accuracy model with respect to microstructure phases. It can be determined by experiments for evalution of heat flux between steel and quenching media. (Kesner 2015; Chotěborský & Linda 2015b), also

chemical composition of steels, specific heat capacity c_p and thermal conductivity λ must be set with the highest possible accuracy. Specific heat capacity and thermal conductivity during the heat treatment show different values. Phase transformations during the heat treatment depend on physical properties of the material. When the cooling rate increases, the diffusive process is interrupted causing a change in the metallurgical microstructure which will affect steel properties (Lara-Guevara et al., 2016).

Size of the specific heat capacities and thermal conductivities reported at room temperature is dependent on the condition of heat treatment. Technical literatures are not given information about dependency between microstructure of steel and physical properties. A higher thermal conductivity reduces temperature gradients at the surface of a tool. A high thermal conductivity is beneficial for hardening because determines the cooling rate of a metal blank from the austenitization temperature and thereby directly influences cycle time and productivity (Kessler & Reich, 2009; Wilzer et al., 2013). The thermal diffusivity and the thermal conductivity decreased as the carbon content increased (Lara-Guevara et al., 2016).

Thermal conductivity and specific heat capacity are increases with increasing carbon content (Lara-Guevara et al., 2016).

Specific heat capacity and thermal conductivity are obtained: using photoacoustic techniques and thermal relaxation (Kessler & Reich, 2009), generating regression analysis, a simple extrapolation of data (Kuepferle et al., 2015) or deriving by calculation from electrical resistance depending on temperature (Rabin et al., 2013).

The aim of this work is to determination of physical properties of material like specific heat capacity and thermal conductivity for FEM models of agriculture tools. Physical properties of material were determined by algorithm where we compared experimetal data with model.

MATERIAL AND METHODS

Specific heat capacity and thermal conductivity was determined for the material 25CrMo4. The chemical composition of the material used is shown in Table 1.

Table 1. Chemical composition of steel 25CrMo4 in wt. %

	C	Mn	Si	P	S	Cr	Ni	Mo	Cu	V
25CrMo4	0.250	0.710	0.230	0.018	0.022	1.030	0.090	0.210	0.230	0.004

Specific heat capacity and thermal conductivity was determined using FEM model. Heat flux was measured during cooling. The results of heat flow were used for comparison of experimentally measured curves and cooling curves.

Some authors (Kesner, 2015) have been described measuring of heat flux. Samples (ø25–50 mm) were heated at temperatures 800, 900 and 1,000 °C for 30 minutes. Water was used as the quenching media. Cooling time lasted until cool the sample throughout the volume (water has 20 °C). Sample cooling was repeated three times for each measured sample. Dependency of heat flux on absolute temperature was transformed to relative temperature (dimensionless temperature-from 0 to 1). Iterative method algorithm of solution was used for the calculation of heat capacity and thermal conductivity. SCILAB 5.5.1. was used to compilation the algorithm – see Fig. 1.

Neumann boundary condition heat flux used for iterative calculation (Telejko 2004; Chotěborský & Linda 2015a).

Heat flux was determined from the measured temperatures for the constant c_p and λ, settings data inclueded boundary conditions (heat flux) and material characteristic (nonstacionar c_p and λ). The next step was run FEM model. Comparison measured and modeled temperature field and determination of suma of error temperature. Last step was setting new c_p and λ. After full iteration the file suma of error was evaluated and minimal suma of errors was found.

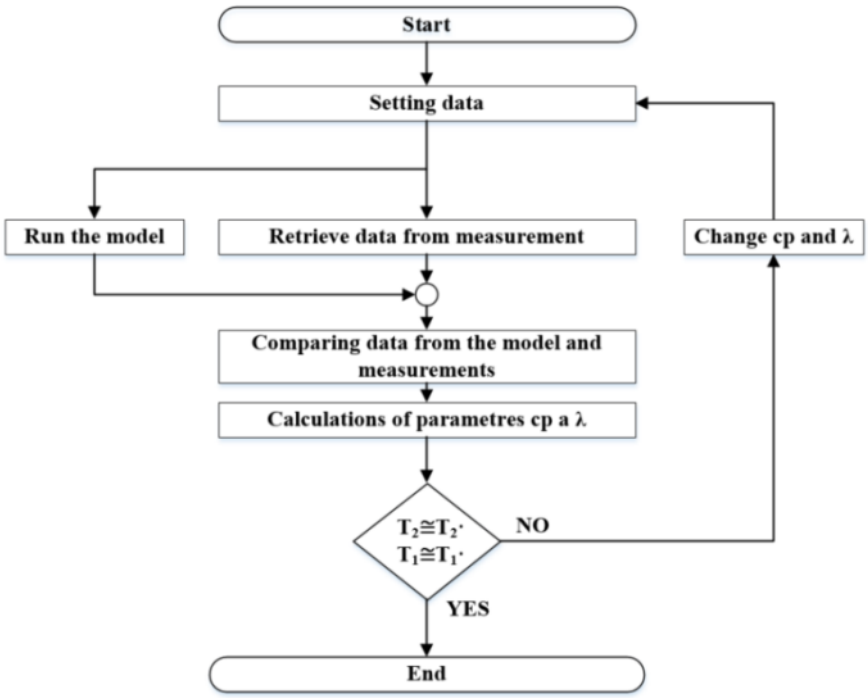

Figure 1. Algorithm for finding the smallest difference between calculeted and measured temperatures field. T_1 and T_2 are measured temperatures, T_1 and T_2 are modeled temperatures.

Iterations were assembled into the matrix. Each iteration included a combination of values of specific heat capacity and thermal conductivity. Relative temperatures were assigned to each value (in table labeled c_0 – constant of boost, c_{sop}, c_1 – constants of slope from the peak) of the specific heat capacity and thermal conductivity. The range of values is shown in the Table 2. The first row contains the smallest set value and the last row of the highest set value. Heat capacity and thermal conductivity were found in the material sheet 25CrMo4 for a constant temperature at 20 °C (λ = 46.44 W m^{-1} K^{-1}, c_p = 590 J kg^{-1} K^{-1}). Step 0.05 was used to shift the relative temperature (in places where it counts a given size thermal conductivity and heat capacity). The algorithm was designed for calculating and comparing iterations. The values were loaded from the first iteration. Cooling curves were calculated for the core and the surface. Heat equation was used to calculate (Eq. 1).

$$\frac{\partial}{\partial x}\left(\lambda\frac{\partial T}{\partial x}\right)+\frac{\partial}{\partial y}\left(\lambda\frac{\partial T}{\partial y}\right)+\frac{\partial}{\partial z}\left(\lambda\frac{\partial T}{\partial z}\right)+Q=\rho\times c_p\times\frac{\partial T}{\partial t} \quad (1)$$

λ – thermal conductivity, Q – is the inner heat–generation rate per unit volume, T – temperature, ρ – density, c_p – heat capacity, t – time.

Calculation began by thermal conductivity, which has a high sensitivity to the temperature cooling rate. The procedure was run for all iterations. Cooling curves, which were experimentally measured, they were also loaded to algorithm. The calculated and experimentally measured cooling curve were compared after simulation. The differences between the calculated and experimentally measured curves were compared. The smallest difference between measured and calculated values of temperature is closest to the fair value of specific heat capacity and thermal conductivity. Iterations are calculated for the cooling time up to 30 seconds, which is the high heat transfer from the the material and the phase transformation.

Newton polynomials were used to calculate (Eq. 2). Triangular matrix is composed of iterations (Eq. 3).

$$n_j(x):=\prod_{i=0}^{j-1}(x-x_i) \quad (2)$$

$$\begin{bmatrix}1 & 0\\ x_1-x_0 & 1\\ x_1-x_0\ (x_1-x_0) & 2\end{bmatrix} \quad (3)$$

For the calculation was used software Windows 7 Enterprise, Intel® Xeon® Processor CPU E5 – 1650 v3@, processor base frequency 3.50 GHz.

Table 2. Combinations of iterations for calculating the heat capacity and thermal conductivity

Shift of point	Thermal conductivity			Shift of point	Heat capacity		
	c_0	c_{sop}	c_1		c_0	c_{sop}	c_1
0.35	20	37.5	20	0.35	1,150	750	1,050
0.4	20	37.5	20	0.35	1,150	750	1,050
.	.	.	.	.	.	.	.
.	.	.	.	.	.	.	.
.	.	.	.	.	.	.	.
0.4	25	42.5	25	0.45	1,250	850	1,150
0.45	25	42.5	25	0.45	1,250	850	1,150

RESULTS AND DISCUSSION

Dependence between the sum of errors and iterations temperature is shown in Fig. 2. The differences (errors) of temperatures were calculated and compared separately for core and separately for the sample surface. The differences in core temperature and surface were added up for each iteration.

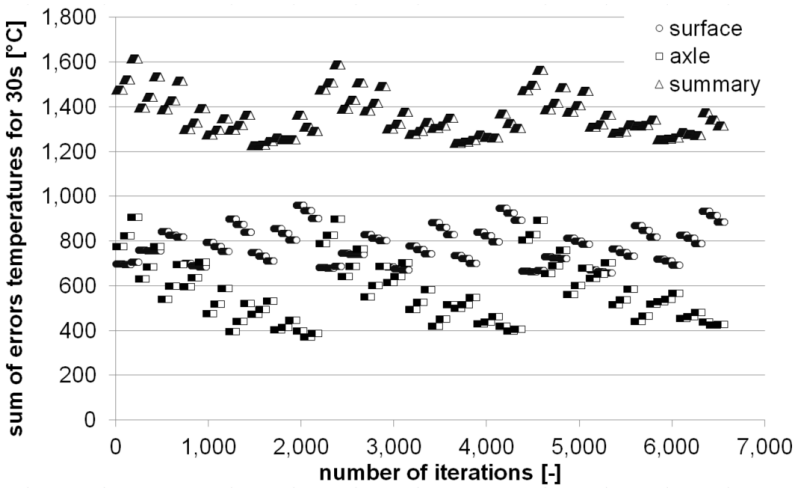

Figure 2. Dependency between sum of errors temperatures.

The smallest difference sum of the temperature was found to closest to the real values of thermal capacity and thermal conductivity. The smallest difference sum of temperature was detected for the iteration which is shown in Table 3.

Table 3. Iteration for the smallest difference sum of temperature

Shift of point	Thermal conductivity			Shift of point	Heat capacity		
	c_0	c_{sop}	c_1		c_0	c_{sop}	c_1
0.4	22.5	42.5	22.5	0.35	1,150	850	1,050

Table 3 show the values of specific heat capacity and thermal conductivity at a given relative temperature which is closest to real values. Fig. 3 shows the course of the thermal capacity and thermal conductivity depending on the relative temperature.

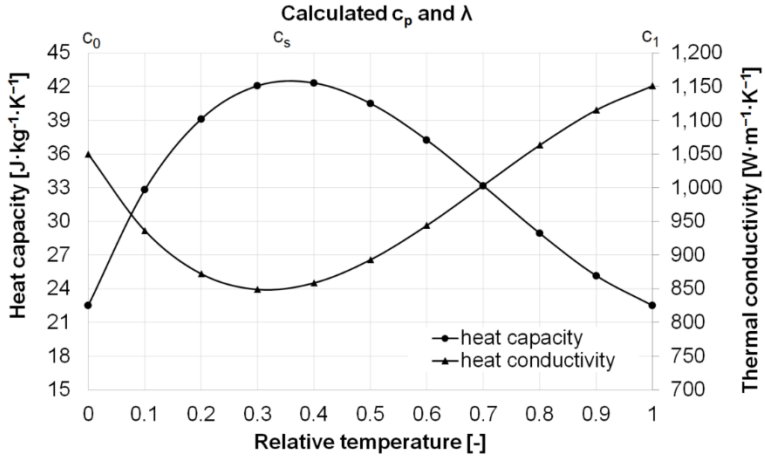

Figure 3. The dependence of the heat capacity and thermal conductivity to relative temperature differential for the smallest experimentally measured and calculated temperatures.

Values c_p and λ can be application in the FEM model, which can be used for a simulation of the thermal treatment of the material 25CrMo4. FEM model was created for simulation with the size of the thermal capacity and thermal conductivity at a given temperature. The advantage is more precise simulation of heat treatment than if they had entered constant the value from the material sheets – see Fig. 4.

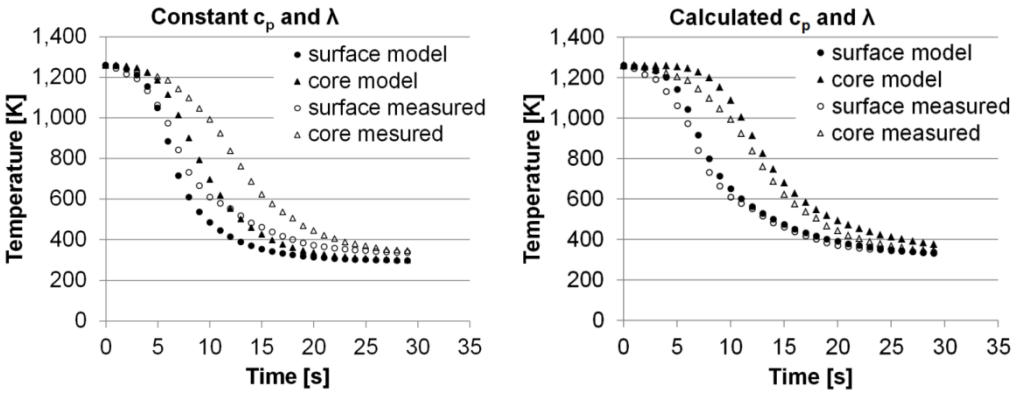

Figure 4. Left side: cooling curves for stacionary c_p and λ in FEM model, right side: cooling curves for nonstacionary c_p and λ in FEM model.

The procedure is relatively time demanding for software. Processor total time was 336 hours for all iterations. Processor time could be reduced by better choice matrix iterations. Iteration could be adjusted by using the adaptive testing algorithm. The program would be assembled with the value of the exact error. The algorithm would not calculated all steps, but only steps with the smallest error until the set conditions. The number of steps is not known with these settings iteration. Large differences between the actual data and calculated data can be adjusted refining steps. Bigger time for calculation and memory software is required for this procedure.

(Prasanna Kumar, 2013) in their work indicates that the accuracy of calculations based on the finite element method depends on the discretization and the time step. Effect of errors has been studied in setting a time step of 0.1 and 0.5 seconds to simulate hardening material C45. The error for time step 0.1 seconds was below 0.50%. The error for time step 0.5 seconds was below 2.25%. The errors were compared with experimentally measured data. Calculations for time step 0.1 seconds were CPU intensive, error for time step 0.5 seconds is considered acceptable.

(Teixeira et al. 2009) shows the heat capacity and thermal conductivity depending on the temperature. The course of thermal conductivity and heat capacity are characterized by at least five points. But we were given three points in this work. More points have higher demands on the software, respectively processor time for calculates. More iterations or choosing a larger time step should be done. Choosing a larger time step could increased again error.

(Wang et al., 2008) in their work compares experimentally calculated and measured temperature during cooling. Cooling was calculated for the constant and variable thermal conductivity and heat capacity. Their results indicate that the variable thermal conductivity and heat capacity values approaching to the experimentally measured data.

CONCLUSIONS

The following findings can be summarized from the calculattions this work:

- Thermal conductivity and heat capacity dependency on the temperature can be calculated by the procedure describe in this work.
- The values of the heat capacity and thermal conductivity dependency on the relative temperature may be used to heat equation FEM model. The algorithm will be more accurate than if we used algorithm without constant values heat capacity and thermal conductivity.
- The smallest difference between the temperatures measured and modeled (for variables cp and λ). The smallest difference value (suma error of temperatures for core and surface) was calculated as 1,224 °C for 30 seconds from the start of cooling.
- Processor total time used in this work was 336 hours for all iterations. A shorter time could be achieved by a better choice of iterations for modelling the variable cp and λ.

ACKNOWLEDGEMENTS. Supported by Internal grant 31140/1312/3108 agency of Faculty of Engineering, Czech University of Life Sciences in Prague

REFERENCES

Chotěborský, R. & Linda, M. 2015a. FEM based numerical simulation for heat treatment of the agricultural tools. *Agronomy Research* **13**(3), pp.629–638.

Chotěborský, R. & Linda, M. 2015b. Prediction Of Mechanical Properties Of Quench Hardening Steel. *Scientia Agriculturae Bohemica* **46**(1), 26–32.

Kesner, A. 2015. Determination of the heat flux for FEM models (Stanovení tepelného toku pro MKP modely). In International Scientific Conference of Young in Zvolen 2015, 67–75.

Kessler, O. & Reich, M. 2009. Similarities and differences in heat treatment simulation of aluminium alloys and steels. *Materialwissenschaft und Werkstofftechnik* **40**(5–6), 473–478.

Kuepferle, J., Wilzer, J., Weber, S. & Theisen, W. 2015. Thermo-physical properties of heat-treatable steels in the temperature range relevant for hot-stamping applications. *Journal of Materials Science* **50**(6), 2594–2604.

Lara-Guevara, A., Ortiz-Echeverri, C.J., Rojas-Rodriquez, I., Mosquera-Mosquera, J.C., Ariza-Calderón, H., Ayala-Garcia, I. & Rodriquez-García, M.E. 2016. Microstructural, Structural, and Thermal Characterization of Annealed Carbon Steels. *International Journal of Thermophysics* **37**(10), p. 99.

LIU, H. Song, Z.L., Cao, Q., Chen, S.P. & Meng, Q.S. 2016. Microstructure and Properties of Fe-Cr-C Hardfacing Alloys Reinforced with TiC-NbC. *Journal of Iron and Steel Research International* **23**(3), 276–280.

Narayanaswamy, B., Hodgson, P., Timokhina, I. & Beladi, H. 2016. The Impact of Retained Austenite Characteristics on the Two-Body Abrasive Wear Behavior of Ultrahigh Strength Bainitic Steels. *Metallurgical and Materials Transactions A*, **47**(10), 4883–4895.

Narayanaswamy, B., Hodgson, P. & Beladi, H. 2016. Comparisons of the two-body abrasive wear behaviour of four different ferrous microstructures with similar hardness levels. *Wear* **350–351**, 155–165.

Prasanna Kumar, T.S. 2013. Influence of Steel Grade on Surface Cooling Rates and Heat Flux during Quenching. *Journal of Materials Engineering and Performance* **22**(7), 1848–1854.

Rabin, B.H., Swank, W.D. & Wright, R.N. 2013. Thermophysical properties of Alloy 617 from 25 °C to 1000 °C. *Nuclear Engineering and Design* **262**, 72–80.

Teixeira, M.G., Rincon, M.A. & Liu, I.-S. 2009. Numerical analysis of quenching – Heat conduction in metallic materials. *Applied Mathematical Modelling* **33**(5), 2464–2473.

Telejko, T. 2004. Analysis of an inverse method of simultaneous determination of thermal conductivity and heat of phase transformation in steels. *Journal of Materials Processing Technology* **155–156**, 1317–1323.

Wang, J., Gu, J., Shan, X., Hao, X., Chen, N. & Zhang, W. 2008. Numerical simulation of high pressure gas quenching of H13 steel. *Journal of Materials Processing Technology* **202**(1–3), 188–194.

Wilzer, J., Lüdtke, F., Weber, S. & Theisen, W. 2013. The influence of heat treatment and resulting microstructures on the thermophysical properties of martensitic steels. *Journal of Materials Science* **48**(24), 8483–8492.

Agronomy Research **15**(S1), 1041–1049, 2017

Comparison of PM production in gasoline and diesel engine exhaust gases

M. Kotek*, P. Jindra, P. Prikner and J. Mařík

Czech University of Life Science Prague, Faculty of Engineering, Department of Vehicles and Ground Transport, Kamýcká 129, CZ165 21 Prague, Czech Republic
*Correspondence: kotekm@oikt.czu.cz

Abstract. The article is focused on different kind of combustion engines and their particulate matter production. The first part of experiments dealt with particulate matter production under defined driving cycle and operating regimes. The second part of experiments was carried out to measure the maximal PM production under engine's full load regime. The experimental vehicle engines were manufactured by Skoda Auto a.s., equipped with modern fuel injection systems. Two representatives of diesel engines were chosen: the engine EURO-4 1.4 TDI with PD (Unit injector) injection system and the EURO-6 1.6 TDI with common rail injection system and DPF. As two representatives of gasoline EURO-4 engines were chosen: 1.2 MPI with non-direct fuel injection system and 2.0 FSI with direct stratified fuel injection system. The analysis of the particulate matters was carried out on a TSI Engine Exhaust Particle Sizer 3090 that is able to classify particles from 5.6 nm to 560 nm. In the case of diesel engines the results proved expectable decrease in PM production due to usage of diesel particulate filter (DPF). The older engine without DPF produced more than hundred times higher PM production under all operating regimes of driving cycle. The result of gasoline engines confirmed increased PM production of direct injection systems especially under higher engine load. FSI engine in driving cycle reached up twenty times higher PM production than MPI engine.

Key words: particulate matter, MPI, FSI, DPF, PFI, common rail, carburettor, size distribution, driving cycle.

INTRODUCTION

The diesel engines are often used in trucks, trains and other heavy-duty applications, as a powertrain. The number of diesel vehicles slowly equals the number of vehicles with gasoline engines. In the European Union share of diesel engines was about 41% in 2014 (ACEA). This fact leads to very strict regulations limiting the emission production which manufacturers must respect.

First emission limit Euro-1 was introduced in 1992. Euro-2 in 1996, Euro-3 in 2000, Euro-4 in 2005, Euro-5 in 2009 and last Euro-6 was introduced in 2014. To meet the strict Euro-6 limits the new vehicles have to be equipped with the diesel particulate filter (DPF) for PM reducing and with the SCR (selective catalytic reduction) catalyst to meet the NO_X limits (López et al., 2009).

The most frequently discussed problem of diesel engine emissions are particulate matter (PM) and nitrogen oxides (NOx). The danger of PM lies in the ability to absorb polycyclic aromatic hydrocarbons (Vojtíšek-Lom et al., 2015). Impact of increasing PM

production on human health is often associated with lung cancer and asthma (McEntee et al., 2008).

Size of PM influences the impact on human health. Particles less than tens of nanometres can penetrate through cell membranes into the blood and have a wide and detrimental effect on human health (Künzli et al., 2000). PM may affect reproduction, cardiovascular system or may provoke cancerous growth (Lewtas, 2007).

The number of gasoline direct injection (GDI) engines grows in recent years because of its advantages in terms of fuel economy. The introduction of direct fuel injection to gasoline engines has led to an increase in fuel economy and engine performance in relation to traditional port injection (Mathis et al., 2005). Explanation is that the direct injection allows better control the quantity of fuel injected and because vaporized liquid droplets cause a cooling of surrounding air and it allows to increase air volume in a cylinder. On the other side there is not enough time in GDI engines for complete fuel evaporation which leads to the formation of areas with a locally rich mixture. Therefore more particulate matter is produced from GDI engines compared with PFI engines (Liu, 2013; Short, 2015).

Comparing the production of vehicles according to the PM with depending on the emission standard was solved by Tzamkiozis, 2010. Emissions from actual operations and their dependence to speed or age of vehicle describes Chana, 2004. One of possible way is to reduce the production of PM by the use of alternative fuels or biofuels. A common alternative fuel is LPG. Emissions during the use of LPG in real operation describe Laua, 2011. Positive impact of biofuels in terms of engine emissions was confirmed by many studies (Mařík et al., 2014; Pexa et al., 2014, Kotek et al., 2015; Jindra et al., 2016). But on the other hand emission production is substantially influenced by the driver's behaviour and immediate traffic conditions (Holmén & Niemeier, 1998). Vehicle manufacturers try to solve the problems linked with emissions in several ways.

One the most discussed issue, especially within recent years, is well known scandal so-called ‘Dieselgate’ that is associated with the excessive production of emissions by several types of VW’s diesel engines. The general public is influenced by the media campaign against the use of diesel engines, mainly in case of older engines due to the excessive production of NO_X emissions and particulate matter. Many automobile manufacturers announced a planned limitation of diesel engine production till the year 2020. On the contrary, the use of gasoline direct injection engines is more and more supported but in fact they can produce a significantly higher amount of PM than the diesel engines which are already mandatorily equipped with diesel particulate filters.

This article presents a comparison of the PM production depending on the engine type (spark ignition, compression ignition) and fuel injection system operating at various operating modes.

Five different vehicles from Skoda Auto, a.s. were used for this experiment. The vehicles were manufactured in the years 2004–2016. For better illustrations of development in systems for emission reducing the experiment was extended by the historic Skoda Octavia manufactured in 1960.

MATERIALS AND METHODS

The five different vehicles Skoda (technical information see Table 1) were used in these experiments. Three vehicles were equipped with spark ignition (SI) engine and two with compression ignition (CI) engine.

Table 1. Technical information of tested cars

					
Vehicle	Octavia 2.0 FSI combi	Fabia 1.2 HTP	Rapid 1.6 TDI Spaceback	Roomster 1.4 TDI	Octavia Super 1960
COMBUSTION ENGINE					
Design	SI, atmospheric	SI, atmospheric	CI, turbo charged	CI, turbo charged	SI, atmospheric
Fuel system	direct injection	multi-point injection	common rail	unit injector system	carburettor
Number of cylinders and valves	4, in row, 16 valves	3 in row, 6 valves	4, in row, 16 valves	3 in row, 6 valves	4, in row, 8 valves
Fuel	gasoline	gasoline	diesel	diesel	gasoline
Volume of cylinders	1,984 ccm	1,198 ccm	1,598 ccm	1,422 ccm	1,433 ccm
Power	110 kW at 6,000 rpm	40 kW at 4,750 rpm	85 kW at 4,400 rpm	59 kW at 4,000 rpm	37.5 kW at 4,600 rpm
Torque	200 Nm at 3,500 rpm	106 Nm at 3,000 rpm	250 Nm at 1,500 rpm	195 Nm at 2,200 rpm	88 Nm at 3,000 rpm
EU limit	EU4	EU4	EU6	EU4	EU0
PM limit	-	-	0.005 $g \cdot km^{-1}$	0.025 $g \cdot km^{-1}$	-
Manufacture year	2004	2003	2016	2006	1960 (engine 1990)
Mileage	105,000 km	136,000 km	12,500 km	102,000 km	65,000 km
CAR BODY					
Service weight	1,515 kg	1,055 kg	1,260 kg	1,240 kg	920 kg
DRIVE PERFORMANCE					
Max. speed	212 km h^{-1}	150 km h^{-1}	190 km h^{-1}	165 km h^{-1}	115 km h^{-1}
Acceleration 0–100 km h^{-1}	9.4 s	18.5 s	10.3 s	14.7 s	-
Fuel consumption	8.87/5.18/6.5 (L 100 km^{-1})	7.8/4.8/5.9 (L 100 km^{-1})	5.0/3.4/4.1 (L 100 km^{-1})	5.1/3.76/4.26 (L 100 km^{-1})	8 (L 100 km^{-1})

The experiment was conducted on the chassis dynamometer at the Department of Vehicles and Ground transport, CULS in Prague. This device simulated the real driving resistances according to each vehicle properties. Test procedure was split into two stages.

In the first stage the vehicles were driven according to designed driving cycle (specification see Fig. 1) to attain repeatability and comparability of conducted measurements under conditions that were as close as possible to real driving conditions. This driving cycle was based on the NEDC (New European Driving Cycle), but for the purpose of this experiment was substantially shortened and maximal speed was limited up to 80 km h^{-1}.

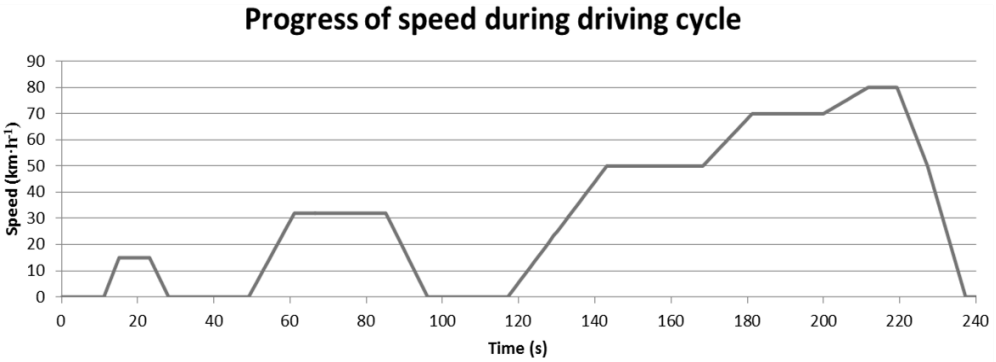

Figure 1. Progress of speed during driving cycle.

The second stage of test procedure was focused on to measure the maximal PM production at full load of engine. The vehicle was driven on chassis dynamometer again; at 3rd gear grade from idle to maximum engine speed with full acceleration. This regime was repeated 3 times.

Classification of PM was analysed by the engine exhaust particle sizer TSI model EEPS 3090 whose detailed specification is shown in Table 2. The analyser enables detection of particle size and also monitors their number. The obtained data are presented as a size range of produced particles. The measured sample was taken from the exhaust gas, and then is diluted by the device. Within the experiments were evaluated only relative changes in the production of solid particles in the diluted exhaust gas.

Table 2. Specification of PM analyser TSI EEPS 3090

Particle size range	5.6–560 nm
Particle size resolution	16 channels per decade (32 total)
Electrometer channels	20
Time resolution	10 size distribution per second
Sample flow	10 L min^{-1}
Dilution accessories	Rotation Disk thermodilution

RESULTS AND DISCUSSION

The result of instantaneous values of PM total concentration during driving cycle for each vehicle is shown in Fig. 2.

The highest PM values were reached by the vehicle Skoda Roomster. This vehicle produced high amount of PM already even at idling speed (compared to other vehicles) and the next increase of PM production is evident under engine load. The second vehicle

with CI engine Skoda Rapid reached expectable minimal PM concentration during the whole cycle due to diesel particulate filter (DPF). There is no noticeable influence of engine operating state on PM production which indicates a very high DPF efficiency. This observation is consistent with Mathis et al. (2005) and Mohr et al. (2006).

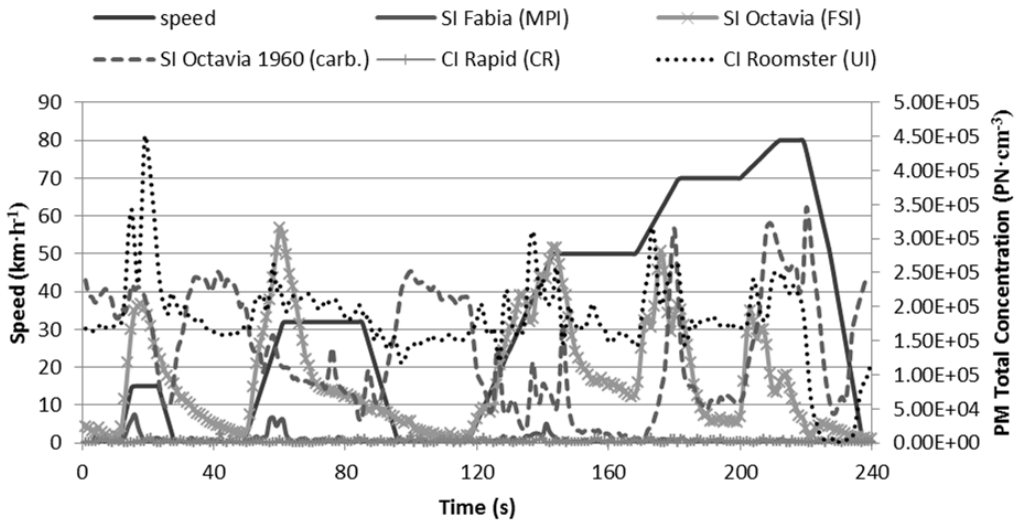

Figure 2. PM total concentration during driving cycle.

In case of vehicles with SI engines the situation is a little complicated. The lowest PM concentration was reached by Skoda Fabia with relatively obsolete non-direct multi-point injection system. On the other hand the vehicle Skoda Octavia FSI with modern direct system of stratified injection produced the highest values of PM. It is probably caused due to combustion strategy. FSI engine management switched from the stoichiometric mode to the lean stratified combustion which caused significantly higher particle emissions especially at higher engine load. A similar conclusion was reached by Mohr et al. (2006) and Chen et al. (2017). The last vehicle Skoda Octavia 1960 was in experiment as interesting attraction and produced expectable very high amount of PM. There was not surprisingly so big difference in the PM production compared to Octavia FSI that is about 40 years younger. It can be caused probably by a big influence of very rich mixture prepared by old carburettor system because of illogical decrease in PM production at higher engine load and increase at idle.

Better overview of reached results is provided in Fig. 3. There are shown average values of PM production during whole driving cycle and separately at idling speed. These two presented regimes demonstrate the influence of engine load. There are not evident fundamental differences between idle and ordinary operating state for Skoda Roomster and Octavia 1960. These vehicles produce almost constantly large amount of PM regardless to engine operating state while Skoda Rapid and Skoda Fabia produced the minimal amount of PM during the whole driving cycle. These results are consistent with Mathis et al. (2005), Mohr et al. (2006) and Chen et al. (2017).

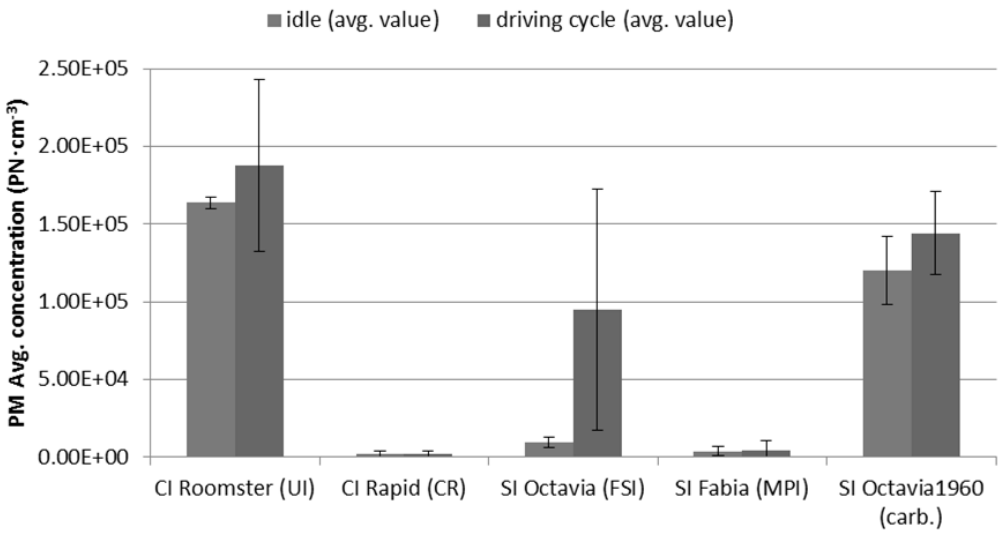

Figure 3. PM average PM concentration during driving cycle and at idle speed.

The results of second stage of experiment are summarised in Fig. 4. There is evident surprisingly the highest PM production of Skoda Fabia MPI. Results of other vehicles correspond approximately to previous Fig. 3. It is important to remark that engine works relatively exceptionally at operating regime of full load during normal drives.

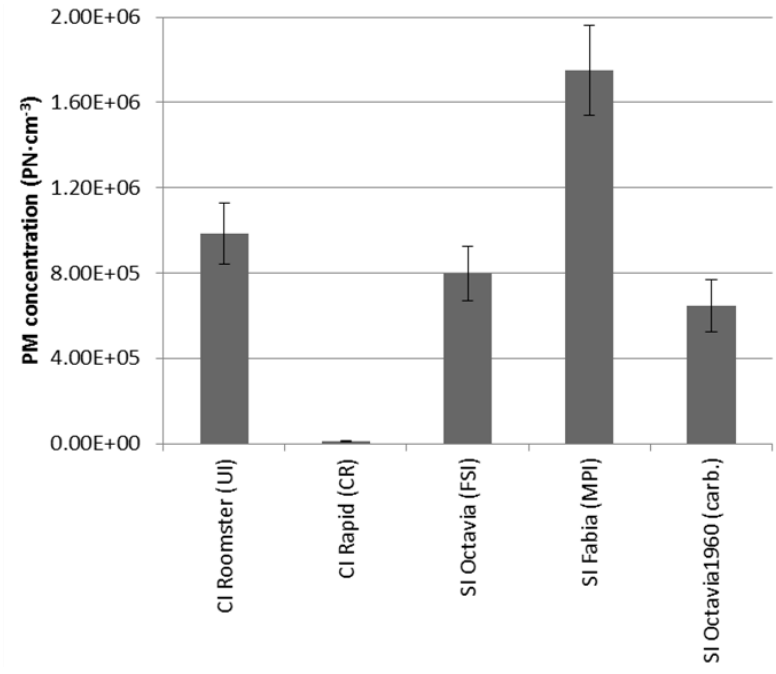

Figure 4. Maximal PM concentration at full load.

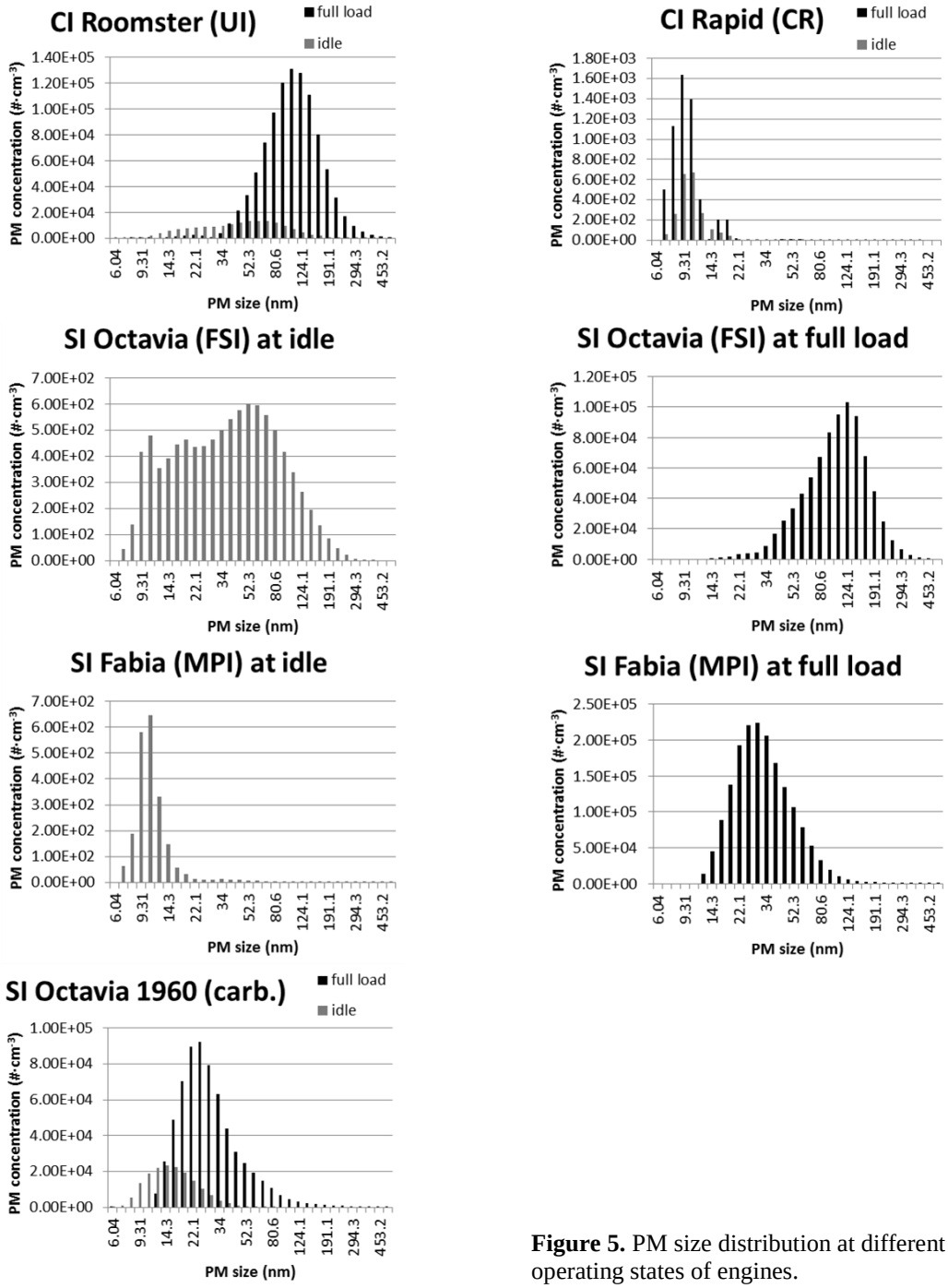

Figure 5. PM size distribution at different operating states of engines.

The Fig. 5 shows PM size distribution at idle speed and at full engine load (respectively at maximal PM production). The vehicle Skoda Roomster produces relatively large PM at both operating regimes. The similar situation is at full load of Skoda Octavia FSI while at idling speed was produced wide PM spectrum but with very

small total concentration. Much better situation is in the case of Skoda Rapid with DPF. There are evident filter abilities of DPF when the PM spectrum decreases up to minimal size and PM total concentration is very low. Skoda Fabia MPI produced very small size and amount of PM at idling speed while at full load the PM spectrum is shifted to middle and the total concentration rapidly grows. Similar PM size distribution can be found in Gupta et al. (2010) and Graves et al. (2017). In case of historic Skoda Octavia 1960 the PM spectrum at idle is little bit similar to Skoda Roomster when the spectrum is shifted to small particles. At full load the PM spectrum is very similar to all other SI engines, the spectrum is again shifted to small particles but the total concentration is the smallest of tested SI engines.

CONCLUSIONS

This paper was focused on measurement of PM (particle number and particle size distribution) emitted from the exhaust of different types of SI and CI engines.

The results of PM production of CI engines confirm that newer vehicles with modern system of fuel injection (common rail) and better systems for emissions reduction (especially DPF) produce absolutely minimal PM. Of course there is a question what happens in case of DPF regeneration process when can be expectable big increase in PM production as was published for example in Ko et al. (2016).

In case of SI engines there is different situation. The older system of non-direct multi-point injection reached minimal PM production (except of full engine load) while the newest direct fuel stratified injection system showed perceptible increase at every engine load. The twenty times higher PM production was reached in driving cycle in compare with MPI engine. It can be expected that in the future DPF could be mandatory for new gasoline engines with FSI technology.

ACKNOWLEDGEMENTS. Paper was created with the grant support – CZU 2016:31150/1312/3111 – Analysis of the impact of biofuels on the operating parameters of internal combustion engines.

REFERENCES

ACEA. http://www.acea.be/. *European Automobile Manufacturers' Association.* [Online] [Cited: 2 1 2016.] http://www.acea.be/statistics/tag/category/passenger-car-fleet-by-fuel-type.

Graves, B.M., Koch, Ch.R. & Olfert, J.S. 2017. Morphology and volatility of particulate matter emitted from a gasoline direct injection engine fuelled on gasoline and ethanol blends. *Journal of Aerosol Science* **105**, 166–178.

Gupta, T., Kothari, A., Srivastava, D.K. & Agarwal, A.K. 2010. Measurement of number and size distribution of particles emitted from a mid-sized transportation multipoint port fuel injection gasoline engine. *Fuel* **89**(9), 2230–2233.

Holmén, B.A. & Niemeier, D.A. 1998. Characterizing the effects of driver variability on real-world vehicle emissions. *Transportation Research Part D: Transport and Environment* **3**(2), 117–128.

Chana, T.L., Ninga, Z., Leunga, C.W., Cheunga, C.S. & Hungb, W.T. 2004. On-road remote sensing of petrol vehicle emissions measurement and emission factors estimation in Hong Kong. *Atmospheric Environment* **38**(14), 2055–2066.

Chen, L., Liang, Z., Zhang, X. & Shuai, S. 2017. Characterizing particulate matter emissions from GDI and PFI vehicles under transient and cold start conditions. *Fuel* **189**, 131–140.

Jindra, P., Kotek, M., Mařík, J. & Vojtíšek, M. 2016. Effect of different biofuels to particulate matters production. *Agronomy Research* **14**(3), 783–789.

Ko, J., Si, W., Jin, D., Myung, Ch-L. & Park, S. 2016. Effect of active regeneration on time-resolved characteristics of gaseous emissions and size-resolved particle emissions from light-duty diesel engine. *Journal of Aerosol Science* **91**, 62–77.

Kotek, T., Kotek, M., Jindra, P. & Pexa, M. 2015. Determination of the optimal injection time for adaptation SI engine on E85 fuel using self-designed auxiliary control unit. *Agronomy Research* **13**(2), 577–584.

Künzli, N., Kaiser, R., Medina, S., Studnicka, M., Chanel, O., Filliger, P., Herry, M., Horak, F.Jr., Puybonnieux-Texier, V., Quénel, P., Schneider, J., Seethaler, R., Vergnaud, J.-C. & Sommer, H. 2000. Public-health impact of outdoor and traffic-related air pollution: a European assessment. *The Lancet* **356**, 9232, pp. 795–801.

Laua, J., Hunga, W.T. & Cheungb, C.S. 2011. On-board gaseous emissions of LPG taxis and estimation of taxi fleet emissions. *Science of The Total Environment* **409**(24), 5292–5300.

Lewtas, J. 2007. Air pollution combustion emissions: Characterization of causative agents and mechanisms associated with cancer, reproductive, and cardiovascular effects. *Mutation Research/Reviews in Mutation Research* **636**, pp. 95–133.

Liu, H., Ronkko, T. & Keskinen, J. 2013. Impact of vehicle development and fuel quality on exhaust nanoparticle emissions of traffic. *Environmental Science and Technology* **47**(15), 8091–8092.

López, J.M., Jiménez, F., Aparicio, F. & Flores, N. 2009. On-road emissions from urban buses with SCR + Urea and EGR + DPF systems using diesel and biodiesel. *Transportation Research Part D: Transport and Environment* **14**(1), 1–5.

Mařík, J., Pexa, M., Kotek, M. & Hönig, V. 2014. Comparison of the effect of gasoline - ethanol E85 - butanol on the performance and emission characteristics of the engine Saab 9-5 2.3 l turbo. *Agronomy Research* **12**(2), 359–366.

Mathis, U., Mohr, M. & Forss, A.-M. 2005. Comprehensive particle characterization of modern gasoline and diesel passenger cars at low ambient temperatures. *Atmospheric Environment* **39**(1), 107–117.

McEntee, J.C. & Ogneva-Himmelberger, Y. 2008. Diesel particulate matter, lung cancer, and asthma incidences along major traffic corridors in MA, USA: A GIS analysis. *Health & Place* **14**(4), 817–828.

Mohr, M., Forss, A.-M. & Lehmann, U. 2006. Particle Emissions from Diesel Passenger Cars Equipped with a Particle Trap in Comparison to Other Technologies. *Environmental Science and Technology* **40**(7), 2375–2383.

Pexa, M. & Mařík, J. 2014. The impact of biofuels and technical engine condition to its smoke - Zetor 8641 Forterra. *Agronomy Research* **12**(2) 367–372.

Short, D., Vu, D., Durbin, T., Karavalakis, G. & Asa-Awuku, A. 2015. Particle speciation of emissions from iso-butanol and ethanol blended gasoline in light-duty vehicles. *Journal of Aerosol Science* **84**, 39–52.

Tzamkiozis, T., Ntziachristos, L. & Samaras, Z. 2010. Diesel passenger car PM emissions: From Euro 1 to Euro 4 with particle filter. *Atmospheric Environment* **44**(**7**), 909–916.

Vojtíšek-Lom, M., Pechout, M., Dittrich, L., Beránek, V., Kotek, M., Schwarz, J., Vodička, P., Milcová, A., Rossnerová, A., Ambrož, A. & Topinka, J. 2015. Polycyclic aromatic hydrocarbons (PAH) and their genotoxicity in exhaust emissions from a diesel engine during extended low-load operation on diesel and biodiesel fuels. *Atmospheric Environment* **109**, 9–18.

Agronomy Research **15**(S1), 1050–1056, 2017

Development and testing of apparatus for wooden chips voids measurement

V. Křepčík[1*], J. Lev[2] and F. Kumhála[1]

[1]Czech University of Life Sciences in Prague, Faculty of Engineering, Department of Agricultural Machines, Kamýcká 129, CZ165 00 Praha 6 – Suchdol, Czech Republic
[2]Czech University of Life Sciences in Prague, Faculty of Engineering, Department of Physics, Kamýcká 129, CZ165 00 Praha 6 - Suchdol, Czech Republic
[*]Correspondence: krepcik@tf.czu.cz

Abstract. The interparticle porosity of wooden chips (commonly called voids) is a very important factor which significantly affects properties of wooden chips, i.e. bulk density, combustion speed or dielectric properties. Dielectric properties can be used for the measurement of its moisture content and it is the moisture content which is one of the most important factors that affect wooden chips calorific value. This paper is focusing on the development of measuring apparatus for wooden chips voids measurement. The principle of measuring apparatus is based on a gas displacement method. Measuring apparatus is composed from two chambers; both with the same volume. One from chambers is comparative one and second is experimental one. The pressure operating range was from 1,000 to 1,500 Pa. Results showed nontrivial behaviour of wooden material with the change of moisture content which was probably caused by different structures of tested materials.

Key words: wooden chips, porosity, gas displacement method.

INTRODUCTION

Wood chips are typically used as a fuel in various facilities. Common use cases include home boilers for individual family housesor sophisticated heating apparatuses capable of supplying a large number of households with energy.

The moisture content is very important property of wood chips because the water contained within a fuel significantly influences its calorific value (Nyström & Dahlquist, 2004), which is a crucial factor in this case. The moisture content of wood chips can differ significantly, usually between 20% and 55%. From this point of view, autonomous measurement of wood chips moisture content just before this fuel enters a boiler could make the combustion control much more effective.

It is a well-established fact that the dielectric properties of materials are significantly influenced by the water content. Nelson (2005) has published many important articles in this area. James (1975) has focused directly on wood and has published the measurement statistics in the frequency voltage from 20 Hz to 50 MHz for various moisture contents and temperatures. Another important parameter affecting the dielectric properties is the bulk density (Nelson, 1991; Nelson, 2015). Paz et al. (2011) tested dielectric mixing models for the purpose to determine the dielectric constant of

woody biomass at different water contents. An important component of their model was the air volumetric content. Another possibility for wood chips moisture measurement is x-ray. X-radiation is absorbed by material in relation to the total mass in the radiation beam. It is clear that this method is significantly influenced by the material bulk density as well (Nyström & Dahlquist, 2004).

The knowledge of material porosity is crucial for development of universal method for wood chips moisture contend measurement. Several methods for material porosity measurement are available. One of them is the gas displacement method – GDM (Karathanos & Saravacos, 1993; Rahman, 2003; Sahin & Sumnu, 2006). This method can be fast and effective. Several researches used this method for volume/density measurement of seeds (Thompson & Isaacs, 1967; Fang & Campbell, 2000). Authors reported that their measurements were influenced by material internal pores. Another similar experimental methods are liquid and solid displacement method. However, the usage of the liquid displacement method is problematic in case a material that quickly absorbs the liquid (Rahman, 2005; Sahin & Sumnu, 2006). The solid displacement method is similar to liquid displacement method but instead of liquid it uses fine particulate material (sand, glass bead, seed, etc.). The disadvantage of this method is its duration and labour intensity (Sahin & Sumnu, 2006). The bulk density of the agricultural materials can be estimated based on the acoustic measurement (Adamchuk et al., 2004). However, this method is affected by a material modulus of elasticity and material structure.

As it follows from previous text, fast determination of wood chips voids could be a way to better use its calorific value by better combustion control. That is why the main aim of the work presented in this article was to apply GDM for wooden chips voids measurements.

MATERIALS AND METHODS

A new apparatus for wooden chips voids measurement was developed. The measuring apparatus for measurement of voids of wooden chips (Fig. 1) is composed from two chambers with the same volume. Chambers are attached to bearing frame together with connecting line (Fig. 2), which the aim to haul the medium (in our case the air). The connecting line is divided into two parts with the help of three closing valves when digital pressure meter is attached to the first part. Basically, this design is well-known as it was described eg. by authors Sahin & Summu (2006).

Samples from three kinds of wood were (pine, beech, oak) prepared for our experiment. All samples had a cubic shape with 20 mm edge length (see Fig. 3). Samples were measured and weighed before each measurement to determine its volume and moisture. The fault of determining the samples volume did not exceed 3%. At the beginning of the measurement, the samples were dried to the dry matter in the hot-air oven under the temperature of 105 °C (ASABE Standard S358.2, 2006). After taking samples out, their weighing and proportions measurement was done. Then, the samples were inserted into the measuring chamber and the chamber was together with the samples inserted into the pressure mechanism of the measuring chamber.

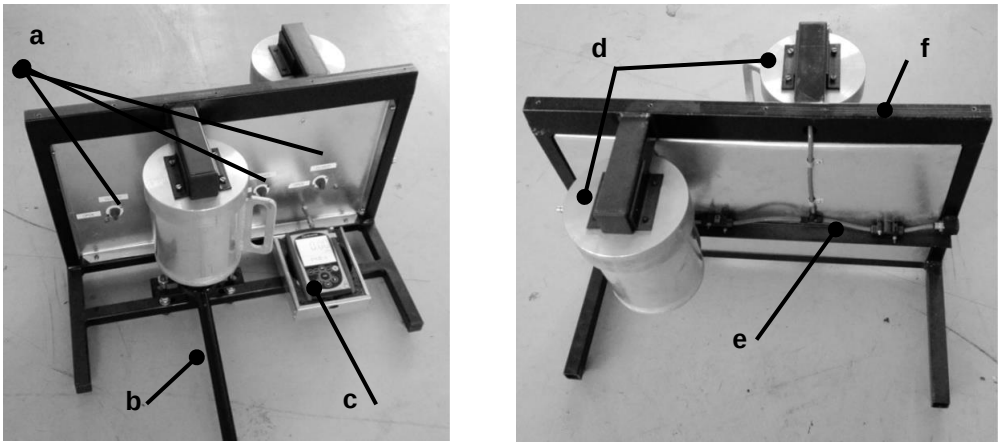

Figure 1. Measuring apparatus: a) closing valves; b) pressure mechanism of measuring chambers; c) digital pressure meter; d) measuring and comparing chambers; e) connecting line; f) bearing frame of the measuring apparatus.

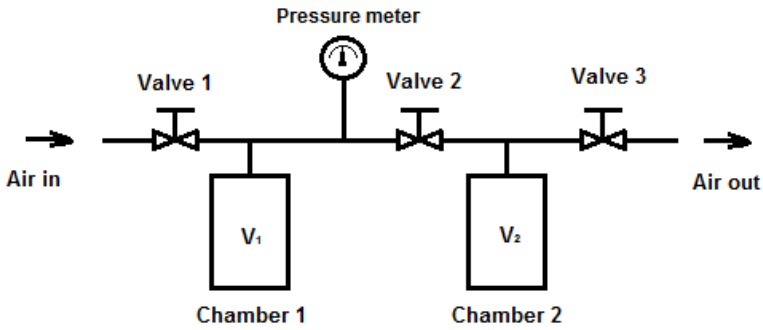

Figure 2. Linking conduct of the measuring apparatus.

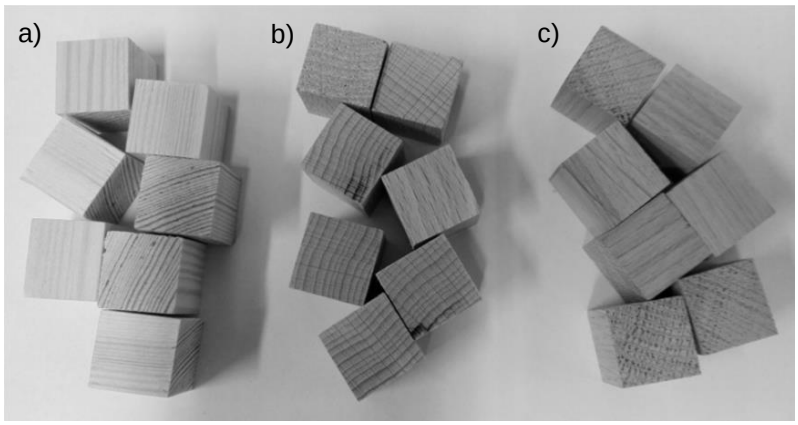

Figure 3. Testing samples: a) pine, b) beech, c) oak.

After the connecting the source of pressure medium, the first valve was opened and the other two valves were closed. The pressure from 1,000 to 1,500 Pa was put into the first part of the connecting line and, subsequently, the first valve was closed. After the pressure was ballanced in the first part, the value of the pressure in the first part of connecting line was recorded from digital pressure meter.

Then the second closing valve was closed and the pressure was released into the second part of connecting line when first and third valves were still closed. The value which was at the pressure gauge after the connecting both branches of connecting line was recorded from the pressure meter. The volume of the sample was counted with the help of the following equation (Sahin & Sumnu, 2006):

$$V_s = V_2 - V_1\left(\frac{P_1 - P_2}{P_2}\right) \quad (1)$$

where: V_s – calculated volume of the sample (m^3); V_1, V_2 – volume of the chambers (m^3); $P_1,\ P_2$ – measured pressures (Pa).

Then, samples were inserted into water with the temperature 15 ± 3 °C for one hour. After this time, samples were taken out and inserted into the hermetic plastic bag where they were kept for 12 hours in order to balance the moisture content of all samples at the same level. After the balancing the moisture content, the samples were weighed again and its dimensions were measured in order to determine its moisture content and volume. After that, the measurement described above was repeated.

Volume measurements by the GDM method was 15 times repeated. All together the samples were macerated four times. First three times for one hour and within the forth maceration, for 36 hours. The samples from pine reached moisture content 6.4%, 20.6%, 28.0% a 35.6%. The samples of oak reached moisture content 12.7%, 15.6%, 30.3% a 53.9%, and the samples of beech reached moisture content 6.1%, 26.2%, 39.1% a 43.7%.

RESULTS AND DISCUSSION

Results of the measurement are charted in the graphs in Fig. 4. Each of the three graphs contains three curves. First curve presents the real volume of measured samples as it was determined by hand measurement. From all three diagrams, obvious effect of samples swelling can be seen. The degree of volume change for individual materials approximately coincided with an increase of moisture content. However, the response of individual materials was different. The second curve presents the course of volume which was measured by our measuring apparatus. Volumes measured corresponded with the volume of samples, without pores in the material. The difference between both measured values present a part of pores volume in the material. In Fig. 4, these data are displayed as percentage share from the real volume of the samples.

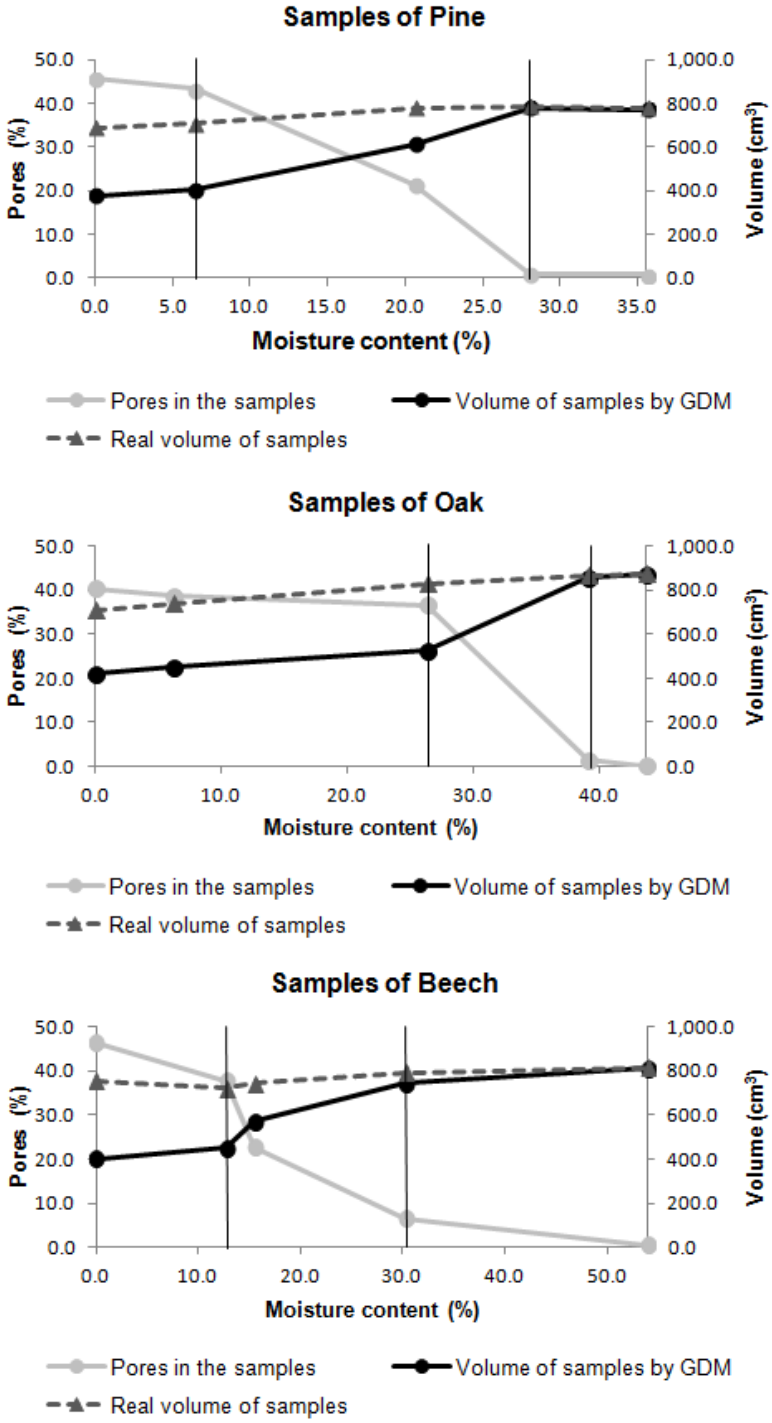

Figure 4. Graphs of the dependence of filling of pores by water,samples real and samples measured volume on material moisture content. GDM – gas displacement method.

It is possible to distinguish between three different areas in the graphs in Fig. 4. Slight change of proportional volume of pores during moistening was typical for the first area. This area was relatively short for pine and beech wood; nevertheless for oak wood it reached 30% of moisture content. In this area, water penetrated into the material but most of bigger pores still remained full of air. The second area was typical by fast change of pores percentage volume with the increasing moisture content. It can be assumed that, in this phase, the gradual filling of bigger pores by water was observed. The fastest change was observed for oak wood again. In the third area, most of the pores were filled with water and volumes measured by apparatus almost matched to the real volumes. In this area, it is possible to still expect the growth of moisture content. Nevertheless, the movement of water was determined by diffusion processes, which are considerably slower.

The Fig. 4 showed that from 40% up to 45% shares of the pores were observed for completely dry material. When using the method and the apparatus presented in this article, measured porosity values presented not only voids (space between particles), but also bigger part of inner pores volume. This fact can be evaluated as a positive one, because this volume also fundamentally influences dielectric properties of material (Nelson, 1991). Our results also indicated that the knowledge of the kind of material is important not only to explain different materials dielectric properties, but also different behaviour of water in material. Arrangement and shape in which water is located in the material influences its dielectric properties as well (Serdyuk, 2008; Paz et al., 2011).

CONCLUSIONS

New apparatus for wooden chips voids measurement, which function is based on gas displacement method, was developed.

Developed aApparatus was successfully tested on three types of samples and with different samples moisture content. Results indicated nontrivial behaviour of material with the change of moisture content. Three different areas of the curve describing the dependence of measured pores on material moisture content can be distinguished. These areas were different for different wood tested. This was probably caused by different structures of tested materials.

This behaviour is needed to be taken into consideration when developing methods for fast measurement of wooden chips moisture content made from different wood materials.

ACKNOWLEDGEMENTS. This project was funded by CULS Prague, The University Internal Grant Agency, project CIGA No. 20163001 (31160/1313/3102).

REFERENCES

Adamchuk, V.I., Hummel, J.W., Morgan, M.T. & Upadhyaya, S.K. 2004. On-the-go soil sensors for precision agriculture. *Computers and Electronics in Agriculture* **44**, 71–91.

ASABE Standards. 2006. *S358.2 Moisture measurement-Forages.* St. Joseph, Michigan, USA.

Fang, C. & Campbell, G.M. 2000. Effect of Measurement Method and Moisture Content on Wheat Kernel Density Measurement. *Food and Bioproducts Processing* **78**, 179–186.

James, W.L. 1974. Dielectric properties of wood and hardboard: variation with temperature, frequency moisture content, and grain orientation. Madison, WI: US Department of Agriculture, Res. Pap FPL 245.

Karathanos, V.T. & Saravacos, G.D. 1993. Porosity and pore size distribution of starch materials. *Journal of Food Engineering* **18**, 259–280.

Nelson, S.O. 2005. Dielectric Properties Measurement for Agricultural Applications. *ASAE Paper No: 053134*.

Nelson, S.O. 1991. Dielectric properties of agricultural products-measurements and applications. *IEEE Transactions on Electrical Insulation* **26**, 845–869.

Nelson, SO. 2015. *Dielectric Properties of Agricultural Materials and Their Applications.* Academic Press, Elsevier, UK, USA. 292 p.

Nyström, J. & Dahlquist, E. 2004. Methods for determination of moisture content in woodchips for power plants – a review. *Fuel* **83**, 773–779.

Paz, A., Thorin, E. & Topp, C. 2011. Dielectric mixing models for water content determination in woody biomass. *Wood Sci Technol*. **45**, 249–259.

Rahman, M.S. 2003. A theoretical model to predict the formation of pores in foods during drying. *International Journal of Food Properties* **6**, 61–72.

Rahman, M.S. 2005. Mass-volume-area-related properties of foods. In M.A. Rao, S.S.H. Rizvi & A.K. Datta (Eds.), *Engineering Properties of Foods*, 3rd ed. (pp. 1–39). Boca Raton, FL: CRC Press Taylor & Francis.

Sahin, S. & Sumnu, S.G. 2006. Physical Properties of Foods. *Springer New York*, 257.

Serdyuk, V.M. 2008. Dielectric Study of Bound Water in Grain at Radio and Microwave Frequencies. *Progress In Electromagnetics Research* **84**, 379–406.

Thompson, R.A. & Isaacs, G.W. 1967. Porosity Determinations of Grains and Seeds with an Air-Comparison Pycnometer. *Transactions of the ASAE* **10**(5), 0693–0696.

Agronomy Research **15**(S1), 1057–1066, 2017

Influence of chemical cleaning of adhesive bonded surface on working environment and adhesive bond quality

A. Krofova[1,*], M. Müller[1] and P. Kic[2]

[1]Czech University of Life Sciences Prague, Faculty of Engineering, Department Material Science and Manufacturing Technology, Kamýcká 129, CZ165 21, Czech Republic
[2]Czech University of Life Sciences Prague, Faculty of Engineering, Department of Technological Equipment of Buildings, Kamýcká 129, CZ165 21, Czech Republic
[*]Correspondence: krofovaa@tf.czu.cz

Abstract. Undesirable chemical substances are released into the environment at single manufacturing operations, namely at a chemical treatment /cleaning of an adhesive bonded surface. The chemical treatment /cleaning of namely metal adhesive bonded surface before an application of the adhesive represents a significant factor having an influence on a resultant adhesive bond strength, i.e. adhesive and cohesive strength.
Producers do not provide information about releasing harmful substances into the atmosphere, i.e. mass values of a flow of polluting substances used at the chemical cleaning of the adhesive bonded surface. These cleaning agents were experimentally investigated.
The aim was to evaluate an adhesive bond quality depending on the chemical treatment of the adhesive bonded surface and the intensity of the chemical agent release into the atmosphere. The adhesive bond quality was evaluated by means of mechanical tests and SEM analysis.
The increase of the adhesive bond strength does not conclusively occur when using the chemical treatment of the adhesive bonded surface compared to the adhesive bonds with only mechanical treatment of the adhesive bonded surface, except for the chemical cleaning in the acetone bath. This treatment proved always in a positive way.

Key words: adhesive bond, chemical treatment, chemicals contamination, evaporation.

INTRODUCTION

Undesirable chemical substances are released into the environment at single manufacturing operations. Chemical substances or aerosols should be caught and ventilated according to technical possibilities directly at their source, i.e. e.g. in a production hall. Namely the production of adhesive bonds at using the chemical cleaning of the adhesive bonded surfaces is a problem (Bjørgum et al., 2003; Lunder et al., 2004; Müller et al., 2011; Müller & Valášek, 2013; Müller, 2015).

The proper preparation of the surface by different mechanical, physical or chemical processes or by their combination removes impurities, i.e. 'weak boundary layer'. If the impurity is not removed from the surface or if there are layers on the surface which are not firmly connected to the adhesive material, the adhesive is either not able to wet the adhesive bonding surface or a thin adhesive layer is made, thus it is reducing the strength of the adhesive bond (Messler, 2004; Prolongo et al., 2006).

Treatments of the adhesive bonded surface usually involve mechanical, chemical and combined methods of the preparation (Müller & Valášek, 2014; Cidlina & Müller, 2015; Krofová & Müller, 2016. It is not always technologically desirable to use all combinations of the adhesive bonded surface treatments (Krofová & Müller, 2016).

The chemical cleaning of the adhesive bonded surface represents a significant factor having an influence on the resultant adhesive bond strength (Lunder et al., 2004; (Rudawska, 2014). Producers of chemical cleaning agents usually do not provide technical data about releasing these undesirable substances. Most of manufacturing facilities are equipped with ventilation equipment which do not sometimes fully remove polluting substances. Subsequently, namely the working environment is significantly deteriorated.

Owing to the fact that producers do not provide information about releasing harmful substances into the atmosphere, i.e. mass values of a flow of polluting substances used at the chemical cleaning of the adhesive bonded surface, these cleaning agents were experimentally investigated. The research based on determining the mass flow of polluting substances which leak into the production hall was performed at different chemical agents used for the adhesive bonded surface cleaning. An intensity of the ventilation equipment was calculated in a model space determined for the production of adhesive bonds for different chemical cleaning agents used for the adhesive bond preparation.

The chemical cleaning is a process in which we remove coarse impurities and an antiadhesive layer. Its task is to create an original clean surface by removing the fats, oils, grease etc. on the surface of the adherent. It is also used to increase the adhesion of the adhesive to the adherent surface which results in a creation of surface chemical bonds allowing the reaction molecules of the adherent and the adhesive to form strong bonds (Comyn, 1990; Habenicht, 2002; Krofová & Müller, 2016).

The secondary aim was to evaluate an adhesive bond quality depending on the chemical treatment of the adhesive bonded surface and the intensity of this chemical agent release into the atmosphere. The adhesive bond quality was evaluated by means of mechanical tests and SEM analysis.

A benefit of this research is a comparison of reached values of the adhesive bond strength and a wettability of the adhesive bonded surface depending on values of an evaporation of chemical cleaning agents.

MATERIALS AND METHODS

The amount of substances released into the air during handling with them is not defined by a producer anywhere, due to the many different factors that affect the speed and the amount of evaporated substances. For example depending on the area of evaporation (Fig. 1). The requirements of health and safety at work are summarized in Decree no. 361/2007 Coll., (Act No. 262/2006 Coll.). Referred Exposure Limits OEL and MEL valid for the Czech Republic may be in some cases slightly different (usually higher) from exposure limits valid in the EU or in other countries, however, the principles and solution of this research these small differences do not affect. The evaporation was determined in the following way. The experiment was performed in a ventilated laboratory at 22 ± 2 °C, humidity of 60 ± 3% and an atmospheric pressure of 986 hPa. For the determination of the evaporation laboratory bowls of three different

areas (diameter: 190 mm, 95 mm and 60 mm) were used and using analytical weights mass losses were recorded in real time to the laptop for each substances used for the chemical preparation of the surface of bonded specimens at intervals of 45 minutes.

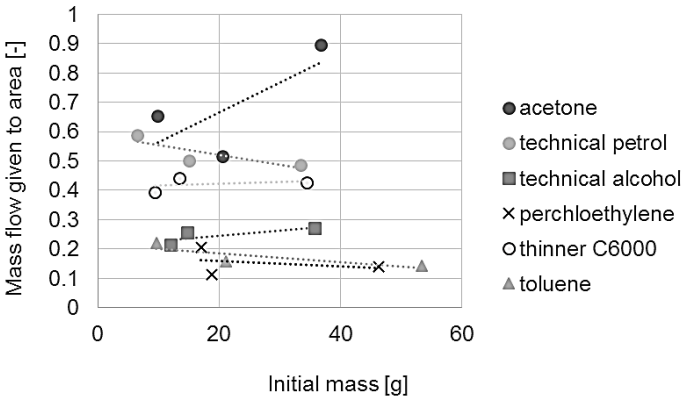

Figure 1. Influence of area on mass flowing.

The evaluation of the adhesive bond quality depending on the chemical treatment of the adhesive bonded surface was performed in accordance with the standard CSN EN 1465. Experiments were performed on standardized test specimens of structural carbon steel S235J0 and manufactured according to the standard EN 1465 by cutting the steel workpiece (100 x 25 x 1.5 mm). The overlapping length of the adhesive bond was 12.5 ± 0.25 mm. Test specimens with the mechanical treatment of the adhesive bonded surface were used for the bonding. The grit blasting by a garnet MESH 80 was the mechanical treatment. The adhesive bonded surface was chemically treated prior to the bonding process. The chemical cleaning of the adhesive bonded surface was performed in the following substances: a bath of acetone, a bath of technical petrol, a bath of technical alcohol, a bath of perchlorethylene, a bath of thinner C6000 and a bath of toluene.

The comparing standard was the surface only mechanically treated by grit blasting without the chemical cleaning. Ethanol was mechanically treated surface the grid blasting without chemical cleaning adhesive bonding surface.

For bonding three structural two-component epoxy adhesives were applied. Structural epoxy adhesives are particularly applied in an industrial manufacturing. The epoxy based adhesive-bonded steel is known to have a good stiffness and the strength, providing a potentially wide range of applications, especially in vehicle structures (Lin et al., 2011; Lu et al., 2011; Krofová & Müller, 2016).

Following adhesives were used: two-component epoxy adhesives Bison metal (further marked as BM), GlueEpox Rapid (further marked as GER) and GlueEpox Rapid F (further marked as GEF).

The roughness parameters Ra and Rz were measured on the adherent's surface designated for the adhesive bonding. Roughness parameters were measured with the portable profilometer Mitutoyo Surftest 301. The boundary wave length of cut-off was placed to 0.8 mm. The roughness parameter Ra was 1.82 ± 0.19 μm and Rz was 11.16 ± 0.97 μm.

Adhesive bonds were chemically cleaned in a chemical bath (except for the comparing standard). The adhesive was applied to the first adhesive part (adherent). Subsequently, the second bonded part (adherent) was attached and the adhesive bond was fixed with a weight of 750 g.

The testing sample was kept with the laboratory temperature 22 ± 2 °C for 48 hours after the fixation of the adhesive bond. After that the destructive testing followed.

Fig. 2 shows the cut through the adhesive bond. The cohesive layer of the adhesive, the adhesive layer of the adhesive and the adhesive bonded material at the same time are essential for the adhesive bond strength.

The tensile strength test (according to CSN EN 1465) was performed using the universal tensile strength testing machine LABTest 5.50ST (a sensing unit AST type KAF 50 kN, an evaluating software Test&Motion). The loading speed of the deformation corresponded to 5 mm min^{-1}. The failure type was determined at the adhesive bonds according to ISO 10365.

Fracture surfaces and an adhesive bond cut were examined with SEM (scanning electron microscopy) using the microscope MIRA 3 TESCAN (the fracture surfaces were dusted with gold) at the accelerating voltage of the pack (HV) 5.0 kV and the stereoscopic microscope Arsenal. The surface of specimens was coated with the gold dust using the device Quorum Q150R ES – Sputtering Deposition Rate using Gold.

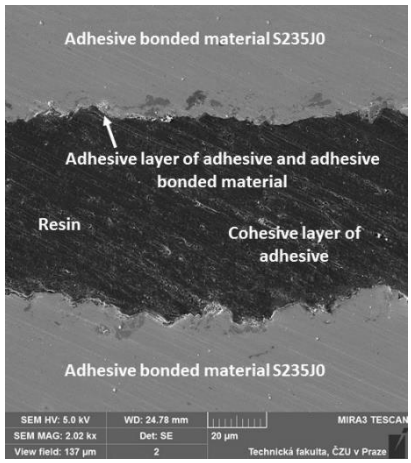

Figure 2. SEM images of cut through adhesive bond (MAG 2.02 kx).

The results of measuring were statistically analysed. Statistical hypotheses were also tested at measured sets of data by means of the program STATISTICA. A validity of the zero hypothesis (H_0) shows that there is no statistically significant difference ($p > 0.05$) among tested sets of data.

RESULTS AND DISCUSSION

Results of the effect of the surface treatment of the structural carbon steel S235J0 to an adhesive bonding strength (Fig. 3) did not prove the essentiality of this factor at all chemical treatments of the adhesive bonded surface compared to the comparing standard. The adhesive bond strength was not conclusively increased when using the chemical treatment of the adhesive bonded surface.

When using the chemical treatment (acetone, technical petrol, technical alcohol, thinner C6000 and toluene) of the bonded surface the adhesive bond strength was increased in the interval from 7.5 to 51.5% at the adhesive BM. When using the chemical treatment (perchlorethylene) of the bonded surface the adhesive bond strength was decreased of 1.3% at the adhesive BM.

When using the chemical treatment (acetone, technical petrol, technical alcohol, thinner C6000 and toluene) of the bonded surface the adhesive bond strength was increased in the interval from 1.2 to 7.7% at the adhesive GEF. When using the chemical treatment (perchlorethylene) of the bonded surface the adhesive bond strength was decreased of 3.8% at the adhesive GEF.

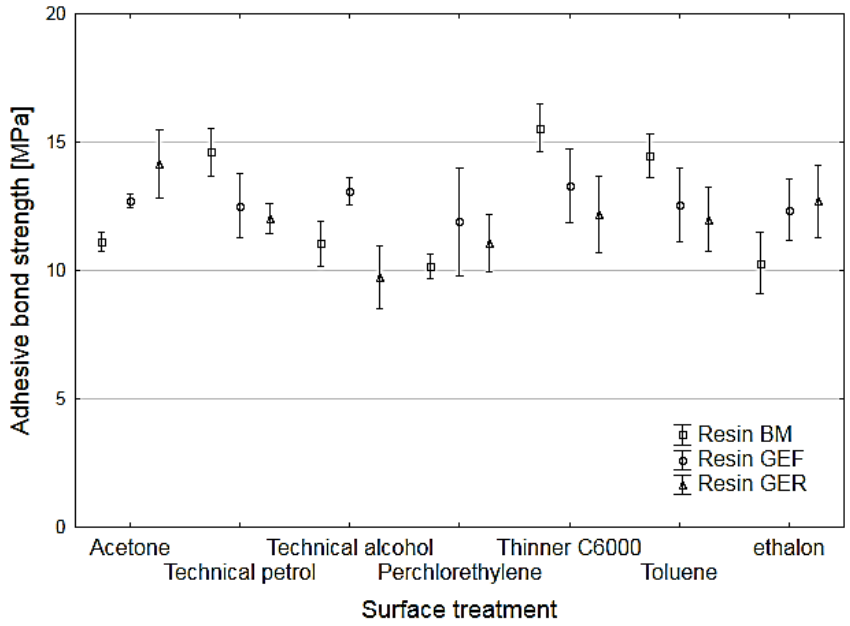

Figure 3. Influence of different treatments on adhesive bond strength.

For the adhesive GEF it was not been demonstrated so significant effect of the bonding surface treatment as for other tested adhesives.

When using the chemical treatment (technical petrol, technical alcohol, thinner C6000, toluene and perchlorethylene) of the bonded surface the adhesive bond strength was decreased in the interval from 4.1 to 23.5% at the adhesive GER.

When using the chemical treatment (acetone) of the bonded surface the adhesive bond strength was increased of 11.4% at the adhesive GER.

It follows from the results that most of chemical treatment affect the adhesive bond strength (the adhesive GER) in a negative way.

The influence of different chemical treatments of the adhesive bonded surface on the adhesive bond strength was proved. These conclusions are also agreed by other researches (Krofová & Müller, 2016).

In terms of the statistical testing of the effect of the surface treatments it is possible to state that different chemical treatments are statistically non-homogeneous groups at the application of adhesives BM and GER. The hypothesis H_0 of these adhesives was not confirmed, i.e. there is a difference in the strength of the adhesive bond at a significance level of *0.05* among different treatments of the adhesive bonded surface. From the statistical analysis it is obvious that the treatment of the adhesive bond

significantly influences the adhesive bond strength, i.e. adhesive BM ($p = 0.000$) and adhesive GER ($p = 0.001$).

In terms of the statistical testing of the effect of the surface treatments it is possible to state that various chemical treatments are statistically homogeneous groups at the application of the adhesive GEF. The hypothesis H_0 was certified, i.e. there is not difference in the adhesive bond strength in the significance level *0.05* among single adhesive bonded surface treatments when using the adhesive GEF. It is visible from the statistical testing that the adhesive bond treatment does not significantly influence the adhesive bond strength at the adhesive GEF ($p = 0.446$).

Fig. 4 presents results of the elongation of the adhesive bonds. A significant change of the elongation occurred only at the adhesive bonds bonded with BM (technical petrol, thinner C6000 and toluene). The hypothesis H_0 was certified, i.e. there is no difference in the elongation of the adhesive bond in the significance level 0.05 among single adhesive bonded surface treatments when using the adhesives GEF and GER. It is visible from the statistical testing that the adhesive bond treatments does not significantly influence the elongation of the adhesive bond when using the adhesive GEF ($p = 0.140$) and GER ($p = 0.163$).

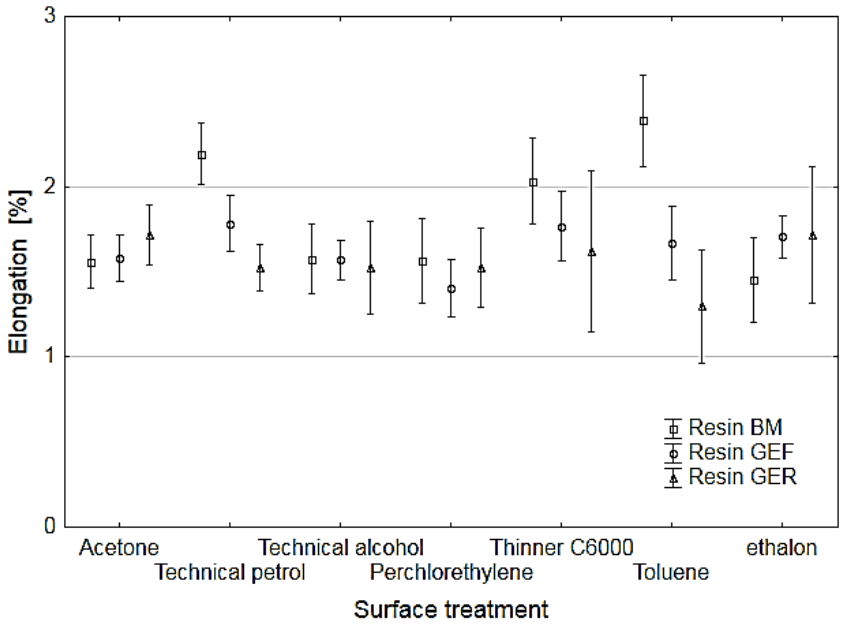

Figure 4. Influence of different treatments on adhesive bond elongation.

In terms of statistical analysis of the velocity (Fig. 5) of the evaporation of chemical substances intended for the chemical treatment of the bonded surface, it is possible to state that this is a statistically inhomogeneous group, i.e. the difference between the individual chemicals.

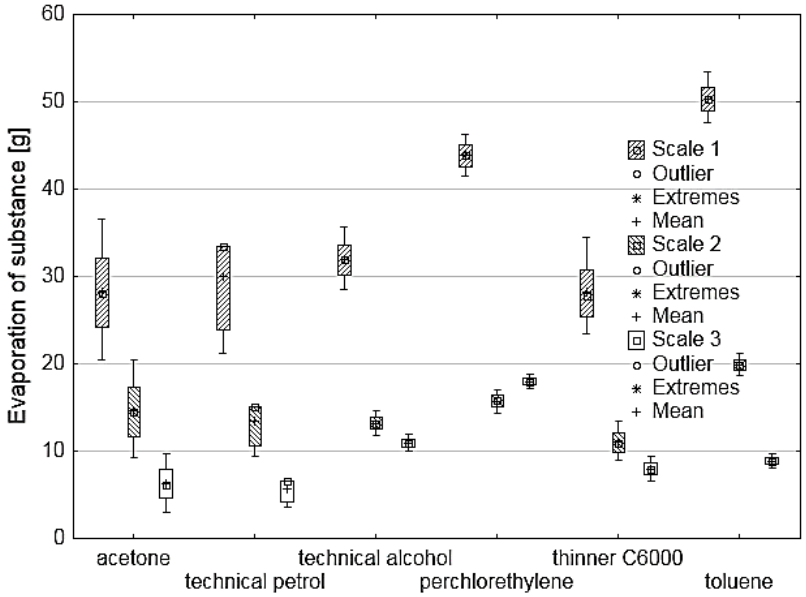

Figure 5. Velocity of the evaporation of chemical substances.

H_0 hypothesis was not confirmed, ie. there is a difference in significance level of *0.05* between the test chemical degreasers, ie. $p < 0.05$ even at the level of different sizes, from which there were evaporation (scale1: $p = 0.000$, scale2: $p = 0.000$ and scale3: $p = 0.000$). Statistically difference was detected in the tested products intended to modify the chemical bonding surface. Toluene and trichloroethylene are agents which vaporized the most significantly. Other tested agents for the chemical treatment showed similar values evaporation.

The mass flow values of produced pollutant according to the different surfaces M_{sm} were measured experimentally in the laboratory. Determined productions M_{sm} of harmful substances presented at the Table 1.

Table 1. Evaporation of chemical substances

Agent	Equation
acetone	$y = 0.0101M_p + 0.4630$
technical petrol	$y = -0.0033M_p + 0.5873$
technical alcohol	$y = 0.0017M_p + 0.2117$
perchlorethylene	$y = -0.0009M_p + 0.1783$
thinner C6000	$y = 0.0006M_p + 0.4089$
toluene	$y = -0.0015M_p + 0.2160$

* y = mass flow given to area, Mp = initial mass.

The cohesive failure was ascertained at all treatments of the adhesive bonded surface at the adhesive BM. The adhesive failure was ascertained at all treatments of the adhesive bonded surface at the adhesive GER. The adhesive/cohesive failure was ascertained at the chemical treatments with acetone, toluene and perchlorethylene at the adhesive GEF.

A presence of cracks in the interface of the adhesive boned material and the adhesive was proved by use of the electron microscopy (SEM) within the experimental research (Fig. 6, A, B). So, there was a poor wettability. The poor wettability was namely at the grit blasting without the chemical cleaning of the adhesive bonded surface (Fig. 6, A). The abrasivum from the mechanical treatment of the adhesive bonded

surface was left between the adhesive bonded material and the adhesive layer (Fig. 6, A). Nor the chemical cleaning of the adhesive bonded surface did not secure a sufficient wettability of the adhesive bonded surface, i.e. the presence of cracks in the interface of the adhesive bonded material and the adhesive was proved (Fig. 6, B). Good wetting of the adhesive bonded surface is obvious from Fig. 6, C.

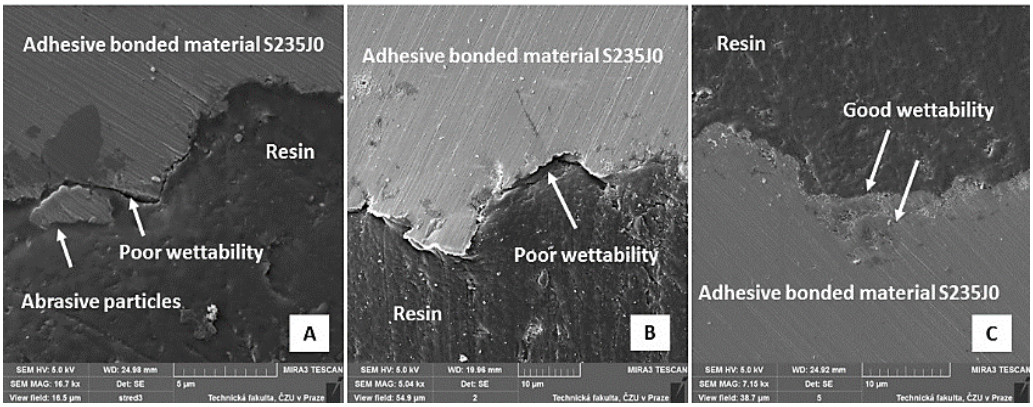

Figure 6. SEM images of interaction of adhesive layer and adhesive bonded material, adhesive GER (secondary electron): A: mechanical treatment (grit blasting) without chemical cleaning of adhesive bonded surface (MAG 16.7 kx), B: mechanical treatment (grit blasting) with chemical treatment, technical alcohol (MAG 5.04 kx), C: mechanical treatment (grit blasting) with chemical treatment, acetone (MAG 7.175 kx).

The research results showed that the adhesion of the adhesive layer was strongly dependent on the type of the treatment of the adhesive bonded surface (Bajat et al., 2007; Müller, 2015; Krofová & Müller, 2016). The efficiency of chemical methods was not as crucial to the adhesive bonding strength (Bockenheimer et al., 2002). That conclusion was confirmed for the adhesive GEF. It was not confirmed for the adhesives BM and GER.

The surface preparation was done in order to achieve the maximum surface wettability of selected adhesives. This creates ideal conditions for contacting the adhesive with the adherent surface and the formation of adhesive bonds (Gent & Lai, 1994; Harris & Beevers, 1999; Elbing et al., 2003; Packham, 2003).

Experimental results clearly demonstrated that different values of the adhesive bond strength depending on the type of the chemical cleaning of the bonded surface had been achieved even with the same roughness of the adhesive bonded surface. Analogical conclusions were reached also at the electrolytic galvanized steel (Krofová & Müller, 2016).

CONCLUSIONS

The paper describes the influence of the adhesive bonded surface treatment and the intensity of releasing the chemical cleaning agents into the air on the strength and the quality of the adhesive bond. The comparison of reached values of the adhesive bond strength and the wettability of the adhesive bonded surface depending on the values of the evaporation of the chemical cleaning agents was done within the research.

Following conclusions can be deduced from the research results:

- When using the chemical treatment of the adhesive bonded surface (the structural carbon steel S235J0) the adhesive bond strength increase did not conclusively occur compared to the adhesive bonds with only the mechanical treatment of the adhesive bonded surface. The difference in the adhesive bond strength values ranged in the horizon: a fall of ca. 25% and an increase up of ca. 51%. The strength increase was always only at the chemical treatment with acetone, at all three tested structural adhesives.
- The presence of cracks in the interface of the adhesive bonded material and the adhesive was proved by the use of the electron microscopy (SEM) within the experimental research at the mechanical treatment by the grit blasting (without the chemical cleaning of the adhesive bonded surface) and at the mechanical treatment by the grit blasting and with the chemical treatment with the technical alcohol. The residues of the abrasivum from the grit blasting process remains on the surface at the comparing standard, i.e. only at the mechanical treatment.
- There is a difference between the test chemical degreasers. Statistically difference was detected in the tested products intended to modify the chemical bonding surface. Toluene and trichloroethylene are agents which vaporized the most significantly.

ACKNOWLEDGEMENTS. This paper has been done when solving the grant IGA TF.

REFERENCES

Act No. 262/2006 Coll. Government Regulation No. 361/2007 Coll. Laying down the conditions for the protection of health at work. Changes: 9/2013 Coll. 48 pp. (in Czech).

Bajat, J.B., Mišković-Stanković, V.B., Bibić, N. & Dražić, D.M. 2007. The influence of zinc surface pretreatment on the adhesion of epoxy coating electrodeposited on hot-dip galvanized steel. *Progress in organic coatings* **58**, 323–330.

Bjørgum, A., Lapique, F., Walmsley, J. & Redford, K. 2003. Anodising as pre-treatment for structural bonding. *International journal of adhesion and adhesives* **23**, 401–412.

Bockenheimer, C., Valeske, B. & Possart, W. 2002. Network structure in epoxy aluminium bonds after mechanical treatment. *International Journal of Adhesion and Adhesives* **22**, 349–356.

Cidlina, J. & Müller, M. 2015. Influence of adhesive bonded surface treatment of alloy AlCu4Mg and increased environmental temperature on adhesive bond strength. *Manufacturing Technology* **15**, 520–526.

Comyn, J. 1990. Surface treatment and analysis for adhesive bonding. *International Journal of Adhesion and Adhesives* **10**, 161–165.

Elbing, F., Anagreh, N., Dorn, L. & Uhlmann, E. 2003. Dry ice blasting as pretreatment of aluminum surfaces to improve the adhesive strength of aluminum bonding joints. *International journal of adhesion and adhesives* **23**, 69–79.

Gent, A.N. & Lai, S.-M. 1994. Interfacial bonding, energy dissipation, and adhesion. *Journal of Polymer Science Part B: Polymer Physics* **32**, 1543–1555.

Habenicht, G. 2002. Kleben: Gundlagen, Technologien, Anwendung (Adhesive bonding: Principles, Technologies, Application).

Harris, A.F. & Beevers, A. 1999. The effects of grit-blasting on surface properties for adhesion. *International Journal of Adhesion and Adhesives* **19**, 445–452.

Krofová, A. & Müller, M. 2016. Influence of chemical treatment of electrolytic galvanized sheet on adhesive bond strength. *Manufacturing Technology* **16**, 965–971.

Lin, J., Lu, Z., Yang, H. & Wang, P. 2011. A design of experiments assessment of moisture content in uncured adhesive on static strength of adhesive-bonded galvanized SAE1006 steel. *International Journal of Adhesion and Adhesives* **31**, 478–485.

Lu, Z., Wang, P., Lin, J., Wang, L. & Li, G. 2011. Effect of moisture content in uncured adhesive on static strength of bonded galvanized DP600 steel joints. *International Journal of Adhesion and Adhesives* **31**, 202–208.

Lunder, O., Lapique, F., Johnsen, B. & Nisancioglu, K. 2004. Effect of pre-treatment on the durability of epoxy-bonded AA6060 aluminium joints. *International journal of adhesion and adhesives* **24**, 107–117.

Messler, R.W. 2004. Joining of Materials and Structures: From Pragmatic Process to Enabling Technology, Elsevier Inc., 816 pp.

Müller, M. 2011. Influence of surface integrity on bonding process. *Research in Agricultural Engineering* **57**, 153–162.

Müller, M. 2015. Research on surface treatment of alloy Alcu4mg adhesive bonded with structural single-component epoxy adhesives. *Manufacturing Technology* **15**, 629–633.

Müller, M. & Valášek, P. 2013. Assessment of bonding quality for several commercially available adhesives. *Agronomy Research* **11**, 155–162.

Müller, M. & Valášek, P. 2014. Optimization of surface treatment of carbon steel in area of adhesive bonding technology with application of quik-setting adhesives. *Manufacturing Technology* **14**, 579–584.

Packham, D.E. 2003. Surface energy, surface topography and adhesion. *International Journal of Adhesion and Adhesives* **23**, 437–448.

Prolongo, S.G., del Rosario, G. & Ureña, A. 2006. Comparative study on the adhesive properties of different epoxy resins. *International Journal of Adhesion and Adhesives* **26**, 125–132.

Rudawska, A. 2014. Selected aspects of the effect of mechanical treatment on surface roughness and adhesive joint strength of steel sheets. *International Journal of Adhesion and Adhesives* **50**, 235–243.

Agronomy Research **15**(S1), 1067–1071, 2017

Multilayer material for electromagnetic field shielding and EMI pollution prevention

V. Lapkovskis[1*], V. Mironovs[1], I. Jevmenov[2], A. Kasperovich[3] and V. Myadelets[3]

[1]Riga Technical University, Scientific Laboratory of Powder Materials, Kipsalas str. 6B-331, LV-1048 Riga, Latvia
[2]Rubber Products Llc, Jurkalnes str. 15/25, LV-1046 Riga, Latvia
[3]Belarussian State Technological University, Department of Technology of petrochemical Synthesis and Polymer Materials Processing, Sverdlova str. 13a, BY220006 Minsk, Belarus
[*]Correspondence: lap911@latnet.lv

Abstract. A significant growth of scientific activities related to electromagnetic fields interaction with equipment and living organisms have turned into an up-to-date research trend in recent decades. Power transmission lines, electric devices, and portable electronics have become a source of electromagnetic pollution. Therefore, a question of electromagnetic shielding is a substantial criterion for workplace safety. Current paper suggests a possible solution based on loose materials and rubber compounds for essential protection of people and equipment against electromagnetic influence.

Key words: crumb rubber, iron powder, electromagnetic shielding, perforated steel, multilayer structures.

INTRODUCTION

The European countries recognise non-ionising electromagnetic fields (EMF) as a significant concern of modern life (Health Protection Agency 2012). Meanwhile, ultra-low electromagnetic frequencies (50–60 Hz) are of importance in case of industrial and residential electrical installations and wirings (European_Commission, 2015b). According to research activities carried out by international scientific groups, low-frequency range (Jain & Tyagi, 1999) can be considered as an electromagnetic hazard (European_Commission, 2015a), especially for industrial (Mild & Sandström, 2015) (machinery) and transportation (Muc, 2001) environments. Non-ionising electromagnetic fields can be isolated by providing a conductive barrier enveloping an electrical equipment or sources of electromagnetic fields. Moreover, shielding is needed for protection against interferences between electrical and electronics equipment at industrial and household levels (Chung, 2000).

Shielding effectiveness (SE) is characterised by ratio of the electromagnetic field energy on one side of the shield to the electromagnetic field energy on the other side of the shield (Nichols, 2013). At the same time, the theory describes the shielding

effectiveness as a combination of following effects: shield material's absorption, reflection loss, and multiple reflection loss inside the shield (Morari et al., 2011).

Applications of steel materials for damping of magnetic fields produced in lab-scale equipment along with electromagnetic fields in contemporary workplaces have been outlined in several *Agronomy research* papers (Koppel et al. 2013; Mironovs et al., 2014). In previous work (Mironovs et al., 2016) a method for obtaining a new material by transformation of end-of-life crumb rubber wastes (Rubber. Products, 2016) to crumb rubber-iron powder mixture has been introduced. Meanwhile, in current paper an application of crumb rubber-iron powder mixture (CRIP) for electromagnetic shielding is investigated.

MATERIALS AND METHODS

Bulk CRIP was used as a perspective raw material for electromagnetic shielding tests (Figs 1, 2). Iron powder M20/80-19 was used as a reference material. For experimental trials, loose powders were packed in rectangular multilayer blocks approximately 100 x 100 mm with respected thickness of 20, 40, and 35 mm (Table 1.).

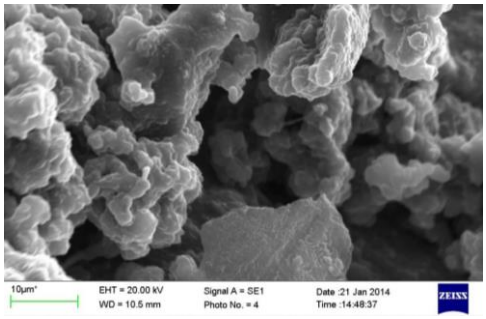

Figure 1. Developed devulcanised crumb rubber (NGR) surface structure enables high strength interaction with non-rubber particles (Rubber.Products 2016).

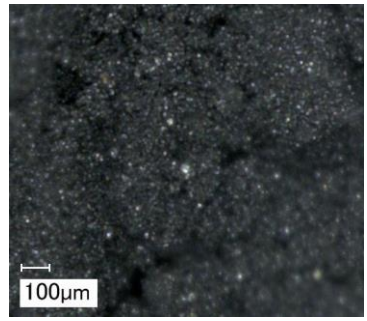

Figure 2. Crumb rubber – iron powder mixture (Mironovs et al. 2016).

Table 1. Shielding materials used in experimental trials

Shielding material	Block dimensions, mm	Iron (Fe) contents, %
Multilayer CRIP blocks	100 x 100 x 20 and 100 x 100 x 40	~ 30%
Multilayer iron powder (Höganäs M20/80-19) block	100 x 100 x 35	> 99%

An experimental rig (Fig. 3) for measurements of electromagnetic fields shielding consisted of electromagnetic field (EMF) source (300W desktop computer power source), shielding block made multilayer CRIP blocks, or iron powder M20/80-19 filling, and the portable electromagnetic radiation tester (teslameter GM3120) has been designed. Magnetic fields were measured in microteslas (µT) (Energy Networks Association 2013).

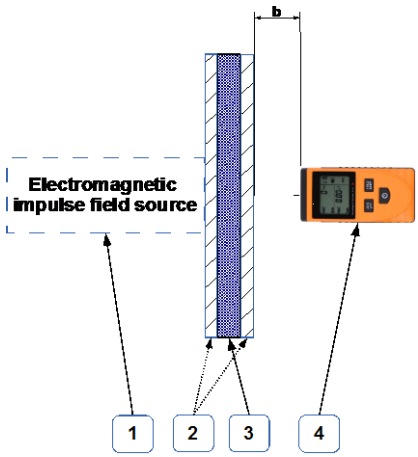

Figure 3. Schematics of experimental rig used for local EMF strength measurements: 1 – Source of electromagnetic impulse fields; 2 – Layer made of crumb rubber; 3 – Layer made of crumb rubber – iron powder mixture (CRIP); 4 – Electromagnetic radiation tester-teslameter GM3120.

RESULTS AND DISCUSSION

Experimental trials have demonstrated a feasibility of suggested shielding materials based on CRIP. 20 mm CRIP block have resulted a reduction of magnetic field strength for about 1.5–2.0 times (13.00 μT vs. 8.50 μT) comparing to unshielded measurements (Fig. 4). Investigated CRIP shielding elements have shown an effectiveness up to 60 mm distance from EMF source (with background electromagnetic field strength 0.70–0.80 μT).

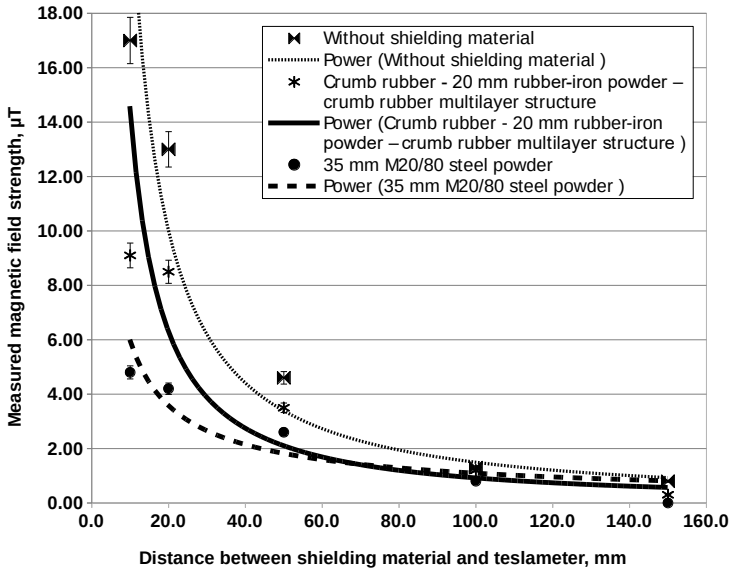

Figure 4. Measured magnetic field strength vs. distance between shielding materials and teslameter (*b* in Fig. 3).

A suggested material was investigated in multilayer elastomeric compositions, which can be used for applications requiring EMI shielding (Morari et al., 2011) in combination with shock and sound absorption features.

FURTHER DEVELOPMENTS

Further research activities will cover multilayer structures containing CRIP, rubber mat, and reinforcment with perforated steel bands. One of multilayer realisations is shown in (Fig. 5). Specifications of reinforcement material are listed in Table 2.

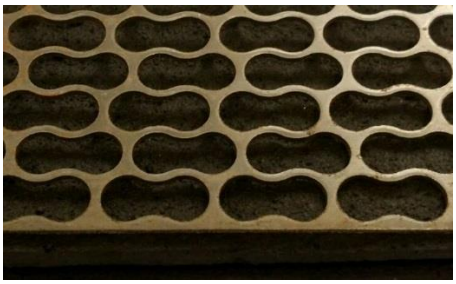

Figure 5. Preparation of multilayer structure composed of crumb rubber / CRIP reinforced by perforated steel tapes.

Table 2. Perforated steel tape specifications

Steel Standard	50-T-C-H, GOST 2284-79
Thickness, mm	1.2
Width, mm	80
Permeable area, %	72.25
Effective cross-sectional area, mm^2	18.12
Tensile load bearing capacity, N	9,314
Strain, %	1.35

Suggested multilayer structure is characterised by its multifunctional performance: electromagnetic field shielding with shock and sound absorption features. Further modification of rubber substrate with copper or aluminium containing components may be considered for shielding of radio-frequency (Weibler, 1993), as well as for shielding of microwave sources (Micheli et al., 2011).

CONCLUSIONS

An experimental investigations of materials based on crumb rubber (devulcanised crumb rubber (NGR)) have proved that crumb rubber – iron powder mixture can be used for shielding of electromagnetic field of ultra-low frequency, thus minimising an electromagnetic pollution.

Multilayer materials made of crumb rubber – iron powder mixture filling can be considered as a shielding media for low-frequency EMF emitting sources (household and industrial equipment).

Further development of low-cost shielding materials based on crumb rubber fully supports the European Union trend to the circular economy (European_Commission 2015a) by introduction of materials re-use and recycling and, therefore, industrial wastes minimisation (European_Commission 2016).

ACKNOWLEDGEMENTS. Support for this work was provided by the Riga Technical University through the Scientific Research Project Competition for Young Researchers No. ZP-2016/37.

REFERENCES

Chung, D.D.L. 2000. Materials for electromagnetic interference shielding. *Journal of Materials Engineering and Performance*, 9(Compendex), pp. 350–354. Available at: https://wings.buffalo.edu/eng/mae/cmrl/Materials for electromagnetic interference shielding.pdf.

Energy Networks Association. 2013. *Electric and Magnetic Fields*, Available at: http://www.emfs.info/wp-content/uploads/2014/07/EMF_The_Facts_260613.pdf.

European_Commission. 2015a. *Potential Health Effects of Exposure to Electromagnetic Fields (EMF)*. doi:10.2772/75635.

European_Commission. 2015b. 'An EU Action Plan for the Circular Economy'. *Com* 614: 21. doi:10.1017/CBO9781107415324.004.

European_Commission.2016. Landfill Waste - Environment - European Commission." http://ec.europa.eu/environment/waste/landfill_index.htm.

Health Protection Agency. 2012. *Health Effects from Radiofrequency Electromagnetic Fields*. *Advisory Group on Non-Ionizing Radiation AGNIR*. http://www.hpa.org.uk/webc/hpawebfile/hpaweb_c/1317133827077.

Jain, S.C. & Tyagi, K. 1999. Effects of extremely low frequency electromagnetic fields on health. *Indian journal of biochemistry & biophysics* **36**(5), 348–351.

Koppel, T., Tasa, T. & Tint, P. 2013. Electromagnetic fields in contemporary office workplaces. *Agronomy Research* **11**(2), 421–434.

Micheli, D.C. Apollo, R. Pastore, R.B. Morles, M. Marchetti & Gradoni, G. 2011. Electromagnetic Characterization of Composite Materials and Microwave Absorbing Modeling. *Advances in Nanocomposites - Synthesis, Characterization and Industrial Applications*, 360–384. doi:10.5772/15215

Mild, K.H. & Sandström, M. 2015. *Guide Electromagnetic fields in working life. A guide to risk assessment*, 1st edition. http://www.etui.org/Publications2/Guides/Electromagnetic-fields-in-working-life.-A-guide-to-risk-assessment

Mironovs, V., Boiko, I., Koppel, T., Zemchenkov, V. Lapkovskis, V & Shishkin, A. 2014. Cellular structures from perforated metallic tape and its application for electromagnetic shielding solutions. *Agronomy Research* **12**(1), 279–284.

Mironovs, V., Ozernovs, O., Lapkovskis, V. & Golyandin, D. 2016. Production of Crumb Ruber — Iron Powder Mixture for perspective synthesis of Carbon-Iron powder sorbent. *Agronomy Research* **14**(S1), 1063–1068.

Morari, C., Balan, I. & Pintea, J. 2011. Electrical conductivity and electromagnetic shielding effectiveness of silicone rubber filled with ferrite and graphite powders. *Progress In*, **21**, 93–104.

Muc, A. 2001. Electromagnetic fields associated with transportation systems. *Health Canada, Toronto*, 52.

Nichols, L. 2013. *A Compliance Handbook for Electrical Engineers* InCompliance, ed., Available at: http://incompliancemag.com/issue/march-2013/.

Rubber.Products. 2016. *Devucanised crumb rubber (NGR)*, Available at: http://www.rubber-products.net/files/nrg-presentation-2016.pdf.

Weibler, J. 1993. Properties of Metals Used for RF Shielding. *EMC Test & Design*. http://www.ets-lindgren.com/pdf/emctd_1293_weibler.pdf.

Agronomy Research **15**(S1), 1072–1083, 2017

A dynamic model of electric resistor's warming and its verification by micro-thermocouples

M. Linda, G. Künzel and M. Hromasová*

Czech University of Life Sciences in Prague, Faculty of Engineering, Department of Electrical Engineering and Automation, Kamýcká 129, CZ165 21 Prague, Czech Republic
*Correspondence: hromasova@tf.czu.cz

Abstract. The object of research is a resistor, a real electronic component, loaded by constant or impulse power. As a first approximation, resistor follows 1st order dynamic system, i.e. heating of the hottest spot on its surface is exponential to the power increase. The validity of this model is confirmed by measurements in a constant power loading regime. In an impulse power loading, it is only valid when the pulse duration approaches time constant of the resistor. The aim of this article is to show more credible model warming of the resistor, which is valid even for the case of pulse duration (ms) much shorter than the time constant of the resistor. The model can reveal an overload which does not lead to destruction of the resistor. Dynamic model of the resistor is based on its construction. Typically, an insulating ceramic rod is coated with a resistive layer connected with outlet wires on both sides, all being coated with insulating lacquer layer. The resistive layer is a source of heat flow. Formulation of the model comes from general power balance in a form of three differential equations and it is solved using Scilab. The input variable is the impulse power and the outputs are temperature changes in the ceramic rod, the resistive layer and the lacquer layer, compared to the ambient temperature. The simulation allows to determine solutions for various parameters including very short power pulses, which are confirmed experimentally.

Key words: load factor, model, resistor, thermocouple, warming.

INTRODUCTION

Resistors with power loading mostly between 0.1–2 W, or alternatively power resistors with power handling capacity of 10–100 W are the significant heat-sources in electric devices. Since the electric power in the resistor changes into a heat flux, and thus it's operated at a loss, this passive electrical component, from the heat transfer point of view, is probably the most interesting, and in many cases, also the solution of the heat and temperature field (O'Sullivan & Cotterell, 2001; Song et al., 2016). It is necessary, when designing the electrical devices to project correctly a nominal value of the resistor and its type with regard to its power load. In case of inappropriate choice the component might be destroyed.

This paper deals with the formulation, design, and experimental verification of a dynamic model of a resistor in a pulse-loaded mode by the power. A typical application would be reduction of a capacitor's charging current, soft starter of transformer, or an inrush current suppression of an induction motor (Osmanaj & Selimaj, 2009).

The object of the research is a resistor with a metal-oxide layer 100 Ω and with power of 2 W (type MO–300) (GMElectronic, 2008). The parts manufacturer usually states the pulse load only for special power and pulse resistors (Shin et al., 2009). A Graph of an energy absorption 'energy capability' is provided for short pulses of 100 ms. So called overload characteristic is provided for longer pulses. A limitation based on shock wave test is used for pulses < 1 ms (Batal et al., 2014).

Understanding the damage mechanism of the metal-oxide resistor is shown e.g. in (ROHM, 2012). When power overload occurs, firstly there is an oxide reduction on metal, which results in a slight decrease of the nominal resistance. Longer overload leads to a melting of resistive layer, or cracking and melting in a layer of ceramic rod, or in resistor's coating, until the resistive layer is damaged. The last phase of resistive layer melting is characterized by a significant resistance increase. The component is inoperable and needs to be replaced (Hromasová & Linda, 2016).

Dynamic model of the resistor is based on its structural arrangement. Formulation of electro thermal system respects the power balance of a resistor's part. The simplest model is a first-order model with a time constant substantially greater than the duration of power pulses (Böckh & Wetzel, 2012; Contento & Semancik, 2016). For a very short pulses in ms, the validity of this model is limited, as it's demonstrated by measurements using micro thermocouples (Degenstein et al., 2007). Therefore a more complex dynamic model was designed, which reflects better the warming of the ceramic rod, the resistance layer, and the lacquer layer. After parameter identification and verification, based on measurements, it is possible to simulate on PC model a complex behaviour of the resistor in the pulse mode and determine the conditions of acceptable overload capacity without destruction of the component.

MATERIALS AND METHODS

A typical resistor is usually comprised of a ceramic rod (sometimes tubes), on which surface is applied an electrically conductive resistive layer, which is connected at both ends e.g. by copper wire outlets. This layer is covered by a lacquer insulation layer. From the cybernetic viewpoint, we can see the resistor as a dynamic electro thermal system, which input is loaded constant or pulsed electrical power P (W) and the output is temperature ϑ (°C) (Fig. 1). The resistive layer is a source of a heat flux, which is equivalent to the electric power. Static model of a heat transfer between the heat source and the environment does not define the structure of the resistor. The main problem is that there is no part on the resistor's construction, which would correspond to a thermal circuit's node with temperature ϑ. Therefore the practice of measuring temperature ϑ got stabilised (warming determination given the ambient temperature ϑ_0) at the hottest point of the resistor, usually in the middle of the cylindrical coating (Fig. 2). Warming $\Delta_{\cdot}\vartheta$ (1) in a steady state is considered as directly proportional to the power P on the resistive layer.

$$\Delta\vartheta = \vartheta - \vartheta_0 \tag{1}$$

Figure 1. Block diagram of the power-loaded resistor (Linda & Hromasová, 2016a).

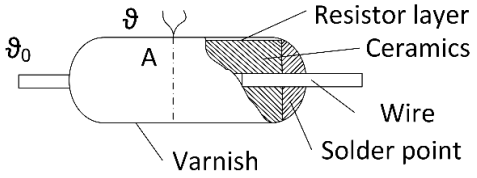

Figure 2. Indication of areas suitable for measuring the resistor's surface temperature (Linda & Hromasová, 2016a).

If we disregard the convention as well as radiation from the coating's surface, the dynamic model of a second-order will be sufficient, based on the ideas of heat flux branching on the resistor according to a replacement RC heat circuit with two loops. Repeated measurements of the warming transition characteristics and their identification showed, that this noncascade model of second-order satisfies, with an adequate accuracy, a real resistor's mode of the rectangular-pulsed power input signals. Warming transition characteristics in standardized form $h(t)$ have a form of (2) (Linda & Hromasová, 2016a)

$$h(t) = 1 - A_1 \exp\left(-\frac{t}{T_1}\right) - (1 - A_1)\exp\left(-\frac{t}{T_2}\right) = \frac{\Delta\vartheta(t)}{\Delta\vartheta_{jm}} \qquad (2)$$

where: A_1 –constant ratio; t –time, s; T_1, T_2 –time constant, s; $\Delta\vartheta(t)$ –immediate warming, °C; $\Delta\vartheta_{jm}$ –nominal value of warming, °C.

The model can be quantified by a regression method, where we determine time constants T_1, T_2 for each sample or type resistor and a constant ratio A_1 for the minimum value of the sum of squared deviations. In the model (2) is a smaller time constant T_1, that always corresponds with a product of heat capacity of the lacquer layer and with thermal resistance between the layer and the environment, while $T_2 > T_1$ is given by the product of heat capacity of the ceramic rod, eventually by the outlets and the thermal resistance between the resistive layer and the surroundings.

Each energy (power) balance is the mathematical expression of the law of conservation of energy (power). Simplified wording of the equation of conservation is (3) (Linda & Hromasová, 2016a; 2016b)

$$\text{INPUT} + \text{SOURCE} = \text{OUTPUT} + \text{ACCUMULATION} \qquad (3)$$

Heat balance of the object's unit volume at the propagation of heat is then (4)

$$\begin{bmatrix}\text{Input}\\ \text{heat flux}\\ \text{into the}\\ \text{element}\end{bmatrix} + \begin{bmatrix}\text{External}\\ \text{source}\\ \text{of heat flux}\end{bmatrix} = \begin{bmatrix}\text{Output}\\ \text{heat flux}\\ \text{from the element}\end{bmatrix} + \begin{bmatrix}\text{Time change of}\\ \text{the inner energy}\\ \text{in the element,}\\ \text{i. e. accumulation}\end{bmatrix} \quad (4)$$

This general approach to the creation of resistor's electro thermal model leads to a system of first-order ordinary differential equations with lumped constant parameters. We compile a power balance for each layer and also the ceramic rod. Block diagram of the distribution of individual heat fluxes q *(w)* (q_i, q_{12}, q_{13}, q_{01}, q_{02}) between the individual elements of the real resistor is on Fig. 3.

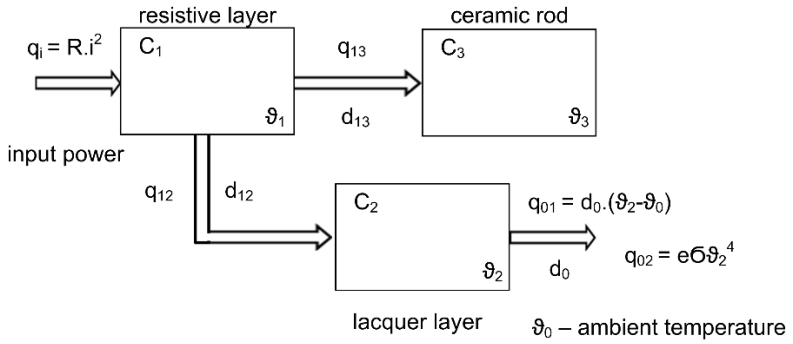

Figure 3. The block diagram of the distribution of heat fluxes.

Power balance of the resistive layer is described by Eq. (5)

$$Ri^2 = C_1\frac{d\vartheta_1}{dt} + d_{12}(\vartheta_1 - \vartheta_2) + d_{13}(\vartheta_1 - \vartheta_3) \quad (5)$$

where: R –electrical resistance of the examined object, Ω; i –the electric current, A; C_1 –the heat capacity of the resistive layer, J K^{-1}; d_{12}, d_{13} –coefficients of heat transfer from the resistive layer to the surface coating and the ceramic rod, W K^{-1}; $\vartheta_1(t)$, $\vartheta_2(t)$, $\vartheta_3(t)$ –the temperatures of the resistive layer, lacquer layer and the ceramic rod, °C.

Power balance of the lacquer layer is described by Eq. (6)

$$d_{12}(\vartheta_1 - \vartheta_2) = C_2\frac{d\vartheta_2}{dt} + d_0(\vartheta_2 - \vartheta_0) + e\sigma S\vartheta_2^4 \quad (6)$$

where: C_2 –the heat capacity of the lacquer layer, J K^{-1}; ϑ_0 = 24 °C –ambient temperature, °C; $e \leq 1$ emissivity of the resistor's surface; σ = 5.78 10^{-8} Wm^{-2}K^{-4} Stefan-Boltzmann constant; S –the surface size of resistor's cylinder; m^2.

Due to the fourth power of temperature $\vartheta_2(t)$ is the differential equation nonlinear. Heat flux q_{02}, which can be emitted during radiation from the surface, is determined by the Stefan-Boltzmann law. Analogous power balance of the resistor's ceramic rod is expressed by the Eq. (7)

$$d_{13}(\vartheta_1 - \vartheta_3) = C_3\frac{d\vartheta_3}{dt} \quad (7)$$

where: C_3 –the rod's thermal capacity, J K^{-1}.

The resistor model is loaded by the input electric power, which is represented by a formula $P = Ri^2$and for constant values of the resistance as well as the current is also constant. If we examine the pulse-loading mode of the resistor, we need to supply periodic rectangular pulses with a pulse power *P*, the duration t_1 (s) with the time period *T* (s) to define the following parameters according to Fig. 4. (O'Sullivan & Cotterell, 2001).

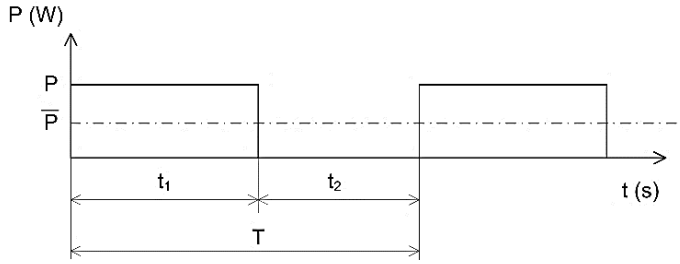

Figure 4. The power pulse.

Load factor *z* (-, %)

$$z = \frac{t_1}{T} \tag{8}$$

Medium power $\bar{P}$ (W)

$$\bar{P} = \frac{P_1 t_1}{T} = P_1 z \tag{9}$$

Medium warming $\Delta\bar{\vartheta}$ (°C) in a steady state

$$\Delta\bar{\vartheta} = k\bar{P} = kP_1 z \tag{10}$$

where: *k* –a constant corresponding to a thermal resistance in a steady state, K W^{-1}.

A warming $\Delta\vartheta_1$ given by continuous power P_1

$$\Delta\vartheta_1 = kP_1 = \frac{k\bar{P}}{z} = \frac{\bar{\vartheta}}{z} \tag{11}$$

These formulas serve as an evaluation of the measured time courses of warming of the particular resistors, but also can be used for a pulse mode of the resistor's dynamic model.

For the model quantification, we need to know the values of heat capacities, which can be calculated using the dimensions of the resistor, cubic density ρ_m (kg m^{-3}) and specific heat *C* (J $kg^{-1}K^{-1}$). The thickness of the resistive layer of the resistor MO-300 100 Ω was measured using a microscope, and it is about 2 microns. The length of the resistor $l = 11$ mm and its radius $r = 2$ mm can be determined from the data (O'Sullivan & Cotterell, 2001). The values of heat capacities of the individual resistor layers are shown in Table 1.

The heat transfer coefficients were identified by comparing with the conducted experiment. Three pieces of the same resistor were chosen, and each of them was continuously loaded by power of 2 W five times. During this, the surface temperatures in the middle of the resistor were also measured. To determine the searched-for parameters, we used a method of least squares of the difference between the measured temperature and the model's temperature. Calculated values of the heat transfer coefficients are in Table 2.

Table 1. Calculated parameters of heat capacity

Layer	Label	Heat capacity (J K^{-1})
Resistive	C_1	1.11 x 10^{-3}
Lacquer	C_2	9.93 x 10^{-3}
Ceramic	C_3	314 x 10^{-3}

Table 2. Averages of calculated coefficients

Parameters	Sample 1	Sample 2	Sample 3
d_{12} (W K^{-1})	0.763	0.758	0.757
d_{13} (W K^{-1})	0.254	0.254	0.253
d_0 (W K^{-1})	0.008	0.008	0.009

In a differential energy balance equations the individual elements participate in a total warming unevenly. By so called Sensitivity analysis we can determine the effect of changes of individual parameters in the equations on a maximum warming of the resistor, and possibly decide, what elements need not be considered when dimensioning the resistors by short repetitive pulses.

Relative sensitivity function S_a^y is defined as the ratio (12)

$$S_{a_{i_3}}^{y} = \frac{\frac{dY}{Y}}{\frac{da_i}{a_i}} = \frac{dY}{da_i}\frac{a_i}{Y} \tag{12}$$

We expect a linear dependence of the relative output variable $\frac{dY}{Y}$ on the relative change of each individual parameter. In our case, the function Y represents a maximum possible temperature in the resistive layer. The relative change of the parameter was chosen $\frac{da_i}{a_i} = 0.01$ ie. 1%.

RESULTS AND DISCUSSION

The complete mathematical model expressed by the Eqs (5–7) was created in Scilab Xcos and its block diagram is on Fig. 5.

The computer model graphically displays the temperature curses $\vartheta_1(t)$resistive layer, $\vartheta_2(t)$ lacquer layer and $\vartheta_3(t)$ ceramic layer for different variants of the entered parameters from Table 1 and Table 2. for the constant as well as a pulse-loaded power entering into the resistor.

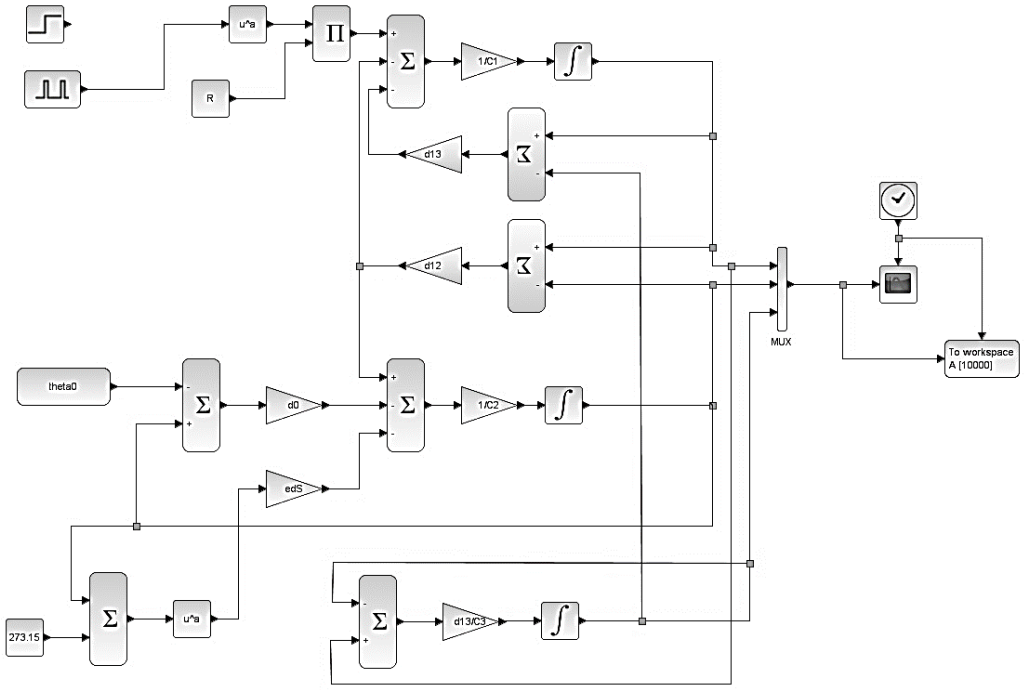

Figure 5. Block diagram of models in Scilab-Xcos.

Fig. 6 show temperature response to steady state. Input signal is step function of electrical current. Final temperature of response is 77.4 °C and electrical current is 70 mA.

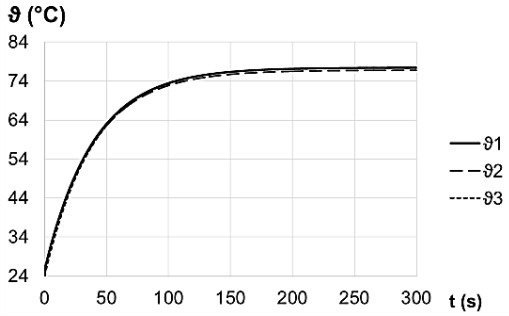

Figure 6. The temperature waveform i = 0.07 A.

Fig. 7 show temperature waveform for sample 1 (Fig. 7, a), 2 (Fig. 7, b) and 3 (Fig. 7, c) with constant current 0.14 A, time to the period 14 ms and pulse duration 7 ms.

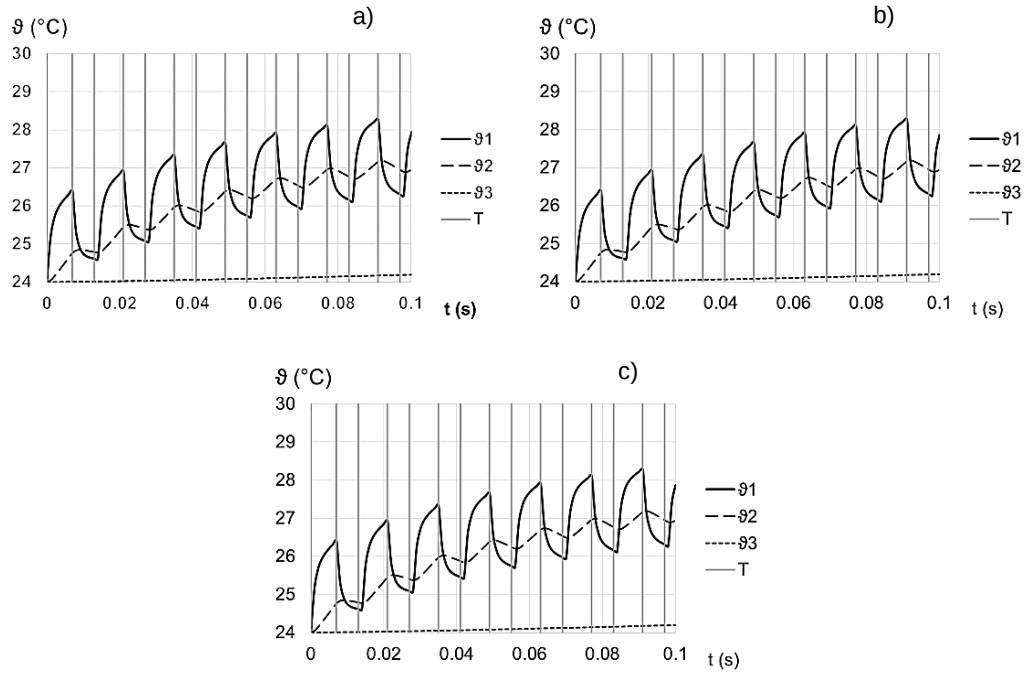

Figure 7. The temperature waveform –sample 1 $_{a)}$, 2 $_{b)}$ and 3 $_{c)}$, T = 14 ms, t_1 = 7 ms.

Fig. 7, a), 8, a), 8, b show temperature waveform for sample 1 with constant current 0.14 A, time to the period was changed to a value 2 ms, 14 ms and 100 ms and pulse duration was changed to a value 1 ms, 7 ms and 50 ms.

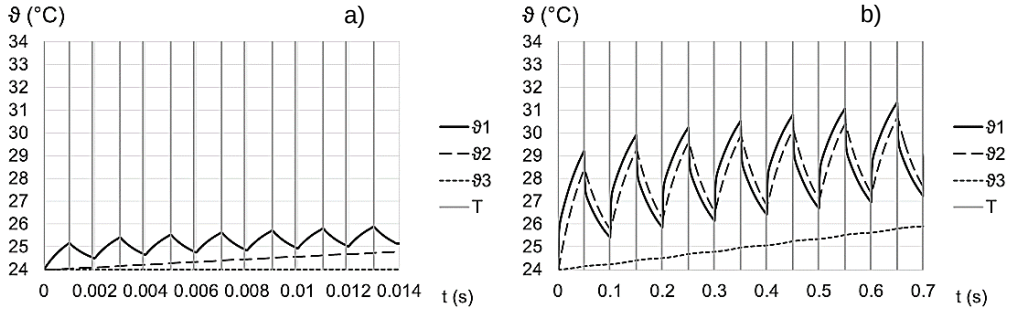

Figure 8. The temperature waveform –sample 1, a) T = 2 ms, t_1 = 1 ms and b) T = 100 ms, t_1 = 50 ms.

Fig. 9 shows temperature waveform sample 1 with constant current 0.42 A, time to the period was changed to a value 2 ms, 14 ms and 100 ms and pulse duration was changed to a value 1 ms, 7 ms and 50 ms.

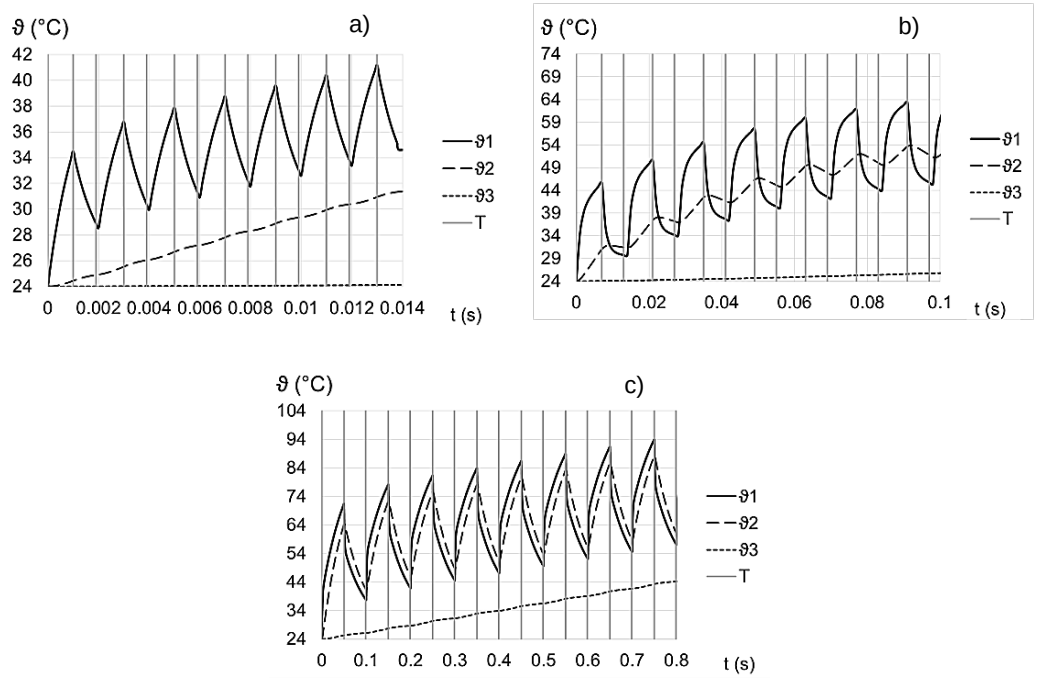

Figure 9. The temperature waveform –sample 1, a) T = 2 ms, t_1 = 1 ms; b) T = 14 ms, t_1 = 7 ms; c) T = 100 ms, t_1 = 50 ms.

Fig. 10 shows temperature waveform sample 1 with constant current 1.4 A, time to the period 32 ms and pulse duration 16 ms.

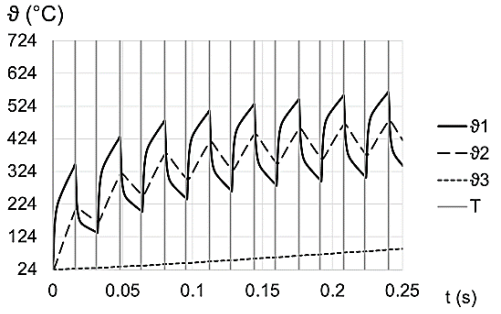

Figure 10. The measured waveform –sample 1, T = 32 ms, t_1 = 16 ms.

It is noticeable from the graphical dependencies of the sensitivity function on parameters' changes at a constant amplitude of the current of 140 m A with rectangular pulses with duration of 0.8 ms, that the warming sensitivity on the thermal capacity change C_1 (resistive layer) is at the highest. At even shorter pulses is not sufficient to fully explore the ability to accumulate the created heat energy. Sensitivity to parameter C_2 (insulating layer) is the highest for 51 ms pulses. The biggest impact on warming, however, has the heat capacity of the ceramic rod C_3, which is higher by 2 orders of magnitude, but it applies itself at longer pulses. The coefficient d_{12} has a high sensitivity when the effect of the thermal capacity of the resistive and the covering insulating layer manifest itself the most. Parameters d_{13} and d_0 have a higher sensitivity by an order of magnitude than d_{12} and their course corresponds with the sensitivity to the thermal capacity C_3.

The simulation of the created model shows that temperature of the insulation layer during short pulses of 1–7 ms lags behind the reached temperature of the resistive layer until the pulse is of 50 ms duration. The ceramic rod does not warm up close to the temperature of the resistive layer, even when pulse-loaded for an order of magnitude of seconds. The simulated course while the temperatures are higher than ca 700 °C, is however unrealistic because the resistive layer was, without a doubt, destructed, as shown in comparisons of the measurement results and the model.

During the loading by the current of 1.4 A and by pulse of 16 ms (50% cycle), the destruction does occur in the examined resistor with resistance of 100 Ω and with maximum allowable continuous power-loading of 2 W. The maximum temperature of the resistive layer in time 0.24 s was identified at 540 °C, the temperature of the lacquer layer at 450 °C and of the ceramic rod at 86 °C.

Measuring of the resistors when the pulse-loading was underway using a created measuring apparatus in a free space. The influence of the environment on short pulses is minimal. The heat from the resistive layer does not suffice to warm up significantly the surface layer of the resistor. Resistors were loaded by pulses of 5 ms duration. Between pulses was the corresponding pulse energy -30 s for the energy of 1 J, because the resistor cooled down to the ambient temperature. At the end of the cooling time was the resistance measured with a multimeter connected by a 4-wire method to the resistor. Resistance does not change its value at first. Initial temperature of the resistances differ in individual pieces, which is in accordance with tolerances stated in the manufacturers' catalogue. The damage mechanism of the metal-oxide resistor occurs successively in three phases, as shown in Table 3, which is developed on the basis of a statistical evaluation of 12 measurements. The resistor was always damaged near the centre of the ceramic rod. Destruction was associated with formation of an electric arc at the point of damage.

Table 3. Individual phases of resistor's damage

Phases	Impulse of current (A)	Pulse of energy (J)
Reduction O_2	1.10–1.30	0.6–0.9
Fusion resistive layer	1.65–1.95	1.6–2
Destruction	1.90–2.20	1.8–2.6

The accuracy of the model can be demonstrated by comparing the warming transition characteristic of the resistor's model $\Delta\vartheta_2(t)$ and the measured warming transition characteristic in the centre of the real resistor's surface, provided that the input power pulses are in both cases the same. The conditions of the correct and sufficiently accurate measurement of the very rapid time courses of temperatures using micro thermocouples are stated in (Hromasová & Linda, 2016; Linda & Hromasova, 2016a, 2016b). Given that, the measurement of the warming using these sensors has a non-zero error, the model's maximum error of 1.5% can be determined based on the statistical processing of 150 samples of transition characteristics.

CONCLUSIONS

Using the power balance, we formulated a mathematical model of a heat transfer in three subsystems of the resistor as a system of differential equations of first-order. Computer model in Scilab Xcos was created after adjusting. The computer model graphically displays the temperature curses $\vartheta_1(t)$, $\vartheta_2(t)$ a $\vartheta_3(t)$ for different variants of the entered parameters from Table 1 and Table 2. for the constant as well as a pulse-loaded power entering into the resistor.

We obtain more information about the loaded resistor from the computer model than during the surface temperature measurement eg. using thermocouples or pyrometers. Usability of the model in practice is possible, based on the experimental identification of the model's parameters. The measurement is irreplaceable, however it only observes how the temperature changes in time but does not explain the physical nature of correlations among quantities.

Comparison of results of the model's behaviour and the measurements show us what impulses can be used to load the resistor, in order not to exceed the maximum allowable warming from the dimensioning viewpoint. The destruction of the component occurs when the temperature of the resistive layer is at about 700 °C.

The mentioned methodology may be used for research of thermal dynamics in more complex components (capacitors, diodes, transistors, thyristors, or integrated circuit), where is certainly necessary to address the related issue of cooling.

REFERENCES

Batal, M.A., Nashed, G. & Jneed, F.H. 2014. Conductivity and thermoelectric properties of nanostructure tin oxide thin films. *Journal of the Association of Arab Universities for Basic and Applied Sciences* **15**, 15–20.

Böckh, P. von. & Wetzel, T. 2012. *Heat transfer: basics and practice*. Springer, 276 p.

Contento, N.M. & Semancik, S. 2016. Thermal characteristics of temperature-controlled electrochemical microdevices. *Sensors and Actuators B: Chemical* **225**, 279–287.

Degenstein, T., Günter, M., Keller, A. & Winner, H. (n.d.). 2007. Dynamic measurement of the temperature of electro conductive objects used for the example of a wheel brake. AMA Service GmbH, 2007, **A1**(4), 1–5.

GMElectronic. 2008. Power metal film resistor. Retrieved from http://www.gme.cz/

Hromasová, M. & Linda, M. 2016. Analysis of rapid temperature changes. *Agronomy Research* **14**(3), 768–778.

Linda, M. & Hromasová, M. 2016a. Analysis of rapid temperature changes of the object with higher thermal constant. In. *Proceeding of 6th international conference on trends in agricultural engineering*, Jelgava. pp. 366–374.

Linda, M. & Hromasová, M. 2016b. Model analysis of temperature sensors. In *Engineering for Rural Development*, Jelgava. pp. 566–573.

O'Sullivan, D. & Cotterell, M. 2001. Temperature measurement in single point turning. *Journal of Materials Processing Technology* **118**(1), 301–308.

Osmanaj, S.F. & Selimaj, R.A. 2009. Thermal Analysis Of Electrical Machines. *TMT*, 16–21.

ROHM. 2012. ROHM Semiconductor. Retrieved from http://www.rohm.com/products/databook/r/pdf/r_siyoujou.pdf

Shin, D., Kim, J., Chang, N., Choi, J., Chung, S.W. & Chung, E.-Y. 2009. Energy-optimal dynamic thermal management for green computing. In *Proceedings of the 2009 International Conference on Computer-Aided Design - ICCAD '09* (p. 652). New York, New York, USA: ACM Press.

Song, H., Zhan, X., Li, D., Zhou, Y., Yang, B., Zeng, K. & Tang, J. 2016. Rapid thermal evaporation of Bi2S3 layer for thin film photovoltaics. *Solar Energy Materials and Solar Cells* **146**, 1–7.

Agronomy Research **15**(S1), 1084–1093, 2017

The dependence of COx and NOx emission concentrations on the excess air coefficient during combustion of selected agricultural briquetted by-products

J. Malaťák*, J. Bradna and J. Velebil

Czech University of Life Sciences Prague, Faculty of Engineering, Department of Technological Equipment of Buildings, Kamýcká 129, CZ165 21 Prague, Czech Republic
*Correspondence: malatak@tf.czu.cz

Abstract. The issue of CO, CO_2 and NOx emissions is very extensive and important. The aim of the paper is the experimental determination of the CO, CO_2 and NOx emission dependencies on the amount of excess air. Materials used for the experiments were several types of briquetted biomass. Crops used were Czech knotweed (*Reynoutria* × *bohemica*), Rumex hybrid OK 2 (*Rumex patientia* × *Rumex tianschanicus*), meadow hay and timothy grass (*Phleum pratense*). For all samples proximate and elemental analyses were performed (semiautomatic calorimeter LECO AC-600 elemental analyser CHN628 + S and analyser LECO TGA-701) and stoichiometric calculations of combustion were made. Combustion device used in combustion tests was a hot air stove with a grate fireplace and with manual fuel supply. The combustion process was monitored by analyser Madur GA-60. Parameters monitored during the combustion tests were primarily the flue gas temperature and the emission levels of carbon monoxide, carbon dioxide and nitrogen oxides.
Analyses and calculations of plant biomass samples indicate their good properties for energy use. The gross calorific value was as high as 19.55 $MJ.kg^{-1}$ in the sample of Rumex OK 2. Limiting factor is the high quantity of ash in plant material. The briquettes from timothy grass achieved 5.77% wt. ash in the dry matter. The excess combustion air had positive influence during combustion test. On the other hand, this caused heat loss by departing flue gases, wherein the flue gas temperature reached high values. The excess air coefficient also significantly affected the emission levels of carbon dioxide and monoxide and nitrogen oxides in the flue gases. Results were statistically analysed and complemented by regression equations, which in practice can be used to optimize the combustion process in boilers with manual fuel supply.

Key words: plant biomass, combustion device, calorific value, combustion gases, heat loss.

INTRODUCTION

Impacts of combustion processes on the environment are evident. Results of Esteban et al. (2014) clearly demonstrate the environmental benefits of using small scale produced biomass instead of fossil fuels. As for the combustion process quality, the first indicators are the levels of carbon oxides (Bradna & Malaťák, 2016). If at low excess air the highest possible concentration of CO_2 is achieved, losses caused by the flue gases at that temperature are minimal (Johansson et al., 2004).

Higher emissions of sulphur and nitrogen oxides observed in plant biomass compared to wood biofuel were reported by Brassard et al. (2014). Also the influence of

discontinuous fuel supply on carbon monoxide and nitrogen oxides does not necessarily lead to a significant increase in the concentration of carbon monoxide emissions as compared with combustion devices with continuous fuel supply (Juszczak, 2016). Diaz-Ramirez et al. (2014) confirmed the influence of fuel nitrogen and higher proportion of air on increasing nitrogen oxides (NOx) emission concentrations. Gaseous emissions are significantly influenced by the type of fuel. High CO emission may be caused by high solid loading and high length to diameter ratios in solid fuels, while high NOx emissions can be caused by a very high content of nitrogen in the fuel (Garcia-Maraver et al., 2014).

This article aims to provide experimental determination of carbon monoxide and nitrogen oxides emission concentrations, and also flue gas temperature in dependence on the excess air coefficient during combustion of briquettes from plant biomass in a grate combustion device. For these materials elemental analyses and stoichiometric calculations were determined.

MATERIALS AND METHODS

To fulfill the objectives of article several plant biomasses were sampled. They were Czech knotweed (*Reynoutria* × *bohemica*), Rumex OK 2 (*Rumex patientia* × *Rumex tianschanicus*), meadow hay and timothy grass (*Phleum pratense*). Czech knotweed at harvest reaches height of 3 m and thanks to its rapid growth it produces a large amount of biomass. This plant due to its characteristics is being considered as a renewable energy source (Strašil & Kára, 2010). Rumex OK 2 for energy purposes was harvested just before reaching full maturity when the seeds were not yet released. Harvested material has good characteristics as a biofuel and the net calorific value approaches that of wood chips (Heděnec et al., 2015). Meadow hay as an agricultural source consisting of various kinds of grasses, legumes and herbs (Riedener et al., 2015), was obtained from the first harvest (having coarser texture) in the temperate climate of the Czech Republic. Timothy grass is often grown as fodder in the dry areas of the Czech Republic. The significance of this plant for its energetic value is generally described in (Naik et al., 2010).

Each sample was disintegrated by a hammer mill and pressed into the form of briquettes. The briquetting press BrikStar 150 with a hydraulic unit was used for the samples processing. Density of the briquettes was up to 1,100 kg m^{-3} at the operating pressure up to 18 MPa and the operating temperature of 60 °C. Briquettes have a cylindrical shape with a diameter of 65 mm and length 50 mm.

Samples of biomass briquettes were analysed for fuel properties. The first task is to determine the chemical composition (by elemental analysis) on the combustible components such as carbon (C), hydrogen (H), nitrogen (N) and sulphur (S). The analyses were repeated six times and are carried out in an elemental analyzer LECO CHN628 + S. Detection method for carbon and hydrogen is dispersive infrared absorption, for nitrogen thermal conductivity and for sulphur infrared absorption. Accuracy range from 0.01 mg to 0.05 mg.

Non-combustible substances, i.e. ash and total moisture content, were determined in the thermogravimetric analyzer LECO TGA-701 with an accuracy of ± 0.02%. The gross calorific value of assessed biofuel samples was determined by burning in a isoperibolic calorimeter LECO AC-600 according to DIN 14918 (2010). The net calorific value was determined by calculation using the results of elemental and proximate analysis of individual samples (see Table 1).

Table 1. The average values from proximate and elemental analysis

Sample / Average values	Water Content (% wt.)	Ash (% wt.)	Gross Calorific Value (MJ.kg^{-1})	Net Calorific Value (MJ.kg^{-1})	Carbon C (% wt.)	Hydrogen H (% wt.)	Nitrogen N (% wt.)	Sulphur S (% wt.)	Oxygen O (% wt.)
	W	*A*	Q_s	Q_i	*C*	*H*	*N*	*S*	*O*
Czech knotweed original sample	**5.93**	**3.99**	17.62	**16.31**	45.87	5.33	0.30	0.03	**38.48**
Czech knotweed dry matter	-	**4.242**	18.73	**17.34**	48.76	5.66	0.32	0.03	**40.91**
Rumex OK 2 original sample	**7.75**	**2.75**	18.04	**16.86**	46.43	4.54	0.69	0.07	**37.72**
Rumex OK2 dry matter	-	**2.98**	19.55	**18.27**	50.33	4.92	0.75	0.07	**40.89**
Meadow hay original sample	**4.63**	**5.08**	17.25	**15.76**	42.86	6.34	0.44	0.08	**40.37**
Meadow hay dry matter	-	**5.33**	18.09	**16.52**	44.94	6.65	0.46	0.084	**42.33**
Timothy grass original sample	**10.65**	**5.16**	15.90	**14.38**	44.68	5.82	0.68	0.10	**32.54**
Timothy grass dry matter	-	**5.77**	17.79	**16.08**	50.01	6.51	0.76	0.11	**36.42**

The relationship between the gross calorific value Q_s (kJ kg^{-1}) and the net calorific value Q_i (kJ kg^{-1}) was expressed in the following equation:

$$Q_i = Q_s - (0.02442 \cdot 1{,}000) \cdot (W + 8.94 \cdot H) \quad (1)$$

where: W – the water content in test sample (*%*); *8.94* – coefficient for the conversion of hydrogen to water; H – hydrogen content in test sample (*%*); 0.02442 – value that corresponds to energy consumed in heating *1%* of water at 25 °C.

Stoichiometric calculations were made for calculation of other combustion characteristics, such as the excess air coefficient (*n*) expressed in the equation:

$$n = 1 + \left(\frac{CO_{2,max}}{CO_2} - 1\right) \cdot \frac{V_{sp.min}}{L_{min}} \quad (2)$$

where: $CO_{2,max}$ – theoretical volumetric concentration of carbon dioxide in dry flue gases (*%*); CO_2 – volumetric concentration of carbon dioxide in dry flue gases (*%*); $V_{sp.min}$ – theoretical mass amount of dry flue gas (m^3_N kg^{-1}); L_{min} – theoretical amount of air for complete combustion (m^3_N kg^{-1}).

The test device calculates the CO_2 content on the basis of measured values and characteristics of the fuel according to the formula:

$$CO_2 = CO_{2,max}\left(1 - \frac{O_{2,m}}{20.95}\right) \quad (3)$$

where: $CO_{2,max}$ – theoretical volumetric concentration of carbon dioxide in dry flue gases (%); $O_{2,m}$– real (measured) volumetric concentration of oxygen in dry flue gases (%); 20.95 – concentration of oxygen in atmosphere (%).

In stoichiometric calculations real molar volumes of gases. are used. Stoichiometric calculations are described in the paper of Malaťák et al. (2016). Results of stoichiometric calculations further serve to adjust the characteristics of the samples for flue gas analyzer and other essential combustion characteristics. Stoichiometric calculations are converted to standard conditions (to the temperature T = 0 °C and pressure p = 101.325 kPa).

Experimental measurements were carried out using a hot air grate combustion device with manual fuel supply from the company CALOR CZ. The nominal power of the combustion device is 12 kW and standard fuel consumption is 3.6 kg h^{-1}. The samples of biomass briquettes were monitored during sustained combustion. The emission concentrations were not monitored during ignition, start-up and extinguishing of fire.

Each sample was combusted for six hours. During the whole combustion process a nominal heat output was maintained which is rated for the combustion device at 12 kW with an efficiency of 80%. The corresponding hour supply of samples was for Czech knotweed m_p = 3.31 kg h^{-1}, Rumex OK 2 m_p = 3.20 kg h^{-1}, samples of meadow hay m_p = 3.43 kg h^{-1} and timothy grass m_p = 3.76 kg h^{-1}. For each fuel sample the measurement was carried out for 6 hours. The interval of fuel loading was set to 30 minutes. The measurements took place under stable combustion conditions during intervals of 15 minutes and the data was averaged for each measurement after one minute. During the whole combustion process the supply of primary combustion air is regulated, which is monitored by the amount of oxygen in the flue gas by the flue gas analyzer.

The emission concentration measurement was performed by flue gas analyser Madur GA-60. During all measurements the analyser monitored the ambient temperature, flue gas temperature and concentration of gases O_2, CO, NO, NO_2 in flue gas. Signal of converters is proportional to the volume concentration of the measured component in *ppm*. Recording interval of average individual components is set to one minute. Before each sample measurement was performed calibration of the measuring apparatus. The emission concentrations of dry flue gas are converted from *ppm* levels to normal conditions and transferred to the concentration in mg m^{-3} and reference oxygen content in the flue gas of 13%. Results of air emission measurements are processed by regression statistical analysis to express dependencies of carbon monoxide and carbon dioxide, flue gas temperature and nitrogen oxides on the excess air coefficient.

RESULTS AND DISCUSSION

The values from the elemental analysis indicated in Table 1 confirmed the fact from other authors Müller et al. (2015) and Ružbarský et al. (2014) that most decisive for the energetic utilization of selected biomass samples is the net calorific value, which depends on the water content and ash in the fuel. The best results in the net calorific value of dry matter on average reached samples of Rumex OK 2, which had compared to the other samples the lowest amount of ash.

A higher percentage of ash content is determined generally in samples of herbaceous biomass such as straw (Gurdil et al., 2009), in contrast to wood biomass (Johansson et al., 2004). Timothy grass had the highest concentration of ash up to 5.77% in the dry matter, which resulted in low gross calorific value. Low water content in the samples is a positive factor because moisture affects their behavior in combustion

process and exhaust gas volume produced per unit of energy (Malaťák & Bradna, 2014). Another essential element in samples of plant biomass is the amount of oxygen which reduces the amount of oxidizable elements in the fuel. The average oxygen content of all samples was determined at 40.14% in the dry matter, which corresponds to the results presented in this work Tao et al. (2012).

The values from stoichiometric calculations (see Table. 2) did not reveal fundamental differences in the theoretical air consumption, the theoretical concentration of dry flue gases of individual samples. Larger differences were determined in the theoretical maximum concentration of carbon dioxide in flue gas in the samples of Rumex OK 2, where the values reached 21.30% vol. This fact should be reflected in the emission measurements.

Table 2. The results of stoichiometric calculations

Sample / Average values	Theoretical amount of air		Theoretical amount of dry flue gases		Theoretical concentration of carbon dioxide in dry flue gases	
	kg kg^{-1}	m^3 kg^{-1}	kg kg^{-1}	m^3 kg^{-1}	% wt.	% vol.
Czech knotweed original sample	5.45	4.20	7.80	4.13	21.56	20.59
Rumex OK 2 original sample	5.28	4.07	7.69	4.04	22.12	21.30
Meadow hay original sample	5.38	4.14	7.63	4.03	20.59	19.72
Timothy grass original sample	5.74	4.42	7.98	4.29	20.53	19.32

The graph of the emission measurements for Czech knotweed depending on the excess air coefficient is shown in Fig. 1.

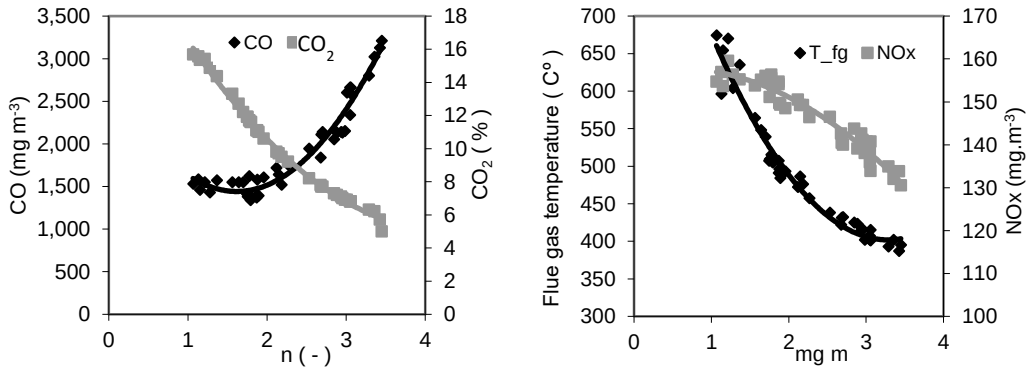

Figure 1. Graph of the emission measurements for Czech knotweed.

The combustion process quality during stable combustion is described by regression equations for Czech knotweed depending on the excess air coefficient *n* (-):

$$CO = 504.43n^2 - 1{,}631.3n + 2{,}760.8;\ R^2 = 0.9515 \quad (4)$$

$$CO_2 = 2.4138n^2 - 15.965n + 32.782;\ R^2 = 0.9869 \quad (5)$$

$$NOx = -3.1361n^2 + 3.3643n + 156.93;\ R^2 = 0.9368 \quad (6)$$

$$T_{\_fg} = 52.64n^2 - 345.54n + 968.92;\ R^2 = 0.9624 \quad (7)$$

where: *CO* – carbon monoxide emission concentration (mg m^{-3}); CO_2 – carbon dioxide emission concentration (%); *NOx* – nitrogen oxides emission concentration (mg m^{-3}); $T_{\_fg}$ – flue gas temperature (°C).

The graph of the emission measurements for Rumex OK 2 depending on the excess air coefficient is shown in Fig. 2.

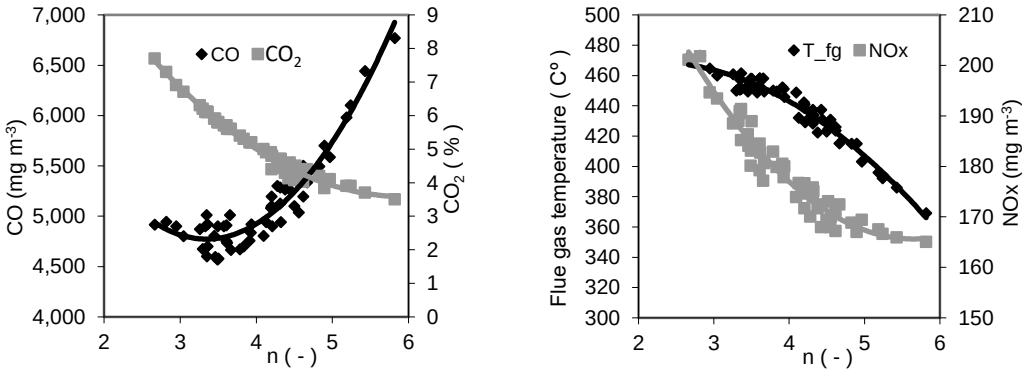

Figure 2. Graph of the emission measurements for Rumex OK 2.

The combustion process quality is described by regression equations for Rumex OK 2 depending on the excess air coefficient *n* (-):

$$CO = 352.36n^2 - 2{,}357.6n + 8{,}716.4;\ R^2 = 0.9124 \quad (8)$$

$$CO_2 = 0.3773n^2 - 4.482n + 16.897;\ R^2 = 0.9812 \quad (9)$$

$$NOx = 4.1513n^2 - 46.934n + 298.27;\ R^2 = 0.942 \quad (10)$$

$$T_{\_fg} = -7.6581n^2 + 32.954n + 433.61;\ R^2 = 0.9515 \quad (11)$$

where: *CO* – carbon monoxide emission concentration (mg m^{-3}); CO_2 – carbon dioxide emission concentration (%); *NOx* – nitrogen oxides emission concentration (mg m^{-3}); $T_{\_fg}$ – flue gas temperature (°C).

A graph of the emission measurements for Meadow hay depending on the excess air coefficient is shown in Fig. 3.

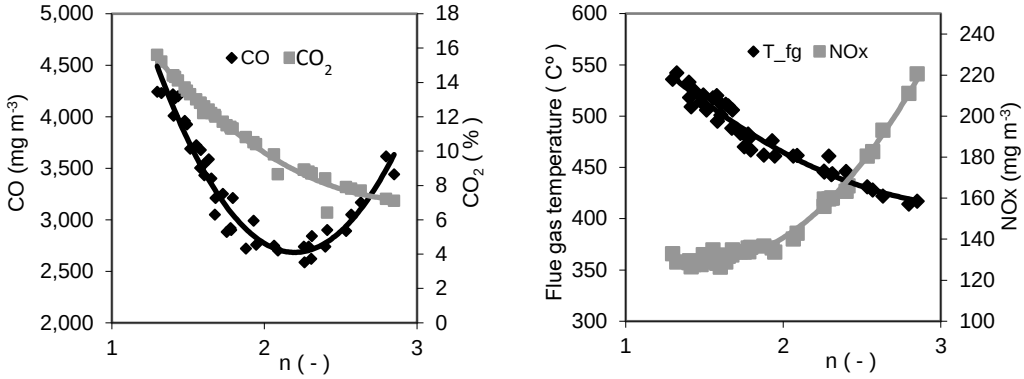

Figure 3. Graph of the emission measurements for Meadow hay.

The combustion process quality is described by regression equations for the Meadow hay depending on the excess air coefficient *n* (-):

$$CO = 2{,}231.2n^2 - 9{,}805.3n + 13{,}456;\ R^2 = 0.9376 \quad (12)$$

$$CO_2 = 2.9569n^2 - 17.529n + 33.14;\ R^2 = 0.9817 \quad (13)$$

$$NOn = 50.639n^2 - 154.81n + 247.79;\ R^2 = 0.9888 \quad (14)$$

$$T_{fg} = 31.81n^2 - 209.63n + 756.73;\ R^2 = 0.9456 \quad (15)$$

where: *CO* – carbon monoxide emission concentration (mg m^{-3}); CO_2 – carbon dioxide emission concentration (%); *NOx* – nitrogen oxides emission concentration (mg m^{-3}); T_{fg} – flue gas temperature (°C).

A graph of the emission measurements for Timothy grass depending on the excess air coefficient is shown in Fig. 4.

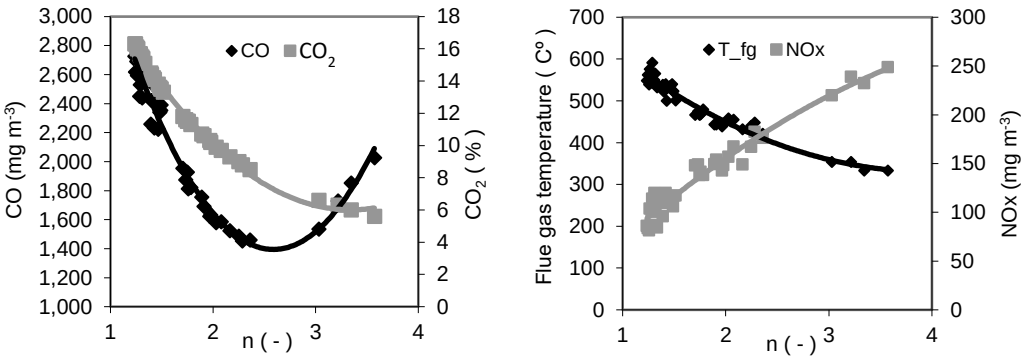

Figure 4. Graph of the emission measurements for Timothy grass.

The combustion process quality is described by regression equations for Timothy grass depending on the excess air coefficient *n* (-):

$$CO = 718.7n^2 - 3720n + 6{,}208.2;\ R^2 = 0.9595 \quad (16)$$

$$CO_2 = 2.2576n^2 - 15.093n + 31.233;\ R^2 = 0.9953 \quad (17)$$

$$NOn = -9.5214n^2 + 111.63n - 29.756;\ R^2 = 0.9528 \quad (18)$$

$$T_{\_fg} = 30.44n^2 - 242.2n + 812.06;\ R^2 = 0.9509 \quad (19)$$

where: CO – carbon monoxide emission concentration (mg m^{-3}); CO_2 – carbon dioxide emission concentration (%); NOx – nitrogen oxides emission concentration (mg m^{-3}); $T_{\_fg}$ – flue gas temperature (°C).

Under conditions of low excess air coefficient ($n < 2$) incomplete combustion occurs and high concentrations of carbon monoxide are found. Conversely with higher excess air coefficient ($n > 3$) rising concentration of carbon monoxide emissions occurs, mainly due to low temperature and premature cooling of the flue gas. These trends are observed in all examined samples. For samples of Rumex OK 2 particularly high excess air coefficients were tested as well and with *n* approaching 6 carbon monoxide in the flue gas got up to 6,500 mg m^{-3}. The increasing trend of carbon monoxide concentration in the flue gas is a result of the lowering temperature and high excess air coefficient in combustion zone, where the high CO concentration in flue gas is firstly resulted by cooling of the burning furnace. This fact is also confirmed in the combustion test in Malaťák & Bradna (2017) and also in Liu et al. (2010).

Similar trends for emission concentrations were achieved by Eskilson et al. (2004) during the combustion of pellets from plant biomass. Strehler (2000); Houshfar et al. (2012) & Černý, et al. (2016) achieved similar results during combustion of wood pellets. In their case decreasing amount of air in the combustion chamber reduced amount of nitrogen oxides in flue gas, but on the other hand increased emissions of unburned carbon.

All samples reach an optimal concentration of nitrogen oxides below 250 mg m^{-3}. For samples of meadow hay and timothy grass with rising excess air coefficient an increase of nitrogen oxides emission occurred. These trends were also observed by Diaz-Ramirez et al. (2014). The highest flue gas temperatures 680 °C were observed for Czech knotweed.

CONCLUSIONS

The results of experimental measurements confirm the fact, that the proximate and elemental composition affect not only the net calorific value, but also the behaviour during the combustion process. Especially high amount of oxygen and ash in plant biomass samples will affect the final emission concentrations. This difference is primarily visible in the samples of Czech knotweed and Timothy grass compared to other analysed samples. The higher consumption of combustion air and high amount of flue gas affect setting of the combustion device.

The results of emission measurements confirm also the fact, that the excess air coefficient is an important parameter for achieving optimum combustion of plant

biomass of the selected samples. The main factors are the concentration of carbon monoxide and nitrogen oxides, but also the flue gas temperature. Especially with samples of Rumex OK 2 higher concentrations of carbon monoxide at higher excess air coefficient were achieved. Under optimal conditions, the achieved reduction of CO and NOx, with the greatest reduction represents case with excess air coefficient around 2. The results of measurements confirm the fact that the emissions of CO and NOx were very sensitive to the excess air ratio. By regulating an optimal combustion air amount for each type of biomass fuel heat losses can be prevented thereby increasing the efficiency of the combustion device.

ACKNOWLEDGEMENTS. The article was financially supported by the Internal Grant Agency of the Czech University of Life Sciences Prague, Czech Republic, Grant No. 20173003.

REFERENCES

Bradna, J. & Malaťák, J. 2016. Flue gases thermal emission concentration during waste biomass combustion in small combustion device with manual fuel supply. *Research in Agricultural Engineering* **62**(1), 1–7

Brassard, P., Palacios, J.H., Godbout, S., Lagacé, R., Larouche, J.P. & Pelletier, F. 2014. Comparison of the gaseous and particulate matter emissions from the combustion of agricultural and forest biomasses. *Bioresource Technology* **155**, 300–306.

Čedík, J., Pexa, M., Pražan, R., Kubín, K. & Vondřička, J. 2015. Mulcher energy intensity measurement in dependence on performance. *Agronomy Research* **13**(1), 46–52.

Černý, D., Malaťák, J. & Bradna, J. 2016. Influence of biofuel moisture content on combustion and emission characteristics of stove. *Agronomy Research* **14**(3), 725–732.

Díaz-Ramírez, M., Sebastián, F., Royo, J. & Rezeau, A. 2014. Influencing factors on NOX emission level during grate conversion of three pelletized energy crops. *Applied Energy* **115**, 360–373.

DIN 14918: 2010. Solid biofuels – Determination of calorific value. Standard is the Czech version of the European Standard EN 14918: 2009. *Czech Office for Standards, Metrology and Testing*, 52.

Eskilsson, D., Rönnbäck, M., Samuelsson, J. & Tullin, C. 2004. Optimisation of efficiency and emissions in pellet burners. *Biomass and Bioenergy* **27**, 541–546.

Esteban, B., Riba, J.-R., Baquero, G., Puig, R. & Rius, A. 2014. Environmental assessment of small-scale production of wood chips as a fuel for residential heating boilers. *Renewable Energy* **62**, 106–115.

Garcia-Maraver, A., Zamorano, M., Fernandes, U., Rabaçal, M. & Costa, M. 2014. Relationship between fuel quality and gaseous and particulate matter emissions in a domestic pellet-fired boiler. *Fuel* **119**, 141–152.

Gurdil, G.A.K., Malatak, J., Selvi, K.C. & Pinar, Y. 2009. Biomass utilization for thermal energy. *AMA, Agricultural Mechanization in Asia, Africa and Latin America* **40**(2), 80–85.

Heděnec, P., Novotný, D., Ust'ak, S., Honzík, R., Váňa, V., Petříková, V. & Frouz, J. 215. Effect of long term cropping hybrid sorrel (Rumexpatientia x Rumex tianshanicus) on soil biota. *Biomass and Bioenergy* **78**, 92–98.

Houshfar, E., Løvås, T. & Skreiberg, Ø. 2012. Experimental investigation on NO x reduction by primary measures in biomass combustion: Straw, peat, sewage sludge, forest residues and wood pellets. *Energies* **5**(2), pp. 270–290.

Johansson, L.S., Leckner, B., Gustavsson, L., Cooper, D., Tullin, C. & Potter, A. 2004. Emission characteristics of modern and old-type residential boilers fired with wood logs and wood pellets. *Atmospheric Environment* **38**(25), 4183–4195.

Juszczak, M. 2016. Comparison of CO and NOx concentrations from a 20 kW boiler for periodic and constant wood pellet supply. *Environment Protection Engineering* **42**(3), 95–107.

Liu, H., Qiu, G., Shao, Y. & Riffat, S.B. 2010. Experimental investigation on flue gas emissions of a domestic biomass boiler under normal and idle combustion conditions. *International Journal of Low-Carbon Technologies* **5**(2), 88–95.

Malaťák, J. & Bradna, J. 2017. Heating and emission properties of waste biomass in burner furnace. *Research in Agricultural Engineering* **63**(1), 16–22.

Malaták, J. & Bradna, J. 2014. Use of waste material mixtures for energy purposes in small combustion devices. *Research in Agricultural Engineering* **60** (2), pp. 50–59.

Malat'ák, J., Bradna, J. & Velebil, J. 2016. Combustion of briquettes from oversize fraction of compost from wood waste and other biomass residues. *Agronomy Research* **14**(2), 525–532.

Müller, M., Horníčková, Š., Hrabě, P. & Mařík, J. 2015. Analysis of physical, mechanical and chemical properties of seeds and kernels of Jatropha curcas. *Research in Agricultural Engineering* **61**(3), 99–105.

Naik, S., Goud, V.V., Rout, P.K., Jacobson, K. & Dalai, A.K. 2010. Characterization of Canadian biomass for alternative renewable biofuel. *Renewable Energy* **35**(8), 1624–1631.

Riedener, E., Melliger, R.L., Rusterholz, H.-P. & Baur, B. 2015. Changes in landscape composition of differently irrigated hay meadows in an arid mountain region. *Applied Vegetation Science* **18** (2), pp. 242–251.

Ružbarský, J., Müller, M. & Hrabě, P. 2014. Analysis of physical and mechanical properties and of gross calorific value of Jatropha curcas seeds and waste from pressing process. *Agronomy Research* **12**(2), 603–610.

Strašil, Z. & Kára, J. 2010. Study of knotweed (Reynoutria) as possible phytomass resource for energy and industrial utilization. *Research in Agricultural Engineering* **56**(3), 85–91.

Strehler, A. 2000. Technologies of wood combustion. *Ecological Engineering* **16**, S25–S40.

Tao, G., Lestander, T.A., Geladi, P. & Xiong, S. 2012. Biomass properties in association with plant species and assortments I: A synthesis based on literature data of energy properties. *Renewable and Sustainable Energy Reviews* **16**(5), 3481–3506.

Agronomy Research **15**(S1), 1094–1100, 2017

Mathematical model describing the drying curves of false banana´s fibre (Ensete ventricosum)

Č. Mizera[1,*], D. Herák[2] and P. Hrabě[3]

[1,2]Czech University of Life Sciences Prague, Faculty of Engineering, Department of Mechanical Engineering, Kamýcká 129, CZ165 21 Praha 6 Suchdol, Czech Republic
[3]Czech University of Life Sciences Prague, Faculty of Engineering, Department of Material Science and Manufacturing Technology, Kamýcká 129, CZ165 21 Praha 6 Suchdol, Czech Republic
[*]Correspondence: mizera@tf.czu.cz

Abstract. Drying processes play an important role in the preservation of agricultural products. They are defined as a process of moisture removal due to simultaneous heat and mass transfer. This study was focused on the analysis of drying curves of fibres of false banana (*Ensete ventricosum*). The fibres of *Ensete ventricosum*, originally from Ethiopian region Hawasa, were used in this experiment. Moisture content of freshly harvested fibres $M_c = 78.4 \pm 1.4$ % (w.b.) were determined. The fibres were dried at different air temperatures $T_d = 40$, 60, 80 and 100 ± 1 °C. To determine the drying curves the drying moisture balance (Radwag, MA 50.R, Poland) was used. Measured data were analysed by computer software Mathcad 14. Experimental drying curves at different temperatures and drying rate were determined. Basic mathematical model describing the loss of mass by drying of the Ensete fibres was represented. The model coefficients were statistically significant suggesting that the determined model could be used as a background for further research focused on Ensete fibre application.

Key words: drying kinetics, moisture content, drying rate.

INTRODUCTION

False banana fibre (*Ensete ventricosum*) belongs to the family *Musa*, and is a lucrative natural fibre with good mechanical and physical properties (Mizera et al., 2017). In general natural fibres are an interesting and environmentally friendly alternative to the replacement of synthetic material. The natural fibres are environmentally friendly, biodegradable and recyclable, and also they can help in the reduction of waste and environmental pollution (Kalia et al., 2013). Natural fibres are good substitute for synthetic polymeric fibres since they are available in fibrous forms at low cost (Aseer et al., 2013). The Ensete plant is a perennial herb that grows in Ethiopia and it is primarily intended for human consumption and animal feeding (Vincent et al., 2013; Herak et al., 2014). Over centuries the Ensete fibres have been extracted from the leaves of this plant as major material for the weaving, ropes and cord production, as well as for baskets production (Diriba et al., 2013; Yirmaga, 2013). Some of the mechanical properties of Ensete fibres have already been determined (Mizera et al., 2016a; Mizera et al., 2016b). For using of natural fibres as a construction material it

is necessary to reduce their moisture content. Because of their relatively high moisture content fresh fibres have short shelf-life as they are sensitive to microbial spoilage and formation of mould. A decrease of moisture content reduces their biological activity as well the chemical and physical changes that occur during storage. Drying is one of the oldest methods of agriculture products preservation and improves the shelf life of agriculture products (Larrauri, 1999). Water loss from agriculture products is a very energy – intensive process and it is necessary to find the optimum drying conditions for economical operation (Agrawal & Methekar, 2017). Energy and time efficiency is one of the most significant design and operation parameters in drying processing (Mongpraneet et al., 2002; Sharma et al., 2005; Adak et al., 2017). For better understanding of drying processes is necessary to know the drying curves under various drying temperatures. Experimental data are usually transformed into mathematical drying models, which are routinely used in the design and analysis of dryers. In view on the fact that no literature was available on the drying characteristics of *Ensete ventricosum* fibres, the present study aims are to measure drying curves and to determine drying rate and basic mathematical model of drying under different temperatures.

MATERIALS AND METHODS

Materials

Samples of fibres produced from *Ensete ventricosum*, obtained from Hawassa region, Ethiopia were used for this experiment. Fibres were harvested at natural moisture content. The moisture content $M_c = 78.4 \pm 1.4$ % (w.b.) of the freshly harvested fibres was determined using standard oven method, ASAE method (ASAE S410.1 DEC97, ASAE, 1998). Samples of *100 g* mass from a batch of Ensete fibres were randomly selected for the moisture content determination. For measuring of mass of each sample m_s *(g)* an electronic balance (Kern 440–35, Kern & Sohn GmbH, Balingen, Germany) was used. All the obtained results were expressed as mean of three replicates. After harvesting the fibres were packaged by vacuum atmosphere in polyethylene (PE) bag. Packed samples of fibres were transported using air transport to the laboratory of CULS Prague. All the fibres were stored in a refrigator at 5 ± 1 °C prior to the experiments.

Drying experiments

Drying of samples were carried out in the drying moisture balance (Radwag, MA 50.R, Poland). Moisture balance is equipped with IR emiter heating module 400 W and was set to a standard drying profile (Fig. 1). To explore the effect of drying temperature on drying rate of fibres, drying experiments were carried out at temperatures of *40, 60, 80* and 100 ± 1 °C. The fibres were prepared for drying by chopping them into short fibres of approximately *25 mm* length. The randomly selected samples of weight $m_0 = 10 \pm 1$ *g* were inserted into the moisture balance and gradually dried. The weight loss changes per minute were recorded in the memory.

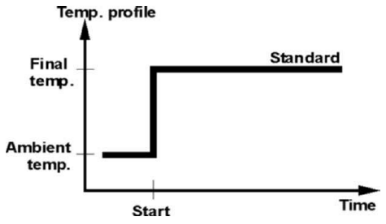

Figure 1. Drying profile: Standard for moisture balance Radwag

Mathematical modelling of drying curves

The measured values of weight loss for different drying temperstures were analysed with computer program Mathcad 14 (MathCAD 14, PTC Software, Needham, MA, USA), (Pritchard, 1998) uses Levenberg-Marquardt algorithm for data fitting (Marquardt, 1963). The determined models of drying curves were statisticaly verified by using ANOVA.

RESULTS AND DISCUSSION

Fig. 2 shows the moisture ratio as a function of drying time of Ensete fibres at the air temperature range of *40–100 °C*. The initial moisture content of freshly harvested Ensete fibres was observed to be $M_c = 78.4 \pm 1.4\%$ (w.b.), which is characteristic of most natural fibres (Faruk et al., 2012). Drying continued until the final moisture content was ca. *5%* (w.b.). Fig. 2 shows that, as expected, drying rate increases significantly as the drying air temperature increases. Drying time was estimated at *473, 112, 77* and *51 min* at *40, 60, 80* and *100 °C*, respectively. The results indicate that increasing drying air temperature can extensively enhance drying process. The drying time at air temperature of 40 °C was approximately four times longer that required at a drying air temperature of 60 °C. The drying time of Ensete samples at 80 °C was 43% shorter than the drying period at temperature of 60 °C. This phenome due to the fact that high temperature could enhance heat transfer between drying air and fibre samples (Wang et al., 2017).

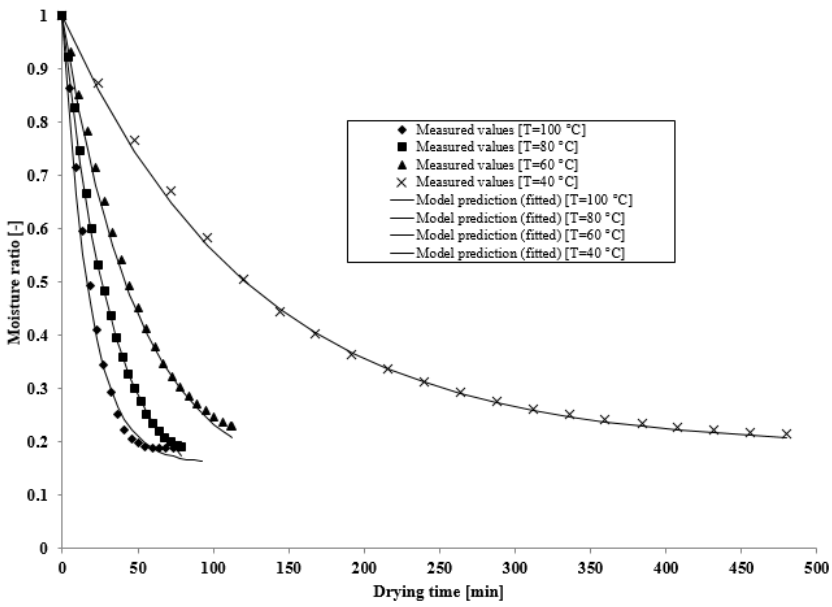

Figure 2. Comparison of measured values of moisture ratio and fitted models in the air temperature range of 40–100 °C.

The drying curves of the Ensete fibres at 4 drying temperatures with the model fit are presented in Fig. 2. Measured and calculated values for different drying curves were fitted by exponential curve using Marguardt Levenberg algorithm and it is described by Eq. 1.

$$\xi(d,t) = d_0 + d_1.e^{d_2.t} \tag{1}$$

where: d_0 – ratio of dry matter, -; d_1 – ratio of water, -; d_2 – slope of the tangent at zero time, min^{-1}.

The values of coefficients d_0, d_1, d_2 from Eq. 1 are presented in Table 1.

Table 1. Estimated values of coefficients for Eq. 1

Temperature of drying	d_0 (-)	d_1 (-)	d_2 (min^{-1})
40	0.192	0.8169	-0.00793
60	0.1158	0.9001	-0.02
80	0.0962	0.9082	-0.031
100	0.1632	0.8665	-0.056

From statistical analysis ANOVA (Table 2) follows, that measured amounts of drying curves at diferent temperatures and results from the general exponential model (Eq. 1) were statistically significant at significance level 0.05, that is, the values of F_{crit} (critical value comparing a pair of models) were higher than the F_{rat} values (value of the F – test) for all the measured Ensete fibres and values of P_{value} (significance level at which it can be rejected the hypothesis of equality of models) (Table 2) were higher than 0.05 which is also confirmed by very high coefficients of determination R^2.

Table 2. Statistical analysis of general model

Drying temperature (°C)	F_{rat} (-)	F_{crit} (-)	P_{value} (-)	R^2 (-)
40	$-1.147.10^{-14}$	4.085	1	0.999
60	$-1.523.10^{-14}$	4.073	1	0.998
80	$-1.798.10^{-14}$	4.085	1	0.999
100	$-1.963.10^{-14}$	4.073	1	0.994

F_{rat} – value of the F test; F_{crit} – critical value that compares a pair of models; P_{value} – hypothesis of the study outcomes significant level; R_2 – coefficient of determination.

The variation of drying rate with moisture content is shown in Fig. 3. From the Fig. 3 is evident, that the drying rate decreased continuously with decreased moisture content. A trend of drying rate decrease showed no constant drying rate period for Ensete fibres. Different drying rate decrease is determined by the structure of the sample being dried and the mechanism of internal liquid migration (Simović et al., 2016). Some previous authors determined, that moisture diffusion represents the dominant physical mechanism affecting drying rate decrease during the drying of vegetable products (Singh & Gupta, 2007; Xiao et al., 2010).

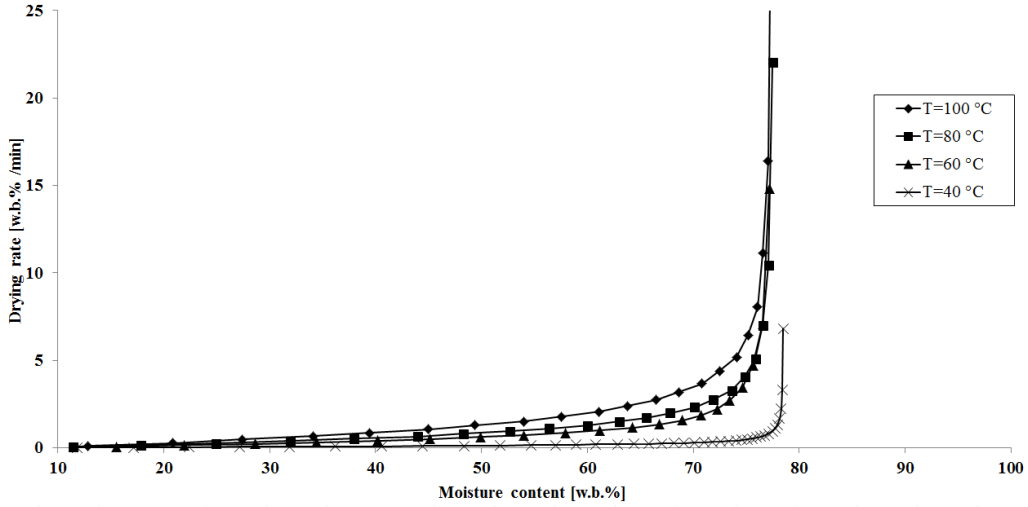

Figure 3. Drying rate versus moisture content at different air temperatures.

This effect can also be seen in the drying of Ensete fibres indicating that the absence of constant water supply to the sample surface lowered the drying rate, which is expressed through the rapid decline of drying rate values (Fig. 3). Similar values were measured also for other natural fibers (Stamboulis et al., 2001). Drying of coton fibres explored Soomro (2014). Drying is a very energy demanding process and also has a large effect on the mechanical and physical properties (Mohanty et al., 2005). Therefore it is very important to know the drying process of Ensete fibres and to determine the basic mathematical description. Modeling of drying process for agricultural products also published some authors (Karathanos & Belessiotis, 1996; Krokida et al., 2003).

CONCLUSIONS

This study has focussed on the drying process of Ensete fibres. Dependency between weight loss and drying time was observed and transformed into general mathematical model describing hot air drying of Ensete fibres. Results indicate that the fibres are very sensitive to the drying air temperature and air temperature enhance extensively drying process. The drying time at air temperature of 60 °C was approximately four times shorter that required at a drying air temperature of 40 °C, which can occur by drying with sunshine. The drying rate was also determined. Mathematical model in this study could by used for the development of further models which will describe drying process of Ensete fibres and it can help to design of technology for drying of Ensete ventricosum fibres.

ACKNOWLEDGEMENTS. This paper has been supported by Internal Grant Agency of Faculty of Engineering – Czech University of Life Sciences Prague – IGA 2016: 31130/1312/3111.

REFERENCES

Adak, N., Heybeli, N. & Ertekin, C. 2017. Infrared drying of strawberry. *Food Chemistry* **219**, 109–116.

Agrawal, S.G. & Methekar, R.N. 2017. Mathematical model for heat and mass transferduring convective drying of pumpkin. *Food and Bioproducts Processing* **101**, 68–73.

Aseer, J.R., Sankaranarayanasamy, K., Jayabalan, P., Natarajan, R., Dasan, K.P. 2013. Morphological, Physical and Thermal Properties of Chemically Treated Banana Fiber. *Journal of Natural Fibers* **10**, 365–380.

ASAE S410.1 DEC97. 1998. Moisture measurement of peanut. In: ASAE standards, 45th edition. 560–561.

Diriba, H.D., Mazancová, J., Rušarová, K. & Havrland, B. 2013. Possibilities and Acceptance of Alternative Energies from Farm Solid Waste Material (Kocho): Case Study from Kembata Tenbaro Zone. *EthiopiaTropentag 2013 International Research on Food Security, Natural Resource Management and Rural Development Agricultural development within the rural-urban continuum*, Gottingen.

Faruk, O., Bledzki, A.K., Fink, H.-P. & Sain, M. 2012. Biocomposites reinforced with natural fibers: 2000–2010. *Progress in Polymer Science* **37**, 1552–1596.

Herák, D., Hrabě, P., Kabutey, A., Jaweso, D.E. & Diriba, H.D. 2014. Mechanical behavior of enset (ensete ventricosum) pulp under compression loading - A multipurpose product in Ethiopia. *Journal of Food Process Engineering* **37**, 588–595.

Kalia, S., Thakur, K., Celli, A., Kiechel, M.A. & Schauer, C.L. 2013. Surface modification of plant fibers using environment friendly methods for their application in polymer composites, textile industry and antimicrobial activities. *Journal of Environmental Chemical Engineering* **1**, 97–112.

Karathanos, V.T. & Belessiotis, V.G. 1997. Sun and Artificial Air Drying Kinetics of some Agricultural Products. *Journal of Food Engineering* **31**, 35–46.

Krokida, M.K., Karathanos, V.T., Maroulis, Z.B. & Kouris, M.D. 2003. Drying kinetics of some vegetables. *Journal of Food Engineering* **59**, 391–403.

Larrauri, J.A. 1999. New approaches in the preparation of high dietary fibre powders from fruit by-products. *Trends in Food Science & Technology* **10**, 3–8.

Marquardt, D.W. 1963. An Algorithm for Least-Squares Estimation of Nonlinear Parameters. *Journal of the Society for Industrial and Applied Mathematics* **11**, 431–441.

Mizera, Č., Herák, D. & Hrabě, P. 2016a. Relaxation and creep behaviour of false banana's fibre (Ensete ventricosum). *Agronomy Research* **14**, 1069–1077.

Mizera, Č., Herák, D., Hrabě, P., Müller, M. & Kabutey, A. 2016b. Mechanical Behavior of Ensete ventricosum Fiber Under Tension Loading. *Journal of Natural Fibers* **2**, 287–296.

Mohanty, A.K., Misra, M. & Drzal, L.T. 2005. Natural fibers, biopolymers, and biocomposites. Taylor & Francis Group, USA.

Mongpraneet, S., Abe, T. & Tsurusaki, A. 2002. Accelerated drying of welsh onion by far infrared radiation under vacuum conditions. *Journal of Food Engineering* **55**, 147–156.

Pritchard, P.J. 1998. Mathcad: A tool for engineering problem solving. McGraw-Hill Science Engineering, New York.

Sharma, G.P., Verma, R.C. & Pathare, P.B. 2005. Thin-layer infrared radiation drying of onion slices. *Journal of Food Engineering* **67**, 361–366.

Simović, D.Š., Šereš, Z., Maravić, N., Djordjević, M., Djordjević, M., Luković, J. & Tepić, A. 2016. Enhancement of physicochemical properties of sugar beet fibres affected by chemical modification and vacuum drying. *Food and Bioproducts Processing* **100**, 432–439.

Singh, B. & Gupta, A.K. 2007. Mass transfer kinetics and determination of effective diffusivity during convective dehydration of pre-osmosed carrot cubes. *Journal of Food Engineering* **79**, 459–470.

Soomro, N. 2014. Effect of drying methods on quality of cotton fibers before ginning. *European Scientific Journal* **10**, 24.

Stamboulis, A., Baillie, C.A. & Peijs, T. 2001. Effects of environmental conditions on mechanical and physical properties of flax fibers. *Composites: Part A* **32**, 1105–1115.

Vincent, H., Wiersama, J., Kell, S., Fielder, H., Dobbie, S., Castaneda-Alvarez, N.P., Guarino, L., Eastwood, R., Leon, B. & Maxted, N. 2013. A prioritized crop wild relative inventory to help underpin global food security. *Biological Conservation* **167**, 265–275.

Wang, J., Fang, X.M., Mujumdar, A.S., Qian, J.Y., Zhang, Q., Yang, X.H., Liu, Y.H., Gao, Z.J. & Xiao, H.W. 2017. Effect of high-humidity hot air impingement blanching (HHAIB) on drying and quality of red pepper (Capsicum annuum L.). *Food Chemistry* **220**, 145–152.

Xiao, H.W., Pang, C.L., Wang, L.H., Bai, J.W., Yang, W.X. & Gao, Z.J. 2010. Drying kinetics and quality of Monukka seedless grapes dried in an air-impingement jet dryer. *Biosystem Engineering* **105**, 233–240.

Yirmaga, M.T. 2013. Improving the Indigenous Processing of Kocho, an Ethiopian Traditional Fermented Food. *Journal of Nurition and Food Science* **3**, 1–6.

Agronomy Research **15**(S1), 1101–1106, 2017

Seabed sediment – a natural seasonal heat storage feasibility study

A. Mäkiranta*, B. Martinkauppi and E. Hiltunen

University of Vaasa, Faculty of Technology, Electrical Engineering and Energy Technology, P.O. Box 700, FI-65101 Vaasa, Finland
*Correspondence: anne.makiranta@uva.fi

Abstract. The new discovery among renewable energy resources, seabed sediment, has been utilised as a heat source for 42 houses in Vaasa since 2008. Sediment heat is annually loaded by the Sun. In this study the amount of annually charged energy is estimated. The difference of sediment temperatures between the coldest and the warmest month during the year is a key value in the approximation of the loaded energy. Sediment temperatures are measured once per month via optical cable by distributed temperature sensing (DTS) method. The monitoring period is three years, 2014–2016. The estimation of incoming energy (575 MWh) versus known exploited energy (560 MWh) is reasonable. Despite of the extraction this seasonal heat storage in the seabed of the Baltic Sea seems to reload well annually.

Key words: renewable energy, sediment heat, distributed temperature sensing, heat storage.

INTRODUCTION

Renewable, Sun-based energies are often available when the need of energies is low. Especially in the Northern countries, the demand of heat is greater in wintertime but a lot of renewable heat is available in summertime. Due to the seasonal nature of the solar energy, its utilisation requires storing. Water tanks, bedrock batteries and aquifers are the most used applications as heat storages. Old flooded mines have also been studied as potential heat storages (Watzlaf et al., 2006; Martinkauppi & Hiltunen, 2015). There are also natural seasonal heat storages like seabed sediment. The natural seasonal storing guarantees that the heat is available in winter time when the heating season is going on. The advantages of natural storage are also automatical annual function, fewer infrastructure constructions and thus less CO_2 emissions.The aim of this study is to estimate the amount of reloaded energy. This will help to estimate how much energy is exploited without detrimental effects.

Local renewable energy sources are available almost everywhere on Earth. The seabed sediment heat is one geothermal heat energy source which has been utilized in Vaasa, Finland since 2008. Actually the heat of this source is mainly coming from the Sun which is a common feature of natural heat sources in the upper crust. In Finland, the seasonal variation in air temperatures is observed to correlate even to the depth of 10–15 meters from the soil surface (Mäkiranta et al., 2016a).

Geological Survey of Finland made a geological analysis of the sediment in Suvilahti area in 2006. They also measured the sediment temperatures in house fair area

in 2008–2009 (Martinkauppi, 2013). Valpola (2007) discovered that the annual air temperature variation is observed only to the depth of 3 m in the seabed sediment in Vaasa area. Instead in the ground that variation is observed even to the depth of 10–15 m. The Research group of Renewable Energies from University of Vaasa continued temperature measurements in 2013 in the same site, Suvilahti suburb.

Hiltunen et al. (2015) and Mäkiranta et al. (2016b) have investigated the dependency between the air temperature, the sediment heat collection fluid (water ethanol mixture) temperature and the sediment temperature on the residential area which is utilizing the seabed sediment as a heat source. They observed that there is a clear correlation between the heat carrier liquid temperature and the sediment temperature of the next month and the temperatures of the same month as well. The conclusions of that study were that there is heat energy sufficiently available for all the houses included in the low energy network, the collection pipeline is sized correctly.

In this study, the annual recovery of the sediment heat is examined. The annually loaded energy is estimated by means of the seasonal temperature variation in sediment when the composition of sediment is known to be wet clay.

MATERIALS AND METHODS

Seabed sediment has been utilised since 2008 as a heat source in the residential area in Vaasa next to the Gulf of Bothnia in the Baltic Sea. This low energy network is used for heating and cooling houses throughout the year. The main heating season starts on October continuing to May. During the summer season cooling is used occasionally. Instead the loading occurs from April to October. The sediment temperature measurements have been executed there starting from the year 2013 by the Renewable Energy Research group of University of Vaasa. The used measurement method is distributed temperature sensing (DTS) method and the device is a product of Sensornet, Oryx DTS. The method and more detailed description of measurements are presented by Mäkiranta et al. (2016c).

Figure 1. The measurement site is located in Ketunkatu street. A box including optical fibers with connectors is placed in the distribution well.

There is assembled an optical cable along one heat collection pipe in Ketunkatu street (Fig.1). In measurement session the laser pulse travels along the optical glass fiber inside the cable. So the cable functions as a thermal profile sensor transferring temperature data with spatial resolution of 1 meter. The cable is 300 meters long and it is diagonally drilled to the depth of 3–4 meters, see Fig. 2. During the drilling action there was noticed some rocks and the direction of drilling had to be changed. Because of this variety in the composition of sediment layer the depth position of cable may vary from the supposed one.

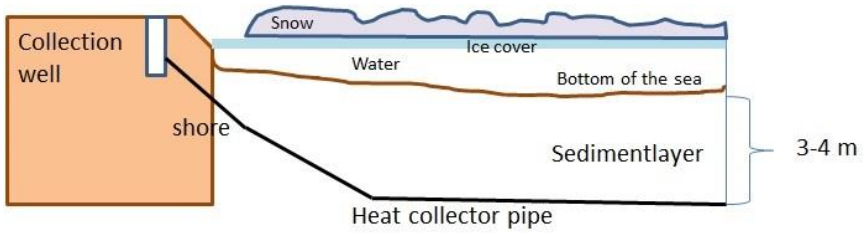

Figure 2. The conjectural position of the collection pipe and measurement cable along it in the seabed sediment is visualized in this graphical presentation. (not in scale).

The measurements were made once per month throughout the years. To discover the annual reloading of sediment heat the temperature difference between the warmest and the coldest month of the year were calculated. Year 2013 was measured only partly, thus the first year for observing the reloading of the seabed sediment heat was 2014. The highest sediment temperatures were observed in October 2014, 2015 and 2016. Instead the time of the coldest month varied being February in 2014 and March in 2015 and 2016. The temperature difference curves are shown in Fig. 3. The *x*-axis shows the length and the distance of the cable from the shore. The zero point is on the shore in the well and the sediment layer occurs after about 5 meters distance from the well. The first hundred meter is partly covered by reeds and there is located a pedestrian route with a bridge, too. They may have an effect on temperatures. Therefore, the starting point for calculating the differences was decided to be at 100 meter distance from the shore. The sediment temperature differences are presented 100–300 meters distance from the shore in years 2014–2016 in Fig. 3.

According to the Finnish Meteorological Institute (2017) the annual average air temperature in Finland during the year 2016 was the warmest compared to the long term average in 1981–2010. Sediment temperatures in 2016 were indicating the warming too. Based on the previous research by Mäkiranta et al. (2016b) the sediment temperature correlates strongly with the air temperature of two previous months.

The amount of annually loaded energy in the sediment layer is estimated with help of the facts that how much energy is bound to close range around the collection pipe while the annual temperature variation in sediment is known. The calculated energy is compared to the experimental extraction of energy which is known to be 560 MWh per year in the low energy network (Energy Vaasa, 2016).

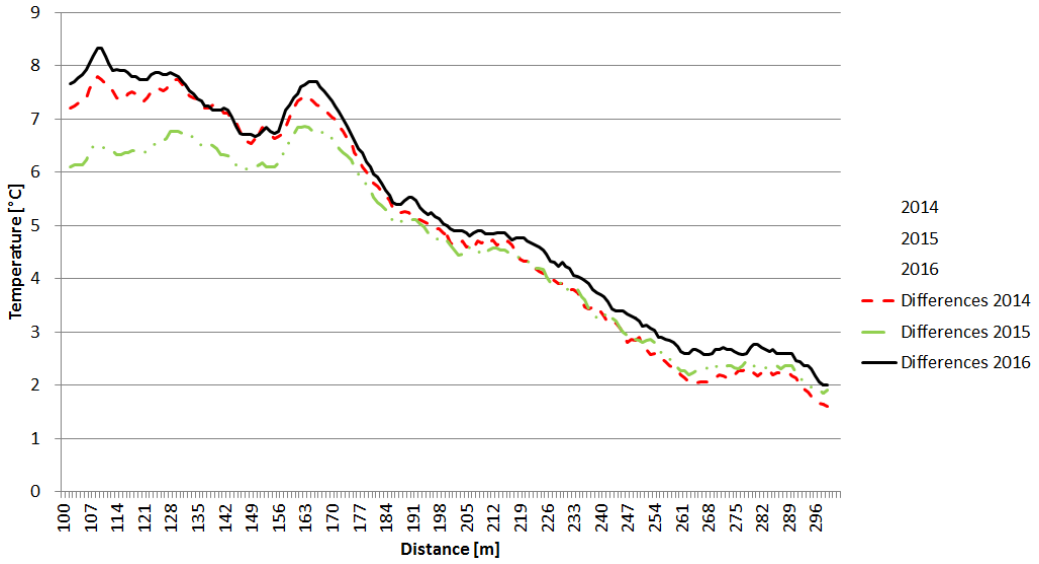

Figure 3. Temperature differences between the warmest and the coldest months during three annual loading periods in 2014, 2015 and 2016 as a function of length and distance of the cable from the shore. (Note: data is smoothed in Excel with the following option: moving averages with period 3, as the original data is very noisy).

The estimation of loaded and later extracted energy by the Sun is calculated as follows. First, the volume

$$V = \pi r^2 h \quad (1)$$

The volume of heat collection pipeline (26 pipes, h = 300 m, Ø = 84 mm) in the sediment is 43 m³ calculated with Eq. 1. The volume of seabed sediment around the pipeline with a radius of 2 m is 98.0 10^3 m³. The mass of the volume is calculated using the basic formula (Eq. 2):

$$m = \rho \cdot V \quad (2)$$

The calculation gives the value of mass as 172 10^6 kg when density of wet clay ρ = 1,760 kg m^{-3} is used. The heat energy is:

$$Q = cm\Delta T \quad (3)$$

The quantity of heat energy Q in the seabed sediment for heat collection is calculated with help of Eq. (3), when the average variation of annual sediment temperature (ΔT) is 5 °C and specific heat capacity of wet clay c =2.4 kJ kg^{-1} °C. By using these consumptions the quantity of heat energy is counted to be 2,070 10^6 kJ which is equal to 575 MWh.

RESULTS AND DISCUSSION

The absolute temperatures at the distances of 100–170 m are variating from 3–14 °C. This reveals that the depth of the heat collection pipe is not more than 3 m. The annual air temperature variation is clearly affecting to the sediment temperatures. Instead the effect of air temperature is not noticed in winter months measured sediment temperatures. The ice cover and snow form an isolating layer against the effect of the air temperature.

The absolute temperatures at the distances of 180–230 m variate from 5–12 °C and at the distances 240–300 m about 6–10 °C throughout the year. According to these last values (h = 300 m - 240 m = 60 m and ΔT = 10 °C – 6 °C = 4 °C), the heat energy Q = 92 MWh is available in the sediment layer.

The temperature difference (ΔT) between the warmest and the coolest month remain almost at the same level year after year. The variation is only between 0–2 °C and the difference curve follows the same shape every year. After 180 m distance the variation in the temperature differences is about 0.5 °C. This may indicate the fact that the sediment heat collection pipe is located deeper in the sediment layer at the distance of 180–300 m than closer to the shore. Thus the air temperature has not such a great impact on the sediment temperature.

The annual variation of the sediment temperature indicates the fact that the heat energy is truly naturally loaded to the seabed sediment despite of the usage for heating houses in the residential area.

The estimation of incoming energy compared to known exploited energy is reasonable when the estimated influence area`s radius is 1°m around the heat collection pipe and ΔT = 5 °C. The annual extraction of energy is 560°MWh and the calculated value for annually loaded heat energy is 575°MWh. Despite of the extraction the sediment heat seems to reload well annually.

CONCLUSIONS

Sediment temperature measurements were made once per month for three years period by using distributed temperature sensing (DTS) method. With help of the temperature differences of coldest and warmest month the annual reloading of heat was calculated and verified. The stage of annual charging may vary due to the average air temperature level of the year but still the variation is only 0–2 °C. Regardless of the heat extraction the annual reloading of sediment heat seems to be complete and even in the long run no cooling is expected.

This study shows that nature formulates seasonal storages to the watercourse sediment layers. The renewable heat will stay there waiting for the utilization.

ACKNOWLEDGEMENTS. We thank for Geological Survey of Finland for sharing the data and knowledge of seabed sediment in Vaasa area.

REFERENCES

EnergyVaasa. Available on the Internet (last access on 10.10.2016): < http://energyvaasa.vaasanseutu.fi/en/cases/case-renewable-energy/>

Finnish Meteorological Institute FMI (2017). Available on the Internet (last access on 28.3.2017): < http://ilmatieteenlaitos.fi/tiedote/291348664>. Only in Finnish.

Hiltunen, E., Martinkauppi, J.B., Mäkiranta, A., Rinta-Luoma, J. & Syrjälä, T. 2015. Seasonal temperature variation in heat collection liquid used in renewable, carbon-free heat production from urban and rural water areas. *Agronomy Research* **13**, 485–493.

Martinkauppi, B & Hiltunen, E. 2015. *Water heat battery-preliminary survey* (Vesilämpöakku-esiselvitys). EAKR-project. Final report. 18 p. Only in Finnish.

Martinkauppi, Ilkka. 2013 Private communications.

Mäkiranta, A., Martinkauppi, B. & Hiltunen, E. 2016a. Seasonal temperature variations under lawn and asphalt fields: *Proceedings of the11th Conference on Sustainable Development of Energy, Water and Environment Systems*, SDEWES2016.0281, 1–6.

Mäkiranta, A., Martinkauppi, J.B. & Hiltunen, E. 2016b. Correlation between temperatures of air, heat carrier liquid and seabed sediment in renewable low energy network. *Agronomy Research* **14**, 1191–1199.

Mäkiranta, A., Martinkauppi, B. & Hiltunen, E. 2016c. Design of Asphalt Heat Measurement in Nordic Country. *Proceedings of the11th Conference on Sustainable Development of Energy, Water and Environment Systems*, SDEWES2016.0580, 1–7.

Valpola, Samu. 2007. Unpublished results.

Watzlaf, G. & Ackman, T.E. 2006. Underground Mine Water for Heating and Cooling using Geothermal Heat Pump Systems. *Mine Water and the Environment* **25**, 1–14.

Agronomy Research **15**(S1), 1107–1118, 2017

Mechanical properties of resin reinforced with glass beads

M. Müller

Department of Material Science and Manufacturing Technology, Faculty of Engineering, Czech University of Life Sciences, Kamýcká 129, CZ165 21 Prague, Czech Republic
Correspondence: muller@tf.czu.cz

Abstract. The research was focused on the evaluation of a loading speed and a size of the particle filler in a form of glass beads B159 and B112 on resultant behaviour of a composite material and during its application in a structural adhesive bond. A fall of the tensile strength of the composite material of ca. 60% is obvious from the experiment results when adding both fillers (B159 as well as B112). This composite material showed in the positive way as the adhesive at the adhesive bonds. The experiment results proved the positive influence of adding the particle filler of the spherical shape – glass beads B159 (the fraction size 85.23 ± 31.23 μm) on the adhesive bond strength. The adhesive bond strength was increased up of 14% at the filler glass beads B159. However, adding the filler into the resin proved that this filler eliminated the influence of various loading speeds. Adding the filler into the resin changed a fracture surface. An analysis of a scanning electron microscopy (SEM) proved a good wettability of the filler, the resin and the adhesive bonded material (a structural carbon steel S235J0). A crack propagation was concentrated around the filler B112 (151.59 ± 53.04 μm), namely at higher value of the loading speed, i.e. 10 mm min^{-1}. The crack propagation is a consequence of this. Higher particles show in a negative way namely at an initiation of the fracture surface.

Key words: Loading speed, particle filler, SEM, strength.

INTRODUCTION

The use of the adhesive bonding technology in the construction of transport means and agricultural machines secures a stiffness comparable with mechanical fasteners or spot-welds (Borselino et al., 2009). Further, the adhesive bonding technology increases an energy absorption reducing a noise and vibrations (Borselino et al., 2009).

The adhesive bonding strengthens its position in a number of agricultural machinery and tools. It can be mentioned e.g. the cooperation of the firms Henkel and New Holland in the area of the agriculture (Müller, 2013; Müller & Valášek, 2013). An example of the adhesive bonding application in the agriculture is an adhesive bonding of a breakwater in an agricultural fertilizer sprayer and holders for fixing of plough shares on a plough body (Müller, 2013).

The adhesive bonding technology belongs among significant bonding methods of diverse materials (Šleger & Müller, 2016). A present trend is to add a filler into the adhesive. A reason is mainly a decrease of the adhesive price and an improvement of mechanical properties (Kim & Khamis, 2001; Kawaguchi & Pearson, 2003; Agoudjil et al., 2008; Ramazan et al., 2008; Müller & Valášek, 2012; Müller et al., 2015; Valášek &

Müller, 2015; Šleger & Müller, 2016). Some polymers can be toughened by rigid inorganic fillers (Lee & Yeeb, 2000).

Polymer particle composites are usually applied in a renovation area where they are used namely as cements (Cho et al., 2006; Ruggiero et al., 2015; Valášek, 2015a; Valášek, 2015b; Müller, 2016). An improvement of the adhesive bond properties can be reached at a suitably chosen filler type, its size and a concentration. The properties of the composite mixture are similar as of the adhesive itself. Particle-reinforced polymers are widely used in load-carrying applications (Tjernlund et al., 2006). Fillers of various dimensions are frequently added to make polymers stiffer, cheaper and improve on properties such as heat resistance, dimensional stability, fracture toughness and colour control (Tjernlund et al., 2006; Kawaguchi & Pearson, 2003).

The strength strongly depends on the stress transfer between the particles and the matrix (Shao-Yun et al., 2008). For well-bonded particles, the applied stress can be effectively transferred to the particles from the matrix, this clearly improves the strength (Shao-Yun et al., 2008). However, for poorly bonded microparticles, the strength reductions occur by adding particles (Shao-Yun et al., 2008).

The mechanical properties of polymer particle composites depend strongly on a particle size, a particle–matrix interface adhesion (wettability) and a particle loading (Kawaguchi & Pearson, 2003). A crack propagation along the interface between the filler and the epoxy matrix threatens at the use of the filler (Tjernlund et al., 2006). This propagation largely depends on the size and the shape of the particles.

According to this mechanism, particles in a brittle matrix can resist the crack propagation by making the crack front bow out between particles (Lee & Yeeb, 2000). The amount of the line energy in the bowed crack front reflects the toughness increase due to the existence of particles (Lee & Yeeb, 2000). This mechanism explains the common generalization on the effect of the inherent matrix toughness, i.e. the toughening effect of the inorganic particle incorporation into polymers decreases as the inherent matrix toughness increases (Lee & Yeeb, 2000).

The former research results proved a positive influence of adding particle filler of the spherical shape – glass beads B159 with the fraction size 90 ± 20 μm on the adhesive bond strength (Müller, 2016). The highest increase of the adhesive bond strength was at the adhesive bond with the adhesive in the form of the composite (150 g of filler: 100 g of matrix) (Müller, 2016). Also Sanchez-Soto et al. (2007) came to similar conclusions that adding glass microballs with the dimension to the diameter 120 μm increases tensile properties of resulting particle composites. The filler of composite materials is different Al_2O_3, SiC, glass beads, minerals, various metals, rubber particles. Although the use of particles as fillers in many polymers is widespread, the knowledge about the fracture behaviour of inorganic particle filled composites has developed very slowly (Lee & Yeeb, 2000).

The research subject is the influence of the particle filler (glass beads) on mechanical properties of the composite mixture with the evaluation of the interaction of the matrix and the reinforcement by means of the fracture surface at the same time. The research aim was not to determine the influence of the filler concentration. This had been already done and the pieces of knowledge were used from another study.

The research focused on the evaluation of the influence of the loading speed and the particle size on the resultant behaviour of the composite material and during its application in the area of the structural adhesive bond. The influence of the fracture

surface at various loading speeds on the composite system strength was investigated by means of SEM. The composite system strength is based on the transfer of the stress between the matrix and the filler. Also the adhesive layer between the adhesive and the adhesive bonded material is the essential factor at the adhesive bond (Shao-Yun et al., 2008).

MATERIALS AND METHODS

The subject of performed experiments was the polymer composite whose continuous phase was in a form of the structural two-component adhesive CHS Epoxy 1200 (resin) and a discontinuous phase / reinforcing particles in a form of glass beads B159 (a fraction size 85.23 ± 31.23 μm) and B112 (a fraction size 151.59 ± 53.04 μm) which was applied on the structural carbon steel S235J0. Figs 1 and 2 show a histogram of a frequency of glass beads filler. It is obvious from the results that the highest portion was at the glass beads B112 among 100 to 200 μm and B159 among 60 to 140 μm. The polymer filler was of very different dimensions.

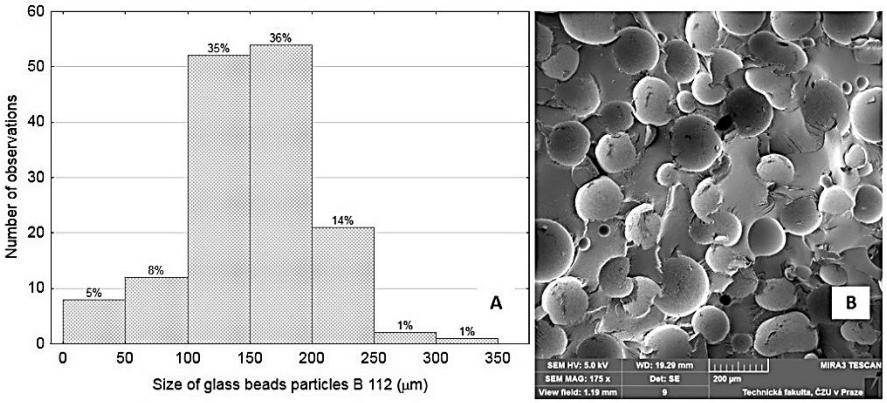

Figure 1. Filler in form of glass beads B112: A) Histogram, B) composite with spherical particles (SEM image, secondary electrons, MAG 175 x).

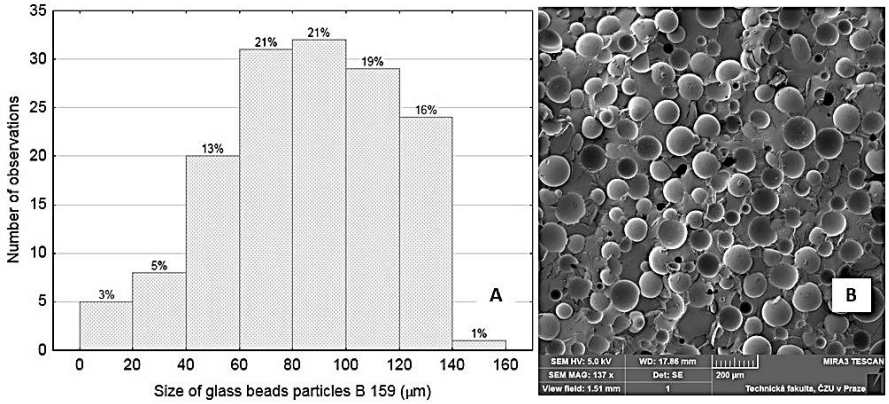

Figure 2. Filler in form of glass beads B159: A) Histogram, B) composite with spherical particles (SEM image, secondary electrons, MAG 137 x).

The filler concentration 40 vol.% was used at the research on the influence of the loading speed on mechanical properties of the composite material. This concentration corresponded to reaching the optimum composite strength (Müller, 2016).

The research focused on the evaluation of the influence of the loading speed and the particle size on resultant behaviour of the composite material and during its application in the area of the structural adhesive bond by means of the static tensile test and the adhesive bond strength.

The test specimens for the tensile properties determination according to the standard CSN EN ISO 527-1 (Plastics – Determination of tensile properties – Part 1: General principles) were prepared according to the standard CSN EN ISO 3167 (Plastics – Multipurpose test specimens, Czech Standard Institution). The tensile strength was the evaluated parameter. The test specimens were cast into the moulds from Lukapren N which corresponded to the requirements of the standard by their shape and dimensions. The universal tensile strength testing machine LABTest 5.50ST (a sensing unit AST type KAF 50 kN, an evaluating software Test&Motion) was used for the determination of the tensile strength. The loading speed of the deformation corresponded to 1, 5 and 10 mm min^{-1}.

The hardness of the tested materials was determined on the base of the standard CSN EN ISO 2039 by means of a ball of a diameter 5 mm on the device Durajet (the Struers company), a loading force corresponded to 961 N.

The adhesive bond strength was analysed owing to a verification of the composite mixture behaviour in the interaction with the adhesive bonded material.

Laboratory tests were performed using the standardized test specimens made according to the standard CSN EN 1465 (dimensions 100 ± 0.25 x 25 ± 0.25 x 1.5 ± 0.1 mm and lapped length of 12.5 ± 0.25 mm) from the structural carbon steel S235J0. The adhesive bonded surface was mechanically treated (grit blasted by Garnet MESH 80, a fraction size 0.1–0.3 mm) and chemically treated (cleaned in the acetone bath). The roughness parameters Ra and Rz were measured on the surface of grit blasted adherents, $Ra = 1.76 \pm 0.16$ μm, $Rz\ 10.92 \pm 0.85$ μm. Roughness parameters were measured with a portable profilometer Mitutoyo Surftest 301. A limit wavelength of the cut-off was set as 0.8 mm. Adhesive bonds were hardened for 72 ± 5 hours with a temperature 22 ± 2 °C.

The universal tensile strength testing machine LABTest 5.50ST (a sensing unit AST type KAF 50 kN, an evaluating software Test&Motion) was used for the determination of the adhesive bond strength. The loading speed of the deformation corresponded to 1, 5 and 10 mm min^{-1}. A fracture surface of the adhesive bonds was evaluated according to the standard ISO 10365.

Fracture surfaces and an adhesive bond cut was examined with SEM (scanning electron microscopy) using a microscope MIRA 3 TESCAN at the accelerating voltage of the pack (HV) 5.0 kV. The samples were dusted with gold by means of the equipment Quorum Q150R ES – Sputtering Deposition Rate using Gold.

Data were also evaluated means of the program STATISTICA (*F-test*). A validity of the zero hypothesis (H_0) shows that there is no statistically significant difference ($p > 0.05$) among tested sets of data. On the contrary, the hypothesis H_1 denies the zero hypothesis and it says that there is a statistically significant difference among tested sets of data or a dependence among variables ($p < 0.05$).

RESULTS AND DISCUSSION

The hardness of the tested materials is following: resin 153.85 ± 4.78, composite B159 256 ± 9.74 and composite B112 275 ± 16.09. Composite mixture was considerably increased with the resin (matrix), of ca. 67 to 79%.

The results of the loading speed influence of the resin and the composite material based on the glass beads on the static tensile strength are visible in Fig. 3. The fall of the tensile strength by adding both fillers glass beads B159 as well as B112 is visible from the experiment results. The tensile strength at the polymer particle composite reinforced with the glass beads B159 was reduced of 61.5% and with B112 of 55.2%.

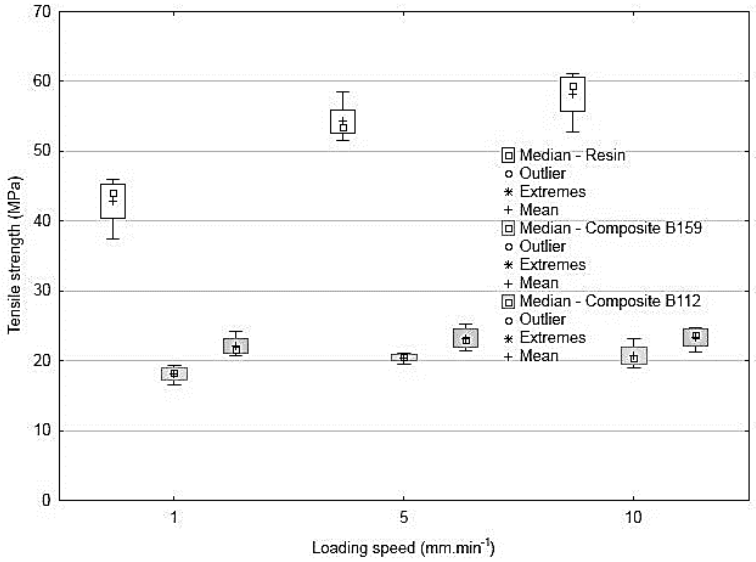

Figure 3. Influence of loading speed on tensile strength of resin and polymeric particle composite.

It is possible to say in terms of the statistical testing of the resin that the loading speeds are statistically non-homogeneous groups ($p = 0.004$), i.e. there is the difference in the resultant tensile strength among single loading speeds 1, 5 and 10 mm min^{-1}. The hypothesis H_0 was not certified in the significance level 0.05. It is obvious from the results that different loading speed influences the tensile strength. The experiment results proved the increase of the tensile strength of the resin due to increasing loading speed of 27 to 3%.

It is possible to say in terms of the statistical testing of the polymer particle composites based on the glass beads B159 and B112 that the loading speeds are statistically homogeneous groups ($p_{B159} = 0.336$, $p_{B112} = 0.489$), i.e. there is no difference in the resultant tensile strength among single loading speeds 1, 5 and 10 mm min^{-1}. The hypothesis H_0 was certified in the significance level 0.05. It is obvious from the results that different loading speed does not influence the tensile strength. The loading speed cannot be regarded as the statistically significant at the application of the tested polymer particle composite.

Other parameters determined from the tensile test (Elongation and Time of destruction) are presented in Table 1. An average elongation at the resin was $6.81 \pm 1.02\%$. The average elongation at the composite B159 and B112 was $1.96 \pm 0.18\%$. The elongation did not significantly change owing to the loading speed. The loading speed considerably influenced the time of the destruction. By adding the filler, the elongation and the loading speed were considerably changed (decreased).

Table 1. Tensile test (CSN EN ISO 527-1) (**Elongation ε, Time of destruction t**)

Abbr.	Properties	Resin			Composite B 159			Composite B 112		
	Loading speed (mm min^{-1})	1	5	10	1	5	10	1	5	10
ε	Mean (%)	5.41	7.19	7.82	1.44	1.79	1.75	1.37	1.47	1.77
	Standard deviation (%)	0.41	0.55	0.51	0.13	0.14	0.16	0.11	0.15	0.11
	Variation coefficient (%)	7.55	7.66	6.55	8.74	7.65	9.23	8.21	9.99	6.11
t	Mean (s)	163	46.7	23.7	59.7	10.7	5.27	36.1	7.09	4.48
	Standard deviation (s)	11.5	2.47	1.78	6.47	0.82	0.49	2.45	0.72	0.5
	Variation coefficient (%)	7.04	5.29	7.49	10.8	7.66	9.2	6.79	10.2	11.22

SEM (scanning electron microscopy) analysis was used for the study of fracture surfaces and cuts through the adhesive bonds. SEM analysis enabled to display a quality of the interaction of the reinforcing phase (glass beads) and the resin. A better understanding of the tested material behaviour was the reason for the research by means of SEM. The fracture surface of the resin and the composite systems after the tensile test are visible in Fig. 4. The interaction between the filler and the resin is good (Fig. 4, A & B). However, a reduction of the wetting was possible to observe in some places, i.e. the interaction between the resin and the glass beads B 159 and B 112 was lower 0.13 ± 0.06 μm (Fig. 4, B).

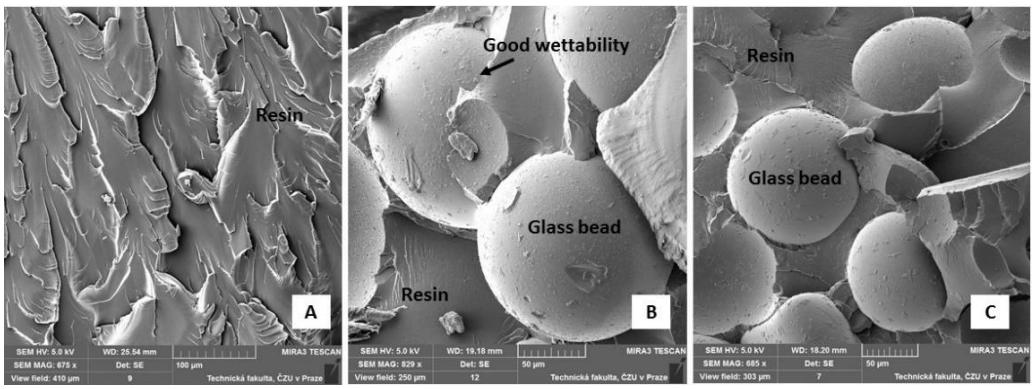

Figure 4. SEM images of fracture surface after tensile test (secondary electrons): A: Resin (MAG 675 x), B: interaction of resin and glass beads B112 (MAG 829 x), C: interaction of resin and glass beads B159 (MAG 829 x)

Results of the influence of the loading speed of the resin and the composite material based on glass beads on the adhesive bond strength are visible in Fig. 5. The fall of the adhesive bond strength of ca. 1.5% by adding the glass beads B112 filler is obvious from the experiment results. The increase of the adhesive bond strength of ca. 14.3% by

adding the glass beads B159 filler is obvious from the experiment results. The adhesive bond strength was increased by adding the spherical filler of smaller dimension.

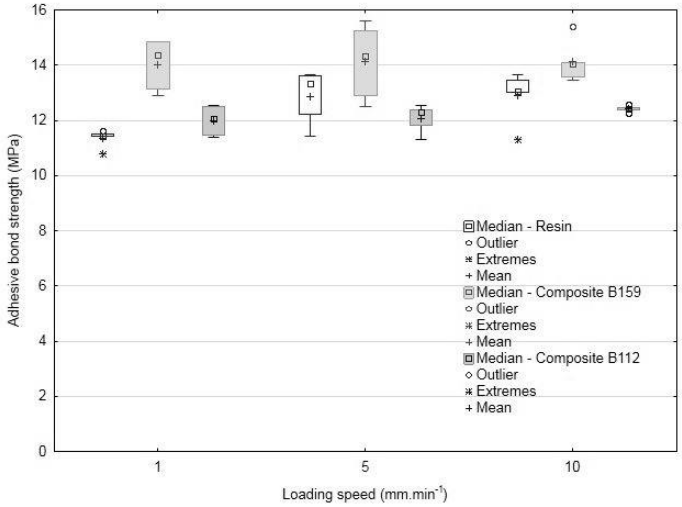

Figure 5. Influence of loading speed on adhesive bond strength of resin and polymer particle composite.

It is possible to say in terms of the statistical testing of the resin that the loading speeds are statistically non-homogeneous groups ($p = 0.015$), i.e. there is the difference in the resultant adhesive bond strength among single loading speeds 1, 5 and 10 mm min^{-1}. The hypothesis H_0 was not certified in the significance level *0.05*. It is obvious from the results that different loading speed influences the adhesive bond strength. The experiment results proved the increase of the adhesive bond strength at the resin owing to the loading speed of ca. 13%. The considerable difference in the adhesive bond strength did not occur at the loading speeds 5 and 10 mm min^{-1}.

It is possible to say in terms of the statistical testing of the polymeric particle composites based on glass beads B 159 and B112 that the loading speeds are statistically homogeneous groups ($p_{B159} = 0.986$, $p_{B112} = 0.290$), i.e. there is no difference in the resultant adhesive bond strength among single loading speeds 1, 5 and 10 mm min^{-1}. The hypothesis H_0 was certified in the significance level *0.05*. It is evident from the results that different loading speed did not influence the strength of the composite adhesive bond. The loading speed cannot be regarded as statistically significant at the application of the tested polymer particle composite.

The layer thickness of the adhesive is essential (Naito et al., 2012). The layer thickness of the adhesive was considerably different depending on the filler type. The highest adhesive bond thickness 291.56 ± 12.29 μm was measured at the adhesive bonds reinforced with glass beads B 112. It was 224.32 ± 12.46 μm at the adhesive bonds reinforced with glass beads B159. The layer thickness was the smallest at the adhesive bonds bonded only with the resin – 162.25 ± 48.56 μm. However, it is evident from the results that the layer of the adhesive bond was uneven, i.e. the variation coefficient was 29.9%. The layer was even at the adhesive bonds reinforced with the filler, i.e. the variation coefficient was 4.2 to 5.6%.

The type of the fracture surface differed for various variants of the experiment. The adhesive bond failure was of the adhesive type, i.e. the adhesive bond failure occurred between the adhesive bonded material (adherent) and the resin. The adhesive bonds reinforced with the glass beads showed the adhesive – cohesive type of the fracture surface. The loading speed did not changed the fracture surface.

Other parameters determined from the adhesive bonds testing are presented in Table 2. The average elongation was 2.46 ± 0.16%. The considerable changes of the elongation owing to the loading speed occurred at the resin and the composite B112. The loading speed significantly influenced the time of the destruction. A considerable change occurred between the speed 1 and 5 mm min^{-1}.

Table 2. Adhesive bond strength (CSN EN 1465) (Elongation ε, Time of destruction t)

Abbr.	Properties	Resin			Composite B 159			Composite B 112		
	Loading speed (mm min^{-1})	1	5	10	1	5	10	1	5	10
ε	Mean (%)	2.20	2.39	2.48	2.50	2.49	2.54	2.24	2.52	2.77
	Standard deviation (%)	0.27	0.25	0.11	0.18	0.30	0.17	0.18	0.21	0.20
	Variation coefficient (%)	12.29	10.4	4.44	7.36	12.1	6.88	8.13	8.42	7.07
t	Mean (s)	62.06	14.3	6.84	82.56	14.5	7.83	63.55	14.2	8.45
	Standard deviation (s)	3.84	1.08	0.94	8.96	2.02	0.22	6.31	2.02	0.30
	Variation coefficient (%)	6.18	7.57	13.8	10.85	13.9	2.81	9.94	14.22	3.57

SEM analysis proved a good wettability of the adhesive and the adhesive bonded material (carbon steel S235J0) (Fig. 6 A, B & 7, A).

This conclusion is essential because the wettability of the adhesive bonded surfaces is crucial for good adhesive strength (Rudawska, 2012; Müller & Valášek, 2013; Rudawska et al., 2016; Šleger & Müller, 2016). The fracture surface of the adhesive bond is visible in Fig. 6, C. The fracture surface was concentrated around the filler B 112, namely at higher values of the loading speed, i.e. 10 mm min^{-1} (Fig. 7, B). A spreading of the fracture surface is a consequence of this. Higher particles show themselves in a negative way.

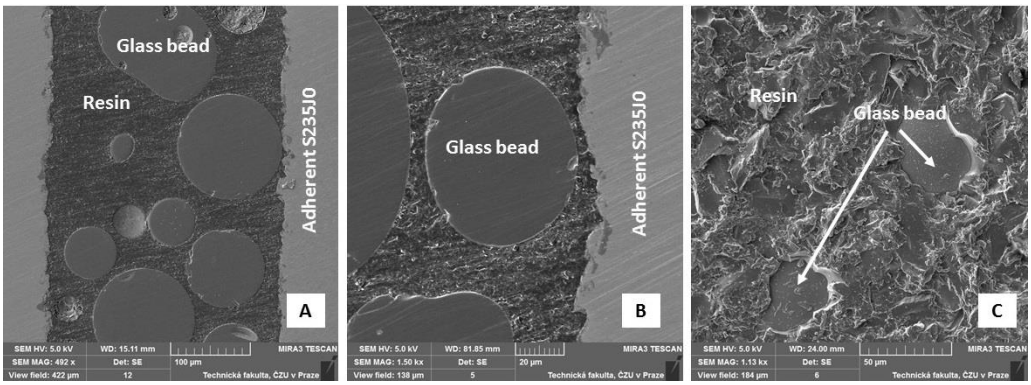

Figure 6. SEM images of cut through adhesive bond reinforced with glass beads (secondary electrons): A: cut through adhesive bond of resin reinforced with glass beads B 112 (MAG 492 x); B: good wettability of glass beads B 112 filler with resin (MAG 1.50 kx); C: adhesive – cohesive type of fracture surface of adhesive bond (MAG 1.13 kx).

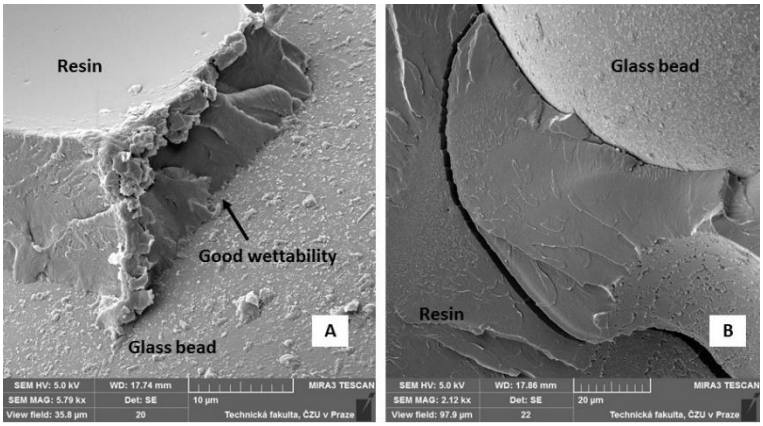

Figure 7. SEM images of fracture surface after shear tensile strength test of adhesive bonds (secondary electrons): A: good interaction of resin and glass beads B112, loading speed 1 mm min^{-1} (MAG 579 kx); B: fracture surface within adhesive layer stopped by glass beads B112 filler, loading speed 10 mm min^{-1} (MAG 212 kx).

The tensile strength is decreased at the epoxies which filled with glass beads when increasing the loading speed of the composite material (Gurusideswar & Velmurugan, 2014). The presence of the filler considerably influences the mechanical properties. The experiment results proved significant fall of the tensile strength by adding the filler. The fall of the tensile strength was of ca. 62% at the filler B159 and ca. 55% at the filler B112 (Valášek, 2011). Similar results were gained also in other researches which state to 80% fall of the tensile strength at using the glass beads B159 (Valášek, 2011). The fall of the composite strength with increasing mass portion is attributed to an agglomeration and poor interfacial bonds between the matrix and the filler Gurusideswar & Velmurugan, 2014). A visual check of tested samples shows significant changes in the fracture surface with increased loading speed Gurusideswar & Velmurugan, 2014). It is obvious from the results that the loading speed of the adhesive bonds has a positive influence on the strength results of tested adhesive bonds (Müller et al., 2016).

The increase of the adhesive bond strength by adding the glass beads B 159 filler of ca. 14.3% is obvious from the experiment results. The adhesive bond strength was increased by adding the spherical filler of smaller dimensions. The glass beads B 112 filler which is of greater fraction did not caused the increase of the adhesive bond strength values. Mild fall of the adhesive bond strength was proved also at Fe based particles (Valášek et al., 2016). Similar increase of the adhesive bond strength of ca. 14% occurred also in other studies (Müller, 2016).

The assumption that the stress in the polymer particle composite filled with the glass beads is concentrated around the filler of higher dimensions was certified (Lee & Yeeb, 2000). Spreading of the fracture surface is the consequence of this. This state was visible in SEM image – see Fig. 7, B.

The cohesive strength can be related to the strain energy release rate of a material through a decohesion process occurring at the crack tip (Kawaguchi & Pearson, 2003). Yield behaviour is also related to the strain energy release rate through plastic zone formation at the crack tip (Kawaguchi & Pearson, 2003).

Even thickness of the adhesive layer is essential (Naito et al., 2012). The experiment results certified that the adhesive bond without the filler is of huge uneven thickness of the adhesive layer, the difference is up to ca. 30% (Lee & Yeeb, 2000). On the contrary when using the filler the dispersion of the layer thickness was reduced to max. 5.6%.

CONCLUSIONS

The experiment subject is the behaviour of the particle filler (glass beads) in relation to mechanical properties of the composite mixture at simultaneous evaluation of the interaction of the matrix and the reinforcement by means of the fracture surface. The experiment focused on the evaluation of the influence of the loading speed and the particle size on resultant behaviour of the composite material and at its application in the structural adhesive bond. Following conclusions can be deduced from the experiment results:

- A fall of the tensile strength by adding the filler – glass beads B159 and B112 is obvious from the experiment results. The tensile strength of the polymeric particle composite reinforced with the glass beads B159 filler was reduced of 61.5% and with the glass beads B112 of 55.2%. It is obvious from the results that different loading speed influenced the tensile strength of the resin. It is also obvious that different loading speed does not influence the tensile strength of the resin filled with the glass bead microparticles. The loading speed cannot be regarded as the statistically significant at the application of tested polymer particle composite. The loading speed considerably influenced the time of the destruction and the elongation. By adding the filler the significant change (fall) of the elongation and the loading speed occurred.
- The experiment results proved a positive influence of adding the particle filler of the spherical shape – glass beads B159 on the adhesive bond strength. The adhesive bond strength was increased up of 14%. The glass beads B112 filler which is of greater fraction did not influence the adhesive bond strength (neither an increase nor a fall). The adhesive bond strength was similar as at the resin. It is obvious from the results that different loading speed influences the adhesive bond strength. The experiment results proved the increase of the adhesive bond strength at the resin owing to the loading speed of ca. 13%. The adhesive bond strength was not so different at the loading speed 5 and 10 mm min^{-1}. However, adding the filler into the resin proved that this filler eliminated the influence of different loading speed. The loading speed cannot be regarded as the statistically significant at the application of tested polymer particle composite. The loading speed considerably influenced the time of the destruction and the elongation, namely at the resin and the composite B112. The loading speed did not change the fracture surface. Adding the filler into the resin changed the fracture surface.
- SEM analysis proved good wettability of the filler and the adhesive bonded material (adherent – carbon steel S235J0) with the resin. The fracture surface spreading was concentrated around the filler B112, namely at higher values of the loading speed, i.e. 10 mm min^{-1}. Greater particles show themselves in a negative way, namely at the initiation of the cracks.

ACKNOWLEDGEMENTS. Supported by Internal grant agency of Faculty of Engineering, Czech University of Life Sciences in Prague.

REFERENCES

Agoudjil, B., Ibos, L., Majesté, J.C., Candau, Y. & Mamunya, Ye P. 2008. Correlation between transport properties of Ethylene Vinyl Acetate/glass, silver-coated glass spheres composites. *Composites Part A: Applied Science and Manufacturing* **39**, 342–35.

Borsellino, C., Bell, G.Di. & Ruisi, V.F. 2009, Adhesive joining of aluminum AA6082: The effects of resin and surface treatment. *International Journal of Adhesion and Adhesives* **29**, 36–44.

Cho, J., Joshi, M.S. & Sun, C.T. 2006. Effect of inclusion size on mechanical properties of polymeric composites with micro and nano particles. *Composites Science and Technology* **66**, 1941–1952.

Gurusideswar, S. & Velmurugan, R. 2014. Strain rate sensitivity of glass/epoxy composites with nanofillers. *Materials and Design* **60**, 468–478.

Kawaguchi, T. & Pearson, R.A. 2003. The effect of particle–matrix adhesion on the mechanical behavior of glass filled epoxies: Part 1. A study on yield behavior and cohesive strength. *Polymer* **44**, 4229–4238.

Kim, H. & Khamis, M.A. 2001. Fracture and impact behaviours of hollow micro-sphere/epoxy resin composites. *Composites Part A: Applied Science and Manufacturing* **32**, 1311–1317.

Lee, J. & Yeeb, A.F. 2000. Role of inherent matrix toughness on fracture of glass bead filled epoxies. *Polymer* **41**, 8375–8385.

Müller, M. & Valášek, P. 2012. Abrasive wear effect on Polyethylene, Polyamide 6 and polymeric particle composites. *Manufacturing Technology* **12**, 55–59.

Müller, M. 2013, Research of liquid contaminants influence on adhesive bond strength applied in agricultural machine construction. *Agronomy Research* **11**, 147–154.

Müller, M. & Valášek, P. 2013. Assessment of bonding quality for several commercially available adhesives. *Agronomy Research* **11**, 155–162.

Müller, M., Cidlina, J., Dědičová, K. & Krofová, A. 2015. Mechanical properties of polymeric composite based on aluminium microparticles. *Manufacturing Technology* **15**(4), 624–628.

Müller, M. 2016. Effect of saline environment on mechanical properties of structural adhesive bonds. *Acta universitatis Agriculturae et Silviculturae mendelianae Brunensis* **64**, 1609–1617.

Müller, M., Valášek, P., Ruggiero, A. & D´amato, R. 2016. Research on influence of loading speed of structural two-component epoxy adhesives on adhesive bond strength. *International Conference on Manufacturing Engineering and Materials. Procedia Engineering*. Nový Smokovec, Slovak Republic, pp. 340–345.

Naito, K., Onta, M. & Kogo, Y. 2012. The effect of adhesive thickness on tensile and shear strength of polyimide adhesive. *International Journal of Adhesion and Adhesives* **36**, 77–85.

Ramazan, K., Mehmet, S. & Bekir, Y. 2008. Influence of adhesive thickness and filler content on the mechanical performance of aluminium single-lap joints bonded with aluminium powder filled epoxy adhesive. *Journal of materials processing technology* **205**. 183–189.

Rudawska, A. 2012. Surface Free Energy and 7075 Aluminium Bonded Joint Strength Following Degreasing Only and Without Any Prior Treatment. *Journal Adhesion Science and Technology* **26**, 1233–1247.

Rudawska, A., Danczak, I., Müller, M. & Valášek, P. 2016. The effect of sandblasting on surface properties for adhesion. *International Journal of Adhesion and Adhesives* **70**, 176–190.

Ruggiero, A., Valášek, P. & Merola, M. 2015. Friction and wear behaviors of Al/Epoxy Composites during Reciprocating Sliding tests. *Manufacturing technology* **15**, 684–689.

Sanchez-Soto, M., Pagés, P., Lacorte, T., Briceno, K. & Carrasco, F. 2007. Curing FTIR study and mechanical characterization of glass bead filled trifunctional epoxy composites. *Composites Science and Technology* **67**, 1974–1985.

Shao-Yun, F., Xi-Qiao, F., Bemd, L., Emd, L. & Yiu-Wing, M. 2008. Effects of particle size, particle/matrix interface adhesion and particle loading on mechanical properties of particulate-polymer composites. *Composites: Part B* **39**, 933–961.

Šleger, V. & Müller, M. 2016, Low-Cyclic Fatigue of Adhesive Bonds. *Manufacturing Technology* **16**, 1151–1157.

Tjernlund, J.A., Gamstedt, E.K. & Gudmundson, P. 2006. Length-scale effects on damage development in tensile loading of glass-sphere filled epoxy. *International Journal of Solids and Structures* **43**, 7337–7357.

Valášek. P. 2011. Strength characteristics of polymer particle composites with filler on the basis of waste from mechanical surface treatment. *International Scientific Conference Engineering for Rural Development*. Jelgava, Latvia, pp. 434–439.

Valášek, P. & Müller, M. 2015. Abrasive wear in three-phase waste based polymeric particle composites. *Tehnicki Vjesnik-Technical Gazette* **12**, 257–262.

Valášek, P. 2015a. Polymer microparticles composites with waste EPDM rubber powder. *Agronomy Research* **13**, 723–731.

Valášek, P. 2015b. Influence of surface treatment of steel adherends on shear strength of filled resins. *Manufacturing Technology* **15**, 468–474.

Valášek, P. Ruggiero, A., D´amato, R. & Machado, J. 2016. Two-body abrasion of Fe-based particle epoxy composites – experimental approach. *6th International Conference on Trends in Agricultural Engineering*. Prague, Czech Republic. pp. 673–678.

Agronomy Research **15**(S1), 1119–1126, 2017

The use of unsteady method for determination of thermal conductivity of porous construction materials in real conditions

P. Neuberger[1*] and P. Kic[2]

[1]Czech University of Life Sciences Prague, Faculty of Engineering, Department of Mechanical Engineering, Kamýcká 129, CZ165 21 Prague, Czech Republic
[2]Czech University of Life Sciences Prague, Faculty of Engineering, Department of Technological Equipment of Buildings, Kamýcká 129, CZ165 21 Prague, Czech Republic
[*]Correspondence: neuberger@tf.czu.cz

Abstract. The possibility to determine the thermal conductivity of construction materials outside the laboratory conditions is useful for professional practice mainly for control and inspection activities on real existing buildings. The requirement to determine the thermal conductivity can be useful above all for different thermal insulation materials but for other materials as well, even for compact soils or rocks. This paper describes methods and instrument which can be used for these measurements, as well as the results of measurement of porous building materials. Measurements presented in this paper were carried out by the needle and surface sensor. Four different materials were selected for verification of technical parameters of Isomet 2104. Besides the thermal conductivity there were determined also thermal diffusivity and volume-specific heat capacity of materials. The carried out measurements confirmed the applicability of this device for practical measurements of thermal conductivity in real conditions. For porous materials, there were determined significant differences between the data presented by the manufacturer or in the literature and measured values, in some cases. Differences between the measured values of thermal diffusivity and volume-specific heat capacity of porous materials were always statistically significant. Authors tested different materials including thermal insulation based on agricultural products.

Key words: dynamic method, measurement, sensor, thermal properties.

INTRODUCTION

Thermal conductivity is an important parameter of thermal-technical properties of materials. It is used mainly in civil engineering. Its real value is a function several internal and external variables (density, moisture, temperature, porosity, chemical and mineralogical composition and phase composition, crystalline modification etc.). The attention is paid to the problems of insulation properties in different publications, e.g. (Muizniece et al., 2015; Kocova & Kic, 2016; Pleiksnis et al., 2016; Týbl & Kic, 2016; Valasek et al., 2016).

There are used steady and unsteady methods to determine the thermal conductivity of the material used. Stationary methods are characterized by steady state temperature of measured material sample. These methods determine steady heat flux through the

material from the surface of a higher temperature to the surface of a lower temperature. Stationary methods are based on the use of sensors with special shape, e.g. plate method, cylinder method or ball method. These methods are suitable for laboratory conditions.

Unsteady methods are characterized by monitoring of dynamic development of temperatures. They do not require steady thermal state. They are based on monitoring of thermal wave transmission through the measured sample. Unsteady methods include a method of unsteady heat flux and heat pulse method (Hot Wire Method), laser flash method and other methods based on monitoring of heat pulse. Heat energy may be supplied in these methods either at the beginning of the measurement (impulse heat source) or continuously during the whole measurement (continuous heat source), or periodically by constant power (periodic heat source). The methods are applied mainly in laboratory instruments.

The construction of modern laboratory techniques emphasizes rapid measurement, ease manipulation and durability. Therefore some new methods based on dynamic unsteady method are useful and more popular. Examples might be the instrument Shotherm QTM (Showa Denko, Japan) THASYS, THESYS, MTN01 (HUKSEFLUX Thermal Sensors, Netherlands) and Isomet 2114 (Applied Precision, Ltd., Bratislava, Slovakia).

The instrument Isomet 2114 has suitable construction and properties which enable its use also in real buildings (control and revision measurements). Determination of thermal conductivity can be important even for compact soils and rocks. Determination of thermal conductivity of plasters in reconstruction of historical buildings is described in some publications, e.g. Cerny, R. et al. (2006).

The aim measurements described in this article is to verify the use of a dynamic method, applied in design and construction of the instrument Isomet 2104, for the measurement of thermal conductivity of porous thermal insulating materials (polystyrene, Thermo HANF® Premium Plus, ...). Results obtained from the measurements with the needle and surface sensors were compared.

Porous materials do not transfer the heat only by conduction. A significant part of the heat radiation is transmitted between the individual particles. Non-porous materials (e.g. metals) transfer the heat only by conduction. Problems of heat transfer within the porous heat insulating materials are published e.g. in Koru (2016) and Antonyová et al. (2016).

The instrument Isomet 2104 was also used according to the manufacturer's recommendation for determination of thermal diffusivity and volumetric heat capacity, also termed volume-specific heat capacity. Results of measurements of thermal conductivity of polystyrene published e.g. Tsutsumi (1997). The aim of this research was to compare the results of these measurements with data reported in the literature and confirm the applicability of this measuring instrument for this purpose.

MATERIALS AND METHODS

Isomet 2104 (Applied Precision, Ltd., Bratislava, Slovakia) is a portable instrument controlled by microprocessor, to which the manufacturer supplies exchangeable needle and surface sensors of various ranges. The calibration constants are stored in the sensors memory.

This instrument measures the thermal conductivity of compact and loose materials in a range of 0.015–2 W m^{-1} K^{-1}. For the thermal conductivity in the range 0.015–0.050 W m^{-1} K^{-1} is permissible measurement error 5% of reading + 0.003 W m^{-1} K^{-1}. There is also measured the temperature (measurement error of ± 1 °C) and specific heat capacity of materials (the measurement error of 15% of the value of + 1,000 J m^{-3} K^{-1}). The measured values can be stored in the internal memory of the instrument. The content of memory is accessible via display. Data can be transferred via RS-232 interface to a PC. The instrument can be powered from AC or battery.

To determine the thermal conductivity of the material is used unsteady method. This compared to stationary methods significantly reduces the time of measurement. The device analyses the time dependence of thermal responses to impulses of heat flux supplied to the material. The heat flux creates scattered electric output from the resistor located in the sensor. The sensor has a thermally conductive connection with the analysed material. Temperature resistance is sensed by a semiconductor sensor.

Temperature variation as a function of time is tested in discrete points. The obtained points are interleaved by regression polynomials using the method 'least squares'. The coefficients of the regression polynomials are used to calculate the thermo-physical parameters using analytical formulas.

Air temperatures and relative humidity were measured by sensor FHA 646–21 including temperature sensor NTC type N with operative range from –30 to +100 °C with accuracy ± 0.1 °C, and air humidity by capacitive sensor with operative range from 5 to 98% with accuracy ± 2% connected to the measuring instrument ALMEMO 2590-9 (Ahlborn GmbH, Germany).

There was used for the indirect measurement of material moisture the capacitive sensor FH A696–MF with operative range of mineral construction materials from 0 to 20% with accuracy 0.1%. The sensor was connected to the data logger ALMEMO 2690-8 (Ahlborn GmbH, Germany).

Measurements presented in this paper were carried out by needle and surface sensors. Four different materials were selected for verification of technical parameters of Isomet 2104.

The first material is expanded polystyrene foam (density 15 kg m^{-3}) removed from an old building during the demolition. It is an inexpensive lightweight material of white colour used in constructions for decades because of its thermal insulating properties. There is a formula according to the CSN EN 13163+A for determination of thermal conductivity λ based on the density of this material presented in the Eq. (1).

$$\lambda = 0.02714 + 5.1743 \cdot 10^{-5} \cdot \rho + \frac{0.173606}{\rho} \quad (1)$$

where: λ – thermal conductivity, W m^{-1} K^{-1}; ρ – material density, kg m^{-3}.

Hejhálek (2012) gives the Eq. (2) describing the dependence of a thermal conductivity on temperature for expanded polystyrene (density of 15 kg m^{-3}).

$$\lambda = 0.0354 + 2.00 \cdot 10^{-4} \cdot t + 4.77 \cdot 10^{-7} \cdot t^2 \quad (2)$$

where: λ – thermal conductivity, W m^{-1} K^{-1}; t – temperature of material, °C.

The second material is extruded polystyrene foam of blue colour, manufactured by the Dow France S.A.S. (France) under the trademark AGMA XL-X. The product is designed for heat insulation of agricultural buildings, especially for ceilings and

sloping side walls. The material has a homogeneous cellular structure preventing water absorption; it is a barrier to water vapour. Manufacturer declares possibility to use the low pressure water for washing and possibility to use disinfectants.

The third material is Thermo HANF® Premium Plus, which is a natural insulation material manufactured from hemp by company Thermo Natur GmbH & Co. KG (Nördlingen, Germany). As a binder of hemp particles is used a corn-starch. This material can be used as good quality insulation.

Eight to ten measurements were carried out for each experimental material. Measurements were carried out under laboratory conditions at 20–26 °C. Measurements simulating operating non-laboratory conditions were carried out in non-heated hall at 14–15 °C. If the dimensions allow, the sensor was placed at various locations of material sample. In case of material Thermo HANF® Premium Plus were available two samples.

The fourth material is a paper with a low volume of voids.

RESULTS AND DISCUSSION

The sample size and density of materials are given in Table 1.

Table 1. Dimension and density of materials according to the catalogue values given by producers and measured values

Material	Dimensions of material samples			Density of material, kg m^{-3}	
	Height, m	Width, m	Length, m	Catalogue	Measured
Expanded polystyrene	0.060	0.367	0.497	10–60	15
AGMATE XL-X	0.047	0.147	0.148	38	34.6
TERMO HANF Premium Plus	0.080	0.110	0.110	30–42	39.9
Paper	0.296	0.210	0.040	700–1,300	771

The Table 2 shows the values of thermal conductivity λ_m of polystyrene calculated according to the Eq. 1 (column A), thermal diffusivity a, volume-specific heat capacity c, measured by the needle probe (column B) and by the surface probe (column C). The Table 2 also presents material temperature t_m and moisture w_m and the temperature t_e and relative humidity φ_e of the ambient air determined together with measurement of thermal conductivity. The table also contains statistical indicators of measured values. The data are the mean values ± SD. Different letters (a, b, c) in the superscript are the sign of high significant differences *(ANOVA; Tukey HSD Test*; $p \leq 0.05$*).*

Table 2. Expanded polystyrene (density of material 15 kg m^{-3})

Parameter	A	B	C
$\lambda_m \pm SD$, W m^{-1} K^{-1}	0.039^{b}	0.0279 ± 0.00035^{a}	0.0402 ± 0.00051^{b}
$c \pm SD$, J m^{-3} K^{-1}	$1.905\ 10^{4\,c}$	$1.40\ 10^{6} \pm 0.0^{a}$	$6.63\ 10^{4} \pm 0.37\ 10^{4\,b}$
$a \pm SD$, m^2 s^{-1}	$2.05\ 10^{-6\,c}$	$2.00\ 10^{-8} \pm 6.62^{-24\,a}$	$6.08\ 10^{-7} \pm 0.32^{-7\,b}$
$t_m \pm SD$, °C	20.00 ± 3.23^{a}	21.93 ± 3.74^{a}	23.76 ± 0.84^{a}
$w_m \pm SD$, %	---	2.71 ± 0.25^{a}	2.71 ± 0.25^{a}
$t_e \pm SD$, °C	---	21.44 ± 3.67^{a}	22.13 ± 1.14^{a}
$\varphi_e \pm SD$, %	---	39.31 ± 2.41^{a}	28.40 ± 1.74^{b}

Fig. 1 shows values of thermal conductivity calculated according to the Eq. 2 (data A), measured using a needle probe (data B) and by the surface probe (C data).

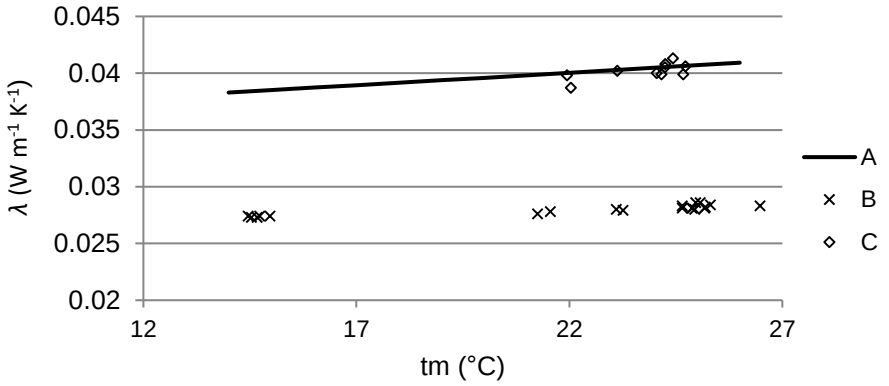

Figure 1. Dependence of thermal conductivity λ_m of polystyrene on the material temperature t_e.

Table 3 presents values of thermal conductivity λ_m of material AGMATE XL-X declared by the manufacturer (column A), thermal diffusivity *a*, volume-specific heat capacity *c*, measured using a needle probe (column B) and by the surface probe (column C). The Table 3 also presents material temperature t_m and moisture w_m and the temperature t_e and relative humidity φ_e of the ambient air determined together with measurement of thermal conductivity. The table also contains statistical indicators of measured values. The data are the mean values ± SD. Different letters (a, b, c) in the superscript are the sign of high significant differences *(ANOVA; Tukey HSD Test; $p \leq 0.05$).*

Table 3. AGMATE XL-X (density of material 34.6 kg m^{-3})

Parameter	A	B	C
$\lambda_m \pm SD$, W m^{-1} K^{-1}	0.029 [a, b]	0.0274 ± 0.00026 [a]	0.0365 ± 0.0005 [b]
$c \pm SD$, J m^{-3} K^{-1}	7.13 10^4 [c]	1.40 10^6 ± 0.0 [a]	9.54 10^4 ± 0.41 10^4 [b]
$a \pm SD$, m^2 s^{-1}	4.07 10^{-7} [c]	1.97 10^{-8} ± 4.08^{-10} [a]	3.83 10^{-7} ± 1.22^{-8} [b]
$t_m \pm SD$, °C	---	20.63 ± 4.86 [a]	23.55 ± 1.14 [a]
$w_m \pm SD$, %	---	undetectable	undetectable
$t_e \pm SD$, °C	---	20.46 ± 5.16 [a]	20.70 ± 2.84 [a]
$\varphi_e \pm SD$, %	---	36.37 ± 42.91 [a]	27.70 ± 2.14 [b]

Table 4 presents values of thermal conductivity λ_m of material Thermo HANF® Premium Plus declared by the manufacturer (column A), thermal diffusivity *a*, volume-specific heat capacity *c*, measured using a needle probe (column B1 and B2). Columns B1 and B2 are values of two different samples. Surface probe with its weight caused a deformation of the material; therefore the measurement was not carried out. The Table 4 also presents material temperature t_m and moisture w_m and the temperature t_e and relative humidity φ_e of the ambient air determined together with measurement of thermal conductivity. The table also contains statistical indicators of measured values. The data

are the mean values ± SD. Different letters (a, b) in the superscript are the sign of high significant differences *(ANOVA; Tukey HSD Test; $p \leq 0.05$).*

Table 4. Thermo HANF® Premium Plus (density of material 39.9 kg m^{-3})

Parameter	A	B1	B2
$\lambda_m \pm SD$, W m^{-1} K^{-1}	0.040 [a]	0.041 ± 0.001 [a]	0.041 ± 0.001 [a]
$c \pm SD$, J m^{-3} K^{-1}	6.4 10^4 [b]	1.4 10^6 ± 0.0 [a]	1.4 10^6 ± 0.0 [a]
$a \pm SD$, m^2 s^{-1}	6.25 10^{-7} [b]	3.0 10^{-8} ± 0.0 [a]	2.98 10^{-8} ± 4.33^{-10} [a]
$t_m \pm SD$, °C	---	20.63 ± 4.86 [a]	23.55 ± 1.14 [a]
$w_m \pm SD$, %	---	2.12 ± 0.268 [a]	2.22 ± 0.308 [a]
$t_e \pm SD$, °C	---	21.6 ± 4.85 [a]	21.7 ± 5.24 [a]
$\varphi_e \pm SD$, %	---	31.6 ± 0.18 [a]	31.6 ± 0.23 [a]

Table 5 shows values of thermal conductivity λ_m, thermal diffusivity a, volume-specific heat capacity c of the paper material with a density of 771 kg m^{-3} according to Ražnjević (1984) (column A) and the values measured using the surface probe (column B). There are presented in the Table 5 also material temperature t_m and moisture w_m, and the temperature t_e and relative humidity φ_e of the ambient air determined in the measurement of thermal conductivity. The tables also contain statistical indicators of measured values. The data are the mean values ± SD. Different letters (a, b) in the superscript are the sign of high significant differences *(ANOVA; Tukey HSD Test; $p \leq 0.05$).*

Table 5. Paper (density of material 771 kg m^{-3})

Parameter	A	B
$\lambda_m \pm SD$, W m^{-1} K^{-1}	0.151 [a]	0.160 ± 0.0013 [b]
$c \pm SD$, J m^{-3} K^{-1}	1.03 10^6 [a]	7.4 10^5 ± 0.09 10^5 [b]
$a \pm SD$, m^2 s^{-1}	1.46 10^{-7} [a]	2.15 10^{-7} ± 0.01 10^{-7} [b]
$t_m \pm SD$, °C	---	24.27 ± 1.27
$w_m \pm SD$, %	---	9.53 ± 0.23
$t_e \pm SD$, °C	---	23.8 ± 1.55
$\varphi_e \pm SD$, %	---	31.2 ± 1.41

By measurement of thermal conductivity λ_m of polystyrene were confirmed statistically non-significant differences between the values calculated according to the Eq. 1 and the values measured by surface probe. The values measured by needle probe are statistically different by from the values calculated according to the Eq. 1. Results of the measurement of volume-specific heat capacity c and thermal diffusivity a, determined by the needle and surface probes are different from each other, as well as they are different from the results presented in the literature, e.g. Yucel (2013). Differences of measurements of conditions were non-statistically significant; there was different only the relative humidity of air (Table 2).

The values of thermal conductivity λ_m obtained by measurement using surface probe are statistically consistent with the values calculated according to the Eq. 2 (see Fig. 1). The values of thermal conductivity λ_m measured by needle probe are statistically different by from the values calculated according to the Eq. 2. However, the growth of thermal conductivity λ_m of the material with increasing temperature t_m confirmed both

measurements (see Fig. 1). The growth of thermal conductivity with increased temperature of a material corresponds with the trends reported in the literature, e.g. EPS CR Association or TZBinfo.

The values of thermal conductivity λ_m of material AGMATE XL-X obtained by measurement using needle probe are statistically consistent with the values declared by the producer. The values of thermal conductivity λ_m measured by the surface probe are statistically different from the value indicated by manufacturer.

Results of the measurement of volume-specific heat capacity *c* and thermal diffusivity *a*, determined by the needle and surface probes are different from each other, as well as they are different from the values presented by the producer. Operating conditions of the measurements were statistically consistent (Table 3). The minimal growth of thermal conductivity with temperature in the case of the material AGMATE XL-X confirms resistance of extruded polystyrene to the temperature fluctuations.

The values of thermal conductivity λ_m of both samples B1 and B2 of material Thermo HANF® Premium Plus obtained by measurement using the needle probe are statistically consistent with the values declared by the producer. The surface probe cannot be used for this material because it causes deformation of material samples. Results of the measurement of volume-specific heat capacity *c* and thermal diffusivity *a*, determined by the needle and surface probes are different are different from the values presented by the producer. Operating conditions of the measurements were statistically consistent (Table 4).

Due to unsatisfactory results in the detection of volume-specific heat capacity *c* and thermal diffusivity *a* (of previous porous materials) determined by the instrument Isomet 2104, there were carried out the control measurements of materials with a low volume of voids. The suitable material is a paper with density 771 kg m^{-3}.

The statistically significant consistence of thermal conductivity λ_m of paper measured by the surface probe with the values presented by Ražnjević (1984) was not confirmed. Results of the measurement of the volume-specific heat capacity *c* and thermal diffusivity *a* also cannot be considered as statistically consistent with the literature data. However, it can be stated that from all measured values *c* and *a* presented in Tables 2–5, the determined values of paper are approaching the values reported in the literature.

CONCLUSIONS

The measurement confirmed the suitability of the tested instrument Isomet 2104 based on the non-stationary method of measurement for the rapid determination of thermal conductivity λ_m of porous materials, but there were also found statistical differences between the measured values and values reported in the literature or declared by the manufacturers.

The measurements did not confirmed the suitability of the instrument Isomet 2104 to measure the volume-specific heat capacity *c* and thermal diffusivity *a*. The results of measurement are not statistically consistent with the values presented in the literature or declared by the manufacturer of tested materials.

There is not confirmed the consistence of results obtained by the measurements with needle and surface probes. The suitability of the instrument Isomet 2104 for the measurement of the volume-specific heat capacity *c* and thermal diffusivity *a* of homogeneous materials should be tested in the future.

The instrument is able to register the changes of thermal conductivity with temperature changes of materials. This feature can be suitably used in the preparation of laboratory exercises for university students of engineering study.

Portability and short duration of the tests make it ideal for the use outside the laboratory. It will be useful in real conditions for inspection and audit activities on already completed buildings.

REFERENCES

Antonyová, A., Antony, P. & Korjenic, A. 2016. Laboratory measurement of thermal distribution throughout the insulation materials using the Peltier module while managing elimination of external influences. *Energy and Buildings* **128**, 336–348.

CSN EN 13163+A Thermal insulation products for buildings – Factory made expanded polystyrene (EPS) products – Specification. 2016.

Černý, R., Kunca, A., Tydlitát, V., Drchalová, J. & Rovnaníková, P. 2006. Effect of pozzolanic admixtures on mechanical, thermal and hygric properties of lime plasters. *Constructon and Building Materials* **20**, 849–857.

EPS CR Association. http://stavba.tzb-info.cz/tepelne-izolace/8482-vlastnosti-expandovaneho-penoveho-polystyrenu-eps. Accessed 13.4.2012.

Hejhálek, J. 2012 Součinitel tepelné vodivosti – praxe a teorie. *Stavebnictví a interiér* **12**, www.stavebnictvi3000.cz/c4059. Accessed 7.1.2012 (in Czech).

Kocova, D. & Kic, P. 2016. Technical and economic aspects of thermal insulation of buildings. In: *15th International Scientific Conference Engineering for Rural Development*. Latvia University of Agriculture, Jelgava, 50–55.

Koru, M. 2016. Determination of Thermal Conductivity of Closed-Cell Insulation Materials That Depend on Temperature and Density. *Arabian Journal for Science and Engineering* **41**, 4337–4346.

Muizniece, I, Vilcane, L. & Blumberga, D. 2015. Laboratory research of granulated heat insulation material from coniferous forestry residue. *Agronomy Research* **13**, 690–699.

Pleiksnis, S., Skujans, J., Visockis, E. & Pulkis, K. 2016. Increasing fire proofness of sapropel and hemp shive insulation material. In: *15th International Scientific Conference Engineering for Rural Development*. Latvia University of Agriculture, Jelgava, 403–408.

Ražnjević, K. 1984. *Termodynamické tabuĺky*. Alfa, Bratislava, 336 PP. (in Slovak).

Tsutsumi, N., Kizu, S., Sakai, W. & Kiyotsukuri, T. 1997. Thermal diffusivity study of polystyrene/poly(vinyl methyl ether) blends by flash radiometry. *Polymer Science Part B: Polymer Physic* **35**, 1869–1876.

Týbl, J. & Kic, P. 2016. Thermal properties and reduction of energy consumption of buildings. *Agronomy Research* **14**, 1222–1231.

TZBinfo. *http://stavba.tzb-info.cz/tepelne-izolace/297-polystyrenove-izolace*. Accessed 5.12.2017 (in Czech).

Valasek, P., Chocholous, P. & Muller, M. 2016. Mechanical properties of thermal insulating sandwich materials. In: *15th International Scientific Conference Engineering for Rural Development*. Latvia University of Agriculture, Jelgava, 324–328.

Yucel, K., Basyigit, T. & Ozel; C. 2003. Thermal insulation properties of expanded polystyrene as construction and insulating material. In: *15th Symposium in Thermophysical Properties. 2003.* National Institute of Standards and Technology, Boulder, 54–66. Shttp://www.allbeton.ru/upload/mediawiki/760/thermal-insulation-properties-of-expanded-polystyrene-as-construction-and-insulating-materials.pdf

Agronomy Research **15**(S1), 1127–1140, 2017

Measurement of weld joint parameters and their mathematical modelling

D. Novák[1,*], P. Kvasnová[1], J. Volf[2] and V. Novák[2]

[1]Matej Bel University, Faculty of Natural Sciences, Department of Technology, Tajovského 40, SK974 01 Banská Bystrica, Slovakia
[2]Czech University of Life Sciences Prague, Faculty of Engineering, Kamýcká 129, CZ165 21 Prague, Czech Republic
[*]Correspondence: daniel.novak@umb.sk

Abstract. The article deals with verifying of weld quality of weld joints created by laser beam welding technology, primarily in agricultural components such as reel screws. We presents both metallographic check of the weld structure using electron microscopy, RTG-microanalysis and micro hardness measurement as well as used mathematical models of the welding process and respective weld joints geometry.
First the laser beam welding technology and concerned agricultural components are introduced. Further we specify individual steel types as well as laser types and we define specific welding parameters used in our measurements. We selected several samples of weld joints, which are further examined them in detail using optical microscopy, micro hardness measurements and RTG microanalysis. We further determined the weld shape, measured dimensions of individual weld joints as well as we checked the weld joints structure.
We further introduced a mathematical model based on the program ANSYS. The model can simulate temperatures, speed field and tensions within the weld joint, basing on known thermal conductivity of the base material and specified welding conditions. Using the model, we can predict the shape of the weld and the temperatures within the material. Finally, individual welding parameters and obtained weld joint samples are briefly discussed and the applicability of the model is evaluated.

Key words: steel, mathematical modelling, screw, laser welding, metallographic check.

INTRODUCTION

The scope of our research is to simulate the welding process using a mathematical model and to verify the weld joint parameters of selected stainless steels used in a reel in a combine harvester. Given the high cutting speed, this particular part requires high quality steel material and also high weld quality to guarantee the required toughness and sharpness of the components. A reel with the screw and its position are depicted in Fig. 1 and it is labelled with (1).

1

Figure 1. Reel with a screw (1).

Simulation represents imitation of the real things, states, relationships and processes. Its advantages include quick verification of systems' behaviour and detecting of potential problems and specific restrictions. It all leads to cost savings in the areas of use. The disadvantages of simulation are higher initial costs and a simplified approach. We created computer models of the weld joints using the simulation program ANSYS. This way we simulate the weld joints using temperature fields and we compare the simulation with the visual analysis of the welds.

To evaluate the structure of welded joints, we performed a metallographic check by means of electron microscopy and micro hardness measurement as proposed by Tillová et al. (2011). We further performed RTG microanalysis to study the concentration of individual alloy elements across the material. Finally, we also created computer models of the weld joints using the simulation program ANSYS.

Screw

A screw is one of the oldest methods known to transport materials of various kinds. The use of screws applies extensively, either attached to a machine as a combined harvester, mill, filter, metering device for feeding poultry and livestock. Or they are used as a separate screw conveyor. The screw is capable of transporting all kinds of loose, granular or granular materials, and even fluids. For the construction of reels are used high-quality materials such as aluminium and stainless steels, associated with robust mechanics and top hydraulic systems, for more information see Krupička & Rybka (2016).

Effective use of screws includes improved flow of the crop from the entire reel, its smooth flow to the trashing mechanism and minimizing of losses in the cutter bar, as stated by Pečenka & Hoffmann (2015) and Čedík et al. (2016).

Laser welding technology

Laser welding is a relatively complicated technological process, which includes several co-acting physical phenomena. The basic process of laser welding is a heat cycle that includes following steps: heating of welded materials, their melt, mixing the meltage in the weld bath and subsequent solidification of the meltage. The quality of steel material itself and weld joints affects also the structure stability, i.e. to resistance to external effects, such as temperature, pressure, corrosion and others, as discussed by Novotný et al. (2015; 2016).

Laser beam welding belongs – together with plasma and electron beam welding methods – to new, special melt welding methods. Their basic common features include a significant reduction of thermal energy consumption, which is achieved by increasing the energy density on the impact surface. If the surface energy density reaches value higher than 10^5 W cm^{-2}, the welded material heats rapidly above its boiling point and a cavity is being formed – a capillary tube, so called keyhole. The hole penetrates the material to a considerable depth, or even through its entire cross section.

The key features of laser beam welding processes include high temperature, high rate of heating and cooling and a strong concentration of power in a small space. These assumptions enable enhancing of the quality of welds compared to conventional methods; however, they expect use of advanced technology.

These features yield advantages like high welding accuracy, cleanness and possibility of operational automation. High heating rate limits the heat diffusion to the surroundings, which limits the transformation changes in the material. High density of power keeps the heat affected zone narrow that lowers tensions and deformations in the material. Other notable advantage of the laser welding method is so called remote welding, when the laser source may be placed up to 1.5 m from the welded object. This yields incomparable dynamics, limited only by the focusing speed. For more information about new welding technologies and more detailed description of their principles see Kubíček (2006) and Radek et al. (2014).

Various types of lasers used for the laser welding technology vary according to the environment from which the laser draws its energy. In our experiments we used three types of lasers: Nd:YAG, fibre and CO_2 laser. The energy for the laser beam is gained from the electron transition within an atom orbital of the active medium. A brief description of the used laser types gives the following summary:

- ✓ Nd:YAG: neodymium-doped yttrium aluminium garnet; Nd:$Y_3Al_5O_{12}$; crystal, the most used solid-state laser; infrared light with wavelength 1.064 μm.
- ✓ fiber: the active gain medium is an optical fibre doped with rare-earth elements, laser light is conducted by the fiber, the wavelength is determined by the doping element.
- ✓ CO_2: gas mixture from He + N_2 + CO_2 closed in a glass tube. Since its wavelength of 10.9 μm the beam cannot be conducted by optical fibres, mirrors have to be used.

MATERIALS AND METHODS

RTG microanalysis

RTG microanalysis is a method based on dispersion of X-rays, to obtain qualitative and quantitative data about the chemical composition of the studied material. We applied so called Line RTG microanalysis to study the concentration change of selected element across the sample. The measurements were performed at Slovak University of Technology in Bratislava, using Superprobe 733 spectrometer.

Welding parameters and steel composition

We modelled and subsequently checked several combinations of welding parameters as well as steel types. Following tables give the overview about the individual chemical composition of steels and they also state the exact welding parameters using various types of lasers.

Table 1 presents the chemical composition of Cr-Ni steels of types 17 246 (ISO X6CrNiTi18-10), 17 249 (ISO X2CrNi19-11) and 17 022 (ISO X20Cr13) determined by the RTG microanalysis.

Table 1. Chemical composition of used stainless Cr-Ni steels (average values)

Chemical element	Steel 17 246	Steel 17 249	Steel 17 022
C (%)	0.06	0.20	0.20
Cr (%)	18.5	16.5	11
Mn (%)	1	1	0.5
Ni (%)	9.5	9.5	-
Si (%)	0.5	0.35	0.5

Technical parameters, e.g. power, wavelength, focus distance etc. of all used laser types (CO_2, Nd:YAG and fiber) are stated Table 2.

Table 2. Technical parameters of used lasers

Laser type	Wavelength (μm)	Laser mode	Focus distance (mm)	Laser power (kW)	Welding gas	Gas flow ($l.min^{-1}$)
Fiber	1.11	TEM00-Gaus	120	2.3	Ar	25
CO_2	10.9	TEM00-Gaus	100	4	Ar	25
Nd:YAG	1.064	TEM00-Gaus	127	3.7	Ar	12

We further designed a variety of different welding parameters of Cr-Ni steels by given laser types. The proposed welding parameters presented in Table 3.

Table 3. Individual welding parameters

Laser type	Material (thickness)	Power (kW)	Welding speed (m min^{-1})	Focusing
Fiber	Steel 17 246 (2.5 mm)	2,3	3; 5; 8	0; +2; -2; -4
Nd:YAG	Steel 17 246 (2.5 mm)	1; 2,3; 3	3; 5; 8	0
CO_2	Steel 17 249 (5 mm)	3,7	1,2; 1,8; 2,4; 3,0	0; -1
CO_2	Steel 17 022 (5 mm)	3,7	1,2; 1,8; 2,4; 3,0	0; -1

RESULTS AND DISCUSSION

RTG microanalysis

First present the results of line RTG microanalysis, by means of which we analyse the concentration course of selected alloy elements within the steel. Fig. 2 presents the RTG microanalysis of all used steel types.

The graph presents the concentration change of selected alloy elements across the steel sample. Despite one peak of Si concentration (steel 17 246) there is no change that exceeds normal fluctuations of the alloy element concentration.

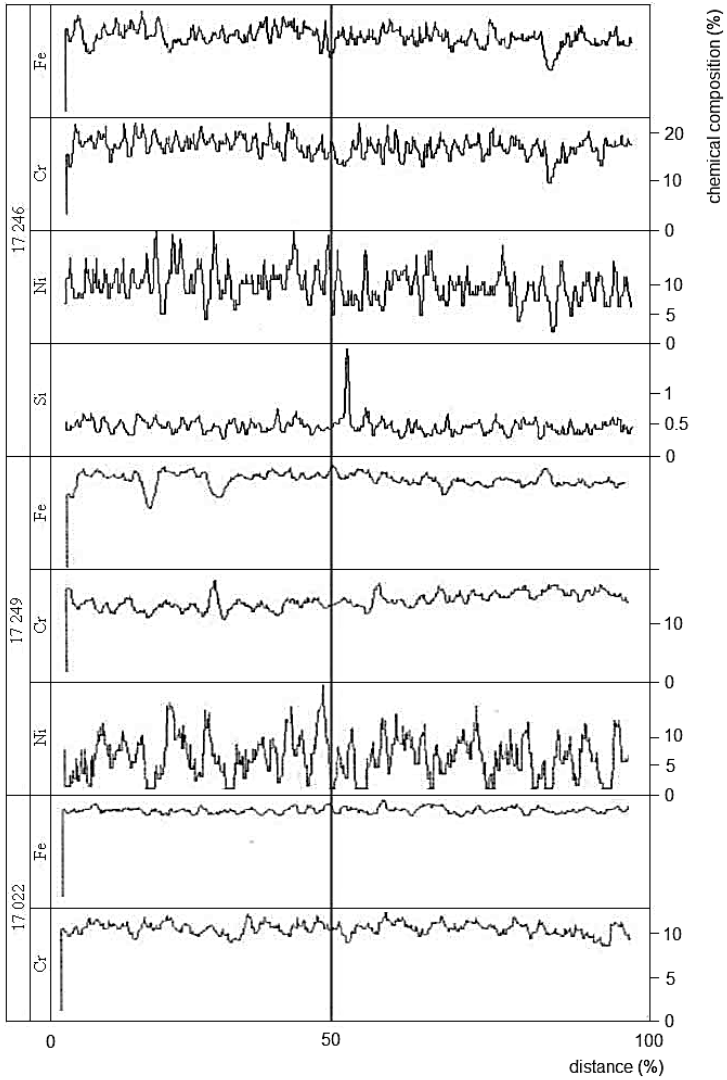

Figure 2. RTG microanalysis across the sample of steel types 17 246 (fiber laser), 17 249 and 17 022 (CO_2 laser).

Metallographic check

We further performed a metallographic check using electron microscopy, and micro hardness measurement, for further detail about these methods see Kardas (2013) and Meško et al. (2014). The macrostructure of the welds was assessed by electron microscope Carl Zeiss Axio A1M using software Proimage 4 at Technical University München. In total 29 individual samples of Cr-Ni steel 17 246, welded by fiber and Nd:YAG laser and Cr-Ni steels 17 249 and 17 022, welded by CO_2 laser have been prepared and analysed. In following Figs 3–6 we present eight selected pictures of the weld macrostructure from different steel types; individual geometrical parameters of the samples are given by Table 4.

Table 4. Parameters of steel samples

Sample No.	Steel	Laser type	Power (kW)	Welding speed ($m.min^{-1}$)	Focusing	Weld depth (mm)	Weld area (mm^2)
1	17 246	fiber	2.3	3	0	2.5	1.8
2	17 246	fiber	2.3	5	-2	2.5	1.3
3	17 246	Nd:YAG	3	5	0	2.3	1.7
4	17 246	Nd:YAG	2.3	8	0	1.1	1.2
5	17 249	CO_2	3.7	2.4	0	4.5	3.2
6	17 249	CO_2	3.7	3	-1	3.3	2.4
7	17 022	CO_2	3.7	3	-1	4	2.7
8	17 022	CO_2	3.7	1.2	0	5.2	5.1

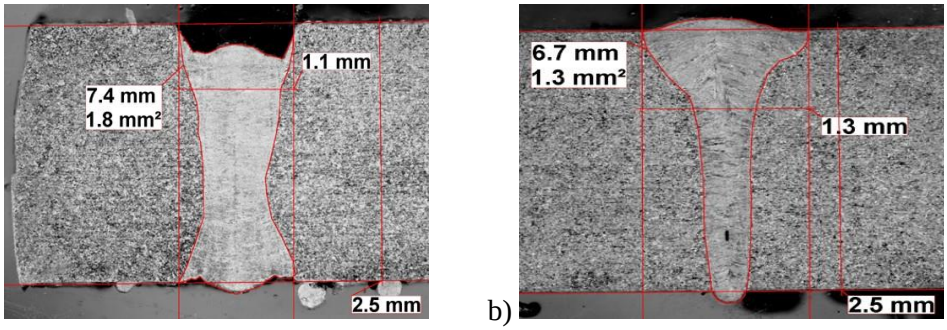

Figure 3. Weld macrostructure. Steel 17 246, fiber laser. Sample 1 (a) and sample 2 (b).

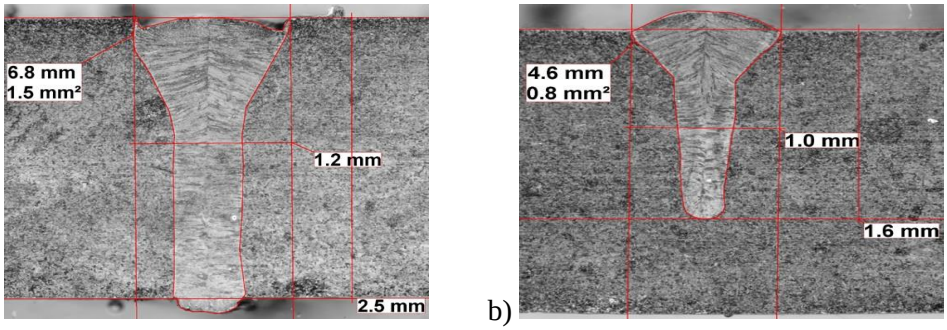

Figure 4. Weld macrostructure. Steel 17 246, Nd:YAG laser. Sample 3 (a) and sample 4 (b).

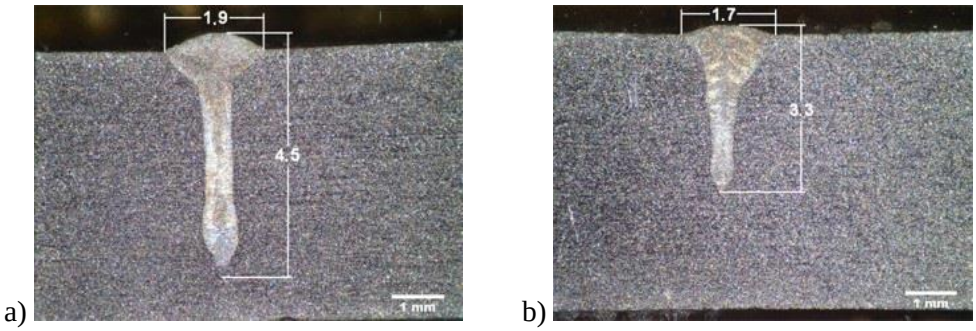

Figure 5. Weld macrostructure. Steel 17 249, CO_2 laser. Sample 5 (a) and sample 6 (b).

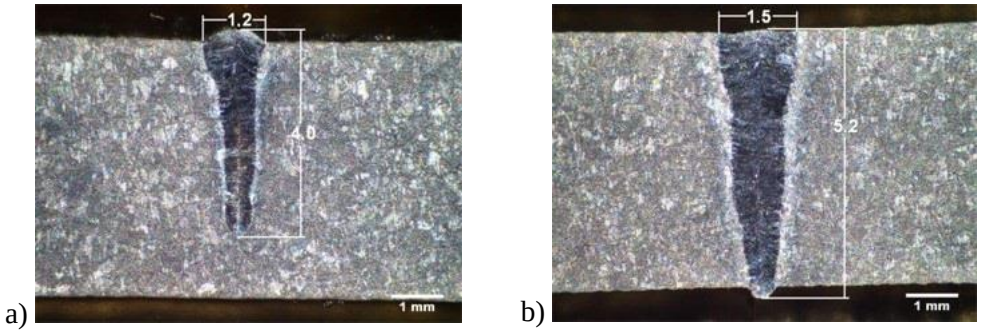

Figure 6. Weld macrostructure. Steel 17 022, CO_2 laser. Sample 7 (a) and sample 8 (b).

The weld geometry is affected by the combination of all welding parameters, i.e. laser type, power, welding speed and focusing. Notable are also shape similarities within one material, compare samples No. 5 and 6 with No. 7 and 8. All the prepared samples exhibit typical high depth-width-ratio, with narrowest weld parts below one millimetre. There is also a notable impact of negative values of laser focusing on the decreasing width and depth of the weld; however, to prove this we would need a dedicated experiment. As the heat flux of 2.3 to 3.7 kW is concentrated on the area of units of square millimetres (depending on the focusing), the welds' area is very small, between 1–5 mm^2.

Micro hardness measurement

Finally, there was also performed micro hardness measurement to determinate the hardness in the cross section of the welded area. The measurement was carried out using Vickers hardness test according to STN EN ISO 6507-1 (load of 100 g, load time 10 s) by means of optical NEOPHOT 21 metalgraph microscope.

The scheme of the micro hardness measurement is depicted in Fig. 7; the hardness was measured in 7 points in the transverse direction along the black bold line in the scheme with highlighted special points (weld, weld boundary, heat affected zone). The course of the hardness in the cross section of three selected samples from different steel types is graphically depicted in Figs 8–10; corresponding data are also presented in Table 5.

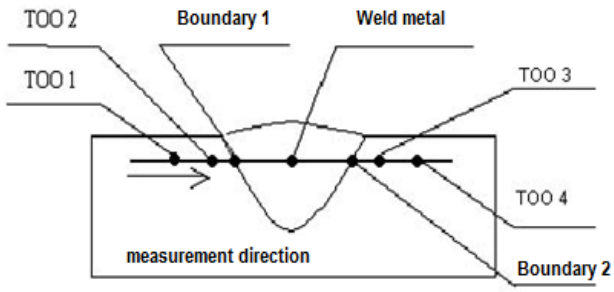

Figure 7. Micro hardness measuring scheme.

Table 5. Measured hardness of 17 246, 17 249 and 17 022 steel types

Point	HV, sample 1	HV, sample 5	HV, sample 8
TOO1	262	203	198
TOO2	254	207	204
Boundary 1	230	210	335
Weld	262	230	543
Boundary 2	238	210	336
TOO3	245	206	206
TOO4	254	203	198
Standard deviation	11.25	8.64	119.23

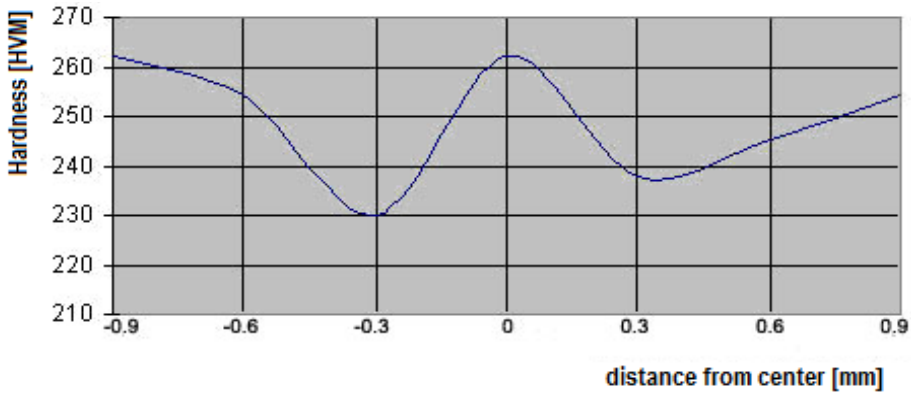

Figure 8. Course of hardness in cross section, sample 1 (steel 17 246).

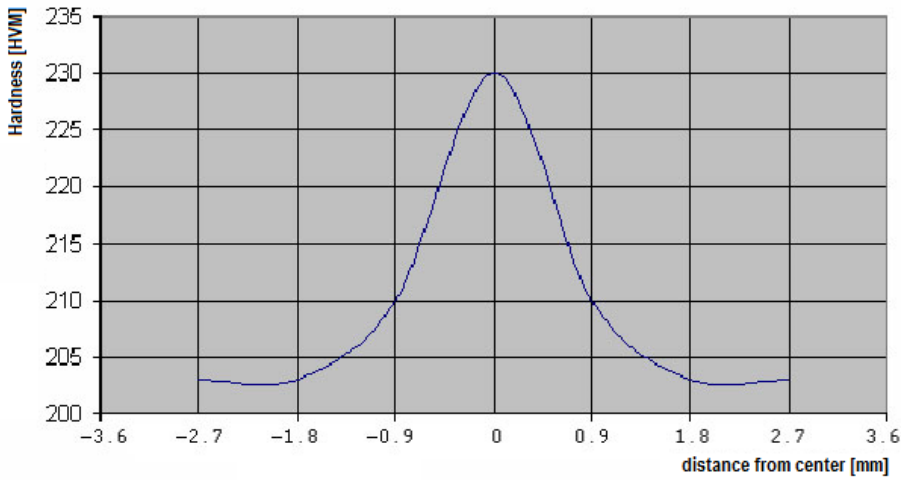

Figure 9. Course of hardness in cross section, sample 5 (steel 17 249).

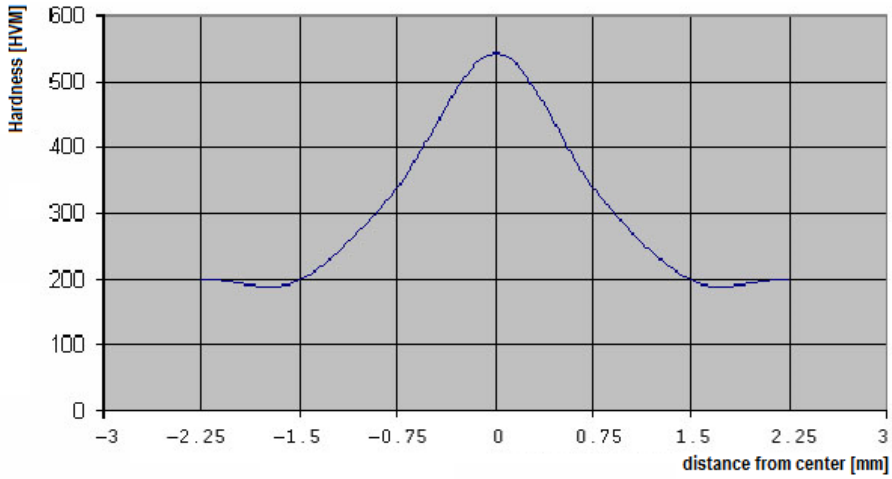

Figure 10. Course of hardness in cross section, sample 8 (steel 17 022).

The course of the hardness across the welded area is different for individual steel types. The hardness of steel 17 246 (Fig. 8) in the centre of the weld is about the same as of the base material; on the boundary of the weld the hardness drops of cca. 10%. In case of steel 17 249, the hardness in the middle of the weld is about 10% higher than of the base material (Fig. 9). However, due to the chemical composition and subsequent material changes during the welding process, the hardness of steel 17 022 is in the centre of the weld almost three times higher than the hardness of the base material. We can conclude that in one case there was observed 10% hardness drop compared to the base material; we do not consider this as a substantial degradation of the welded material. Compared to conventional welding technique, limited material degradation and narrow heat affected due to energy concentration into small area belong to prominent benefits of the laser welding technology.

Computer simulation

Finally we present the some pictures of the weld geometry and temperature fields using the program ANSYS, nearly described by Moravec et al. (2014) and Arslan et al. (2016). The scope of the modeling is to determine the effect of the moving laser beam across the material surface on the temperature field and to determinate the shape and geometry of the hat affected area. The simulation bases on the analysis of temperature and speed fields of the melt, which is considered as a dynamic fluid system. In the model, melted steel is assumed as uncompressible fluid loaded by the heat flux from the laser beam.

The mathematical model of the weld was created for the steel type 17 246 (thickness 2.5 mm) and fiber laser (2.3 kW, welding speed 3 m min^{-1}, focusing +2). The exact thermo-physical and thermo-mechanical parameters of the steel used in the simulation are stated in Table 6.

Table 6. Simulation parameters; steel type 17 246

Thermal conductivity												
T [K]	293	473	673	873	1,073	1,273	1,473	1,673	1,873			
λ [W m^{-1} K^{-1}]	15	17.3	20.05	22.85	25.6	27.9	30.2	32.6	35			
Mass heat capacity												
T [K]	293	473	673	873	973	1,173	1,273	1,473	1,673	1,723	1,823	1,873
c_p [J kg^{-1} K^{-1}]	469	472	477	515	540	600	632	696	760	770	760	745
Density												
T [K]	293	373	473	673	873	1,073	1,273	1,473	1,673	1,873		
ρ [kg m^{-3}]	7,900	7,831	7,763	7,700	7,620	7,580	7,500	7,450	7,400	7,350		
Heat transfer coefficient												
T [K]	323	373	473	573	673	773	873	973	1,073	1,273	1,473	1,673	1,873
h [Wm^{-2}K^{-1}]	13	17	23	30	38	49	63	79	99	150	217	305	357
Linear thermal expansion coefficient												
T [K]	293	373	473	673	873	1,073	1,273	1,473	1,673	1,873		
α_l.10^6 [K^{-1}]	16.8	17.2	17.5	18	18.5	19	19.4	19.8	20.1	20.3		
Young's modulus												
T [K]	293	373	473	673	873	1,073	1,273	1,473	1,673	1,873		
E [GPa]	200	195	187	172	157	135	50	26	15	5		
Yield strength												
T [K]	293	473	673	873	1,073	1,273	1,473					
R_e [MPa]	235	230	210	137	50	23	15					
Young's modulus (tangential)												
T [K]	293	473	673	873	1,073	1,273	1,473					
E_t [MPa]	1,185	1,160	938	690	250	120	30					

On basis of the thermal capacity and conductivity coefficients, we can create a base 2D model, which enables the analysis of temperature and speed fields of the material. The model assumes the dynamical viscosity of the meltage as function of temperature. The surface of the material is loaded by heat flux from the laser beam and by overpressure of 300 Pa in the axis of the laser beam with gausian course; setting this condition is neccessery to calculate the speed fields.

The temperature field is time variable and it determines the heat profile of the weld bath of the molten material under given material and parameters. The simulation of the temperature field in time t = 0.018 s from the welding start is depicted in Fig. 11; it shows the temperature distribution with color marked areas of specified teperature levels. The simulation of the temperature in dependency on time within selected positions of the weld is presented in following Fig. 12.

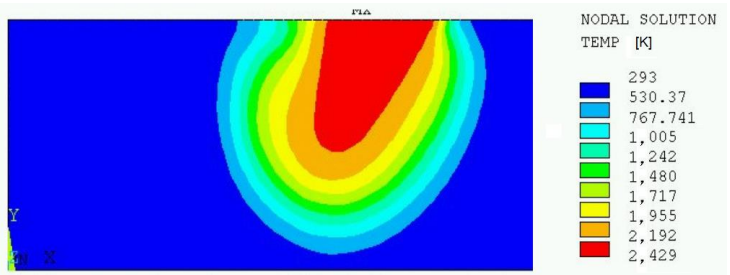

Figure 11. Simulation of the temperature field [K] in time t = 0.018 s from the welding start.

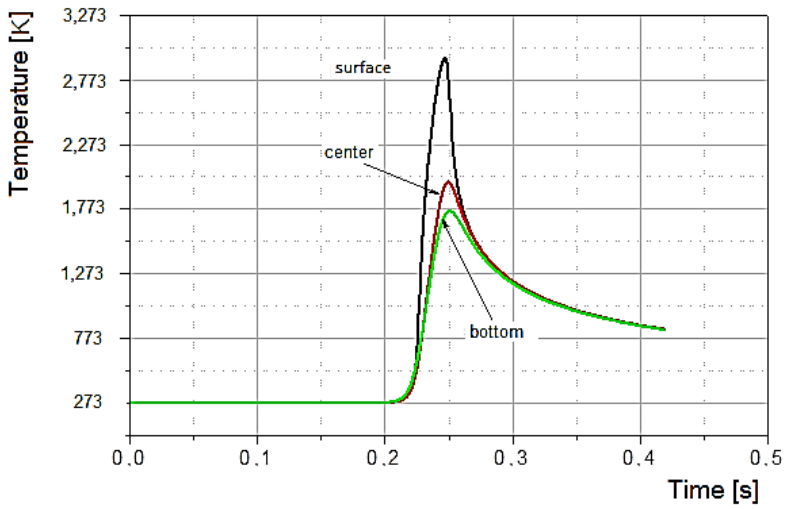

Figure 12. Time course of temperatures [K] in selected points.

In the previous figure, it is shown the time course of temperatures in the three nodes of the network model (surface, middle and bottom) with identical x-coordinate. It is apparent a rapid increase of temperature due to the laser beam effect and subsequent cooling due to conducting of the heat into the surrounding material, due to heat convection into the bypassing gas and due to radiation into the environment.

The final 3D model further enables to simulate non-stationary temperature fields and connected thermo-elastic and thermo-plastic tensions within the material, including residual (Mieses) tensions. Hereby we need to set the stated material parameters as function of temperature. In the 3D model (see Fig. 13), calculated tensions can be displayed as 3D fields. Here the laser beam moves from the low left to the upper right corner. Prior to impact of the laser beam, there is a 'tension wall' with increased tension (red color). The tension vanishes under the passing laser beam (blue color – liqid state). After passing arises a field of increased tension, the residual tension.

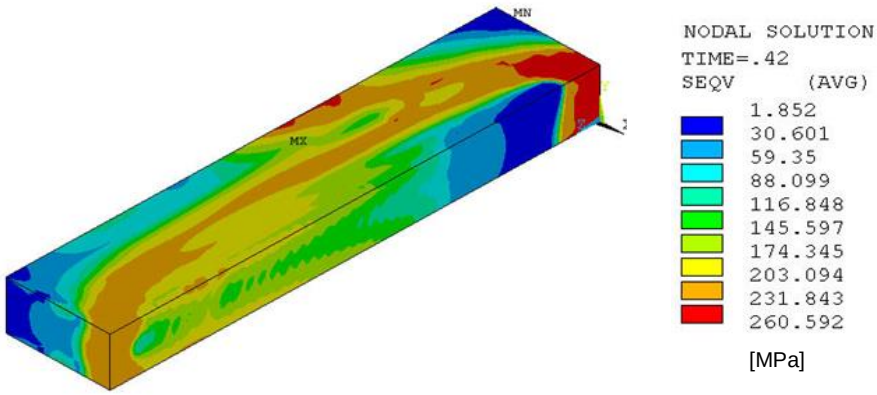

Figure 13. Tensions [MPa] under moving laser beam, t = 0.42 s.

The model of the geometrical profile of the weld in 3D-view can be seen in Fig. 14, where the boundary of the melted area is highlighted. The geometrical shapes of the boundary of the melted area obtained by the simulation are similar to the real shapes of the weld macrostructure under same conditions; see Fig. 15 with the real weld joint under the same welding parameters (steel 17 246, thickness 2.5 mm, fiber laser 2.3 kW, welding speed 3 m min^{-1}, focusing +2). The main issue when simulating the shape and dimensions of the weld joint is to specify exactly the material parameters, particularly its thermal conductivity. In order to near the real shapes, it is necessary to consider the welded part as orthotropic material and perform recalculations of its thermal conductivity.

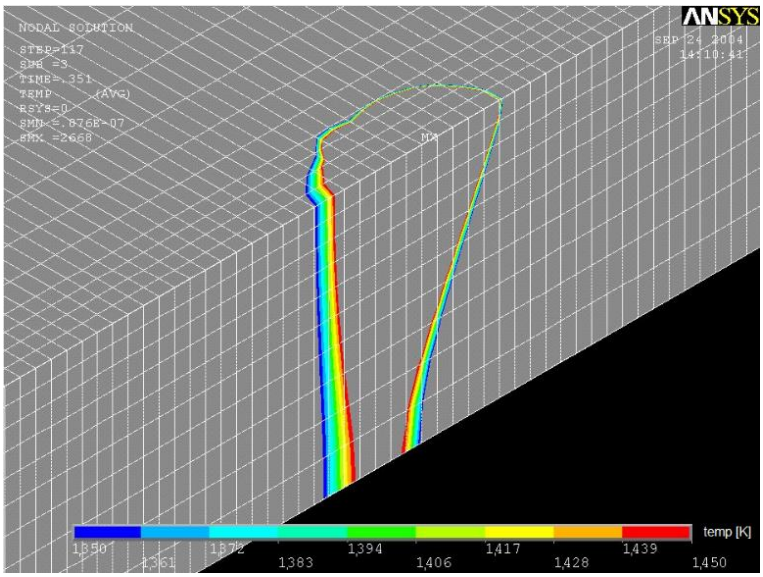

Figure 14. 3D view on the melted area boundary.

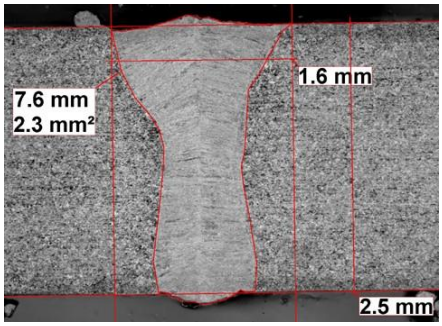

Figure 15. Weld macrostructure; steel 17 246, fiber laser.

CONCLUSIONS

Our research focuses on quality check and mathematical simulation of welds created by the laser welding technology. We prepared weld samples from several types of steels using different laser welding methods. We examined these samples using metallographic check by electron microscopy, micro hardness measurement and RTG-microanalysis. Hereby we obtained a detailed analysis of the welds. Using the above-described methods, we could determine the geometry of the weld, hardness and alloy concentration within the weld and surrounding area.

Using the laser welding technology, we measured in case of one sample only a 10% strength drop compared to the strength of the base material; other samples exhibit increase of strength in the weld area. Basing on the measurements of the weld geometry and structure, we proved the generally stated advantages of the laser welding technology, such as narrow heat affected zone, low deformations, high preciseness etc. The typical nail shape of the welds with high depth-with ratio was also observed; however, the final geometry of the weld joint depends not only on the laser parameters, but on the welded material, too. Further it has to be noted that the weld appearance change with focusing. Although we observed an impact of selected focus values on the weld geometry, a general prove would need a dedicated experiment.

Finally we presented a mathematical simulation of the welding process using the program ANSYS. Using the program we can simulate the temperature distribution within the weld, the temperature change in dependency on time, the geometrical shape of the weld and last but not least the residual tensions within the material. To simulate the thermal behaviour of the material exactly, it is necessary to set many material parameters (such as thermal conductivity and others), but it is also required to perform some recalculations with respect to real material characteristics. Fulfilling these conditions, the mathematical model is capable to simulate the real shape of the weld quite precisely; thus it makes use of the cost-saving effect of the simulation.

In further research, we would like to concentrate in detail on impact of laser focusing on the weld structure and geometry; as well as on the influence of used gases on the weld. We would also like to continue our work on increasing the accuracy of the mathematical model.

REFERENCES

Arslan, S., Tursun, N., Kurtulmus, F. & Gülec, D. 2016. Use of thermal images for optimizing burner height, operating pressure, and burner angle of a weed flamer. *Agronomy Research* **14**(1), 14–24.

Čedík, J., Pexa, M., Chyba, J., Vondrášek, Z. & Pražan, R. 2016. Influence of blade shape on mulcher blade air resistance. *Agronomy Research* **14**(2), 337–344.

Kardas, E. 2013. The analysis of quality of ferrous burden materials and its effect on the parameters of blast furnace process. *Metallurgy* **52**(2), 149–152.

Krupička, M. & Rybka, A. 2016. New design of roller separation line and its effect on the separation of hop mater. *Agronomy Research* **14**(2), 450–459.

Kubíček, J. 2006. *Special methods of melt welding. Pressure welding*. VUT v Brně, Brno, Czech Republic (in Czech).

Meško, J., Zrak, A., Mulczyk, K. & Tofil, S. 2014. Microstructure analysis of welded joints after laser welding. *Manufacturing technology* 1**4**(3), 355–359.

Moravec, J., Bradáč, J. & Nováková, I. 2014. Ways of numerical prediction of austenitic grain size in heat-affected zone of welds. In: *7th International Conference on Innovative Technologies for Joining Advanced Materials*, TIMA 2014, Trans Tech Publications Ltd.

Novotný, J., Honzíková, J., Pilous, V. & Stránský, K. 2015. Properties of welded joints in Power Plant. *Manufacturing Technology* **15**(6).

Novotný, J., Honzíková, J., Pilous, V. & Stránský, K. 2016. Verification for the causes of the degradation of welded joints in power plant. *Manufacturing Technology* **16**(5), 1106–1110.

Pečenka, R. & Hoffmann, T. 2015. Harvest technology for short rotation coppices and costs of harvest, transport and storage. *Agronomy Research* **13**(2), 361–371.

Radek, N., Meško, J. & Zrak, A. 2014. Technology og laser forming. *Manufacturing technology* **14**(3), 428–431.

Tillová, E., Chalupová, M., Hurtalová, L. & Ďuriníková, E. 2011. Quality control of micro-structure in recycled Al-Si cast alloys. *Manufacturing Technology* **11**, 70–76.

Agronomy Research **15**(S1), 1141–1151, 2017

Optimization of the balancer for $LiFePO_4$ battery charging

V. Papez[1] and S. Papezova[2,*]

[1]Czech Technical University in Prague, Faculty of Electrical Engineering, Department of Electrotechnology, Technicka 2, CZ166 27 Pague 6, Czech Republic
[2]Czech University of Life Sciences in Prague, Faculty of Engineering, Department of Electrical Engineering and Automation, Kamycka 129, CZ165 21 Prague 6 - Suchdol, Czech Republic
[*]Correspondence: papezovas@etf.czu.cz

Abstract. Balancers of various constructions are currently used for the operation control of the batteries connected in series. Unidirectional balancers ensure proper charging of all battery cells in a way that the first loaded cells should not be overcharged. Active balancers distribute the power, supplied to already-charged cells, to other cells; the power is further consumed by the passive balancers. Bidirectional balancers enable distributing the power between the cells during the discharge process, as well. This process thus protects the fastest discharging cells against the deep discharge. Passive balancers are most often used in batteries charged by the currents up to 20 A. If there are not big differences between individual cells in the battery, passive balancers reduce the efficiency of the charging process by only a few percent. They are the cheapest and most reliable. Optimally adjusted balancers with very low internal resistance deteriorate the efficiency only by about 1%. Commercially available balancers, working on the principle of a switch, periodically connecting the load resistor to the cell, deteriorate the efficiency to a greater extent, by about 5%. Optimized balancers, whose construction is described in the paper, work on a principle of a linear feedback controller. They can work with a maximum charging current up to 20 A, they have very low dynamic resistance of about 1 mΩ, and are absolutely stable. Their properties are further compared both with previously used circuits and commercial circuits.

Key words: balancer, $LiFePO_4$ accumulator, isolated solar power system.

INTRODUCTION

$LiFePO_4$ batteries in operation must be meticulously protected against over-charging. The manufacturers specify a maximum terminal voltage at the accumulator cells during charging. After achieving it, the charging must be ended. In charging a set of cells connected in series, the charging based on the total voltage in the entire battery will be markedly inaccurate. If the method were used, the cells with minimum capacity or maximum charge cycle efficiency could be overcharged. Reliable protection against overcharging can be guaranteed only by evaluating the voltage of each single cell and by terminating their charging after reaching the maximum terminal voltage. The battery can be controlled, only if the cells are absolutely identical. The voltage characteristic of two not entirely identical batteries of the same type in the cyclic charging and discharging is shown in Fig. 1.

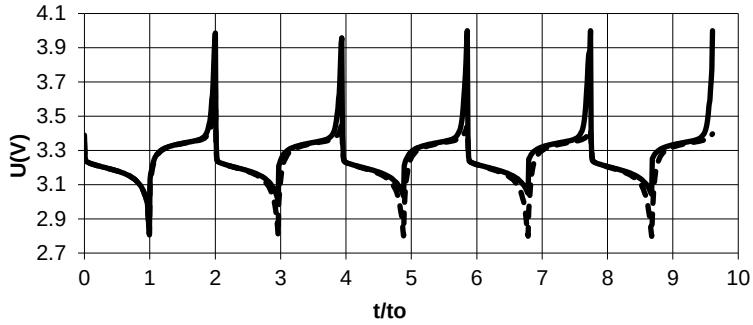

Figure 1. Voltage characteristics at two cells in the cyclical charging and discharging without balancers.

A voltage characteristic in Fig. 1 is based on the assumption that the cells are discharged and charged by a constant current, which corresponds to the charge and discharge of the first cell (a green curve) per time t_0. The charging efficiency of the second cell is by 3% lower than that at the first cell. The battery is controlled both by the total voltage (8 V for the charge and 5.6 V for the discharge) and by the minimum and maximum voltages of individual cells 4 V for the charge and 2.8 V for the discharge (Winston, 2017; Thunder Sky, 2017). In the first part of the characteristic, both cells are fully charged; discharging ends when the total battery voltage drops to 5.8 V. Subsequent charging is unbalanced. It ends after the first cell is charged, while the second cell does not reach full charging and is discharged to the lower voltage than the first cell. The total available capacity of the battery gradually decreases, and the difference between the voltage levels of the two cells gradually grows. Multi-cell battery cannot be effectively operated in this way (Papez & Papezova, 2015).

The solution lies in cell balancing. Each cell is connected in parallel to the electronic circuit. If a cell terminal voltage reaches the desired value during charging, the circuit consumes charging current supplied from the cell and stabilizes the terminal voltage at a desired value. Therefore, the battery charging is not necessary to terminate immediately, and other cells connected in series are still charged by a charge current to the maximum voltage.

Currently, passive and active balancers of various constructions are commonly used. Passive balancers simply consume the superfluous power, supplied to the already charged cell. Electric energy is converted to heat, which reduces the efficiency of the charging process (Albertronic, 2015). An active unidirectional balancer distributes the superfluous power to the terminals of other cells or to the entire battery. In this way the power is utilized for charging other cells. The balancer includes an isolated flyback converter that enables transferring the power between two ports of different voltages and voltage shift in between.

An active bidirectional balancer enables transferring power between the cells both in charging and discharging processes (Linear technology, 2017). In charging, it works as a unidirectional balancer. In discharging, it can transfer the power from the terminals of the whole battery or other cells to the terminals of the earliest discharged cells. Therefore, the discharging process may not be completed by discharging the cells with the lowest capacity. Thus the bidirectional balancer ensures that all cells are discharged

evenly to the required minimum voltage. The balancer includes a bidirectional isolated flyback converter that allows transferring the power between two ports in both directions.

MATERIALS AND METHODS

The balancer function analysis is based on its expected use for the operation control of the battery with 10 $LiFePO_4$ cells with the capacity of 300 Ah in the isolated solar power system. The battery is composed of cells of a small difference. The battery is charged from the photovoltaic generator by a relatively small current which is less than one twentieth to one tenth of an ampere-hour cell capacity. Sometimes the battery has to supply a high short-term power during the discharge. The maximum discharge current can reach up to a third of an ampere-hour cell capacity. A full discharge (100% DOD) is not expected due to the requirement to achieve maximum battery lifetime.

The charging process should be optimized over a wide range of charging currents, because the output of the photovoltaic system is determined by the instantaneous intensity of solar radiation, which strongly varies during charging. The battery can be charged many tens of hours by small currents. Therefore, the balancer may consume only the current in the region of a maximum cell voltage. At a lower cell voltage or at times when it is not charged, the current consumed by the balancer from the battery must be minimal, at any circumstances, i.e., the long-running charging process must be minimally affected by the balancer.

As shown in Fig. 2, the charging process is completed by reaching the maximum defined value of the cell terminal voltage. To reach minimal dependence on the termination of charging on the instantaneous charging current, the real voltage value at the balancer terminals should be minimally affected by the passing current. Only this way, the charging can terminate under the condition that the cell terminal voltage is close to its defined maximum value, and the cells will be charged by the charge, close to their maximum capacity.

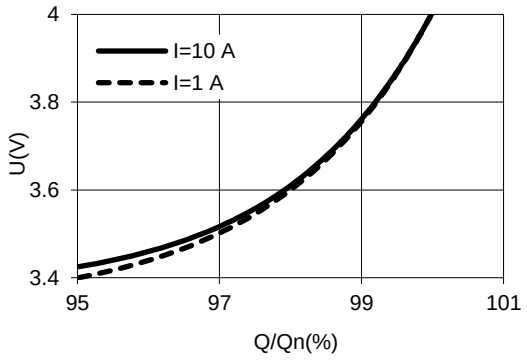

Figure 2. Cell terminal voltage at the end of the charging process.

Such a state is evident from the courses of the charging processes of the cells with the balancers having different internal resistances and being charged by different currents, as shown in Figs 3. The waveforms depicting a cell charging process are compared. The cell is charged by 2 A (Fig. 3, a, b) or 10 A (Fig. 3, c, d) currents and is connected to the balancer with the internal resistance of 10 mΩ (Fig. 3, a, c) or 40 mΩ (Fig. 3, b, d). Both balancers are adjusted to 4 V voltage, at the current of 10 A. The thin curve in Fig. 3 represents a cell charge waveform at the end of charging by a constant current without using the balancer (at a scale of a proportional charge). The thick curve shows the cell charge waveform with using the balancer. The dotted curve on the right

axis depicts the charge consumed by the balancer during charging (at a scale of a proportional charge).

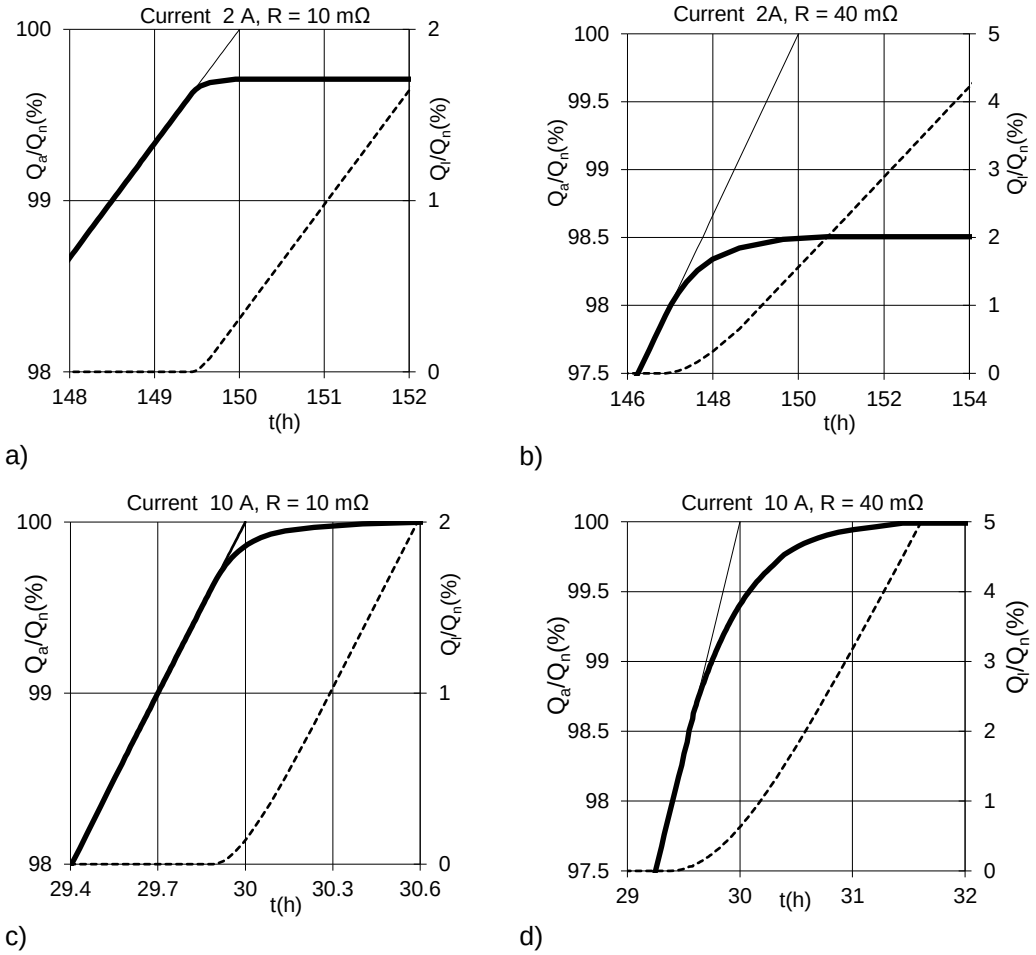

Figure 3. Charging process of the cell by 2 A or 10 A currents with balancers with internal resistance 10 mΩ or 40 mΩ; Q_a – instantaneous charge of the cell, Q_n – nominal charge of the cell, Q_l –charge consumed by the balancer.

To exploit effectively the supplied power, a minimal internal resistance of the balancer is important. At the end of the charging process, in a certain voltage range, whose width corresponds to the internal resistance of the balancer, the current consumed by the balancer increases up to the value of the charging current, and, at a constant voltage, the charging circuit is then balanced. Figs 3 show that the balancer with low internal resistance consumes the current for a shorter time and the stability is reached earlier. At the end of the charging process, it consumes less energy supplied to the battery in all cases. If there are not big differences between the individual cells in the battery, the balancers with very low internal resistance consume from the terminals cca 1% of energy that was supplied by the battery throughout the charging cycle.

At the end of the charging process of the battery with more cells, which are not completely identical, the energy, dissipated from the terminals of each cell, will be higher by the value corresponding to the difference between the charge of the longest charged cell and the charge of the reference cell. The size of this energy at all cells reaches cca 2.5% of the energy needed for charging the battery, provided the battery is in a standard condition, when the differences between charges, which charge single cells, do not exceed 3% of the total charge. In case of active balancers, this energy will be redistributed between cells, while in case of passive balancers it will be lost.

All cells will reach the same level of charging that corresponds to the terminal voltage at the balancers, if the mean value of the current passing through equals to the charge current. A balancer with less internal resistance allows achieving less dependence of the degree of charging on the charge current. The balancers can control the discharge process of the battery with difficulties due to the expected size of the discharge current. They should be designed for the current exceeding 100 A, which would be very costly. In doing so, they could extend the potential discharge time by about 2–3 minutes only.

In the first phase of designing autonomous photovoltaic power system, commercially available balancers were observed for their potential use. Primarily, the possible devices are passive balancers working on the switchable principle with fixed bypass resistors. They differ in their connection in series, adjusting or programming, and by the maximum operating currents ranging from 0.5 A to 20 A. Balancers with dissipated power higher than c. 5 watts use external load resistors that are placed on the coolers (HS series, 2017).

Two types of commercial balancers were tested: balancing module CBM1 (CBM1, 2017) for $LiFePO_4$ cell and current of 1.7 A and balancing module BS1V4 (BS1V4, 2017) for $LiFePO_4$ cell and current up to 13 A. Both balancers operate on the same principle of a switch that is controlled by the Schmitt trigger, as shown in Fig. 4.

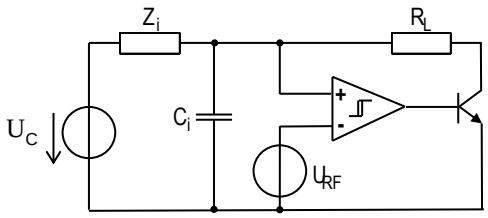

Figure 4. Block diagram of the balancer operating on the principle of trigger and switch.

The cell is replaced with power supply U_c, equivalent internal impedance Z_i and capacity C_i. The circuit works as a relaxation generator. When the voltage of the capacitor C_i increases above a reference voltage, a Schmitt trigger starts working and opens the output switch. Current passing through the load resistor R_L starts discharging the capacitor C_i. If this current causes sufficient voltage drop at the impedance Z_i, and Ci voltage drops below the reference voltage, reduced by the trigger hysteresis, the output switch is closed. This way, R_L current is extinguished, C_i starts recharging and after charging above the reference voltage, the process periodically continues. Balancer relaxation oscillations are mostly determined by the impedance in the cell circuit. The impedance may affect the voltage-current characteristic, which can be shifted even by several tenths of V.

The first mentioned balancer CBM1 is tested in a static mode, when it is connected to a voltage source with an internal resistance of the order of milliohms. The balancer switches up at a terminal voltage of 3.65 V and disconnects at the voltage of 3.55 V. When switched, the value of the current is 1.7 A. Due to a high Z_i impedance and the own Schmitt trigger time constant, the balancer will get into a regime of relaxation oscillations when it is connected to a voltage source with a high Z_i impedance of about 0.5 Ω.

Voltage and current characteristics for the balancer CBM1 are shown in Fig. 5. If the voltage is 3.8 V, the passing current reaches only c. 0.25 A. In contrast, the manufacturer declares thse current of 1.7 A at a voltage of 3.6 V. The waveforms for the second tested module BS1V4 with external load resistor 0.33 Ω, 50 W are shown in Figs 6 and 7. The source has an internal resistance of 30 mΩ, and capacity of 15 mF; open-circuit voltage is 3.6 V and 3.75 V. The mean value of the supplying current is controlled by the switching time of the power switch at an approximately constant period. The internal resistance of the balancer, set up according to the average values of its terminal voltages and currents, is relatively high, i.e. c. 36 mΩ. Following the above mentioned analysis, such a value would cause c. 5% charge loss during the charging of every single cell.

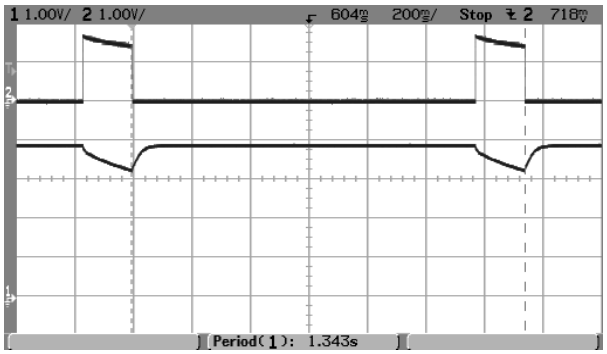

Figure 5. Current-voltage characteristics of the balancer CBM1 for the current 0.25 A.

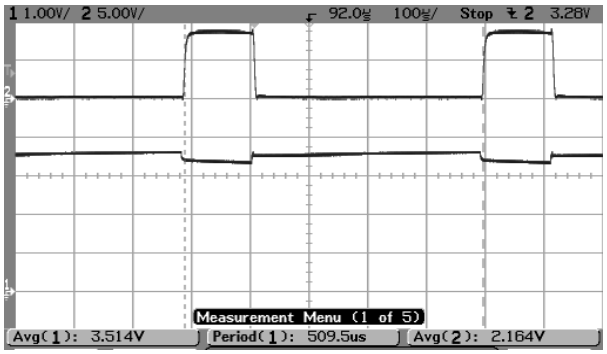

Figure 6. Current-voltage characteristics of the balancer BS1V4 for the current 2.16 A.

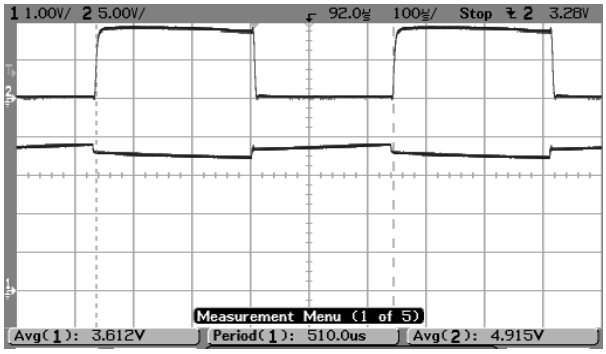

Figure 7. Current-voltage characteristics of the balancer BS1V4 for the current 4.9 A.

Using an active bidirectional balancer is, due to the large discharge current, unrealistic. In charging, the active balancer causes shortening the charging time of the battery by c. 2.5%.

As the price of an active balancer is 2–4 times higher than the price of a passive balancer and equals, in principle, the price of the entire photovoltaic generator, it is twenty times more efficient to slightly increase the power of the photovoltaic generator.

Design and construction of an optimal balancer

The design and construction of an optimal balancer is based on the following conditions. The balancer is passive and operates on the principle of the linear feedback controller. In the voltage range, corresponding to that at the end of the charging process, its current-voltage characteristic must show very low dynamic resistance in the order of mΩ units; for lower voltages, the passing current must reach only hundreds of μA. Further, it is also necessary to prevent the balancer from oscillating in any of the regimes. If the balancer starts to oscillate, its current-voltage characteristic will significantly divert from the desired static characteristics, and the balancer will lose its function. Specifically, the stability condition can be expressed, e.g., by the immittance criterion (Gajdosik, 2011). It states that if the balancer with the admittance $Y_b(\omega) = G_b(\omega) + j\,B_b(\omega)$ is connected in parallel with the cell with the admittance $Y_a(\omega) = G_a(\omega) + j\,B_a(\omega)$, it will start oscillating (in case that conditions (1) and (2) apply for some of the frequencies), see Fig. 8.

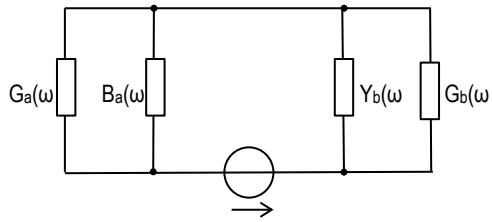

Figure 8. Immittance stability criterion in the battery – balancer circuit.

$$G_a(\omega) + G_b(\omega) < 0 \qquad (1)$$

$$B_a(\omega) + B_b(\omega) = 0 \qquad (2)$$

As $G_a(\omega) > 0$ applies to the cell absolutely, the balancer will be stable (without any further conditions), if is valid that $G_b(\omega) > 0$. The balancer must be designed also with respect to achieving the maximum operation reliability. The possibility of any

defect of the components increases the probability of the failure of the entire device. The refore the balancer should be constructed with a minimum number of components. Then the components will work at significantly lower operating temperatures than their maximum operating temperature.

The first balancer constructed according to the above mentioned conditions was used in $LiFePO_4$ battery systems, which were designed in 2015 (Papez & Papezova, 2015; 2016a; 2016b). The basic configuration of the balancer consisted of a reference voltage stabilizer, differential amplifier with a double transistor, Darlington power transistor and five resistors. The balancer could operate with currents up to 10 A. For higher currents, the circuits were arranged in parallel. A current-voltage characteristic of a pair of circuits is shown in Fig. 9 (a thin curve). The balancer works quite well in the current range greater than c. 2 A, where its dynamic resistance is less than 10 mΩ and may be loaded by the current up to 20 A. In the range of smaller currents, a fuzzy knee of a current-voltage characteristic is basically very disadvantageous, because it may cause undesired current leakage from a charged cell.

The other construction of the balancer uses a rail-to-rail operational amplifier to increase the gain in a feedback loop. Simple differential amplifier is replaced with the operational amplifier and power Darlington transistor is controlled from its output (see Fig. 9).

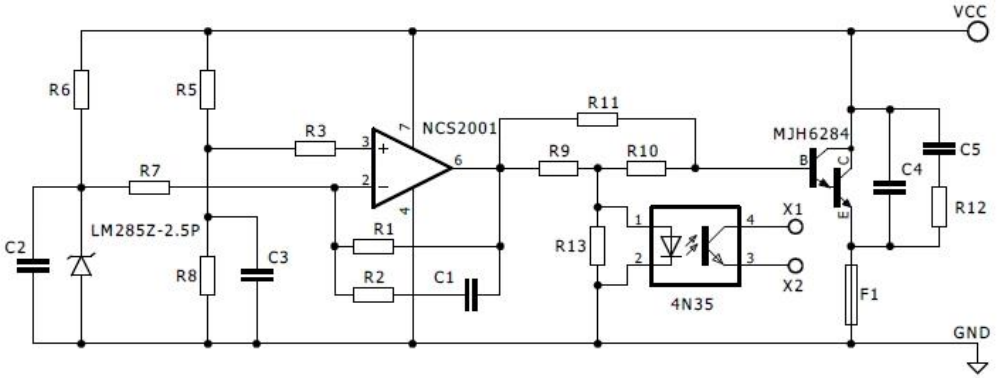

Figure 9. Circuit diagram of the new balancer.

The balancer in this modification has a very low dynamic resistance (c. 1 mΩ), as shown in Fig. 10 (a thick curve). The stability of its feedback loop was solved by using typical frequency compensation in a negative feedback loop, i.e., by an operational amplifier. The achieved characteristic of complex admittance, which satisfies the condition of absolute stability, is shown in Fig. 11. The balancer can be loaded by the current of up to 20 A.

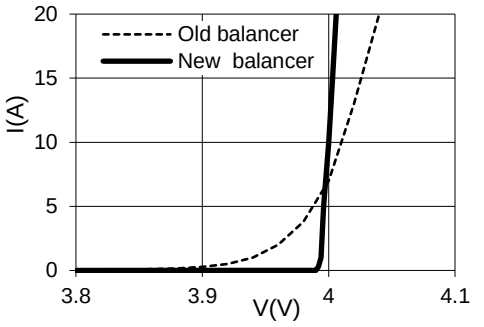

Figure 10. Current-voltage characteristics of the balancers.

The problem of cooling the power transistor, which is loaded with the power dissipation of 80 W, must also be strongly solved. The example of the prototype of the balancer with a cooler is shown in Fig. 12.

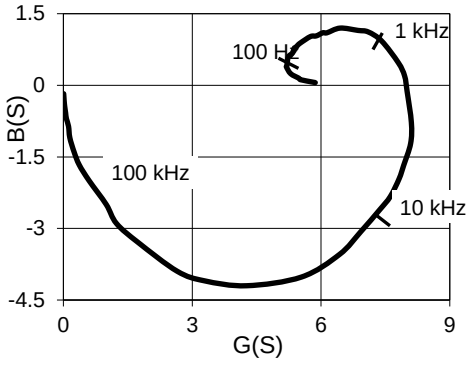

Figure 11. Complex admittance characteristic of the balancer.

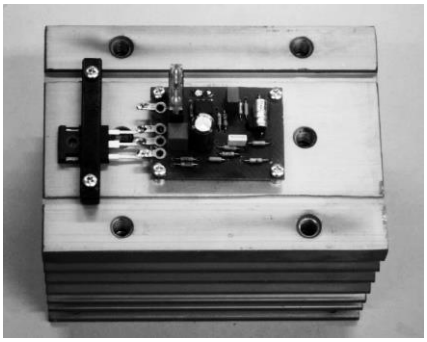

Figure 12. Prototype of the balancer with a cooler.

For using the balancer in the automated measuring station for testing accumulator (Papez & Papezova, 2016b) there was implemented a simpler construction, controlled by a circuit of three-terminal adjustable shunt regulator, whose output amplifier is extended by another external amplifier which allows loading the balancer with the current of 10–16 A (see Fig. 13). The external amplifier stage further reduces the dynamic resistance of the shunt regulator by 2–3 orders, in proportion to its current gain, thus achieving a very small value, i.e., c. 1 mΩ. A simple connection of an external amplifier, however, causes also the input admittance with a negative real part in a frequency range of tens to hundreds kHz, as illustrated in Fig. 14 (a dashed line). In the situation, when the internal frequency compensation at the amplifier shunt regulator cannot be changed, two external damping Boucherot RC circuits are applied to reach system stability. The characteristic of the balancer complex admittance with the frequency compensation is shown in Fig. 14 (a solid line).

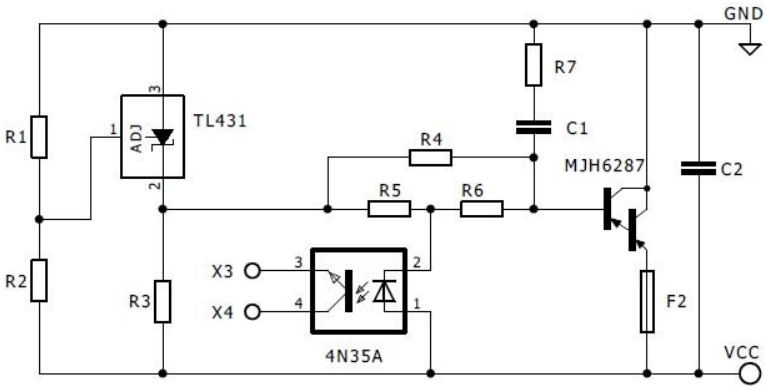

Figure 13. Circuit diagram of the simple balancer.

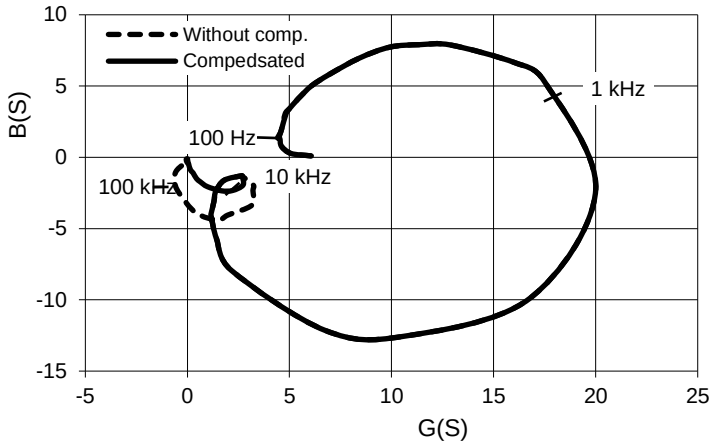

Figure 14. Complex admittance characteristic without frequency compensation (dashed line) and with frequency compensation (solid line).

RESULTS AND DISCUSSION

The analysis of the functions of balancers designed for the controlled charging of $LiFePO_4$ batteries has been carried out. The worst operating parameters are exhibited by the balancers working on the principle of a switch that periodically connects load resistor across the cell terminals. The relaxation oscillations are completely determined by the impedance in the cell circuit, which can shift the current-voltage characteristic even by 0.5 V.

Better parameters show the balancers working on the principle of a dipole with a nonlinear static current–voltage characteristic. Simple circuits, however, show a large internal resistance. Moreover, the circuits operating on the principle of feedback control regulator are often potentially unstable.

Both the implementation and construction of the two types of balancers optimized for the maximum charge currents of 16 A and 20 A, operating on the principle of feedback controller are described. Their properties are further compared with the previously used circuits and commercial circuits. The designed circuits contain 20 components at maximum, their internal resistance is approx. 1 mΩ and they are absolutely stable.

CONCLUSIONS

At the passive balancers, a minimum internal resistance is necessary for the efficient power utilization during charging. The balancer with a lower internal resistance consumes the current for a shorter period of time and the stability is reached earlier. In all cases of the charging process, it consumes less power at its end than the balancer with a higher internal resistance. If there are not big differences between the single cells in the battery, the balancers with a very low internal resistance consume from terminals c. 1% of the energy supplied to the battery throughout the whole charging cycle. At a lower

cell voltage, off the battery charging, the current consumed from the battery must be at such a level not to cause an apparent increase in self-discharge.

ACKNOWLEDGEMENTS. Thanks for cooperation belong to Laboratory of Photovoltaic Systems Diagnostics, Faculty of Electrical Engineering, Czech Technical University in Prague and Department of Electrical Engineering and Automation, Faculty of Engineering, Czech University of Life Sciences in Prague.

REFERENCES

Albertronic, B.V. *http://www.123electric.nl.* Accessed 23.1.2017.

Bidirectional Battery Management System. *http://www.tesvolt.com/bidirectional-battery-management-system.html.* Accessed 21.1.2017.

BS1V4. *http://www.bateriovеboxy.cz/domains/bateriovеboxy.cz/produkty-2/.* Accessed 23.1.2017.

CBM1. *http://gwl-power.tumblr.com/post/5199241412/cell-balancing-solved-the-cbm1-module-is-here.* Accessed 21.1.2017.

HS series. *https://store.comet.bg/download-file.php?id=15455*. Accessed21.1.2017.

Gajdosik, L. 2011. *Methods for analyzing linear circuits*, Ben–technical literature, Praha, 315 pp. (in Czech).

Linear technology LT 1213. High Efficiency Bidirectional Multicell Battery Balancer LTC 3300-1, REV B. *http://www.linear.com/product/LTC3300-1*. Accessed 23.1.2017.

Papez, V. & Papezova, S. 2015. Isolated Solar Power Station. In: *14th International Scientific Conference Engineering for Rural Development Proceedings*. University of Agriculture, Jelgava, Latvia, pp. 458–465.

Papez, V. & Papezova, S. 2016a. Optimization of a solar power station with LiFePO44 accumulators. *Agronomy Research* **14**(S1), 1200–1211.

Papez, V. & Papezova, S. 2016b. Automated measuring station for accumulator testing. *Agronomy Research* **14**(S1), 1212–1221.

Thunder Sky. *http://www.thunderstruck-ev.com/Manuals/Thundersky%20Product%20Manual.pdf.* Accessed 11.4.2017.

Winston. *http://en.winston-battery.com/index.php/products/power-battery/item/wb-lyp40aha?category_id=176.* Accessed 21.2.2017.

Agronomy Research **15**(S1), 1152–1161, 2017

Endurance $LiFePO_4$ battery testing

S. Papezova[1,*] and V. Papez[2]

[1]Czech University of Life Sciences in Prague, Faculty of Engineering, Department of Electrical Engineering and Automation, Kamycka 129, CZ165 21, Prague 6 - Suchdol, Czech Republic
[2]Czech Technical University in Prague, Faculty of Electrical Engineering, Department of Electrotechnology, Technicka 2, CZ166 27 Pague 6, Czech Republic
[*]Correspondence: papezovas@etf.czu.cz

Abstract. A lithium-iron-phosphate ($LiFePO_4$) battery is nowadays considered one of the best types of batteries. Manufacturers and mostly suppliers indicate that $LiFePO_4$ batteries have much longer lifespan than other batteries, and thus convincing their customers of lower operating costs than at other types of batteries, although their purchase price is several times higher. In connection with the problem of replace Pb batteries in the backup sources of security systems with $LiFePO_4$ batteries, there has been necessary to determine the real parameters of available cells under conditions in which they operate. The paper describes the battery tests, in which their real parameters, comparable with the parameters indicated by the suppliers, are tested. The tests lie in automatic long-term cyclical charging and discharging of the multi-cell battery. Operating parameters are continuously monitored, recorded and evaluated by the computer. Individual cells are equipped with balancers and protection circuits that prevent from exceeding the maximum voltage during charging, as well as the voltage drop below a minimum level during discharging. The results of long-term tests on $LiFePO_4$ WB-LYP40AHA Winston Battery are presented. The first test was conducted with 100% depth of discharge (DOD). New cells, after the first charge and discharge, showed the capacity about 115% of the rated capacity, the capacity drop c. 0.015 to 0.02% per cycle and the capacity drop to 80% after 950 cycles, which represents a lifetime of about 5% less than state the manufacturers.
A second test was conducted with 50% depth of discharge. Here, again after the first charge and discharge, new cells exhibited the same capacity as in the first case, i.e. c. 113% of the rated capacity. After 1,000 cycles, the cell capacity decreased to 107% of the rated capacity, which corresponds to the expected lifetime of 5,000 cycles.

Key words: $LiFePO_4$ battery, lifespan, capacity drop, depth of discharge.

INTRODUCTION

One of the barriers for usage of all types of accumulators is their lifespan. Their producers and retailers are providing to their potential end users information about their products. But there are especially accentuated their beneficial properties – the possibility of charging and discharging by high currents, minimum influence of the discharge time on capacity, long durability. Measuring of lifespan according to producers specifications is done in cycles, discharging the cells to defined DOD and then charging it to a maximal

allowed value, then after many cycles, deterioration of the parameters is observed, as well (Cenek et al., 2003; Lust, 2010).

The lifetime at standard $LiFePO_4$ batteries is usually indicated in the range of 1,000–7,000 cycles, DOD 70–100% and usually stated capacity drop of 80% of the nominal value, as shown in Fig. 1. It is valid for LYP, LFP and CA batteries from different manufacturers (Scrosati et al., 2013; Liberty, 2017; Sinopoly, 2017; Thunder-Sky, 2017; Winston-Battery, 2017a).

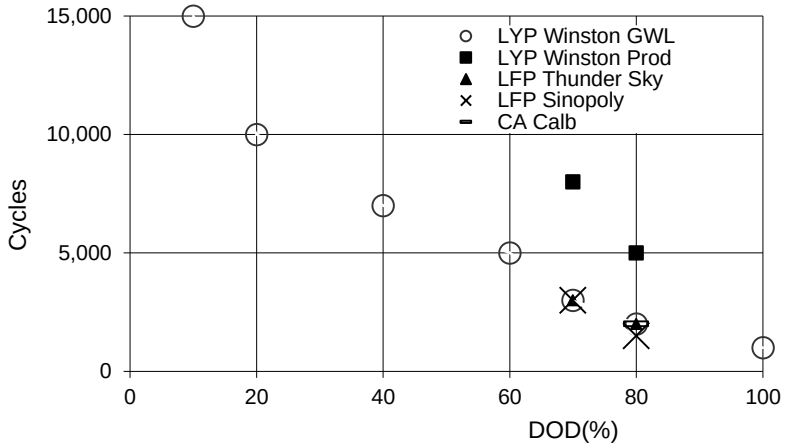

Figure 1. $LiFePO_4$ battery lifetime according to different sources.

Indicated values sometimes differ by more than 100%, even at the same products from the same manufacturer. The data published by the manufacturer or the distributor often differs.

The most important criterion for determining real quality of the supplied batteries is to verify a real lifetime of $LiFePO_4$ batteries.

Testing of the $LiFePO_4$ accumulators is practiced on the special testing station where charging and discharging is automated (Papez & Papezova, 2016).

MATERIALS AND METHODS

The evaluation of operational parameters of specific $LiFePO_4$ cells during the long-term measurement is performed by a special testing system. Charging and discharging processes are controlled by a computer and are fully automated. Operating parameters of the tested accumulator are continuously scanned, recorded and evaluated by the personal computer (Srovnal, 2002; Kreidl & Svarc, 2006).

Individual cells are equipped with balancing and protection circuits that prevent the cell from exceeding the maximum voltage during charging and also from voltage drops below the minimum level during discharging. The testing system consists of a DC power supply, electronic load, switch control unit, cell balancers, input-output card and a computer see Fig. 2.

The source of electricity is the laboratory MANSON HCS source 3402 with maximum output voltage of 32 V and current of 20 A. The charging current and voltage can be set manually or from the computer.

STATRON 3227 with 200 W power output is used as an electronical load, it has maximum voltage of 80 V and current of 25 A. Discharging current can be set manually, its stability reaches 1% from the set value for 4 cells of $LiFePO_4$ accumulators. The load also has an automatic protection of the accumulator against unintended discharging after turning off and when the terminal voltage drop below the set value. This controlling algorithm was not used because of its low reliability.

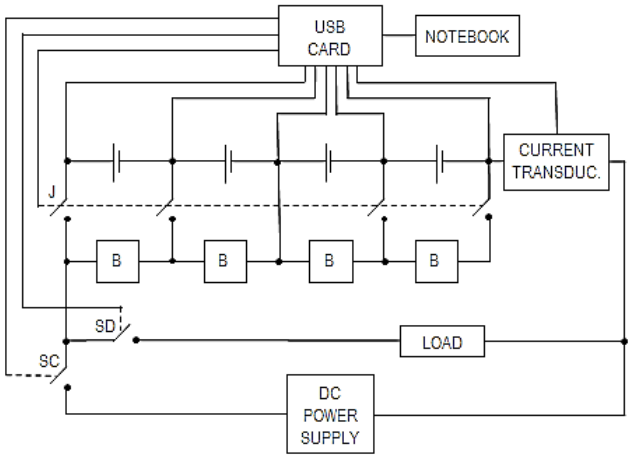

Figure 2. Block diagram of a testing workplace; B – balancer, SC – charging relay, SD – discharging relay, J – breaker.

The relay switches control the high power circuits. These relay switches have high reliability and robust construction. Bistable relays J which are used in this system do not need constant control current. Relays are controlled by logical signals from the interface card, which are connected to the transistor switches through opto-couplers.

The charging of not quite identical cells connected in series is controlled by the network of balancers. Each cell is connected in parallel to the electronic circuit. If a cell terminal voltage reaches the desired value during charging, the circuit consumes charging current supplied from the cell and stabilizes the terminal voltage at a desired value. Other cells connected in series are still charged by a charge current to the maximum voltage and full charge.

The balancer is designed as an electronic load controlled by a circuit of three-terminal adjustable shunt regulator, whose output amplifier is extended by another external amplifier which allows loading the balancer with the current of 10−16 A. The external amplifier stage further reduces the dynamic resistance of the shunt regulator by 2–3 orders. The balancer has a very low dynamic resistance (c. 1 mΩ), as shown in Fig. 3. In the situation, when the internal frequency compensation at the amplifier shunt regulator cannot be changed, two external damping Boucherot RC circuits are applied to reach system stability. The achieved characteristic of complex admittance satisfies the condition of absolute stability. The balancer can be loaded by the current of up to 20 A.

The problem of cooling the power transistor, which is loaded with the power dissipation of 80 W, must also be strongly solved.

When using the charging current of 10 A, the balancer safely reduces the maximum voltage to 4V at the charged cell. Through discharging time, during the inactivity, the balancer consumes less than 1 mA, which causes negligible discharging of the cell.

The relay switches control the high power circuits. These relay switches have high reliability and robust construction. Bistable relays J which are used in this system do not need constant control current. Relays are controlled by logical signals from the interface card, which are connected to the transistor switches through opto-couplers.

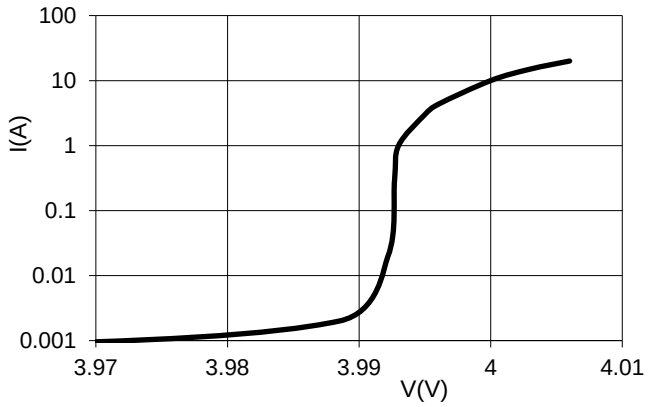

Figure 3. Balancer I–V characteristic.

The charging and discharging networks of accumulators are operated by SC and SD switches. During the accumulator charging, the charging source is connected by an SC switch. The accumulator discharge occurs by switching off the SC switch and subsequent switching on the SD. The accumulator discharge occurs by disconnecting the SC switch and subsequent contacting the SD switch.

Scanning the analogue electrical signals from the accumulators and generating control signals for controlling the function of switches, which set the desired mode and ensure continuous emergency protection of the operating modes, is provided by a measuring card USB 6211. An input card with 16-bit converters enables achieving an absolute error in determining cell voltage of 0.3 mV at a chosen input range of the ± 10 V analogue inputs. Switches SC and SD are controlled by the logic signals of the card.

The temperature of the accumulator cells was continuously monitored by a thermal imager, because we were initially afraid of possible overheating, or, in the worst case, of possible inflammation of the cells. But under the applied current, nothing like happened during the operation. The temperature of the cells was practical equal to the ambient temperature of 20 °C.

The testing workplace control is provided by the program in a system-design platform LabVIEW implemented in the PC.

In the first part of the program, it is necessary to set the technical parameters of the cells for testing. These parameters are given by producers and their limits must not be exceeded. For accumulator protection there are limit values of voltage. After reaching

this limit value, the program will generate signal for disconnecting the bistable relays. Accumulators are then disconnected from the DC power supply and from the load. The testing is ended so the damage of the accumulator is prevented. In program, these parameters can be set: maximum voltage on the cell, when the bistable relays is set on U_{max_L}, minimal voltage on the cell, when the bistable relays is set on U_{min_L}, terminate charging voltage of the cell, when the system will be switched to the discharging U_{max_C} and the terminate discharging voltage of the cell when the system will by switched to the charging U_{min_D}.

The monitoring of the measured data is provided by the graphic recording to the Waveform graph placed on a virtual front panel in a LabVIEW program. There are recorded all four cell voltage waveforms and the current waveform. Apart from a continuous display of the measured data and control signals for charging or discharging on the front panel, the data are also recorded directly into the archive file. The data serve for displaying the charge and discharge waveforms, and if necessary, the data can be subjected to further analysis.

RESULTS AND DISCUSSION

The measuring workplace in operation is shown in Fig. 4. The example of the measured data record for a period of 1200 minutes, which corresponds to three charge and discharge cycles, is shown in Fig. 5.

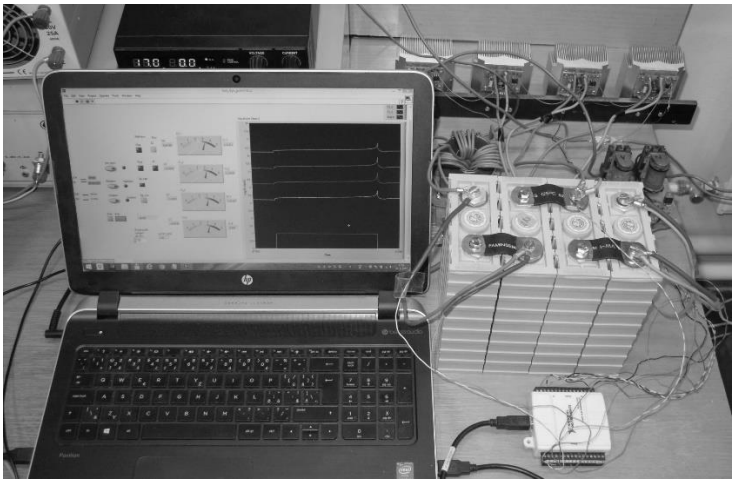

Figure 4. Photo of a measuring workplace.

Parameter measurements are performed by a cyclic discharge of the cells to a predefined minimum voltage and their recharge to a predefined maximum voltage. Gradually deteriorating battery parameters during hundreds of cycles are being monitored and evaluated.

There were tested commercially available Winston batteries, model WB-LYP40AHA, with a nominal capacity of 40 Ah (Winston Battery, 2017a) on the batteries with four in series-connected cells.

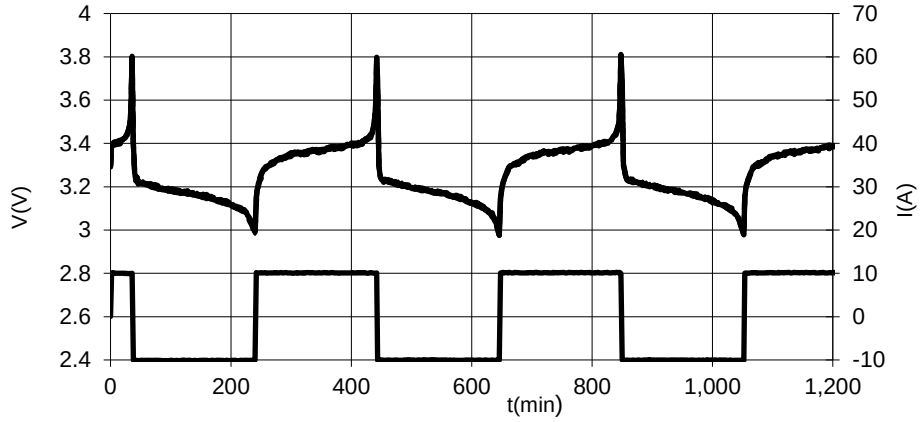

Figure 5. Example of the measured voltage (the upper curve) and current (the lower curve) waveforms on the cells within 1,200 minutes.

One battery was operated at the limits provided by the manufacturer with the DOD = 100%. Both charging and discharging currents were chosen the same, i.e., 10 A, which corresponds to the current CA/4 (Winston Battery), according with anticipated operational conditions as power backup of the alarm system. During a mains power failure the system takes the current of several tens of mA in the sleep mode but the current up to 10 A in the event of an alarm. The charging was controlled by the balancers and terminated after reaching the voltage, ranging from 3.95 V to 4 V, simultaneously by all the battery cells. The discharge terminated when the voltage of any of the cells dropped below 2.9 V. The cells were loaded by the deepest possible discharge within the done limits. The charge, corresponding to cell nominal capacity, is consumed from the cells during the discharge.

The batteries were placed in a heated laboratory at the temperature 20 ± 1 °C and the cells temperature was monitored by infrared thermography. View of the upper wall of the cell is shown in Fig. 6, a. Photo with a temperature field on the surface of cells is shown in Fig. 6, b. Temperature distribution along the axis designated L1–L2 is graphically illustrated in Fig. 6, c. The temperature of individual cells differ by 0.4 °C, the maximum temperature deviation of the cells from room temperature in the laboratory is 1.1 °C.

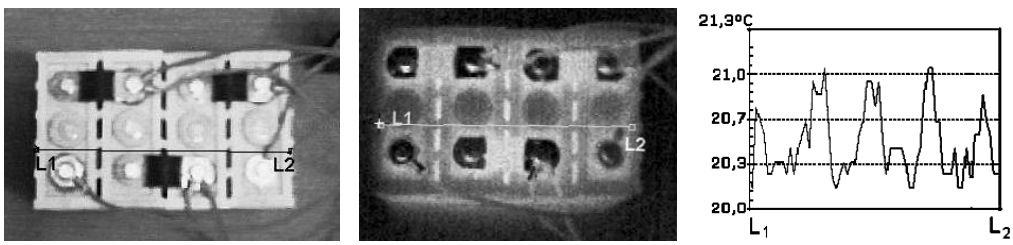

a) b) c)

Figure 6. The temperature of the cells, a) real photo, b) infra photo, c) a distribution of temperature on the cells.

The electrical test results are shown in Table 1.

Table 1. Test results of 4 cells WB-LYP40AHA Winston Battery with DOD = 100%

After	Dischar. voltage (V)	Charging voltage (V)	Full discharge (Ah)	Full dis-charge (%)	Full charge (Ah)	Charging efficiency (%)	Capacity drop (Ah)
0 c.	11.94	15.8	46.3	115.8	46.6	99.3	
100 c.	11.94	15.9	44.4	111.0	45	98.6	1.9
200 c.	11.93	15.86	42.33	105.8	42.8	98.9	4.0
300 c.	11.87	15.85	41.3	103.3	41.7	99.1	5.0
400 c.	11.88	15.83	39.6	99.0	40	99.0	6.7
500 c.	11.89	15.8	37.2	93.0	37.9	98.1	9.1
600 c.	11.88	15.9	35.8	89.5	36.2	98.9	10.5
700 c.	11.87	15.86	35.	87.5	35.4	98.9	11.3
800 c.	11.87	15.85	33.8	84.5	34.1	99.1	12.5
900 c.	11.86	15.85	32.6	81.5	32.9	99.1	13.7
1,000 c.	11.86	15.84	31.4	78.5	31.7	99.0	14.9

The test results can be summarized as follows: after initialization charging, the capacity of all cells was approximately 46 Ah, during the next approximately 20 cycles, the capacity dropped about 0.03% per cycle. The drop further gradually decreased to the value of 0.017% per cycle, and then it remained constant until the test was completed. The drop of the capacity to 80% of the nominal capacity was recorded after 950 charging cycles and is shown in Fig. 7. The efficiency of the charge cycle throughout the whole test was for all cells practically constant, i.e. at 99%.

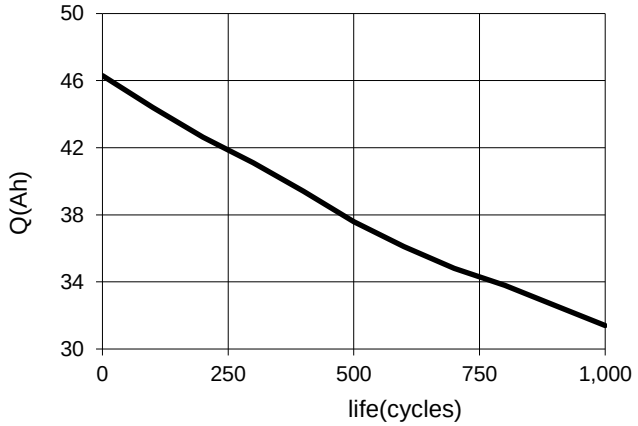

Figure 7. Drop of the capacity of cells operated with the DOD = 100%.

Second battery was operated at the limits provided by the manufacturer with the DOD = 50%. Both charging and discharging currents were chosen the same, i.e., 10 A, which corresponds to the current CA/4. The charging was controlled by the balancers and terminated after reaching the voltage, ranging from 3.95 V to 4 V, simultaneously by all the battery cells. The cells with nominal capability 40 Ah were loaded by the charge 20 Ah and the voltage of the cells dropped approximately to 3.2 V.

The test results are shown in Table 2.

Table 2. Test results of 4 cells WB-LYP40AHA Winston Battery with DOD = 50%

After	Dischar. voltage (V)	Charging voltage (V)	Full discharge (Ah)	Full discharge (%)	Full charge (Ah)	Charging efficiency (%)	Capacity drop (Ah)
0 c.	12.87	15.24	45.00	112.5	45.50	98.90	
100 c.	12.87	15.28	44.55	111.4	45.08	98.81	0.45
200 c.	12.86	15.26	44.10	110.3	44.56	98.98	0.90
300 c.	12.85	15.13	43.67	109.2	44.15	98.93	1.33
400 c.	12.86	15.20	43.26	108.2	43.72	98.96	1.74
500 c.	12.86	15.18	42.86	107.1	43.33	98.91	2.14
600 c.	12.87	15.22	42.48	106.2	42.98	98.83	2.52
700 c.	12.87	15.15	42.11	105.3	42.53	99.01	2.89
800 c.	12.86	15.15	41.74	104.4	42.23	98.83	3.26
900 c.	12.87	15.09	41.39	103.5	41.83	98.95	3.61
1,000 c.	12.86	15.10	41.05	102.6	41.49	98.94	3.95
1,100 c.	12.86	15.13	40.72	101.8	41.18	98.89	4.28
1,200 c.	12.87	15.15	40.40	100.0	41.86	98.88	4.60
1,300 c.	12.86	15.18	40.09	100.2	40.49	98.92	4.91
1,400 c.	12.86	15.19	39.79	99.5	40.20	89.99	5.21

The test results can be summarized as follows: after initialization charging, the capacity of all cells was approximately 45 Ah, during the next approximately 20 cycles, the capacity dropped 0.015 per cycle. The drop further gradually decreased to the value of 0.01% per cycle, and then it remained constant until the test was completed. The drop of the capacity to 90% of the initial capacity was recorded after 1,000 charging cycles and is shown in Fig. 8.

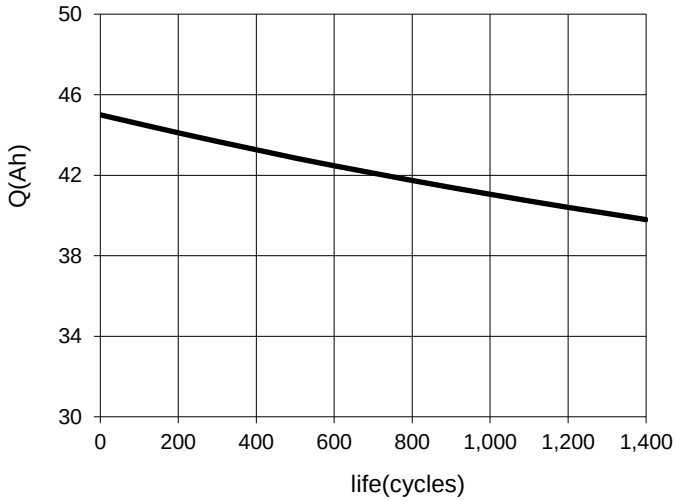

Figure 8. Drop of the capacity of cells operated with the DOD = 50%.

The given capacity and its drop correspond to the expected lifetime of 4,000–5,000 cycles. The efficiency of the charge cycle throughout the whole test was for all cells practically constant, i.e. at 99%.

CONCLUSIONS

The batteries were tested on two automated testing stations (Papez & Papezova, 2016), which were upgraded using the balancers with very low internal resistance and a galvanic isolated current transducer. For the discharge control with the preset DOD, the control program was completed with the function of continuous evaluation of the consumed charge. Two tests with 1,000 and 1,400 discharge cycles were performed at two four-cell batteries of the type WB-LYP40AHA Winston Battery during one-year period of time. There were verified voltage waveforms of both sets during charge and discharge by a constant current in the range of voltage levels recommended by the manufacturer. Their ampere–hour capacity and charging efficiency was also determined.

The lifetime of the first battery with 100% DOD relative to 80% of the nominal capacity of the worst cell was set to 950 cycles. The lifetime of the second battery with a DOD of 50% relative to 80% of the nominal capacity of the worst cell was calculated on 3800 cycles according to the measurement results. The measured maximal initial capacity of the cell was 46.3 Ah at a discharge current of 0.25 CA. The manufacturer indicates the battery capacity of the cell of approximately 110% of the nominal capacity at a discharge current of 0.5 CA in the datasheet (Winston-Battery, 2017b).
Manufacturer probably elects a greater initial capacity of the battery for reliable security of a guaranteed cell lifetime.

Valve Regulated Lead-Acid batteries (VRLA batteries) 12 V, 40 Ah (Reddy, 2010) has the lifetime of 300 cycles at 100% DOD and the lifetime of 900 cycles at 50% DOD. An acquisition cost of VRLA battery is approximately equal to 45% of acquisition cost of $LiFePO_4$ battery with the same parameters 12 V, 40 Ah. The comparison of these results shows that the operating costs of $LiFePO_4$ battery are definitely lower. But there is necessary to respect that $LiFePO_4$ battery has a slightly higher operating voltage and requires strict compliance of the prescribed operational mode.

ACKNOWLEDGEMENTS. Thanks for cooperation belong to Laboratory of Photovoltaic Systems Diagnostics, Faculty of Electrical Engineering, Czech Technical University in Prague and Department of Electrical Engineering and Automation, Faculty of Engineering, Czech University of Life Sciences in Prague.

REFERENCES

Cenek, M. Jindra, J., Jon, M., Kazelle, J., Kozumplík, J. & Vrba, J. 2003. *Accumulator from principle to practice*. FCC Public. Praha. 248 pp. (in Czech).

Kreidl, M. & Svarc, R. 2006. *Technic Diagnostic*. BEN – technicka liteartura. Praha. 408 pp. (in Czech).

Liberty Electric Bikes. *http://www.iloveebikes.com/batteries.html.* Accessed 23.1.2017.

Lust, R. 2010. *Accumulator Capacity Measurement*. Bachelor's thesis. VUT Brno. Supervisor Kolka.Z. 36 pp. (in Czech).

Papez, V. & Papezova, S. 2016. Automated measuring station for accumulator testing. *Agronomy Research* **14**(S1), 1212–1221.

Reddy, T. 2010. *Linden's Handbook of Batteries.* McGraw Hill Professional. New York, 1456 pp.
Scrosati, B., Abraham, M., Schalkwijk, W. & Hassoun, J. 2013. *Lithium Batteries Advanced Technologies and Applications.* Wiley. New Jersey. 392 pp.
Sinopoly Battery Limited. http://www.sinopolybattery.com/en/products.aspx?cid=10&pages=1, Accessed 23.1.2017.
Srovnal, V. 2002. *Electrotechnical Measurements*. BEN – technicka literatura. Praha. 255 pp. (in Czech).
Thundersky Product Manual *http://www.thunderstruckev.com/Manuals/Thundersky_Product_Manual.pdf.* Accessed 23.1.2017.
Winston-Battery. *http://en.winston-battery.com/index.php/products/power-battery/category/lyp-battery.* Accessed 23.3.2017.
Winston-Battery. *http://en.winston-battery.com/index.php/products/power-battery/item/wb-lyp-40aha.* Accessed 11.4.2017.

Agronomy Research **15**(S1), 1162–1169, 2017

Comparison of exhaust emissions and fuel consumption of small combustion engine of portable generator operated on petrol and biobutanol

B. Peterka[1,*], M. Pexa[1], J. Čedík[1], D. Mader[1] and M. Kotek[2]

[1]Czech University of Life Sciences Prague, Faculty of Engineering, Department for Quality and Dependability of Machines, Kamycka 129, CZ165 21 Prague 6, Czech Republic
[2]Czech University of Life Sciences Prague, Faculty of Engineering, Department of Vehicles and Ground Transport, Kamycka 129, CZ165 21 Prague 6, Czech Republic
[*]Correspondence: peterka@oikt.czu.cz

Abstract. The paper is focused on the comparison of exhaust emissions and fuel consumption of small internal combustion engines operated on petrol and biobutanol. In case of this research, small engines are represented by combustion engine of portable power generator with nominal power of 4.8 kW equipped with carburettor for fuel mixture preparation. Exhaust emissions and fuel consumption were measured while gradual loading of the combustion engine. BrainBee emission analyser, Bruker FTIR spectrometer and EEPS particle analyser was used for the measurement. The mass fuel consumption was monitored using laboratory scale Vibra. The initial hypothesis expected that exhaust emissions and fuel consumption will be higher in case of use of nonstandard fuels. From the viewpoint of particles count can be stated, that their productions are at very low level for both kinds of used fuels. Production of carbon monoxide and hydrocarbons is higher than in case of usual automobile engine due to simple engine control system and absence of additional emission control device (catalytic converter). The fuel consumption increased while using n-butanol as a result of its lower calorific value.

Key words: biobutanol, petrol, emission, fuel consumption.

INTRODUCTION

In the Europe the biofuels are widely used as an alternative to fossil fuels. They reduce the increase of greenhouse gasses in the atmosphere, dependency on fossil fuel products and their import, furthermore the biofuels are usually produced from local crops and thus supports the local production (Demirbas, 2009). In the Europe the aim is to achieve a 10% share of energy from renewable sources in transport in 2020 according to EU directive 2009/28/EC.

For SI engines the alcohol based biofuels are most commonly used. The ethanol is mostly used as an alcohol based biofuel for spark ignition engines. However, the ethanol has many disadvantages such as its affinity to the water, aggression to the most of rubber and plastic sealing elements, low calorific value etc. (Čedík et al., 2014a, 2014b).

The alternative to ethanol as alcohol-based biofuel could be butanol. Butanol is the second generation biofuel and it is mainly studied as an admixture in diesel or biodiesel fuels in compression ignition engines (Rakopoulos et al., 2010; Altun et al., 2011; Tüccar

et al., 2014; Yilmaz et al., 2014). Butanol can be produced by fermentation or in petrochemical way, so its production is very similar as ethanol (Ezeji et al., 2003). Properties of butanol are closer to fossil fuels. However use of pure butanol in spark ignition engines mainly requires the modification of the air-fuel mixing ratio, due to lower stoichiometric ratio of butanol, similar as when using ethanol. Butanol has several advantages over ethanol, such as a lower ignition temperature and higher calorific value. Butanol is more mixable with hydrocarbon fuels and its stoichiometric ratio is closer to gasoline than when using ethanol. This ratio allows the use of higher concentrations of butanol in gasoline without engine modification. Butanol is also less corrosive due to lower affinity for water. (Durre, 2007; Qureshi et al., 2008; Shapovalov & Ashkinazi, 2008; Andersen et al., 2010; Harvey & Meylemans, 2011; Swana et al., 2011; Serras-Pereira et al., 2013). Gasoline fuel blended with butanol was studied in the range of 3–100% vol. butanol (Rice et al., 1991; Alasfour, 1997; Yacoub et al., 1998; Gautam & Martin, 2000a; Gautam & Martin, 2000b; Dagaut & Togbé 2008; Dagaut & Togbé, 2009; Wallne et al., 2009; Williams et al., 2009; Yang et al., 2009; Dernotte et al., 2010; Wigg et al., 2011; Gu et al., 2012; Feng et al., 2013; Elfasakhany, 2014). The results show that addition of butanol reduces fuel emissions of CO, HC, CO_2, but NO_X emissions are increased depending on concentration and conditions, as compared with gasoline. Increase the emissions of CO and HC and NOx emissions are reduced at concentrations greater than 60% butanol. Due to lower heating value than gasoline the specific fuel consumption is higher and the torque and power are lower compared with gasoline. Better combustion efficiency can be achieved due to better anti-detonation characteristics of butanol compared with gasoline and higher oxygen content. Some sources indicate the increase torque and reduce energy consumption at 35% concentration of butanol in gasoline (Feng et al., 2013). Other sources state that the engine power is maintained in proportion to 80% by volume of gasoline and 20% butanol. (Yang et al., 2009). Most of the above studies were carried out on the engines with fuel injection. Sources indicate small ratios to (3, 7, 10 vol.% Butanol) mixture of butanol in gasoline for testing engine carburettor (Elfasakhany, 2014).

The aim of this paper is to compare the emissions production and fuel consumption of the generator when operating at biobutanol and petrol. Monitored will be those emissions components: CO – carbon monoxide, CO_2 – carbon dioxide, NO_X – nitrogen oxides, HC – hydrocarbons, PM – particles and K – smoke).

MATERIALS AND METHODS

Measurements were carried out on mobile generator ProMax 3500A with a rated power of 2.7 kW powered by small Briggs and Stratton engine type Vanguard 6.5HP with a rated power of 4.8 kW. Assembly of small combustion engine and the alternator is suitable for the quick and easy driving of load of the engine. In this case, value of the output current of the alternator is proportional to combustion engine load.

During loading of the combustion engine, there is measured frequency, electrical current and voltage of the output of the generator. Simultaneously with the measurement of electrical parameters is also measured fuel mass flow rate using Vibra AJ 6200 standard precision scale. In order to monitor the operating parameters of the engine during measurements, the oil temperature sensor, fuel temperature sensor and intake air temperature sensor was mounted on the engine. BrainBee emission analyser, Bruker

FTIR spectrometer and EEPS particle analyser was used as testing devices of emissions production (Table 1). All data are stored to the PC memory using RS482 to RS232 interface and for this purposes software application was developed.

Table 1. Parameters of the emission analyzer BrainBee

Component	Resolution	Accuracy
CO	0.01% vol.	0.03% vol. or 5% read value
CO_2	0.1% vol.	0.5% vol. or 5% read value
HC	1 ppm vol.	10 ppm vol. or 5% read value
O_2	0.01% vol.	0.1% vol. or 5% read value
NO	1 ppm	10 ppm vol. or 5% read value
Opacity	0.1%	2%
Temperature	1 °C	2.5 °C

From measured data the mass emissions production was calculated according to Eqs 1 and 2.

$$Q_a = M_p \cdot FA \cdot 3{,}600 \tag{1}$$

where: Q_a – amount of intake air (g h^{-1}); M_p – fuel consumption (g s^{-1}); FA – mixing ratio (kg_{air} kg_{fuel}^{-1})

$$PE_i = \frac{Q_a \cdot E_i}{100} \tag{2}$$

where: $PE_i i$ – amount of produced emission component (g h^{-1}); E_i – mass share of the emission component (%)

The principle of measurement is based on the principle of operation of the internal combustion engine and electric generator. The internal combustion engine operates in the range around 3,000 rpm, corresponding to a frequency of 50 Hz of electric generator output. During loading of the internal combustion engine decreases its speed according to the control part of the engine characteristics. Properly adjusted governor of the engine keeps the engine speed steady regardless of engine load. At the moment when the engine load reaches external speed characteristics, there is a significant change in engine speed and thus the output frequency of the electric generator.

Measurement is aimed at monitoring of fuel consumption and emissions production of internal combustion engine during gradual loading by heating elements connected to electric generator. Emission values are measured in units of volume and based on the intake air quantity converted into units of weight.

Based on engine operation while using pure BA 95 petrol there was selected several measurement points in steps approximately 25% (675 W), 50% (1,350 W), 72% (1,944 W) and 95% (2,565 W) of rated power. Measurement point at full load (100%) is not selected because of possibility of reaching the external speed characteristic of the engine.

Transmission losses and the change in viscosity of oil are not considered. The measurement is performed at an operating temperature, which is dependent on the engine load and ranges from 90 °C to 110 °C of the engine oil temperature.

Used fuels are biobutanol (n-butanol – BUT) and petrol BA95. Especially for this measurement there was fitted BA 95 petrol without any bio-components required by law.

In the Czech Republic ethanol is mainly used as this component. Basic properties of the used fuels are shown in the Table 2.

During the measurement the air–fuel equivalence ratio was monitored (BrainBee – Brettschneider equation). Consequently the air-fuel ratio (AFR) was changed using the choke shutter according to stoichiometric ratio for each fuel. Stoichiometric ratio for pure octane is commonly 14.7:1 and 12:1 for butanol.

Table 2. Basic properties of used fuels (Feng et al., 2015)

Property	n-Butanol	Petrol
Chemical formula	C_4H_9OH	C_4–C_{12}
Molecular weight (g mol^{-1})	74	100–105
Density (kg m^{-3})	810	720–760
Carbon content (%)	65	86
Hydrogen content (%)	13.5	14
Oxygen content (%)	21.5	–
Auto ignition temperature (°C)	343	257
Calorific value (MJ kg^{-1})	33.1	42.9
Latent heat of vaporization (KJ kg^{-1})	716	380–500
Stoichiometric air-fuel ratio	11.2	14.7
Octane number	89	86–94
Boiling temperature (°C)	118	25–275
Adiabatic flame temperature (K)	2,340	2,370

RESULTS AND DISCUSSION

The resulting values of the individual components of the emissions, fuel consumption, engine speed and load are an average of 2 minutes recording with a sampling frequency of 1 Hz. Solid components of the emissions were excluded from the evaluation. Content of solid particles is negligible in case of the SI engine and in terms of measuring devices it is at the border of sensitivity.

Table 3 shows the volume fraction of emission components in exhaust gas of the internal combustion engine. Table 4 gives the calculated values of mass emissions production (with the inclusion of the combustion process, which is dependent on the air-fuel ratio and on the mixture preparation process).

Table 3. Volume fraction of emission components in exhaust gas of observed engine

	Speed rpm	Load W	NO_X ppm	CO %	CO_2 %	HC ppm	Fuel consumption g h^{-1}	Specific fuel consumption g kWh^{-1}
BA 95	3,142	656	88.9	3.82	7.91	104.1	600.1	914.8
	3,121	1,331	175.9	3.92	7.74	120.5	789.4	592.7
	3,101	1,939	363.2	4.09	8.61	129.4	960.3	495.0
	2,989	2,566	660.8	4.68	10.56	137.3	1,162.5	452.9
BUT	3,141	656	155.2	0.77	9.65	44.3	665.8	1,013.9
	3,122	1,330	361.2	1.59	9.35	56.1	883.0	663.8
	3,091	1,941	714.6	2.08	9.82	77.9	1,106.6	570.1
	2,915	2,591	818.3	3.35	11.26	90.9	1,408.8	543.6

According to Table 3 and Table 4 it is obvious that better results was reached by using fuel BA95 in case of emissions of nitrogen oxides, carbon dioxide and fuel consumption. Conversely, by using BUT fuel, there was achieved better emissions of carbon monoxide and hydrocarbons. Interestingly, just production of carbon monoxide and hydrocarbons has decreased by about 50% when using BUT fuel. In contrast, the carbon dioxide emissions and fuel consumption increased by about 10%. Considerable increase in emissions production was achieved in case of nitrogen oxides namely about 60% in comparison with BA95.

Table 4. Calculated values of mass emissions of observed engine

	Speed rpm	Load W	NO_x g h^{-1}	CO g h^{-1}	CO_2 g h^{-1}	HC g h^{-1}	Fuel consumption g h^{-1}	Specific fuel consumption g kWh^{-1}
BA 95	3,142	656	0.797	0.0320	1,040.3	1.37	600.1	914.7
	3,121	1,331	2.076	0.0431	1,340.4	2.09	789.4	592.7
	3,101	1,939	5.215	0.0549	1,813.8	2.73	960.3	495.0
	2,989	2,566	11.485	0.0759	2,690.7	3.51	1,162.5	452.9
BUT	3,141	656	1.261	0.0058	1,150.4	0.53	665.8	1,013.9
	3,122	1,330	3.892	0.0160	1,477.1	0.89	883.0	663.8
	3,091	1,941	9.651	0.0262	1,945.9	1.55	1,106.6	570.1
	2,915	2,591	14.070	0.0537	2,838.3	2.30	1,408.8	543.5

Fig. 1 shows the percentage comparison of the average values of harmful emissions production and fuel consumption when operating at BUT compared to BA95.

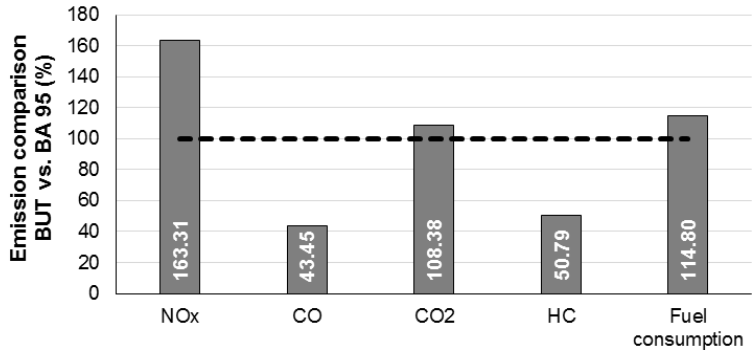

Figure 1. Percentage comparison of emissions and fuel consumption as average for all load modes when operating at BUT where BA95 is represented as 100%.

Fig. 2 shows detailed percentage comparison of emissions of the engine operated at BUT for selected load levels compared with BA95. It is evident, that at low load level when BUT is used emissions of nitrogen oxides, carbon dioxide and fuel consumption are increased in comparison with the BA95 fuel. On the contrary, there is visible decrease in production of carbon monoxide and unburned hydrocarbons. With increasing engine load the production of carbon monoxide, unburnt hydrocarbons and fuel consumption increases. This is probably caused due to the enrichment of the fuel mixture at a higher load. Reduced combustion efficiency at higher loads confirms the declining production of carbon dioxide. With increasing loads, temperature of combustion rises

due to a larger amount of mixture delivered into the combustion chamber, which corresponds with higher production of nitrogen oxides. At full load, there is probably insufficient amount of oxygen in the mixture and nitrogen oxides emissions are significantly lower.

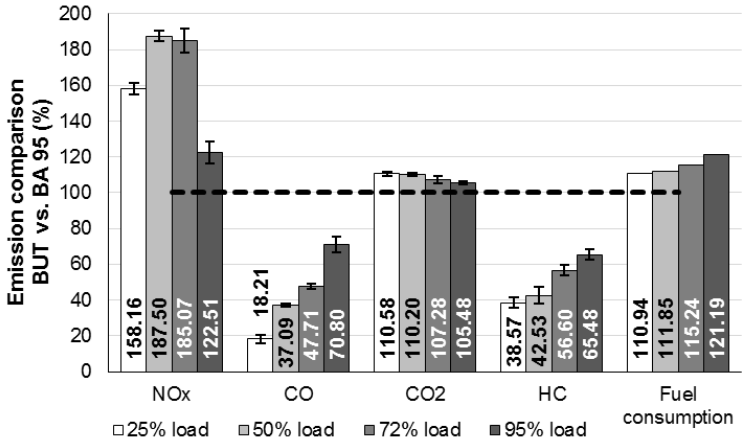

Figure 2. Percentage comparison of harmful emissions and fuel consumption for particular load levels when operating at BUT where BA95 is represented as 100%.

CONCLUSIONS

This paper was aimed on the comparison of exhaust emissions (CO_2, CO, NO_X, HC) of small internal combustion engines fuelled by carburettor, controlled by governor and operated on BA95 petrol and biobutanol. According to results, it can be concluded:

- It was expected that fuel consumption will be higher when operating at butanol due to lower calorific value of butanol. Fuel consumption was about 15% higher in case of butanol.
- When operating at BA95, there was achieved better values of emissions production of NO_X and CO_2 (which is related to fuel consumption). Emissions of NO_X and CO_2 were approximately about 65% and 10% lower than when operating at butanol.
- Conversely, when operating at butanol the better results was achieved in case of CO and HC emissions. Emission decreased significantly about 50%.

Significant improvement in CO and HC emissions during operation at butanol can be associated to a better regulation of the combustion process. When operating at BA95 fuel, the engine operated unattended. When operating at butanol, the air-fuel ratio was monitored and mixture ratio of butanol and air was manually adjusted in order to maintain stoichiometry mixture. Without this intervention the operation of the combustion engine is almost impossible when operating at pure butanol.

The overall engine operation time also influences the production of the exhaust emissions. Therefore, the long-term measurement is needed to confirm the results in real operation conditions.

ACKNOWLEDGEMENTS. Paper was created with the grant support – CZU CIGA 2015-20153001 – Utilization of butanol in internal combustion engines of generators.

REFERENCES

Andersen, V.F., Anderson, J.E., Wallington, T.J., Mueller, S.A. & Nielsen, O.J. 2010. Distillation curves for alcohol-gasoline blends. *Energy and Fuels* **24**(4), 2683–2691.

Alasfour, F.N. 1997. Butanol - A single-cylinder engine study: Availability analysis. *Applied Thermal Engineering* **17**(6), 537–549.

Altun, S., Öner, C., Yaşar, F. & Adin, H. 2011. Effect of n-butanol blending with a blend of diesel and biodiesel on performance and exhaust emissions of a diesel engine. *Industrial and Engineering Chemistry Research* **50**(15), 9425–9430.

Commission of the European Communities. 2009. Directive 2009/28/EC of the European Parliament and of the Council of 23 April 2009 on the promotion of the use of energy from renewable sources and amending and subsequently repealing Directives 2001/77/EC and 2003/30/EC. *Official journal of the European Union L series* **140**(52), 16–62.

Čedík, J., Pexa, M., Kotek, M. & Hromádko, J. 2014a. Effect of E85 Fuel on Harmful Emissions -Škoda Fabia 1.2 HTP. *Agronomy Research* **12**(2), 315–322.

Čedík, J., Pexa, M., Kotek, M. & Hromádko, J. 2014b. Effect of E85 fuel on performance parameters. fuel consumption and engine efficiency - Škoda Fabia 1.2 HTP. *Agronomy Research* **12**(2), 37–314.

Čedík, J., Pexa, M., Mařík, J., Hönig, V., Horníčková, Š. & Kubín, K. 2015. Influence of butanol and FAME blends on operational characteristics of compression ignition engine. *Agronomy Research* **13**(2), 541–549.

Demirbas, A. 2009. Biofuels securing the planet's future energy needs. *Energy Convers Manage*. **50**, 2239–2249.

Dagaut, P. & Togbé, C. 2008. Oxidation kinetics of butanol-gasoline surrogate mixtures in a jet-stirred reactor: Experimental and modeling study. *Fuel* **87**(15–16), 3313–3321.

Dagaut, P. & Togbé, C. 2009. Experimental and modeling study of the kinetics of oxidation of butanol-n-heptane mixtures in a jet-stirred reactor. *Energy and Fuels* **23**(7), 3527–3535.

Dernotte, J., Mounaim-Rousselle, C., Halter, F. & Seers, P. 2010. Evaluation of butanol-gasoline blends in a port fuel-injection. spark-ignition engine. *Oil and Gas Science and Technology* **65**(2), 345–351.

Durre, P. 2007. Biobutanol: an attractive biofuel. *Biotechnol. Journal* **2**, 1525–1534.

Elfasakhany, A. 2014. Experimental study on emissions and performance of an internal combustion engine fueled with gasoline and gasoline/n-butanol blends. *Energy Conversion and Management* **88**, 277–283.

Ezeji, T.C., Qureshi, N. & Blaschek, H.P. 2003. Production of acetone. butanol and ethanol by Clostridium beijerinckii BA101 and in situ recovery by gas stripping. *World Journal of Microbiology Biotechnology* **19**, 595–603.

Feng, R., Fu, J., Yang, J., Wang, Y., Li, Y., Deng, B. & Zhang, D. 2015. Combustion and emissions study on motorcycle engine fueled with butanol-gasoline blend. Renewable Energy **81**, 113–122.

Feng, R., Yang, J., Zhang, D., Deng, B., Fu, J., Liu, J. & Liu, X. 2013. Experimental study on SI engine fuelled with butanol-gasoline blend and H_2O addition. *Energy Conversion and Management* **74**, 192–200.

Gautam, M. & Martin, D.W. 2000a. Emission characteristics of higher-alcohol/gasoline blends. *Proceedings of the Institution of Mechanical Engineers. Part A: Journal of Power and Energy* **214**(2), 165–182.

Gautam, M. & Martin, D.W. 2000b. Combustion characteristics of higher-alcohol/gasoline blends. *Proceedings of the Institution of Mechanical Engineers. Part A: Journal of Power and Energy* **214**(5), 497–511.

Gu, X., Huang, Z., Cai, J., Gong, J., Wu, X. & Lee, C.-F. 2012. Emission characteristics of a spark-ignition engine fuelled with gasoline-n-butanol blends in combination with EGR. *Fuel* **93**, 611–617.

Harvey, B.G. & Meylemans, H.A. 2011. The role of butanol in the development of sustainable fuel technologies. *Journal of Chemical Technology and Biotechnology* **86**, 2–9.

Hönig, V., Orsák, M. & Táborský, J. 2015b. The analysis of the influence of biobutanol and bioethanol mixture with ethers on the vapour pressure of gasoline. *Agronomy Research* **13**(2) pp. 568–576.

Hönig, V., Táborský, J., Orsák, M. & Ilves, R. 2015c. Using gas chromatography to determine the amount of alcohols in diesel fuels. *Agronomy Research* **13**(5), 1234–1240.

Hönig, V., Smrčka, L., Ilves, R. & Küüt, A. 2015a. Adding biobutanol to diesel fuel and impact on fuel blend parametres. *Agronomy Research* **13**(5), 1227–1233.

Qureshi, N. & Ezeji, T.C. 2008. Butanol, a superior biofuel production from agricultural residues (renewable biomass): recent progress in technology. *Biofuels Bioprod Bioref*. 2: 319–330.

Rakopoulos, C.D., Dimaratos, A.M., Giakoumis, E.G. & Rakopoulos, D.C. 2010. Investigating the emissions during acceleration of a turbocharged diesel engine operating with bio-diesel or n-butanol diesel fuel blends. *Energy* **35**(12), 5173–5184.

Rice, R.W., Sanyal, A.K., Eirod, A.C. & Bata, R.M. 1991. Exhaust gas emissions of butanol. ethanol. and methanol-gasoline blends. *Journal of Engineering for Gas Turbines and Power* **113**(3), 377–381.

Serras-Pereira, J., Aleiferis, P.G., Walmsley, H.L., Davies, T.J. & Cracknell, R.F. 2013. Heat flux characteristics of spray wall impingement with ethanol. butanol. iso-octane. gasoline and E10 fuels. *International Journal of Heat and Fluid Flow* **44**, 662–683.

Shapovalov, O.I. & Ashkinazi, L.A. 2008. Biobutanol: Biofuel of second generation. *Russian Journal of Applied Chemistry* **81**(12), 2232–2236.

Swana, J., Yang, Y., Behnam, M. & Thompson, R. 2011. An analysis of net energy production and feedstock availability for biobutanol and bioethanol. *Bioresource Technology* **102**(2), 2112–2117.

Tüccar, G., Özgür, T. & Aydin, K. 2014. Effect of diesel-microalgae biodiesel-butanol blends on performance and emissions of diesel engine. *Fuel* **132**, 47–52.

Wallner, T., Miers, S.A. & McConnell, S. 2009. A comparison of ethanol and butanol as oxygenates using a direct-injection. spark-ignition engine. *Journal of Engineering for Gas Turbines and Power* **131**, 1–9.

Wigg, B.R., Coverdill, R.E., Lee, C.F. & Kyritsis, D.C. 2011. Emissions characteristics of neat butanol fuel using a port fuel-injected. spark-ignition engine. *SAE*, 1–902.

Williams, J., Goodfellow, C., Lance, D., Ota, A., Nakata, K. & Kawatake, K. 2009. Impact of butanol and other bio-components on the thermal efficiency of prototype and conventional engines. *SAE*, 1–1908.

Yacoub, Y., Bata, R. & Gautam, M. 1998. The performance and emission characteristics of C1-C5 alcohol-gasoline blends with matched oxygen content in a single-cylinder spark ignition engine. *Proceedings of the Institution of Mechanical Engineers. Part A: Journal of Power and Energy* **212**(5), 363–379.

Yang, J., Yang, X.L., Liu, J.P., Han, Z.Y. & Zhong, Z.H. 2009. Dyno test investigations of gasoline engine fueled with butanol–gasoline blends. *SAE*, 1–1891.

Yilmaz, N., Vigil, F.M., Benalil, K., Davis, S.M. & Calva, A. 2014. Effect of biodiesel–butanol fuel blends on emissions and performance characteristics of a diesel engine. *Fuel* **135**, 46–50.

Agronomy Research **15**(S1), 1170–1181, 2017

Mechanical qualities of adhesive bonds reinforced with biological fabric treated by plasma

S. Petrásek and M. Müller

Department of Material Science and Manufacturing Technology, Faculty of Engineering, Czech University of Life Sciences in Prague, Kamýcká 129, CZ165 21 Prague, Czech Republic
*Correspondence: petrasek@tf.czu.cz

Abstract. The paper deals with the utilization of a biological reinforcement in the area of an adhesive layer at structural adhesive bonds. A significant disadvantage of adhesive bonds is uneven layer of an adhesive, which can be eliminated by various technological procedures. One possibility is to use a reinforcing even layer. The primary aim of this paper was to experimentally investigate an influence of the surface plasma treatment of natural fabrics (flax, cotton) at different intervals of plasma affecting (0 to 90 seconds and power 350 W) on mechanical properties of the adhesive bond. There were positive results from reinforcing the adhesive bond by a layer of linen and cotton. Strength characteristics of reinforced adhesive bond were increased compared to non–reinforced adhesive bonds. When the linen was used, the strength was increased by 43.2% and when the cotton then 15.5% strength increase could be seen. When modifying the surface by plasma, next adhesive bond's strength increase was seen. Using the linen there was approx. 47% strength increase, using the cotton the strength increase was approx. 38% compared to non–reinforced adhesive bonds (without reinforcing phase). It is obvious from the results that plasma modifying showed better results when the cotton was used as the reinforcing material. SEM analysis proved that adhesion was improved with plasma surface modification of biological fibres. In other words the distance between the warp and the resin was significantly decreased for 87.1% when using the cotton and by 46.5% when the linen was used.

Key words: Cotton, flax, plasma treatment, SEM.

INTRODUCTION

Adhesive bonding technology is a common method of linking in the industry. Various researches deal with different possibilities of how to increase adhesive bond's strength, which would contribute to better results at the practical application. A significant disadvantage of adhesive bonds is an uneven layer of an adhesive, which can be eliminated by various technological procedures. One possibility is to use a reinforced even layer. Main goal in the adhesive bonding technology research is the quality increase of the adhesive bond, especially the strength increase and the increase of the resistance to external factors.

The aim of the adhesive bonding process is to create a bond, which can provide maximum strength and quality for each adhesive and adherent combinations at minimum costs. According to Messler (2004) following conditions have to be met in order to reach that goal:

- Appropriate modification and surface cleanness of adherents before the application of the adhesive. This will cause proper wetting of the adherent by the adhesive.
- Proper choose of the adhesive for each single adherent and prevailing conditions of use.
- To assure constant layer of the adhesive.
- To take into consideration external surrounding factors that can affect adhesive bonds

Use of reinforcing fabrics in the adhesive layer means better distribution of the adhesive. This distribution has to be even. There are different deformations of adhesive layers in adhesive bonds, where even distribution of the adhesive is not guaranteed. This causes less strength of the adhesive bond.

Due to uneven deformation there is different adhesive deformation through a thickness of the adhesive layer. The deformation is biggest at the end of lapping. So called 'stress peaks' are emerged at the edge of the adhesive layer which causes a hyperbolic course of the stress in the whole length of the lapping.

The concentration of the stress at the edge of the adhesive bond is increased by the impact of bending moment. This causes a breach of the adhesive bond. The reason is uneven distribution in the adhesive layer caused by a flexibility and deformations of adhesive materials. This creates pulling stress at the edge of the bond which is a reason of peeling off with related decrease of the strength. A consequence is a spread of leaks and following destruction of the adhesive bond. A significant contribution for adhesive bonds is a reinforcing layer with fabrics. (Researches with fabrics from glass fibres showed positive influence on strength increase of the adhesive bond). Possibilities and limits of fibre–composite materials are subjected to long–term research in different research fields (Fu et al., 2002; Pothan, 2005; Wong et al., 2010; Hong et al., 2012; Zavrtálek & Müller, 2016b).

Composites made from natural (Idicula et al., 2005; Pothan et al., 2007; Zavrtálek & Müller, 2016b) and biologically flawless matrixes play big part in recent researches Schorr et al., 2014; Thakur et al., 2014). Composites made from these materials decrease the impact on nature surroundings during the production process and also after a lifespan of the fibre composites (Shi et al., 2012; Patlolla & Asmatulu, 2013).

The use of the synergic effect which leads to improved adhesive bond's mechanical qualities is well–known technology and nanoparticles are used for this in particular (Park et al., 2009; Dorigato et al., 2010; Ahmad et al., 2012). But the production of nanoparticles is often very costly. Next problem is their even layout in the matrix, caused for example by a sedimentation. This is technologically very difficult process. This fact leads to the research of the appropriate alternatives which use the synergic effect in adhesive bonds. For example the use of synthetic and natural reinforcing fabrics.

Basic characteristics of the fabric are very important in order to use natural and synthetic fabrics in the field of composite materials (material, fibre orientation, specific weight), their wetting with matrix etc. (Fowler et al., 2006; Karbhari & Abanilla, 2007; Lee et al., 2010; Maheri, 2010; Mizera et al., 2016a; Mizera et al., 2016b).

Already published studies showed that natural fibres like linen, jute, hemp, sisal and pineapple have serious advantage compared to the conventional fibres due to their low density (Sankari, 2000; Munawar et al. 2006; Rao & Rao, 2007; Silva et al., 2008;

Alves et al., 2010; Faruk et al., 2012). Thanks to the low density they have high measured strength and toughness.

The most used fibres are from the following plants: sisal, linen, hemp, cotton, jute. Fibres of natural origin are used as cheaper alternative to the glass fibres.

The main disadvantages of natural fillers utilized in the polymeric composites are their low wettability and non–homogeneity (Herrera–Franko & Valadez–Gonza´lez, 2005; Mizera et al., 2016a). The fibres are mostly hydrophilic natural fibres. Especially these factors are a reason for their low tensile strength (Sharifah & Martin, 2004; Alkbir et al., 2016).

These problems can be alleviated through the use of suitable compatibilisers and plasma surface treatment (Hrabě et al., 2016).

The main disadvantage of plant fibres lies in a combination of a non–polar polymer matrix (hydrophobic) and polar plant fibres (hydrophilic). This combination creates a poor interface with a low adhesion of both components. That implies a poor wettability of fibres by the polymer matrix and low mechanical properties of composites (Boruvka et al., 2016).

The good wettability of the matrix and the reinforcement improves an efficiency of a stress transmission from the matrix to the fibre (Müller et al., 2013; Hrabě et al., 2016). The plasma surface treatment is a suitable method. The plasma can influence the surface energy and clean the surface at the same time (Hrabě et al., 2016).

Generally, plasma treatments have the ability to change the surface properties through the formation of free radicals, ions and electrons in the plasma stream (Boruvka et al., 2016; Hrabě et al., 2016). During the plasma treatment, the surface of the substrate is bombarded with high–energy particles. Surface properties such as the wettability, the surface chemistry and the surface roughness of the substrate can be altered as a result, without the need for any hazardous chemicals or solvents (Boruvka et al., 2016).

A major advantage of employing low pressure plasma treatments is that such plasma can be generated at the low power output. The use of the plasma technology is among the most efficient and economical methods of modifying the surface properties of polymers and fibres without affecting the internal structure. The plasma modifies the surface of microfibres by removing weakly attached surface layers and forming new functional groups on the surface (Boruvka et al., 2016).

The paper deals with the utilization of a biological reinforcement in the area of the adhesive layer. An advantage of the biological reinforcement application is a simplification of following recycling of adhesive bonds compared to used carbon and glass fibre based reinforcements. A good wettability of the reinforcing layer improves an efficiency of a stress transfer in the layer of the adhesive. Plasma can influence a surface energy and clean the surface at the same time.

A chemical cleaning is another possibility of a natural fibre treatment. A rise of waste chemical substances is a disadvantage of the chemical cleaning.

The primary aim of this paper was to experimentally investigate an influence of the surface plasma treatment of natural fabrics (flax, cotton) at different intervals of plasma affecting (0 to 90 s and power 350 W) on mechanical properties of the adhesive bond.

MATERIALS AND METHODS

Waste fabrics from the manufacturing industry was used for the research. Cuttings in a form of strips were used. This fabric cannot be used in the textile industry due to its size.

Samples were cut from flax and cotton into strips of 30 x 200 mm. The samples were modified by the plasma treatment (Fig. 1).

The strengthening reinforcement was the fabric of cotton and flax. Flax: the mass of the fabric ca. 300 g m^{-2}, cotton: ca. 150 g m^{-2}. Plasma was generated from a plasma generator (Plasma Reactor KPR 200 mm RM 54) while supplying the reaction gas (oxygen) and maintaining the reactor´s pressure at 0.1 Torr with the use of a vacuum pump.

To determine the properties that depend on the discharge power and the treatment time, the plasma treatment was conducted in the power range 350 W for 15, 30, 60 and 90 s.

Adhesive bonds were prepared in accordance with requirements of the Czech standard ČSN EN 1465. The length of adhesive bonds lapping was 12.5 ± 0.25 mm. Adherents from the structural carbon steel S325J0 were used for the research. Those adherents are in accordance with the Czech standard ČSN EN 1465 as far as the size and the shape are concerned (100 x 25 x 1.5 mm). Samples were lit up by the plasma. There was 48 hours delay before the plasma treatment and the adhesive procedure. A construction of the composite reinforced adhesive bond can be seen in Fig. 2, A.

The arrangement of the reinforcing fabrics, i.e. a weft and a warp in the layer of the adhesive is visible in Fig. 2, A. The warp is a bearing element of the fabric, the weft serves for connecting of fabric.

The surface of adherents was mechanically and chemically treated before the adhesive bonding. The mechanical treatment consisted in grit blasting by the garnet MESH 80 under the angle 90 °. The chemical treatment consisted in the cleaning in a bath of acetone. Using the profilograph Surftest 301 the following values were determined: Ra 1.18 ± 0.08 μm, Rz 6.4 ± 0.96 μm.

A structural two–component epoxy adhesive Glue Epox Rapid (next only Resin) was used in the adhesive bonding process. The reinforcing fabric was put into the layer of the adhesive whose surface was treated for various times in the plasma. The principle consisted in putting the adhesive layer on the first adhesive bonded part, subsequently the fabric was applied and the second adhesive bonded part was attached on which the layer of the adhesive was also deposited. A resulting bond was fixed by a pressure 0.02 MPa. Adhesive bonds were hardened for 48 h under the temperature 22 ± 2 °C and the moisture 65 ± 8%.

The tensile strength test (according to CSN EN 1465) was performed using the universal tensile strength testing machine LABTest 5.50ST (a sensing unit AST type KAF 50 kN, an evaluating software Test&Motion). The course of the test is visible in Fig. 2, B. A speed of the deformation was 5 mm min^{-1}. The deformation speed influences the adhesive bond strength. The research results proved that the adhesive bond strength increased with increasing deformation speed. The research results proved that the time of the adhesive bond destruction according to the requirements of the standard CSN EN 1465 was reached at this speed (Muller et al., 2016). Ten test samples were always tested in single series. The failure type was determined at the adhesive bonds according to ISO 10365.

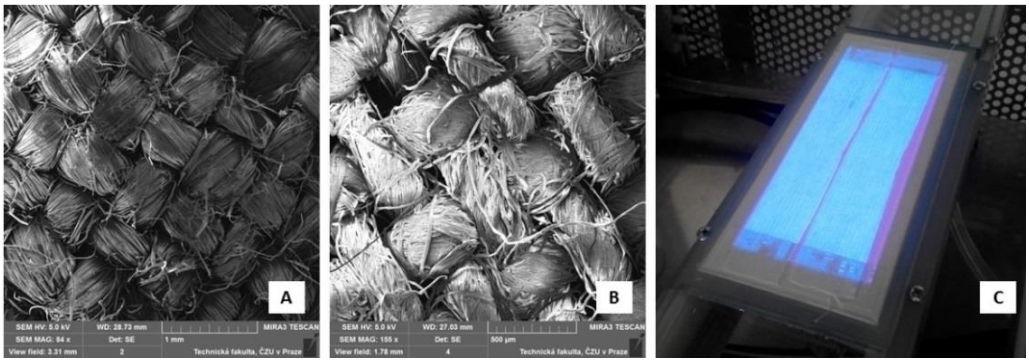

Figure 1. Reinforcing phases. A: SEM images of cotton MAG 84 x, B: SEM images of flax MAG 155 x, C: surface treatment of flax using plasma discharge at 350 W.

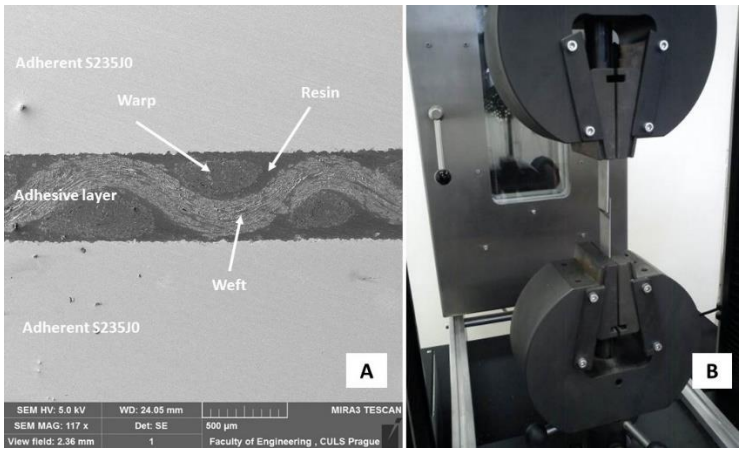

Figure 2. Adhesive bond testing: A: SEM images of cotton – construction of adhesive bond using biological reinforcing fabric (MAG 117 x, secondary electrons), B: tensile strength testing of adhesive bond in universal testing machine LABTest 5.50ST (according to CSN EN 1465).

Fracture surfaces and an adhesive bond cut was examined with SEM (scanning electron microscopy) using a microscope MIRA 3 TESCAN (the fracture surfaces were dusted with gold) at the accelerating voltage of the pack (HV) 5.0 kV and a stereoscopic microscope Arsenal. The difference of the saturation of the various types of fabrics with the epoxy adhesive was observed with SEM.

An evaluation of the shape and the dimensions was performed using the program Gwiddion. The results of measuring were statistically analysed.

Statistical hypotheses were also tested at measured sets of data by means of the program STATISTICA (*F–test*). A validity of the zero hypothesis (H_0) shows that there is no statistically significant difference ($p > 0.05$) among tested sets of data. On the contrary, the hypothesis H_1 denies the zero hypothesis and it says that there is a statistically significant difference among tested sets of data or a dependence among variables ($p < 0.05$).

RESULTS AND DISCUSSION

This experiment brings new pieces of knowledge of how to use biological fabrics in the field of adhesive bonds in order to increase the strength of the adhesive bonds. In the Table 1 there are basic parameters of the adhesive bond. A support frame for the fabric reinforcement is the warp, the weft is used for the fabric connection. The adhesive width showed difference of 9.5%. When the reinforcing fabric was used the difference was decreased to approx. 4.5%. The adhesive layout showed more even distribution when the reinforcing fabric from the flax was used. This finding is very important for the construction of adhesive bonds.

Table 1. Basic characteristics of tested adhesive bonds

Adhesive bond characteristic	Adhesive bond thickness (μm)	Warp – Fabric thickness (μm)
Resin	238.93 ± 22.48	–
Resin and reinforcement in form of linen fabrics	266.05 ± 11.92	9.55 ± 3.36
Resin and reinforcement in form of cotton fabrics	496.66 ± 24.42	14.99 ± 4.04

A graphic presentation of the results of the adhesive bond strength can be seen from Fig. 3. There were positive results from the reinforcing adhesive bond by the layer of the flax and cotton. Strength characteristics of the reinforced adhesive bond were increased compared to non–reinforced adhesive bonds. When the flax was used, the strength was increased of 43.2% and when the cotton then 15.5% strength increase could be seen. When modifying the surface by the plasma, next adhesive bond's strength increase was seen. Using the linen there was approx. 47% strength increase, using the cotton the strength increase was approx. 38% compared to non–reinforced adhesive bonds (without reinforcing phase). It is obvious from the results that the plasma modifying showed better results when the cotton was used as the reinforcing material.

Adhesive bonds without the reinforcing fabric showed an adhesive type of the failure. When the reinforcing material was added, the adhesive failure type changed to adhesive–cohesive type, where the adhesive type was dominating. This result was caused by even distribution of the adhesive.

It is obvious from the results that the reinforcing fabric influences the strength of the adhesive bond, so there is the difference between the adhesive bonds with and without the reinforcement ($p = 0.000$).

The hypothesis H_0 was not certified so there is the difference among tested variants in relation to the adhesive bond strength on the reliability level 0.05. Use of the biological reinforcement from the flax and the cotton can be considered as the significant factor which has the impact on final strength of the adhesive bond.

If we check statistics of testing of the plasma surface modification, we can conclude following findings: When the flax was used as the reinforcing material, the plasma modification did not have any proved effect on the strength of the adhesive bond ($p = 0.641$), when the cotton was used as the reinforcing material, the plasma modification statistically proved the impact on the strength of the adhesive bond ($p = 0.000$).

It is also obvious from the results that different time of the plasma surface modification in interval between 15 up to 90 seconds does not have any impact on the final strength of the adhesive bond (flax $p = 0.872$, cotton $p = 0.343$) on 0.05 reliability level.

The time used for the plasma surface modification of tested biological fabrics cannot be considered as the significant factor in the adhesive bond application.

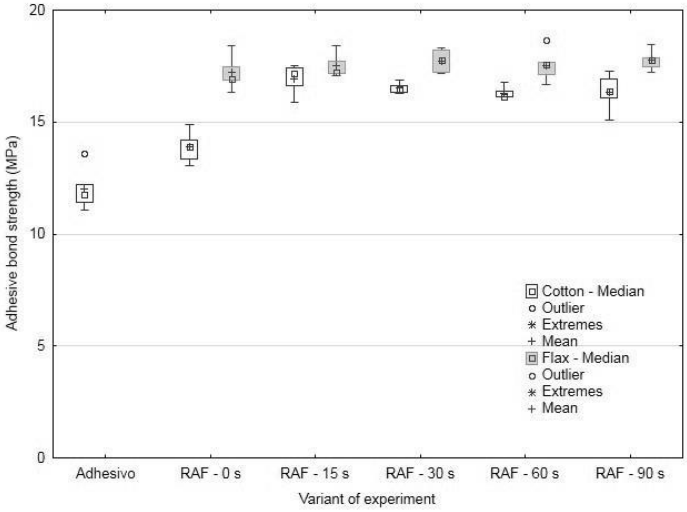

Figure 3. Dependence of adhesive bond strength on plasma surface modification of reinforcing fabric. (adhesive – without reinforcing phase, RAF – adhesive reinforced with fabric, number shows duration for how long plasma was affecting reinforcing fabric in seconds).

SEM (scanning electron microscopy) analysis was used for a study of the fracture surfaces and cuts of the adhesive bonds. SEM analysis enabled to display the quality of the interaction of the reinforcing biological fabric and the resin. It proved better wetting of the structural epoxy adhesive and the reinforcing phase. SEM analysis proved a good wettability of the adhesive bonded material with the adhesive, see e.g. Fig. 4, A and 4, D. This conclusion is essential because the wettability of the adhesive bonded surfaces is crucial for good adhesive strength (Müller, 2011; Rudawska, 2012; Müller & Valášek, 2013; Müller & Valášek, 2014; Müller, 2015; Müller, 2016; Rudawska et al., 2016).

On the Fig. 4, A the layout of the reinforcing fabric is visible, i.e. the weft and the warp in the adhesive layer. The warp is the bearing element of the fabric. On the Fig. 4, A the warp shape of the cotton is apparent. The diameter of the cotton warp was 14.99 ± 4.04 μm. From the Fig. 4, C the flax warp shape is apparent. The diameter of the flax warp was 9.55 ± 3.36 μm. From the Fig. 4, B and 4, C a bad wetting of the warp with the resin is visible. Bad wetting of the reinforcing cotton fabric (warp) and resin was ascertained with the optical analysis, this was showed by the distance 1.16 ± 0.86 μm (Fig. 4, A). Bad wetting of the reinforcing flax fabric (warp) and resin was ascertained with the optical analysis, this was showed by the distance 0.98 ± 0.43 μm. The adhesion was improved by the plasma treatment of biological fibres, i.e. the distance between the warp and the resin was decreased dramatically (Fig. 4, D; 4, E).

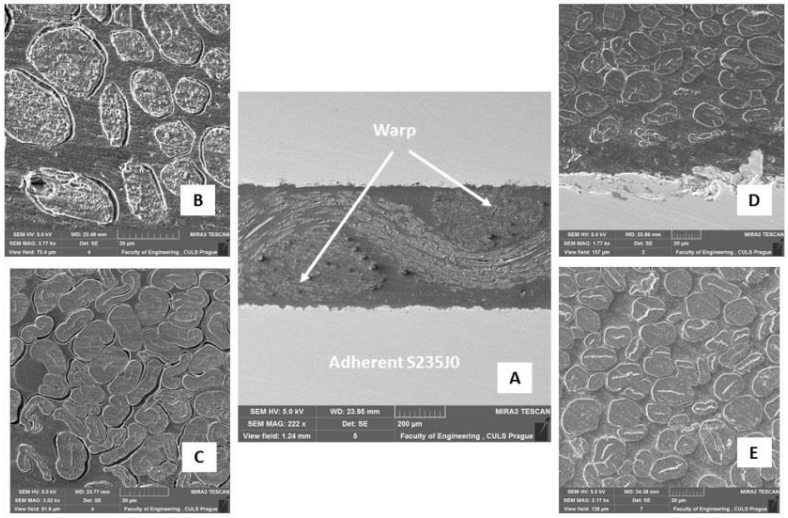

Figure 4. SEM images of cut through adhesive bond reinforced with biological reinforcing fabric (secondary electrons): A: resin reinforced with fabric from cotton MAG 222 x, B: cut through adhesive bond, poor wettability of reinforcing fabric (cotton) with resin (interaction of warp and resin) MAG 3.77 kx, C: cut through adhesive bond, poor wettability of reinforcing fabric (flax) with resin (interaction of warp and resin) MAG 3.02 kx, D: cut through adhesive bond, satisfactory wettability of reinforcing fabric (cotton) with resin after 30 seconds, reinforcing fabric treated by plasma (interaction of warp and resin) MAG 1.77 kx, E: cut through adhesive bond, good wettability of reinforcing fabric (cotton) with resin after 90 seconds reinforcing fabric treated by plasma (interaction of warp and resin) MAG 2.17 kx.

It is obvious from the results shown in Table 2 that the surface plasma treatment improved the adhesion of the resin and biological reinforcing fabric. A significant fall of the distance between the untreated and the plasma treated biological reinforcing fabrics is visible from the experiment results. More significant fall of the distance was at the cotton, up of 75% already at 15 s. The fall was milder at the flax.

Table 2. Impact of surface plasma treatment on distance between biological reinforcing fabrics (warp) and resin

Time of effect of plasma treating of biological material surface (s)		0	15	30	60	90
Cotton	Mean (μm)	1.16	0.29	0.26	0.20	0.15
	Standard deviation (μm)	0.86	0.15	0.09	0.12	0.10
	Variation coefficient (%)	74.51	51.72	35.75	60.00	65.65
Flax	Mean (μm)	0.98	0.68	0.46	0.25	0.23
	Standard deviation (μm)	0.43	0.34	0.20	0.10	0.08
	Variation coefficient (%)	44.26	50.00	43.73	40.00	33.58

The adhesive type of the adhesive bond failure was at the resin. Adhesive bonds with the reinforcing phase were of adhesive (85–95%) – cohesive (5–15%) type (Fig. 5, A & 6, A). It was proved by the SEM that the resin was broken away from the reinforcing fabric at the adhesive bond destruction (Fig. 5, A & 6, A). The cohesive fracture surface was increased up to 80% after reinforcing fabric surface treating by the

plasma (Fig. 5, B & 6, B). This caused much better strength increase of the adhesive bond reinforced with the reinforcing fabrics from cotton. The strength increased by 22.5%. There was no significant strength increase of adhesive bonds reinforced with the flax when they were treated by the plasma. The strength was increased only by 1.5%. However there was the adhesive material deformation when adhesive bonds were weighted, which caused peeling off that consequently causes the formation of the fracture surface. It is obvious from the cohesive/adhesive fracture surface that there is destruction in the adhesive layer (Figs 5, B & 6, B). The destruction in the adhesive layer is caused by a bending moment at the deformation of the adhesive bonded material. This state is caused at thinner adhesive bonded material above all.

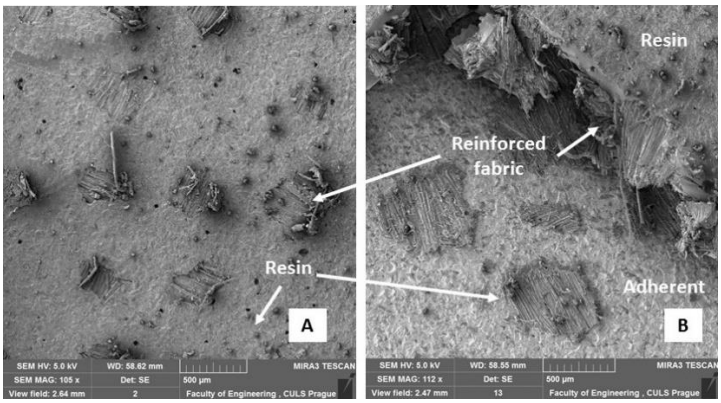

Figure 5. SEM images of fracture surface of adhesive bond reinforced with cotton (secondary electrons): A: Adhesive/cohesive failure – reinforcing fabric without plasma treatment MAG 105 x, B: Cohesive/adhesive failure – reinforcing fabric treated by plasma for over then 90 s MAG 112 x.

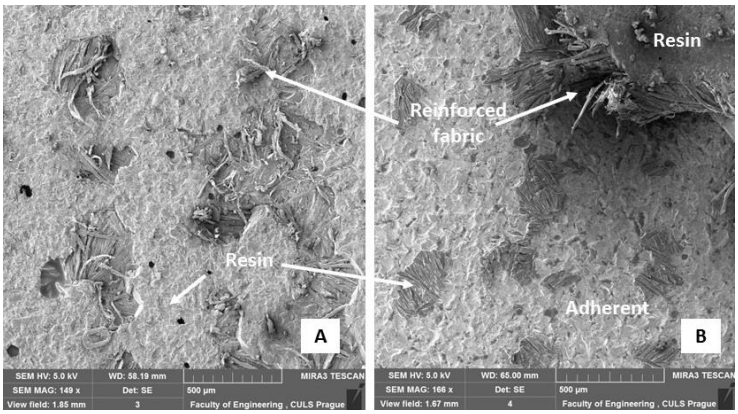

Figure 6. SEM images of fracture surface of adhesive bond reinforced with flax (secondary electrons): A: Adhesive/cohesive failure – reinforcing fabric without plasma treatment MAG 149 x, B: Cohesive/adhesive failure – reinforcing fabric treated by plasma for over then 90 s MAG 166 x.

A positive influence on the adhesive bond strength was proved by using the biological reinforcement. This positive effect was increased by the plasma treatment of the cotton fabric surface. Analogous effect was observed also at synthetic fibres (Müller & Cidlina, 2015; Müller et al., 2016; Zavrtálek et al., 2016; Zavrtálek & Müller, 2016a). Results proved the statement about the positive effect of natural and synthetic fabrics in the adhesive layout. SEM analysis proved worse wetting of the biological reinforcement without previous modification (flax, cotton).

CONCLUSIONS

The experiment results proved a benefit of the reinforcing biological fabric in the layer of the adhesive. The adhesive bond strength was increased of 15.5% at the reinforcing layer based on the cotton and up of 43.2% at the reinforcing layer based on the flax. The reinforcing of the adhesive bond by the layer of the flax and the cotton showed itself in the positive way. However, the biological reinforcement was not fully wetted with structural epoxy adhesive, which did not fundamentally influence the adhesive bond quality. A fracture surface of the adhesive and the adhesive reinforced with the fabric was of the adhesive type, i.e. the strength of the adhesive was not fully utilized. The fracture surface changed when using the plasma treating of the fabric surface. The fracture surface was of the cohesive/adhesive type with prevailing cohesive failure. Ca. 20% increase of the adhesive bond strength at the reinforcement based on the cotton is connected with it. The plasma surface treatment of biological fibres improved the adhesion i.e. the distance between the warp and resin was decreased significantly.

ACKNOWLEDGEMENTS. Supported by Internal grant agency of Faculty of Engineering, Czech University of Life Sciences in Prague.

REFERENCES

Ahmad, Z., Ansell, M.P., Smedley, D. & Md Tahir, P. 2012. The Effect of Long Term Loading on Epoxy–Based Adhesive Reinforced with Nano–Particles for In Situ Timber Bonding. *Advanced Materials Research* **545**, 111–118.

Alkbir, M.F.M., Sapuan, S.M., Nuraini, A.A. & Ishak, M.R. 2016. Fibre properties and crashworthiness parameters of natural fibre reinforced composite structure: A literature review. *Composite Structures* **148**, pp. 59–73.

Alves, C, Ferrao, P.M.C., Silva, A.J., Reis, L.G. Freitas, M., Rodrigues L.B. & Alves, D.E. 2010. Ecodesign of automotive components making use of natural jute fiber composites. *Journal of Cleaner Production* **18**, pp. 313–327.

Boruvka, M., Ngaowthong, Ch., Cerman, J. Lenfeld, P. & Brdlik, P. 2016. The Influence of Surface Modification Using Low–Pressure Plasma Treatment on PE-LLD/α-Cellulose. *Composite Properties* **16**–**1**, 29–34.

Dorigato, A., Pegoretti, A., Bondioli, F. & Messori, M. 2010. Improving Epoxy Adhesives with Zirconia Nanoparticles. *Composite Interfaces **17***–**9**, pp. 873–892.

Faruk, O., Bledzki, A.K., Fink, H.P. & Sain, M. 2012. Biocomposites reinforced with natural fibers: 2000–2010. *Progress in Polymer Science* **37**, 1552–1596.

Fowler, P.A., Hughes, J.M. & Elias, R.M. 2006. Biocomposites: Technology, environmental credentials and market forces: *Journal of the Science of Food and Agriculture* **86**(12), 1781–1789.

Fu, S.Y. Mai, Y.W. Lauke, B. & Yue, C.Y. 2002. Synergistic effect on the fracture toughness of hybrid short glass fiber and short carbon fiber reinforced polypropylene composites. *Materials Science and Engineering A*, **323**(1–2), pp. 326–335.

Hrabe P., Müller, M. & Mizera, C. 2016. The Effect of Plasma Treatment on Tensile Strength of Ensete Ventricosum Fibres. *Manufacturing Technology* **16**–**5**, 928–933.

Herrera Franco, P.J. & ValadezvGonza´lez, A. 2005. A study of the mechanical properties of short natural–fiber reinforced composites. *Composites: Part B* **36**, 597–608.

Hong, H.M. Li, M. Zhang, J.Y. & Zhang, Y.N. 2012. Compressive Strength of CCF300/QY8911 Composite Laminates with LVI Damage. *Advanced Materials Research* **583**, pp. 203–206.

Idicula, M. Malhotra, S.K. Joseph, K. & Thomas, S. 2005. Effect of layering pattern on dynamic mechanical properties of randomly oriented short banana/sisal hybrid fiber-reinforced polyester composites. *Journal of Applied Polymer Science* **97-5**, pp. 2168–2174.

Karbhari, V.M. & Abanilla, M.A. 2007. Design factors, reliability, and durability prediction of wet layup carbon/epoxy used in external strengthening. *Composites Part B: Engineering* **38**(1), 10–23.

Lee, J., Cho, M., Kim, H.S. & Kim, J.S. 2010. Layup optimization of laminated composite patches considering uncertainty of material properties. In *Collection of Technical Papers - AIAA/ASME/ASCE/AHS/ASC Structures, Structural Dynamics and Materials Conference*. Retrieved from http://www.scopus.com/inward/record.url?eid=2-s2.0-84855621588&partnerID=tZOtx3y1

Maheri, M.R. 2010. The effect of layup and boundary conditions on the modal damping of FRP composite panels. *Journal of Composite Materials **45***(**1**3), 1411–1422.

Messler, R.W. 2004. Joining of Materials and Structures Structures: From Pragmatic Process to Enabling Technology. Burlington, *Elsevier*, pp. 790.

Mizera, Č., Hrabě, P. Müller, M. & Herák, D. 2016a. Creep behaviour of the polymer composite with false banana's fibres (Ensete Ventricosum). *Manufacturing Technology* **16**(1), 188–192. ISSN: 1213–2489.

Mizera, Č., Herák, D., Hrabě, P., Müller, M. & Kabutey, A. 2016b. Effect of Length of False Banana Fibre (Ensete ventricosum) on Mechanical Behaviour under Tensile Loading. *Scientia Agriculturae Bohemica* **47**(2), 90–96. ISSN: 1211–3174.

Munawar, S.S., Umemura, K. & Kawai, S. 2006. Characterization of the morphological, physical, and mechanical properties of seven nonwood plant fiber bundles. *Journal of Wood Science* **53**, 108–113.

Müller, M. 2011. Influence of surface integrity on bonding process. *Research in Agricultural Engineering (Zemědělská technika)* **57**(4) 153–162. (in Czech)

Müller, M. 2015. Research on surface treatment of alloy AlCu4Mg adhesive bonded with structural single–component epoxy adhesives. *Manufacturing Technology* **15**(4), 629–633.

Müller, M. 2016. Experimental research on load capacity, treatment of adhesively bonded surface and failure process of structural t–joint. *Acta Universitatis Agriculturae et Silviculturae Mendelianae Brunensis* **64**(2), 473–479.

Müller, M. & Cidlina, J. 2015. Research of loading of structural bonds created with one–component epoxy adhesives. *Manufacturing Technology* **15**(2), 183–188. ISSN: 1213–2489.

Müller, M., Herák, D. & Valášek, P. 2013. Degradation limits of bonding technology depending on destinations Europe, Indonesia. In: *Tehnicki Vjesnik–Technical Gazette* **20**(4), 57–575.

Müller, M. & Valášek, P. 2013. Assessment of bonding quality for several commercially available adhesives. *Agronomy Research* **11**(1), 155–162.

Müller, M. & Valášek, P. 2014. Optimization of surface treatment of carbon steel in area of adhesive bonding technology with application of quik–setting adhesives. *Manufacturing Technology* **14**(4), 579–584.

Müller, M., Valášek, P., Ruggiero, A. & D´Amato, R. 2016. Research on influence of loading speed of structural two–component epoxy adhesives on adhesive bond strength. In *International Conference on Manufacturing Engineering and Materials 06.06.2016, Nový Smokovec*. Nový Smokovec: Procedia Engineering, pp. 340–345.

Park, S.W., Kim, B.C. & Lee, D.G. 2009. Tensile Strength of Joints Bonded With a Nano–particle–Reinforced Adhesive. *Journal of Adhesion Science and Technology* **23**(1), 95–113.

Patlolla, V.R. & Asmatulu, R. 2013. Recycling and reusing fiber-reinforced composites. In Recycling: *Technological Systems, Management Practices and Environmental Impact Nova Science Publishers*, Inc., pp. 193–207.

Pothan, L.A. 2005. The Static and Dynamic Mechanical Properties of Banana and Glass Fiber Woven Fabric-Reinforced Polyester Composite. *Journal of Composite Materials* **39**(11), pp. 1007–1025.

Pothan, L.A., Cherian, B.M., Anandakutty, B. & Thomas, S. 2007. Effect of layering pattern on the water absorption behavior of banana glass hybrid composites. *Journal of Applied Polymer Science* **105**(5), 2540–2548.

Rao, K.M.M. & Rao, K.M. 2007. Extraction and tensile properties of natural fibers: Vakka, date and bamboo. *Composite Structures* **77**, 288–295.

Rudawska, A. 2012. Surface Free Energy and 7075 Aluminium Bonded Joint Strength Following Degreasing Only and Without Any Prior Treatment. In: *Journal Adhesion Science and Technology* **26**, pp. 1233–1247.

Rudawska, A., Danczak, I., Müller, M. & Valášek, P. 2016. The effect of sandblasting on surface properties for adhesion. *International journal of adhesion* **70**, 176–190.

Sankari, H.S. 2000. Comparison of bast fibre yield and mechanical fibre properties of hemp (Cannabis sativa L.) cultivars. *Industrial Crops and Products* **11**, 73–84.

Sharifah, H.A. & Martin, P.A. 2004. The effect of alkalization and fiber alignment on the mechanical and thermal properties of kenaf and hemp bast fiber composites: Part 1 – polyester resin matrix. *Composites Science and Technology* **64**, 1219–30.

Shi, J.., Bao, L., Kobayashi, R., Kato, J. & Kemmochi, K. 2012. Reusing recycled fibers in high-value fiber-reinforced polymer composites: Improving bending strength by surface cleaning. *Composites Science and Technology **72***(11), pp. 1298–1303.

Schorr, D., Diouf, P.N & Stevanovic, T. 2014. Evaluation of industrial lignins for biocomposites production. *Ind.Crop. Prod*. **52**, 65–73.

Silva, F.A., Chawla, N. & Filho, R.D.T. 2008. Tensile behavior of high performance natural (sisal) fibers. *Composites Science and Technology* **68**, 3438–3443.

Thakur, V.K., Thakur, M.K., Raghavan, P. & Kessler, M.R. 2014. Progress in green polymer composites from lignin for multifunctional applications: A review. *ACS Sustain. Chem. Eng.* **2**, 1072–1092.

Wong, K., Nirmal, U. & Lim, B. 2010. Impact behavior of short and continuous fiber-reinforced polyester composites. *Journal of Reinforced Plastics and Composites* **29-23**, 3463–3474.

Zavrtálek, J. & Muller, M. 2016a. Low-cyclic fatigue test of adhesive bond reinforced with biodegradable fabrics. *Manufacturing technology*, **6**, 1205–1211.

Zavrtálek, J. & Müller, M. 2016b. Research on mechanical properties of adhesive bonds reinforced with fabric with glass fibres. *Manufacturing Technology* **16**(1), 299–304.

Zavrtálek, J., Müller, M. & M. Šleger, V. 2016. Low–cyclic fatigue test of adhesive bond reinforced with glass fibre fabric. *Agronomy Research* **14**, 1138–1146.

Agronomy Research **15**(S1), 1182–1188, 2017

Indirect measurement of the battery capacity of smart devices

H. Pihlap*, A. Annuk, A. Allik and M. Hovi

Institute of Technology, Estonian University of Life Sciences, Kreutzwaldi 56, EE51014, Tartu, Estonia
*Correspondence: heino.pihlap@student.emu.ee

Abstract. A crucial part of portable electronic devices (smartphones, smart watches, Tablet PCs, GPS devices, etc.) are the batteries. The dominant trend in the design of these devices is such that the users are not supposed to replace the batteries, i.e. the device's battery is meant to last for the entire lifetime of the device. This makes it important to know the capacity of the battery in order to estimate the expected life of the portable device. As there is no access to the terminals of these batteries, it is not possible to use traditional direct methods to evaluate the capacity of the battery and an indirect method needs to be used. The aim of the given research is to propose different indirect methods of battery capacity measurement and assess their accuracy.

Key words: smart device, battery life, capacity, indirect measurement.

INTRODUCTION

The present study focuses on universal indirect capacity measurement methods for lithium-ion batteries. As more and more devices (smartphones, tablets, GPS devices, e-readers, video cameras, etc.) are designed in such a way that their batteries cannot be replaced by the consumer, it is important to know the capacity of these batteries, because the expected life of the equipment is directly dependent on it. The problem with these batteries is, that the terminals of integrated batteries are not accessible for measurement and therefore indirect methods are needed.

The vast majority of portable devices use a Lithium-Ion (Li-on) battery. There is even a need to assess the capacity of unused or less used Li-on batteries, because the capacity of batteries decreases over time, regardless of use (Williard et al., 2013, Keil et al., 2016). Previous research on Li-on battery charging has been done by (Chun et al., 2015; Vo et al., 2015) and specifically on the capacity of Li-on batteries by (Weng et al., 2013; Weng et al., 2016). The algorithms for state of charge and energy estimation of Li-on batteries have been explored by (He et al., 2011; Chaoui & Gualous 2016; Zhang et al., 2017).

Li-on batteries are extremely sensitive to both overloading and excessive emptying and, as a result, are always equipped with a control module. The purpose of the module is to interrupt the connection between the battery and the charger and/or energy consuming device if necessary, depending on whether the battery temperature has risen too high, the battery is fully charged or the battery has emptied to the allowed limit (Chao et al., 2014). Overcharging of Li-on batteries should be avoided, because it leads to a

rise of the internal temperature, which can cause the battery to ignite (Wang et al., 2012). Excessive emptying, in turn, can lead to deterioration of the battery (Zheng et al., 2015).

There are several CPU based (software) methods, which measure the capacity of a device's battery (Rong & Pedram, 2006). In these cases, the control module acts as a measurement tool by being in direct contact with the terminals of the battery. As such, these methods should be classified as methods of direct measurement because the calculations are made based on the results measured from the terminals. All devices that use Android or iOS operating systems, and for which numerous applications have been created, belong in this category. However, there also exist many devices, with which these methods cannot be used because the end user is unable to install applications (e.g. GPS devices, power banks).

Consequently the proposed method of capacity measurement for these devices is to measure the energy used in the charging process and assess how much of the energy stored in the battery is usable.

MATERIALS AND METHODS

Method 1

The units Wh and mAh are usually used to describe the maximum usable energy E_n stored in the batteries of the analysed devices e.g. 4,000 mAh /14.8Wh. However, these are units of electric charge and do not directly describe the usable energy in the battery. The more frequently used unit Ah is not a SI unit and describes a situation in which the battery provides the stated current during an hour, operating at the rated voltage V_n. For the purpose of this paper, we will instead use their corresponding energy values. In order to express the receivable energy from the battery in SI units (J), the Ampere hours must be multiplied by the nominal voltage V_n and 3,600 seconds.

The first step in this method for the measurement of the capacity of an integrated battery, is to apply a load to the device until it shuts down. As the device turns itself off before the battery is fully discharged, a residual energy of E_r remains in the battery, which with the usable energy E_{usable} forms the actual energy $E_{actural}$. Since the capacity of each Li-on battery decreases with time, then $E_{usable} < E_N$. By leaving the device in the the off position, and by charging its battery to full capacity, we can measure the energy (E_{charge}) that is used to charge the battery. The energy can be calculated with formula 2.

$$E_{charge} = \sum_{i=1}^{n} I_i \cdot V_i \cdot t_i, \quad (1)$$

where n – number of measurements, I_i – charging current (A); V_i – charging voltage (V); t_i – measurement interval (s).

The stored useful energy can be calculated with the following formula:

$$E_{charge} = E_{usable} + E_{loss} + E_{cm}\,, \quad (2)$$

where E_{usable} – stored useful energy (J); E_{loss} – energy loss while charging the battery (J); E_{cm} – self-consumption of control module (J). Hence

$$E_{usable} = E_{charge} - E_{loss} - E_{cm}, \quad (3)$$

E_{loss} can not be measured but it is known that the efficiency factor of Li-on batteries typically is in the range of 95 % (Espinar & Mayer, 2011). Hence:

$$E_{usable} = 0.95(E_{charge} - E_{cm}) \quad (4)$$

E_{cm} can be found by measuring the off-mode power consumption of the fully charged device. All energy consumed in that state is used for the self-consumption of the control module, because when the battery is fully charged, the control module disconnects the device from the charger to prevent overcharge.

Taking into account the time spent on charging, we can calculate the E_{cm}:

$$E_{cm} = \sum_{i=1}^{n} I_{cm} \cdot V_{cm} \cdot t_i, \quad (5)$$

where n is the number of measurements; I_{cm} – charging current of disconnected battery (A) ; V_{cm} – charging voltage of disconnected battery (V); t_i – measurement interval (s).

How much of the initial capacity of the battery is maintained can be calculated with the following equation:

$$\frac{E_{cm}}{E_N} \cdot 100\%, \quad (6)$$

How much of the initial capacity of the battery is maintained depends on the number of cycles that the battery has underwent and on the age of the battery.

Method 2

The second method (Method 2) uses a separate power bank to measure the battery (Table 1). For this purpose the test device is burdened until it switches off, the power bank is fully charged and used to charge the test device, and after the charging is complete, the remaining energy in the power bank is measured.

Table 1. Used equipment

Equipment	Method 1	Method 2
Tested device	Sony Xperia V	Sony Xperia V
Battery	E_N = 1,700 mAh and V_N = 3.7 V	E_N = 1,700 mAh and V_N = 3.7 V
Charger	LG, 5 V, 0.7 A	LG, 5 V, 0.7 A
Measurement device	Agilent 34972a	Agilent 34972a
Power bank	-	RIVACASE VA2004 4,000 mAh
Additional load	-	USB powered lamp, P_N = 3W
Used software	Spreadsheet software	MathCad

Knowing the capacity of the power bank, we can easily calculate the amount of energy spent on charging the device. Since it is possible to burden the power bank with a USB device, then by knowing the power it consumes (P_N) and measuring the time until it shuts down, we can calculate the total receivable energy E_{pb} from the power bank.

$$E_{pb} = P_N \cdot t, \quad (7)$$

The residual energy (E_r) in the power bank after charging the test device can be calculated similarly by using the time (t_r) during which the residual power is consumed.

$$E_r = P_N \cdot t_r, \quad (8)$$

Energy spent on charging test device (E_{charge}) can be calculated with:

$$E_{charge} = E_{pb} - E_r, \tag{9}$$

It is not possible to measure the self-consumption of the control module (E_{cm}) using this method, so it will not be taken into account for this experiment.

$$E_{usable} = 0.95 \cdot E_{charge}, \tag{10}$$

$$\frac{E_{usable}}{E_N} \cdot 100\%, \tag{11}$$

The phone's battery (described in Table 1) was previously burdened with an electrical load to a state, where it had shut off automatically (the battery control module had disconnected the battery from the device before it was fully discharged. The phone was connected to the charger through the measuring device and the voltage and current were measured with 2 second intervals. The experiments were held at room temperature 20 °C.

RESULTS AND DISCUSSION

Method 1

The course of the charging process in relation to the power consumption is characterized by Fig. 1. The total· E_{charge} calculated according to Eq. (2) is 19,350.55 J. We can see from Fig. 2 that the current stabilizes at 0.075 (A) at the end of the charging, which is the self-consumption of the control module (I_{cm}), therefore according to Eq. (6) E_{cm} = 3,631.76 J and according to Eg. (5) E_{usable} = 14,932.85 J. On the basis of the aforementioned findings the the maximum usable energy (E_N) is 22,644 J. Hence E_{usable}/E_N =65.95% (Eq. 10). So 65.95% of the initial capacity has remained. Fig. 1 shows the strength of current during the charging process.

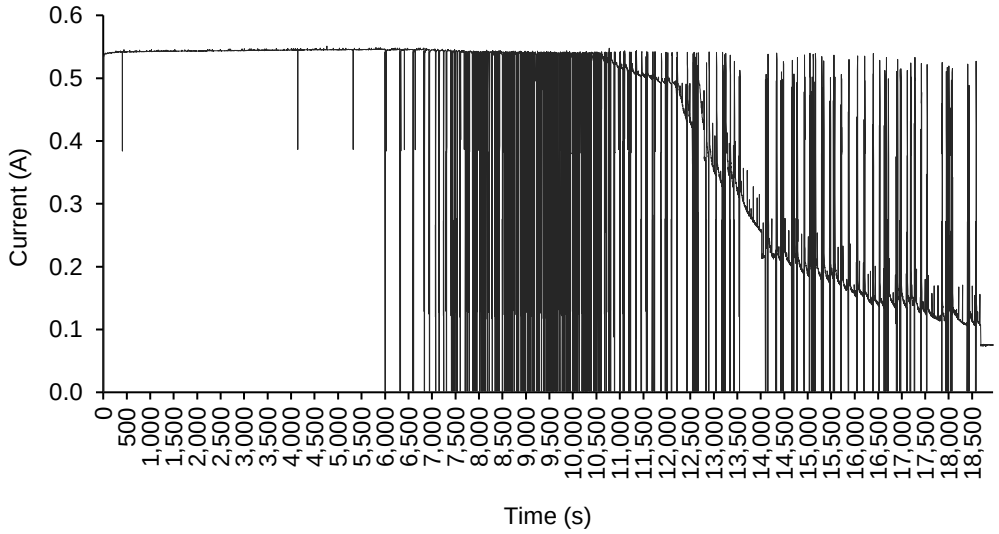

Figure 1. Current during the charging process.

The battery is charged with current pulses with changing frequency during the charging process. The frequency is high until the middle and begins to drop towards the end of the charging process. The charging rate is controlled by varying the width of the pulses. Rest periods between pulses allow chemical reactions to stabilize in the battery. This enables to charge the battery faster and with higher efficiency (Yin et al., 2015). Fig. 2 shows a close up of the current strength at the end of the charging process.

The current drops when the charging process reaches its end (Fig. 2).

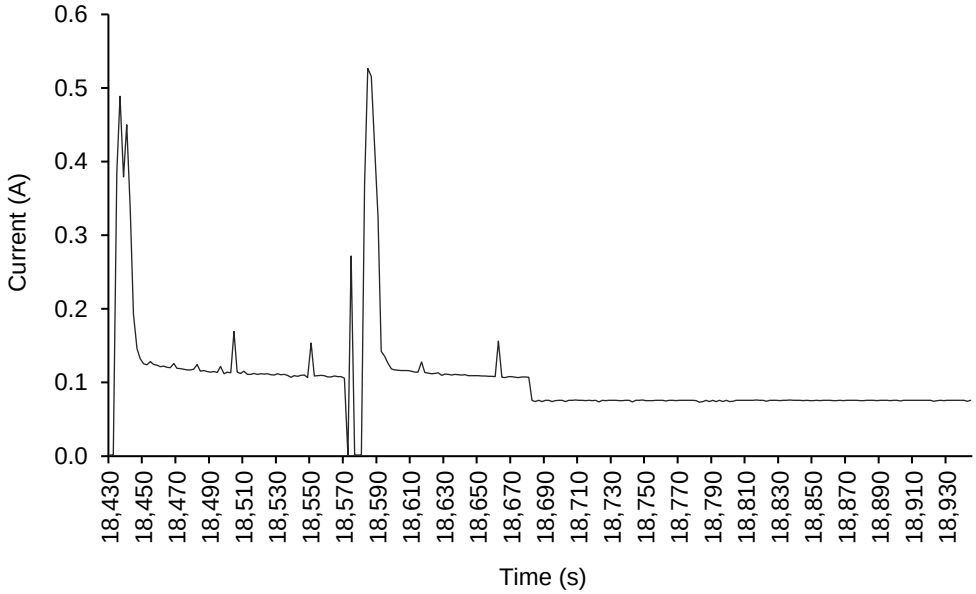

Figure 2. Current at the end of the charging process.

Method 2

The second method involved the discharging of the fully charged power bank. The power bank was connected to a 3 W lamp until it was discharged, which took 13,306 seconds. Thus, the receivable energy from the power bank is E_{pb}=3·13,306=39,918 J.

The test device was burdened until the battery was fully discharged and was then charged using the precharged power bank until the test device signalled that the battery was fully charged. The power bank was then again burdened with a 3W lamp until it was discharged, which took 8,014.00 seconds (2 hours and 14 minutes). The experiments were made at room temperature 20 °C.

Consequently:

E_r = 8,014·3 = 24,042.00 J;

E_{charge} = 39,918 – 24,042 = 15,276.00 J;

E_{usable} = 0.95·15,276 = 14,512.20 J;

$E_{cm}/E_n \cdot 100\%$=64.00%.

From Table 2 can be seen that the both applied methods give similar results. The differences were insignificant. Despite that, it has to be considered that method 2 is designed to be used by everyone, and therefore there is some trade-off in accuracy.

Table 2. Comparizon of results from the applied methods

	Method 1	Method 2
E_{usable}, J	14,932.00	14,512.20
E_{usable}, mAh	1,121.15	1,089.50
E_{usable}, %	65.95	64.00

CONCLUSIONS

Despite the different degrees of precision between methods, the results were within the error margin, so that reasonable assumptions can be made about the supposed service life of the test device. An interesting result is that the capacity results were lower using the second method than with the first method. In theory, the second method should have shown a higher result than the first method, as the self-consumption of the control module was included in the useful energy. The reason for this not being the case is probably a result of the test device prematurely signalling that the battery is fully charged.

For further research, different devices should be tested numerous times using both methods in order to gain more information about the precision of the measurements. In this study, it can be said that the second method is accurate enough to measure the capacity of the test device, especially if a power bank with a marginally bigger capacity is used, which shortens the time spent on testing the battery.

ACKNOWLEDGEMENTS. This research was funded by the Estonian Centre of Excellence in Zero Energy and Resource Efficient Smart Buildings and Districts, ZEBE, grant TK146 funded by the European Regional Development Fund.

REFERENCES

Caihao, W., Cui, Y., Sun, J. & Peng, H. 2013. On-Board State of Health Monitoring of Lithium-Ion Batteries Using Incremental Capacity Analysis with Support Vector Regression. *Journal of Power Sources* **235**, 36–44.

Chao, P.C.P., Wei, D.C. & Ruo, H.W. 2014. A Battery Charge Controller Realized by a Flyback Converter with Digital Primary Side Regulation for Mobile Phones. *Microsystems Techn*ologies **20**(8–9), 1689–1703.

Chaoui, H. & Gualous, H. 2016. Adaptive State of Charge Estimation of Lithium-Ion Batteries With Parameter and Thermal Uncertainties. *IEEE Transaction on Control Systems Tech*nology **25**(2), 752–759.

Chun, C.Y., Baek, J., Seo, G., Cho, B.H., Kim, J., Changc, I.K. & Lee, S. 2015. Current Sensor-Less State-of-Charge Estimation Algorithm for Lithium-Ion Batteries Utilizing Filtered Terminal Voltage. *Journal of Power Sources* **273**, 255–263.

Espinar, B. & Mayer, D. 2011. The role of energy storage for mini-grid stabilization, Report, IEA-PVPS T11-0X:2011.

He, W., Williard, N., Osterman, M. & Pecht, M. 2011.Prognostics of lithium-ion batteries based on Dempster–Shafer theory and the Bayesian Monte Carlo method. *Journal of Power Sources* **196**(23), 10314–10321.

Keil, P., Schuster, S.F., Wilhelm, J., Travi, J. & Hauser, A. 2016. Calendar Aging of Lithium-Ion Batteries: I. Impact of the Graphite Anode on Capacity Fade . *Journal of The Electrochemical Society* **163**(9), 1872–1880.

Rong, P. & Pedram, M. 2006. An Analytical Model for Predicting the Remaining Battery Capacity of Lithium-Ion Batteries. *IEEE Transactions on Very Large Scale Integration (VLSI) Systems* **14**(5), 441–451.

Vo, T.T., Xiaopeng, C., Weixiang, S. & Ajay, K. 2015. New Charging Strategy for Lithium-Ion Batteries Based on the Integration of Taguchi Method and State of Charge Estimation. *Journal of Power Sour*ces **273**, 413–422.

Wanga, Q., Pinga, P., Zhaoa, X., Chub, G., Suna, J. & Chenc, C. 2012. Thermal Runaway Caused Fire and Explosion of Lithium Ion Battery. *Journal of Power Sources* **208**, 210–224.

Weng, C., Yujia, C., Jing, S. & Huei, P. 2013. On-Board State of Health Monitoring of Lithium-Ion Batteries Using Incremental Capacity Analysis with Support Vector Regression. *Journal of Power Sour*ces **235**, 36–44.

Weng, C., Xuning, F., Jing, S. & Huei, P. 2016. State-of-Health Monitoring of Lithium-Ion Battery Modules and Packs via Incremental Capacity Peak Tracking. *Applied Energy* **180**, 360–368.

Williard, N., He, W., Osterman, M. & Pecht, M. 2013. Comparative analysis of features for determining state of health in lithium-ion batteries. *International Journal of Prognostics and Health Management* **4**, 1–7.http://www.calce.umd.edu/articles/abstracts/2013/13_comparative_analysis_of_features_for_determining_state_of_health_in_lithium_ion_batteries.html

Yin, M. Di, Youn, J., Park, D. & Cho, J. 2015. Dynamic Frequency and Duty Cycle Control Method for Fast Pulse-Charging of Lithium Battery Based on Polarization Curve. *Ninth International Conference on Frontier of Computer Science and Technology* **9**, 40–45.

Zhang, Y., Rui, X., Hongwen, H. & Weixiang, S. 2017. Lithium-Ion Battery Pack State of Charge and State of Energy Estimation Algorithms Using a Hardware-in-the-Loop Validation. *IEEE Transactions on Power Electronics* **32**(6), 4421–431.

Zheng, Y., He, Y., Qian, K., Li, B., Wang, X., Li, J., Chang, S., Miao, C., Kang, F. & Zhang, J. 2015. Deterioration of Lithium Iron Phosphate/graphite Power Batteries under High-Rate Discharge Cycling. *Electrochimicia Acta* **176,** 270–279.

Agronomy Research **15**(S1), 1189–1197, 2017

Experimental evaluation of hydraulic design modifications of radial centrifugal pumps

M. Polák

Czech University of Life Sciences in Prague, Faculty of Engineering, Kamýcká 129, CZ165 21, Praha 6, Czech Republic
Correspondence: karel@tf.czu.cz

Abstract. In the field of small hydropower, pump units in turbine mode (PAT) are frequently used as alternative to conventional turbines. In order to maximize their operation efficiency, it is possible to optimize the performances of these engines through various simple innovative modifications which relate mainly to the geometry of the flow parts. This paper deals with the results of several successful modifications verified on one such engine. While various simple modifications led to the increase of overall efficiency and power output by few percentages, power output increased by nearly 30% with the innovated runner blades geometry. The modifications also had positive effects on the pump's operation, with significant increases in flow rate, head and total efficiency.

Key words: pump as turbine (PAT), efficiency, inovation, turbine mode, pump mode.

INTRODUCTION

One major driving force for innovations has been the effort to improve the efficiency of machines in operation, a trend which in recent time has been supported by EU legislation (Directive 2009/125/EC). Regulations focused specifically on hydraulic machines (Commission regulation (EU) No 547/2012) specify a so called minimum energy efficiency index (MEI) of at least 0.1 which means in practice that 10% of pumps with the lowest efficiency must be withdrawn from the EU market. From January 1, 2015, this index must be at least 0.4, which means it will be necessary to replace 40% of the pumps on the European market (Nevěřil, 2012).

Centrifugal pumps are often used in hydropower as alternative to conventional water engines due to their reversibility – their ability to convert hydraulic energy to mechanical energy. Such applications are financially highly attractive alternatives to conventional turbines. Properties of pumps in turbine mode are described in literature (Alatore 1994; Derakhshan, et al. 2008; Sedlář 2009; Bláha 2011; Nautiyal, et al. 2011; Singh & Nestmann, 2011; Pochylý, et al. 2013; Raman, et al. 2013). Since smaller pumps usually have lower efficiency, the issue of their optimization in turbine mode can be targeted. Although some modifications have been tested and described (Gülich 2003; Singh 2005; Singh, et al. 2012), results of detailed studies on the subject are still missing in literature. This article follows on research published in (Poláková & Polák, 2016).

MATERIALS AND METHODS

Pump modifications and verification tests

Based on above mentioned existing researches and own hydraulic calculations, innovative modifications for pump optimization were proposed. They are designed primarily to increase the efficiency of the turbine pump operation but, at the same time not to reduce the effectiveness of the pumping operation. The concept of the modifications is based on the theory of fluid flow through radial hydrodynamic machines according to Hýbl (1928), Nechleba (1962), Nechleba (1966), Melichar et al. (1998), Munson et al. (2006), Ulrych (2007), Polák & Polak (2010). Other minor modifications resulted from technical documentation and the experiences described in Singh (2005), Polák (2013), Poláková & Polák (2016). Modifications were designed to be, in terms of feasibility as simple as possible while being at the same timeapplicable to already existing pumps. Summary description of the two 'most successful' modifications is given below in Table 1.

Table 1. Summary of tested variations

Variation	Description
A	Original unmodified pump – in characteristics indicated by dashed lines.
B	Pump with modified impeller and modified spiral casing – in characteristics indicated by full lines. Modifications consisted in arrangements that led to reduction of local and friction losses in impeller and spiral casing
C	Pump with new impeller blades geometry and modified spiral casing – in characteristics indicated by double lines. New geometry of the blades was designed on the base of the theory of fluid flow in specific low-speed hydrodynamic machines. Spiral casing modification is the same as in variation B – minimization of friction and local losses

For experimental verification of the proposed modifications, a single-stage centrifugal pump with spiral casing was selected. The pump's scheme, including its parameters as provided by the manufacturer is shown in Fig. 1.

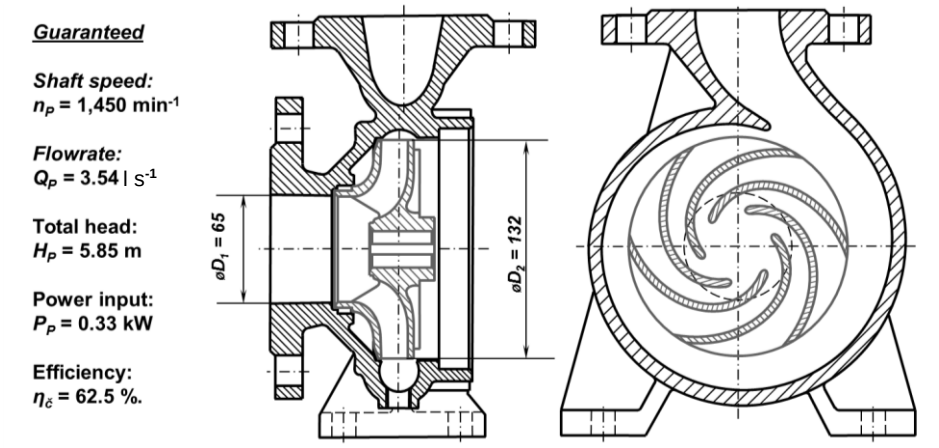

Figure 1. Centrifugal pump for experimental tests and original pump parameters.

Verification tests were conducted on a hydraulic circuit in the Fluid Mechanics laboratory at the Faculty of Engineering, Czech University of Life Sciences Prague. The circuit diagram is shown in Fig. 2. In the first stage characteristics of the pump and its modifications in the turbine mode were measured. Subsequently the effect of the modifications in the pump operation was verified.

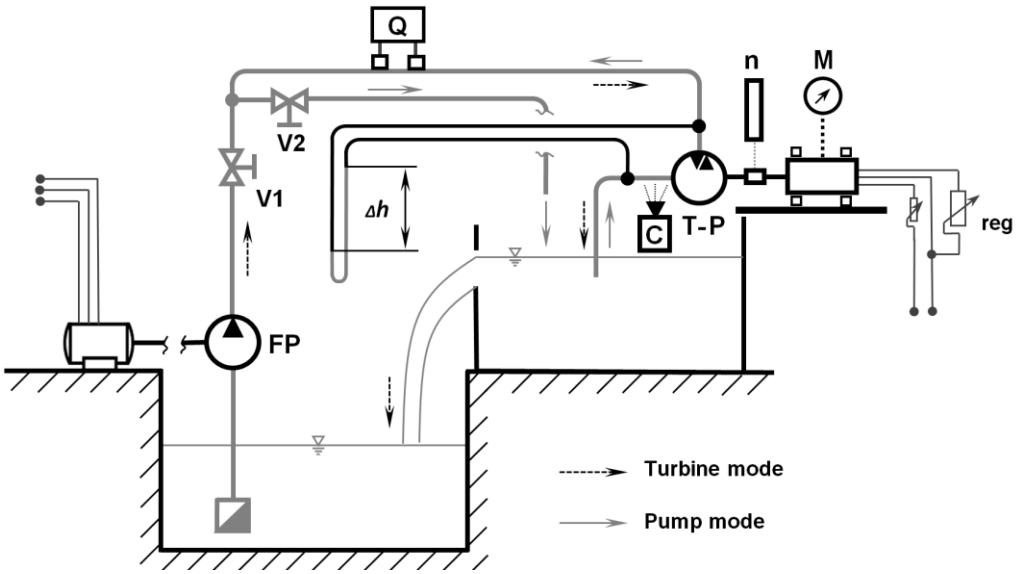

Figure 2. Hydraulic circuit scheme for testing turbines/pumps: Q – flowmeter; FP – feed pump (for turbine mode); T–P tested pump/turbine; V1, V2 – control valves; M – dynamometer, *n* – revolution counter, reg – load/drive control of the turbine/pump.

The testing circuit consisted of a set of two reservoirs with pipes and control and measuring elements. With this setting the tested pump (T-P) was measured in turbine mode – by closing valve V2 while regulating valve V1, the water flows in the direction of dashed arrows, while the feeding pump (FP) creates the hydro-technical potential for the turbine. After rearranging the valves V1and V2, the machine (T-P) was tested in the pumping operation on the same circuit – by closing the valve V1 and controlling valve V2 the water flows in the direction of gray arrows. The dynamometer (M) with continuous revolutions control allows operation in motor and braking mode. The dynamometer has cylindrical stator. It is placed on a bed allowing a slight rotation, which enables a measurement of the reaction torque at load. Dynamometer is a DC machine connected to continuous resistance load control unit. The water flow was measured using an ultrasonic flowmeter, Q (the Siemens SITRANS FUP1010). Specific energy of the turbine was determined on the basis of flow rate, Q_T and the value of differential pressure of mercury manometer, Δh connected to the pipe by collecting probes according to (ČSN EN ISO 9906; Hodák 1982), as detailed in Fig. 4. The turbine shaft speed was measured using an infrared sensor (TESTO 465).

In addition to measured values, flow character in both operating modes was recorded with a CCD camera (C) in transparent flow suction tube. Measured performance parameters were synchronously assessed with camera records and then

used to design other optimization. Two images illustrating the flow in turbine and consequently pump mode can be seen in Fig. 3.

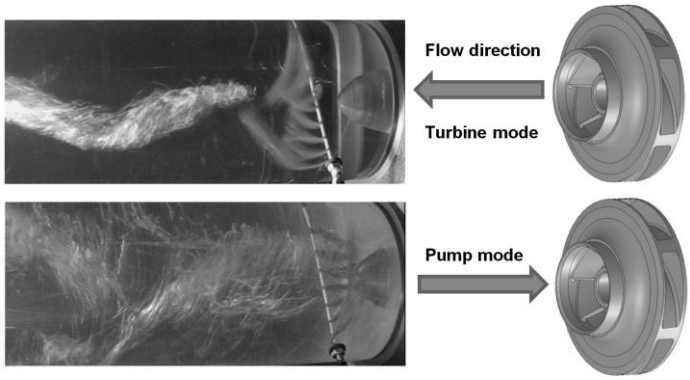

Figure 3. Flow inside the suction tube in turbine and pump operation.

Based on the measured values of differential pressure Δh, water flow Q, shaft speed *n* and torque M_T on dynamometer, other parameters were calculated for the purpose of creating characteristics in both operating modes of the machine.

Power of the water flow transferred to the turbine (or passed on by the pump) is determined from specific energy according to Bernoulli's equation and from measured values by calculation:

$$P_{T-P} = Q \cdot \rho_W \cdot \left[\frac{\rho_{Hg}}{\rho_W} \cdot \Delta h \cdot g + \frac{8 \cdot Q^2}{\pi^2}\left(\frac{1}{d_p^4} - \frac{1}{d_s^4}\right) + g \cdot y\right] [W] \qquad (1)$$

where: Q – volumetric flow rate [$m^3\ s^{-1}$]; ρ_{Hg} – specific weight of mercury (ρ_{Hg} = 13,540 kg m^{-3} at 20 °C); ρ_W – specific weight of water [kg m^{-3}]; Δh – measured level difference in U-pipes [m]; d_p, d_s – inner diameter of pressure and suction pipe respectively [m s^{-1}]; y – vertical distance of zones generating pressure [m] (see Fig. 4).

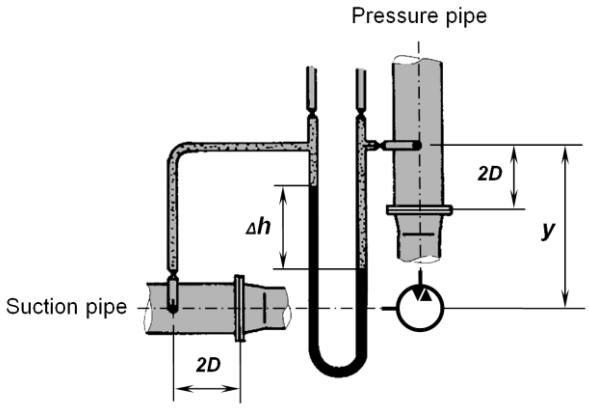

Figure 4. Diagram of pressure measurements according to EN ISO 9906.

The mechanical power output/input of the machine is given by torque M_T and shaft speed, n. The overall efficiency of the machine is then expressed by the ratio of mechanical and hydraulic power.

RESULTS AND DISCUSSION

Before beginning with verification of the individual innovative modifications, the properties of original unmodified machine were tested on the hydraulic circuit – both in turbine and pump mode. Thus obtained characteristics became a basis for assessment of the influence of individual modifications. They were then tested on the same test circuit under the same conditions as the original, unmodified machine – first in turbine and subsequently in pump mode. A number of modifications were experimentally tested in this way but only those with the best influence were selected for the following evaluation. Descriptions of all tested variations are summarized in Table 1. More details of structural design can not be published because they are subjected to law protection of intellectual ownership.

The very measurements in turbine mode were conducted so that the machine was gradually loaded from idle speed up to 900, or 800 rpm. The test results (Figs 5 & 6) illustrate the basic performance characteristics, mainly efficiency, power output, torque, and flow rate in dependence to shaft speed. Optimal operation or best efficiency points (BEP) are indicated for the characteristics of the three variants.

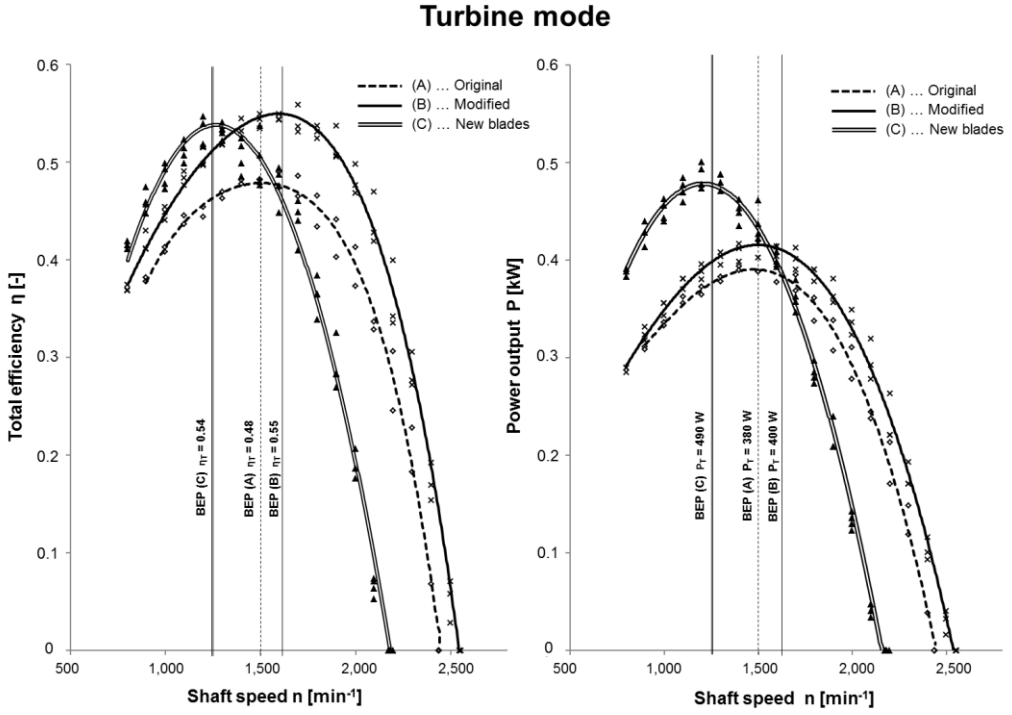

Figure 5. Turbine mode – efficiency and power output in dependence to shaft speed.

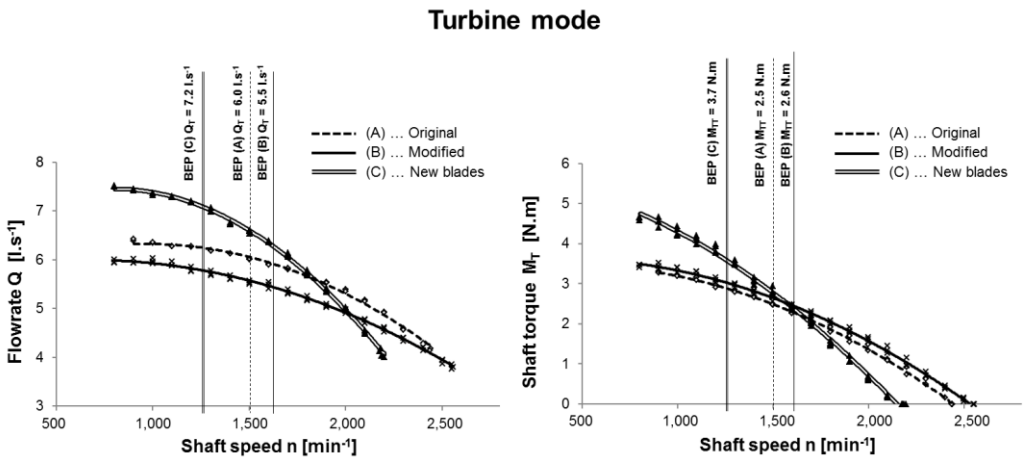

Figure 6. Turbine mode – flow rate and shaft torque in dependence to shaft speed.

Properties of above mentioned variants were subsequently verified in pump mode. Measurements were carried out at a constant speed, n = 1,450 rpm, according to specifications of manufacturer of the original pump. The two mostimportant measured characteristics are shown in Fig. 7, being the dependence of total efficiency and head on flow rate. The charts also indicate corresponding optimum points (BEP).

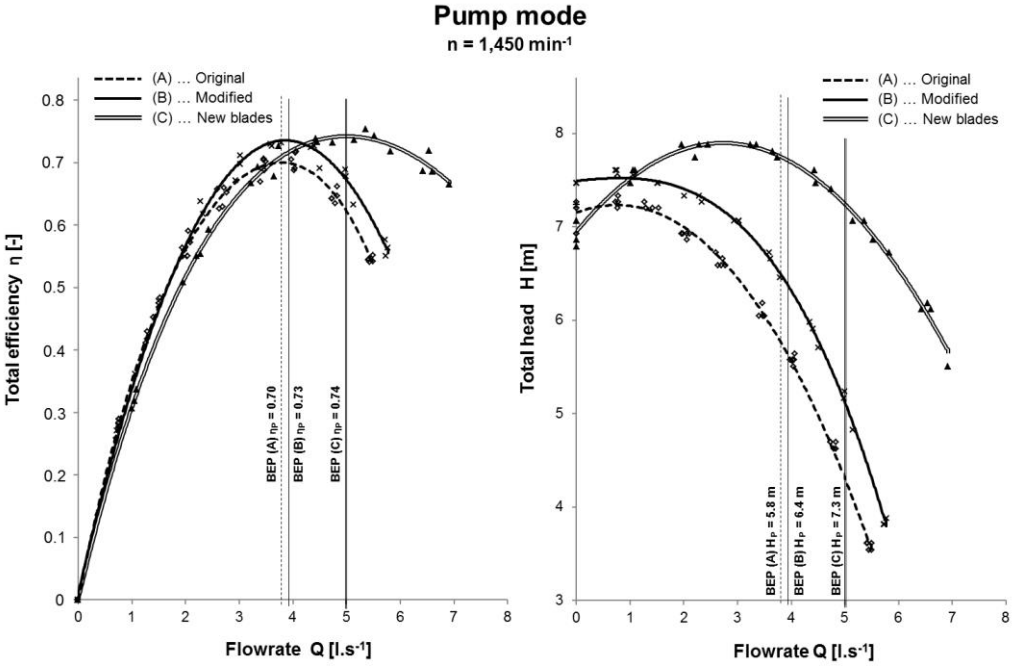

Figure 7. Pump mode – efficiency and head in dependence of flowrate.

For quantified evaluation of the proposed innovative modifications, key parameters of the measured characteristics are explicitly summarized in Table 2. Relative increases of monitored values corresponding to optimal operation (BEP) in both turbine and pump modes of operation are shown for the two variants, B and C. Relative increase of the parameters were computed in relation to those of variant A – the unmodified pump.

Table 2. Changes in parameters due to innovative modifications (at BEP)

Variant	Turbine mode					Pump mode			
	$\Delta\eta_T$ [%]	ΔP_T [%]	ΔM_{TT} [%]	ΔQ_T [%]	ΔH_T [%]	$\Delta\eta_P$ [%]	ΔP_P [%]	ΔQ_P [%]	ΔH_P [%]
B	14.6	5.3	4.0	-8.3	2.2	4.3	9.7	2.6	10.3
C	12.5	28.9	48.0	20.0	-6.7	5.7	61.3	35.5	25.9

In its original, unmodified state, the centrifugal pump used in this study had a head, H_P = 5.8 m, flow rate, Q_P = 3.8 ls^{-1}, power input, P_P = 310 W and efficiency, η_P = 70%. The values refer to the optimum operation, i.e. the highest achieved efficiency (BEP). The same unmodified machine, in turbine mode indicated a head, H_T = 13.5 m, flow rate, Q_T = 6.0 ls^{-1}, power output, P_T = 380 W and total efficiency, η_T = 48%, at optimum point. The pump therefore has a significantly higher efficiency than the manufacturer guarantees. However, if the pump is used in the turbine mode, its efficiency as a machine decreases by 22%. The aim of the innovative modifications was to reduce such a significant decline. Via simple, additional modifications to the existing machine – variant B – a proportional increase in efficiency in the turbine mode was achieved (up to $\Delta\eta_T$ = 14.6%). At the same time, torque increased by ΔM_{TT} = 4% and power output of the turbine by ΔP_T = 5.3%.

When the same pump was fitted with an impeller with new blade geometry, efficiency in the turbine mode increased only by $\Delta\eta_T$ = 12.5%, but the torque increased by ΔM_{TT} = 48% and power output almost by ΔP_T = 29% (!). Moreover, these parameters were achieved at a lower gradient. The cause of the higher power output was an increased rate of flow through the impeller by as much as ΔQ_T = 20%.

Manufacturers of pumps are, interested in the influence of modifications in the pump mode. For the modified pump (variant B), a slight increase in flow rate of ΔQ_P = 2.6% occurred, while head increased by ΔH_P = 10.3%. Increase in efficiency of $\Delta\eta_P$ = 4.3% confirmed positive impact of the innovation also in the pump mode.

The impeller with new blades geometry indicated even a higher increase in performance parameters in the pump mode. Flow rate increased significantly by ΔQ_P = 35.5%, head by ΔH_P = 25.9% and efficiency by $\Delta\eta_P$ = 5.7%. However, given the concept of impeller blades, it can be expected that the impeller with such geometry in the pump mode will have deteriorated cavitation characteristics. This has however not yet been experimentally verified.

CONCLUSIONS

In this study, two variants to a centrifugal pump were selected following several modifications on the pump's geometric parameters and their performances both as turbine and pump were evaluated and compared with those of the original machine. The original machine's total efficiency as a turbine was 22% below its performance as a

pump. As a pump, variant B gave slight increases in flow rate, head and overall efficiency (2.6, 10.3 and 4.3%, respectively) over the original pump. When fitted with an impeller with new blade geometry (variant C) the machine indicated up to 48% increase in torque output and 29% increase in power output over the original machine when tested in the turbine mode. The proposed innovative modifications of the radial centrifugal pump are therefore clearly beneficial for the turbine mode. Due to increased power output of the machine, variant C is especially suitable for this purpose. In variant B, benefits were also demonstrated for the pump mode. In summary, it can be said that the application of these innovations brings to their users benefit in terms of increased efficiency in their use for hydroelectric power. Manufacturers of pumps can then benefit from higher market attractiveness of their products.

REFERENCES

Alatorre-Frenk, C. 1994. Cost minimization in microhydro systems using pumps-as-turbines, Ph.D. Thesis, University of Warwick.

Bláha, J., Melichar, J. & Mosler, P. 2011. Contribution to the use of hydrodynamic pumps as turbines. *Energetika* **5**, 1–5 (in Czech)

Commission regulation (EU) No 547/2012. http://eur-lex.europa.eu/legal-content/EN/TXT/?qid=1486033967314&uri=CELEX:32012R0547. Accessed 10. 1. 2017

ČSN EN ISO 9906: Hydrodynamic pumps – Acceptance tests of hydraulic performance parameters – Degrees accuracy of 1, 2 and 3, ČSNI. (in Czech)

Directive 2009/125/EC. *http://eur-lex.europa.eu/legal-content/EN/TXT/?qid=1486034114 994& uri=CELEX:32009L0125.* Accessed 10. 1. 2017

Derakhshan, S. & Nourbakhsh, A. 2008. Theoretical, numerical and experimental investigation of centrifugal pumps in reverse operation. *Experimental Thermal and Fluid Science* **32**, 1620–1627.

Gülich, J.F. 2003. Effect of Reynolds Number and Surface Roughness on the Efficiency of Centrifugal Pumps. *Journal of Fluid Engineering* **125**(4), 670–679.

Hodák, T., Vodzinský, V., Ondrušek, V. 1982. *Utilization of hydropower (Instructions for exercise).* SVŠT, Bratislava, 1982. (in Slovak)

Hýbl, J. 1928. *Water engines I, II, III*. Czech Technical Institute, Prague. (in Czech)

Melichar, J., Vojtek, J. & Bláha, J. 1998. *Small hydro turbines, construction and operation.* ČVUT, Praha. pp 296. (in Czech)

Munson, B.R., Zouny, D.F. & Okishii, T.H. 2006. *Fundamentals of Fluid Mechanics, Fifth edition*, John Wiley & Sons, Inc., New York.

Nautiyal, H.V., Kumar, A. & Yadav, S. 2011. Experimental investigation of centrifugal pump working as turbine for small hydropower system. *Energy Science and Technology* **1**(1), 79–86.

Nechleba, M. 1962. *Water turbines – their design and accessories*, 2nd Edition. SNTL, Praha. pp 673 (in Czech)

Nechleba, M. & Hušek, J. 1966. *Hydraulic machines*. SNTL, Prague. pp 388 (in Czech)

Nevěřil, J. 2012. Limits of energy demands. *Sigmaprofil* **20**(4), 10. (in Czech)

Pochylý, F., Haluza, M., Rudolf, P., Habán, V., Klas, R., Hudec, M., Himr, D. & Stejskal, J. 2013. Mutual cooperation SIGMA GROUP, Inc. Lutin, SIGMA RDI, Ltd. Lutin and the Department of Fluid Engineering of V. Kaplan FSI in Brno in research pumps. In Proceedings of the Scientific–Technical Conference on ‚Current trends pumping equipment'.Sigma Group a.s., Lutín. (in Czech)

Polák, M. & Polák, V. 2010. Application of the theory of physical similarity in calculation program for the design of hydraulic turbines. *Jemná Mechanika a Optika* **10**, 281–284. (in Czech)

Polák, M. 2013. The issue of energy utilization of low-potential water sources. CULS Prague, Prague 2013. [hab. thesis] (in Czech)

Poláková, Z. &Polák, M. 2016. Centrifugal pump in turbine mode for small hydropower. In Proceedings of the 6th International Conference on Trends in Agricultural Engineering. CULS, Prague. pp 500–505.

Raman, N., Hussein, I., Palanisamy, K. & Foo, B. 2013. An experimental investigation of pump as turbine for micro hydro application. In Proceedings of 4th International Conference on Energy and Environment (ICEE 2013), 5–6 March, Putrajaya, Malaysia. IOP Conference Series: Earth and Environmental Science **16**(1), 012064.

Sedlář, M., Šoukal, J. & Komárek, M. 2009. CFD analysis of middle stage of multistage pump opereting in turbine regime. *Engineering Mechanics* **16**(6), 413–421.

Singh, P. 2005. Optimization of internal hydraulics system design for pumps as turbine with Field Implementation and Evaluation. PhD thesis, Universität Fridericiana, Karlsruhe.

Singh, P. & Nestmann, F. 2011. Internal hydraulic analysis of impeller rounding in centrifugal pumps as turbines. *Experimental Thermal and Fluid Science*, 35, 121–134.

Ulrych, E. 2007. *Applied hydromechanics I – Basics of hydropower*. Powerprint s.r.o., Prague. pp 126. (in Czech)

Agronomy Research **15**(S1), 1198–1203, 2017

Selection and evaluation of degradation intensity indicators of gas combustion engine oil

J. Pošta, B. Peterka, Z. Aleš, J. Pavlů* and M. Pexa

Faculty of Engineering, Czech University of Life Sciences Prague, Kamycka 129, CZ16521 Prague 6, Czech Republic
*Correspondence: jindrichpavlu@seznam.cz

Abstract. The paper is focused on the analysis of data obtained during the operation of gas combustion engines running on biogas. The observed engines were running continuously in cogeneration units of biogas plants. The long-term operational monitoring of engines operating on biogas was carried out using tribotechnical diagnostics methods focused on oil properties. Each of individual indicators was determined in obtained time series. As critical indicators oils were identified oxidation, sulfation, nitration and total acid number. The prerequisite for correct selection of the oil change interval is knowledge on evolution of critical indicators over time. In the reference case, oil oxidation was identified as critical indicator. This knowledge allows to optimize intervals of oil sampling and oil change interval on the basis of time series evaluation.

Key words: biogas, engine oil, oxidation, sulfation, oil change.

INTRODUCTION

Long-term monitoring of oil filling and diagnostic of engine together with monitoring of particles content creates conditions for sustainable and reliable operation of engine during whole service life (Novacek, 2015).

The first prerequisite in order to correctly diagnosis is proper sampling of engine oil. During oil sampling those basic rules must be maintained: a) avoid external contamination of a sample; b) sampling should be done with the engine running or as soon as engine is stopped; c) sampler should be immediately marked with both sample and engine identification data (Novacek, 2015).

During the last decade, the tribological analysis of industrial lubricants was done by using well-known tests. Those tests provided early warnings of possible problems, so there was sufficient time to take proactive action. According to the American Petroleum Institute (API), base oils fall into five main groups (Group I–V). This breakdown is based on the refining method and the base oil's properties in terms of, among other things, viscosity and the proportion of saturates and sulfur content. Transition of actual oils from Group I to Group II and III was accompanied with general changes in oil composition. Oils belonging to Group II and III have inferior natural oxidation stability in comparison with oils of Group I. This is main reason why those kinds of oils are highly doped with antioxidants (Novacek & Novak, 2013; Cerny, 2015). Antioxidants are not able to stop the process of oxidation, but this process can be significantly slowed down. Antioxidants

are consumed and if their amount in the oil drops below a certain threshold, there is an appreciable acceleration of oxidation of the oil, as is shown in Fig. 1.

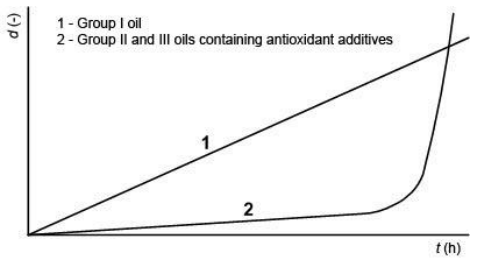

Figure 1. Progress of oil degradation.

Biogas is produced by processing of organic waste and biomass in bio-gas stations and then is burned using gas engine cogenerations units. Gas combustion engines of cogeneration units are operated continuously at constant speed but under variable load. This load depends mostly on requirements of electricity distribution network and on actual composition of used biogas. Because of the forced breaks, load variation or gas composition variation, the thermal load of engines and oil fillings varies. This operational mode has extremely high requirements on engine oils (Posta et al., 2016).

Engine oils specified for gas engines belongs to most challenging products of his kind. The progress and level of degradation of those oils was long-term monitored in order to full utilization of their potential. Scientific problem can be presented as verification of hypothesis assuming that for given type of engine and specific working conditions can be expected similar progress as is shown in Fig. 1. Therefore, results from earlier analyses can be used for determination of a limit value of critical indicators and corresponding operating time.

MATERIALS AND METHODS

Long-term monitoring of operation and condition of engine oil of two identical engines of cogeneration units was carried out. Both engines was supplied with biogas from the same fermenter. Cogeneration units, shown in Fig. 2, was marked as KJ3 a KJ4. Units KJ1 and KJ3 was not monitored due to their different operational mode. Monitored units consist of Scania-Schnell ES 2507 combustion engine and Stamford HCI434F2 generator. Basic parameters are shown in Table 1. Engines was filled with engine oil with zero content of zinc and medium content of sulphated ash, specified for use in all kinds of stationary gas engines running at sewage gas, biogas or woodgas. Basic oil parameters are shown in Table 2.

Figure 2. Cogeneration units.

Table 1. Basic technical parameters of cogeneration unit

Engine		Generator	
Model	Scania-Schnell ES 2507	Model	Stamford HCI434F2
Cylinder volume	12,000 cm^3	Voltage	400/230 V
Rated power	250 kW	Rated power	280 kW
Oil capacity	41 l	Frequency	50 Hz

Table 2. Basic technical parameters of engine oil used in cogeneration units

Property	Units	Value	Testing standard
Density at 15°C	kg m^{-3}	866	DIN 51 757
Fire point	°C	260	DIN ISO 2592
Pour point	°C	-35	DIN ISO 3016
Kinematic viscosity at 40 °C	$mm^2 s^{-1}$	105.00	DIN 51 562-1
Kinematic viscosity at 100 °C	$mm^2 s^{-1}$	13.40	DIN 51 562-1
Sulphur ash	% of mass	0.7	DIN EN ISO 6245
TBN	mg KOH g^{-1}	8.9	DIN ISO 3771

Condition monitoring of oils was performed using tribotechnical diagnostics by independent and certified laboratory. Standards used for analyses are described in Table 3. Oil samples were acquired by authorized employee according to methodology given by laboratory. At the time of sampling, the overall operation time of engine was read from the control unit of engine. Procedure of oil sampling for analysis has to follow certain order. The sample should be extracted so that the concentration of information is consistent and representative. During the sampling process, it is essential to make sure that the sample does not become contaminated (dust, debris, water, etc.). It is important to take sample always from the same spot of crankcase immediately after turning off the engine.

Table 3. Standard test methods

Method	Standard
Determination of elements in oil using OES-ICP	ASTM D 5185
Oxidation, sulfation, nitration, water and glycol content	ASTM E 2412
Acidity number TAN	ČSN ISO 6619
Base number TBN	ČSN ISO 3771
Viscosity	ČSN EN ISO 3104

RESULTS AND DISCUSSION

In the period of years 2014–2016 there was performed 30 analyses (approximately 1 sampler per month) of engine oil for each of monitored engine. List of mostly exceeded thresholds values is shown in Table 4. In all cases when threshold of sulfation and nitration was exceeded, threshold of oxidation was also exceeded. Therefore, it is evident that the critical indicator of oil condition in the monitored engine is oxidation.

Table 4. Exceed count for selected threshold parameters in period of years 2014–2016

Parameter	Treshold	KJ3	KJ4	Total /%
Oxidation	20 Abs·cm^{-1}	29	26	55 / 92
Sulfation	20 Abs·cm^{-1}	7	9	16 / 27
Nitration	20 Abs·cm^{-1}	8	3	11 / 18
Viscosity 100°	16.4 mm^2 s^{-1}	7	6	13 / 22
TAN > TBN	mg KOH g^{-1}	17	18	35 / 59

Relation between values of oxidation and oil filling uptime in case of monitored engines is shown in Fig. 3, using calculation according to Formula 1.

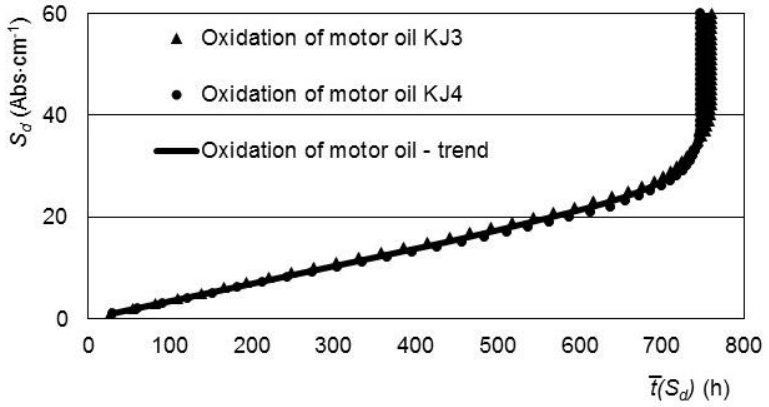

Figure 3. Oxidation of engine oil.

$$\bar{t}(S_d) = \frac{1}{n}\left[\sum_{i=1}^{m(S_d)} t_i(S_d) + \sum_{j=1}^{n-m(S_d)} t_j(S_d)\right] \quad (1)$$

where: n – the range of the entire sample of monitored elements; $m(S_d)$ – the number of elements operating at certain value of diagnostic signal S_d; $t_i(S_d)$ – operating time of *i*-th element, which is functional at certain value of diagnostic signal S_d; $t_j(S_d)$ – operating time of *j*-th element, which is in failure mode at certain value of diagnostic signal S_d.

Speed and mode of degradation process of engine oil can be affected by fuel used in combustion engine. As states (Vesela et al., 2014) when is used fuel E85 containing 85% of ethanol and 15% of BA95 petrol, the significant degradation index is reduction of viscosity. While monitoring, in case of this study, the progress of degradation of engine oil in gas engines burning biogas, viscosity was in either case an indicator excessing critical value and therefore does not lead to oil change, as shown in Table 4. Exceeding of viscosity, TAN/TNB indicators was (with single exception) accompanied with significant exceed of oxidation.

As shown by the results of the performed operational monitoring of engines operating on biogas, the significant degradation index of engine oil is oxidation or sulfation.

Results of performed operational monitoring can be also used to set the value of diagnostic signal, which corresponds with optimal time of change of oil filling.

Method of determining the normative diagnostic signal and determining optimal time for preventive maintenance gives (Teringl et al., 2015; Legat et al., 2017). Principle of such as determination process is presented by specific samples of data collected during operation monitoring in Fig. 3.

Analogously, we can determine the optimal time for an oil change for each of additional diagnostic signal. First diagnostic signal, which exceeded limit value, will be used as decisive for real oil change.

Results of carried operational monitoring, shown in Fig. 3, confirms the hypothesis that for specific engine in specific working conditions course as shown in Fig. 1 can be expected.

In particular case of monitored oils, the appropriate procedure is further described. Oil service time will be monitored and in the moment of optimal time, oil filling will be either changed or the oil sampling followed by analysis has to be done. If the analysis confirms reached or exceeded limit values, oil change will be performed immediately or the deadline of oil change will be resolved. Values given by oil analysis will be added to data history, so next time will be included again both in optimization process of oil change interval and in process of adjusting of threshold value of diagnostics signal.

CONCLUSIONS

Modern engine oils are highly doped with antioxidants additives. Oil degradation continues rapidly after depletion of additives. This moment can be captured using frequent tribotechnical analyses, or can be estimated from early service periods reached before the breakpoint of degradation curve. Using execution of qualified estimation, the preventive maintenance of oil fillings including oil analysis can be driven.

Results of monitoring of engine oils demonstrate that in this particular case, the reason of oil degradation is mainly oxidation, which led to execution of 98% of oil change events.

Recommendation for operators of referenced kinds of gas engines:

- Monitoring of oil service interval and oil sampling at that time, when limit value of selected parameter is close to his threshold, based on acquired knowledge (respecting shape of time progress of critical parameter) of this research it is possible to predict remaining service interval of oils belonging to Group II and Group III in similar operation conditions.
- According to results of obtained analysis, either perform of oil change or set its deadline.
- Add the values given by oil analysis to data from earlier analyses, so they will be included again in optimization process of both setting of oil change interval and adjusting of threshold value of diagnostic signal.

By this approach, the highest possible utilization of the potential of engine oil without excessive risk of shortening the technical life of the engine can be achieved.

ACKNOWLEDGEMENTS. Paper was created with the grant support – CZU CIGA 2015 – 20153001 – Utilization of butanol in internal combustion engines of generators.

REFERENCES

Černý, J. 2015: The properties of motor oils - Oxidation stability, nitration oil. Oleje-cz. Available from <http://www.oleje.cz/clanek/Vlastnosti-motorovych-oleju---Oxidacni-stabilita--nitrace-oleje>, (in Czech)

Legát, V., Mošna, F., Aleš, Z. & Jurča, V. 2017. Preventive maintenance models – higher operational reliability. [Modele konserwacji zapobiegawczej a wyższa niezawodność eksploatacyjna] *Maintenance and Reliability Eksploatacja i Niezawodnosc* **19**(1), 134–141. doi:10.17531/ein.2017.1.19

Nováček, V. & Novák, J. 2013: A new approach to monitoring oil condition. In: Tribotechnika, Vol. VI., No. 6/2013, pp. 26–28, ISSN 1338-0524, Available from <http://www.tribotechnika.sk/application_data/tribo/uploads/Data/tribotechnika_6_2013.pdf>, (in Czech)

Nováček, V. 2015. Analysis of motor oils and antifreeze liquids for diesel. In: Tribotechnické informace, Januar 2015. Vol. **45**(1), pp. 8–9. Available from <http://www.techmagazin.cz/ke_stazeni/TRIBO012015.pdf>, (in Czech)

Posta, J., Peterka, B., Ales, Z., Pexa, M., Pavlu, J. & Vutan, H. 2016, "Lubricity of thermo-oxidized engine oils". *MM Science Journal*, vol. 2016, no. NOVEMBER, pp. 1214–1217.

Teringl, A. & Aleš, Z. & Legát, V. 2015 Dependability characteristics - indicators for maintenance performance measurement of manufacturing technology. *Manufacturing Technology* **15**(3), 456–461. Retrieved from www.scopus.com

Veselá, K., Pexa, M. & Mařík, J. 2014: The effect of biofuels on the quality and purity of engine oil. *Agronomy Research* **12**(2), 425–430.

Agronomy Research **15**(S1), 1204–1222, 2017

Existing state of art of free-piston engines

V. Raide,* R. Ilves, A. Küüt, K. Küüt and J. Olt

Institute of Technology, Department of Agricultural and Production Engineering, Estonian University of Life Sciences, Fr.R. Kreutzwaldi 56, EE51014 Tartu, Estonia
*Correspondence: veljo.raide@emu.ee

Abstract. Free-piston engines (FPE), as power generators for electricity and hydropower solutions, have come under intensive research and development during the last decade. The rapid development of information technology provides an opportunity to return to FPE technology development due to better levels of control and management in terms of the engine's work. What is more, changed environmental requirements are imposing stricter conditions upon the development of internal combustion engines. More effective solutions which ensure lower exhaust emissions, which are able to consume a variety of conventional and renewable fuels without any engine modification or rebuild taking place, and which work well with a very wide variety of ambient temperature conditions. However, commercially available or production-ready compact and stable free-piston engine solution are still absent. The objectives of this article are the innovative and novel features of FPE and their influence on engine operations and power production. The article maps the FPE technology and conducts a fact analysis. Various technical solutions, experiments, and mathematical calculations are discussed and are presented critically, along with potential pros and cons. This paper will epitomise the discussions outlined above with one possible theoretical technical solution for FPE, this being the electrical power generator.

Key words: internal combustion engine, free-piston linear alternator, engine generator.

INTRODUCTION

The world's growing electricity deficit forces us to evaluate other options when it comes to energy resources and technology. Over the next two decades, oil will remain the world's main energy source but it will not cover the growing demand for energy. This perspective compels us to develop combustion technology and to find energy alternatives. Fuel converted to electrical power via 'engine generators' (GENSET) is a relatively quick process. Mobile power generation is under constant development (Lund, 2008) and solutions are sought in many sectors. The US Land Forces stated that, in 2020, new technology will produce 75% of operation electricity (Defence Update, 2003), and the EU will replace conventional fuels with 20% renewable energy. These objectives determine the development directions in all energy areas including the automotive industry.

Environmentally-friendly combustion technology will be progressively introduced and engine production will evolve in the direction of hybrid engines. In terms of the automobile industry, significant technological developments focus primarily on electric and hybrid cars which have the potential to consume less energy and reduce emissions. Developments influence and determine mobile electricity production with renewable

fuels as being key to progress. One internal combustion engine research area is the free-piston engine (FPE), which was abandoned in the middle of the previous century but which is currently making something of a comeback in terms of low levels of power production. The return of FPE technology is significantly influenced by IT developments which provide faster processors and more sensitive sensors to control the way engines work. Technology compactness and improved capacity parameters make FPE an attractive and promising technology. More deeply FPE-related concepts are being studied by Achten and Aichlamyr (Achten, 1994; Aichlmayr, 2002) but technology has evolved and improved in the meantime.

In this article, FPE studies are provided with an overview and are cited in association with the developments of the previous decade. Chapters are divided based upon problems and in highlighting the pros and cons of the technology. According to the analysis which has been carried out, (1) FPE concepts are mapped out and the list of usable technology developments is improved by the addition of the latest inventions (Table 1); (2) the engine mechanics are debated in connection with simulations and engine control; (3) the principles behind starting-up an engine are critically reviewed, along with the provision of technical examples; and (4) focuses on engine combustion stability and starting an analysis which was carried out in particularly changing load conditions. Finally, an overview is presented and discussed along with the provision of an FPE solution for the mobile GENSET.

ENGINE CONCEPTS

The FPE can be divided into three groups by its actions and extractions (Mikalsen & Roskilly, 2007), and by more complex configurations using three cylinders and four pistons (Hung et al., 2015). The configurations mentioned use piston motion in order to achieve any useful work. For example, the technology implements and supercharges power turbine rotational movement. The single piston FPE consists of only a few parts: (1) the cylinder; (2) the load device; and (3) the rebound device which stores energy for the next compression. The surplus energy is directed towards hydraulic, pneumatic, or electrical power production. The dual FPE configuration skips the rebound chamber since combustion provides compression for the next stroke. This omission increases the overall power to weight ratio. Dual technology is the area which sees the most research and development, so a number of patented designs are available. The patents are found in all three types of hydraulic, pneumatic, and electrical power production. The challenge in terms of FPE is in achieving control of: (1) the piston motion; (2) the stroke length; and (3) compression due to sensitivity to load and cycle-to-cycle variations (Aichlmayr, 2002). The most common designs are illustrated and general pros, cons, and loads are described in Table 1.

Table 1. Common free-piston engine designs

Configuration	Representation	Pros / Cons/General description/ Load
a) Single piston and one cylinder solution (Achten et al., 2000; Zhang et al., 2015a; Zhang et al., 2015b Zhao et al., 2010; Zhao et al., 2013; Zhao et al., 2014; Brunner et al., 2005; Hibi&Ito, 2004; Kock et al., 2013)	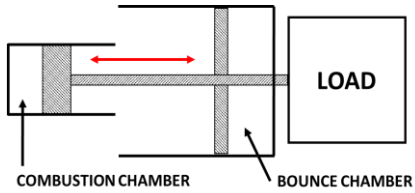	Simple design, compact, unbalanced, counterweights may be needed, allows long stroke, scavenging or injection fuelling, exhaust ports or valves for the outlet.
b) Single piston rod, two piston and two cylinder solution (Mikalsen et al., 2010; Jia et al., 2014a; Jia et al., 2015a; Jia et al., 2015b, Mikalsen & Roskilly, Part 1, 2010; Xiao et al., 2010; Tikkanen et al., 2000; Clark et al., 1998; Blarigan et al., 1998; Fredriksson & Denbratt, 2004; Xu & Chang, 2010; Robinson & Clark, 2016)	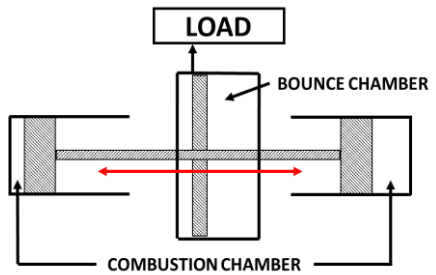	Every revolution two power strokes, better power output, massive piston causes unbalance, long stroke, challenge to control, great power output, loading hydraulic or electric generator, scavenging or injection fuelling, exhaust ports or valves for outlet.
c) Two opposed piston, two piston rods and one cylinder solution (Wu et al., 2014; Xu et al., 2011; Zhou et al., 2005)	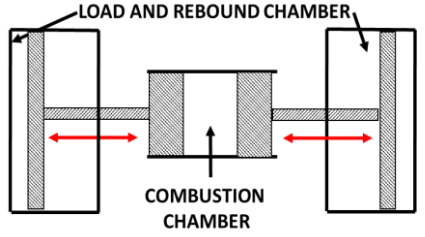	Concurrent combustion, separate bounce, and load chambers, challenge to control, loading hydraulic or producing high pressure for the turbine, scavenging or injection fuelling, exhaust ports or valves for the outlet.
d) Two opposed piston, two piston rods and one cylinder with synchronisation rods (Achten, 1994; Hanipah et al.,2015; Mikalsen & Roskilly, 2007a; Aichlmayr, 2002)	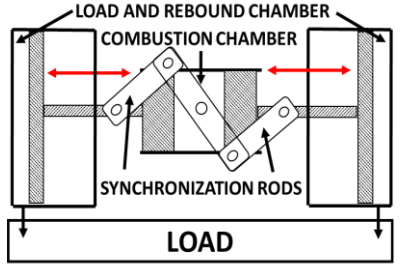	Concurrent combustion, piston synchronization, minimal vibration, separate bounce and load chambers, loading hydraulic or producing high pressure for turbine, scavenging or injection fuelling, exhaust ports or valves for the outlet.

Table 1 (continued)

e) Four piston, opposed – dual, two piston rods and three cylinders solution (Nguyen et al., 2015)	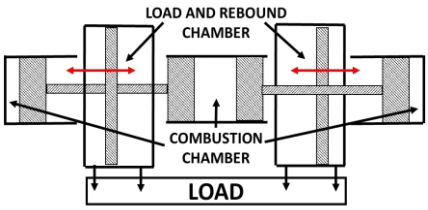	Four pistons, three combustion chambers, two separate bounce and load chambers, loading hydraulic, injection fuelling, exhaust ports.
f) Four piston, opposed, two cylinder solution (Li et al., 2015; Zhang et al., 2015)	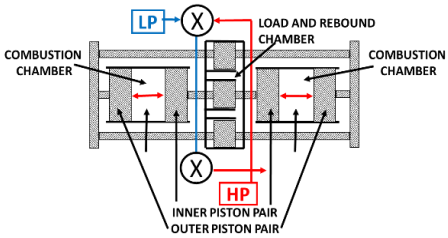	Four pistons, two combustion chambers, concurrent combustion, compression ignition, three interconnected hydraulic chambers, intake and exhaust ports.

The FPE is a reciprocating engine, one which is frequently termed a linear piston engine, in which the steady piston moves and transforms thermal energy into power. Unlimited piston motion and the variable clearance volume V_c between the 'top dead centre' (TDC) and the 'bottom dead centre' (BDC) is missing from the rod and crank mechanism. The FPE configurations differ but at least have: (1) a combustion chamber; (2) rebound or bounce-storing energy; (3) load absorbing or consuming energy. Fewer moving parts decrease friction and increase system efficiency as piston rings, bearings, bounce, and rebound result in minimal kinematic constraints (Aichlmayr, 2002). The FPE compression and expansion (power) stroke is similar to the revolution of a two-stroke engine. The compression stroke starts at BDC, after the charge is sucked in to the cylinder and it ends when the charge is compressed until the pressures equalise. The compression stroke uses released rebound storage energy. The compression or spark initiates combustion in TDC and thermal energy converts into kinetic energy through rapidly expanding gasses. The expansion lasts until blow-down is achieved, in BDC, since the exhaust port or valve opens and releases exhaust gasses. The inlet port or valve opens and scavenges (compresses) a charge into the cylinder and then the cycle repeats. The FPE designs may vary but operational principles are the same (Mikalsen & Roskilly, 2007a).

The FPE is exploited by electric generators, and by hydraulic and pneumatic systems. In hydraulic systems, pressures are achieved via a small piston mass and the efficiency rate is relatively high. The hydraulic control system keeps the discharge pressure constant. Linear electric generators are compact power packs due to the use of ferromagnetic materials or permanent magnets in pistons mechanisms. In linear electric generators, the oscillation frequency is set in accordance with the load. The FPE advantages and challenges are as follows:

The FPE advantages:

- A structurally simple machine;
- A variable compression ratio during operation;
- Variable compression allows high compression ratios;

- Allows for multi-fuel operation;
- Each stroke generates power;
- Piston movement is not limited by crankshaft radius;
- The missing crankshaft reduces the geometry significantly;
- A significant kW to kg ratio;
- Allows a long piston stroke to be implemented;
- Small frictional losses;
- Good volumetric efficiency;
- Lower temperature release due to a rapid burning process;
- Lower fuel consumption due to lower frictional losses;
- Reduced emissions;
- Able to work in very low temperature conditions;
- Low vibrations due to the crankshaft being absent.

Challenges to overcome are these:

- The starting process;
- Piston movement control;
- Variable piston stroke which leads to poor volumetric efficiency;
- Precise load control;
- An accurate fuel mixture;

In conclusion, normally the crankshaft controls and stores energy for the next stroke. The FPE employs a two-stroke principle as it needs a power stroke in every cycle. The one-piston FPE reciprocates in terms of combustion and for the necessary rebound force in balance with the controlled load. The proper combustion characteristics ensure that the engine works as expected and the residue is diverted for power production. The FPE needs enough computing power, accurate algorithms, quick reaction sensors, and powerful enforcement mechanisms to control the piston, scavenging, ignition, and exhaust release. Otherwise, the engine management process fails.

ENGINE MECHANICS

The FPE is missing a crankshaft, and instead the load force is directly coupled to the piston. The calculations and simulations based on the balance of piston motion on the engine power mode. The compression ratio r_c (r_c = total cylinder volume V_t / cylinder clearance volume V_c) and cylinder volume V (m^3) calculates in a similar way to calculations for crankshaft engines, but volume V at any crank angle φ (degrees) is problematic. The piston location calculations for crankshaft engines are take into account the connecting rod length l (cm), crank radius α (cm), and time- change rate dependent on crank angle φ. In terms of FPE, piston motion is derived from free-body motion and, therefore, excludes crankshaft radius and piston friction by side forces. The main piston motion characteristics in the FPE are shown in Fig. 1 (Aichlmayr, 2002; Mikalsen & Roskilly, 2007a).

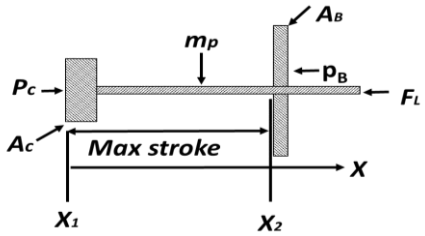

Figure 1. FPE body diagram and generalised loads and friction acting on a piston (Aichlmayr, 2002; Mikalsen & Roskilly, 2007a).

Determining the location of the piston requires variables; piston mass m_p (kg); and combustion chamber pressure P_c (bar); and combustion chamber area A_c (m^2); and load force F_L (N). The load force F_L (N) consists of the bounce chamber area A_B (m^2), and rebound or bounce pressure p_B (bar). The combustion force acts in the x-direction, and in applying Newton's second law a force balance (Mikalsen & Roskilly, 2007b) can be described:

$$\sum F_x = m_p \frac{d^2x}{dt^2} = P_c A_c - F_L \tag{1}$$

The piston velocity (v) can be calculated from the FPE work function. Velocity can be calculated between the set points x_1 and x_2 (Fig. 1) and, after integration, the equation is expressed as follows: (Mikalsen & Roskilly, 2007b):

$$\underset{1\to2}{W} = m_p \left(\frac{\bar{V}_2^2 - \bar{V}_1^2}{2}\right) = A_c \int_{x_1}^{x_2} P_c dx - \int_{x_1}^{x_2} F_L dx \tag{21}$$

The x_1 and x_2 are the piston dead points, and velocities v_1 and v_2 are set at zero, so the equation can be reducing as follows (Mikalsen & Roskilly, 2007b):

$$A_c \int_{x_1}^{x_2} P_c dx = \int_{x_1}^{x_2} F_L dx \tag{3}$$

The assumption that piston position determines as a function of combustion pressure $P_c = P_c(x)$, and x_1 is known (Eq. 3), in which case more variables should be available for precise control. One important variable is preparation of air-fuel mixture. The air-fuel mixture preparation consists of: (1) the exact calorific value of the fuel; (2) the air-fuel ratio; (3) the air-fuel mixture quality; and (4) the temperatures (Aichlmayr, 2002). In order to be able to control all of the aforementioned parameters, the control unit has been designed to analyse the information it receives from sensors and processes according to the algorithms that have been set for just this purpose. The FPE needs proactive intervention to be able to manage the piston as any failure to do so causes a collision in dead centres. The management system senses and calculates piston movement and load force F_l by the prescribed function. The location x_2 computation starts after combustion, in fairly quick time, and it is impossible to conduct this without controlling F_L. So it excludes sudden load changes.

ENGINE START UP PRINCIPLES

The absence of a flywheel concludes any remaining problems which need to be overcome. The FPE piston's missing connection with any mechanical parts directly influences the start-up process. The start-up problems occurred regardless of configuration, and researchers report that the start for a dual-piston engine is the real problem (Noren & Erwin, 1958; Aichlmayr, 2002; Nemecek & Vysoky, 2006; Mikalsen & Roskilly, 2007a; Zulkifli et al., 2008; Xu & Chang, 2010). The FPE must start the combustion on the first stroke (Braun & Schweitzer, 1973) and the start-up requires additional technical equipment. The cylinder is fuelled, the piston is positioned on the maximum value, and required pulse energy is released (Farmer, 1947; Noren & Erwin, 1958; Aichlmayr, 2002). The FPE is started with a spring or a hydraulic system that can generate the piston movements in the cylinder (bounce or rebound), (Farmer, 1947; Aichlmayr, 2002), with this being the most widely-used practical method (London & Oppenheim, 1952).

The latest General Motors patent is similar to the Sigma GS-34 gas generator and differs in terms of its physical synchronisation mechanism which controls the piston movement with levers (Durrett et al., 2012; Nait et al., 2012). The piston synchronises with bounce chambers and the permanent magnets generate electricity in coils. Magnets are added in the piston and the coil windings are enveloped around the cylinder. (Hanipah et al., 2015). The solution need piston cooling when the *Fe* magnet works on the temperature 770 °C and more. When using other alloys in the magnets, the temperature is even lower. The temperature decreased the ability of the magnet and the power producing of the FPE linear generator is inhibited. (Kittel, 1995). The two stroke FPE design by General Motors is shown in Fig. 2.

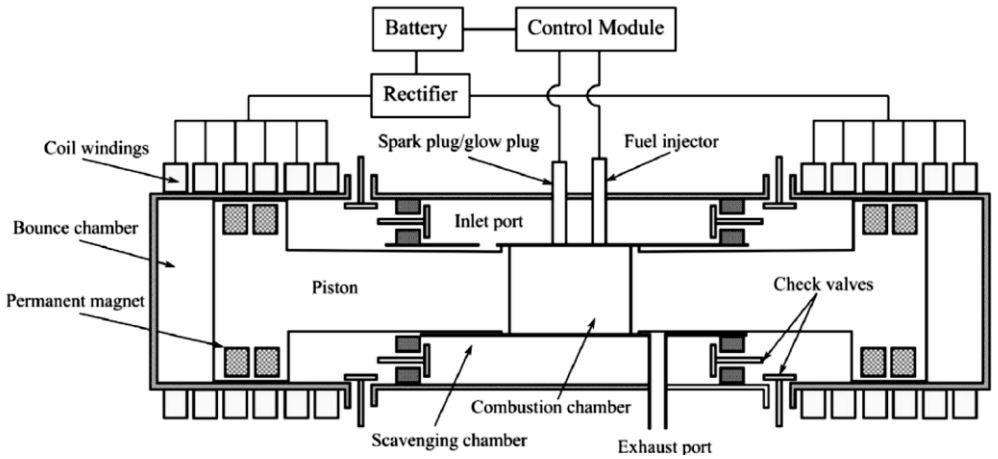

Figure 2. GM's opposed piston two stroke design FPE linear alternator (FPLA) (Xu et al., 2011).

In terms of FPLA, Patent No US 20110012367A1 (2011), Holmes resolves the engine starting conundrum by using an electrical flywheel. The opposed piston simplified linear alternator is shown in Fig. 3. The engine driving system (1) which includes a linear machine (2) with a linearly-moving piston (3). With that in mind, (3)

moves along a path between the first end (4) with a first combustion chamber (5) which has a first fuel source and spark plug (6), and a second end (7) with a second combustion chamber (8) with a second fuel source and spark plug (9). A first coil (10) has windings around the path of the linearly-moving piston. It can be seen that (3) is positioned towards the first end (4). Similarly, a second coil (11) is also wound around the path and is positioned towards the second end (7) (12). Other items are a third coil (13) rotary machine, (14) fourth coil, (15) transmission, (16) variable speed motor, (17) rotor, (15) transmission of speed. The FPLA connects electrically via two sets of coils to a rotary machine (middle) and a battery source via a converter. In addition, a variable-speed motor connects mechanically via a gear box to the rotary machine as well as being electrically connected to the whole system via two sets of coils. This FPLA uses stored energy from batteries to create a starting electrical current in the first and second coils. The starting magnetic field moves the piston and creates the magnetic field in the cylinder coils. The converter starts the engine and converts electricity. The external coils and rotating bodies are kept limited in size and mass. The alternative solution is a programmable controller which generates the needed current and oscillation directly in the engine coils (Holmes, 2011).

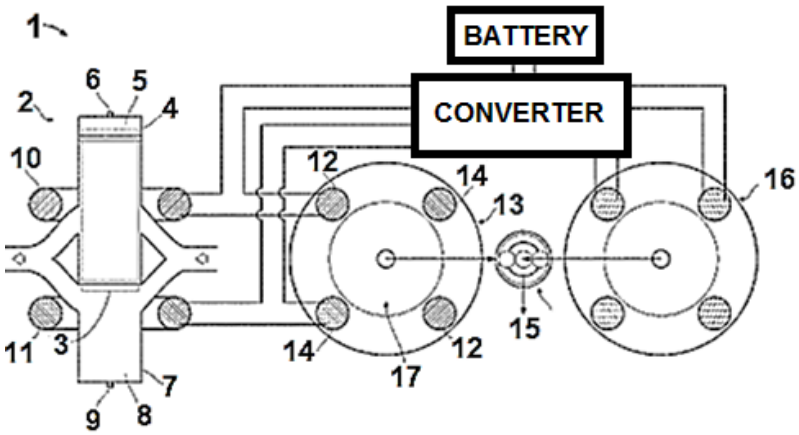

Figure 3. FPE starting system principle (Holmes, 2011).

The turbo charged energy converter, Patent No EP 1540155B1 (Max et al., 2005), is shown in Fig. 4. The energy converter system (1) consist of, comprising piston (2 & 3), combustion chamber (4 & 5), inlet (6 & 7), and outlet (8 & 9) manifold, inlet and outlet valves (10, 11, 12, & 13). One inlet and one outlet valve are controllable separately by control unit in order to regulate the beginning of suction and compression stroke. When piston starts moving, the magnets in the generator affect electromagnetically the coil windings. Differences compare to solution in Fig. 2 is, that magnets are added in to the piston rod. This solution is less sensitive to temperatures but load of generator has impact for piston velocity.

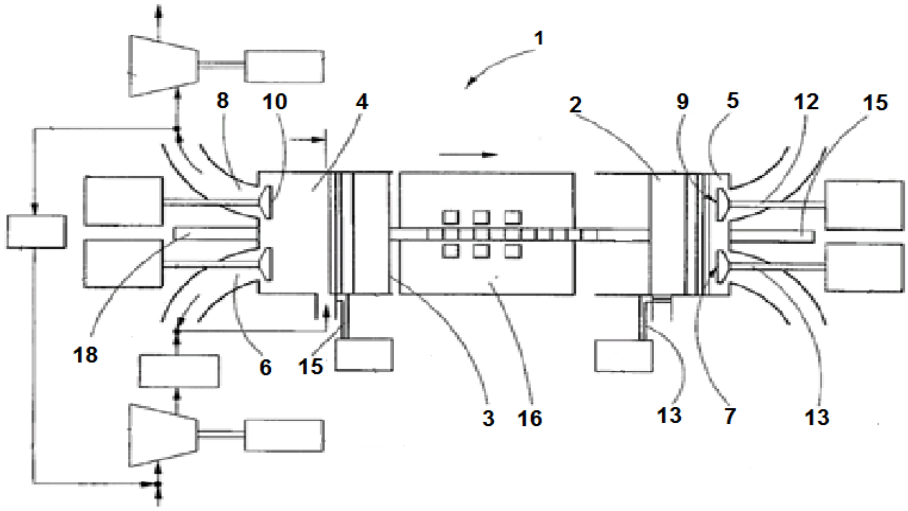

Figure 4. FPE linear alternator (Max et al., 2005).

The batteries operate the linear alternator as a linear motor. The piston is oscillated in the cylinder, building to a higher compression each cycle until sufficient compression is developed for auto-ignition. The fuel which is introduced into the engine ensures self-powered operation. A cold starting process is a special case since a considerable amount of compression is required to achieve the automatic ignition temperature (Max et al., 2005).

The linear alternator allows the FPE to be started without the need for any additional systems and this restrains FPE to compact dimensions. An engine which starts up by means of a battery or supercapacitor is a reasonable prospect when it comes to smoothing out load peaks which can cause malfunctions in engine operation. Any FPE starting without external aids ensures system compactness. When using the spring, hydro or pneumatic systems as engine starters, additional developments in FPE construction are necessary. What's more, when using pneumatic pumps or electrical engines as FPE starters, the mass of the FPE increases. This is problematic in terms of the transportation of FPE.

ENGINE START-UP COMBUSTION STABILITY

The opposed piston FPE generator (FPEG) consists of mechanical resonance starting (Atkinson et al., 1999; Li et al., 2008; Jia et al., 2014a; Jia et al., 2015b). The spring theoretical model was researched and the start-up experiment was conducted on a prototype engine. They investigated engine control, input parameters and misfire reasons. The FPEG (a) simplified scheme and (b) prototype is shown in Fig. 5. The stoichiometric mixture takes place in the intake manifold. The ignition system consists of a 2V battery, ignition coil, and spark plug, which is activated automatically after the required compression has been achieved. The generator motors the start-up process and switches the generator mode after the starting-up process has been completed. The magnets are placed in the centre of the piston and the stator coil is connected to an electrical load absorber. All three starting phases: 1) starting; 2) the electrical motor

phase; and 3) the generator switch phase is to be coupled up to a proper control system in order to ensure transition and stable running. All of the processes are measured by system sensors and data is sent to electrical controllers: 1) starting; 2) ignition; 3) electrics; and 4) the external load control system (Jia et al., 2015b).

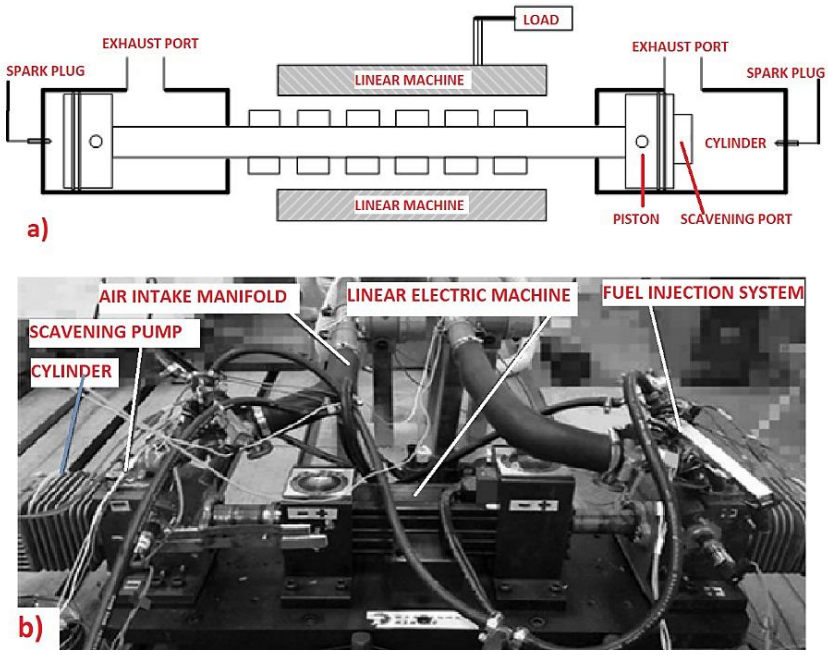

Figure 5. FPE generator simplified design (a) (Jia et al., 2014a) and the prototype (b) (Jia et al., 2015b).

Practical tests of FPE starting are carried out. Testing theory based on the factor that the FPEG is free of side forces, and system friction is low in proportion to electrical force within the start-up. In the practical tests, the theoretical starting force of FPE was 60*N* and in this case, it illustrates the crossing of the friction forces. The practical experimental results are illustrated in Fig. 6. Piston displacement extends step-by-step, until it reaches to maximum value. Gas pressure in the cylinder and maximum velocity of the piston increases with each stroke. Suitable compression value in FPE cylinder was reached in less than a second (Jia et al., 2014). The amplitude of piston movements and velocity increased in respect to the completion of the stroke time (Fig. 6). Fig. 6 shows that, in addition to friction, air leakage, heat transfer, and vibration all exist as additional drains on energy production. Piston movement amplitude, maximum piston velocity, and cylinder pressure peak which increases gradually by resonance and also increases rapidly (at *0.8* fractions of a second) all serve to achieve the target for ignition. Later research will need to focus on new targets, these being achieving the compression ratio (8:1) and the cylinder pressure (*10 bar*). The crossing of the friction forces, the static friction force (*60N*), was set as a maximum theoretical force. In practical experiments it emerged that it was twice as much as *60N*. In FPE tests, forces were applied which were between *80N* to *125N* at a *15N* interval. At *80N* (*8.5Hz~510 cycle per min*), the maximum cylinder pressure of *5 bar* after four cycles was achieved and remained at the same level.

A motoring force of *95N* (*10Hz ~600 cycle per min*) achieved *7 bar* in six cycles and remained stable afterwards (Jia et al., 2015b).

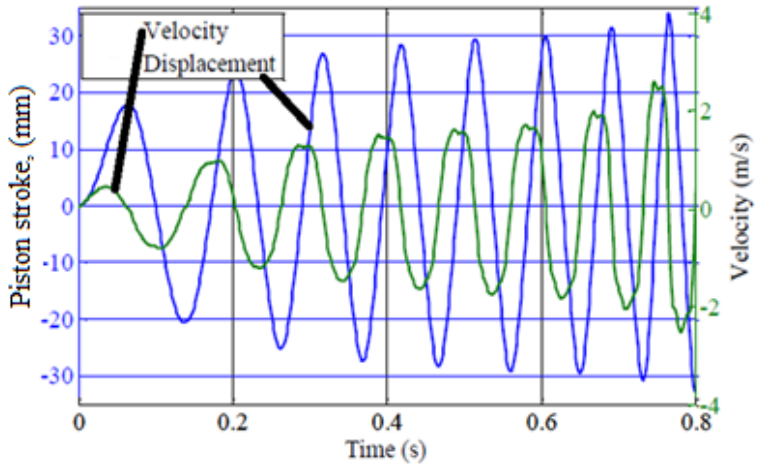

Figure 6. The experimental results of piston stroke and velocity (Jia et al., 2015b).

The starting force needs to exceed *103N* to be able to start the engine smoothly. After several cycles a motor force over *103N* (650 cycles per min) provides conditions which ensure that ignition can take place. The fixed motoring force of *125N* with ignition timing set 27mm from the central position was implemented for the start-up process. The prototype runs using the stoichiometric air-fuel ratio ($\lambda = 1.0$). The velocity profile is close to symmetrical before and after BDC/TDC as the difference in acceleration is small. The maximum piston velocity is achieved in the middle of the stroke. With a higher starting force having been achieved, the piston velocity and compression is higher. The piston moves at a high and relative constant speed at the middle portion of the stroke. The slowdown of the piston takes place at the bottom dead centre (BDC) and top dead centre (TDC). The FPEG prototype output maximum force reaches *232N* and a piston velocity of 3.1 m s^{-1}. The higher figures result in overheating of the stator coil and, after starting, the piston velocity declined. The piston decline increased gas flow through the piston rings and the heat transfer. Limiting of the piston movement velocity caused misfires in the combustion process. For this reason, the FPE control unit is adjusted as follows: when the electrical generator is being used as a motor, continuous ignition and combustion were both achieved. After a period of 1.2 seconds, the system obtains the stability it requires (Jia et al., 2015b).

Considerably more complex starting-up operations are being researched by Carlson. The ports are closed and the trapped air is compressed by the piston towards the TDC point. The trapped compressed air behaves like a mechanical spring and supports the next stroke. The pistons are cyclically reciprocated to suit the air charge pressure rise and combustion pressure rise. Finally, a spark plug initiates combustion in the first cylinder and then in the second cylinder. The spark plugs are used until maximum cylinder pressure achieves the required compression ignition level and, after the HCCI mode is working, the SI is disabled (Carlson, 2005). The FPE linear generator (FPLA) start-up and mechanical problems are being researched by Zulkifli et al., 2008.

The spark ignited dual FPE uses a brushless linear motor to produce the required start-up force. The research focuses on the FPLA mechanical model and provides simulations for different motoring force values. The start-up strategy proposes the presence of air compression in the engine cylinders prior to combustion (Zulkifli et al., 2008).

The generator coils will be loaded with a fixed DC voltage, and an open-loop, rectangular commutation of the input current and a high motoring force reciprocates the translator at small amplitudes until the amplitude and speed of the mechanical resonance reach the required parameters for combustion (Zulkifli et al., 2008). A starting method which uses the resonance in a diesel free-piston linear alternator with a commercial permanent magnet tubes has shown that: (1) the FPLA can be started by using the air-spring characteristics and with a comparatively small thrust force, but a greater thrust force will engage the start-up in a few less cranking cycles; (2) the load on the linear alternator is associated with the cylinder bore measure and the maximum electromagnetic force is approximately proportional to the bore square measure; (3) with the same fuel/air equivalence ratio and external load resistance, a longer effective stroke length helps to increase the compression ratio and also served to indicate the efficiency of the free-piston engine; (4) with the same fuel/air equivalence ratio and external load resistance, it can generally be seen that a longer effective stroke length leads to a higher power output level (Mao et al., 2011). Researches of the diesel FPE start-up and working parametric analysis (Mikalsen & Roskilly, 2010), and detailed engine control strategies (Mikalsen & Roskilly, Part 1, 2010; Mikalsen & Roskilly, Part 2, 2010; Mikalsen et al., 2010) reached on the similar results.

The FPE idea is simple and compact power pack technology, which is easily maintained due to a few simple engine parts. The engine's external starting extras include system ballast, which means that linear or rotational electrical generators maintain the preliminary measurements and are used for operation of normal engine. The stable duty-cycle is achieved by controlling the piston stroke and energy storage. After solving the FPE management process satisfactorily, the unique features of this resource can be released onto markets so that they can compete with existing crankshaft engine technology. The scavenging, spark, or compression ignition and exhaust release process represent a major challenge for all types of FPE. The piston dictates consequent processes which include compress control. In order to be able to ensure smooth running, the control systems have to start with the nature of the fuel itself and the fuel preparation process. When it comes to piston motion calculations using different fuels, the algorithms can be developed. FPE control requires precise algorithms and optimised operating software for the 'virtual crankshaft'. The piston speed is high, and data traffic needs to be extremely rapid when it comes to sending and receiving sensor information and executing commands. Control functions can only be carried out by using sensitive sensors and high speed reaction valves.

OUTLOOK

The FPE frequency depends upon P_0 and L loads. Therefore the fuel mixture, the moving piston (of between 4–15 kg), the ignition position, and the loads need advanced combustion control strategies in place to be able to properly manage them. FPE load regulation is one method of controlling the combustion process. Fuel injection and exhaust manipulation have only a limited level of influence on the engine's operation

and the methods used for fine tuning. Stroke-to-stroke manipulation is carried out by reducing the external excitation and increasing the damping coefficient. The method prevents engine damage and bounce chamber damping. The piston rod stiffness provides a positive effect on external excitation and ignores the initial state. The pressure peaks and working cycle variations are controlled by the piston motion estimation and by accurate injection timing. When using one piston hydraulic FPE, the process of controlling it is less problematic than when using rigidly connected pistons, because every revolution consists of two power strokes. The first piston's compression is the second piston's, which means that the system management reaction rates must be higher. The timing-based injection method reduces pressure variability and means that the resultant kinetic energy will be used. The aforementioned method has a significant effect on the reliability and simplicity of engine operations. The method allows the pressure in the combustion to be controlled, along with the forming of the air-fuel mixture. Accordingly, the most important controlling principle is the control of the entire fuel system, starting from fuel chemical kinetics and subsequent gas dynamics.

The varied stroke causes fuel injection timing problems. The problem can be solved by limiting of the piston stroke interval. The piston oscillation frequency must be increased step by step, until the piston stroke has reached to the maximum value. The load control must restrained within tight limits otherwise the piston hits the cylinder head and the engine stops. The same problem was revealed in the engine starting process, where valve actuation and timing may cause abnormal combustion. FPE misfiring can be caused by a lack of energy storage and, due to the unstable load, the electrical generator cannot work as a flywheel. The engine stops if any interruption is experienced in compression, combustion, ignition, or injection, or a mistiming occurs.

Geometrically, the FPE allows the maximum stroke of the piston to be used, but the long piston stroke and the rapid piston movement are problems when it comes to controlling the FPE. The piston movement frequency and stroke length are directly related. The piston management in hydro/gas/spring bounce or electrical load systems remains within a very limited range. The FPE can operate on limited conditions, when the precise compression into the cylinder and control of the engine are guaranteed. The aforementioned operation parameters serve to limit the power output range of FPE. The bounce and rebound systems are controlled by the 'pulse with modulation' method. This method needs pre-defined mathematical functions, controllers, highly-sensitive sensors, and fast-acting valves to be able to control the engine operation. The precise piston motion control is complicated, mainly in terms of the engine's full load regime.

When a controllable hydraulic cylinder is used in the engine, the piston can be stopped at the BDC, until combustion energy is released at the top of the parallel piston (Fig. 7). This speciality allows the engine to be operated at very low operational frequencies in terms of piston usage, but efficiency is decreased in the optimum range.

The FPE and reciprocating engine comparison is shown in Fig. 7. The rigid connection FPE and regular reciprocating engine piston stroke and velocities are presented in the Fig. 7. The engines have a similar piston stroke and compression ratio (13.9). The piston motion frequency was 48.8 Hz. The time, when FPE piston velocity is equal to zero ($v = 0$ m s^{-1}) (around to the TDC), is longer, compare to reciprocating engine piston velocity (point A in the Fig. 7). The FPE combustion process is quicker compare to reciprocating engine (after the point B). In a conventional engine, the crank

mechanism rotates and continuously changes the geometry of the combustion chamber, thereby disrupting the process of complete oxidation. In the FPE, free body motion allows better fuel oxidation to be developed and rapid combustion is directly related to a peak cylinder temperature and heat release in the cylinder which is significantly lower than in traditional IC engines. The complete combustion and the combustion temperature are ways in which emissions can be reduced to a remarkable degree. In the author's opinion, a unique feature of the FPE is between points A and B, as shown in Fig. 7. Fuel mixture burning is a chemical process, which means that the precise fuel mixture preparation process and the related chemical equations must be known in advance. The rate of expansion for burning hydrogen-oxygen is far better than it is for carbon-oxygen and, thermodynamically, the stoichiometric limitations are different, as is adiabatic efficiency. The FPE is capable of working at very low fuel consumption rates, based on lean (30:1) and super lean (50:1) fuel mixtures. Important is adiabatic efficiency not rich air-fuel mixture. When combustion takes place, the shock wave which passes through the fuel makes it burn differently, which is close to the detonation point and is key when it comes to extracting more energy from each kilogramme of fuel. Lean mixtures release more power because more oxygen is in the combustion process, burning carbons and hydrogen. During the TDC piston's dead time there is enough of an opportunity to create the pressure required for burning a very lean mixture and, in a very short time, the temperature will increase enough to support the hydrogen-oxygen reaction. Due to the fast combustion process in the cylinder, cylinder walls are not affected by flame. In addition, in to the cylinder sucked air-fuel mixture is cooling the cylinder wall. From this it can be seen that noise levels are reduced, exhaust gasses do not consist of any useful heat energy, and polluting carbon monoxides are greatly lessened in quantity.

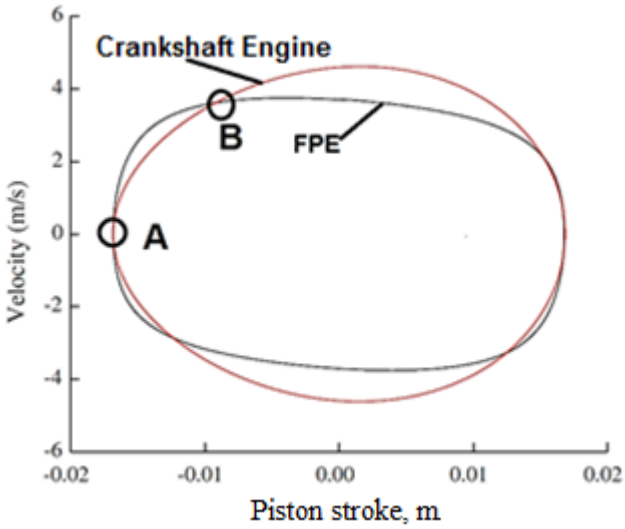

Figure 7. Compared FPE and IC engine velocity and piston stroke (Xiao et al., 2010).

The FPE and reciprocating engine comparison is shown in Fig. 7. The rigid connection FPE and regular reciprocating engine piston stroke and velocities are presented in the Fig. 7. The engines have a similar piston stroke and compression ratio (13.9). The piston motion frequency was 48.8 Hz. The time, when FPE piston velocity is equal to zero ($v = 0$ m s^{-1}) (around to the TDC), is longer, compare to reciprocating engine piston velocity (point A in the Fig. 7). The FPE combustion process is quicker compare to reciprocating engine (after the point B). In a conventional engine, the crank mechanism rotates and continuously changes the geometry of the combustion chamber, thereby disrupting the process of complete oxidation. In the FPE, free body motion allows better fuel oxidation to be developed and rapid combustion is directly related to a peak cylinder temperature and heat release in the cylinder which is significantly lower than in traditional IC engines. The complete combustion and the combustion temperature are ways in which emissions can be reduced to a remarkable degree. In the author's opinion, a unique feature of the FPE is between points A and B, as shown in Fig. 7. Fuel mixture burning is a chemical process, which means that the precise fuel mixture preparation process and the related chemical equations must be known in advance. The rate of expansion for burning hydrogen-oxygen is far better than it is for carbon-oxygen and, thermodynamically, the stoichiometric limitations are different, as is adiabatic efficiency. The FPE is capable of working at very low fuel consumption rates, based on lean (30:1) and super lean (50:1) fuel mixtures. Important is adiabatic efficiency not rich air-fuel mixture. When combustion takes place, the shock wave which passes through the fuel makes it burn differently, which is close to the detonation point and is key when it comes to extracting more energy from each kilogramme of fuel. Lean mixtures release more power because more oxygen is in the combustion process, burning carbons and hydrogen. During the TDC piston's dead time there is enough of an opportunity to create the pressure required for burning a very lean mixture and, in a very short time, the temperature will increase enough to support the hydrogen-oxygen reaction. Due to the fast combustion process in the cylinder, cylinder walls are not affected by flame. In addition, in to the cylinder sucked air-fuel mixture is cooling the cylinder wall. From this it can be seen that noise levels are reduced, exhaust gasses do not consist of any useful heat energy, and polluting carbon monoxides are greatly lessened in quantity.

In conclusion, the piston ridged rod principle should be maintained due to the absence of side forces and lower levels of friction on the piston. According to the engine start-up and operations control problems, useful energy must instantly be withdrawn via the centre of the rigid piston rod and sent to the rotational movement. Not having been subject to cooling, the reciprocating moving magnets or ferromagnets are not stable and cannot produce sufficient current at a stable frequency. It is possible to use an external frequency converter to produce the current at the stable frequency but this is an additional cost and also acts as extra ballast for the system.

The solution which is being proposed by the author is as follows: the rotating flywheel is polyfunctional, and is positioned on top of the two piston one-rod engine, and rotates horizontally as shown in Fig. 8. The flywheel ensures the stability of the generator and stores energy for the next load peak. The rotating flywheel carries magnets which are placed on the outer side of flywheel.

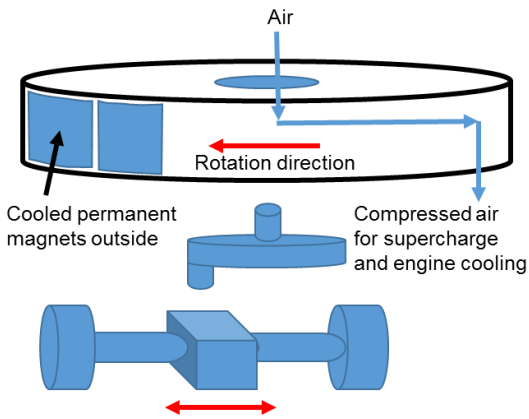

Figure 8. The simplified design of the FPE generator.

The permanent magnets and coil windings are kept outside and are constantly cooled. The normal port scavenging in a lean mixture situation is insufficient, and as a result the engine must be supercharged. The flywheel compresses air for supercharging and engine cooling via inner channels. The air cooled engine is powerful and excludes the outer cooling system. Finally, the flywheel serves to stabilizes the combustion engine and reduces piston movement vibrations. Such a configuration keeps the engine-generator (GENSET) flat, with a very low centre of gravity, and horizontal rotation adds stability. The solution is a two-stroke engine, with two power strokes per revolution. Combustion will be carried out after each 180^{o} degrees stroke. The recommended piston stroke is 1.8 of the piston diameter and should not be variable. The piston rod consists of two parts: (1) a lightweight piston with sleeve; and (2) the reciprocating rigid rod. The sleeve keeps the piston in TDC for a longer period of time as it moves freely on the piston rod. The compression stroke starts and the air-fuel mixture compresses until TDC is reached. The connected flywheel with its piston rod moves towards the BDC and the spark ignites the mixture. From this point forwards, combustion continues towards the BDC. The engine has outlet and inlet ports and charging takes place through electric valves which are located on top of the cylinder. The heat exchanger pre-treats the fuel and uses exhaust gasses for heating and breaking down fuel molecules. The engine lubricates itself from the crankcase, which is a small area of the engine and which uses the piston rod reciprocating motion for pumping oil. Crankcase lubrication allows fuel injection without any oil admixtures. The flywheel with its magnets acts in a contrary fashion and works as the engine starter.

CONCLUSIONS

The different technical solutions which are available in terms of FPE have been reviewed from the point of the system's invention until the present day. The simulations and empirical experiments have all been discussed. Any weaknesses or strong points related to FPE have been mapped out and discussed in a critical fashion. The most important findings are these: 1) there exists a significantly lower kW kg^{-1} ratio in proportion to crankshaft engines; 2) lower fuel consumption rates have been registered

against those of crankshaft engines due to the lower friction levels; 3) the missing crankshaft allows the engine dimensions to be significantly reduced and, at the same time, allows the maximum piston stroke to be applied and lower temperature release to be achieved due to the rapid burning process which in turn reduces the levels of emissions.

The most important points to identify in relation to FPE are these: 1) piston movement is too complicated to control; 2) during engine operations, three variables should be precisely controlled at the same time, with these being the following; 3) air-fuel mixture, engine load, and volumetric efficiency.

The technical solution which involves a new power generator is described with the general description of generator operation. The most important advantages in this novel solution are these: a slim motor-generator with the aforementioned planetary moving flywheel/generator rotor which stabilises the system based on the spinner effect; the flywheel is also supercharger; two stroke engine with crankcase lubrication allows to use fuels without oil; internal combustion engine combustion process is controlled by crankshaft, what is connected to ridged rod of piston.

REFERENCES

Achten, P.A. 1994. Review of Free Piston Engine Concepts. *SAE Technical Paper* **941776**, 1994, doi: 10.4271/941776.

Achten, P.A., Oever J.P.J., Potma, J. & Vael, G.E.M. 2000. Horsepower with brains: the Design of the Chiron free piston engine. *SAE paper* **2000-01-2545**, 2000.

Aichlmayr, H.T. 2002. Design Considerations, Modeling, and Analysis of Micro-Homogeneous Charge Compression Free-Piston Engines, Ph.D. thesis, University of Minnesota, 2002. Ignition Combustion.

Atkinson, C.M., Petreanu, S. & Clark, N.N. 1999. Numerical simulation of a two stroke linear engine-alternator combination. *SAE Paper* 1999-01-0921, 1999.

Blarigan, P., Paradiso, N. & Goldsborough, S. 1998. Homogeneous charge compression ignition with a free piston: a new approach to ideal Otto cycle performance. *SAE paper* 982484, 1998.

Braun, A.T. & Schweitzer, P.H. 1973. The Braun Linear Engine. *SAE Technical Paper* **730185**.

Brunner, H., Dantlgraber, J., Feuser, A., Fichtl, H., Schäffer, R. & Winger, A. 2005. Renaissance einer Kolbenmachine. *Antriebstechnik* **4**, 66–70.

Carlson, C. 2005. Compression Pulse Starting of a Free Piston Internal Combustion Engine Having Multiple Cylinders, US 6,966,280 B1, 2005.

Chang, J., Guralp, O., Filipi, Z., Assanis, D., Kuo, T.W., Najt, P. & Rask, R. 2004. New heat transfer correlation for an HCCI engine derived from measurements of instantaneous surface heat flux. *SAE Technical paper*, 2004–01-2996, 2004.

Clark, N., Nandkumar, S., Atkinson, C., Atkinson, R., McDaniel, T. & Petreanu, S. 1998. Modelling and development of a linear engine. *ASME Spring Conf Int Combust Engine Div*. **30**(2), 49–57.

Defence Update. 2003. (http://defense-update.com/features/du-1-04/batteries-lessons-iraq.htm).

Durrett, R.P., Gopalakrishnan, V. & Najt, P.M. 2012. Turbocompound Free Piston Linear Alternator, US 2012/112469 A1, 2012.

Farmer, H.O. 1947. Free-Piston Compressor-Engines. *Proceedings of the Institution of Mechanical Engineers*, vol. **156**, pp. 253–271.

Fredriksson, J & Denbratt, I. 2004. Simulation of a two-stroke free-piston engine. *SAE paper* 2004-01-1871, 2004.

Hibi, A. & Ito, T. 2004. Fundamental test results of a hydraulic free piston internal combustion engine. *Proceedings of Institute of Mechanical Engineering* **218**, 1149–1157.

Hanipah, M.R., Mikalsen, R. & Roskilly, A.P. 2015. Recent commercial free-piston engine developments for automotive applications. *Applied Thermal Engineering* **75** (2015) 493e503.

Holmes, A.G. 2011. Free-piston Linear Alternator Systems and Methods, US 20110012367A1, 2011.

Nguyen, B.H., Ocktaeck, L. & Norimasa, I. 2015. The effects of key parameters on the transition from SI combustion to HCCI combustion in a two-stroke free piston linear engine. *Applied Energy* **137,** 385–401.

Jia, B., Zhengxing, Z., Huihua, F., Guohong, T. & Roskilly, A.P. 2014a. Investigation of the starting process of free-piston engine generator by mechanical resonance. *Energy Procedia* **61**, 572–577.

Jia, B., Zuo, Z., Feng, H., Tian, G., Roskilly, AP. 2014b. Development approach of a spark ignited free-piston engine generator. SAE Technical Paper 2014-01-2894.

Jia, B., Zuo, Z., Tian, G., Feng, H. & Roskilly, A.P. 2015a. Development and validation of a free-piston engine generator numerical model. *Energy Conversion and Management* **91**, 333–341.

Jia, B., Tian, G., Feng, H., Zuo, Z. & Roskilly, A.P. 2015b. An experimental investigation into the starting process of free-piston engine generator. *Applied Energy* **157**, 798–804.

Kock, F., Haag, J. & Horst, F.E. 2013. The Free Piston Linear Generator – Development of an Innovative, Compact, Highly Efficient Range- Extender Module. SAE Technical Paper 2013-01-1727.

Kittel, C. 1995. Hardcover; Hoboken, Nj, U.S.A.: John Wiley & Sons Inc, 1995 *Introduction to Solid State Physics*. ISBN: 9780471874744 / 0471874744.

Li, K., Zhang, C. & Sun, Z. 2015. Precise piston trajectory control for a free piston engine. *Control Engineering Practice* **34**(2015)30–38.

Li, Q.F., Xiao, J. & Huang, Z. 2008. Simulation of a two-stroke free-piston engine for electrical power generation. *Energy Fuel* **22**, 3443–9.

Lund, P. 2008. Puolustusvoimien Teknillinen Tutkimuslaitos 2008. (Defense Forces Technical Research) *Sotatekninen arvio ja ennuste 2025 STAE 2025, osa 1*. Energian Tuotto, Siirto Ja Varastointi, 109–110 pp. (in Finland).

London, A.L. & Oppenheim, A.K. 1952. The Free-Piston Engine Development Present Status and Design Aspects.Transactions of the ASME, vol. **74**, no. 2, pp. 1349–1361. *Based upon ASME Technical Paper* **52**-S-17.

Mao, J.L., Zuo, Z.X. & Feng, H.H. 2011. Parameters coupling designation of diesel free-piston linear alternator, *Appl. Energy* **88** (Dec 2011) 4577e4589.

Max, E., Lundgren, S., Somhurst, J., Hoglund, A., Wirmark, G., Gertmar, L. & Denbratt, I. 2005. Energy Converter, Sweden Patent EP 1 540 155 B1, 2005.

Mikalsen, R. & Roskilly, A.P. 2007a. A review of free-piston engine history and applications. *Applied thermal Engineering* **27**, 2339–2352.

Mikalsen, R. & Roskilly, A.P. 2007b. The design and simulation of a two-stroke free-piston compression ignition engine for electrical power generation. *Applied Thermal Engineering, 2007.04.009.*

Mikalsen, R., Jones, E. & Roskilly, A.P. 2010. Predictive piston motion control in a free-piston internal combustion engine. *Applied Energy* **87**, 1722–1728.

Mikalsen, R. & Roskilly, A.P. 2010. The control of a free-piston engine generator. Part 1: Fundamental analyses. *Applied Energy* **87**, 1273–1280.

Mikalsen, R. & Roskilly, A.P. 2010. The control of a free-piston engine generator. Part 2: engine dynamics and piston motion control. *Appl Energy 2010*; **87**(4):1281–7.

Najt, P.M., Durrett, R.P. & Gopalakrishnan, V. 2012. Opposed Free Piston Linear Alternator, US 2012/112468 A1, 2012.

Nemecek, P. & Vysoký, O. 2006. Control of two-stroke free-piston generator, in: *Proceedings of the 6th Asian Control Conference*, vol. 1, 2006.

Nguyen, B.H., Ocktaeck, L. & Norimasa, I. 2015. The effects of key parameters on the transition from SI combustion to HCCI combustion in a two-stroke free piston linear engine. *Applied Energy* **137**, 385–401.

Noren, O.B. & Erwin, R.L., 1958. The Future of the FREE-PISTON ENGINE in commercial Vehicles. *SAE Transactions* **66**, 305–314.

Robinson, M. & Clark, N.N. 2016. Study on the Use of Spring in a Dual Free Piston Engine Alternator, *SAE Technical Paper* 2016-01-2233.

Tikkanen, S., Lammila, M., Herranen, M. & Vilenius, M. 2000. First cycles of the dual hydraulic free piston engine. *SAE paper* 2000-01-2546, 2000.

Wu, Y., Wang, Y., Zhen, X., Guan, S. & Wang, J. 2014. Three-dimensional CFD (computational fluid dynamics) analysis of scavenging process in a two-stroke free-piston engine. *Energy* **68** (2014) 167–173.

Xiao, J., Li, Q. & Huang, Z. 2009. Motion characteristic of a free piston linear engine. *Applied Energy 2009*. doi:10.1016/japenergy.2009.07.005.

Xu, Z. & Chang, S. 2010. Prototype testing and analysis of a novel internal combustion linear generator integrated power system, *Appl. Energy 87* (2010) 1342–1348.

Xu, S., Wang, Y., Zhu, T., Xu, T,. Tao, C. 2011. Numerical analysis of two-stroke free piston engine operating on HCCI combustion. *Applied Energy* **88** (2011) 3712–3725.

Zhang, C., Li, K. & Sun, Z. 2015. Modeling of piston trajectory-based HCCI combustion enabled by a free piston engine. *Applied Energy* **139**, 313–326.

Zhang, S., Zhao, C. & Zhao, Z. 2015a. Stability analysis of hydraulic free piston engine. *Applied Energy* **157,** 805–813.

Zhang, S., Zhao, C., Zhao, Z Z. & Ma, F. 2015b. Combustion characteristics analysis of hydraulic free piston diesel Engine. *Applied Energy* **160**(2015) 761–768.

Zhao, Z., Huang, Y., Zhang, F., Zhao, C. & Han, K. 2010. Experimantal Study on Hydraulic Free Piston Diesel Engine. SAE Technical Paper 2010-01-2149.

Zhao, Z., Zhang, F., Huang, Y. & Zhao, C. 2013. An experimental study of the cycle stability of hydraulic free-piston engines. *Applied Thermal Engineering* **54** (2013) 365–371.

Zhou, S., Xu, B. & Yang, H.Y. 2005. Oscillation characteristic of dual hydraulic free piston engine piston component assemble. *J Chin Coal Soc.* **30**, 1–4 (in Chinese).

Zulkifli, S.A., Karsiti, M.N. & Aziz, A.R.A. 2008. Starting of a free-piston linear engine-generator by mechanical resonance and rectangular current commutation, in: *Vehicle Power and Propulsion Conference, 2008*. VPPC '08, IEEE, 2008, pp. 1–7.

Agronomy Research **15**(S1), 1223–1231, 2017

Biomass combustion research studying the impact factors of NOx formation and reduction

T. Sereika[1,*], K. Buinevičius[1,2], E. Puida[1] and A. Jančauskas[2,4]

[1]Kaunas University of Technology, Faculty of Mechanical Engineering and Design, Department of Thermal and Nuclear Energy, Studentų st. 56, LT–51424 Kaunas, Lithuania
[2]UAB 'Enerstena' Centre of Research and Development, Partizanų st. 89, LT–50312 Kaunas, Lithuania
[*]Correspondence: titas.sereika@ktu.edu

Abstract. Aim of this study was to identify potential NOx reduction factors and determine impact of nitrogen quantity in the fuel, during combustion process and conversion to nitrogen oxides. Experiments were performed using moving grate biofuel boiler with two staged air inlets, which represents industrial boiler operating principles. Combustion was performed using agricultural wastes: grain middlings, buckwheat hulls, corn pellets and mixtures with wood pellets. These types of fuels in combustion process generate about two times bigger amount of nitrogen oxides than wood pellets. The result of research shows, that the amount of nitrogen in the fuel has the greatest impact for NOx generation compared to all NOx formation forms. It was found that a smaller quantity of nitrogen, has bigger impact factor, than higher quantity of nitrogen, in biomass, for NOx formation during combustion. It was noticed that during combustion process the amount of carbon monoxide is inversely proportional to NOx values. The impact factor of nitrogen conversion to NOx and CO potential of reducing NOx is presented by formula in this paper.

Key words: biomass combustion, NOx formation, CO.

INTRODUCTION

In Lithuania 60% of thermal energy is produced from renewable resource biofuel. Biofuel resources are wood, cutting wastes, straw and leaves. Growing demand of biofuel encourages to look for new renewable energy resources which could supplement the list of fuel variety.

For this purpose, the attention was paid to agricultural waste. However, agricultural waste is characterized by higher nitrogen oxide concentrations during combustion, but usage of agricultural waste is limited because of valid environmental protection standards. The first aim of this study was to identify potential NO_x reduction factors. The second aim was to determine the impact of nitrogen quantity in the fuel to the NO_x formation during combustion process.

In this work examined alternatives for biofuel include agricultural wastes: grain middlings, buckwheat hulls, corn pellets. These types of fuel during combustion process generate about two times higher amount of nitrogen oxides. The paper presents

combustion techniques of the examined fuel types, experimental study results, evaluation of emission concentrations in flue gases and dependence on fuel composition. Experiments have demonstrated that the higher the content of nitrogen contained in the shape of compounds, the lower the share of this nitrogen transitioning into nitrogen oxides. The conducted studies formed the basis for the development of a formula for calculating NO_x concentrations from nitrogen contained in fuel. Main designations used in paper presented in Table 1.

Table 1. Nomenclature

Mark	Explanation	Mark	Explanation
NO_x	nitrogen oxides	W	Fuel moisture content, %
CO_2	carbon dioxide	α	excess air coefficient
K_N	nitrogen conversion factor, %	V_a^t	theoretical content of air necessary for combustion, m^3
N_K	nitrogen content in the fuel	V_g^t	theoretical flue gas volume, m^3

MATERIALS AND METHODS

Materials

The experiments were accomplished on the basic fuel – agricultural wastes (grain middlings, buckwheat hulls, corn pellets). These fuels were used as high NO_x concentration generating fuels (with high nitrogen content in mass). (Table 2) illustrates results of the used fuel nitrogen content and calorific value.

Table 2. Properties of the substances used in the research

Fuel	W, %	N_k, %	Ash, %	$Q_{w.f.l}$ kJ kg^{-1}
Grain middlings	8.0	0.59	0.38	15,617
Buckwheat hulls	8.7	0.57	0.27	15,912
Corn pellets	7.0	1.24	0.32	14,934
Wood pallets	8.7	0.13	0.17	17,100

Agricultural wastes are formed every year. During the annually cutting, cereal processing and other technological process of agricultural products, some of it remains as a waste. Consequently, agriculture companies show and interest to use these wastes to meet their own energy needs.

In Lithuania, a large amount of such wastes are created and cannot be used as a fuel due to large quantities of nitrogen oxides generated during combustion process. However, in case of a successful reduction of the nitrogen contents conversion to nitrogen oxides, type of such biomass could be used in energy production. Moreover, it could reduce amounts of waste disposed in landfills and decrease the amount of wood used in energy production.

Fuels used for research were not additionally treated just dried up. All type of fuels are small fraction 2–5 mm size middlings, hulls and small pallets (6 mm diameter). Fuel is supplied to the combustion chamber by the mechanical feeder. Fuel in combustion zone is blown by primary air, which does not take away unburned particles to the chamber and combustion process going smoothly.

Methods

Experiments were carried out in the Combustion research laboratory of Kaunas University of Technology, which has an installed pellets-fired industrial boiler model and all other system elements shown in (Fig. 1).

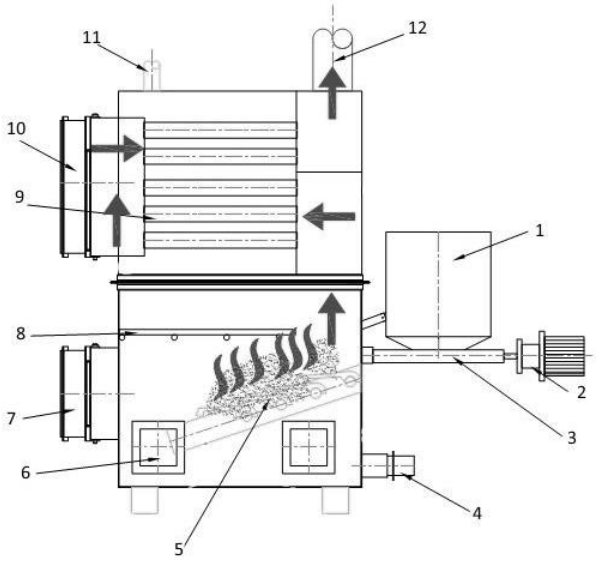

Figure 1. Laboratory combustion research stand: 1 – Fuel container; 2 – Electric motor; 3 – Mechanical feeder; 4 – Primary air inlet; 5 – Moving grate; 6 – Ash hopper; 7 – Inspection window; 8 – Secondary air inlet; 9 – Fire tube boiler; 10 – Inspection door; 11 – Heated water outlet; 12 – Chimney.

The main component of the stand is furnace, which has systems for fuel and air feeding. Furnace and heat exchange surfaces, are the main two components of the water boiler. The operating load of the boiler can vary from 25 to 40 kW Draft fan with a frequency converter assists to emit flue gases to the chimney to keep stable pressure in the combustion chamber.

Branch pipe for flue gas analysis probe is installed in the flue gas pipe in order to be able to make flue gas analysis and temperature measurements. About 20 °C temperature air for combustion is fed from the surrounding environment. Boiler water temperature is maintained to stay in between 65 °C and 70 °C. Cooling system consists of a heater block with a cooling fan which is constantly fed with pumping water in order to ensure uninterruptible heat transfer.

There are two parameters that control a combustion of all fuel types. First is fuel feeding rate and second is the amount of air that is supplied to the combustion chamber. Flue gas analyser measures generated pollutant concentrations. This analyser measures temperatures and concentrations of nitrogen oxides, nitrogen monoxide, oxygen and carbon monoxide in the exhaust gases.

All the measured made from the dry gasses and concentration of CO and NOx emissions normalized to 6% of O_2.

Frequency converter, which is mounted on the side of the furnace, is used to determine the constant rate of fuel feeding and according to this value, it also regulates the amount of air for combustion. Tank for ash is at the bottom of the grate.

The fuel is burnt so that the temperature in the combustion zone would not exceed 1,200 °C; burning at such temperature mode would allow examining solely the generation of 'fuel NOx', because this temperature is insufficient for the formation of 'thermal NOx' (Hodžic et al., 2016). At this temperature range, its share in the NOx content is so small, that it has no practical value (Javed et al., 2007).

In order to examine biomass samples in a larger total nitrogen spectrum, blends of agriculture waste and wood pellets were prepared. Wood pellets used in the preparation of blends had small nitrogen content up to 0,13 percent, while lower calorific value of fuel was 17,1 MJ kg^{-1}. Blends mechanically were mixed by mass proportions shown in (Table 3).

Table 3. Properties of the fuel blends

Fuel blends	W, %	N_k, %	Ash, %	$Q_{w.f.l}$ kJ kg^{-1}
Blend of grain middlings	8,35	0.36	0.28	16,359
Blend of buckwheat hulls	8.7	0.35	0.22	16,506
Blend of corn pellets	7.85	0.69	0.25	16,017

All the blends made with mass proportion in 50 percent wood pallets and 50 percent original fuel.

COMBUSTION RESEARCH

Experimental fuel combustion research was conducted with the aim to examine the amount of pollutants contained in flue gases.

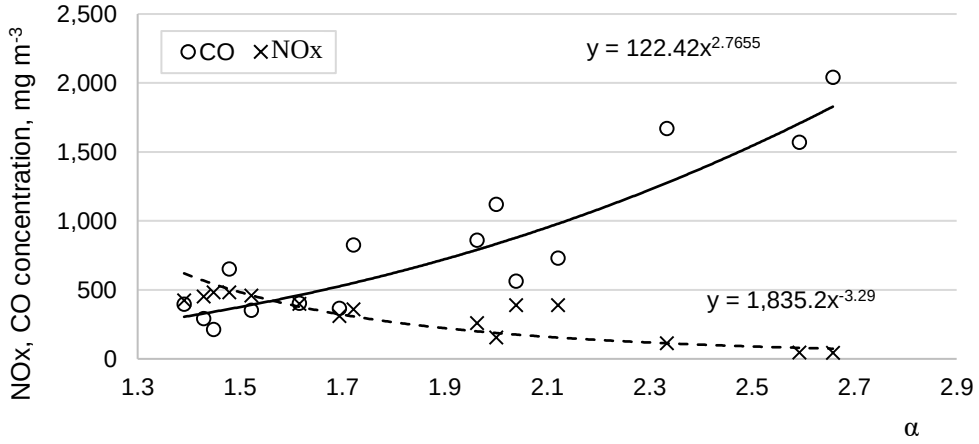

Figure 2. NOx and CO emissions values dependent on excess air ratio (α). Fuel – grain middlings.

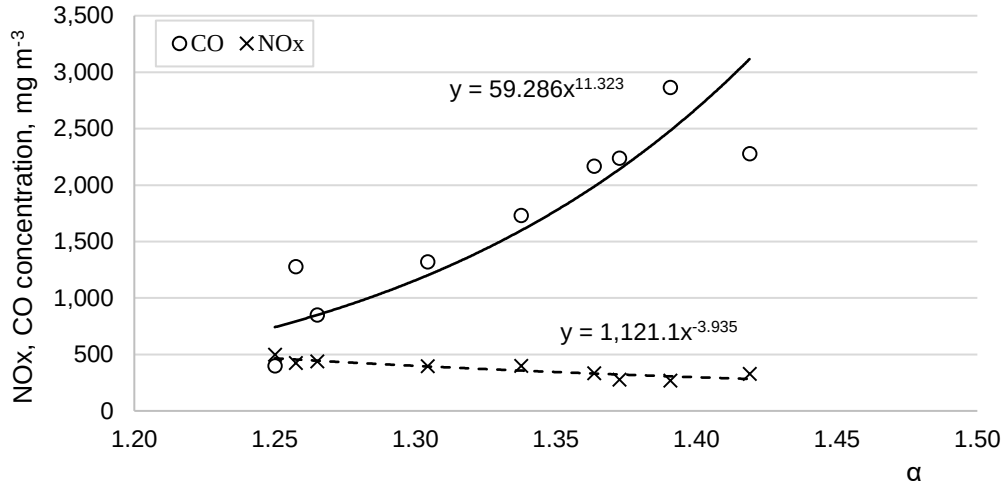

Figure 3. NO_X and CO emissions values dependent on excess air ratio (α). Fuel – buckwheat hulls.

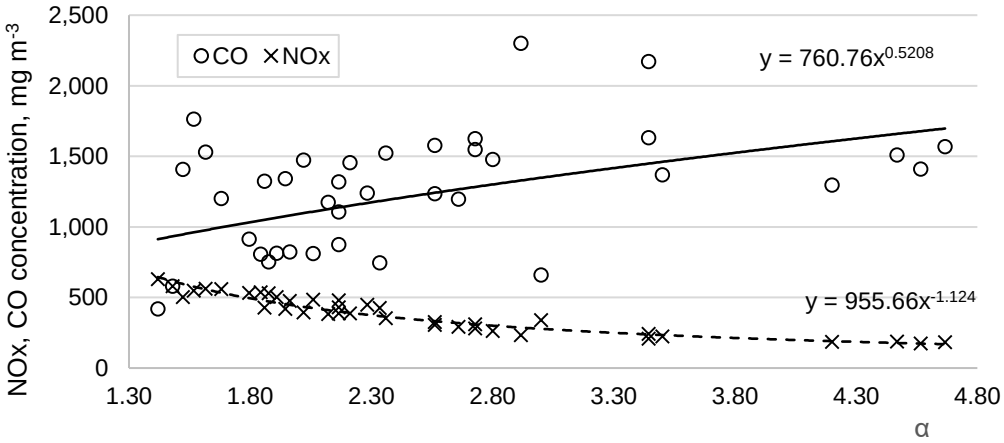

Figure 4. NOx and CO emissions values dependent on excess air ratio (α). Fuel – Corn pellets.

Summary research graphs of the examined waste reveal that the corn pallets with highest nitrogen content generates large amounts of nitrogen oxides of up to 700 mg m^{-3}. Burning other agricultural waste with two times smaller nitrogen content in fuel NO_X concentration reaches 500 mg m^{-3}. This shows that different N content in the substances turns to nitrogen oxides unevenly, and the lower the nitrogen content in the substance, the greater part of it converts to nitrogen oxides.

The highest recorded CO concentrations ranged from 2,100 mg m^{-3} when burning grain middlings and to 2,700 mg m^{-3} when burning buckwheat hulls.

A trend was observed that with an increasing excess air in the furnace above 1.4, NOx concentration in flue gases decreased (Carroll et al., 2015). It has already been

known from other sources (Li et al., 2012) and observed in the conducted experimental research, increasing CO concentration in flue gases has a decreasing effect on NOx generation in flue gases.

Thus in order to determine the dependence of the formation of nitrogen oxides on the content of nitrogen in substances, calculations of the values of the conversion coefficient were conducted. The K_N coefficient of nitrogen conversion to NO_X is calculated as the share of nitrogen contained in fuel having transitioned to NO_X, according to the equation (Buinevičius et al., 2011):

$$K_N = \frac{\left(V_g^t + (\alpha - 1)V_a^t\right) \cdot C_{NO_X}}{328.6 \cdot N_K} \quad (1)$$

where: α – excess air coefficient in flue gases; C_{NO_X} – nitrogen oxides concentration in flue gases, mg m^{-3}; 328.6 – recalculation coefficient;

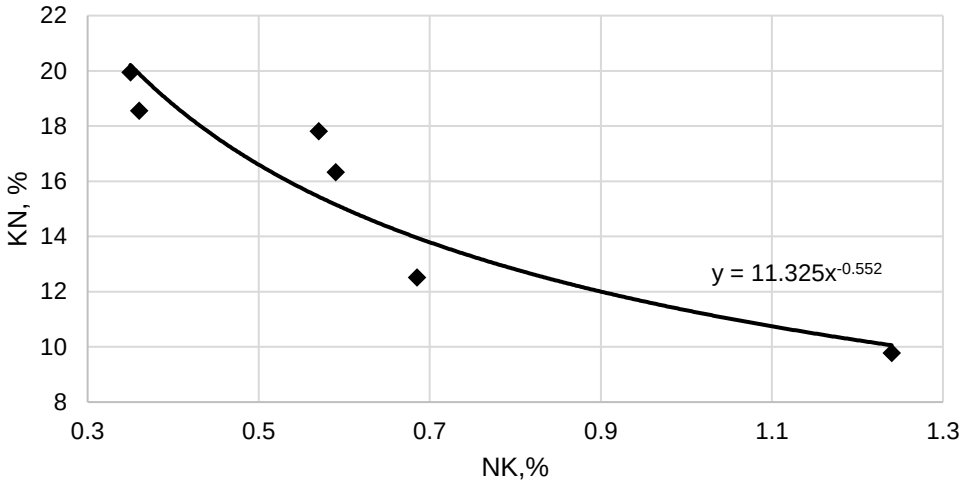

Figure 3. The total approximating nitrogen curve of nitrogen conversion from fuel.

In summary of all the examined materials with higher nitrogen content, a summary graph is drawn up (Fig. 3), with a derived function describing a conversion factor of all examined fuel samples:

$$K_N = 11.325 \cdot N_K^{-0,552} \quad (2)$$

This function may be used to calculate the nitrogen oxides conversion factor in agricultural waste where N amount in mass is less than 1.3%.

Calculation of NO_X concentrations

In order to evaluate the NO_X generation dependence on the nitrogen conversion factor described in formula (3), a formula was drawn up allowing calculating NOx concentration (mg m^{-3}) forming during the combustion process:

$$C_{NO_X} = \frac{328.6 \cdot K_N \cdot N_K}{V_a^t \cdot (\alpha - 1) + V_g^t} \quad (3)$$

The calculation on NO_X concentration by formula (3) gives deviation when in flue gas appears higher amount of carbon monoxide. In order to avoid this error CO influence to NO_X is calculated. The graphs below show the CO influence to NO_X correction.

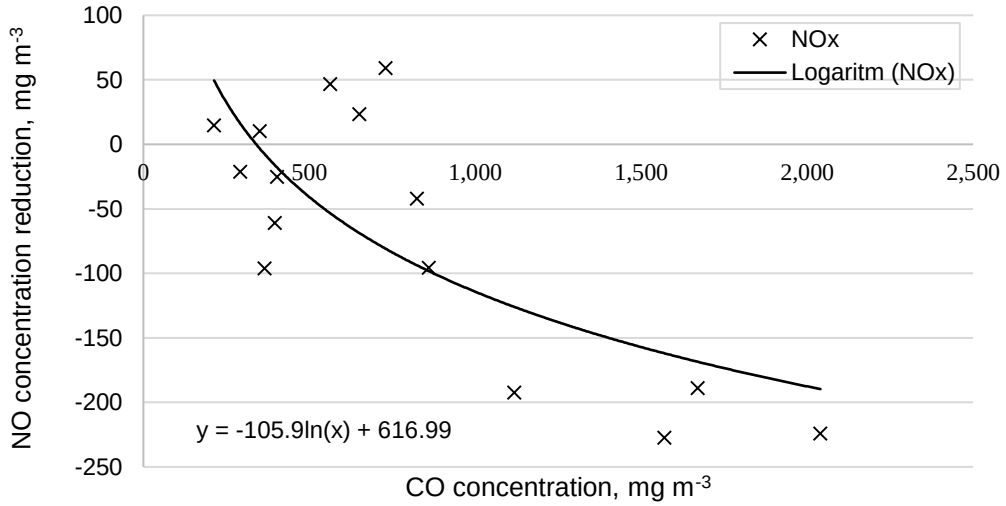

Figure 5. The CO influence to NO_X concentration. Burning grain middlings.

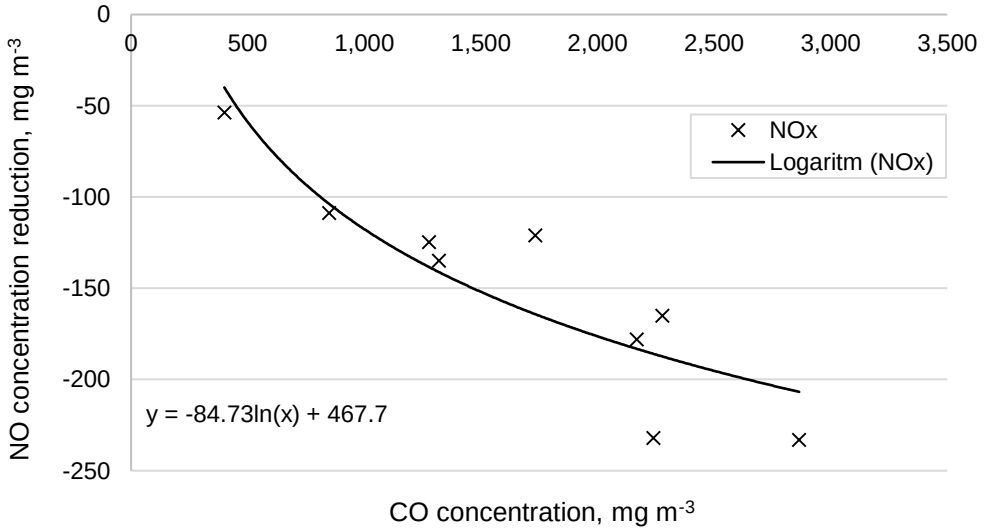

Figure 6. The CO influence to NO_X concentration. Burning grain middlings.

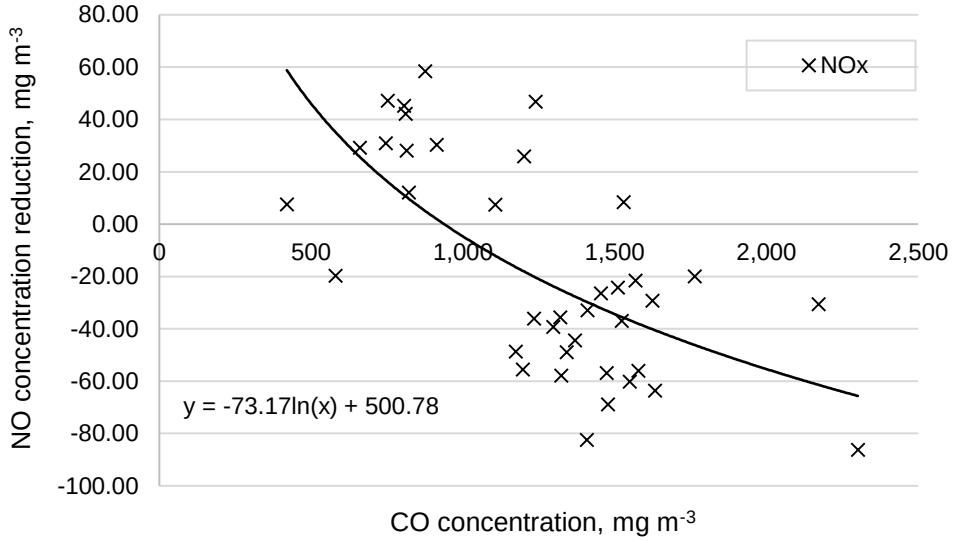

Figure 7. The CO influence to NO_X concentration. Burning corn pallets.

According to (Fig. 5–7), the highest NO_x concentration reduction was measured while burning buckwheat hulls up to 250 mg m^{-3}. It was determined that the CO concentration greater than 500 mg m^{-3} has a noticeable influence to NO_X concentration reduction.

To specify the formula (3) and additionally evaluate the carbon monoxide impact factor for agricultural wastes, approximates formula was derived:

$$K_{CO} = -87.93ln\ (C_{CO})\ + 528.49 \tag{4}$$

where: C_{CO} – carbon monoxide concentration in flue gases, mg m^{-3}

Summing up the formulas (3 and 4) is written new formula:

$$C_{NO_X} = \frac{328.6 \cdot\ K_N \cdot\ N_K}{V_a^t \cdot\ (\alpha - 1) +\ V_g^t} - 87.93ln\ (C_{CO})\ + 528.49 \tag{5}$$

The obtained result reveals that NO_X concentration in flue gases depends on the volume of flue gases. It has a direct dependence on lower calorific value of fuel (Plečkaitienė & Buinevičius, 2011) and values of excess air coefficient (Kuang et al., 2014), nitrogen content in fuel (Wang et al., 2012) and the compiled nitrogen conversion coefficient, which is expressed via the recalculation coefficient and the CO concentration in exhaust gases.

CONCLUSIONS

Noticed that different N content in the substances turns to nitrogen oxides unevenly, and the lower the nitrogen content in the substance, the greater part of it converts to nitrogen oxides. Confirmed in experimental research, that increasing CO concentration in flue gases has a decreasing effect on NO_X generation in flue gases.

To additionally evaluate the carbon monoxide impact factor for agricultural wastes, approximates formula was derived and summed up the formulas for NO_X concentration calculation. The new formula assess hat NO_X concentration in flue gases depends on the volume of flue gases, which has a direct dependence on lower calorific value of fuel and values of excess air coefficient, nitrogen content in fuel and the compiled nitrogen conversion coefficient, which is expressed via the recalculation coefficient and the CO concentration in exhaust gases.

REFERENCES

Buinevičius, K., Plečkaitienė, R., Norinkevičiūtė, R., Černiauskas, E. 2011. Research of NO_X formation from the nitrogen of fuel. *Environmental engineering* **4**, 58–63. (in Lithuanian).

Carroll, J.P., Finnan, J.M., Biedermann, F., Brunner, T., Obernberger, I. 2015. Air staging to reduce emissions from energy crop combustion in small scale applications. *Fuel* **155**, 37–43.

Hodžic, N., Kazagic, A., Smajevic, I. 2016. Influence of multiple air staging and reburning on NO_X emissions during co-firing of low rank brown coal with woody biomass and natural gas. *Applied Energy* **168**, 38–47.

Javed, M.T, Irfan, N., Gibbs , B.M.. 2007. Control of combustion-generated nitrogen oxides by selective non-catalytic reduction. *Journal of the Environmental Management* **83**, 251–289.

Kuang, M, Li, Z, Ling, Z, Zeng, X. 2014. Evaluation of staged air and overfire air in regulating air-staging conditions within a large-scale down-fired furnace. *Applied Thermal Engineering* **67**, 97–105.

Li, J., Yang, W., Blasiak, W., Ponzio. A. 2012 Volumetric combustion of biomass for CO_2 and NO_X reduction in coal-fired boilers. *Fuel* **102**, 624–633.

Plečkaitienė, R., Buinevičius, K., Puida, E. 2013 'Analysis of solid phase nitrogen conversion process to gaseous oxides *Mechanika* **19**, 531–538p.

Wang, J., Fan, W., Li, Y., Xiao, M., Wang K., Ren, P. 2012 The effect of air staged combustion on NO_X emissions in dried lignite combustion. *Energy* **37**, 25–36.

Agronomy Research **15**(S1), 1232–1241, 2017

Effects of sulphur on the storage stability of the bio and fossil fuel blends

K. Sirviö*, S. Niemi, S. Heikkilä and E. Hiltunen

University of Vaasa, Faculty of Technology, PL 700, FIN-65101 Vaasa, Finland
*Correspondence: katriina.sirvio@uva.fi

Abstract. In this study, the aim was to find out if mixing two common fuels together could be beneficial for both the environment and storage stability of fuel. It is obvious, that adding biodiesel to fossil fuel will decrease its sulphur content and reduce its carbon monoxide and hydrocarbon, sulphur dioxide and soot emissions. But will the high sulphur content enhance the storage stability of the biodiesel? Four B20 samples were produced, consisting of 20 vol% biodiesel and 80 vol% fossil diesel. The samples were prepared from rapeseed methyl ester (RME), low sulphuric fossil diesel fuel and high sulphuric diesel solvent. The blends had different sulphur contents of 6, 76, 149 and 226 mg kg^{-1}. For these B20 fuel samples, the parameters were compared that correlate with the storage stability of the fuel blends. The studied parameters were the oxidation stability (OSI, according to EN 15751:2015), acid number (AN, according to EN 14104:2003) and kinematic viscosity (KV, by Stabinger SVM 3000 rotational viscometer). The measurements were carried out straight after mixing the blends, and again after 4, 8 and 12 weeks. According to the results, the fuel containing less sulphur slightly lost its oxidation stability within three months. Instead, the oxidation stability of high sulphuric samples improved within the same time frame. As a conclusion, the study gave a reason to assume that – in spite of its known drawbacks – the sulphur may be favourable to fuel blends' storage stability but the phenomenon and chemistry should be studied in more detail.

Key words: Biofuel, blending, FAME, diesel fuel, B20, stability, sulphur.

INTRODUCTION

During the recent decades, the sulphur content of liquid engine fuels has drastically decreased to reduce harmful effects of exhaust sulphur compounds. The reasons for the fuel sulphur limitations are both technical and environmental; sulphur pollutes the air and poisons the catalysts in emission control systems. Fuel sulphur also increases soot and particulate matter emissions in the exhaust of all kind of internal combustion engines, causes corrosion and also has a deleterious effect on advanced after treatment systems used for CO, HC, NOx and particulate reduction (Kalghatgi, 2014; Zhao et al., 2016). Moreover, the fuel sulphur causes corrosion inside the engine cylinder. In combustion processes, sulphur oxidizes to sulphur dioxide SO_2. It will be further oxidized to SO_3 and then again react with water. Formed sulphuric acid, H_2SO_4, will condensate on the metal surfaces and cause corrosion (Heywood, 1988). This aspect makes the de-sulphurization important but refining processes which remove the sulphur from the fuel simultaneously reduce fuels lubricity.

Sulphur emissions, both gaseous and particles, are also harmful for human health. An acute exposure can cause trouble in breathing and a long-time exposure for those emissions can cause heart disease, pulmonary illness or even untimely death. In the environment, sulphur oxides are reactive and form H_2SO_4 which comes down with the rain and the acid rain again depletes the nature in many ways. Moreover, buildings disintegrate because of the acid rain (Pan, 2011).

In parallel with the fuel de-sulphurization development, the need to increase the use of renewable fuels continues to grow to also reduce greenhouse gas (GHG) emissions. In countryside, there may also be possibilities to utilize own yield of rapeseed or other oils as biodiesel fuel through transesterification and this could be financially beneficial for the farmers. In rural areas, there is an increasing need for cheap, both fossil and renewable, fuels in agricultural engine applications. Due to the environmental aspects, the fuel sulphur content is widely regulated but the content still remains quite high in the developing countries in Asia and Southern America. The cheapest fuels are not the cleanest, i.e., the sulphur contents in non-road fuel may in those regions be as high as 500 mg kg^{-1} while in Europe, the automotive diesel fuel standard, EN 590:2013 allows the fuel to contain a maximum of 10 mg kg^{-1} (SFS-EN 590:2013, 2013).

Due to the environmental reasons on one hand and to the agricultural needs, on the other hand, different blends of bio- and fossil fuels are becoming more popular. High sulphuric fossil fuels and the effect, they have on blends' properties, need to be studied further to find an economic, environmental and technical balance between de-sulphurization, fuel blending, and the usage of renewable components. It is also noteworthy that after de-sulphurization processing, the fuel lubricity must usually be returned by adding lubricity additives into the fuel. However, biodiesels or fatty acid methyl esters (FAMEs) have also been found to enhance the lubricity when they are mixed with diesel fuel oil (Guibet, 1999; Kalghatgi, 2014). Blending of FAME with low sulphur fossil diesel thus also improves the fuel lubricity.

The storage stability is one of the main quality parameters related to FAMEs. The deterioration of the properties of FAMEs during storage is more serious than for fossil fuels. Storage conditions, like ambient temperature, have of course an effect on storage time. Improving oxidation and storage stability is an important issue for commercializing the biodiesel (Bouaid et al., 2009). Some studies indicate that higher sulphur contents may beneficially affect the oxidation stability of the fuel blends (McCormick & Westbrook, 2007; Sirviö et al., 2016). Sulphur is an essential compound for living organisms. For a long time, organic sulphuric compounds, like glutathione, have been well known of their action to protect cells from free radicals and reactive oxygen compounds (Meister & Anderson, 1983). It has also been shown that glutathione can reduce the lipid peroxidation caused by reactive oxygen radicals (Roxas et al., 1997). In other words, an example of the anti-oxidative effect of sulphur compounds can be found from biochemistry. Biodiesel oxidation is a complex process of radical chain reactions. Hydroperoxides are formed first during degradation and they react further to form secondary oxidation products (Fattah et al., 2014). In living organisms and fuel blends, the reaction environments and reaction chains differ and it cannot be stated that the phenomenon is the same. Still, there is an interesting similarity and it needs to be studied further.

To investigate how the sulphur of fossil diesel may affect the OSI and other properties of biodiesel-fossil fuel blends, fuel blends were prepared having different sulphur contents. In Europe, the maximum FAME content in diesel fuel is 7 vol% according to the EN 590:2013 (SFS-EN 590:2013, 2013) but higher percentages are also available and targeted around the world. For example in the United States, the 20% blend fraction is becoming more common. B20 and B30 fuels do even have their own Standard, EN 16709, which specifies the quality of those fuels with a high biodiesel content (SFS-EN 16709:2015, 2015). That is why B20 fuels were chosen to be investigated in this study. Fuel blending may, however, cause operating risks. The fuels need to be stable and compatible with engine and other blended fuels. Several studies have been made to figure out how biodiesels and their blends affect the lifetime of the engines. A review of short run tests reports that biofuels can replace conventional diesel fuel but a long run analysis is needed for assessment of the engine life. Problems that may occur are carbon deposition, lubricating oil dilution, piston ring sticking and injector nozzle choking (Patel et al., 2016).

In this study, the aim was to find out how sulphur affects the storage stability of the prepared fuel blends. It was interesting to see if mixing two common non-road fuels could be beneficial for both the environment and storage stability of fuel in developing countries. It is clear, that adding non-sulphuric biodiesel to fossil fuel will decrease their blends' sulphur content and reduce emissions and other adverse effects. But will the high sulphur content enhance the storage stability of the biodiesel?

MATERIALS AND METHODS

In the current study, the parameters were investigated that correlate with the storage stability of the fuel blends. Four B20 fuel samples were compared consisting of 20 vol% biodiesel and 80 vol% fossil diesel. All of the samples were prepared by mixing rapeseed methyl ester (RME), diesel fuel oil (DFO) containing 6.6 mg kg^{-1} sulphur, and high sulphuric diesel solvent. Different amounts of sulphuric diesel solvent were added into the B20 samples. The achieved sulphur concentrations were 6 mg kg^{-1} (B20 1), 76 mg kg^{-1} (B20 2), 149 mg kg^{-1} (B20 3), and 226 mg kg^{-1} (B20 4). The aim was to figure out how the storage stability of the fuel blends change as a function of time when the samples were stored in stable conditions (in dark, at 20 °C) for 12 weeks.

The fuel samples were made by mixing three different compounds; RME, DFO and ICP diesel solvent, which contained 1,000 mg kg^{-1}, sulphur. The total volumes of the samples were 500 ml and the dilution was carried out as presented in Table 1.

Table 1. Dilution ratios of the B20 samples

Sample	RME (ml)	DFO (ml)	Diesel solvent (ml)
B20 1	100	400	0
B20 2	100	360	40
B20 3	100	320	80
B20 4	100	280	120

The analyses carried out for these four samples were the oxidation stability (OSI), acid number (AN) and kinematic viscosity (KV). The samples were analysed straight after mixing and after 4, 8 and 12 weeks of storage. The storage conditions were a dark

cupboard at room temperature (around 20 °C). The OSI, AN, and KV of both RME and DFO were determined before mixing them together and adding high sulphuric diesel solvent. For the prepared sulphur containing B20 samples, the sulphur contents were measured straight after mixing. After the whole storage time, the elemental analysis (CHNO) was carried out for the samples.

RME used as the bio component in the fuel blends was a product of ecoMotion GmbH, Germany. RME is ISCC EU certified and meets Standard EN14214:2012 (SFS-EN 14214:2012, 2012). Fuel had been produced three years before this study and delivered to the University of Vaasa in 2012. Still, RME fulfilled the requirements of Standard EN 14214:2012 in terms of the properties measured in this study. The ester content of RME was not measured. Any information about the most likely added antioxidant of RME was not available.

DFO was a product of Neste and it had been produced in Finland. It did not contain any bio component before mixing it with RME. DFO contained 6.6 mg kg^{-1} sulphur.

CONOSTAN Premisolv™ ICP Solvent containing 1,000 mg kg^{-1} sulphur was a product of Conostan®, Canada. Conostan® is a division of SCP SCIENCE. According to the safety data sheet of this solvent, it contained sulphur as n-dibutyl sulphide in diesel fuel.

Acid number

The acid number of the blends was analysed by a titrator Metrohm Titrando 888. The method is a potentiometric titration method. The sample is diluted with iso-propanol and titrated by potassium hydroxide. The measurement was produced according to Standard EN 14104:2003 (SFS-EN 14104, 2003).

Oxidation stability

The oxidation stability was measured by a Biodiesel Rancimat 873 instrument. The method describes the accelerated oxidation stability of biodiesel. The sample is heated and air flow is conducted through it. The vaporizing compounds of the sample drift with air into water and the conductivity of the water is measured. The end point is achieved when the conductivity increase is at its highest. The method is described in Standard EN 15751:2014 and according this Standard the maximum induction period is 48 hours (SFS-EN 15751, 2014).

Viscosity

The viscosities were measured by a Stabinger SVM 3000 rotational viscometer. The measurement is based on torque and speed measurements. The device calculates the dynamic viscosity from the rotor speed. The device also has a density measuring cell that employs an oscillating U-tube principle. The kinematic viscosity is calculated automatically based on these measurements (Anton Paar, 2012).

Elemental analysis

The elemental analysis was measured by a Thermo Scientific Flash 2000 instrument. It determines the mass fractions of carbon, hydrogen, nitrogen and oxygen. Sulphur may also be analyzed in case its amount is high enough. The analysis was produced according to Standard ASTM D5291 (ASTM D5291-16, 2016).

Sulphur content

The sulphur contents were measured by a Thermo Scientific, iCAP 6500 duo instrument. In this method, the samples are decomposed by an ultrasonic oven and transformed from organic to water-soluble form. The solution is injected to spectrometers plasma. Calibration was made by the known concentrations of the standards. The defined standards (emission intensities in known concentrations) and the presence and concentration of the element are evaluated by comparing the intensity of the light to these standards. The method was an in-house method produced based on Standard ISO 10478 (ISO 10478, 1994).

RESULTS AND DISCUSSION

The analyses results related to storage stability are presented in Table 2 and elemental analyses results in Table 3. All the obtained results are arithmetic means of at least two replicate measurements. The OSI, AN and KV results are also depicted in Figs 1, 2 and 3, respectively, and the elemental analyses in Fig. 4.

Table 2. The storage stability analyses results for DFO, RME and B20 fuels

Property	DFO	RME	B20 1	B20 2	B20 3	B20 4
Oxidation stability (h)						
Fresh	72*	11	45	47	47	51
4 weeks			44	47	51	54
8 weeks			42	48	52	55
12 weeks		10	42	47	53	56
Acid number (mgKOH g^{-1})						
Fresh		0.19	0.07	0.06	0.06	0.07
4 weeks			0.06	0.06	0.06	0.06
8 weeks			0.07	0.06	0.08	0.07
12 weeks			0.07	0.07	0.07	0.07
Kinematic viscosity, 40 °C (mm^2 s^{-1})						
Fresh	3.5	4.5	3.6	3.4	3.2	3.1
4 weeks			3.6	3.4	3.2	3.1
8 weeks			3.6	3.4	3.2	3.1
12 weeks			3.7	3.4	3.2	3.1

The relative standard deviations are: KV 1%, AN 7.9%, and OSI 4.5%. These had been determined for the analysis methods earlier. For the OSI results above 48 hours, the reproducibility is approximately 9.5 hours. The OSI results above 48 hours should be announced >48 hours according to Standard EN 15751.
*The measurement was stopped after 72 hours.

Table 3. Elemental analyses result for B20 fuels

Property	B20 1	B20 2	B20 3	B20 4
C (m-%)	83.7	83.5	84	83
H (m-%)	13.2	13.2	13.8	13.7
N (m-%)	0.2	0.2	0.2	0.2
O (m-%)	2.2	2.2	2.2	2.2
S (mg kg^{-1})	6	76	149	226

The relative standard deviations for these methods were not determined.

Fig. 1 shows how the oxidation stability of the samples changed during 12 weeks:

- B20 1, decreased 5% (from 46 to 42 h)
- B20 2, remained almost constant (varied between 47 and 48 h)
- B20 3, increased 12% (from 47 to 53 h)
- B20 4, increased 10% (from 51 to 56 hours).

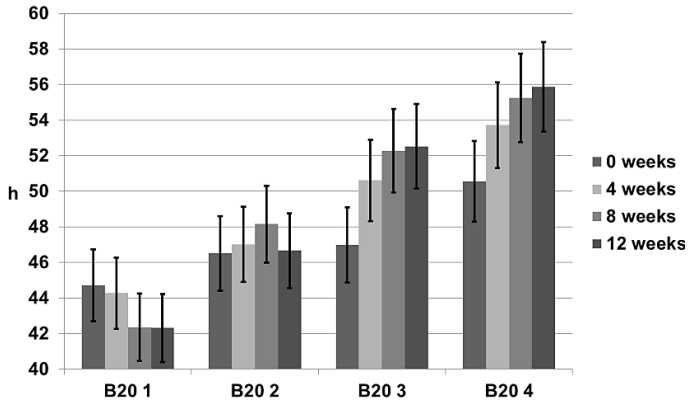

Figure 1. Oxidation stability results for B20 fuels. The sulphur concentrations were 6 mg kg^{-1} (B20 1), 76 mg kg^{-1} (B20 2), 149 mg kg^{-1} (B20 3), and 226 mg kg^{-1} (B20 4).

For the OSI results of above 48 hours, the reproducibility is approximately 9.5 hours. According to Standard EN 15751:2014, the OSI results of above 48 hours should therefore be announced as > 48 hours. In this study, the trend in the results was, however, so clear that the actually measured values were chosen to announce.

It should also be noted that, as fresh, the OSI was the longer, the higher was the sulphur content.

Fig. 2 shows that the acid numbers of all the samples remained within 0.06–0.08 mgKOH g^{-1} during the whole study. There were no significant differences between the samples and the results did not change during the storage. Thus, the sulphur content did not either seem to affect the AN.

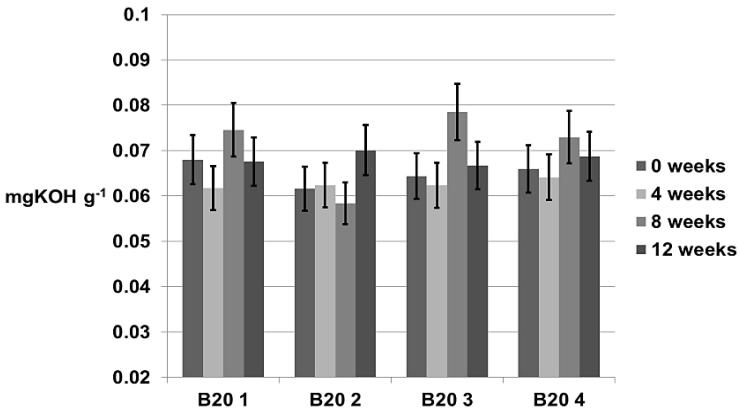

Figure 2. Acid number results for B20 fuels. The sulphur concentrations were 6 mg kg^{-1} (B20 1), 76 mg kg^{-1} (B20 2), 149 mg kg^{-1} (B20 3), and 226 mg kg^{-1} (B20 4).

Fig. 3 shows that the kinematic viscosities remained quite constant during the storage time of 12 weeks for all the samples. The differences between the samples were due to different mixing ratios. For the samples B20 2, 3 and 4, the diesel solvent containing sulphur lowered the KV in relation to its mixing ratio.

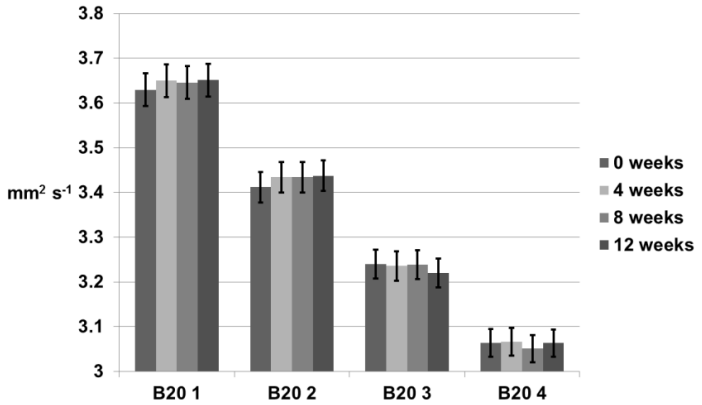

Figure 3. Kinematic viscosity results for B20 fuels. The sulphur concentrations were 6 mg kg^{-1} (B20 1), 76 mg kg^{-1} (B20 2), 149 mg kg^{-1} (B20 3), and 226 mg kg^{-1} (B20 4).

Pölczmann et al. (2016) studied the storage stability of diesel fuels containing biodiesel and made a mathematical correlation between a) the viscosity increase and oxidation stability decrease and b) between the acid number increase and oxidation stability decrease. As a result of their study, the authors conclude that the found correlation could reduce the number of needed analyses in biodiesel quality follow-up. According to them, the kinematic viscosity and acid number could be estimated based on the oxidation stability result (Pölczmann et al., 2016).

However, this was not clearly seen in the present study because no correlation was observed between the oxidation stability and acid number nor kinematic viscosity. In the current study, the amount of samples was, though, small and the timescale was shorter (12 weeks against 150 weeks in Pölczmann et al., 2016).

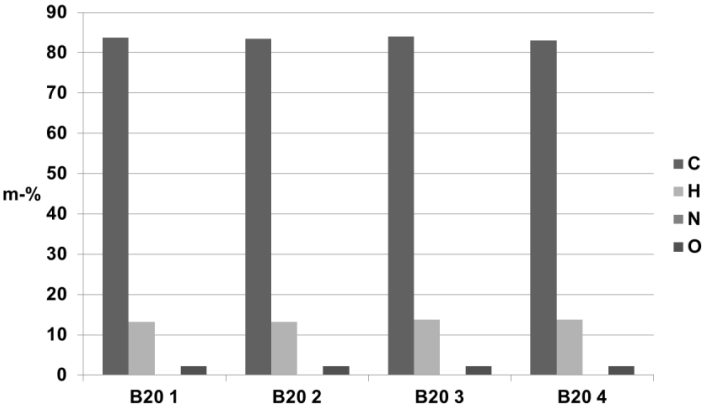

Figure 4. Elemental analyses result for B20 fuels. The sulphur concentrations were 6 mg kg^{-1} (B20 1), 76 mg kg^{-1} (B20 2), 149 mg kg^{-1} (B20 3), and 226 mg kg^{-1} (B20 4).

Fuels mainly consist of carbon and hydrogen and some small quantities of sulphur, nitrogen, and oxygen (Riazi, 2005). Even at its highest in the present study, the amount of added sulphur was not high enough to cause differences in elemental contents of the fuels, Table 2, Fig. 4. It can, thus, be assumed that adding diesel solvent did not affect the elemental composition of the samples. It needs, however, to be kept in mind, that the elemental contents are approximate. The measured sulphur values of 6, 76, 149 and 226 mg kg^{-1} were very close to the calculated values of 5, 78, 151 and 226 mg kg^{-1}.

The form of the sulphur compound is determining. In fossil fuel, sulphur can be found in cyclic compounds such as thiophenes and benzothiophenes as well as in noncyclic compounds such as mercaptanes and sulphides (Ma, 2010). In this study, the added sulphur was n-dibutyl sulphide which is a simple hydrocarbon chain that contains sulphur in the middle, and it is a noncyclic compound, Fig. 5.

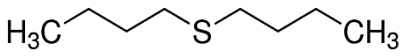

Figure 5. Structure of n-dibutyl sulphide. (Sigma Aldrich, 2016).

In the presence of water, sulphur may form sulphuric acid and the acids will promote oil thickening and oxidation, e.g., in lubricating oils (Folkson, 2014). This phenomenon may also occur within fuels. Biodiesel is hydrophilic and it is possible that its moisture content will increase during three years of storage. The water content of RME was not measured. Most likely, based on the other analysis results, it can be assumed that no water was present in the studied samples and the increasing amount of sulphur did not affect adversely the oxidation stability, quite the contrary.

McCormick & Westbrook (2007) mentioned that sulphur compounds can work as antioxidants and the same conclusion is also supported by the studies of Karavalakis et al. (2010) and Sirviö et al. (2016). Sirviö et al. (2016) was a prestudy in relation to this research theme. In that study, the B20 sample containing more sulphur loosed its oxidation stability less than the B20 sample containing less sulphur. Karavalakis et al.(2010) have found that the oxidation stability behaviour of biodiesel blends is a very complicated process. They say that the most important factors affecting the blends' oxidation are the biodiesel composition and used antioxidants. Additionally, according to McCormick & Westbrook (2007), the stability of the biodiesel is the most important factor from the point of view of the blends storage stability.

In this study, the biodiesel and fossil diesel were the same in all samples but the mixing ratios of the diesel solvent containing sulphur varied from 0 (B20 1) to 22% (B20 4). Most likely, the reason for the difference in the oxidation stability of the fresh blend samples was, thus, the different sulphur content. For the diesel solvent, the oxidation stability was not measured but the oxidation stability of the DFO was high (measurement was stopped at 72 hours). The DFO quality was, thus, not a threat to the stability of the blends.

As mentioned above, the decrease in OSI was 5% for the sample B20 1 while the oxidative stability increased by 12 and 10% for the samples B20 3 and 4, respectively. This may indicate the antioxidative effect of sulphur. To prove this thesis, again indicated by the current study, the chemistry of the fuel blends and organic sulphur should be studied more detailed.

Karavalakis et al. (2011) showed in another study, that even a 4–6 weeks storage time may cause OSI to decrease below the 20 hours' limit due to natural ageing. The 20 hours' limit is set in Standard EN 590:2013 for automotive diesel fuels. In this study, the OSI of all the samples remained clearly above the 20 hours' limit for 12 weeks. The other measured properties were also at a proper level though the adopted RME was produced 3 years before this study.

CONCLUSIONS

The aim of this study was to find out if increasing sulphur content is beneficial for storage stability of the fuel blend. Four B20 fuel samples were produced consisting of 20 vol% biodiesel and 80 vol% fossil diesel. All the samples were prepared from rapeseed methyl ester (RME), diesel fuel oil (DFO) containing 6.6 mg kg^{-1} sulphur, and a high sulphuric diesel solvent (n-dibutyl sulphide in diesel fuel). The measured sulphur contents of the samples were 6, 76, 149 and 226 mg kg^{-1}. The effects of the sulphur content on the oxidation stability, acid number (AN) and kinematic viscosity (KV) of the blends were investigated. Based on the study, the following conclusions could be drawn:

- There is a reason to assume that the sulphur may be favourable to fuel blends' storage stability. The decrease in oxidation stability was 5% for the sample B20 containing the lowest amount of sulphur while the other samples behaved differently. During the storage, the oxidation stability of the sample containing 76 mg kg^{-1} sulphur remained quite constant and for the samples containing 149 and 226 mg kg^{-1} sulphur, the OSI increased by 12 and 10%, respectively. This may indicate the antioxidative effect sulphur has. The phenomenon and chemistry should, however, be studied more thoroughly and for a longer period to confirm this statement.
- The other properties related to storage stability, i.e., AN and KV seemed not to vary much within the storage time of 12 weeks. Any clear correlations between the oxidation stability and the acid number and kinematic viscosity were not observed in the examined samples.

ACKNOWLEDGEMENTS. The authors would like to acknowledge Mr. Jukka Nuottimäki, Ms. Jenni Nortio and Mr. Markku Kuronen from Neste for their expertise and comments for the study. The diesel fuel utilized in this study was also supplied by them. The biodiesel of this study was purchased within the TREAM project which was funded by the Finnish Funding Agency for Technology and Innovation (TEKES). The authors would also like to thank Mrs. Pia Välimäki for her indispensable help with the analyses.

REFERENCES

ASTM D5291-16. 2016. *Standard Test Methods for Instrumental Determination of Carbon, Hydrogen, and Nitrogen in Petroleum Products and Lubricants.*ASTM International. P. 7.

Bouaid, A., Martinez, M. & Aracil, J. 2009. Production of biodiesel from bioethanol and Brassica carinata oil: Oxidation stability study. *Bioresource Technology* **100**, 2234–2239.

Fattah, R.I.M., Masjuki, H.H., Kalam, M.A., Hazrat, M.A., Masum, B.M. & Imtenan, S. 2014. Effect of antioxidants on oxidation stability of biodiesel derived from vegetable and animal based feedstocks. *Renewable Sustainable Energy Review* **30**, 356–370.

Folkson, R. (edit.) 2014. *Alternative Fuels and Advanced Vehicle Technologies for Improved Environmental Performance.* Woodhead Publishing Series in Energy: Number 57, UK. 760 pp.

Guibet, J.C. 1999. *Fuels and Engines.* Éditions Technip, Paris, France. 771 pp.

Heywood, J.B. 1988. *Internal Combustion Engine Fundamentals.* McGraw-Hill Book Co, USA. 930 pp.

ISO 10478. 1994. *Petroleum products. Determination of aluminium and silicon in fuel oils. Inductively coupled plasma emission and atomic absorption spectroscopy methods*. International Organization for Standardization. P. 7.

Kalghatgi, G. 2014. Fuel/Engine Interactions. *SAE International*, Warrendale, Pennsylvania, USA. 255 pp.

Karavalakis, G., Stournas, S. & Karonis, D. 2010. Evaluation of the oxidation stability of diesel/biodiesel blends. *Fuel* **89**, 2483–2489.

Karavalakis, G., Hilari, D., Givalou, L., Karonis, D. & Stournas, S. 2011. Storage stability and ageing effect of biodiesel blends treated with different antioxidants. *Energy* **36**, 369–374.

Ma, T. 2010. The Desulfurization pathway in Rhodococcus. *Research Gate*, 208–230.

Meister, A. & Anderson, M.E. Glutathione. 1983. *Annual Review of Biochemistry* **52**, 711–760.

McCormick, R.L. & Westbrook, S.R. 2007. Empirical Study of the Stability of Biodiesel and Biodiesel Blends. *Milestone Report.* NREL/TP-540-41619. 86 pp.

Pan, X. 2011. Sulphur Oxides: Sources, Exposures and Health Effects. *Encyclopedia of Environmental Health*, 290–296.

Patel, P.D., Lakdawala, A., Chourasia, S. & Patel, R.N. 2016. Bio fuels for compression ignition engine: A review on engine performance, emission and life cycle analysis. *Renewable and Sustainable Energy Reviews* **65**, 24–43.

Pölczmann, G., Tóth, O., Beck, Á. & Hancsók, J. 2016. Investigation of storage stability of diesel fuels containing biodiesel produced from waste cooking oil. *Journal of Cleaner Production* **11**, 85–92.

Riazi, M.R. *Characterization and properties of petroleum fractions*. 2005. 1st ed. ASTM manual series: MNL50. P. 407.

Roxas, V.P., Wang, J., Lohdi, S. & Allen, R.D. 1997. Engineering stress tolerance in transgenic plants. *Acta Physiol. Plant.* **19**, 591–594.

SFS-EN 14104:2003. 2003. *Fat and oil derivatives. Fatty acid methyl esters (FAME). Determination of acid value.* Finnish Petroleum Federation. 1+9 pp.

EN 14214:2012+A1:2014 *Liquid petroleum products - Fatty acid methyl esters (FAME) for use in diesel engines and heating applications - Requirements and test method.* Finnish Petroleum Federation. P. 22.

SFS-EN 15751:2014. 2014. *Automotive fuels. Fatty acid methyl ester (FAME) fuel and blends with diesel fuel. Determination of oxidation stability by accelerated oxidation method.* Finnish Petroleum Federation. P. 18.

SFS-EN 16709:2016. 2016**.** *Automotive Fuels - High Fame Diesel Fuel (B20 and B30) - Requirements and Test Methods*. Finnish Petroleum Federation. P. 5.

SFS-EN 590:2013. 2013. *Automotive fuels. Diesel. Requirements and test methods.* Finnish Petroleum Federation. 1+13 pp.

Sigma Aldrich Catalog, www.sigmaaldrich.com.

Sirviö, K., Niemi, S., Heikkilä, S. & Hiltunen, E. 2016. The effect on sulphur content on B20 fuel stability. *Agronomy Research* **14**, 244–250.

SVM 3000 Stabinger Viscometer -brochure. 2012. Anton Paar 1/10. C18IP007EN-K. 8 pp.

Zhao, Y., Ma, Q., Liu, Y. & He, H. 2016. Influence of sulfur in fuel on the properties of diffusion flame soot. *Atmospheric Environment* **142**, 383–392.

Agronomy Research **15**(S1), 1242–1250, 2017

Influence of sisal fibres on tribological properties of epoxy composite systems

P. Valášek* and K. Habrová

Department of Material Science and Manufacturing Technology, Faculty of Engineering, Czech University of Life Sciences Prague, Kamýcká 129, CZ16521 Prague, Czech Republik
*Correspondence: valasekp@tf.czu.cz

Abstract. Composite are materials, which synergically combine properties of the matrix and fillers. An interaction of polymers – resins – with biological kind of fillers can optimize their mechanical properties in the same way as synthetic fillers. Biological fillers have many advantages, which include low price and satisfying mechanical properties. Significant disadvantages are different properties of fibers – for example, fibre diameter and strength – which are caused by the biological essence of this material. The design of new composite materials based on natural renewable resources is essential for an environment and is also attractive from an economic point of view. This paper describes the hardness and resistance to abrasive wear of epoxy resins filled with unordered short sisal fibers (3, 6 and 9 mm). Scanning electron microscopy was used to assess the fibers and interaction between fibers and epoxy resin.

Key words: Abrasive wear, Agave Sisalana, electron microscopy.

INTRODUCTION

Composite materials can be described as materials that combine two or more phases. These phases are interdependent and can create a synergistic effect (Muller, 2015). Among the most widely used composite materials include composites with the filler in fiber form (Muller, 2011; Valasek & Muller, 2013; Ruggiero et al., 2015; Muller, 2016).

The materials which contain one or both phases from natural materials are increasingly expanding at present (Ruggiero et al., 2016). Natural materials so very often replace conventionally used synthetic materials. This substitution has many advantages, but also disadvantages. The benefits may include low cost of natural fillers, low density, as well as availability. The most significant disadvantage is their very natural character when individual features may differ from each other depending on a growth rate, an area of the growth and other environmental conditions. Among the natural fibers, which often substitute synthetic ones include not only the fibers of coconut, oil palm fibers, banana fibers, but also fibers of sisal (Abdul Khalil et al., 2012; Valasek, 2016).

Sisal fibers are extracted from the plant Agave Sisalana; it is a multi-year xerophyte plant from the family Asparagaceae. This plant grows mostly in tropical and subtropical areas. The sisal fibers are obtained from the leaves of the plants.

Sisal fibers are commonly used in composite systems where they optimize basic mechanical characteristics. Hari Om Maurya et al. (2015) for example show that the presence of short sisal fibers (5, 10, 15 and 20 mm) in an epoxy resin led to improvements in flexural strength and impact strength, but the strength properties did not increase – tensile strength. To improve the interfacial interaction between the sisal fibers and the matrix, it is possible to use alkali treatment, benzoyl peroxide treatment or treatment with maleic anhydride, (Mohit Sood et al., 2015). According to the conclusions of Badrinath & Senthilvelan (2014), the composite systems based on sisal fibers and epoxy have a greater tendency to absorb water than composites with banana fibers, but they also indicate that the composites with sisal fibers in comparison with banana fibers reached a higher flexural strength.

The aim of this paper is to describe two-body abrasion of short-fiber undirected composite systems with fibers of sisal and epoxy matrix. Tribological characteristics are complemented by necessary information about the composite system, i.e., hardness, density, and porosity. Sisal fibers were modified before application of alkali and to optimize interfacial interactions. The partial objective of this paper is to describe the impact of this treatment on sisal fibers. Electron microscopy was used to assess a wear area and to describe the morphology of the fibers. The experimentally obtained data were statistically analyzed.

MATERIALS AND METHODS

Matrix

The epoxy resin based on bisphenol A and F suitable for lamination was used in this experiment. This resin very readily wets the synthetic as well as organic materials. Cycloaliphatic amines with high reactivity towards the resin were used as a hardener. The resin was cured according to the manufacturer' technological instructions; the resin-curing was conducted at a higher temperature of 50 °C to increase the resistance of the resin. When curing at elevated temperatures, it may lead to increase the stability of the resin. Resulting concentration corresponded by its volume percentages to 2.5–10 vol.%

Filler

The filler used was fibers from the leaves of Agave sisalana – sisal fibers. The fibers were chemically modified with 6% aqueous solution of NaOH. After removal from the bath, the fibers were washed with distilled water and were then cut into a required fiber length 3 mm, 6 mm and 9 mm. Essential characteristics of sisal fibers are shown in Table 1. The length of fibers (3–9 mm) was chosen with regard to the description of the changes which are induced by increasing of the fiber length.

Table 1. Mechanical properties of sisal fibres (Mieck et al., 1994; Boopalan et al., 2012)

Cellulose [%]	Hemi cellulose [%]	Lignin [%]	Density [g cm^{-3}]	Tensile strength [MPa]	Young´s modulus [GPa]
67–78	10.0–14.2	8.0–11.0	1.45	468–640	9.4–22.0

Experimental program

The porosity of the composite system was determined as the difference between the theoretical and real density – expressed as a percentage.

Hardness was tested according to ČSN EN ISO 2039-1 (Plastics – Determination of hardness – Part 2: Rockwell hardness), the ball with a diameter of 5 mm was used, load force was 961 N.

The two-body abrasion was tested on a rotating cylindrical drum device with the abrasive cloth of the different grain size (P120 Al_2O_3 grains) according to the standard ČSN 62 1466 (Units used in the field of rubber technology), see Fig. 1. The testing specimen is in contact with the abrasive cloth, and it covers the distance of 60 m. During one drum turn of 360°, it is provoked the testing specimen left above the abrasive cloth surface. Consequent impact of the testing specimen simulates the concussion. The pressure force is 10 N. The mean of the testing specimens was 15.5 ± 0.1 mm and their height was 20.0 ± 0.1 mm. The mass decreases were measured on analytic scales weighing on 0.1 mg.

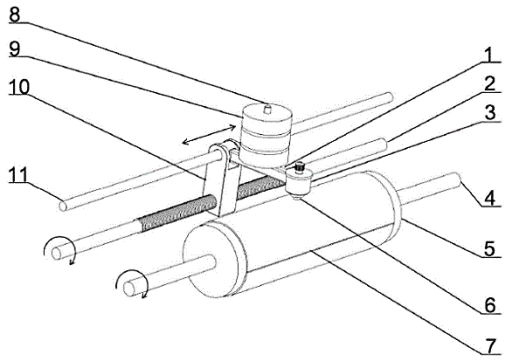

Figure 1. Schema of equipment for two-body abrasive wear testing: 1 – arm, 2 – motion screw, 3 – head, 4 – shaft, 5 – roller, 6 – test sample, 7 – abrasive cloth, 8 – weight holder, 9 – weight, 10 – sliding matrix, 11 – guide rod.

Electron microscopy assessed fiber morphology, interfacial interactions and the influence of chemical treatment of the surface on fiber morphology.

RESULTS DISCUSSION

Fiber morphology was evaluated on the electron microscope before preparing the composition systems. Fig. 2 (left) shows the fibers before mechanical mixing with used matrix; the right figure shows the structure of sisal fiber and the interaction with the epoxy resin itself.

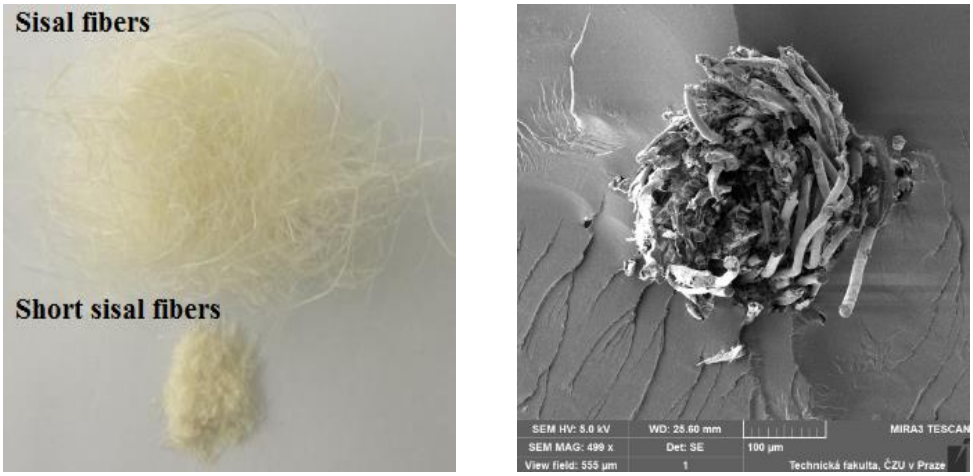

Figure 2. Sisal fiber (left), sisal fiber structure in interaction with the epoxy resin Mag. 499 x (right).

Microscopy determined the real dimensions of fibers (diameter and length) before the application of fibers in an epoxy matrix. The fiber diameter corresponded to 126 ± 42 µm, the original fiber length for 3, 6 and 9 mm shows the following histogram Fig. 3: 3 mm correspond to an average length of 3,053 µm, 6 mm correspond to 5,858 µm and 9 mm correspond to 9,116 µm.

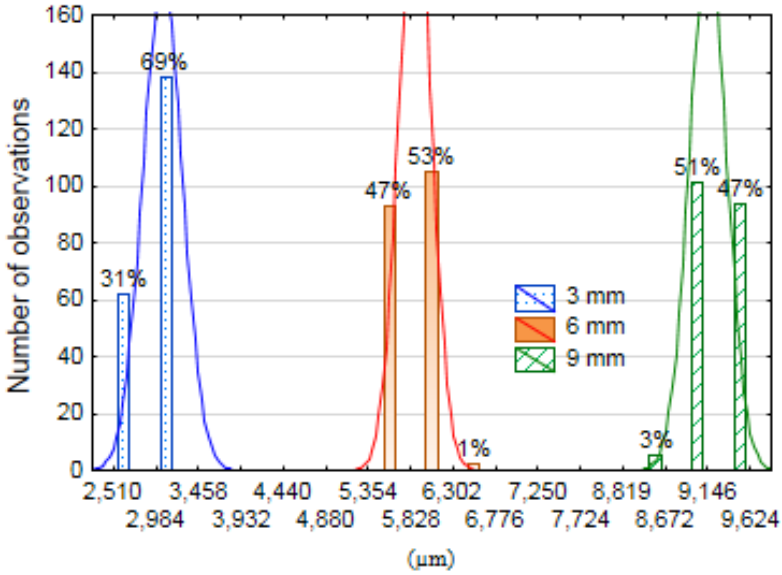

Figure 3. Histogram – real length of sisal fibers.

Performed chemical treatment of fibers surface with 6% NaOH solution leads to removal of surface structures from the fiber surface. The presence of undesirable surface features on the surface has the effect the smoothness of the untreated surface. This fact

was proven by electron microscopy, which is presented in Fig. 4.

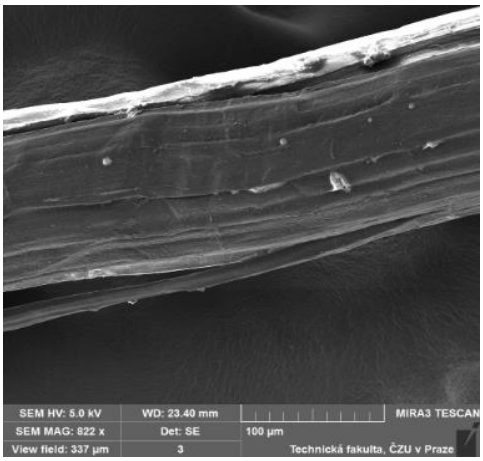

Figure 4. Sisal fiber surface before surface treatment (Mag. 822 x).

Removal of the waxy layers on the surface with chemical treatment of NaOH leads to the removal of smoothness caused by this layer, and the fiber becomes more rugged – its roughness increases. Such treatment process is in accordance with the conclusions of Mohit Sood et al. (2015) who state that apart from the cleaning of the fibers itself it also increases the roughness of the fiber. This treatment is then reflected on the interfacial interactions between the fibers and the matrix. Orue et al. (2016) state that the alkali-treated surface has a cavity, which causes better mechanical properties of composite systems than the systems with untreated fibers.

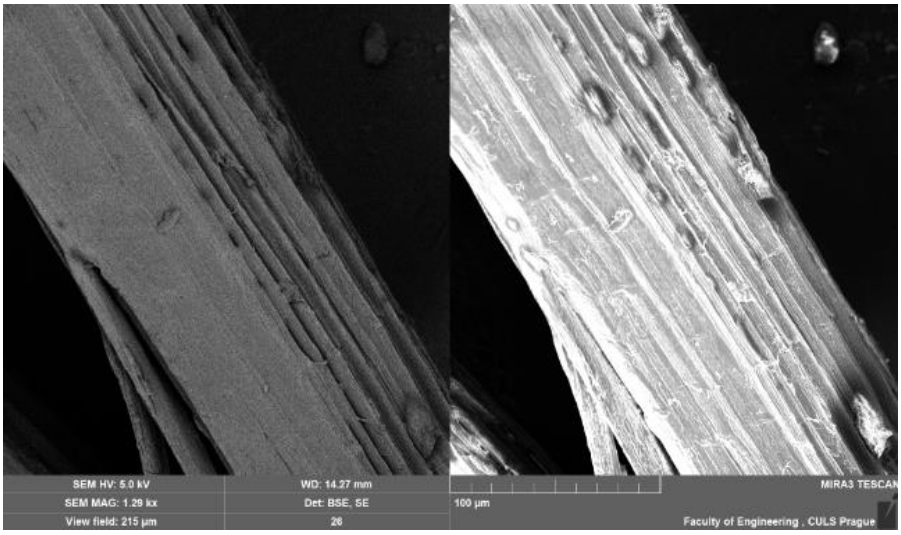

Figure 5. Surface of sisal fiber after chemical treatment with solution of NaOH (Mag. 1.29 kx): BSE, SE.

Essential characteristics of the composite systems are summarized in Table 2, which shows the theoretical density of the composite systems that was calculated based on the density of the resin (manufacturer's declared value 1.15 g cm^{-3}) and an average density of sisal fibers: i.e. 1.45 g cm^{-3}. High values of porosity may result in the initiation of cracks. The porosity can be reduced by vacuum technique – e.g. vacuum infusion.

Table 2. Density and porosity of composite systems

Properties	vol. % of sisal fibers				
	0%	2.5%	5.0%	7.5%	10.0%
Theoretical density [g cm^{-3}]	1.15	1.16	1.17	1.17	1.18
Porosity [%]	-	5.6	4.3	8.0	9.2

Hardness was assessed as an important characteristic that can be in direct correlation with resistance to abrasive wear. Due to the nature of the composite system was as indenter chosen a ball with diameter 5 mm. An inclusion of fibers of sisal has led to a decrease in hardness values of the composite system. The measured values together with their variances are shown in Fig. 6.

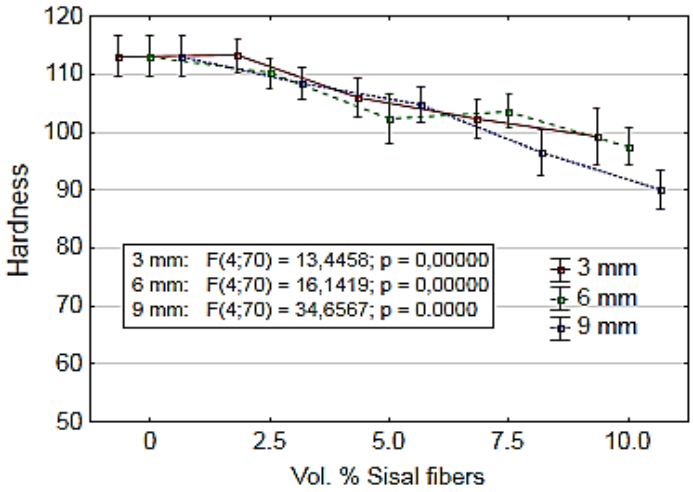

Figure 6. Hardness of composite systems with sisal fiber and after surface treatment with NaOH (ČSN EN 2039).

Resins without sisal fibers reached the hardness 113.11 ± 6.23. This hardness decreased with the inclusions of fibers to a value of 90.16 ± 5.78 (9 mm/10.0%).

Abrasion resistance, i.e. two-body abrasion, was evaluated through weight loss, which was with the help of theoretical density of composite systems converted to volume losses. The following graph (Fig. 7) displays the abrasive wear for the observed period of the proportion of sisal fiber in the matrix.

The inclusion of sisal fibers did not significantly affect the resistance to two-body abrasion. The volume loss of unfilled resins reached 0.5181 cm^3, and there was the highest volume loss from this value in the composite 9 mm/10.0%, the loss was 0.0121 cm^3. There was a decrease in volume loss in some composites; Composite

6 mm/7.5% reached the most significant decrease, the loss was 0.0450 cm^3. The coefficient of variation of measurement did not exceed 10%.

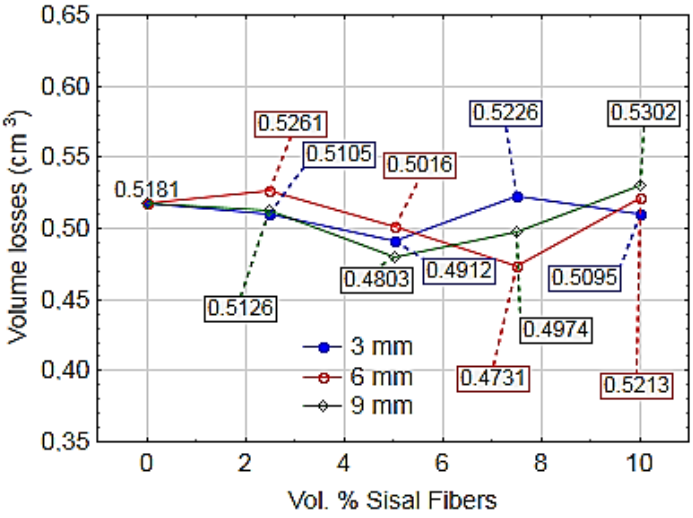

Figure 7. Volume losses – two-body abrasion (ČSN 62 1466).

Surfaces exposed to the two-body abrasion were evaluated with the electron microscope, see Fig. 8.

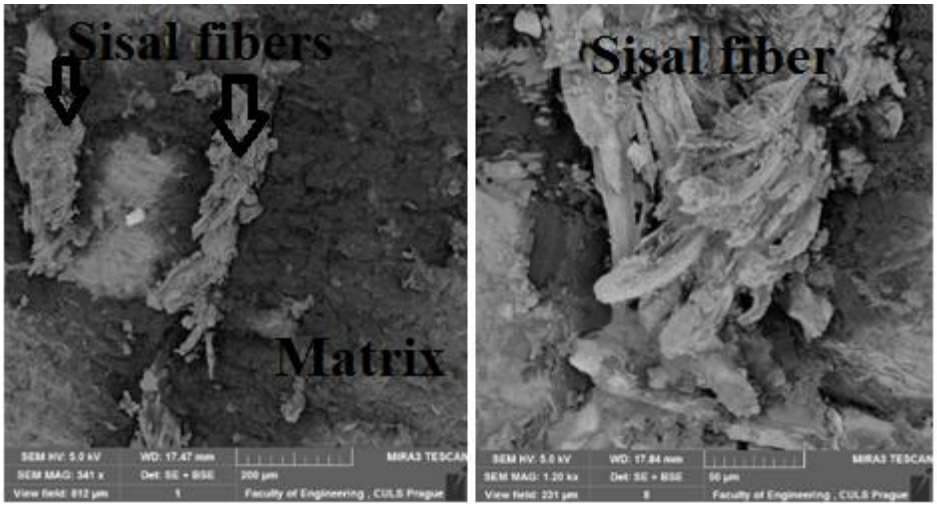

Figure 8. Worn out area of composite systems: Mag. 341 x (left), Mag. 1.20 x (right).

Niu et al. (2005) reported that sisal fibers affect the wear resistance of matrices, the authors demonstrated that sisal fibers might increase the resistance of polymers, the authors achieved the most significant increase in a composite with 15% of sisal fibers. These findings were not completely confirmed, some concentration of sisal fibers slightly increased the wear resistance, but there was also a decrease in wear resistance.

This might be due to the technological process of composite preparation, where the pressing was not used, the fibers were tentative, and the vacuum was not applied. They used technologically undemanding preparation, where the composite systems showed an increase in porosity. Wei et al. (2007) indicate that the surface treatment of sisal fibers with alkali positively affect the durability of the resulting composite system without surface treatment. It is therefore concluded that the treatment of fibers to optimize their surface was an adequate treatment for increasing the wear resistance. Dwivedi et al. (2010) also state that the abrasive wear of composites with sisal fiber depends on, besides other things, the fiber arrangement and just random arrangement could affect the disparate trend of volume losses depending on the concentrations of sisal fibers in the matrix. The composite systems based on biological fillers as sisal/epoxy are of high potential. Fibers composite on epoxy/sisal basis can be used for boards and a surface layers in industry and construction, these materials have significant design benefits in terms of appearance.

CONCLUSIONS

The article describes the hardness and wear resistance of epoxy resin filled with short disordered sisal fibers treated with 6% NaOH solution. The results of the experimental program can be summarized in the following points:

- Surface treatment of the sisal fibers led to the removal of surface layers of fiber and increased the surface segmentation.
- Hardness of the composite systems decreased with the inclusion of treated sisal fibers, namely by 12.3% (3 mm/10.0%), 13.8 (6 mm/10.0%) and by 20.3% (9 mm/10.0%).
- Wear of the individual phases during a two-body abrasion were the same, without significant pulling of fibers from the matrix.
- Increase of the volume losses (two-body abrasion, grit P120) reached 2%, the maximum decrease was 9%.

ACKNOWLEDGEMENTS. This paper has been made with the assistance of the grant CULS – IGA TF.

REFERENCES

Abdul Khalil, H.P.S., Bhat, I.U.H., Jawaid, M., Zaidon, A., Hermawan, D. & Hadi, Y.S. 2012. Bamboo fibre reinforced biocomposites: A review. In: *Materials and Design* **42**, 353–368.

Badrinath, R. & Senthilvelan, T. 2014. Comparative Investigation on Mechanical Properties of Banana and Sisal Reinforced Polymer based Composites. In: *Procedia Materials Science* **5**, 2263–2272.

Boopalan, M., Umapathy, M.J., Jenyfer, P. 2012. A Comparative Study on the Mechanical Properties of Jute and Sisal Fiber Reinforced Polymer Composites. In: *Silicon* **4**(3), 145–149.

Dwivedi, U.K., Shah, H. & Chand, N. 2010 Development of empirical model for abrasive wear volume of sisal fibre-epoxy composites. In: *Tribology – Materials, Surfaces and Interfaces* **4**(2), 86–90.

Hari Om Maurya, Gupta, M.K., Srivastava, R.K. & Singh, H. 2015. Study on the mechanical properties of epoxy composite using short sisal fibre. In*: Materials Today: Proceedings*, 1347–1355.

Mieck, K.P., Nechwatal, A. & Knobelsdorf, C. 1994. Potential applications of natural fibres in composite materials. In: *Melliand Textilberichte* **75**(11), 892–898.

Mohit Sood, Dharmpal Deepak & Gupta, V.K. 2015. Effect of Fiber Chemical Treatment on Mechanical Properties of Sisal Fiber/Recycled HDPE Composite. In: Materials Today: Proceedings **2**, 3149–3155.

Müller, M. 2011. Polymeric composites based on Al2O3 reinforcing particles. In: *Engineering for Rural Development*, 26.05.2011, Jelgava. Jelgava: Latvia University of Agriculture, 423–427.

Müller, M. 2015. Hybrid composite materials on basis of reactoplastic matrix reinforced with textile fibres from process of tyres recyclation. *Agronomy Research* **13**(3), 700–708.

Müller, M. 2016. Mechanical properties of composite material reinforced with textile waste from the process of tyres recycling. *Research in Agricultural Engineering* **62**(3), 99–105.

Niu, Y., Zhong, J., Yang, X., Yu, X. & Wei, C. 2005. Effect of sisal fiber contents on wear resistance of sisal fiber/phenol formaldehyde resin in-situ composites. In: *International Conference on Advanced Fibers and Polymer Materials*, ICAFPM 2005; Shanghai; China; 19 October 2005 through 21 October 2005; Code 105708

Orue, A., Jauregi, A., Unsuain, U., Labidi, J., Eceiza, A. & Arbelaiz, A. 2016. The effect of alkaline and silane treatments on mechanical properties and breakage of sisal fibers and poly(lactic acid)/sisal fiber composites. In: *Composites Part A: Applied Science and Manufacturing* **84**, 186–195.

Ruggiero, A., Valášek, P. & Müller, M. 2016. Exploitation of waste date seeds of Phoenix dactylifera in form of polymeric particle biocomposite: Investigation on adhesion, cohesion and wear. In: *Composites Part B: Engineering* **104**(1), 9–16.

Ruggiero, A., Valášek, P. & Merola, M. 2015. Friction and wear behaviors of Al/Epoxy Composites during Reciprocating Sliding tests. In: *Manufacturing technology* **15**(4), 684–689.

Valášek, P. 2016. Short sisal fibers reinforced epoxy resins: Tensile strength. In: *Manufacturing Technology* **16**(3), 637–641.

Valášek, P. & Muller, M. 2013. Polymeric composite based on glass powder – usage possibilities in agrocomplex. *Scientia Agriculturae Bohemica* **2,** 107–112.

Wei, C., Niu, Y-L., Mu, Q.-H., Zhong, J.-B. & Yang, X.-W. 2007. Wear resistance properties of sisal fiber/phenol formaldehyde in-situ composites. In: *Cailiao Kexue yu Gongyi/Material Science and Technology* **15**(6), 835–838.

INSTRUCTIONS TO AUTHORS

Papers must be in English (British spelling). English will be revised by a proofreader, but authors are strongly urged to have their manuscripts reviewed linguistically prior to submission. Contributions should be sent electronically. Papers are considered by referees before acceptance. The manuscript should follow the instructions below.

Structure: Title, Authors (initials & surname; an asterisk indicates the corresponding author), Authors' affiliation with postal address (each on a separate line) and e-mail of the corresponding author, Abstract (up to 250 words), Key words (not repeating words in the title), Introduction, Materials and methods, Results and discussion, Conclusions, Acknowledgements (optional), References.

Layout, page size and font

- Use preferably the latest version of **Microsoft Word**, doc., docx. format.
- Set page size to **B5 Envelope or ISO B5 (17.6 x 25 cm)**, all margins at 2 cm.
- Use single line spacing and justify the text. Do not use page numbering. Use indent 0.8 cm (do not use tab or spaces instead).
- Use font Times New Roman, point size for the title of article **14 (Bold)**, author's names 12, core text 11; Abstract, Key words, Acknowledgements, References, tables and figure captions 10.
- Use *italics* for Latin biological names, mathematical variables and statistical terms.
- Use single ('…') instead of double quotation marks ("…").

Tables

- All tables must be referred to in the text (Table 1; Tables 1, 3; Tables 2–3).
- Use font Times New Roman, regular, 10 pt. Insert tables by Word's 'Insert' menu.
- Do not use vertical lines as dividers; only horizontal lines (1/2 pt) are allowed. Primary column and row headings should start with an initial capital.

Figures

- All figures must be referred to in the text (Fig. 1; Fig. 1 A; Figs 1, 3; Figs 1–3). Use only black and white or greyscale for figures. Avoid 3D charts, background shading, gridlines and excessive symbols. Use font **Arial** within the figures. Make sure that thickness of the lines is greater than 0.3 pt.
- Do not put caption in the frame of the figure.
- The preferred graphic format is EPS; for half-tones please use TIFF. MS Office files are also acceptable. Please include these files in your submission.
- Check and double-check spelling in figures and graphs. Proof-readers may not be able to change mistakes in a different program.

References

- **Within the text**

In case of two authors, use '&', if more than two authors, provide first author 'et al.':

Smith & Jones (1996); (Smith & Jones, 1996);
Brown et al. (1997); (Brown et al., 1997)

When referring to more than one publication, arrange them by following keys: 1. year of publication (ascending), 2. alphabetical order for the same year of publication:

(Smith & Jones, 1996; Brown et al., 1997; Adams, 1998; Smith, 1998)

- **For whole books**

Name(s) and initials of the author(s). Year of publication. *Title of the book* (*in italics*). Publisher, place of publication, number of pages.

Shiyatov, S.G. 1986. *Dendrochronology of the upper timberline in the Urals*. Nauka, Moscow, 350 pp. (in Russian).

- **For articles in a journal**

Name(s) and initials of the author(s). Year of publication. Title of the article. *Abbreviated journal title* (*in italic*) volume (in bold), page numbers.

Titles of papers published in languages other than English, German, French, Italian, Spanish, and Portuguese should be replaced by an English translation, with an explanatory note at the end, e.g., (in Russian, English abstr.).

Karube, I. & Tamiyra, M.Y. 1987. Biosensors for environmental control. *Pure Appl. Chem.* **59**, 545–554.

Frey, R. 1958. Zur Kenntnis der Diptera brachycera p.p. der Kapverdischen Inseln. *Commentat.Biol.* **18**(4), 1–61.

Danielyan, S.G. & Nabaldiyan, K.M. 1971. The causal agents of meloids in bees. *Veterinariya* **8**, 64–65 (in Russian).

- **For articles in collections:**

Name(s) and initials of the author(s). Year of publication. Title of the article. Name(s) and initials of the editor(s) (preceded by In:) *Title of the collection (in italics)*, publisher, place of publication, page numbers.

Yurtsev, B.A., Tolmachev, A.I. & Rebristaya, O.V. 1978. The floristic delimitation and subdivisions of the Arctic. In: Yurtsev, B. A. (ed.) *The Arctic Floristic Region*. Nauka, Leningrad, pp. 9–104 (in Russian).

- **For conference proceedings:**

Name(s) and initials of the author(s). Year of publication. Name(s) and initials of the editor(s) (preceded by In:) *Proceedings name (in italics)*, publisher, place of publishing, page numbers.

Ritchie, M.E. & Olff, H. 1999. Herbivore diversity and plant dynamics: compensatory and additive effects. In: Olff, H., Brown, V.K. & Drent R.H. (eds) *Herbivores between plants and predators. Proc. Int. Conf. The 38th Symposium of the British Ecological Society*, Blackwell Science, Oxford, UK, pp. 175–204.

.....……

Please note

- Use '.' (not ',') for decimal point: 0.6 ± 0.2; Use ',' for thousands – 1,230.4;
- Use '–' (not '-') and without space: pp. 27–36, 1998–2000, 4–6 min, 3–5 kg
- With spaces: 5 h, 5 kg, 5 m, 5°C, C : D = 0.6 ± 0.2; $p < 0.001$
- Without space: 55°, 5% (not 55 °, 5 %)
- Use 'kg ha^{-1}' (not 'kg/ha');
- Use degree sign ' ° ' : 5 °C (not 5 ^{O} C).